

## ABSTRACT

ATKINS, RACHEL MARIE. Characterizing Tectonic and Hydrologic Processes Shaping Earth and Mars (Under the direction of Dr. Karl W. Wegmann and Dr. Paul K. Byrne).

Planetary surfaces provide a window into the geologic past of planets and can offer clues into their history of deformation. For example, endogenic forces such as tectonic activity resulting from secular planetary cooling can produce fault-driven topography that can be investigated to understand processes occurring at depth. Conversely, exogenic forces such as impact cratering can provide markers for surface dating and can aid in constraining the timing of unobservable subsurface processes like faulting. Further, humans can act as drivers of surface and environmental changes through modifications of the landscape. The impacts of these changes can be long-lasting and have consequences for interconnected ecosystems in fluvial environments. This dissertation explores how tectonic, impact, and fluvial processes have altered surfaces on Earth and Mars.

Lobate scarps can be found across the Martian surface and, based on similar features on Earth, are interpreted as antiformal fault-propagation folds that form from the distortion of the hanging wall. For Chapter 2, I employed a semi-automated method for extracting surface displacement along fault-strike to produce displacement profiles. Then, spectral analyses, both Fourier and S-Transform, were used to characterize segmentation and infer fault growth histories through fault linkage. Finally, the spectral data were used to compare maximum displacement–length ratios and were further analyzed for fault segmentation. Statistically significant differences were found in  $D_{\max}/L$  ratios using an assumed homoclinal fault dip angle of  $30^\circ$  between faults in the northern lowlands ( $n = 24$ ;  $D_{\max}/L = 2.9 \times 10^{-3} \pm 0.9 \times 10^{-3}$ ) and southern highlands ( $n = 25$ ;  $D_{\max}/L = 9.2 \times 10^{-3} \pm 1.9 \times 10^{-3}$ ), with faults in the north exhibiting less displacement for a given length than faults in the south. As demonstrated through calculations of

differing fault dip angles on calculated  $D_{\max}/L$  scaling, these results may be explained by variations in fault geometry. Contrasting mechanical stratigraphy between successive units can promote fault-bend over homoclinal fault-propagation folding, accommodating horizontal fault displacement without a concomitant vertical surface topographic response.

To explore the age of these structures and thus the timing of global contraction resulting from secular cooling of Mars' interior, buffered crater counting (BCC) was used to constrain the timing of landform formation in Chapter 3. Absolute model ages for individual scarps ranged from 4.4 to 3.5 Ga using a range of 2-13 craters per scarp, falling within the Early Noachian to Early Hesperian periods of Mars' geologic history. An aggregate of 148 craters was used to provide a model age for the area encompassing all 28 scarps. Ages based on the aggregate counts are  $3.8_{-0.02}^{+0.01}$  Ga (per the Hartmann PF and CF) and  $3.9_{-0.01}^{+0.01}$  Ga (for the Neukum/Ivanov models), respectively. As a whole, then, the most recent activity on these faults appears to terminate at the Noachian-Hesperian boundary.

Finally, Chapter 4 investigated landscape responses to c. pre-1930's land forest clearing and farming on the North Carolina Piedmont in a now reforested watershed in William B. Umstead State Park. The predicted unchannelized-to-channelized transition (i.e., channel heads) were located using local slope and contributing drainage area relationships. For the 40 channels used for this analysis, slope-area predicted locations were compared to observed channel heads to determine that 23 channel heads are located downslope of their predicted equilibrium location on the landscape. Using a mean migration distance of 174.4 m [S.D. = 109.6 m] per stream, an average per-channel contribution of  $282.6 \text{ m}^3$  [S.D. =  $177.6 \text{ m}^3$ ] of future erosion is predicted as the channel heads migrate up-valley from their observed (current) to predicted (future) locations. Using an estimate of total erosion ( $90,419 \pm 56,838 \text{ m}^3$ ) for the  $23 \text{ km}^2$  area that encompasses the

state park and an average soil bulk density of  $1.3 \text{ g/cm}^3$ , the mass of soil from future erosion of channel heads is predicted to be  $1.1 \times 10^8 \pm 6.7 \times 10^7 \text{ kg}$  (68% conf.) (i.e.,  $106 \pm 67 \text{ t}$ ). This amount of soil and sediment contains approximately  $9.5 \times 10^5 \pm 2.8 \times 10^5 \text{ kg}$  (68% conf.) ( $951 \pm 277 \text{ t}$ ) of carbon,  $4.4 \times 10^4 \pm 1.2 \times 10^4 \text{ kg}$  ( $44 \pm 12 \text{ t}$ ) of total nitrogen, and  $1.3 \times 10^4 \pm 3.9 \times 10^3 \text{ kg}$  ( $13 \pm 4 \text{ t}$ ) of phosphorus. This work shows that historical land use may play a larger role than typically appreciated, in part and specifically through the re-establishment of equilibrium channel head locations. The impacts of this geomorphic process are likely to continue for hundreds to thousands of years to come.

© Copyright 2021 by Rachel M. Atkins

All Rights Reserved

Characterizing Tectonic and Hydrologic Processes Shaping Earth and Mars

by  
Rachel Marie Atkins

A dissertation submitted to the Graduate Faculty of  
North Carolina State University  
in partial fulfillment of the  
requirements for the degree of  
Doctor of Philosophy

Marine, Earth, and Atmospheric Sciences

Raleigh, North Carolina  
2021

APPROVED BY:

---

Karl W. Wegmann  
Committee Co-Chair

---

Paul K. Byrne  
Committee Co-Chair

---

DelWayne R. Bohnenstiehl

---

Ryan E. Emanuel

## DEDICATION

I dedicate this dissertation to my mom, Ann Marie Atkins. Seeing her navigate being a mother, wife, daughter, and sister, managing difficult life events and a demanding job while always being willing to help others has been a huge inspiration for me in my educational pursuits and to push myself to be better. Mom, you always motivate me to be a better version of myself while appreciating everyone and everything around me. I love you so much and feel so lucky to be your daughter!



## **BIOGRAPHY**

Rachel grew up in Buffalo, NY, and attended SUNY Geneseo for undergraduate study majoring in Geology and Adolescent Education. With aspirations of becoming an Earth Science teacher in New York State, she embarked on a Master's degree in Geoscience Education in the distant land of Raleigh, NC. After taking an MEA 599 course with Karl Wegmann and falling in love with geology all over again, she continued her studies at NC State, working towards a Ph.D. in geology. Her Ph.D. research evolved into not just a multi-disciplinary endeavor but a multi-planetary adventure too, studying geologic processes on both Earth and Mars (yes, the planet).

Having played DIII field hockey at SUNY Geneseo, Rachel missed athletics and the fitness and friends that came along with it. This led to her joining a kickball team and meeting some great friends, most of whom happened to work for a company named Atkins. She also explored Raleigh's greenway system extensively by bike and on foot while training for the Oak City Half Marathon in 2017, which she ran with one of her Geneseo Field Hockey friends whom she convinced to move to Raleigh. And yes, she did beat her goal of running 13.1 miles in under two hours, by six seconds! She is also proud to have biked to all of the breweries in Raleigh, Cary, and Apex (that existed as of 2018). Nowadays, you can catch her shredding the trails on her mountain bike or puzzling in her free time.

## ACKNOWLEDGMENTS

First, I would like to thank my Dad, Mom, and sister Amanda – your unwavering support and many road trips to Raleigh over these past 7(!!!) years have helped make achieving this milestone possible. I can always count on Dad to send a photo of Lexi (‘pup’) with glasses on to our group chat when things get stressful. Amanda – I am so glad you decided to join me in Raleigh; living together again was so much more fun as adults! Tell Callie we miss her! Mom – thanks for always taking my phone calls, even when they are right before a meeting. Thank you all for being patient when I never really had a concrete answer to “so when do you think you are going to finish and get a real job?” Love you guys!

Doug, you have celebrated with me at my best and supported me at my worst. Thank you for always encouraging me to keep going, even when I wanted to quit. Like really wanted to actually quit and walk away. Craft beer cheers to many more milestones together!

To the friends I have made during my time in Raleigh – you have truly made this place and time in my life so special, and I cannot thank you enough for all of the distractions from school-related stresses. Shannon and Tom, Allison and Tim, Nicole, Rowan and Michael, LeeAnna and Nathan, Robert and Rainor, Rachael and Patrick, Mike and Katie, Corbin and Alli, Jake and Kara, Chester, the list goes on...

Karl, even if I was white-knuckled on the first trip I ever drove a van for one of your classes; thanks for helping me get over my van driving fears and for reminding me to go for a run or a bike ride when I am stressed. Paul, while I hated it at first, I appreciate you for forcing me to learn illustrator and teaching me the tricks of the trade; definitely one of the most useful skills I acquired during my Ph.D. To both Karl and Paul, thank you for taking on an orphaned graduate student when other’s turned me away. And to my committee members Del and Ryan for

their help and support in creating this beast of a document. To the members of the research groups I have been in during the last five years (the Planetary Research Group and Surface Processes and Active Tectonics - Corbin, Rashonda, Nuttman, Becca, Mallory, Zach, Matt, Corey, Gantulga, Raja, Grant, Adam), thanks for always providing support, ideas, and lending an ear when I just needed to vent. Finally, to the MEAS staff and faculty that helped me at various stages of my academic journey (Jackie, Laura, Brenda, Greg, Gary, Astrid, Carli, Karen, and many more), thank you for making me feel welcomed!

Funding from the Future Investigator of NASA Earth and Space Science and Technology (FINESST) program (grant number 80NSSC19K1539) made my final two years of grad school possible and helped ease concerns of being able to make ends meet so that I could focus on research. Receiving this grant helped me overcome some self-doubt about whether I belonged in science while providing motivation to get this done, particularly through A GLOBAL PANDEMIC! Of course, despite many rejections – funding, personal, professional, career, and otherwise, I DONE DID IT, BABY!



## TABLE OF CONTENTS

LIST OF TABLES .....	ix
LIST OF FIGURES .....	x

### **Chapter 1: Introduction ..... 1**

### **Chapter 2: A morphometric investigation of large-scale crustal shortening on Mars..... 5**

Key points .....	5
1. Abstract .....	6
2. Introduction.....	7
2.1 Crustal shortening on Mars .....	7
2.2 Displacement–length scaling .....	9
2.3 Displacement profile shape and segmentation.....	10
2.4 Rationale for this study .....	11
3. Methods.....	11
3.1 Measurement of scarp height .....	11
3.2 Analysis of scarp height profiles.....	13
4. Results.....	15
4.1 Displacement–length scaling .....	15
4.2 Scarp profile shape.....	16
4.3 Spectral Analysis .....	17
5. Discussion .....	19
5.1 Displacement–length scaling ratios .....	19
5.2 Displacement profiles .....	22
5.2.1 Profile shapes .....	22
5.2.2 Segmentation and fault evolution .....	23
5.3 Comparison with Mercury and Earth.....	24
6. Conclusions.....	25
References.....	38

### **Chapter 3: Determination of timing of large-scale crustal shortening structures on Mars using crater age dating ..... 46**

Key points .....	46
1. Abstract .....	47
2. Introduction.....	47
2.1 Dating surface features .....	49
3. Methods.....	53
3.1 Mapping .....	53
3.2 Crater counts and area calculations.....	55
4. Results.....	56
4.1 Buffered crater counts.....	57
5. Discussion .....	58
5.1 Timing constraints on the cessation of large-scale faulting.....	58
5.2 Geological observations as constraints for thermal evolution models.....	59
5.3 Fluvial interactions.....	62

5.4 Limitations .....	65
6. Conclusions.....	66
References.....	76

**Chapter 4: Channel head response to anthropogenic landscape modification ..... 83**

Key points .....	83
1. Abstract.....	84
2. Introduction.....	85
2.1 Controls on channel head location.....	85
2.2 Anthropogenic impacts on hillslope erosion.....	86
2.3 Study location: William B. Umstead State Park.....	90
2.4 Research questions.....	91
3. Methods.....	91
3.1 Field and environmental lab methods.....	91
3.2 GIS methods.....	93
3.2.1 Trunk channel delineation.....	93
3.2.2 Predicting channel head locations and migrating distances.....	94
4. Results.....	95
4.1 Predicted vs. observed locations of channel heads .....	95
4.2 Sediment/soil volumes .....	96
4.3 Soil descriptions.....	97
5. Discussion .....	98
5.1 Hillslope-to-valley transition zones in modified landscapes .....	98
5.2 Ongoing response to human disturbances.....	100
5.3 Implications for downstream ecosystems .....	102
6. Conclusions.....	104
7. Acknowledgements.....	105
References.....	124

**Chapter 5: Conclusions ..... 130**

**Chapter 2**

Appendix A: Fault displacement skewness schematic .....	136
Appendix B: N vs. S regression plot.....	137
Appendix C: Fault length vs. number of segments plots .....	138
Appendix D: Fault length vs. number of segments plots (N vs. S) .....	139
Appendix E: Major segment length vs. total cumulative length plots .....	140
Appendix F: $D_{max}/L$ vs. Length with missing lengths added .....	141
Appendix G: Summarized fault metrics .....	142
Appendix H: Detrending process for each fault .....	146
Appendix I: FFT and S-Transform analysis for each fault .....	195

**Chapter 3**

Appendix J: Mars time period boundaries.....	244
Appendix K: Crater dating fault metrics summary table .....	245
Appendix L: Aggregate Hartmann Age CraterStats plot ( $n = 28$ ).....	246

Appendix M: Aggregate Neukum/Ivanov Age CraterStats plot (n = 28)..... 247  
Appendix N: Hartmann Age for each fault (CraterStats plots)..... 248  
Appendix O: Neukum/Ivanov Age for each fault (CraterStats plots)..... 276

**Chapter 4**

Appendix P: Channel head summary table..... 304

## LIST OF TABLES

### Chapter 2

Table 2.1	Summary statistics for morphometric characteristics of study thrust faults for the sampled global population ( $n = 49$ ), in the northern lowlands ( $n = 24$ ), and the southern highlands ( $n = 25$ ).....	37
-----------	--	----

### Chapter 3

Table 3.1	Summary statistics for the morphometric characteristics of the thrust fault-related scarps in this study ( $n = 28$ ).....	75
-----------	--	----

### Chapter 4

Table 4.1	Future erosion potential for Umstead State Park using average erosion volume per stream ( $282.6 \pm 177.6 \text{ m}^2$ ) and drainage density information from a modified Strahler stream order analysis. These values conservatively assume that 50% of channels of a given stream order will migrate.....	122
Table 4.2	Future nutrient contribution potential for Umstead State Park headwater channels resulting from the up-valley expansion of the drainage network. Results, by average soil horizon thickness and in aggregate rely on the average erosion volume, the assumption that 50% of modified 4 <sup>th</sup> -order streams will migrate ( $90,419 \pm 56,838 \text{ m}^3$ , calculated in Table 1), a soil bulk density of $1.3 \text{ g/cm}^3$ (Bradley, 2020), and nutrient values from Fig. 12. Confidence intervals (68%) are listed for each horizon under column SD, totals are calculated using appropriate error propagation techniques.....	123

## LIST OF FIGURES

### Chapter 2

Figure 2.1	(a) Three-dimensional schematic view of one of our studied thrust faults, and its extracted, along-scarp height profile (as a proxy for along-strike displacement). (b) The location of this fault.....	26
Figure 2.2	A global map of selected faults for this study ( $n = 49$ ). The map is in a Robinson projection, centered at $0^\circ\text{E}$ . .....	27
Figure 2.3	Examples of fault scarp fit types and detrended profiles. (a) Selected faults exhibiting multiple fit types, with best-fitting shapes shown in black; four are best fit with triangles, whereas two are best fit with ellipses. (b) Those same scarp height profiles now detrended, with the best-fitting shapes removed, for subsequent analysis. ....	28
Figure 2.4	Examples of our spectral analyses for select faults. (a) Number of segments per fault ( $\leq 14$ ) results from FFT analyses binned by integer fault segments, for segment values with the highest amplitude (red*) indicate number of segments per fault. (b) Spectral frequency results from S-transform analyses (at low frequencies, $\leq 14$ ) displayed for the length of each fault; color indicates spectral power. (c) Number of segments per fault binned as means for each integer frequency across the length of the fault. The highest amplitude frequency (red *) indicates the number of fault segments for each fault. (d) Measured displacement profiles (blue) and filtered profiles (red), constructed from the number of cycles from both analyses. Segment boundaries delineated by vertical black lines. ....	29
Figure 2.5	(a) Log–log plot of $D_{\text{max}}/L$ ratios as a function of fault length, for thrusts in the northern lowlands and southern highlands. Means for each population are solid lines. (b) $D_{\text{max}}/L$ values in linear space. In both panels, the dashed lines mark the 99% confidence intervals. ....	30
Figure 2.6	(left) The number of faults with peaks in each zone for all of our study faults ( $n = 49$ ); (right) The number of faults with peaks in each zone by geographic location .....	31
Figure 2.7	These histograms show the distribution of spatial frequencies (i.e., fault segments). Gray dashed lines indicate the percentage of faults less than or equal to the identified spatial frequency. (a) FFT and S-transform distributions for all studied faults ( $n = 49$ ) (b) FFT and S-Transform distributions for study faults separated by hemispherical location (i.e., northern lowlands (orange) or southern highlands (blue)). ....	32
Figure 2.8	Maximum study thrust fault displacement–length ratio as a function of segments. The black points are means for each segment bin, the vertical blue lines are	

	standard deviation for each number of segments, and regression equations are in red. Both regressions are significant ( $p < 0.05$ ). .....	33
Figure 2.9	(a) Calculated mean $D_{\max}$ - $L$ ratios for faults in the northern lowlands for various fault dip angle assumptions. (b) Confidence interval for the predicted difference in the mean $D_{\max}$ - $L$ (N minus S) as a function of fault dip angle for thrusts in the northern lowlands with a constant dip angle of $30^\circ$ for thrusts in the southern hemisphere. The shaded grey area indicates the range of fault dip angles for northern thrusts that would yield no statistically significant differences in the mean $D_{\max}/L$ between the northern and southern hemispheres. ....	34
Figure 2.10	$D_{\max}$ - $L$ ratios as a function of fault length for thrusts in the southern highlands (orange), northern lowlands (blue), and the intercrater plains of Mercury (black). Mean $D_{\max}/L$ values for each population are shown with solid lines, and the 99% confidence intervals are indicated by dashed lines. ....	35
Figure 2.11	$D_{\max}/L$ values for thrust faults on terrestrial planets from multiple studies, including this one (blue dots). ....	36
<b>Chapter 3</b>		
Figure 3.1	A Robinson projection of Mars, centered at $0^\circ\text{E}$ , showing the spatial distribution of fault scarps and scarp numbers labeled in black. Morphometric characteristics, crater counts, calculated ages, and central coordinates for each scarp are detailed in Table S2 (Appendix K). ....	68
Figure 3.2	An example scarp (#15 in Table S2, Appendix K) for which buffered crater counts were determined, demonstrating our approach. (a) First, the forelimb of a fault-displacement gradient fold is identified and mapped as an area that encompasses the forelimb on the surface. (b) Next, craters that superpose the scarp are mapped, and the buffer around the scarp is determined by the radius of the crater in question. (c) For each successively larger crater included in the BCC, the area of the buffer increases proportionately. (d) This process is repeated for all craters that superpose the fault scarp (outlined in yellow). This view is in an equidistant cylindrical. ....	69
Figure 3.3	A plot of Hartmann (a) and Neukum/Ivanov ages (b) for individual faults (black circles) and for the count areas for all faults combined (red squares, $n = 28$ ). Error bars are the $2\text{-}\sigma$ range in crater counts as reported by Craterstats II. See Table S2 (Appendix K) for crater count locations. ....	70
Figure 3.4	A Robinson projection of Mars, centered at $0^\circ\text{E}$ , showing the spatial distribution of fault scarps and their calculated Hartmann ages in Ga on the left (Hartmann, 2005) and Neukum/Ivanov ages on the right (Ivanov, 2001). See Table S2 (Appendix K) for age uncertainties. ....	71

- Figure 3.5 Crater size–frequency distributions for all scarps in this study ( $n = 28$ ). (a) The “Hartmann” age was calculated with the production function from Hartmann (2005) and chronology function from Hartmann (2005), which was refined by Michael (2013). (b) The “Neukum/Ivanov” age was calculated with the chronology and production functions from Ivanov (2001). ..... 72
- Figure 3.6 (a) A plot comparing  $D_{\max}/L$  ratios for the 49 structures analyzed in Chapter 2 (with the blue and red dots corresponding to those structures in the northern lowlands and the southern highlands, respectively), with the 28 faults from this study (green dots). Solid lines denote the means for both the N and S structures from Chapter 2 and the faults investigated in this study (Chapter 2). Dashed lines indicate the 99% confidence intervals. (b) The distributions of  $D_{\max}/L$  ratios from Chapter 1 and this chapter. Note that from their  $D_{\max}/L$  ratios, faults in Chapter 2 are statistically indistinguishable from this chapter and thus can be regarded as part of the same population as they exhibit similar fault behaviors. .... 73
- Figure 3.7 Examples of major thrust fault systems interacting with fluvial valley networks, as observable in the THEMIS imagery. The colors correspond to elevation, and are from the MOLA–HRSC dataset. Fault scarps are outlined in black, with teeth on the inferred hanging wall. Modeled streams are shown as interconnected networks of green lines, and reveal how water would be hydrologically routed on the present-day landscape. .... 74

## Chapter 4

- Figure 4.1 Schematic of the dominant headwater geomorphic process zones for the Piedmont of North Carolina, denoted by a roll-over from a positive-to-negative relationship between the log of the local slope versus the log of contributing drainage area relationship (adapted from Sweeney et al., 2015, Tarolli & Dalla Fontana, 2009; Montgomery & Foufoula-Georgiou, 1993; Willgoose et al., 1991). Note that hillslopes are not steep or long enough to generate debris flows in the Appalachian Piedmont, so that process zone is excluded. Headwater channels commonly exhibit both alluvial and short bedrock-dominated reaches. .... 107
- Figure 4.2 A time-series schematic of (a) an idealized Piedmont landscape before European arrival, (b) immediately after the era of intensive forest clearing and farming, and before the introduction of soil-erosion control measures. (c) Schematic depiction of the landscape recovery (present-day) following disturbance. In the study area, landscape recovery began about 1935 CE. .... 108
- Figure 4.3 Study area. (a-b) Satellite view and map location of North Carolina’s William B. Umstead State Park (USP) located northwest of Raleigh, in Wake County. (c) Wake County is in the eastern portion of the Piedmont physiographic province of North Carolina. USP location in Wake County is marked by the red star. .... 109

- Figure 4.4 Field photos of channel heads located in William B. Umstead State Park showing differing morphologies. Panels (a) and (b) are examples of low-relief channel initiation points, (c) and (d) are examples of channel heads with more significant plunge pools and wider channels. In (c), note the exposed roots of a *Liriodendron tulipifera* tree that attest to recent headward retreat and soil erosion by this channel head. Soil piping may be occurring at this location. The white lines delineate channel margins. The direction of flow is towards the bottom of the photograph in all cases. .... 110
- Figure 4.5 Examples of *Liriodendron tulipifera* roots exposed by recent headward migration of the channel head location along first-order channels of Umstead State Park. The 2018 channel head locations, identified as the upstream most point with clearly defined banks, are marked by the dashed yellow lines and arrows. Flow is toward the bottom of each photograph. .... 111
- Figure 4.6 The process for modeling channel head initiation locations in Piedmont basins. (a) Scatter plot of the log of local channel slope vs. the log of contributing area for an individual channel whose length is artificially extended to the drainage divide for the sub-basin shown in (b). The observed channel head position (black line) is located where the contributing area is 58,106 m<sup>2</sup>. A smoothing spline fit (curved green line) was fit to 2,000 predicted spline peaks (green points) using a bootstrap resampling approach to determine the predicted location (maximum along the green line) at 95% confidence (red lines) should lie between 14,791 and 9,120 m<sup>2</sup>. (c) Slope vs. area plot for sub-basin shown in d indicating that the observed channel head at 58,294 m<sup>2</sup> is downslope of the predicted range of contributing areas (4,786 to 1,754 m<sup>2</sup>). These two example sub-basins are both located within the larger basin (e). .... 112
- Figure 4.7 Slope-area plots constructed using 0.25 log bins of area. (a) An example where the observed channel head (black line) is positioned down the valley from the predicted location (dashed red lines) as determined by the 2,000 bootstrapped samples (green points) and maximum best fit smoothing spline (curved green line). The channel head in this example is predicted to migrate up the valley until its location falls within the predicted range of contributing area. (b) Example basin where the observed channel head location is within the predicted area range and thus not predicted to migrate. (c & d) Distribution of contributing areas at the peak of each of 2,000 bootstrapped smoothing splines; dashed red lines are the 95% confidence range. .... 113
- Figure 4.8 Slope-area plots constructed using 0.25 log bins of area for (a) all study channels ( $n = 40$ ) and (b) the sub-population ( $n = 23$ ) of those predicted to migrate when fit without binning. The average contributing drainage areas of the observed channel heads are displayed as the vertical black lines and the modeled 95% confidence range of predicted locations as vertical dashed red lines for both plots based upon the results of the smoothing spline fit (curved green line) for 2,000 predicted spline peaks (green points) using a bootstrap resampling

approach. When predicted migration distances are determined using aggregate | data, two of the 23 observed channel head locations predicted to migrate when analyzed individually are no longer predicted to do so (plot-b). A smoothing spline parameter ( $p_{smooth}$ ) = 0.5 is used in both plots..... 114

Figure 4.9 The spatial location of 40 investigated channel heads (green = migration predicted; red = migration not predicted) and their trunk channels (blue lines) in William B. Umstead State Park. The solid black line encloses the park. .... 115

Figure 4.10 Estimated future up-valley channel head migration distances for the 23 channels that are predicted to migrate. Vertical bars represent the range in distances, with the black dots as the midpoint between the minimum and maximum. Dashed black lines indicate one standard deviation from the median (solid green line) of the population of 23 channels..... 116

Figure 4.11 Channel width and depth measurements for 15 channels located 5 to 10 m downstream from current channel heads..... 117

Figure 4.12 A generalized composite soil profile upslope of sampled channel heads in Umstead State Park with soil horizon thicknesses, nutrient (carbon, nitrogen, and phosphorous) content, and grain sizes. Soil horizon abbreviations follow the suggested nomenclature of the Keys to Soil Taxonomy 12<sup>th</sup> edition (Soil survey Staff, 2014)...... 118

Figure 4.13 Examples of anthropogenic topographic features visible in 1m lidar topographic data within the study area are present on parts of the landscape with small flow accumulation area values. (a) Hillshade and (b) profile curvature maps of a sub-basin with several inactive (legacy) gullies. (c) Hillshade and (d) profile curvature maps identifying erosion control terraces and a forest road. The existence of topographic features such as these in lidar data (here and elsewhere) hinders the identification of hillslope-to-channel transitions when using average slopes from basin-binned areas. .... 119

Figure 4.14 Log-log plot of local slope versus contributing basin area as a function DEM resolution for a single catchment used to explore the impact of DEM resolution on slope-area relationships for predicting channel head locations. Note the steeper slopes at very low contributing drainage areas for the highest resolution topography data. The 1, 5, 10, and 20 m data were downsampled from the 1 m QL2 Lidar, while the 6 m data is the 2002 legacy QL1 Lidar for North Carolina, and the 10 m DEM is from the USGS National Elevation Dataset (Gesch et al., 2002)...... 120

Figure 4.15 Comparison of local slope and the contributing area at channel head locations between sites in the western and central North Carolina Piedmont (gray points) reported by Jefferson & McGee (2013) and the eastern Piedmont of this study (black points). .... 121

## CHAPTER 1: Introduction

Geologic processes can be found to modify planetary surfaces across the solar system at various time and spatial scales. Investigating processes across scales can help inform our understanding of the formation of planets, how they evolve, and the increasing role that humans play in these processes. This dissertation is the culmination of five years of investigations into aspects of the planetary surface and tectonic processes through the in-depth study of topographic features on Earth and Mars to understand components of each planet's geologic and geomorphic history. First, the morphometric characteristics of fault-controlled surface scarps on Mars were explored to understand thrust fault behavior and the growth history of faults across the planet. Next, the timing of the thrust faults was constrained using populations of impact craters superposing surface scarps as a method for geologic surface dating. Finally, on Earth, the impact of anthropogenic landscape modification on the initiation position of modern drainage networks was investigated using local slope and contributing basin area relationships, which allows for the modeling of future channel head migration distances and the contributions of sediment and nutrients to stream networks from this process.

Chapter 2 takes a deep dive into planetary tectonics, investigating the surface expressions of large thrust faults on Mars, termed "lobate scarps" (Watters & Robinson, 1999). These scarps can be found across the Martian surface and, based on similar features on Earth, are interpreted as antiformal fault-propagation folds that form from the distortion of the hanging wall (Williams & Chapman, 1983; Mitra, 1990; Suppe & Medwedeff, 1990; Wickham, 1995). On Earth, interpreting tectonics from topography is challenging due to the active hydrologic cycle. Mass wasting degrades surface features while rivers and streams often cut into and even dissect them, making structural interpretations from topographic analysis more difficult unless uplift occurred

in the recent geologic past. Thus, direct cross-sectional measurements or seismic reflection data are often used to study faults directly (e.g., Ellis & Dunlap, 1988; Wickham, 1995; Shaw et al., 2004; Bergen & Shaw, 2010).

In contrast with Earth, Mars and other planetary bodies that lack a substantial atmosphere experience exceedingly slow rates of erosion and surface lowering, rendering the landform degradation due to erosion negligible compared to the contribution of topographic uplift (Golombek & Bridges, 2000). Thus, on distant planetary bodies, surface measurements of fault-related topography (e.g., lobate scarps) may be confidently used as an indirect study of fault displacement in the absence of sub-surface data (e.g., Byrne et al., 2014; Klimczak et al., 2018), even for fault-built topography that is billions of years old. This study first employed a semi-automated method for extracting surface displacement along fault-strike to investigate variations in displacement along the fault. Then, spectral analyses, both Fourier and S-Transform, were used to characterize segmentation and infer fault growth histories through fault linkage. Next, the spectral data were used to compare maximum displacement–length ratios and were further analyzed for fault segmentation. These data reveal differences in fault behavior between Mars’ northern lowlands and southern highlands, suggesting that fault geometry, crustal properties, or fault timing may influence lobate scarp morphometry. Results from this study were also compared to thrust faults on Mercury, a planet with comparable gravity and no hydrologic cycle.

Motivated by the differences in displacement–length scaling of fault scarps found across Mars in Chapter 2, the focus of Chapter 3 is to explore differences in the timing of these trust-related landforms. This research was carried out using a population of craters that superpose the fault-related surface scarp. Using only those craters that directly interact with the fault-related topography, minimum bounds are placed on the timing of the most recent fault activity.

Traditional crater size–frequency distributions (CSFDs) are often used to date planetary surfaces for which direct ages are unobtainable. This method operates under the basic assumption that craters accumulate on a surface over time, such that a geologically old surface will have accumulated more craters than a geologically young surface. By accounting for specific target body properties (e.g., gravity, proximity to other larger bodies, rock strength), the size range, velocities, and impactor frequency distributions are modeled, resulting in a semi-quantitative geochronologic estimate of crater-size-time estimates for a specific planetary surface feature. Two common impactor production and chronology functions (e.g., Hartmann, 2005; Ivanov, 2001) were employed to determine the geologic ages of thrust faults. Buffered crater counting (BCC) is a method used to age date linear features such as fluvial valley networks (e.g., Fassett & Head, 2008; Hoke & Hynes, 2009; Bouley et al., 2010) and fault-related landforms (e.g., Fegan et al., 2017; Galluzzi et al., 2019; Giacomini et al., 2020) by normalizing the number of craters of a given diameter by the area encompassed by a buffer of the same size around the landform. This process revealed that the majority of faulting most likely occurred before the Noachian-Hesperian boundary. Implications for using these ages as constraints in thermal evolution models of Mars are discussed in this chapter.

Finally, Chapter 4 investigates fluvial processes that occur on a shorter timescale and at a smaller spatial scale than was studied in previous chapters. The influence of anthropogenic landscape modification on channel head locations in the North Carolina Piedmont was explored. Non-native settlement and expansion in the southeast U.S. from the late 1600s to 1930s led to unsustainable land clearing and agricultural practices that resulted in the erosion and subsequent accumulation of hillslope sediment in headwater valley bottoms (Jacobson & Coleman, 1986; Walter & Merritts, 2008; Auch et al., 2015). These deposits are often called “legacy sediment” as

they contain a record of erosion, transport, and deposition of sediment derived from anthropogenic disturbances (e.g., Costa, 1975; Trimble, 1975; Jackson et al., 2005; Walter & Merritts, 2008). Even after reforestation of these areas, this practice has had lasting impacts on modern streams through the down-valley displacement of headwater locations (e.g., Jefferson & McGee, 2013; Avcioglu et al., 2017). The work presented in this chapter utilizes local slopes and contributing basin areas to constrain predicted locations of channel heads using Lidar-derived DEMs. These locations are compared to observed channel heads on valley bottoms, and future migration distances were determined. The first-order quantification of sediment volume loss was calculated using measured channel head widths and differences in the distance along the trunk channel between observed and predicted locations. Further, soil samples were taken upslope of several channel heads to quantify the potential future contributions of nitrogen, phosphorous, and carbon as channel heads migrate up-valley. Perturbations of sediment and nutrients to stream networks significantly impact hydrologic, biologic, aquatic, riparian, and chemical functions in downstream environments (Walter et al., 2007; Graeber et al., 2012; Inamdar et al., 2012). Thus, quantification of physical and chemical consequences of legacy sediment influx, including volumes of eroded soil/sediment and associated nutrients, will improve our understanding and modeling of nutrient pollution in piedmont streams and reservoirs (Inamdar et al., 2020; 2021).

## CHAPTER 2: A morphometric investigation of large-scale crustal shortening on Mars

R. M. Atkins<sup>1</sup>, P. K. Byrne<sup>1\*</sup>, D.R. Bohnenstiehl<sup>1,2</sup>, K. W. Wegmann<sup>1,2</sup>

<sup>1</sup>Department of Marine, Earth and Atmospheric Sciences, North Carolina State University, Raleigh, NC, USA, <sup>2</sup>Center for Geospatial Analytics, North Carolina State University, Raleigh, NC, USA

\*Now at Department of Earth and Planetary Sciences, Washington University in St. Louis, St. Louis, MO, USA

Corresponding author: Rachel Atkins (ratkins@ncsu.edu)

### Key Points:

- Topographic measurements of thrust-related landforms on Mars suggest a mean maximum fault displacement–length ratio ( $D_{\max}/L$ ) of  $6.1 \times 10^{-3} \pm 1.4 \times 10^{-3}$  globally, with significant differences in ratios for the northern lowlands ( $2.9 \times 10^{-3} \pm 0.9 \times 10^{-3}$ ) and southern highlands ( $9.2 \times 10^{-3} \pm 1.9 \times 10^{-3}$ ).
- Apparent hemispheric differences in the  $D_{\max}/L$  can be explained by variations in fault geometry (ramp-flat or listric) or dip angle, which may develop due to differences in the stratigraphic architecture between the lowland and highland terrains.
- Analysis of displacement–length profiles shows most are characterized by asymmetric triangular shapes, with an inverse relationship between  $D_{\max}/L$  and the number of segments, similar to patterns observed for Earth faults.

## 1. Abstract

The surface of Mars exhibits abundant topographic expressions of large thrust fault-related folds that have long been attributed to global planetary contraction. Morphometric analyses of such structures can provide insight into their growth history. With global THEMIS imagery and HRSC–MOLA topographic data, 49 thrusts with lengths between 35 and 544 km were mapped across the surface of Mars. Assuming planar fault geometries with dips of  $30^\circ$ , the average ratio between maximum fault displacement and fault length ( $D_{\max}/L$ ) of these structures is  $6.1 \times 10^{-3} \pm 1.4 \times 10^{-3}$ , with smaller average ratios observed for thrust faults within the northern lowlands ( $2.9 \times 10^{-3} \pm 0.9 \times 10^{-3}$ ) compared with those in the southern highlands ( $9.2 \times 10^{-3} \pm 1.9 \times 10^{-3}$ ). However, these differences may be accounted for if mechanical layering in the northern lowland crust promotes a shallowing of the fault dip angle, relative to the southern highlands, or the development of ramp-flat geometries such that the topographic scarp height may under-estimate the total fault displacement. Alternatively, these  $D_{\max}/L$  patterns could be interpreted to reflect hemispheric differences in the brittle-ductile transition depth; however, the observed pattern is inconsistent with the Martian dichotomy, whereby the northern lowlands has thinner (and/or denser) crust and therefore presumably deeper BDT than the southern highlands. Displacement–length profiles are commonly asymmetric, with multiple local minima observed along their lengths. Spectral analysis of these profiles, using Fourier- and S-Transforms, indicates power at a range of spatial frequencies, reflecting their complex history of growth and linkage, with an inverse relationship between the peak spectral frequency, correlated to the number of fault segments, and estimated  $D_{\max}/L$  ratios.

## 2. Introduction

### 2.1 Crustal Shortening on Mars

Planetary surfaces record topographic evidence of tectonic processes. Mars has experienced both extensional and compressional stresses (Solomon, 1978; Hauck, 2002). Planetary bodies that lack a substantial atmosphere exhibit slow erosion rates that minimize topographic degradation processes, unlike planets like Earth with its dense atmosphere and active hydrologic and biologic processes (Golombek & Bridges, 2000). If fault-driven topography ultimately reflects the interaction between tectonics and erosion, but the contribution from erosion is negligible for Mars, then the tectonic activity can be more directly linked to its effect on topography.

Thrust faulting on Mars manifests as surface folds, often termed “wrinkle ridges” or “lobate scarps,” with the major distinction between the two landforms being their size and symmetry. Wrinkle ridges have vertical relief on the order of tens to hundreds of meters, are commonly situated within volcanic smooth plains (Solomon, 1978; Watters, 1988, 2004), and are symmetric in cross-section (Mueller & Golombek, 2004). In contrast, lobate scarps have relief from hundreds to thousands of meters (Watters & Robinson, 1999; Knapmeyer et al., 2006; Klimczak et al., 2018) and tend to present one steep scarp and one gently-sloping back scarp (Figure 2.1). In addition, lobate scarps tend to occur as single discrete landforms, instead of the wider, compound fold-and-thrust belts common within many convergent plate boundaries systems on Earth (e.g., Klimczak et al., 2018).

Wrinkle ridges on Mars likely reflect a combination of localized shortening processes, such as subsidence of basin infill and larger-scale deformation resulting from lithospheric loading, for example, by the emplacement of the Tharsis Rise (Raitala & Kauhanen, 1992; Head,

2002; Mueller & Golombek, 2004). Lobate scarps on Mars may, in turn, reflect the planet-wide contraction of the lithosphere as heat has been lost from the planet's interior (Schubert & Spohn, 1990; Schubert et al., 1992); these structures have been used to estimate the resulting decrease in planetary radius to be between 0.2 and 6.0 km (Nahm & Schultz, 2011; Klimczak, 2015).

Lobate scarps on Mars have been interpreted as antiformal fault-propagation folds that form from the distortion of the hanging wall (Williams & Chapman, 1983; Mitra, 1990; Suppe & Medwedeff, 1990; Wickham, 1995). On Earth, similar structures have been studied using seismic reflection and cross-sectional data to measure fault displacement directly (e.g., Ellis & Dunlap, 1988; Wickham, 1995; Shaw et al., 2004; Bergen & Shaw, 2010). In the absence of subsurface information, fault displacements on Earth (e.g., Davis et al., 2005; Kim & Sanderson, 2005) and other planetary bodies (e.g., Byrne et al., 2014; Klimczak et al., 2018) are often estimated from fault-related topography, under the assumption that a planar fault formed the scarp, or with the aid of forward models used to predict the fault-related topography along scarp-perpendicular topographic profiles.

Forward modeling of individual lobate scarps within the Martian highlands (e.g., Amenthes Rupes, Ogygis Rupes, and Thaumasia regions) indicated a range of depths of 20–45 km and dip angles of 15–40° for these structures (Schultz & Watters, 2001; Grott et al., 2007; Ruiz et al., 2008; Egea-Gonzalez et al., 2017; Herrero-Gil et al., 2019, 2020a, 2020b). Although variations in the maximum depth of faulting could be linked to spatial and temporal changes in brittle layer thickness, individual studies have focused on a limited number of scarps and applied different parameterizations (e.g., Schultz & Watters, 2001; Grott et al., 2007; Ruiz et al., 2008; Egea-Gonzalez et al., 2017; Herrero-Gil et al., 2019, 2020a, 2020b). Moreover, most studies reported uncertainties in the maximum depth of faulting of ~30%, largely reflecting the trade-off

between model parameters in predicting surface uplift (Schultz & Watters, 2001; Mueller et al., 2014; Egea-Gonzalez et al., 2017). Modeled fault geometry can similarly have a large influence on estimates of fault displacement, with larger shortening predicted for ramp geometries that translate slip upwards from shallower dipping structures that root near the brittle–ductile transition (Herrero-Gil et al., 2020a, 2020b).

## 2.2 Displacement–length scaling

Studies of fault populations on Earth indicate a self-similar pattern of fault growth, with many populations displaying a quasi-linear relationship between the maximum displacement ( $D_{\max}$ ) and length ( $L$ ):  $D_{\max} = \gamma L$ , where  $\gamma$  is a scaling coefficient related to the host rock strength (Scholz & Cowie, 1990; Cowie & Scholz, 1992; Clark & Cox, 1996; Schlische et al., 1996). Scatter in the displacement–length ratio for a given population of faults is common and may indicate a linkage between adjacent fault systems (e.g., Cartwright et al., 1995; Gallen et al., 2014), fault interactions that inhibit the lateral propagation of the tips (Nicol et al., 1996; Gupta & Scholz, 2002; Ellis & Barnes, 2015), and the limits on fault growth due to the finite thickness of the brittle layer (e.g., Cartwright et al., 1995; Dawers & Anders, 1995; Wojtal, 1996; Bohnenstiehl & Kleinrock, 2000).

Displacement–length ratios of Earth-based thrust faults are typically  $1.0\text{--}8.0 \times 10^{-2}$  (Watters et al., 2000; Davis et al., 2005; Manighetti et al., 2009, 2015). The  $D_{\max}/L$  for thrust faults on Mars have been reported as  $4.5\text{--}6.2 \times 10^{-3}$  (Watters et al., 1998; Watters & Robinson, 1999; Watters et al., 2000; Schultz et al., 2006; Ruj et al., 2018). Thrust faults on Mercury exhibit  $D_{\max}/L$  ratios of  $6.0\text{--}9.0 \times 10^{-3}$  (Byrne et al., 2014). Schultz et al. (2006) suggested that differences in gravitational acceleration, and its influence on rock yield strength, may help to explain these planetary trends, leading to lower  $D_{\max}/L$  values on Mars ( $g = 3.71 \text{ m/s}^2$ ) and

Mercury ( $g = 3.70 \text{ m/s}^2$ ) compared with Earth ( $g = 9.81 \text{ m/s}^2$ ). However, previous studies of thrust faults on Mars investigated fewer than a dozen fault complexes, and focused exclusively on structures located in the southern highlands or close to the dichotomy boundary (e.g., Klimczak et al., 2018; Watters et al., 2000; Watters & Robinson, 1999). In order to draw conclusions about Mars' tectonic history, it is imperative to further investigate faults that are broadly distributed across the surface.

### 2.3 Displacement profile shape and segmentation

The history of a fault's growth and interaction can be assessed by characterizing the pattern of surface displacement, or resulting fault-generated topography, along the length of that fault (Davis et al., 2005; Klimczak et al., 2018). Although the displacement profiles of isolated faults are predicted to exhibit a centrally peaked profile with bell or elliptical shapes (Cowie & Scholz, 1992), many are better described by a roughly triangular, and often asymmetric, profile shape (Manighetti et al., 2001, 2005, 2009). Profile asymmetries can develop when sub-parallel faults overlap and lateral propagation is inhibited by the stress shadows of the adjacent fault.

These interactions increase the displacement profile taper toward the overlapping tips, relative to its distal ends, and may increase the  $D_{\text{max}}-L$  ratio of a fault or fault segments (Gupta and Scholz, 2000; Scholz and Lawler, 2004). As sub-parallel faults merge laterally, the linkage points between segments are marked by fault displacement minima that may persist as the fault system evolves (Peacock & Sanderson, 1991). A plateaued profile shape can evolve when the ability of the fault to accrue displacement is inhibited by the thickness of the brittle layer in which it is forming (Cowie & Scholz, 1992; Dawers & Anders, 1995; Nicol et al., 1996).

## 2.4 Rationale for this study

This work investigates the population of large-scale (i.e., tens to hundreds of kilometers long) lobate scarps on Mars. The growth histories of thrust faults within the southern highlands and northern lowlands are compared via their  $D_{\max}/L$  values, displacement-profile shapes, and displacement-profile spectra, to investigate how faults in both hemispheres compare given that previous studies have been more spatially localized. The  $D_{\max}/L$  values of Martian thrusts are then compared with thrust structures of a similar scale on Mercury, where crustal composition and gravitational acceleration are similar, to understand how crustal shortening on one-plate planets is manifest generally.

## 3. Methods

### 3.1 Measurement of Scarp Height

The Martian surface was surveyed using the merged digital elevation model (DEM) from the Mars Global Surveyor (MGS) Mars Orbiter Laser Altimeter (MOLA) and Mars Express (MEX) High-Resolution Stereo Camera (HRSC) (200 m/px; 3m vertical accuracy), together with the Mars Odyssey Thermal Emission Imaging System (THEMIS) Global Day-IR Mosaic (100 m/px) for the identification of fault-related folds. Our criteria for visually identifying these features include their curvilinear shape, exhibiting ~100 m or greater of maximum relief along the scarp, and resolvable asymmetry across the scarp, with one side of the scarp being relatively flat and low-lying (i.e., the footwall), and the other exhibiting higher topography that gently decreases in slope away from the scarp (i.e., the folded hanging wall). In total, 143 thrust fault locations were identified, but were downselected to 49 based on their: 1) lack of large (>50 km in

diameter) impacts, which if present could alter the topography and interpretation of the history of fault growth; and 2) geographic distribution (Figure 2.2).

Lobate scarps were identified using the HRSC–MOLA and THEMIS IR data and the trace of each scarp, taken to be the intersection of the uplifted hanging wall and the surrounding plains, was digitized in the ESRI ArcGIS ArcMap 10.6 environment. Initial mapping was performed at 1:1,000,000 scale, but was increased to 1:250,000 scale and augmented with the recently available Mars Reconnaissance Orbiter (MRO) Context Camera (CTX) global image mosaic (5 m/px) to resolve finer topographic (structural) features as needed.

Using the mapped traces, scarp-normal topographic profiles were extracted from the HRSC–MOLA DEM at 1-km intervals. A MATLAB-based graphical user interface assisted in marking the base and top of the scarp, and the change in elevation across the scarp ( $h$ ) was recorded for each profile. Profiles were excluded if the scarp morphology showed evidence of small craters, impact debris, or landslides. These features may display as scarp height minima and could be misinterpreted as segment linkage, when in fact the topographic expression is not the reflection of fault behavior, but rather surface modification. Exclusion occurred in 2.3% of the ~1,200 scarp-normal topographic profiles examined for the 49 mapped structures. In such instances, a piecewise cubic polynomial was used to interpolate the elevation values and maintain a record of scarp height with constant (1-km) spacing along strike.

In the absence of subsurface data with which to establish the geometry of these structures, fault displacement ( $D$ ) was calculated assuming a planar fault with the relation  $D = h/\sin(\alpha)$ , with  $\alpha$  being an assumed fault dip angle. Forward models of Martian lobate scarps suggest that these structures have fault dip angles of 15–40° (Egea-Gonzalez et al., 2017; Herrero-Gil et al., 2019), which is broadly in agreement with the dip angles for large thrust faults

on Earth (e.g., Brewer et al., 1979; Gries, 1983; Stone, 1985). A fault dip angle ( $\alpha$ ) of  $30^\circ$ , per Andersonian fault theory (Anderson, 1942), was adopted in our calculation to maintain consistency with recent studies that have reported  $D_{\max}/L$  data for Mars (Klimczak et al., 2018) and Mercury (Byrne et al., 2014). We assume that the measured relief of these landforms corresponds directly to the throw component of total fault displacement. However, some of this displacement is often accommodated by plastic deformation (i.e., folding) of the hanging wall, as well as potential ramp geometry which accommodates some displacement horizontally, which can also be the case for a fault-bend fold (Suppe & Medwedeff, 1990). Therefore,  $D$  values reported in this study likely represent minimum estimates of thrust fault displacement. The influence of fault dip, and its potential variability, are explored in Section 5.1.

Because the surface imagery has finite resolution, the resolvable height of the lobate scarps at the mapped fault tips is typically non-zero, suggesting that the structures extend laterally beyond those points and that fault length may be underestimated (Pickering et al., 1997). These unresolved fault trace lengths can be approximated by projecting the scarp height from the mapped tips assuming a constant fault tip taper (Kim & Sanderson, 2005). For each scarp, the height at its two mapped tips was averaged and the unresolved length was estimated using the mean  $D_{\max}/L$  of the population to estimate this tip taper angle (Figure S6, Appendix F).

### 3.2 Analysis of Scarp Height Profiles

The height–length profile of each scarp was characterized as having either an elliptical or triangular shape. This selection was made based on which of these shapes displayed the lowest root-mean-square misfit with the observed profile. When fitting the triangular shape model, the position of the peak was allowed to vary along the length of the fault, and the location of the

modeled peak height was cataloged to assess profile asymmetry. Elliptically shaped profiles are, by definition, symmetric.

To further examine the complexity of each scarp height profile, spectral analysis was used to quantify the variance in height along the scarp as a function of spatial frequency. Both Fourier and S-transform analyses were utilized, following the approaches to investigating Earth faults developed by Manighetti et al. (2009, 2015). Prior to spectral analysis, each profile was detrended by subtracting the best-fitting (elliptical or triangular) shape from the observed profile to create a stationary time series with  $m$ -points along the length of the scarp (Figure 2.3). The sample rate was expressed as the number of samples per total fault length ( $fs = m$ ) so that the resulting spatial frequencies are integer values with units of cycles per fault. The detrended profiles were additionally Hanning windowed prior to applying the fast-Fourier transform (FFT).

The Fourier spectrum characterizes the scarp height as a function of spatial frequency, such that each spectral amplitude term ( $A_n$ ) describes the contribution of a sinusoid making  $n$  oscillations over the length of the scarp. Although all scarps display power at a range of spatial scales, the peak spectral amplitude was used to identify the dominant scale of segmentation (Figure 2.4a). For example, a detrended profile displaying a peak spectral amplitude at a spatial frequency of two cycles per fault ( $n = 2$ ) would correspond to a fault profile with two dominant segments, each representing approximately half of the total fault length.

The S-transform (Stockwell et al., 1996) is a spectral localization method that incorporates a wavelet-like analysis using a Gaussian window having widths that vary inversely with the spatial frequency. Whereas Fourier analysis considers segments of fixed length, the S-transform technique is more suitable for tracking changes in the importance of different spatial frequencies (i.e., segment length variations) along the length of the scarp. The spectral

amplitudes are expressed as a matrix, with rows and columns representing spatial frequency (segments) and position along the profile, respectively (Figure 2.4b). Averaging the spectral amplitudes along each row produces an average spectra (Figure 2.4c), similar to the output of the FFT, which was used independently to assess the dominant spatial frequencies contributing to the variance of detrended profiles.

Each fault profile exhibits power across a range of spatial frequencies, reflecting its history of growth and linkage. Following Manigetti et al. (2009, 2015) the spatial frequency (cycles/fault) with the largest spectral amplitude is taken to represent the number of segments along a fault. Although some profile spectra do show similar power at multiple frequencies (Figure 2.4), this approach provides an objective criteria for defining segmentation that can be applied uniformly for faults of different sizes. The number of fault segments identified from the spectral analyses was used to constrain identification of segment boundaries based on our mapping of the fault traces and the visual assessment of their displacement-length profiles.

## **4. Results**

### **4.1 Displacement–Length Scaling**

The 49 scarps investigated ranged in length from 34 to 544 km, and have maximum heights from 85 m to 2,100 m. Population statistics are summarized in Table 2.1, and individual scarp measurements are included in Table S1 (Appendix G). Assuming a planar fault geometry with a dip angle of  $30^\circ$ , the average  $D_{\max}/L$  values for these structures is  $6.1 \times 10^{-3} \pm 1.4 \times 10^{-3}$ . Decreasing the fault dip angle to  $25^\circ$  increases the mean  $D_{\max}/L$  to  $6.2 \times 10^{-3}$ , and increasing the assumed dip angle to  $35^\circ$  decreases ratio to  $4.6 \times 10^{-3}$ . These values are within the range

published for other Martian thrust faults of  $4.5 \times 10^{-3}$  to  $6.2 \times 10^{-3}$  (Watters et al., 1998; Watters & Robinson, 1999; Watters et al., 2000; Schultz et al., 2006; Ruj et al., 2018).

Lengths of measured faults are similar between the structures in the northern and southern hemispheres, with median lengths of 211.5 km and 141.0 km, respectively. Again assuming a planar fault geometry and a dip angle of  $30^\circ$ , faults within the southern highlands exhibit a mean displacement–length ratio of  $9.2 \times 10^{-3} \pm 1.9 \times 10^{-3}$ , roughly a factor of three greater than the  $2.9 \times 10^{-3} \pm 0.9 \times 10^{-3}$  value observed for the northern lowland population of faults (Figure 2.5). When evaluated with a two-sample *t*-test or a non-parametric bootstrap resampling test, this difference in the means is found to be significant ( $p < 0.001$ ).

#### 4.2 Scarp Profile Shape

The along-scarp profiles of 47 of the 49 mapped scarps were described better by a triangular shape than an elliptical shape. To quantify the asymmetry of these profiles, the location of the modeled peak was identified by dividing the scarp length into thirds (Figure S1, Appendix A). Twelve scarps display peak heights in the central third of the fault, seventeen have peak heights within the scarp mid-section, and twenty have peak heights within the third of the scarp near its tips (Figure 2.6). The probability of observing a skewed fault profile is not significantly different between the northern lowlands and southern highlands (binomial test,  $p > 0.05$ ).

### 4.3 Spectral Analysis

Fourier analysis indicates that the detrended scarp profiles exhibit power at a range of spatial frequencies, but that peak spectral amplitudes occur in the lower frequency portion of the spectrum. The distributions of peak spectral amplitudes were similar for both the Fourier and S-Transform analyses, most often falling between two and six, with a few faults exhibiting peak amplitudes at spatial frequencies as high as eight or eleven (Figure 2.7). The median spatial frequency identified by both the FFT and S-Transform analyses is three, and 85% of faults included in this study can be characterized by a spatial frequency of five or fewer. When examining this distribution by fault location (i.e., northern lowlands vs southern highlands: Figure 2.7b), it appears that several northern faults exhibit slightly higher spatial frequencies than those in the south; however, a Kolmogorov-Smirnov test suggests that these distributions are not significantly different ( $p>0.05$ ).

Although detailed photogeologic assessment of these scarps is beyond the scope of this work, the results from spectral analyses were compared with visual assessments of evidence for fault segmentation in displacement profiles and in combined imagery and topography data to ensure that the number of segments being identified was the result of fault linkage instead of unrelated surface processes such as impact cratering or scarp landslides (e.g. Klimczak et al, 2018). Compared with visual assessments, results from the FFT and S-Transform analyses both identified the same number of segments *and* were in agreement with visual analysis for 31 (63%) of our study faults. S-Transform segmentation results most closely aligned with visual analyses for 11 faults (22%), followed by the FFT results (5 faults, 10%).

There were two cases where neither spectral analysis technique matched our visual assessment of fault segmentation. The first of which was a fault in Utopia Planitia in terrain with

prominent mud volcanoes (Ivanov et al., 2014) causing a rough surface that made measurements of the scarp height difficult to extract precisely, resulting in inconsistent measurements of displacement along its length and ultimately differing by five to six segments between spectral analyses and visual assessment. The second scarp was of a relatively short fault (~50 km), which also displayed multiple variations in  $D_{\max}$  along its length that were likely local displacement discrepancies caused by a rough surface. The inclusion of these two faults did not impact our results or interpretations, and therefore were retained for this study.

Comparisons of maximum displacement–length ratios with fault segmentation (Figure 2.8) show that, for both FFT and S-Transform analyses, faults with smaller  $D_{\max}/L$  values are more segmented. Conversely, faults with fewer segments (i.e., fewer troughs in their displacement profiles) have accumulated a greater amount of maximum displacement for a given fault length. The best-fit linear regressions for both the FFT and S-Transform analyses exhibit an inverse relationship between  $D_{\max}$ - $L$  ratios and the number of fault segments, with linear regression slopes of  $-9 \times 10^{-4}$  for the FFT and  $-5 \times 10^{-4}$ , respectively (Figure 2.8). Although the slopes of both regression lines in Figure 2.8 are significant ( $p < 0.001$ ) and comparable to those found by Manighetti et al. (2009) for Earth faults, it is important to note that fault population regressions for the northern and southern components are not significant (Figure S5, Appendix E). As a result of available data resolution, mapped faults for this study do not span multiple orders of magnitude (e.g., meter to sub-meter faults were not considered as they can be on Earth) and may therefore be contributing to the lack of significance for these subpopulations.

## 5. Discussion

The number of thrust-fault related landforms ( $n = 49$ ) investigated for this study represent a substantial increase over the number investigated and compared morphometrically in earlier work; previous structural analyses of displacement–length profiles included eight to thirteen faults (Watters & Robinson, 1999; Watters et al., 2000; Klimczak et al., 2018), and fault modeling studies have included only one or two major fault systems (Grott et al., 2007; Ruiz et al., 2008; Mueller et al., 2014; Egea-Gonzalez et al., 2017; Herrero-Gil et al., 2019, 2020a). At least seven of our faults have been investigated independently in previous studies, including Ogygis, Bosporus, Phrixi, Icaria, and Hiddekel Rupēs, along with several other unnamed faults. Our independently measured lengths and throws for these structures are in agreement with results from other studies (Klimczak et al., 2018; Herrero-Gil et al., 2019).

### 5.1 Displacement–length scaling ratios

Assuming planar fault geometries dipping at  $30^\circ$ , the  $D_{\max}/L$  determined for these 49 thrust faults is  $6.1 \times 10^{-3}$ . This value is comparable to other global ratios found for thrust faults on Mars, which range from  $4.5 \times 10^{-3}$  to  $6.2 \times 10^{-3}$  (Watters et al., 1998; Watters & Robinson, 1999; Watters et al., 2000; Schultz et al., 2006; Ruj et al., 2018). Results from this investigation show significantly different  $D_{\max}/L$  ratios (Figure 2.6) for the northern lowlands ( $n = 24$ ;  $D_{\max}/L = 2.9 \times 10^{-3}$ ) and the southern highlands ( $n = 25$ ;  $D_{\max}/L = 9.2 \times 10^{-3}$ ). This finding indicates that, for a given fault length, thrust faults in the south have accumulated almost three times more vertical displacement than those in the north.

To first order, the amount of displacement that can accumulate on a given fault is limited by the strain rate and the thickness of the brittle layer (e.g., Ackermann et al., 2001; Schulz and

Fossen, 2002). The influence of brittle layer thickness has been proposed to modulate the growth of faults across a range of scales (e.g., Shaw et al., 2004; Hughes et al., 2014). Modeling of thrust faulting on Mars, which has focused on lobate scarps within the southern highlands, suggests that the underlying structures extend to mid-to-lower crustal depths, where they are often interpreted to intersect the brittle-ductile transition (BDT) (e.g., Ruiz et al., 2008; Egea-Gonzalez et al., 2017; Herrero-Gil et al., 2019; 2020a; 2020b). While hemispheric differences in the depth of the BDT could be called upon to explain variations in  $D_{\max}/L$ , the observed trends would imply the presence of an even shallower BDT beneath the northern lowlands. Such an interpretation, however, is not easily reconciled with the Martian crustal dichotomy.

If a constant density is assumed for the Martian crust, beneath the southern highlands, where the crust is 50-60 km thick (Neumann et al., 2004), crustal rocks may become ductile at depth. Whereas, in the lowlands, where the crust is only about 30 km thick, the lower crust and upper mantle likely remain strong and the BDT is expected to occur at greater depths (Montesi & Zuber, 2003). Although variations in crustal density may allow for more similar crustal thickness between the hemispheres (Goosens et al., 2017; Broquet & Wiczorek, 2019), a denser (more mafic) northern hemisphere crust would likely not lead to a shallower BDT, compared to the southern hemisphere crust.

The apparent differences in  $D_{\max}/L$  may alternatively be explained by variation in the geometry of fault systems that are not accounted for when estimating fault displacement from scarp height. Figure 2.9 explores how our assumptions regarding fault dip angle influences these reported differences in scaling. If, for example, the assumed dip of the faults in the southern highlands was held fixed at  $30^\circ$ , but the northern faults systems were assumed to dip at  $\leq 16^\circ$ , then the differences in  $D_{\max}/L$  would become statistically insignificant. Additionally, variations

in structural style (e.g., fault-bend vs. homoclinal fault-propagation folding) could explain apparent  $D_{\max}/L$  differences. The accommodation of some fault displacement horizontally in fault-bend folds may lead to lower scarp heights, thus resulting in under-calculated fault displacements.

More generally, variations in mechanical stratigraphy influences fault geometry. Evidence for multiple substantial resurfacing periods in the northern lowlands suggests the existence of a layered basin (Zuber et al., 2000; Tanaka et al., 2003, 2005; Polit et al., 2009). Stratigraphic sequences comprised of units with contrasting mechanical strength can impede the further vertical propagation of faults (Gross et al., 1997; Wilkins & Gross, 2002). Studies of both Mercury and Mars have argued that the formation of décollements is promoted along proposed mechanically weak interfaces within stratified basaltic and sedimentary units (Andrews-Hanna, 2020; Peterson et al., 2020). Analogue modeling indicates that contrasts in mechanical layer strength, low fault dip angles, and more thinly spaced layering promote the development of fault-bend folds. Conversely, when layer strength is less varied or thicker stratigraphic layers are present, faults have relatively steeper dip angles, and the development of fault propagation folds is more favored (Hughes et al., 2014).

Finally, a further possible explanation for the observed hemispheric differences in fault  $D_{\max}-L$  ratios may be their growth histories, which admittedly cannot be constrained based on our observations. If secular interior cooling resulted in a globally contracting stress field, this may have favored the rapid lengthening of these thrust faults systems early in their development. Conceivably faults in the south were active for longer and accumulated more displacement after this initial lengthening phase than their counterparts in the north.

## 5.2 Displacement profiles

### 5.2.1 Profile shapes

Our method of extracting information on fault throw from topographic data offers the ability to analyze not only the maximum displacement and length relationships, but to assess fault segmentation, shape, and skewness. Although qualitative assessments of these morphometric characteristics (i.e., the degree of segmentation and overall shape) have been explored for Mars in other studies (Klimczak et al., 2018; Ruj et al., 2018), by employing shape-fitting and signal-processing techniques (together with including more faults than those earlier studies), we are able to statistically analyze these metrics and compare with those (i.e.,  $D_{max}/L$ ) previously quantified. Further, this technique minimized human subjectivity in characterizing fault shapes and the extent of segmentation. A triangular shape best fits 96% of our displacement profiles. This finding is in agreement with studies of Terran faults that exhibit linear displacement gradients from their maximum toward the fault tips (Manighetti et al., 2009).

Investigations of displacement peak locations show that the majority of faults in this study are ‘slightly’ to ‘substantially skewed’ ( $n = 37$ , see Figure S1, Appendix A), with peaks in displacement just outside the center third of the fault (from 30% to 60% fault half-length) to nearing the fault tips (from 30% fault half-length to the fault tip), respectively (Figure 2.6). This finding means that only about 24% of the faults included in this study have maximum displacements that occur within the center third of the fault length. When faults grow through radial propagation from a centroid, they exhibit a generally symmetrical displacement profile shape (Cartwright et al., 1995). That most of these faults exhibit skewness (or asymmetric displacement) indicates that, rather than growing in isolation, these faults grew through linkage with adjacent structures.

### 5.2.2 Segmentation and fault evolution

We investigated  $D_{\max}/L$  trends as a function of segmentation to better understand how displacement profiles for our study faults evolved after linkage. Comparing fault characteristics within the study population shows that  $D_{\max}-L$  ratios decrease as fault segmentation increases (Figure 2.8). Thus, faults in the northern lowlands with lower  $D_{\max}/L$  appear more segmented. From a fault evolution perspective, the more segmented a displacement profile is for a continuous fault trace, the earlier the fault is in its developmental stages of growth (Wesnousky, 1988; Cartwright et al., 1995; Stirling et al., 1996; Manighetti et al., 2009). Conversely, when a fault's displacement profile can be characterized by a single segment, that structure may be considered more evolved (i.e., it has been accumulating strain for longer and its smaller segment boundaries have been smoothed over time) and/or that it grew in isolation and there were no other proximal structures with which it could link.

The evolutionary history of a given fault can often be captured in  $D_{\max}/L$  values, where the ratios of the linked faults temporarily decrease as their lengths are incorporated with the previous displacements (Wesnousky, 1988; Cartwright et al., 1995; Stirling et al., 1996; Kim & Sanderson, 2005; Scholz, 2019). During this fault linkage process, the overall  $D_{\max}/L$  value deviates to the right of the idealized growth path (below a line defined by  $D_{\max} = \gamma L$ ) (e.g., Burbank & Anderson, 2011, their fig. 4.12). As the faults evolve together into a single structure, they begin to accumulate more displacement for their newly stabilized increase in length. This stepwise evolution into a single fault system is “complete” when the ratio of maximum displacement to length returns to the idealized growth path, and what could previously be identified as multiple segments in a displacement profile become a single fault (Burbank & Anderson, 2011; Cartwright et al., 1995). The growth of faults through linkage has been seen

with normal faults in the Alba Patera region of Mars as supported by physical analog modeling of the observed topography (Wyrick et al., 2011). Alternatively, deviations from the idealized growth path can also be explained by the presence of a mechanically confining layer at depth (Nicol et al., 1996). This mechanism would allow faults to continue to propagate laterally, although limiting their displacements to below some threshold. Such restriction would be observable in the  $D_{\max}/L$  trends as they would plot along a threshold displacement.

### 5.3 Comparison with Mercury and Earth

Our results enable us to compare structures on Mars with thrust faults on other planetary surfaces. The southern highlands of Mars consists of old, cratered planetary basaltic crust (Carr, 2007) and so are arguably morphologically comparable to the similarly old and textured intercrater plains of Mercury (e.g., Strom et al., 1975), which are also composed of old, mafic crust. Additionally, both surfaces lack evidence of discrete tectonic plates segmenting their surfaces, but rather exhibit large thrust fault-related folds (Byrne et al., 2014). Comparing  $D_{\max}/L$  values from our population of Martian faults ( $n = 25$ ;  $D_{\max}/L = 9.2 \times 10^{-3}$ ) in the southern highlands to those in the intercrater plains of Mercury ( $n = 177$ ;  $D_{\max}/L = 9.7 \times 10^{-3}$ ) measured by Byrne et al. (2014), we find, with 99% confidence, that there is no statistically significant difference in these ratios between the two populations (Figure 2.10). Thus, the average displacement–length ratios for faults formed in ancient, impact-battered mafic crusts on Mars and Mercury are essentially the same. This finding is in agreement with others who have compared faults on these two terrestrial planets and have attributed similarities to comparable gravity fields on Mars ( $g_{\text{Mars}} = 3.72 \text{ m/s}^2$ ) and Mercury ( $g_{\text{Mercury}} = 3.78 \text{ m/s}^2$ ) (Schultz et al., 2006; Watters et al., 2000). Comparisons with thrust faults on Earth (Figure 2.11) show

similarities in the measured  $D_{\max}/L$  for Mars and Mercury, and that fault displacements are smaller for comparable fault lengths on Mercury and Mars compared with Earth.

## 6. Conclusions

Results from this study were used to determine geographic variations in displacement–length ratios for thrust faults on Mars, along with comparisons with similar faults on Mercury, and a variety of fault types on Earth. The  $D_{\max}$ - $L$  ratios for 49 globally distributed thrust faults on Mars is  $6.1 \times 10^{-3} \pm 1.4 \times 10^{-3}$ . However, significant differences have been found for displacement–length relationships between faults in the northern lowlands ( $2.9 \times 10^{-3} \pm 0.9 \times 10^{-3}$ ) and southern highlands ( $9.2 \times 10^{-3} \pm 1.9 \times 10^{-3}$ ). Additionally, investigations of fault segmentation reveal an inverse relationship between  $D_{\max}/L$  and the number of major fault segments, which has also been observed for Earth faults (Manighetti et al., 2009; 2015). Lower fault dip angles for faults in the lowlands compared to highland faults could account for the observed differences in  $D_{\max}/L$ . Additionally, layers of sedimentary and volcanic origin in the northern lowlands might promote fault-bend folding as opposed to the assumed fault-propagation fold geometry assumed in this and other studies for thrust faults on Mars generally, and especially those “lobate scarps” in the southern uplands. Should at least these thrusts in the lowlands be fault-bend folds, measurements of their scarp heights likely considerably underestimate the slip values of those faults.

## Figures

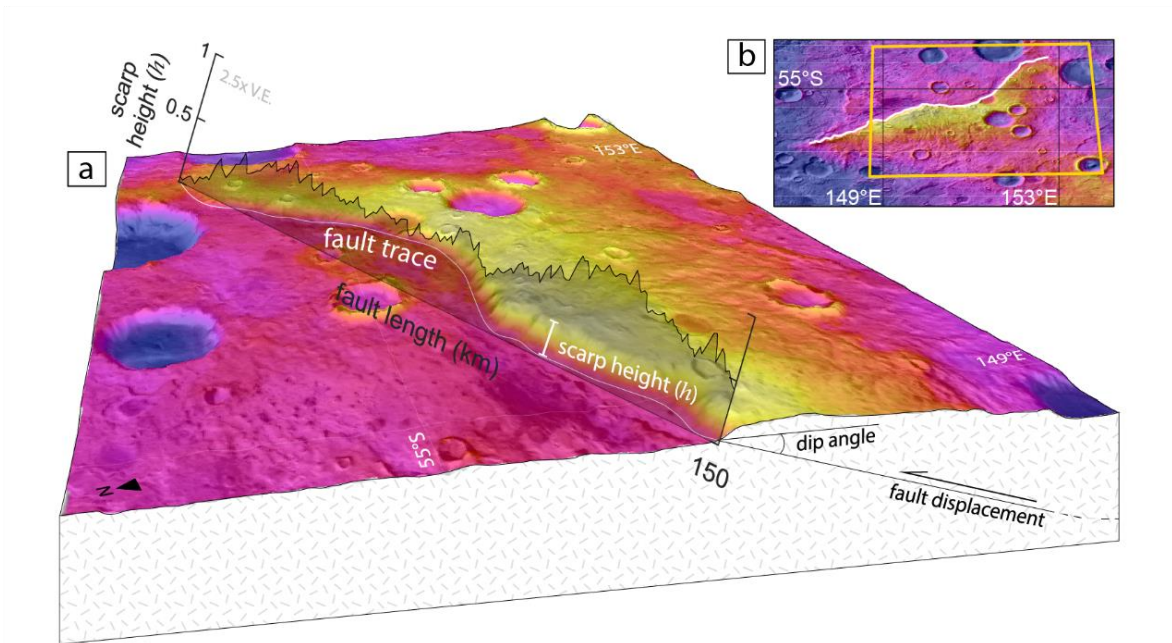


**Figure 2.1** (a) Three-dimensional schematic view of one of our studied thrust faults, and its extracted, along-scarp height profile (as a proxy for along-strike displacement). (b) The location of this fault.

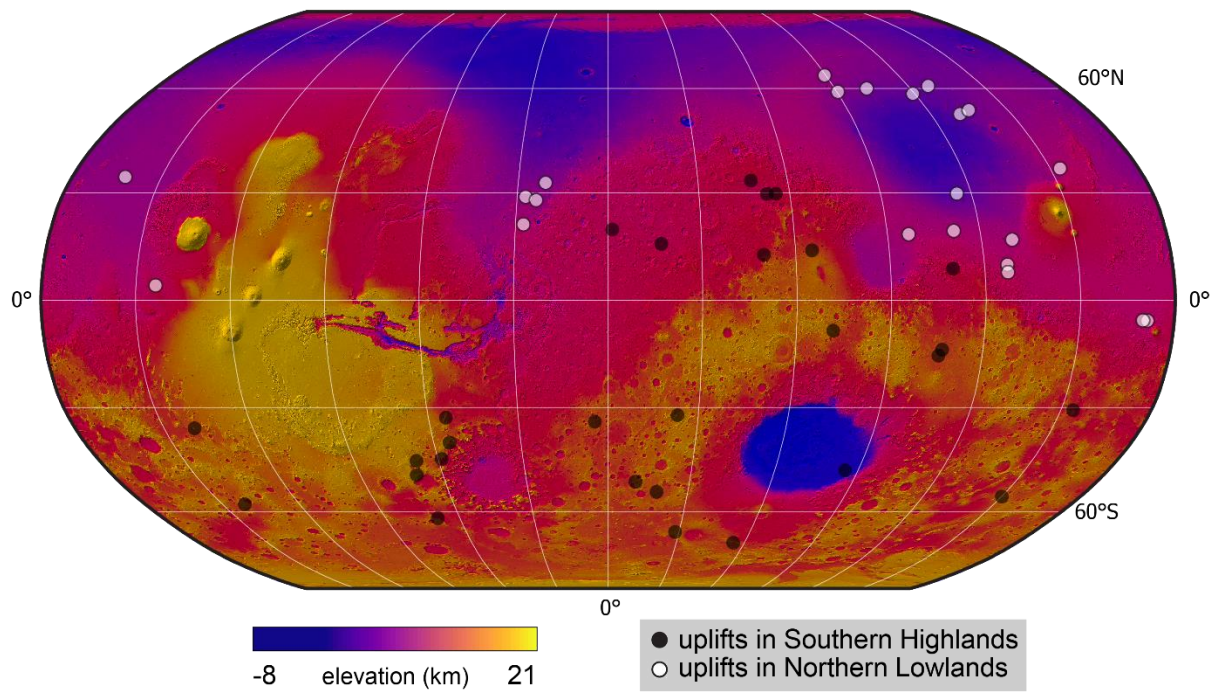


**Figure 2.2** A global map of selected faults for this study ( $n = 49$ ). The map is in a Robinson projection, centered at  $0^\circ\text{E}$ .

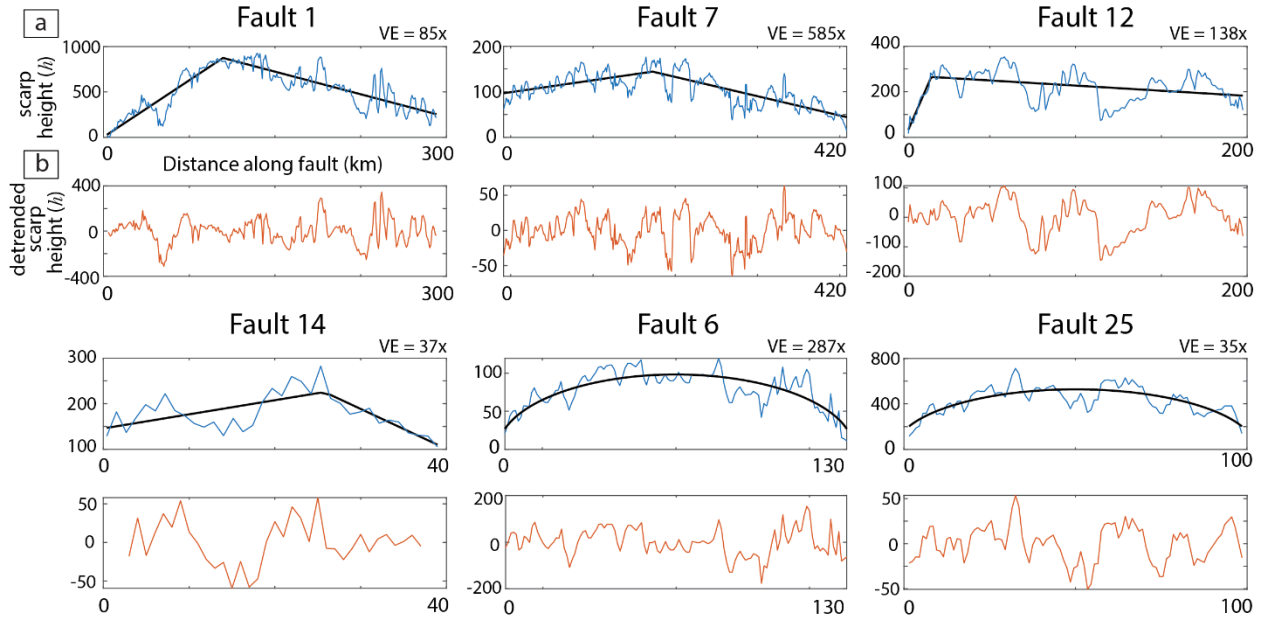


**Figure 2.3** Examples of fault scarp fit types and detrended profiles. (a) Selected faults exhibiting multiple fit types, with best-fitting shapes shown in black; four are best fit with triangles, whereas two are best fit with ellipses. (b) Those same scarp height profiles now detrended, with the best-fitting shapes removed, for subsequent analysis.

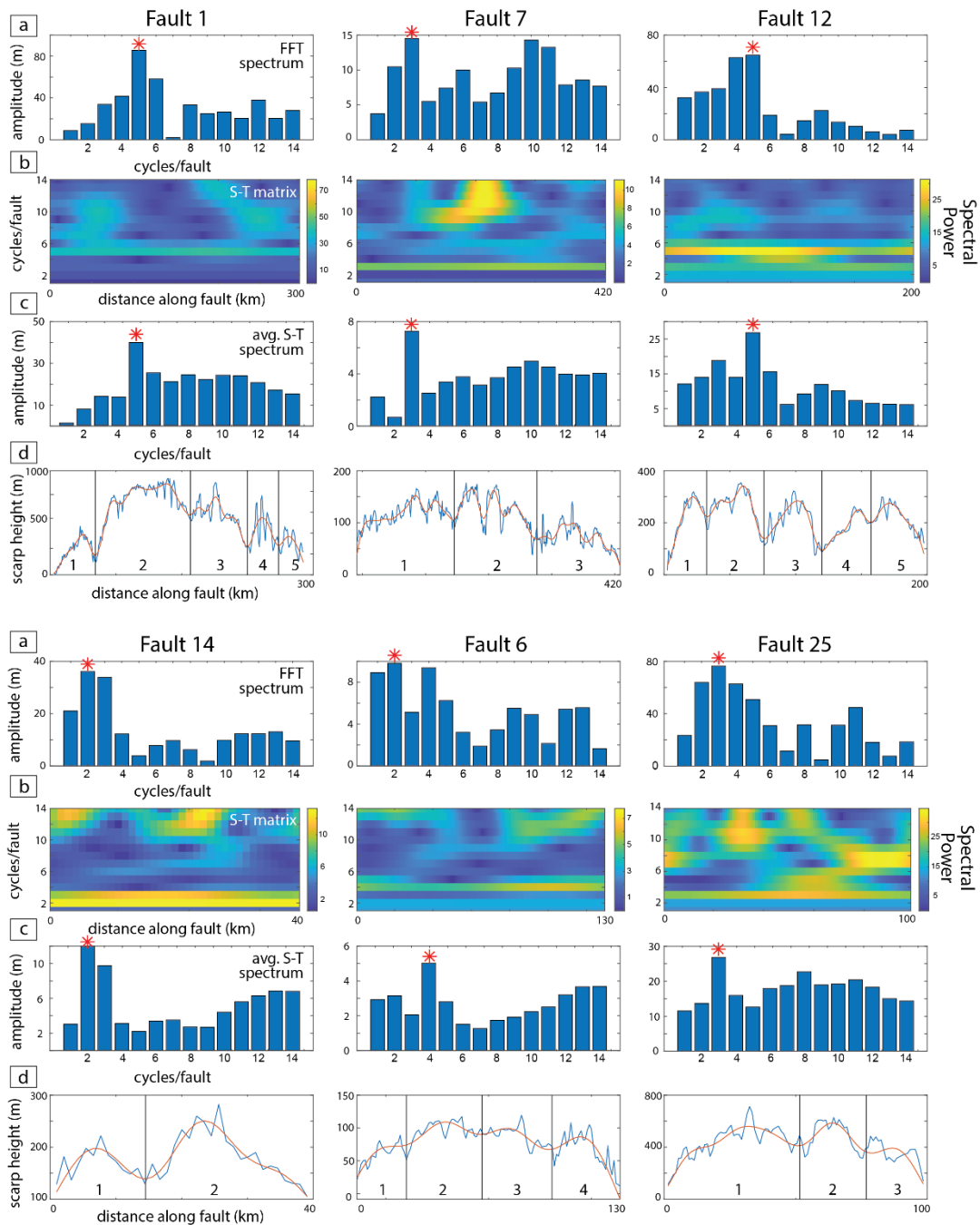


**Figure 2.4** Examples of our spectral analyses for select faults. (a) Number of segments per fault ( $\leq 14$ ) results from FFT analyses binned by integer fault segments, for segment values with the highest amplitude (red\*) indicate number of segments per fault. (b) Spectral frequency results from S-transform analyses (at low frequencies,  $\leq 14$ ) displayed for the length of each fault; color indicates spectral power. (c) Number of segments per fault binned as means for each integer frequency across the length of the fault. The highest amplitude frequency (red \*) indicates the number of fault segments for each fault. (d) Measured displacement profiles (blue) and filtered profiles (red), constructed from the number of cycles from both analyses. Segment boundaries delineated by vertical black lines.

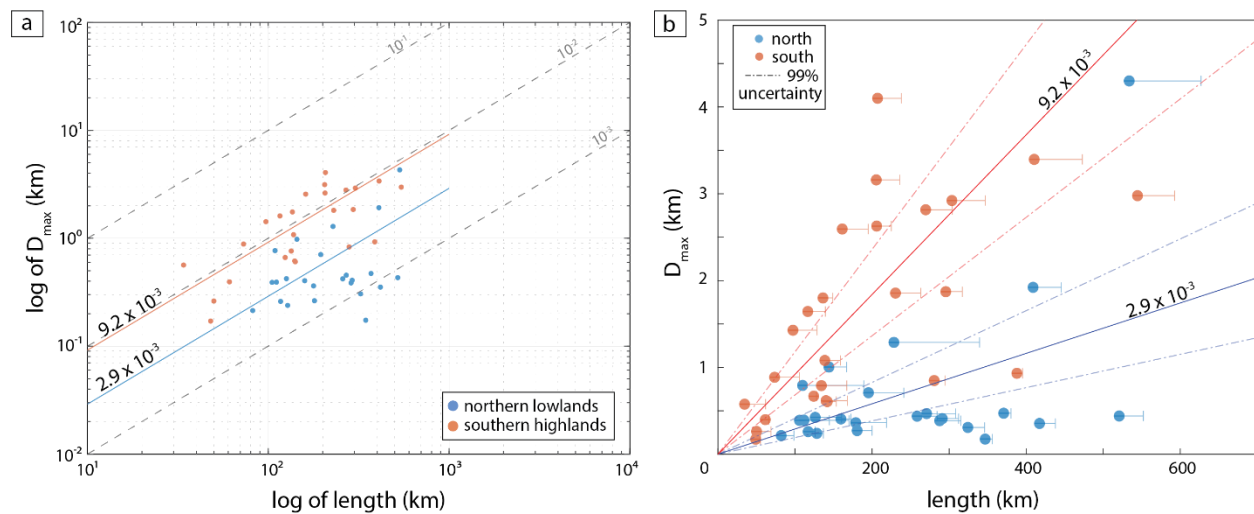


**Figure 2.5** (a) Log–log plot of  $D_{\max}/L$  ratios as a function of fault length, for thrusts in the northern lowlands and southern highlands. Means for each population are solid lines. (b)  $D_{\max}/L$  values in linear space. In both panels, the dashed lines mark the 99% confidence intervals

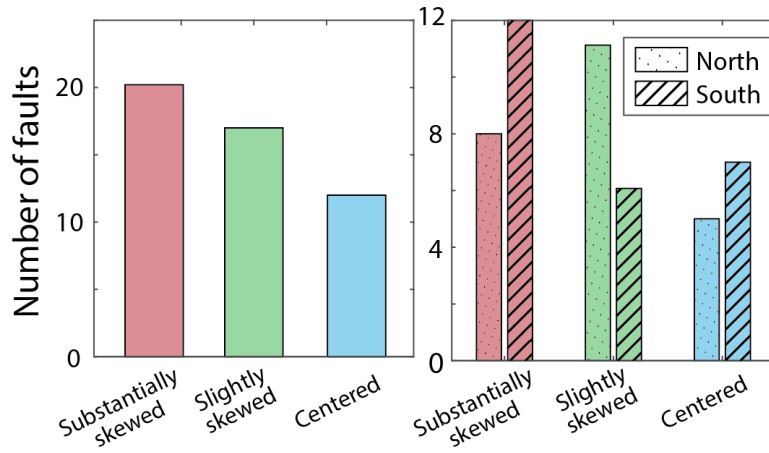


**Figure 2.6** (left) The number of faults with peaks in each zone for all of our study faults ( $n = 49$ ); (right) The number of faults with peaks in each zone by geographic location.

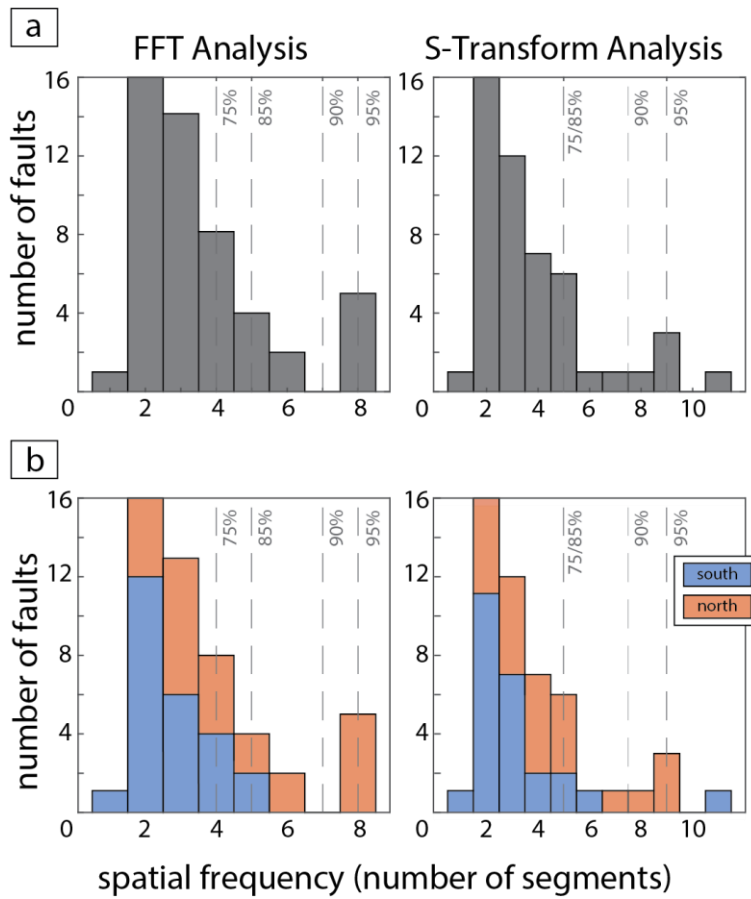


**Figure 2.7** These histograms show the distribution of spatial frequencies (i.e., fault segments). Gray dashed lines indicate the percentage of faults less than or equal to the identified spatial frequency. (a) FFT and S-transform distributions for all studied faults ( $n = 49$ ) (b) FFT and S-Transform distributions for study faults separated by hemispherical location (i.e., northern lowlands (orange) or southern highlands (blue)).

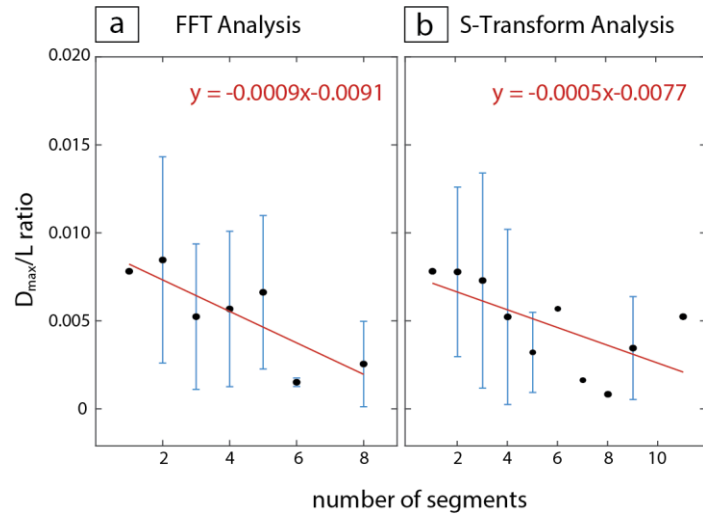


**Figure 2.8** Maximum study thrust fault displacement–length ratio as a function of segments. The black points are means for each segment bin, the vertical blue lines are standard deviation for each number of segments, and regression equations are in red. Both regressions are significant ( $p < 0.05$ ).

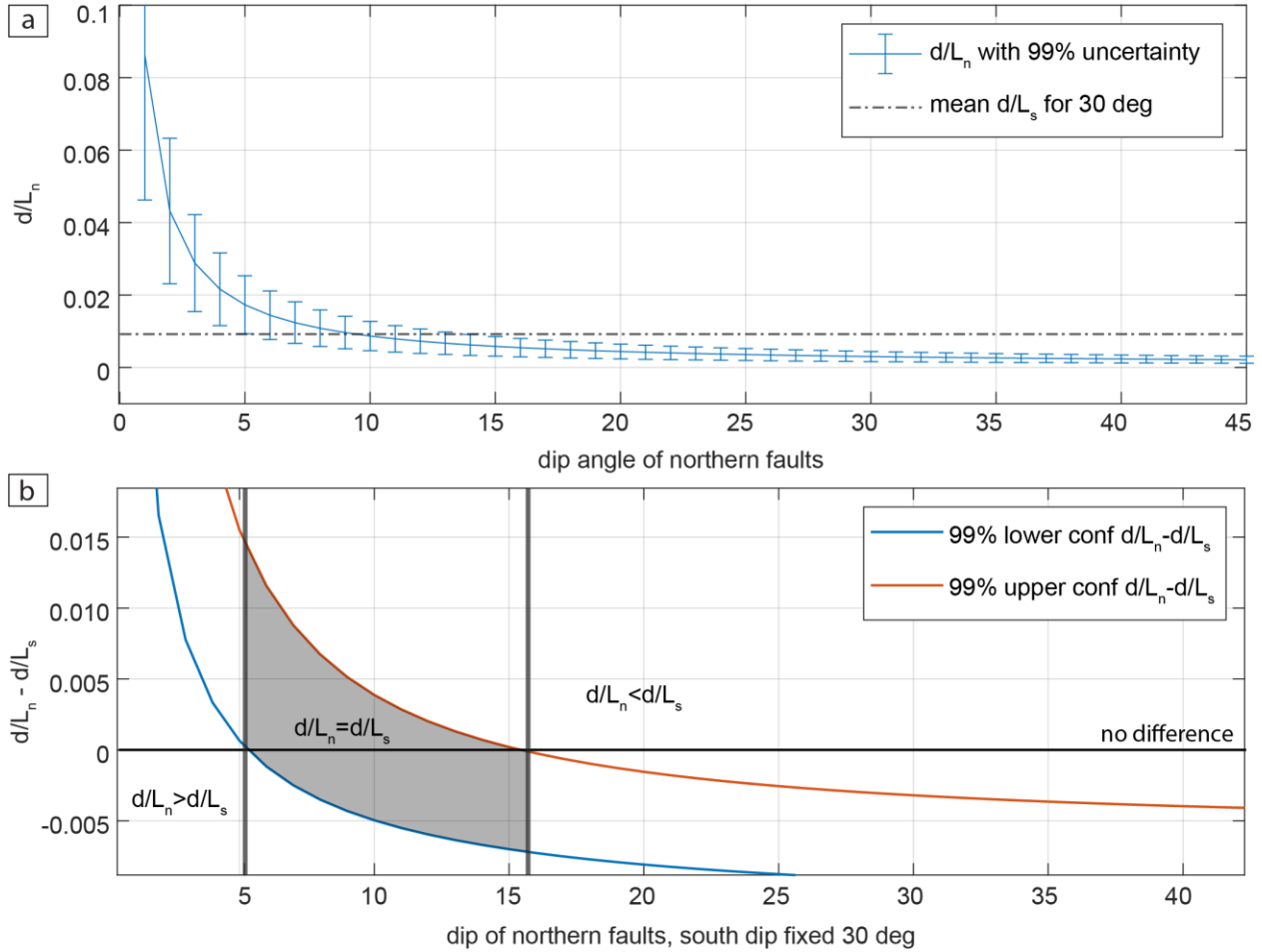


**Figure 2.9** (a) Calculated mean  $D_{\max}$ - $L$  ratios for faults in the northern lowlands for various fault dip angle assumptions. (b) Confidence interval for the predicted different in the mean  $D_{\max}$ - $L$  (N minus S) as a function of fault dip angle for thrusts in the northern lowlands with a constant dip angle of  $30^\circ$  for thrusts in the southern hemisphere. The shaded grey area indicates the range of fault dip angles for northern thrusts that would yield no statistically significant differences in the mean  $D_{\max}/L$  between the northern and southern hemispheres.

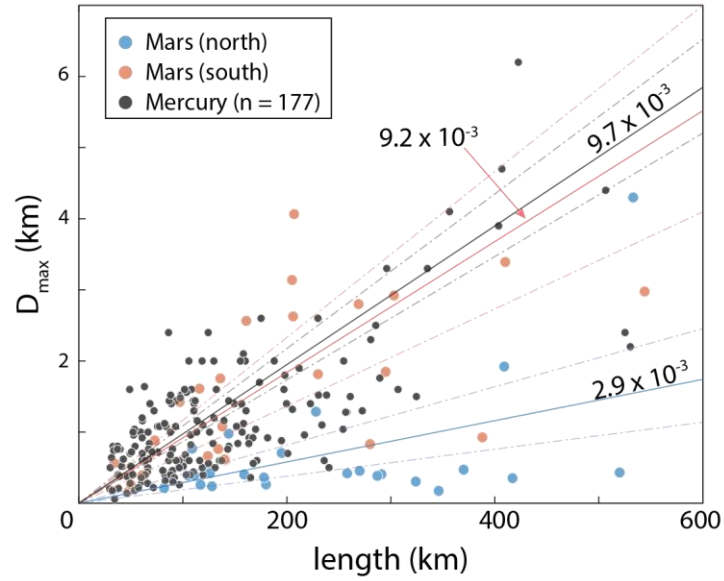


**Figure 2.10**  $D_{\max}$ - $L$  ratios as a function of fault length for thrusts in the southern highlands (orange), northern lowlands (blue), and the intercrater plains of Mercury (black). Mean  $D_{\max}/L$  values for each population are shown with solid lines, and the 99% confidence intervals are indicated by dashed lines.

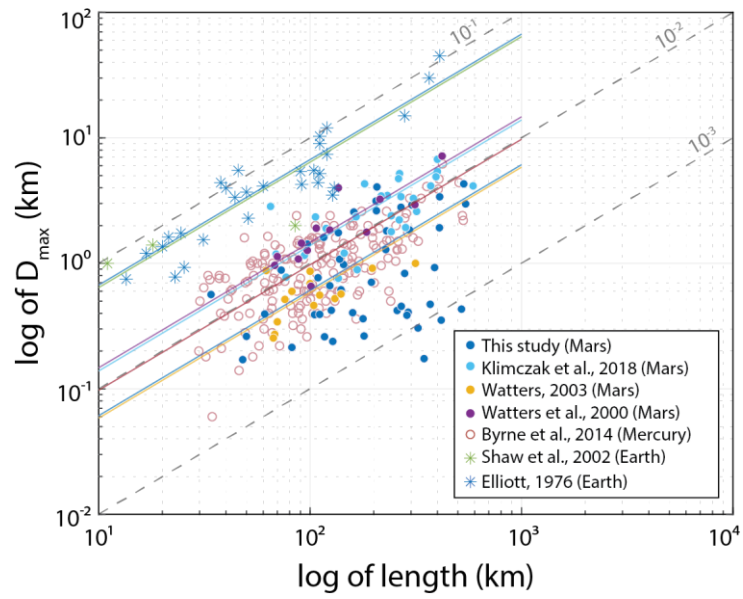


**Figure 2.11**  $D_{\max}/L$  values for thrust faults on terrestrial planets from multiple studies, including this one (blue dots).

**Table 2.1** Summary statistics for morphometric characteristics of study thrust faults for the sampled global population ( $n = 49$ ), in the northern lowlands ( $n = 24$ ), and the southern highlands ( $n = 25$ ).

		<b>Range</b>	<b>Median (<i>Mdn</i>)</b>	<b>Quartiles (Q)</b>
<b>Global</b>	<b>Lengths</b>	34 km–544 km	180.0 km	122.3 km 292.0 km
<b>North</b>		82 km–533 km	211.5 km	127.0 km 335.0 km
<b>South</b>		34 km–544 km	141.0 km	111.3 km 271.8 km
<b>Global</b>	<b>Throws</b>	85.4 m–2.1 km	331.6 m	195.8 m 884.6 m
<b>North</b>		87.0 m–2.1 km	203.0 m	164.5 m 294.6 m
<b>South</b>		85.4 m–2.0 km	712.2 m	325.7 m 1,334.7 m
<b>Global</b>	<b><math>D_{max}</math></b>	170.9 m–4.3 km	663.2 m	391.5 m 1,769.2 m
<b>North</b>		174.0 m–4.3 km	406.0 m	329.0 m 589.2 m
<b>South</b>		170.9 m–4.1 km	1.4 km	651.4 m 2,669.4 m
			<b>Mean (<i>M</i>)</b>	<b>Uncertainty in mean (95%)</b>
<b>Global</b>	<b><math>D_{max}/L</math> ratio</b>	$0.5 \times 10^{-3}$ – $19.6 \times 10^{-3}$	$6.1 \times 10^{-3}$	$\pm 1.4 \times 10^{-3}$
<b>North</b>		$0.5 \times 10^{-3}$ – $8.1 \times 10^{-3}$	$2.9 \times 10^{-3}$	$\pm 0.9 \times 10^{-3}$
<b>South</b>		$2.4 \times 10^{-3}$ – $19.6 \times 10^{-3}$	$9.2 \times 10^{-3}$	$\pm 1.9 \times 10^{-3}$

## Chapter 2 References

- Ackermann, R. V, Schlische, R. W., & Withjack, M. O. (2001). The geometric and statistical evolution of normal fault systems: An experimental study of the effects of mechanical layer thickness on scaling laws. *Journal of Structural Geology*, 23(5), 1803–1819.  
[www.elsevier.com/locate/jstrugeo](http://www.elsevier.com/locate/jstrugeo)
- Anderson, E. M. (1942). The dynamics of faulting and dyke formation with applications to Britain. In *The Journal of Geology*. Oliver and Boyd.
- Andrews-Hanna, J. C. (2020). The tectonic architecture of wrinkle ridges on Mars. *Icarus*, 351, 113937. <https://doi.org/10.1016/j.icarus.2020.113937>
- Andrews-Hanna, J. C., Zuber, M. T., & Banerdt, W. B. (2008). The Borealis basin and the origin of the martian crustal dichotomy. *Nature*, 453(7199), 1212–1215.  
<https://doi.org/10.1038/nature07011>
- Bergen, K. J., & Shaw, J. H. (2010). Displacement profiles and displacement-length scaling relationships of thrust faults constrained by seismic-reflection data. *Bulletin of the Geological Society of America*, 122(7–8), 1209–1219. <https://doi.org/10.1130/B26373.1>
- Bohnenstiehl, D. R., & Kleinrock, M. C. (2000). Evidence for spreading-rate dependence in the displacement-length ratios of abyssal hill faults at mid-ocean ridges. *Geology*, 28(5), 395–398. [https://doi.org/10.1130/0091-7613\(2000\)28<395:EFSDIT>2.0.CO;2](https://doi.org/10.1130/0091-7613(2000)28<395:EFSDIT>2.0.CO;2)
- Brewer, J. A., Smithson, S. B., Oliver, J. E., Kaufman, S., & Brown, L. D. (1980). The Laramide orogeny: Evidence from cocorp deep crustal seismic profiles in the wind river mountains, wyoming. *Tectonophysics*, 62(3–4), 165–189. [https://doi.org/10.1016/0040-1951\(80\)90191-2](https://doi.org/10.1016/0040-1951(80)90191-2)
- Byrne, P. K., Klimczak, C., Sengör, A. M. C., Solomon, S. C., Watters, T. R., & Hauck, S. A. (2014). Mercury’s global contraction much greater than earlier estimates. *Nature Geoscience*, 7(4), 301–307. <https://doi.org/10.1038/ngeo2097>
- Cartwright, J. A., Trudgill, B. D., & Mansfield, C. S. (1995). Fault growth by segment linkage: an explanation for scatter in maximum displacement and trace length data from the Canyonlands Grabens of SE Utah. *Journal of Structural Geology*, 17(9), 1319–1326.  
[https://doi.org/10.1016/0191-8141\(95\)00033-A](https://doi.org/10.1016/0191-8141(95)00033-A)
- Citron, R. I., Manga, M., & Tan, E. (2018). A hybrid origin of the Martian crustal dichotomy: Degree-1 convection antipodal to a giant impact. *Earth and Planetary Science Letters*, 491, 58–66. <https://doi.org/10.1016/j.epsl.2018.03.031>
- Clark, R. M., & Cox, S. J. D. (1996). A modern regression approach to determining fault displacement-length scaling relationships. *Journal of Structural Geology*, 18(2–3), 147–152. [https://doi.org/10.1016/S0191-8141\(96\)80040-X](https://doi.org/10.1016/S0191-8141(96)80040-X)
- Cowie, P. A., & Scholz, C. H. (1992). Displacement-length scaling relationship for faults: data synthesis and discussion. *Journal of Structural Geology*, 14(10), 1149–1156.  
[https://doi.org/10.1016/0191-8141\(92\)90066-6](https://doi.org/10.1016/0191-8141(92)90066-6)
- Davis, K., Burbank, D. W., Fisher, D., Wallace, S., & Nobes, D. (2005). Thrust-fault growth and

- segment linkage in the active Ostler fault zone, New Zealand. *Journal of Structural Geology*, 27(8), 1528–1546. <https://doi.org/10.1016/j.jsg.2005.04.011>
- Dawers, N. H., & Anders, M. H. (1995). Displacement-length scaling and fault linkage. *Journal of Structural Geology*, 17(5), 607–614. [https://doi.org/10.1016/0191-8141\(94\)00091-D](https://doi.org/10.1016/0191-8141(94)00091-D)
- Ding, M., Lin, J., Gu, C., Huang, Q., & Zuber, M. T. (2019). Variations in Martian Lithospheric Strength Based on Gravity/Topography Analysis. *Journal of Geophysical Research: Planets*, 124(11), 3095–3118. <https://doi.org/10.1029/2019JE005937>
- Donald S. Stone. (1985). Geologic interpretation of seismic profiles, Big Horn Basin, Wyoming, Part I: East flank. In R. R. Gries & R. C. Dyer (Eds.), *Seismic Exploration of the Rocky Mountain Region* (pp. 165–174). Rocky Mountain Association of Geologists. <https://doi.org/10.1306/ad462aa6-16f7-11d7-8645000102c1865d>
- Dragoni, M. (1993). The brittle-ductile transition in tectonic boundary zones. *Annals of Geophysics*, 36(2). <https://doi.org/10.4401/ag-4282>
- Egea-Gonzalez, I., Jiménez-Díaz, A., Parro, L. M., López, V., Williams, J. P., & Ruiz, J. (2017). Thrust fault modeling and Late-Noachian lithospheric structure of the circum-Hellas region, Mars. *Icarus*, 288, 53–68. <https://doi.org/10.1016/j.icarus.2017.01.028>
- Ellis, Magdalena A., & Barnes, J. B. (2015). A global perspective on the topographic response to fault growth. *Geosphere*, 11(4), 1008–1023. <https://doi.org/10.1130/GES01156.1>
- Ellis, Michael A., & Dunlap, W. J. (1988). Displacement variation along thrust faults: implications for the development of large faults. *Journal of Structural Geology*, 10(2), 183–192. [https://doi.org/10.1016/0191-8141\(88\)90115-0](https://doi.org/10.1016/0191-8141(88)90115-0)
- Erickson, S. G. (1996). Influence of mechanical stratigraphy on folding vs faulting. *Journal of Structural Geology*, 18(4), 443–450. [https://doi.org/10.1016/0191-8141\(95\)00064-K](https://doi.org/10.1016/0191-8141(95)00064-K)
- Fassett, C. I., & Head, J. W. (2008). Valley network-fed, open-basin lakes on Mars: Distribution and implications for Noachian surface and subsurface hydrology. In *Icarus* (Vol. 198, pp. 37–56).
- Gallen, S. F., Wegmann, K. W., Bohnenstiehl, D. R., Pazzaglia, F. J., Brandon, M. T., & Fassoulas, C. (2014). Active simultaneous uplift and margin-normal extension in a forearc high, Crete, Greece. *Earth and Planetary Science Letters*, 398, 11–24. <https://doi.org/10.1016/j.epsl.2014.04.038>
- Golombek, M. P., & Bridges, N. T. (2000). Erosion rates on Mars and implications for climate change: Constraints from the Pathfinder landing site. *Journal of Geophysical Research E: Planets*, 105(E1), 1841–1853. <https://doi.org/10.1029/1999JE001043>
- Goossens, S., Sabaka, T. J., Genova, A., Mazarico, E., Nicholas, J. B., & Neumann, G. A. (2017). Evidence for a low bulk crustal density for Mars from gravity and topography. *Geophysical Research Letters*, 44(15), 7686–7694. <https://doi.org/10.1002/2017GL074172>
- Gries, R. (1983). Oil and gas prospecting beneath Precambrian of foreland thrust plates in Rocky Mountains. *American Association of Petroleum Geologists Bulletin*, 67(1), 1–28. <https://doi.org/10.1306/03b5b696-16d1-11d7-8645000102c1865d>

- Gross, M. R., Gutiérrez-Alonso, G., Bai, T., Wacker, M. A., Collinsworth, K. B., & Behl, R. J. (1997). Influence of mechanical stratigraphy and kinematics on fault scaling relations. *Journal of Structural Geology*, *19*(2), 171–183. [https://doi.org/10.1016/S0191-8141\(96\)00085-5](https://doi.org/10.1016/S0191-8141(96)00085-5)
- Grott, M., & Breuer, D. (2010). On the spatial variability of the martian elastic lithosphere thickness: Evidence for mantle plumes? *Journal of Geophysical Research*, *115*(E3). <https://doi.org/10.1029/2009JE003456>
- Grott, M., Hauber, E., Werner, S. C., Kronberg, P., & Neukum, G. (2007). Mechanical modeling of thrust faults in the Thaumasia region, Mars, and implications for the Noachian heat flux. *Icarus*, *186*(2), 517–526. <https://doi.org/10.1016/j.icarus.2006.10.001>
- Gupta, A., & Scholz, C. H. (2000). A model of normal fault interaction based on observations and theory. *Journal of Structural Geology*, *22*(7), 865–879. [https://doi.org/10.1016/S0191-8141\(00\)00011-0](https://doi.org/10.1016/S0191-8141(00)00011-0)
- Gupta, V. K., Waymire, E. C., & Wang, C. T. (1980). A Representation of an Instantaneous Unit-Hydrograph from Geomorphology. *Water Resources Research*, *16*(5), 855–862. <https://agupubs.onlinelibrary.wiley.com/doi/pdf/10.1029/WR016i005p00855>
- Hauck, S. A. (2002). Thermal and crustal evolution of Mars. *Journal of Geophysical Research*, *107*(E7), 5052. <https://doi.org/10.1029/2001je001801>
- Head, J. W. (2002). Northern lowlands of Mars: Evidence for widespread volcanic flooding and tectonic deformation in the Hesperian Period. *Journal of Geophysical Research*, *107*(E1), 5003. <https://doi.org/10.1029/2000JE001445>
- Herrero-Gil, A., Egea-González, I., Ruiz, J., & Romeo, I. (2019). Structural modeling of lobate scarps in the NW margin of Argyre impact basin, Mars. *Icarus*, *319*(September 2018), 367–380. <https://doi.org/10.1016/j.icarus.2018.09.027>
- Herrero-Gil, A., Ruiz, J., & Romeo, I. (2020a). 3D modeling of planetary lobate scarps: The case of Ogygis Rupes, Mars. *Earth and Planetary Science Letters*, *532*, 116004. <https://doi.org/10.1016/j.epsl.2019.116004>
- Herrero-Gil, A., Ruiz, J., & Romeo, I. (2020b). Lithospheric Contraction on Mars: A 3D Model of the Amenthes Thrust Fault System. *Journal of Geophysical Research: Planets*, *125*(3), 1–17. <https://doi.org/10.1029/2019JE006201>
- Hoogenboom, T., & Smrekar, S. E. (2006). Elastic thickness estimates for the northern lowlands of Mars. *Earth and Planetary Science Letters*, *248*(3–4), 830–839. <https://doi.org/10.1016/j.epsl.2006.06.035>
- Ivanov, M. A., Hiesinger, H., Erkeling, G., & Reiss, D. (2014). Mud volcanism and morphology of impact craters in Utopia Planitia on Mars: Evidence for the ancient ocean. *Icarus*, *228*, 121–140. <https://doi.org/10.1016/j.icarus.2013.09.018>
- Kim, Y. S., & Sanderson, D. J. (2005a). The relationship between displacement and length of faults: A review. *Earth-Science Reviews*, *68*(3–4), 317–334. <https://doi.org/10.1016/j.earscirev.2004.06.003>

- Kim, Y. S., & Sanderson, D. J. (2005b). The relationship between displacement and length of faults: A review. *Earth-Science Reviews*, 68(3–4), 317–334. <https://doi.org/10.1016/j.earscirev.2004.06.003>
- Klimczak, C. (2015). Limits on the brittle strength of planetary lithospheres undergoing global contraction. *Journal of Geophysical Research: Planets*, 120(12), 2135–2151. <https://doi.org/10.1002/2015JE004851>
- Klimczak, C., Kling, C. L., & Byrne, P. K. (2018). Topographic Expressions of Large Thrust Faults on Mars. *Journal of Geophysical Research: Planets*, 123(8), 1973–1995. <https://doi.org/10.1029/2017JE005448>
- Knapmeyer, M., Oberst, J., Hauber, E., Wählisch, M., Deuchler, C., & Wagner, R. (2006). Working models for spatial distribution and level of Mars' seismicity. *Journal of Geophysical Research E: Planets*, 111(11), 1–23. <https://doi.org/10.1029/2006JE002708>
- Manighetti, I., Campillo, M., Sammis, C., Mai, P. M., & King, G. (2005). Evidence for self-similar, triangular slip distributions on earthquakes: Implications for earthquake and fault mechanics. In *Journal of Geophysical Research: Solid Earth* (Vol. 110, Issue 5, pp. 1–25). Blackwell Publishing Ltd. <https://doi.org/10.1029/2004JB003174>
- Manighetti, Isabelle, Caulet, C., De Barros, L., Perrin, C., Cappa, F., & Gaudemer, Y. (2015). Generic along-strike segmentation of Afar normal faults, East Africa: Implications on fault growth and stress heterogeneity on seismogenic fault planes. *Geochemistry, Geophysics, Geosystems*, 16(2), 443–467. <https://doi.org/10.1002/2014GC005691>
- Manighetti, Isabelle, King, G. C. P., Gaudemer, Y., Scholz, C. H., & Doubre, C. (2001). Slip accumulation and lateral propagation of active normal faults in Afar. *Journal of Geophysical Research: Solid Earth*, 106(B7), 13667–13696. <https://doi.org/10.1029/2000jb900471>
- Manighetti, Isabelle, Zigone, D., Campillo, M., & Cotton, F. (2009). Self-similarity of the largest-scale segmentation of the faults: Implications for earthquake behavior. *Earth and Planetary Science Letters*, 288(3–4), 370–381. <https://doi.org/10.1016/j.epsl.2009.09.040>
- Mitra, S. (1990). Fault-propagation folds. Geometry, kinematic evolution, and hydrocarbon traps. *American Association of Petroleum Geologists Bulletin*, 74(6), 921–945. <https://doi.org/10.1306/44B4B680-170A-11D7-8645000102C1865D>
- Montési, L. G. J., & Zuber, M. T. (2003). Clues to the lithospheric structure of Mars from wrinkle ridge sets and localization instability. *Journal of Geophysical Research E: Planets*, 108(6). <https://doi.org/10.1029/2002je001974>
- Mueller, K., & Golombek, M. P. (2004). Compressional Structures on Mars. *Annual Review of Earth and Planetary Sciences*, 32(1), 435–464. <https://doi.org/10.1146/annurev.earth.32.101802.120553>
- Mueller, K., Vidal, A., Robbins, S., Golombek, M. P., & West, C. (2014). Fault and fold growth of the Amenthes uplift: Implications for Late Noachian crustal rheology and heat flow on Mars. *Earth and Planetary Science Letters*, 408, 100–109. <https://doi.org/10.1016/j.epsl.2014.09.047>

- Nahm, A. L., & Schultz, R. A. (2011). Magnitude of global contraction on Mars from analysis of surface faults: Implications for martian thermal history. *Icarus*, *211*(1), 389–400. <https://doi.org/10.1016/j.icarus.2010.11.003>
- Neumann, G. A., Zuber, M. T., Wicczorek, M. A., McGovern, P. J., Lemoine, F. G., & Smith, D. E. (2004). Crustal structure of Mars from gravity and topography. *Journal of Geophysical Research E: Planets*, *109*(8), E08002. <https://doi.org/10.1029/2004JE002262>Nic
- Nicol, A., Watterson, J., Walsh, J. J., & Childs, C. (1996). The shapes, major axis orientations and displacement patterns of fault surfaces. *Journal of Structural Geology*, *18*(2–3), 235–248. [https://doi.org/10.1016/S0191-8141\(96\)80047-2](https://doi.org/10.1016/S0191-8141(96)80047-2)
- Niño, F., Philip, H., & Chéry, J. (1998). The role of bed-parallel slip in the formation of blind thrust faults. *Journal of Structural Geology*, *20*(5), 503–516. [https://doi.org/10.1016/S0191-8141\(97\)00102-8](https://doi.org/10.1016/S0191-8141(97)00102-8)
- Ojha, L., Mazarico, E., & Goossens, S. (2020). Is There a Crustal Thickness Dichotomy on Mars? *The 51st Lunar and Planetary Science Conference*, Abstract #2386. <https://doi.org/10.1126/science.271.5246.184>
- Okubo, C. H., & Schultz, R. A. (2004). Mechanical stratigraphy in the western equatorial region of Mars based on thrust fault-related fold topography and implications for near-surface volatile reservoirs. *Bulletin of the Geological Society of America*, *116*(5–6), 594–605. <https://doi.org/10.1130/B25361.1>
- Peacock, D. C. P., & Sanderson, D. J. (1991). Displacements, segment linkage and relay ramps in normal fault zones. *Journal of Structural Geology*, *13*(6), 721–733. [https://doi.org/10.1016/0191-8141\(91\)90033-F](https://doi.org/10.1016/0191-8141(91)90033-F)
- Peterson, G. A., Johnson, C. L., Byrne, P. K., & Phillips, R. J. (2020). Fault Structure and Origin of Compressional Tectonic Features Within the Smooth Plains on Mercury. *Journal of Geophysical Research: Planets*, *125*(7). <https://doi.org/10.1029/2019JE006183>
- Pickering, G., Peacock, D. C. P., Sanderson, D. J., & Bull, J. M. (1997). Modeling tip zones to predict the throw and length characteristics of faults. *AAPG Bulletin*, *81*(1), 82–99. <https://doi.org/10.1306/522B4299-1727-11D7-8645000102C1865D>
- Polit, A. T., Schultz, R. A., & Soliva, R. (2009). Geometry, displacement-length scaling, and extensional strain of normal faults on Mars with inferences on mechanical stratigraphy of the Martian crust. *Journal of Structural Geology*, *31*(7), 662–673. <https://doi.org/10.1016/j.jsg.2009.03.016>
- Raitala, J., & Kauhanen, K. (1992). Ridge systems related to Martian impact craters. *Earth, Moon and Planets*, *58*(1), 65–78. <https://doi.org/10.1007/BF00058074>
- Roberts, J. H., & Zhong, S. (2006). Degree-1 convection in the Martian mantle and the origin of the hemispheric dichotomy. *Journal of Geophysical Research E: Planets*, *111*(6), E06013. <https://doi.org/10.1029/2005JE002668>
- Ruiz, J., Fernández, C., Gomez-Ortiz, D., Dohm, J. M., López, V., & Tejero, R. (2008). Ancient heat flow, crustal thickness, and lithospheric mantle rheology in the Amenthes region, Mars. *Earth and Planetary Science Letters*, *270*(1–2), 1–12.

<https://doi.org/10.1016/j.epsl.2008.02.015>

- Ruj, T., Komatsu, G., Pondrelli, M., Di Pietro, I., & Pozzobon, R. (2018). Morphometric analysis of a Hesperian aged Martian lobate scarp using high-resolution data. *Journal of Structural Geology*, *113*, 1–9. <https://doi.org/10.1016/j.jsg.2018.04.018>
- Schlische, R. W., Young, S. S., Ackermann, R. V., & Gupta, A. (1996). Geometry and scaling relations of a population of very small rift-related normal faults. *Geology*, *24*(8), 683–686. [https://doi.org/10.1130/0091-7613\(1996\)024<0683:GASROA>2.3.CO;2](https://doi.org/10.1130/0091-7613(1996)024<0683:GASROA>2.3.CO;2)
- Scholz, C. H. (2019). Mechanics of faulting. In *The mechanics of earthquakes and faulting* (pp. 97–165). Cambridge University Press. <https://doi.org/10.1146/annurev.earth.17.1.309>
- Scholz, C. H., & Cowie, P. A. (1990). Determination of total strain from faulting using slip measurements. *Nature*, *346*(6287), 837–839. <https://doi.org/10.1038/346837a0>
- Scholz, Christopher H., & Lawler, T. M. (2004). Slip tapers at the tips of faults and earthquake ruptures. *Geophysical Research Letters*, *31*(21), 1–4. <https://doi.org/10.1029/2004GL021030>
- Schubert, G., Solomon, S. C., Turcotte, D. L., Drake, M. J., & Sleep, N. H. (1992). Origin and thermal evolution of Mars. *Mars*, 147–183. <http://adsabs.harvard.edu/abs/1992mars.conf..147S>
- Schubert, G., & Spohn, T. (1990). Thermal History of Mars and the Sulfur Content of Its Core. *Journal of Geophysical Research*, *95*(B9), 95–104. <https://doi.org/10.1029/JB095iB09p14095>
- Schultz, R. A. (2000). Localization of bedding plane slip and backthrust faults above blind thrust faults: Keys to wrinkle ridge structure. *Journal of Geophysical Research E: Planets*, *105*(E5), 12035–12052. <https://doi.org/10.1029/1999JE001212>
- Schultz, R.A., Fossen, H. (2002) Displacement–length scaling in three dimensions: the importance of aspect ratio and application to deformation bands. *Journal of Structural Geology* *24*, 1389–1411.
- Schultz, R. A., Okubo, C. H., & Wilkins, S. J. (2006). Displacement-length scaling relations for faults on the terrestrial planets. *Journal of Structural Geology*, *28*(12), 2182–2193. <https://doi.org/10.1016/j.jsg.2006.03.034>
- Schultz, R. A., & Watters, T. R. (2001). Forward mechanical modeling of the Amenthes Rupes thrust fault on Mars. *Geophysical Research Letters*, *28*(24), 4659–4662. <https://doi.org/10.1029/2001GL013468>
- Shaw, J. H., Novoa, E., & Connors, C. D. (2004). Structural controls on growth stratigraphy in contractional fault-related folds. *Thrust Tectonics and Hydrocarbon Systems: AAPG Memoir*, *82*, 400–412. [http://geology.wlu.edu/connors/publications/Shaw\\_AAPG\\_Mem82.PDF](http://geology.wlu.edu/connors/publications/Shaw_AAPG_Mem82.PDF)
- Solomon, S. C. (1978). On volcanism and thermal tectonics on one-plate planets. *Geophysical Research Letters*, *5*(6), 461–464. <https://doi.org/10.1029/GL005i006p00461>

- Stirling, M. W., Wesnousky, S. G., & Shimazaki, K. (1996). Fault trace complexity, cumulative slip, and the shape of the magnitude-frequency distribution for strike-slip faults: A global survey. *Geophysical Journal International*, *124*(3), 833–868. <https://doi.org/10.1111/j.1365-246X.1996.tb05641.x>
- Stockwell, R. G., Mansinha, L., & Lowe, R. P. (1996). Localization of the complex spectrum: the s transform. *IEEE Transactions on Signal Processing*, *44*(4), 998–1001. <https://doi.org/10.1109/78.492555>
- Strom, R. G., Trask, N. J., & Guest, J. E. (1975). Tectonism and volcanism on Mercury. *Journal of Geophysical Research*, *80*(17), 2478–2507. <https://doi.org/10.1029/JB080i017p02478>
- Suppe, J., & Medwedeff, D. a. (1990). Geometry and kinematics of fault-propagation folding. *Eclogae Geologicae Helveticae*, *454*(SEPTEMBER 1983), 409–454. <https://doi.org/10.5169/seals-166595>
- Tanaka, K. L., Skinner, J. A., & Hare, T. M. (2005). Geologic Map of the Northern Plains of Mars. 1:15,000,000, US Geological Survey Scientific Investigations Map 2888. In *U.S. Geological Survey Geologic Investigations: Vol. SIM 2888*. <https://pubs.usgs.gov/sim/2005/2888/>
- Tanaka, K. L., Skinner, J. A., Hare, T. M., Joyal, T., & Wenker, A. (2003). Resurfacing history of the northern plains of Mars based on geologic mapping of Mars Global Surveyor data. *Journal of Geophysical Research: Planets*, *108*(4). <https://doi.org/10.1029/2002je001908>
- Watters, T. R. (1988). Wrinkle ridge assemblages on the terrestrial planets. *Journal of Geophysical Research: Solid Earth*, *93*(B9), 10236–10254. <https://doi.org/10.1029/JB093iB09p10236>
- Watters, T. R. (2004). Elastic dislocation modeling of wrinkle ridges on Mars. *Icarus*, *171*(2), 284–294. <https://doi.org/10.1016/j.icarus.2004.05.024>
- Watters, T. R., McGovern, P. J., & Irwin, R. P. (2007). Hemispheres apart: The crustal dichotomy on Mars. *Annual Review of Earth and Planetary Sciences*, *35*, 621–652. <https://doi.org/10.1146/annurev.earth.35.031306.140220>
- Watters, T. R., & Robinson, M. S. (1999). Lobate scarps and the Martian crustal dichotomy. *Journal of Geophysical Research E: Planets*, *104*(E8), 18981–18990. <https://doi.org/10.1029/1998JE001007>
- Watters, T. R., Robinson, M. S., & Cook, A. C. (1998). Topography of lobate scarps on Mercury: New constraints on the planet's contraction. *Geology*, *26*(11), 991–994. [https://doi.org/10.1130/0091-7613\(1998\)026<0991:TOLSOM>2.3.CO;2](https://doi.org/10.1130/0091-7613(1998)026<0991:TOLSOM>2.3.CO;2)
- Watters, T. R., Schultz, R. A., & Robinson, M. S. (2000). Displacement length relations of thrust faults associated with lobate scarps on mercury and mars comparison with terrestrial faults. *Geophysical Research Letters*, *27*(22), 3659–3662. <https://doi.org/10.1029/2000GL011554>
- Wesnousky, S. G. (1988). Seismological and structural evolution of strike-slip faults. *Nature*, *335*(6188), 340–343. <https://doi.org/10.1038/335340a0>
- Wickham, J. (1995). Fault displacement-gradient folds and the structure at Lost Hills, California

- (U.S.A.). *Journal of Structural Geology*, 17(9), 1293–1302. [https://doi.org/10.1016/0191-8141\(95\)00029-D](https://doi.org/10.1016/0191-8141(95)00029-D)
- Wilkins, S. J., & Gross, M. R. (2002). Normal fault growth in layered rocks at Split Mountain, Utah: Influence of mechanical stratigraphy on dip linkage, fault restriction and fault scaling. *Journal of Structural Geology*, 24(9), 1413–1429. [https://doi.org/10.1016/S0191-8141\(01\)00154-7](https://doi.org/10.1016/S0191-8141(01)00154-7)
- Williams, G., & Chapman, T. (1983). Strains developed in the hangingwalls of thrusts due to their slip/propagation rate: a dislocation model. *Journal of Structural Geology*, 5(6), 563–571. [https://ac.els-cdn.com/0191814183900688/1-s2.0-0191814183900688-main.pdf?\\_tid=dfaa0a2a-051b-11e8-abb6-00000aacb360&acdnat=1517247971\\_940b53af9150faa11867fefbd538e3ff](https://ac.els-cdn.com/0191814183900688/1-s2.0-0191814183900688-main.pdf?_tid=dfaa0a2a-051b-11e8-abb6-00000aacb360&acdnat=1517247971_940b53af9150faa11867fefbd538e3ff)
- Wojtal, S. F. (1996). Changes in fault displacement populations correlated to linkage between faults. *Journal of Structural Geology*, 18(2–3), 265–279. [https://doi.org/10.1016/S0191-8141\(96\)80049-6](https://doi.org/10.1016/S0191-8141(96)80049-6)
- Zhong, S., & Zuber, M. T. (2001). Degree-1 mantle convection and the crustal dichotomy on Mars. *Earth and Planetary Science Letters*, 189(1–2), 75–84. [https://doi.org/10.1016/S0012-821X\(01\)00345-4](https://doi.org/10.1016/S0012-821X(01)00345-4)
- Zuber, M. T. (2000). Internal structure and early thermal evolution of Mars from Mars global surveyor topography and gravity. *Science*, 287(5459), 1788–1793. <https://doi.org/10.1126/science.287.5459.1788>

## **CHAPTER 3: Determination of timing of large-scale crustal shortening structures on Mars using crater age dating**

Rachel M. Atkins<sup>1</sup> and Paul K. Byrne<sup>1\*</sup>

<sup>1</sup>North Carolina State University, Raleigh, NC, USA,

\*Now at Department of Earth and Planetary Sciences, Washington University in St. Louis, St. Louis, MO, USA

Keywords: Mars, buffered crater counting (BCC), tectonics, fluvial, geomorphology, lobate scarp

Key Points:

- Buffered crater counting was used to provide absolute model ages for 28 globally distributed Martian thrust faults-related folds
- Results indicate that global contraction was already underway by the Early Noachian, but was limited to no later than the Noachian–Hesperian boundary
- Several of these scarps have collocated fluvial systems, but the relative timing of these two phenomena is not clear

## 1. Abstract

The surface of Mars exhibits a population of globally distributed lobate scarps interpreted as thrust-related fault propagation folds, where the hanging wall is folded and produces a steep front scarp and gentle sloping backscarp. These tectonic landforms have been taken to be the result of global contraction which occurred as the internal heat of the planet was lost to space. This study investigates the timing of these structures using the buffered crater counting technique to place quantitative constraints on models for the tectonic evolution of Mars. We selected 28 faults for which the folded hanging wall has discernable interactions with impact craters of diameter 1 km or larger. Under the assumption that undeformed impact craters that erase part of the scarp likely post-date the most recent scarp movement, this population of craters was used with successive buffers around the mapped scarp to determine an absolute model age for the cessation of movement on these faults. Absolute model ages found with the Hartmann and Neukum/Ivanov production functions and chronologies were found to be  $3.8_{-0.02}^{+0.01}$  and  $3.9_{-0.01}^{+0.01}$  Ga, respectively. These results suggest that the most recent fault activity in the southern highlands was limited to earlier than the Noachian–Hesperian boundary. Our findings provide quantitative evidence for global contraction having been underway by the Early Noachian  $\sim 4.3$  Ga, in agreement with, but much more expansive in scale than, earlier efforts to acquire absolute model ages that considered only a handful of tectonic structures or those restricted to a particular location or region.

## 2. Introduction

Mars has experienced substantial tectonic deformation as demonstrated by the landforms on its surface. The widespread distribution of normal and thrust faults across the planet indicate

that both extensional and compressional stresses have acted on the planet (Hauck & Phillips, 2002; Solomon, 1978). On the basis of their preferential orientations and localized geographic occurrences, extensional features are often tied to local- or region-scale processes, such as the emplacement of the Tharsis rise and subsidence of volcanic and/or basin infill (e.g., Banerdt et al., 1992; Solomon & Chaiken, 1976). Conversely, the global distribution of crustal shortening features (e.g., Watters et al., 1988) is thought to reflect a planet-wide process such as global contraction from secular interior cooling.

On the basis of similar structures on Earth, shortening features are produced by thrust faults and, on rocky planets including Mars and Mercury, are termed “wrinkle ridges” and “lobate scarps”, with the major difference between the two features being their size and symmetry. Wrinkle ridges have vertical relief on the order of tens to hundreds of meters and are symmetric in cross section (Mueller & Golombek, 2004). In contrast, lobate scarps have relief from hundreds to thousands of meters (Watters & Robinson, 1999; Knapmeyer et al., 2006; Klimczak et al., 2018) and tend to present one steep scarp and one gently-sloping back scarp (Figure 2.1 in Chapter 2). On the basis of comparison with morphologically similar Terran features, lobate scarps are interpreted to be antiformal displacement-gradient folds (Byrne et al., 2018) that form atop thrust faults (Mitra, 1990; Suppe & Medwedeff, 1990; Wickham, 1995; Williams & Chapman, 1983). Although at broad scales (e.g., at 1:500,000) these scarps appear to be a single structure, they are in fact composed of several faults that have linked to form segments in their present, longer form (e.g., Dawers & Anders, 1995; Klimczak et al., 2018). Planetary bodies that lack a substantial atmosphere, as is the case for Mars, exhibit slow erosion rates in contrast to planets like Earth (Golombek & Bridges, 2000), and so topography can be taken to reflect processes that occur at depth more directly. At these view scales, landform shape

and maximum vertical relief ( $t_{\max}$ ) can provide a first-order quantification of fault displacement (Klimczak et al., 2018).

Thermal evolution models of Mars predict that interior cooling of the planet began in the Early Noachian and continues through to the present (Andrews-Hanna et al., 2008; Schubert et al., 1992; Schubert & Spohn, 1990). However, the distribution of wrinkle ridges is concentrated primarily in volcanic plains units dated to be Early Hesperian in age, implying a preferential formation of these landforms during that time (Mueller & Golombek, 2004; Schubert et al., 1992). The formation of wrinkle ridges is attributed primarily to volcanic subsidence due to their preferential locations in the volcanic smooth plains units (Solomon, 1978; Watters, 1988, 2004). In contrast, that lobate scarps are globally distributed has been broadly cited as geological evidence of planet-wide, horizontally compressional stresses (Schubert et al., 1992; Schubert & Spohn, 1990). This finding thus suggests an enhanced period of contraction during the late Noachian to Early Hesperian (Nahm & Schultz, 2011; Schubert et al., 1992).

## 2.1 Dating surface features

The primary dating technique for estimating a modeled absolute age of an extraterrestrial planetary surface employs statistical analyses of crater size–frequency distributions (CSFDs). This method operates under the basic assumption that the population of craters on a given surface increases through time as craters accumulate, so older surfaces will have accumulated more craters than younger surfaces. Since smaller impactors are more numerous than larger objects in the Solar System, and the relative proportion of larger impactors diminishes over time, the number of smaller craters is always greater than that of larger diameter craters on a surface. Once crater counts are acquired (consisting of a number of craters for which diameter values are

recorded), a rate of crater accumulation, also known as a crater production function (PF), can be fit to binned CSFD data to calculate an approximate relative age. For example, all things being equal, older units are characterized by a range of crater sizes and a greater overall number of craters than younger units, which preferentially host fewer and smaller craters. The conventional method for reporting crater frequencies normalizes the number of craters of a given diameter  $D$  (in km) or greater to some normalized area (often, although not always, of  $10^6 \text{ km}^2$ : Crater Analysis Techniques Working Group, 1979). Thus,  $N(2) = 250$  means that there are 250 craters with a diameter of 2 km or greater over some normalized area (e.g.,  $10^6 \text{ km}^2$ ). However, although this metric is often reported as a means for comparison between counts in different areas, less weight should be put on these singular values than on the size–frequency distributions as a whole (e.g., Fassett & Head, 2008).

Once a relative age has been established, an absolute model age of a surface can be determined using a chronology function (CF) specific to that planetary body. Radiometric dating of lunar rock samples from the Apollo missions provided direct age determinations for select portions of the lunar surface that were correlated with mapped CSFDs. These ages were then used as a basis for extrapolating chronology functions for Mercury and Mars (e.g., Hartmann & Neukum, 2001), allowing absolute model ages to be applied to the boundaries between geological epochs on those worlds, which had already been formulated on the basis of relative dating (e.g., through cross-cutting relations) (e.g., Hartmann, 2005). Both PFs and CFs can be used to compare model surface ages of Mars, Mercury, and the Moon when scaled to specific target body properties (e.g., rock strength, gravity, and proximity to other large bodies), and accounting for the influence that target body properties have on impactor characteristics (e.g., velocity, size, and frequency of impacts) (Werner & Tanaka, 2011). For this work, we use the

geologic time period boundaries defined by Tanaka (1986) using  $N(D)$  counts and the corresponding absolute ages calculated by Fassett & Head (2008) for both the Neukum/Ivanov and Hartmann chronology systems for Mars (Table S1, Appendix J).

Early attempts to apply model ages to extraterrestrial surface features began with investigating Martian valley networks with images from NASA's Viking orbiter images (that have resolutions of 125–300 m/pixel). Studies that counted craters superposing valley networks found evidence that most such networks pre-date the Noachian–Hesperian boundary (Pieri, 1980; Carr and Clow, 1981). The availability of higher-resolution image data prompted further investigations of these small-scale features (Tanaka, 1982), and later work attempted to expand count areas using the principle of superposition between valley networks and the units that they incise (e.g., Werner & Tanaka, 2011). That is, where a valley network was seen to have incised a given geological unit, then the fluvial activity must post-date the emplacement of that unit. As geological units occupy greater surface areas than the smaller-scale valleys that incise them, crater size–frequency distributions were shown to be effective for establishing a model date for the timing of valley formation and thus can be used to place upper bounds on the timing of fluvial activity generally (e.g., Carr, 1995).

However, Fassett and Head (2008) noted that this process requires accurate age assessments of all geological units (from CSFD methods), accurate and complete determination of unit boundaries and extents, and a precise understanding of the stratigraphic relationships between valley networks and the units which they incise. Since these processes involve subjectivity and inherent difficulties in satisfying all of the above conditions precisely, Fassett and Head (2008) developed the buffered crater counting (BCC) methodology. This method adapts an early “crater line-count method” (Tanaka, 1982) and relies solely on the spatial

relationship of valley networks to surrounding impact craters. For example, features that have contacts with units that may be gradational, have superposed surficial units such as alluvial fans or dunes, or that suffer from poor illumination conditions can be difficult to map precisely and stratigraphic relationships between surrounding units may be difficult to define (see Figure 4 in Fassett & Head, 2008). Without clear, replicable procedures for mapping such features and their stratigraphic relationships with surrounding units, along with unit extents, errors resulting from count areas that are too large or too small can be introduced to the crater counting process (Fassett & Head, 2008).

The BCC method involves mapping only the linear feature of interest and successive buffers around the feature are created using the diameter of craters that superpose the landform of interest. The BCC technique thus minimizes potential errors and assumptions that also incorporate stratigraphic relationships to geological units and their geographic extents. Specifically, by eliminating the need to map surrounding units and emphasizing the careful mapping of the features themselves (e.g., fault scarps or fluvial networks), assumptions made about stratigraphic relationships between units, and the errors that this can introduce to results, can be minimized. The BCC technique has been employed in several studies to provide model age constraints on various geological features on Mars, including fluvial valleys (e.g., Fassett and Head, 2008; Hoke and Hynek, 2009; Bouley et al., 2010) and graben (e.g., Wichman and Schultz, 1989; Kneissl et al., 2015). In addition to Martian surface features, this method has also been used to date lobate scarps on Mercury (Fegan et al., 2017; Galluzzi et al., 2019; Giacomini et al., 2020), along with wrinkle ridges (Yue et al., 2017) and lobate scarps (Senthil Kumar et al., 2016; van der Bogert et al., 2018) on the Moon.

In an effort to place firmer estimates on the timing of the global contraction of Mars, here we examine the age of lobate scarps on the planet that have been attributed to this process. In this study, we investigate the timing of major crustal shortening structures on Mars using the BCC technique to acquire absolute model ages for select surface scarps. Using morphometric data (i.e., maximum fault displacement–length relationships) to assess similar fault behavior, we also relate the scarps for which we acquire absolute model ages with other studied faults for a more broad understanding of the timing of global contraction. Placing a constraint on the timing of contraction based on observable features will, in turn, help refine thermal evolution models for Mars.

### **3. Methods**

#### **3.1 Mapping**

Fault scarps were mapped using the merged digital elevation model (DEM) from the Mars Orbiter Laser Altimeter (MOLA) and High-Resolution Stereo Camera (HRSC) (200 m/px; 3m vertical accuracy), together with the Thermal Emission Imaging System (THEMIS) Global Day-IR Mosaic (100 m/px) and Context Camera (CTX) global image mosaic (5m/px). Candidate scarps were selected based on their discernable interactions with impact craters (i.e., the crater clearly exhibits deformation due to faults and thus pre-dates the fault, or conversely the crater deforms the scarp and thus post-dates faulting).

For each scarp, a polygon was drawn in ESRI's ArcMap 10.7.1 at a view scale of 1:80,000 to encompass the highest and lowest elevation difference along the fault scarp, thus providing a counting area for the BCC method (described further in section 4.2, below). Glacial activity (e.g., Dickson et al., 2012) may bias crater retention ages at latitudes above 30° in both

hemispheres, because glaciation or other surface processes may preferentially erase and/or infill small, shallow craters and thus return artificially younger model ages (Neukum et al., 2004; Hauber et al., 2005). Therefore, this analysis is limited to faults that are situated within 30° of the equator. As a result of this geographic restriction, the large-scale crustal shortening structures included in this study ( $n = 28$ , Table S2, Appendix K) are all located in the southern highlands (Figure 3.1). These structures range in length from 60 to 610 km and are all located in Noachian highland units (early, middle and late), except for a single structure which is located in an early Hesperian volcanic unit (Tanaka et al., 2014). The studied landforms are distributed throughout four major physiographic regions including Terra Sirenum, Arabia Terra, Noachis Terra, and Terra Cimmeria. Further, there were no observed spatial associations (e.g., preferential orientations) with major landforms in the highlands that encompass the Tharsis region, in Valles Marineris, or in any of the major basins within 30° N or S of the equator (e.g. Isidis).

On planetary bodies such as Mars that lack a substantial atmosphere, erosion rates are slow enough that topographic denudation is minimized and indeed is almost negligible at large scales (Golombek & Bridges, 2000). Thus, measurements of relief can be taken as essentially direct representations of tectonic processes occurring at depth. Here, we use vertical surface relief as a proxy for fault throw ( $t_{\max}$ ), which can then be used to calculate maximum fault displacement ( $D_{\max}$ ) using the relation  $D_{\max} = h/\sin(\alpha)$ , where  $\alpha$  is an assumed fault dip angle. Per Andersonian fault theory for thrust faults (Anderson, 1942), a fault dip angle ( $\alpha$ ) of 30° was adopted in our calculation of maximum displacement. Maximum relief ( $t_{\max}$ ) along each structure was assessed by constructing transects along its length. Variations in the ratio of maximum fault displacement ( $D_{\max}$ ) and length ( $L$ ) ratio for a given population of faults is common and may indicate linkage between adjacent fault systems (e.g. Cartwright et al., 1995; Gallen et al., 2014),

fault interactions that inhibit the lateral propagation of the tips (Nicol et al., 1996; Ellis & Barnes, 2015; Gupta & Scholz, 2000), and limits on fault growth due to the finite thickness of the brittle layer (e.g., Cartwright et al., 1995; Dawers & Anders, 1995; Wojtal, 1996; Bohnenstiehl & Kleinrock, 2000). Here, we compare  $D_{\max}/L$  ratios from Chapter 2 to determine if these ratios are statistically similar to this study (Chapter 3) and if so, we can assume that they exhibit similar fault characteristics and thus both come from the same population.

A global database of Martian craters with diameters  $\geq 1$  km (Robbins & Hynek, 2012) was used as an input for identifying and selecting craters interacting with (i.e., being physically proximal to and cross-cutting) our study fault scarps. To determine the stratigraphic relationship between a crater and a given fault scarp, only those craters for which the rim is situated within one crater radius of the scarp were included in this study. Undeformed craters were assumed to post-date the most recent resolvable activity of a given scarp, and were the population of craters used for this work. Under this assumption, then, the use of this crater–scarp relationship returns a minimum bound on the timing of faulting.

### 3.2 Crater Counts and Area calculations

For calculating absolute model ages of narrow surface features that occupy relatively small ( $\sim 200$  km<sup>2</sup>) areas, as is the case for the thrust fault-related scarps considered here, the BCC method was used to place minimum bounds on the timing of fault activity. The scarp buffers were derived under the assumption that a stratigraphic relationship can be determined when a crater rim is physically located in the same space as a fault scarp, which is termed the ‘simple approach’ to determining crater–feature interactions (e.g., Fassett & Head, 2008; Kneissl et al., 2015). Therefore, the buffer size ( $S_{\text{buffer}}$ ) around each scarp was calculated by  $S_{\text{buffer}} = 1R_{\text{crater}} +$

$0.5W_{\text{scarp}}$ , where  $R_{\text{crater}}$  is the radius of the crater being used for the calculation and the  $W_{\text{scarp}}$  term incorporates the area encompassing the scarp, since the buffer is applied to each side of the fault trace (Figure 3.2). The scarp area was delineated using a combination of THEMIS imagery and the MOLA-HRSC DEM to determine slope changes at the top and bottom of the scarp. The buffered area ( $S_{\text{buffer}}$ ) was re-calculated for each crater that, was determined to superpose and thus post-date the scarp based on cross-cutting relations. The recalculated  $S_{\text{buffer}}$  was then used to determine a frequency of craters of a minimum diameter per unit area,  $N(D)$ . Crater counts and buffer areas were calculated and exported using the CraterTools 2.1 plug-in for ArcMap (Kneissl et al., 2011).

Once cumulative crater frequencies were acquired (i.e., the total number of craters binned by crater diameter), the Craterstats II program (Michael & Neukum, 2010) was used to calculate associated absolute model ages. We report two commonly used ages: the “Hartmann” age calculated with the production and chronology functions given by Hartmann (2005), and the “Neukum/Ivanov” age, which is based on the production and chronology functions of Ivanov (2001). Epoch boundaries were defined by Michael (2013).

#### **4. Results**

For this study, we identified 28 fault scarps for which crater counts were performed (Figure 3.1). These scarps range in length from 60 km to 610 km, with a median length of 157 km. Maximum surface displacements ( $t_{\text{max}}$ ) are between 162 m and  $1,382 \text{ m} \pm 3 \text{ m}$  (vertical accuracy), with a median  $t_{\text{max}}$  of 489 m. Assuming an underlying fault dip angle of  $30^\circ$  (e.g., Klimczak et al., 2018), maximum fault displacement versus length (i.e.,  $D_{\text{max}}/L$ ) ratios were found to range from  $2.1 \times 10^{-3}$  to  $18.8 \times 10^{-3}$ , with an average  $D_{\text{max}}/L$  of  $7.2 \times 10^{-3} \pm 1.3 \times 10^{-3}$  for this

study population. Population statistics are summarized in Table 1 and individual fault characteristics are included in Table S2 (Appendix K).

#### 4.1 Buffered Crater Counts

The surface ages of individual faults and all faults in aggregate, were calculated using the ‘simple approach’ to buffered crater counting that includes, craters whose rims directly superpose fault scarps (Figure 3.3, see section 5.4 for further discussion of errors). Individual Hartmann ages range from 4.2 to 3.5 Ga for this population; most such structures therefore have absolute model ages that fall within the Early to Late Noachian for this chronology. Absolute model ages calculated from the Neukum/Ivanov chronology range from 4.4 to 3.6 Ga, falling between the Early Noachian and Early Hesperian.

The spatial distributions of fault ages are shown in Figure 3.4. The number of craters used to determine ages for individual scarps ranged from 2 to 13; thus, although absolute model ages were determined for individual faults, those ages are necessarily derived from only a very small number of craters. Combining the crater size–frequency distributions and areas of all 28 scarps therefore provides a more robust dataset for statistical power. Taken in aggregate, then, a total of 148 craters were used to determine model ages for the buffered area that encompasses all 28 faults. Ages for the aggregate counts are  $3.8^{+0.01}_{-0.02}$  Ga (per the Hartmann production function and chronology function), and  $3.9^{+0.01}_{-0.01}$  Ga (for the Neukum/Ivanov PF and CF) (Figure 3.5). As a whole, the timing of the most recent fault activity on these structures appears to have been in the mid- to late Noachian (red squares in Figure 3.3).

## 5. Discussion

An overview of the results that places them in context with earlier work that focused on the thermal and tectonic evolution of Mars is presented first, followed by a review of how this study provides further constraints on the timing of Martian global contraction. Preliminary evidence for the co-evolution of faults and fluvial features in the southern highlands is then presented, with the potential for providing additional information regarding the timing of fluvial activity in these regions.

### 5.1 Timing constraints on the cessation of large-scale faulting

Assaying cross-cutting relations between 148 craters and 28 thrust fault scarps in the Martian highlands returned aggregate scarp ages of  $3.8_{-0.02}^{+0.01}$  Ga and  $3.9_{-0.01}^{+0.01}$  Ga for the Hartmann and Neukum/Ivanov models, respectively. This finding indicates a cessation of large-scale thrust fault activity—at least the shortening strain that can be resolved with THEMIS and CTX imagery—by the mid- to late Noachian. Under the assumption that these broadly distributed thrust faults result from global contraction, this finding supports thermal models that predict that the majority of secular cooling occurred early in Mars' history (see section 6.2).

Although observed differences in faults investigated in Chapter 2 motivated this work, those faults were also selected based on their *lack* of superposed impact craters to allow for in-depth morphometric analyses of surface displacement along the length of a given fault scarp. Thus, the second sample of 28 fault scarps was selected for this study, but with a different driving criterion: that these scarps *are required* to have superposed craters. To establish that the faults considered here are representative of those investigated in Chapter 2,  $D_{\max}/L$  values of both sets of structures were compared (Figure 3.6).

It is found that in terms of the  $D_{\max}/L$  metric, the faults assessed in this study are statistically indistinguishable from those situated in the Martian highlands investigated in the previous chapter ( $n = 25$ ) (Figure 3.6). Although there is a difference in aggregate  $D_{\max}/L$  ratio between faults in the northern lowland and southern highlands, the faults used for this study (all of which were sampled from the southern highlands) exhibit statistically similar ratios to highland faults studied in Chapter 2. Therefore, although the buffered crater counting technique cannot be applied to date faults that lack direct cross-cutting relations with impact craters, we can infer that, because their morphometric characteristics are similar, all 53 faults—the 28 in this study and the 25 highland structures from Chapter 2 likely come from the same population and result from the same process. Further, if observed differences in  $D_{\max}/L$  ratios from Chapter 2 can be accounted for by shallower fault dip angles (see section 5.1 in Chapter 2), *all* faults in Chapter 2 and this analysis can be taken to be from the same population—that is, thrust fault-related scarps in both the southern highlands and northern lowlands ( $n = 77$ ).

## 5.2 Geological observations as constraints for thermal evolution models

In the absence of direct, in situ data, planetary thermal evolution models have been used to place constraints on estimates for the physical properties of terrestrial bodies through time. These models use parameters with various ranges to produce optimized scenarios that are capable of matching present-day, observable surface features (e.g., volcanic and tectonic landforms) as well as inferred near-surface conditions (e.g., crustal thickness). For example, through studying the timing and depth of faulting, estimates on the depth of the brittle–ductile transition (BDT) zone can be calculated at a specific time in a planet’s evolution that must be then satisfied by these models.

The thermal evolution of Mercury has been investigated extensively using early orbital observations from the Mariner 10 spacecraft (e.g., Strom et al., 1975; Solomon, 1977; Hauck et al., 2004) and later with data from the MESSENGER spacecraft (e.g., Michel et al., 2013; Tosi et al., 2013; Giacomini et al., 2015; Fegan et al., 2017; Giacomini et al., 2020). Early thermochemical models incorporated interior structure and surface composition (e.g., Grott et al., 2011), with later work also taking into account proposed volcanic and tectonic histories derived from geological investigations of surface features (e.g., Tosi et al., 2013; Michel et al., 2013). Continued, detailed geological investigations of morphometric characteristics and the formation timing of surface features, such as lobate scarps, provided fault penetration depths that offered constraints on estimates for the spatial and temporal location of the brittle–ductile transition zone within Mercury, which in turn helped improve parameterized thermal evolution models (Giacomini et al., 2015; Fegan et al., 2017; Giacomini et al., 2020). Further, model-based estimations of Mercury’s planetary radius decrease as the result of global contraction had been estimated to be between 3 and 7 km (Dombard & Hauck, 2008). However, this estimate was found to be closer to 5–7 km through investigations of ~6,000 globally distributed lobate scarps and wrinkle ridges, some of which were part of fault systems over 1,800 km long (Byrne et al., 2014), and even higher once rock mechanics properties were taken into account (Byrne et al., 2018). These findings emphasized the importance of incorporating geophysical observations into thermal evolution models.

Early thermal evolution models for Mars used topography and gravity measurements (Zuber et al., 2000), geochemical data (Hauck & Phillips, 2002), or radioisotopes from meteorites and their extrapolated concentrations throughout the planet’s evolution (Schubert & Spohn, 1990; Bhatia et al., 2016). More recent models incorporate geophysical information (e.g.,

crustal thicknesses derived from topography and Bouguer and free-air gravity data) (e.g., Plesa et al., 2018). However, some parameters are often derived from observations of localized features, such as inferred mechanical lithospheric thickness values determined from studies of Mars' polar regions (e.g., Wieczorek, 2008). The most recent iterations of thermal evolution models of Mars carefully consider the impact of crustal composition including water content (e.g., Parro et al., 2017; Jimenez-Diaz et al., 2021), and even infer a thermal and rheological history from exploring tidal interactions with its closest satellite, Phobos (Samuel et al., 2019). Importantly, these thermal evolution models rely on geological inputs for the timing of global contraction, a phase in Mars' thermal evolution when cooling started to outpace interior heating.

Geological investigations of lobate scarps and wrinkle ridges laid the groundwork for obtaining estimates of the timing of global contraction resulting from the onset of secular cooling. Anderson et al. (2001) used stratigraphic and crosscutting relationships of tectonic features (namely graben and wrinkle ridges) that were mapped using Viking imagery with geological units that had been dated previously with CSFDs (Tanaka, 1986) to better understand Mars' tectonic history. Anderson and others (2001) identified multiple stages of punctuated, localized shortening related to Tharsis and other regions, but found that the majority of lobate scarps formed in the Late Noachian to Early Hesperian units. These results were determined with geological boundaries mapped at a scale of 1:15,000,000 and utilizing Viking imagery and structures restricted to the western hemisphere, in contrast to the current study that uses faults mapped at 1:80,000 scale and THEMIS/CTX imagery. Building on the work of Anderson et al. (2001), our study was able to refine the timing of thrust faulting globally through the use of higher resolution data and more targeted investigation of the structures themselves (in contrast to

dating geological units as done previously by Anderson et al., 2001), and restrict their formation to the Noachian–Hesperian boundary.

More recently, Ruj et al. (2019) investigated a small cluster of tectonic structures (including lobate scarps, wrinkle ridges, and graben) in Northern Noachis Terra and central/southern Terra Sabaea using THEMIS imagery and both the BCC and CSFD techniques. Those researchers only found absolute model ages for two lobate scarps, but acquired dates similar to what we find here: ~3.6–3.5 Gyr old (i.e., Late Noachian to Early Hesperian). The results of our study are therefore consistent with previous work that placed global contraction relatively early in Mars' history (Anderson et al., 2001; Ruj et al., 2019). But, by including many more scarps with a far wider geographic distribution across all longitudes and at latitudes on Mars for which crater counts can reliably be applied, we show that crustal shortening at a *global* scale on Mars was underway prior to the Early Hesperian.

### 5.3 Fluvial interactions

In several places, fluvial–tectonic superpositions were observed. Records of Mars' hydrological past are preserved in features interpreted as fluvial channels and that are commonly grouped into two distinct categories: small-scale valley networks, and large-scale outflow channels (Carr & Clow, 1981). Valley networks exhibit V-shaped cross-sectional channels, typical widths of 1–10 km, median depths of about 80 m, and characteristic lengths of less than a few hundred kilometers (Fassett & Head, 2008, Irwin et al., 2005). Valley networks often resemble Terran drainage networks with dendritic morphologies, interconnected with branching tributaries, although Martian valleys tend to exhibit lower drainage densities compared with their

counterparts on Earth (Carr & Chuang, 1997; Hynek & Phillips, 2003; Hynek et al., 2010; Seybold et al., 2017; Seybold et al., 2018).

These observations, together with the finding that many Martian valley networks initiate at or near topographic divides (e.g., Irwin & Howard, 2002), suggest that at least some of the fluvial features observed on Mars formed through precipitation and overland flow (Baker et al., 1983; Howard et al., 2005; Irwin et al., 2005; Hynek et al., 2010). Thus, the timing of valley networks gives a valuable insight into when Mars' atmosphere was sufficiently dense, and the surface temperature warm enough, to make available and allow for sufficient water on the Martian surface needed to carve valleys. Results from buffered crater counting suggest that most valley network formation ended around the Noachian–Hesperian boundary (Fassett & Head, 2008; Carr & Head, 2010).

Eight faults investigated in this study show evidence of valley network incision (Figure 3.7). To explore the agreement of paleo-flow direction with present-day, uplifted topography, a hydrologic flow analysis was performed. If fluvial incision clearly pre- or post-dates tectonic uplift, this could provide further evidence to constrain the timing of the formation of valley networks. The cratered topography on these scarps was “filled” using the ‘Fill Sinks’ function within ArcGIS to simulate a pre-impact-event surface, and to also create an interconnected network of modeled streams. Then, D8 flow directions (i.e., water may be routed in one of eight cardinal directions across a surface) and a minimum of 1,000 DEM cells (40 km<sup>2</sup>) was used as a stream initiation threshold (i.e., a stream exists when a minimum flow accumulation of 1,000 contributing cells is reached) in order to delineate a drainage network and determine the locations and directions of streams as they would appear on the landscape today. If visible valley networks pre-dated topographic uplift, it would be only through chance that they would align

with the present-day down-slope topography and delineated drainage network. Further, if valley networks pre-dated uplift, we might expect discontinuous network morphologies if the uplift caused the headwaters to become disconnected to the downstream drainage network.

Alternatively, if valley networks post-dated the cessation of uplift, it would be expected that visible valley networks would be co-located with and oriented in the same down-slope direction as the delineated drainage and, where the topographic gradient changes from steep to flat, that alluvial fans or deltas may be present.

Using indicators of paleo-flow directions such as channel width increasing downstream, and the direction of branching tributaries along with stratigraphic relationships (e.g., Irwin et al., 2008; Seybold et al., 2018), those valley systems in Figures 3.7a, c, and d all appear to have developed an approximate paleo-flow direction from southwest to northeast, which is in agreement with the present-day topography as indicated by the modeled drainage networks. All of these networks appear to cut across the drainage divide formed by the uplift. However, when channelized networks encounter a broad, flat-laying area (e.g., Figure 3.7a), evidence of these networks rapidly depositing their sediment loads and forming alluvial fans or deltas is lacking.

Thus, although it is possible that evidence for these fans and deltas has since been eroded away, it may also be the case that such deposits never existed because the valley networks were abandoned during uplift and/or that alluvial fans or deltas did not develop because sediment supply was too low. Further, while the modeled drainage in Figure 3.7a cross-cuts the fault scarp, there is no visible evidence of channelization across the topographic divide formed by the uplifted topography (i.e., when DEM transitions from red/yellow to blue/purple from southwest to northeast across the fault), providing additional evidence that valleys did not fully post-date uplift (e.g., Howard et al., 2005). It may also be the case that for these particular instances, the

scarp and valley networks co-evolved, with valley incision and uplift occurring at approximately the same time such that no single morphological indicator of relative timing is available because none was formed. The co-evolution of global contraction-related fault scarps and valley networks is in alignment with the proposed timing of valley networks in the southern highlands as between the Late Noachian and Early Hesperian (Fassett & Head, 2008; Hoke et al., 2011). The equivocal evidence for valley networks pre- or post-dating scarp formation warrants more investigation of the relative timing of these features. More detailed fluvial modeling on a reconstructed paleo-surface at a higher spatial resolution than afforded by the MOLA–HRSC dataset may help provide more definitive indications as to whether fluvial networks align with pre-uplifted topography.

#### 5.4 Limitations

It is important to recognize the inherent limitations, and potential error sources, of crater count methods to determine the age of a planetary surface, unit, or landform. First, resurfacing events such as aeolian deposition, lava flows, or glaciation can preferentially erase small, shallow craters ( $\leq 250$  m in diameter) on Mars (Michael & Neukum, 2010). Thus, craters whose diameters are  $\geq 1$  km were used to minimize the potential impact of resurfacing by one or more of these processes on the derived crater statistics. Second, uncertainties reported in our results as returned by Craterstats are caused in part by fitting the CSFD's with expected distributions from the selected production functions—which themselves are extrapolated from the lunar record calibrated with radiometric ages. Our uncertainties can be approximated by  $\sim \sqrt{N}/\text{Area}$ , but Craterstats fails to account for systematic errors of the model arising from uncertainties in production and chronology functions as they are derived from extrapolated lunar records. These

uncertainties can be >100s of Ma (Fassett, C.I., pers. com. 4/23/21). Thus, we take the reported ages to be useful for comparison with each other (i.e., they are generally the same age), and assume that the errors reported by Craterstats are likely minimum estimates of uncertainty, but that they apply more or less equally to each of our count areas.

## 6. Conclusions

This study employed buffered crater counting in an effort to place estimates on the absolute model ages of 28 lobate scarps across Mars' southern highlands. In aggregate, a total of 148 craters were used to determine Hartmann- and Neukum-based model ages of the faulted surfaces, found to be  $3.8^{+0.01}_{-0.02}$  and  $3.9^{+0.01}_{-0.01}$  Ga, respectively. Regardless of the dating system used, results from this work suggest that the most recent fault activity in the southern highlands was limited to earlier than the Noachian–Hesperian boundary, which occurs at approximately 3.7-3.6 Ga, depending on the applied chronology system. Our findings provide quantitative evidence for global contraction having been underway across the planet by the Early Noachian ~4.3 Ga, in agreement but much larger in scale than earlier efforts to acquire absolute model ages for crustal shortening structures on Mars that investigated only a handful of landforms or only those restricted to a particular location or region.

We suggest that future models of thermal and tectonic evolution include BCC-derived absolute model age constraints from thrust faults as inputs for when global contraction was underway. Doing so will help further refine such models, which now must definitively account for major crustal shortening having been a global phenomenon that was underway during the Noachian, a time of considerable geological activity on Mars. Further investigation of fluvial–tectonic interactions is also warranted. Detailed analysis of how fluvial systems temporally relate

to major thrust fault-related scarps might offer new insight into the timing of both features, particularly if faults from both the highlands and lowlands can be investigated. Finally, Earth-analog studies that build on our current understandings of Terran fluvial–tectonic interactions will also help further our understanding of the timing and nature of water on Mars, the role it played in shaping the surface, and even the timing and extent of Mars’ habitability.

## Figures

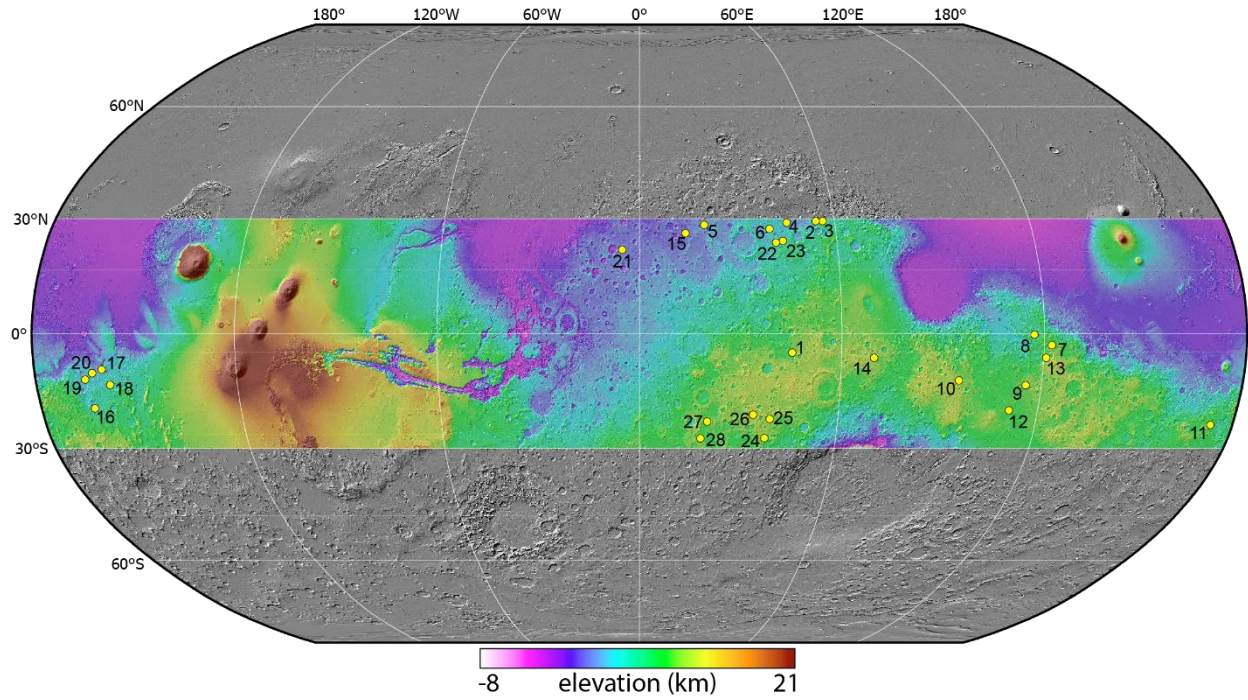


**Figure 3.1** A Robinson projection of Mars, centered at 0°E, showing the spatial distribution of fault scarps (numbered yellow circles). Morphometric characteristics, crater counts, calculated ages, and central coordinates for each scarp are detailed in Table S2 for Chapter 3 (Appendix K).

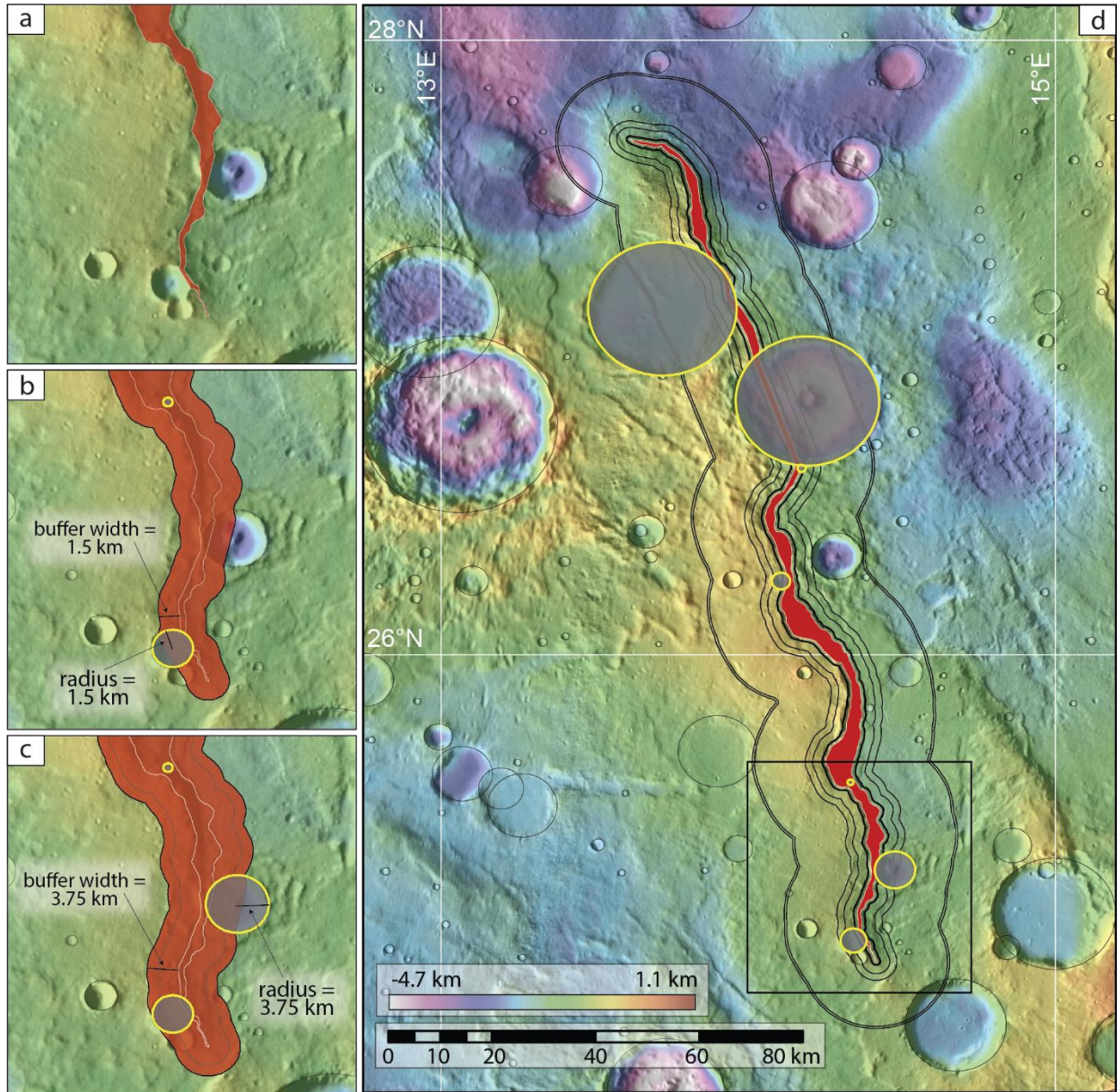


**Figure 3.2** An example scarp (#15 in Table S2 for Chapter 3, Appendix K) for which buffered crater counts were determined, demonstrating our approach. (a) First, the forelimb of a fault-displacement gradient fold is identified and mapped as an area that encompasses the forelimb on the surface (red polygon). (b) Next, craters that superpose the scarp are mapped, and the buffer around the scarp is determined by the radius of the crater in question. (c) For each successively larger crater included in the BCC, the area of the buffer increases proportionately. (d) This process is repeated for all craters (outlined in yellow) that superpose the fault scarp (red polygon). This view is in an equidistant cylindrical.

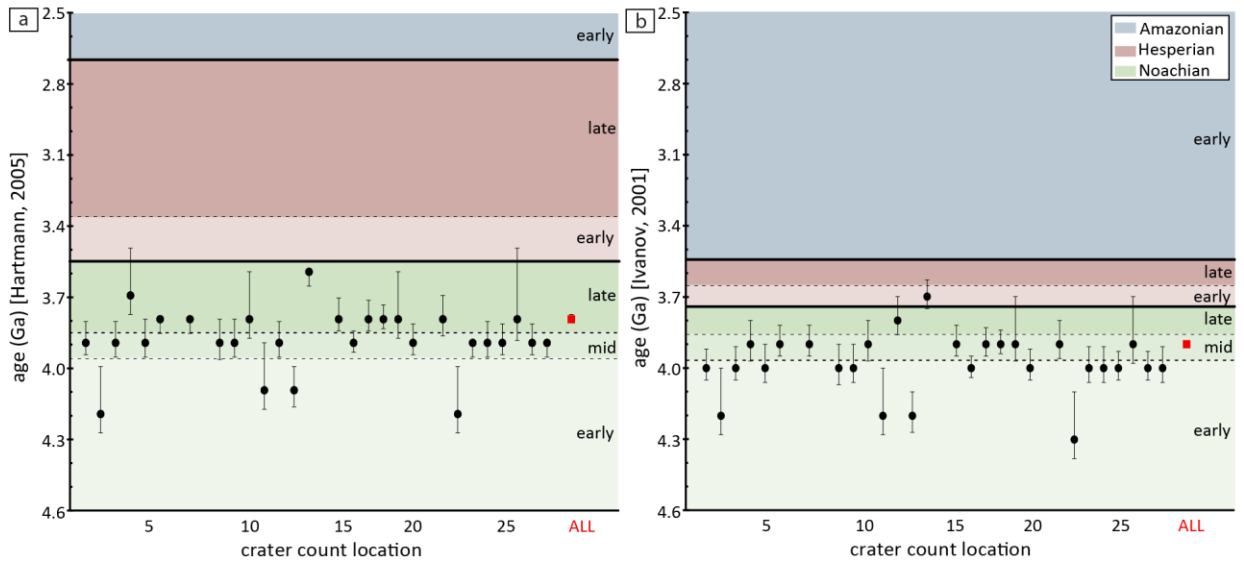


**Figure 3.3** A plot of Hartmann (a) and Neukum/Ivanov ages (b) for individual faults (black circles) and for the count areas for all faults combined (red squares,  $n = 28$ ). Error bars are the 2- $\sigma$  range in crater counts as reported by Craterstats II. See Table S2 for Chapter 3 (Appendix K) for crater count locations.

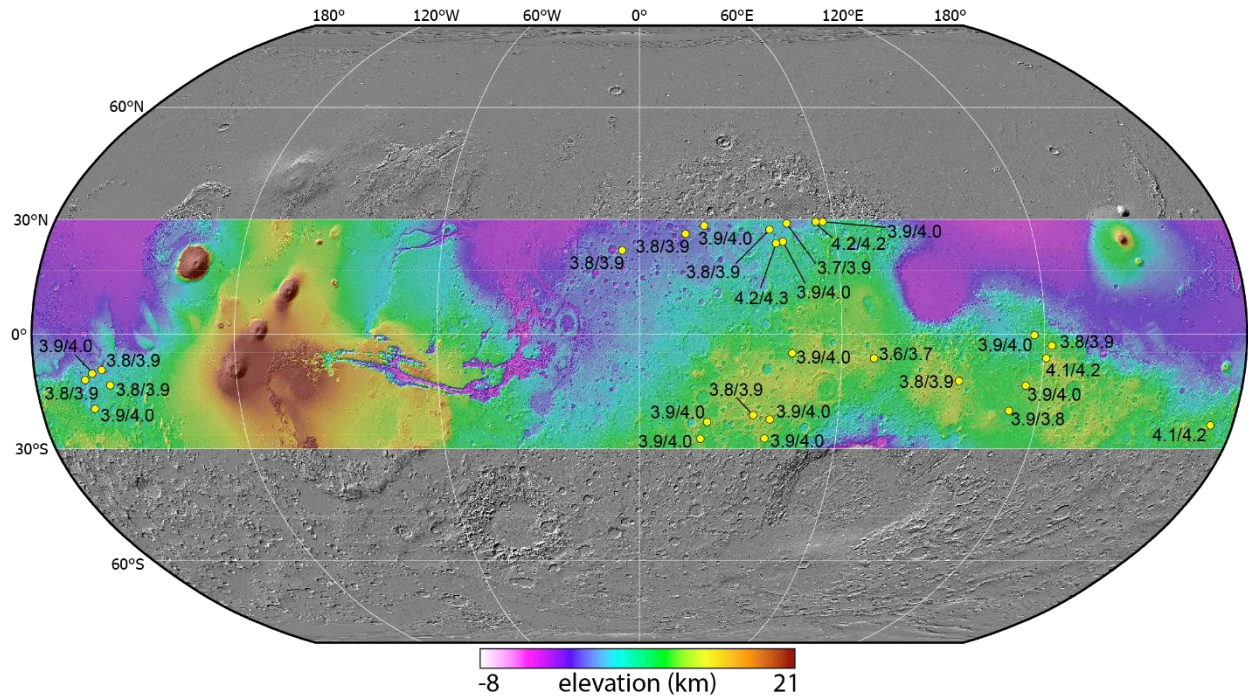


**Figure 3.4** A Robinson projection of Mars, centered at 0°E, showing the spatial distribution of fault scarps and their calculated Hartmann ages in Ga on the left (Hartmann, 2005) and Neukum/Ivanov ages on the right (Ivanov, 2001). See Table S2 in Chapter 3 (Appendix K) for age uncertainties.

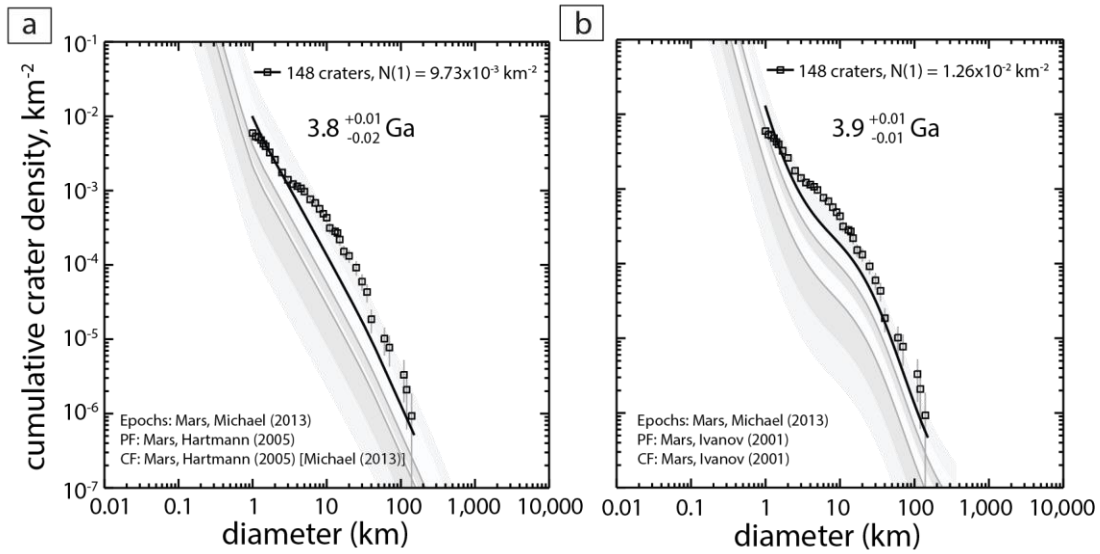


**Figure 3.5** Crater size–frequency distributions for all scarps in this study ( $n = 28$ ). (a) The “Hartmann” age was calculated with the production and chronology functions from Hartmann (2005), which was refined by Michael (2013). (b) The “Neukum/Ivanov” age was calculated with the chronology and production functions from Ivanov (2001).

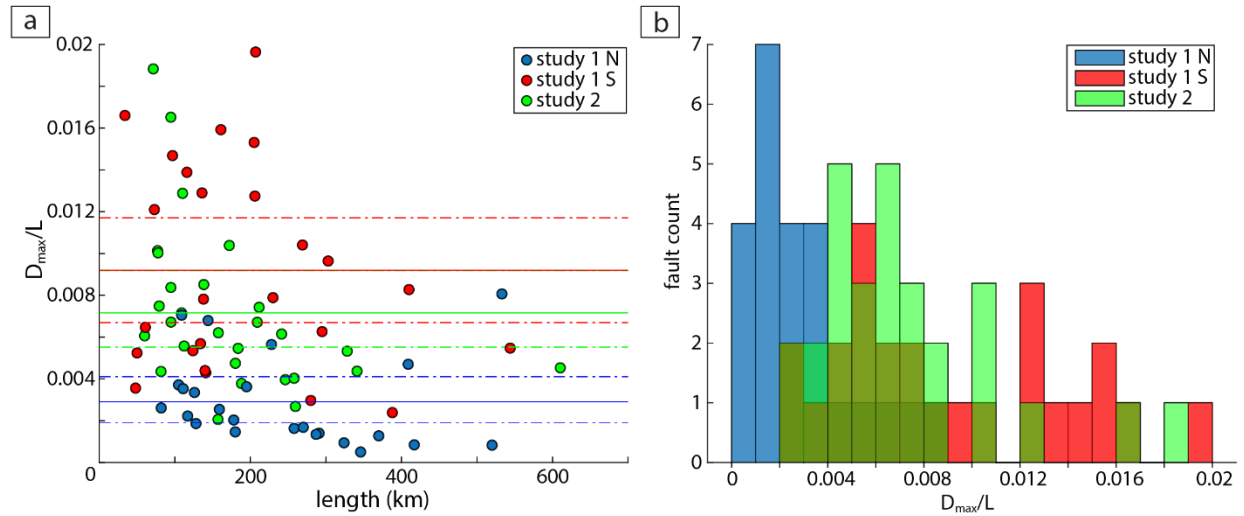


**Figure 3.6** (a) A plot comparing  $D_{max}/L$  ratios for the 49 structures analyzed in Chapter 2 (with the blue and red dots corresponding to those structures in the northern lowlands and the southern highlands, respectively), with the 28 faults from this study (green dots). Solid lines denote the means for both the N and S structures from Chapter 2 and the faults investigated in this study (Chapter 2). Dashed lines indicate the 99% confidence intervals. (b) The distributions of  $D_{max}/L$  ratios from Chapter 1 and this chapter. Note that from their  $D_{max}/L$  ratios, southern faults in Chapter 2 (mean  $D_{max}/L$  ratio indicated by red line) are statistically indistinguishable from this chapter (mean  $D_{max}/L$  ratio indicated by green line) and thus can be regarded as part of the same population as they exhibit similar fault behaviors.

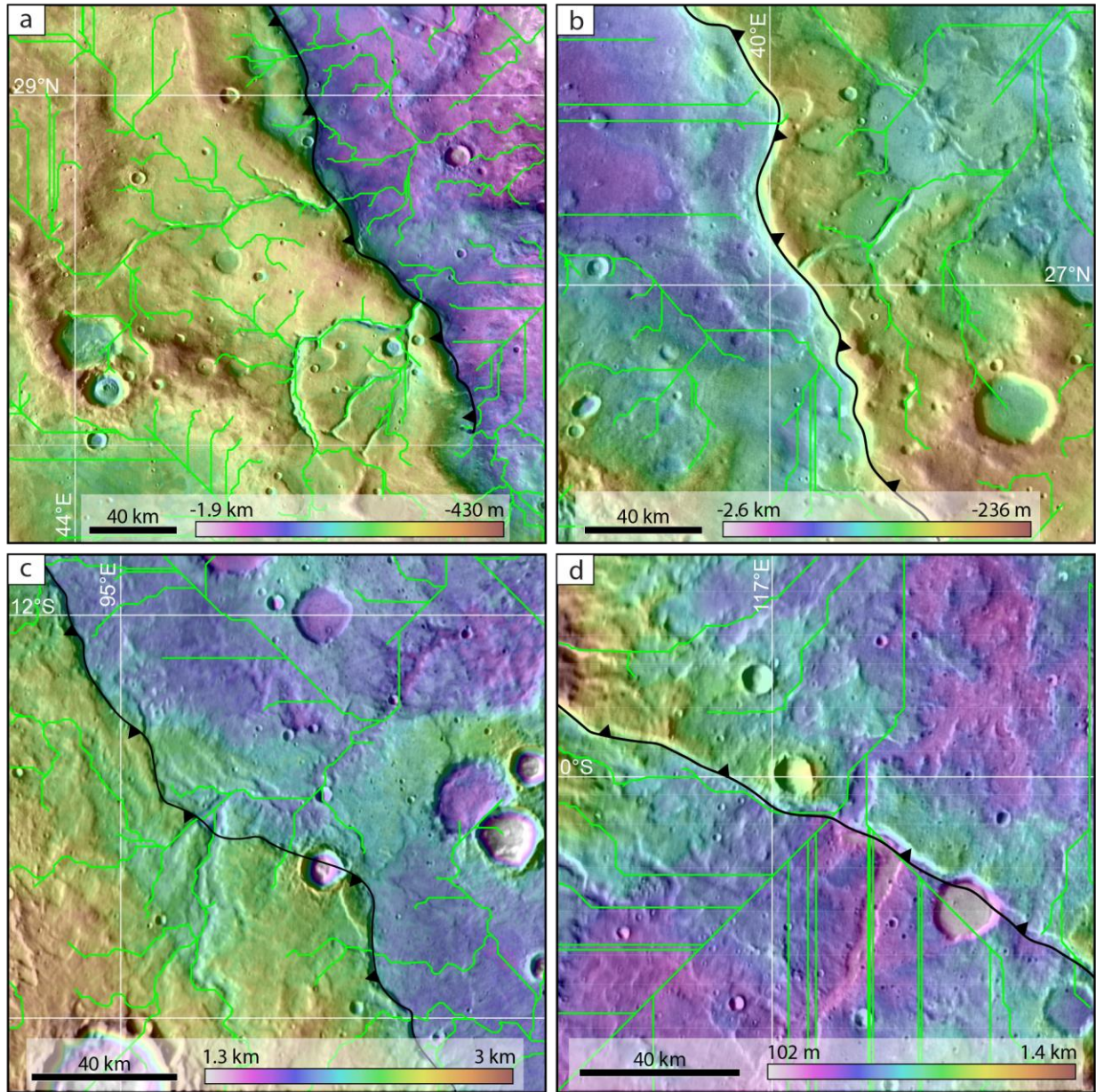


**Figure 3.7** Examples of major thrust fault systems interacting with fluvial valley networks, as observable in the THEMIS imagery. The colors correspond to elevation, and are from the MOLA–HRSC dataset. Fault scarps are outlined in black, with teeth on the inferred hanging wall. Modeled streams are shown as interconnected networks of green lines, and reveal how water would be hydrologically routed across a topographically filled representation of the present-day landscape. Comparing modeled drainage to visible valley networks, no clear relative age could be determined.

**Table 1** Summary statistics for the morphometric characteristics of the thrust fault-related scarps in this study ( $n = 28$ ).

	<b>Range (km)</b>	<b>Median (km)</b>	<b>Quartiles (km)</b>
Length ( $L$ )	60–610	157	62 557
Throw ( $t_{\max}$ )	0.162–1.382	0.489	0.165 1.284
$D_{\max}$	0.324–2.764	0.977	0.330 2.569
		<b>Mean</b>	<b>Uncertainty in mean (95%)</b>
$D_{\max}/L$	$2.1 \times 10^{-3}$ – $18.8 \times 10^{-3}$	$7.2 \times 10^{-3}$	$\pm 1.3 \times 10^{-3}$

### Chapter 3 References

- Anderson, E. M. (1942). The dynamics of faulting and dyke formation with applications to Britain. In *The Journal of Geology*. Oliver and Boyd.
- Anderson, R. C., Dohm, J. M., Golombek, M. P., Haldemann, A. F. C., Franklin, B. J., Tanaka, K. L., Lias, J., & Peer, B. (2001). Primary centers and secondary concentrations of tectonic activity through time in the western hemisphere of Mars. *Journal of Geophysical Research E: Planets*, 106(E9), 20563–20585. <https://doi.org/10.1029/2000JE001278>
- Andrews-Hanna, J. C., Zuber, M. T., & Banerdt, W. B. (2008). The Borealis basin and the origin of the martian crustal dichotomy. *Nature*, 453(7199), 1212–1215. <https://doi.org/10.1038/nature07011>
- Baker, V. R., Boothroyd, J. C., Carr, M. H., Cutts, J. A., Komar, P. D., Laity, J. E., Pieri, D., Thompson, D. E., Lucchitta, B. K., Masursky, H., Malin, M. C., Nummedal, D., & Patton, P. C. (1983). Channels and valleys on Mars. *Bulletin of the Geological Society of America*, 94(9), 1035–1054. [https://doi.org/10.1130/0016-7606\(1983\)94<1035:CAVOM>2.0.CO;2](https://doi.org/10.1130/0016-7606(1983)94<1035:CAVOM>2.0.CO;2)
- Banerdt, W. B., Golombek, M. P., & Tanaka, K. L. (1992). Stress and tectonics on Mars. In *Mars* (pp. 249–297).
- Bhatia, G. K., & Sahijpal, S. (2016). The early thermal evolution of Mars. *Meteoritics and Planetary Science*, 51(1), 138–154. <https://doi.org/10.1111/maps.12573>
- Bouley, S., Craddock, R. A., Mangold, N., & Ansan, V. (2010). Characterization of fluvial activity in Parana Valles using different age-dating techniques. *Icarus*, 207(2), 686–698. <https://doi.org/10.1016/j.icarus.2009.12.030>
- Byrne, P. K., Klimczak, C., & Şengör, A. M. C. (2018). The Tectonic Character of Mercury. In *Mercury* (pp. 249–286). Cambridge University Press. <https://doi.org/10.1017/9781316650684.011>
- Byrne, P. K., Klimczak, C., Sengör, A. M. C., Solomon, S. C., Watters, T. R., & Hauck, S. A. (2014). Mercury's global contraction much greater than earlier estimates. *Nature Geoscience*, 7(4), 301–307. <https://doi.org/10.1038/ngeo2097>
- Carr, M. H. (1995). The Martian drainage system and the origin of valley networks and fretted channels. *Journal of Geophysical Research*, 100, 7479. <https://doi.org/10.1029/95JE00260>
- Carr, M. H., & Chuang, F. C. (1997). Martian drainage densities. *Journal of Geophysical Research E: Planets*, 102(E4), 9145–9152. <https://doi.org/10.1029/97JE00113>
- Carr, M. H., & Clow, G. D. (1981). Martian channels and valleys: Their characteristics, distribution, and age. *Icarus*, 48(1), 91–117. [https://doi.org/10.1016/0019-1035\(81\)90156-1](https://doi.org/10.1016/0019-1035(81)90156-1)
- Carr, M. H., & Head, J. W. (2010). Geologic history of Mars. *Earth and Planetary Science Letters*, 294(3–4), 185–203. <https://doi.org/10.1016/j.epsl.2009.06.042>
- Cartwright, J. A., Trudgill, B. D., & Mansfield, C. S. (1995). Fault growth by segment linkage: an explanation for scatter in maximum displacement and trace length data from the Canyonlands Grabens of SE Utah. *Journal of Structural Geology*, 17(9), 1319–1326.

[https://doi.org/10.1016/0191-8141\(95\)00033-A](https://doi.org/10.1016/0191-8141(95)00033-A)

- Crater Analysis Techniques Working Group. (1979). Standard techniques for presentation and analysis of crater size-frequency data. *Icarus*, *37*(2), 467–474. [https://doi.org/10.1016/0019-1035\(79\)90009-5](https://doi.org/10.1016/0019-1035(79)90009-5)
- Dawers, N. H., & Anders, M. H. (1995). Displacement-length scaling and fault linkage. *Journal of Structural Geology*, *17*(5), 607–614. [https://doi.org/10.1016/0191-8141\(94\)00091-D](https://doi.org/10.1016/0191-8141(94)00091-D)
- Dickson, J. L., Head, J. W., & Fassett, C. I. (2012). Patterns of accumulation and flow of ice in the mid-latitudes of Mars during the Amazonian. *Icarus*, *219*(2), 723–732. <https://doi.org/10.1016/j.icarus.2012.03.010>
- Dombard, A. J., & Hauck, S. A. (2008). Despinning plus global contraction and the orientation of lobate scarps on Mercury: Predictions for MESSENGER. *Icarus*, *198*(1), 274–276. <https://doi.org/10.1016/j.icarus.2008.06.008>
- Ellis, M. A., & Barnes, J. B. (2015). A global perspective on the topographic response to fault growth. *Geosphere*, *11*(4), 1008–1023. <https://doi.org/10.1130/GES01156.1>
- Fassett, C. I., & Head, J. W. (2008). The timing of martian valley network activity: Constraints from buffered crater counting. *Icarus*, *195*(1), 61–89. <https://doi.org/10.1016/j.icarus.2007.12.009>
- Fegan, E. R., Rothery, D. A., Marchi, S., Massironi, M., Conway, S. J., & Anand, M. (2017). Late movement of basin-edge lobate scarps on Mercury. *Icarus*, *288*, 226–234. <https://doi.org/10.1016/j.icarus.2017.01.005>
- Gallen, S. F., Wegmann, K. W., Bohnenstiehl, D. R., Pazzaglia, F. J., Brandon, M. T., & Fassoulas, C. (2014). Active simultaneous uplift and margin-normal extension in a forearc high, Crete, Greece. *Earth and Planetary Science Letters*, *398*, 11–24. <https://doi.org/10.1016/j.epsl.2014.04.038>
- Galluzzi, V., Ferranti, L., Massironi, M., Giacomini, L., Guzzetta, L., & Palumbo, P. (2019). Structural Analysis of the Victoria Quadrangle Fault Systems on Mercury: Timing, Geometries, Kinematics, and Relationship with the High-Mg Region. *Journal of Geophysical Research: Planets*, *124*(10), 2543–2562. <https://doi.org/10.1029/2019JE005953>
- Giacomini, L., Massironi, M., Galluzzi, V., Ferrari, S., & Palumbo, P. (2020). Dating long thrust systems on Mercury: New clues on the thermal evolution of the planet. *Geoscience Frontiers*, *11*(3), 855–870. <https://doi.org/10.1016/j.gsf.2019.09.005>
- Giacomini, L., Massironi, M., Marchi, S., Fassett, C. I., Di Achille, G., & Cremonese, G. (2015). Age dating of an extensive thrust system on Mercury: Implications for the planet's thermal evolution. *Geological Society Special Publication*, *401*, 291–311. <https://doi.org/10.1144/SP401.21>
- Golombek, M. P., & Bridges, N. T. (2000). Erosion rates on Mars and implications for climate change: Constraints from the Pathfinder landing site. *Journal of Geophysical Research E: Planets*, *105*(E1), 1841–1853. <https://doi.org/10.1029/1999JE001043>

- Grott, M., Breuer, D., & Laneuville, M. (2011). Thermo-chemical evolution and global contraction of mercury. *Earth and Planetary Science Letters*, 307(1–2), 135–146. <https://doi.org/10.1016/j.epsl.2011.04.040>
- Gupta, A., & Scholz, C. H. (2000). A model of normal fault interaction based on observations and theory. *Journal of Structural Geology*, 22(7), 865–879. [https://doi.org/10.1016/S0191-8141\(00\)00011-0](https://doi.org/10.1016/S0191-8141(00)00011-0)
- Hartmann, W. K. (2005). Martian cratering 8: Isochron refinement and the chronology of Mars. *Icarus*, 174(2 SPEC. ISS.), 294–320. <https://doi.org/10.1016/j.icarus.2004.11.023>
- Hartmann, W. K., & Neukum, G. (2001). Cratering chronology and the evolution of Mars. *Space Science Reviews*, 96(1–4), 165–194. <https://doi.org/10.1023/A:1011945222010>
- Hauber, E., Van Gasselt, S., Ivanov, B., Werner, S., Head, J. W., Neukum, G., Jaumann, R., Greeley, R., Mitchell, K. L., & Muller, P. (2005). Discovery of a flank caldera and very young glacial activity at Hecates Tholus, Mars. *Nature*, 434(7031), 356–361. <https://doi.org/10.1038/nature03423>
- Hauck, S. A., Dombard, A. J., Phillips, R. J., & Solomon, S. C. (2004). Internal and tectonic evolution of Mercury. *Earth and Planetary Science Letters*, 222(3–4), 713–728. <https://doi.org/10.1016/j.epsl.2004.03.037>
- Hauck, S. A., & Phillips, R. J. (2002). Thermal and crustal evolution of Mars. *Journal of Geophysical Research E: Planets*, 107(7), 5052. <https://doi.org/10.1029/2001je001801>
- Hoke, M. R. T., & Hynek, B. M. (2009). Roaming zones of precipitation on ancient Mars as recorded in valley networks. *Journal of Geophysical Research E: Planets*, 114(8). <https://doi.org/10.1029/2008JE003247>
- Hoke, M. R. T., Hynek, B. M., & Tucker, G. E. (2011). Formation timescales of large Martian valley networks. *Earth and Planetary Science Letters*, 312(1–2), 1–12. <https://doi.org/10.1016/j.epsl.2011.09.053>
- Howard, A. D., Moore, J. M., & Irwin, R. P. (2005). An intense terminal epoch of widespread fluvial activity on early Mars: 1. Valley network incision and associated deposits. *Journal of Geophysical Research E: Planets*, 110(12), 1–20. <https://doi.org/10.1029/2005JE002459>
- Hynek, B. M., Beach, M., & Hoke, M. R. T. (2010). Updated global map of Martian valley networks and implications for climate and hydrologic processes. *Journal of Geophysical Research*, 115(E9), 1–14. <https://doi.org/10.1029/2009je003548>
- Hynek, B. M., & Phillips, R. J. (2003). New data reveal mature, integrated drainage systems on Mars indicative of past precipitation. *Geology*, 31(9), 757–760. <https://doi.org/10.1130/G19607.1>
- Irwin, R. P., & Howard, A. D. (2002). Drainage basin evolution in Noachian Terra Cimmeria, Mars. *Journal of Geophysical Research E: Planets*, 107(7). <https://doi.org/10.1029/2001je001818>
- Irwin, R. P., Howard, A. D., Craddock, R. A., & Moore, J. M. (2005). An intense terminal epoch of widespread fluvial activity on early Mars: 2. Increased runoff and paleolake

- development. *Journal of Geophysical Research E: Planets*, 110(12), 1–38.  
<https://doi.org/10.1029/2005JE002460>
- Ivanov, B. A. (2001). Mars/Moon cratering rate ratio estimates. *Space Science Reviews*, 96(1), 87–104. <https://doi.org/10.1023/A:1011941121102>
- Jiménez-Díaz, A., Egea-Gonzalez, I., Parro, L. M., Tasaka, M., & Ruiz, J. (2021). The thermal structure and mechanical behavior of the martian lithosphere. *Icarus*, 353.  
<https://doi.org/10.1016/j.icarus.2020.113635>
- Klimczak, C., Kling, C. L., & Byrne, P. K. (2018). Topographic Expressions of Large Thrust Faults on Mars. *Journal of Geophysical Research: Planets*, 123(8), 1973–1995.  
<https://doi.org/10.1029/2017JE005448>
- Knapmeyer, M., Oberst, J., Hauber, E., Wählisch, M., Deuchler, C., & Wagner, R. (2006). Working models for spatial distribution and level of Mars' seismicity. *Journal of Geophysical Research E: Planets*, 111(11), 1–23. <https://doi.org/10.1029/2006JE002708>
- Kneissl, T., Michael, G. G., Platz, T., & Walter, S. H. G. (2015). Age determination of linear surface features using the Buffered Crater Counting approach - Case studies of the Sirenum and Fortuna Fossae graben systems on Mars. *Icarus*, 250, 384–394.  
<https://doi.org/10.1016/j.icarus.2014.12.008>
- Kneissl, T., Van Gasselt, S., & Neukum, G. (2011). Map-projection-independent crater size-frequency determination in GIS environments - New software tool for ArcGIS. *Planetary and Space Science*, 59(11–12), 1243–1254. <https://doi.org/10.1016/j.pss.2010.03.015>
- Michael, G. G. (2013). Planetary surface dating from crater size-frequency distribution measurements: Multiple resurfacing episodes and differential isochron fitting. *Icarus*, 226(1), 885–890. <https://doi.org/10.1016/j.icarus.2013.07.004>
- Michael, G. G., & Neukum, G. (2010). Planetary surface dating from crater size-frequency distribution measurements: Partial resurfacing events and statistical age uncertainty. *Earth and Planetary Science Letters*, 294(3), 223–229. <https://doi.org/10.1016/j.epsl.2009.12.041>
- Michel, N. C., Hauck, S. A., Solomon, S. C., Phillips, R. J., Roberts, J. H., & Zuber, M. T. (2013). Thermal evolution of Mercury as constrained by MESSENGER observations. *Journal of Geophysical Research E: Planets*, 118(5), 1033–1044.  
<https://doi.org/10.1002/jgre.20049>
- Mitra, S. (1990). Fault-propagation folds. Geometry, kinematic evolution, and hydrocarbon traps. *American Association of Petroleum Geologists Bulletin*, 74(6), 921–945.  
<https://doi.org/10.1306/44B4B680-170A-11D7-8645000102C1865D>
- Mueller, K., & Golombek, M. P. (2004). Compressional Structures on Mars. *Annual Review of Earth and Planetary Sciences*, 32(1), 435–464.  
<https://doi.org/10.1146/annurev.earth.32.101802.120553>
- Nahm, A. L., & Schultz, R. A. (2011). Magnitude of global contraction on Mars from analysis of surface faults: Implications for martian thermal history. *Icarus*, 211(1), 389–400.  
<https://doi.org/10.1016/j.icarus.2010.11.003>

- Neukum, G., Jaumann, R., Hoffmann, H., Hauber, E., Head, J. W., Basilevsky, A. T., Ivanov, B. A., Werner, S. C., Van Gasselt, S., Murray, J. B., & McCord, T. (2004). Recent and episodic volcanic and glacial activity on Mars revealed by the High Resolution Stereo Camera. *Nature*, *432*(7020), 971–979. <https://doi.org/10.1038/nature03231>
- Nicol, A., Watterson, J., Walsh, J. J., & Childs, C. (1996). The shapes, major axis orientations and displacement patterns of fault surfaces. *Journal of Structural Geology*, *18*(2–3), 235–248. [https://doi.org/10.1016/S0191-8141\(96\)80047-2](https://doi.org/10.1016/S0191-8141(96)80047-2)
- Parro, L. M., Jiménez-Díaz, A., Mansilla, F., & Ruiz, J. (2017). Present-day heat flow model of Mars. *Scientific Reports*, *7*. <https://doi.org/10.1038/srep45629>
- Pieri, D. C. (1980). Martian Valleys: Morphology, Distribution, Age, and Origin. In *Science* (Vol. 210, Issue 21).
- Plesa, A. C., Padovan, S., Tosi, N., Breuer, D., Grott, M., Wieczorek, M. A., Spohn, T., Smrekar, S. E., & Banerdt, W. B. (2018). The Thermal State and Interior Structure of Mars. *Geophysical Research Letters*, *45*(22), 12,198–12,209. <https://doi.org/10.1029/2018GL080728>
- Robbins, S. J., & Hynes, B. M. (2012). A new global database of Mars impact craters  $\geq 1$  km: 1. Database creation, properties, and parameters. *Journal of Geophysical Research E: Planets*, *117*(5). <https://doi.org/10.1029/2011JE003966>
- Ruj, T., Komatsu, G., Pasckert, J. H., & Dohm, J. M. (2019). Timings of early crustal activity in southern highlands of Mars: Periods of crustal stretching and shortening. *Geoscience Frontiers*, *10*(3), 1029–1037. <https://doi.org/10.1016/j.gsf.2018.05.016>
- Samuel, H., Lognonné, P., Panning, M., & Lainey, V. (2019). The rheology and thermal history of Mars revealed by the orbital evolution of Phobos. *Nature*, *569*(7757), 523–527. <https://doi.org/10.1038/s41586-019-1202-7>
- Schubert, G., Solomon, S. C., Turcotte, D. L., Drake, M. J., & Sleep, N. H. (1992). Origin and thermal evolution of Mars. *Mars*, 147–183. <http://adsabs.harvard.edu/abs/1992mars.conf..147S>
- Schubert, G., & Spohn, T. (1990). Thermal History of Mars and the Sulfur Content of Its Core. *Journal of Geophysical Research*, *95*(B9), 95–104. <https://doi.org/10.1029/JB095iB09p14095>
- Senthil Kumar, P., Sruthi, U., Krishna, N., Lakshmi, K. J. P., Menon, R., Amitabh, Gopala Krishna, B., Kring, D. A., Head, J. W., Goswami, J. N., & Kiran Kumar, A. S. (2016). Recent shallow moonquake and impact-triggered boulder falls on the Moon: New insights from the Schrödinger basin. *Journal of Geophysical Research: Planets*, *121*(2), 147–179. <https://doi.org/10.1002/2015JE004850>
- Seybold, H. J., Kite, E., & Kirchner, J. W. (2018). Branching geometry of valley networks on Mars and Earth and its implications for early Martian climate. *Science Advances*, *4*(6), 6692–6719. <https://doi.org/10.1126/sciadv.aar6692>
- Seybold, H., Rothman, D. H., & Kirchner, J. W. (2017). Climate's watermark in the geometry of stream networks. *Geophysical Research Letters*, *44*(5).

<https://doi.org/10.1002/2016GL072089>

- Solomon, S. C. (1977). The relationship between crustal tectonics and internal evolution in the moon and Mercury. *Physics of the Earth and Planetary Interiors*, 15(2–3), 135–145. [https://doi.org/10.1016/0031-9201\(77\)90026-7](https://doi.org/10.1016/0031-9201(77)90026-7)
- Solomon, S. C. (1978). On volcanism and thermal tectonics on one-plate planets. *Geophysical Research Letters*, 5(6), 461–464. <https://doi.org/10.1029/GL005i006p00461>
- Solomon, S. C., & Chaiken, J. (1976). Thermal expansion and thermal stresses in the Moon and terrestrial planets. *Lunar and Planetary Science Conference*, 7, 825–827. <https://ntrs.nasa.gov/search.jsp?R=19770051982>
- Strom, R. G., Trask, N. J., & Guest, J. E. (1975). Tectonism and volcanism on Mercury. *Journal of Geophysical Research*, 80(17), 2478–2507. <https://doi.org/10.1029/JB080i017p02478>
- Suppe, J., & Medwedeff, D. a. (1990). Geometry and kinematics of fault-propagation folding. *Ecolgae Geologicae Helvetiae*, 454(SEPTEMBER 1983), 409–454. <https://doi.org/10.5169/seals-166595>
- Tanaka, K. L. (1982). A new time-saving crater-count technique, with application to narrow features. *NASA Technical Memo, NASA TM-85127*, 132–125.
- Tanaka, K. L. (1986). The stratigraphy of Mars. *Journal of Geophysical Research*, 91(B13), E139. <https://doi.org/10.1029/jb091ib13p0e139>
- Tanaka, K.L., Skinner, J.A., Jr., Dohm, J.M., Irwin, R.P., III, Kolb, E.J., Fortezzo, C.M., Platz, T., Michael, G.G., and Hare, T.M., 2014, Geologic map of Mars: U.S. Geological Survey Scientific Investigations Map 3292, scale 1:20,000,000, pamphlet 43 p., <https://dx.doi.org/10.3133/sim3292>.
- Tosi, N., Grott, M., Plesa, A. C., & Breuer, D. (2013). Thermochemical evolution of Mercury’s interior. *Journal of Geophysical Research E: Planets*, 118(12), 2474–2487. <https://doi.org/10.1002/jgre.20168>
- van der Bogert, C. H., Clark, J. D., Hiesinger, H., Banks, M. E., Watters, T. R., & Robinson, M. S. (2018). How old are lunar lobate scarps? 1. Seismic resetting of crater size-frequency distributions. *Icarus*, 306, 225–242. <https://doi.org/10.1016/j.icarus.2018.01.019>
- Watters, T. R. (1988). Wrinkle ridge assemblages on the terrestrial planets. *Journal of Geophysical Research: Solid Earth*, 93(B9), 10236–10254. <https://doi.org/10.1029/JB093iB09p10236>
- Watters, T. R. (2004). Elastic dislocation modeling of wrinkle ridges on Mars. *Icarus*, 171(2), 284–294. <https://doi.org/10.1016/j.icarus.2004.05.024>
- Watters, T. R., & Robinson, M. S. (1999). Lobate scarps and the Martian crustal dichotomy. *Journal of Geophysical Research*, 104(E8), 981–990. <https://repository.si.edu/bitstream/handle/10088/3257/199905.pdf?sequence=1&isAllowed=y>
- Werner, S. C., & Tanaka, K. L. (2011). Redefinition of the crater-density and absolute-age

- boundaries for the chronostratigraphic system of Mars. *Icarus*, 215(2), 603–607.  
<https://doi.org/10.1016/j.icarus.2011.07.024>
- Wichman, R. W., & Schultz, P. H. (1989). Sequence and mechanisms of deformation around the Hellas and Isidis impact basins on Mars. *Journal of Geophysical Research*, 94(B12), 17333–17357. <https://doi.org/10.1029/jb094ib12p17333>
- Wickham, J. (1995). Fault displacement-gradient folds and the structure at Lost Hills, California (U.S.A.). *Journal of Structural Geology*, 17(9), 1293–1302. [https://doi.org/10.1016/0191-8141\(95\)00029-D](https://doi.org/10.1016/0191-8141(95)00029-D)
- Wieczorek, M. A. (2008). Constraints on the composition of the martian south polar cap from gravity and topography. *Icarus*, 196(2), 506–517.  
<https://doi.org/10.1016/j.icarus.2007.10.026>
- Williams, G., & Chapman, T. (1983). Strains developed in the hangingwalls of thrusts due to their slip/propagation rate: a dislocation model. *Journal of Structural Geology*, 5(6), 563–571. [https://ac.els-cdn.com/0191814183900688/1-s2.0-0191814183900688-main.pdf?\\_tid=dfaa0a2a-051b-11e8-abb6-00000aacb360&acdnat=1517247971\\_940b53af9150faa11867fefbd538e3ff](https://ac.els-cdn.com/0191814183900688/1-s2.0-0191814183900688-main.pdf?_tid=dfaa0a2a-051b-11e8-abb6-00000aacb360&acdnat=1517247971_940b53af9150faa11867fefbd538e3ff)
- Yue, Z., Michael, G. G., Di, K., & Liu, J. (2017). Global survey of lunar wrinkle ridge formation times. *Earth and Planetary Science Letters*, 477, 14–20.  
<https://doi.org/10.1016/j.epsl.2017.07.048>
- Zuber, M. T., Solomon, S. C., Phillips, R. J., Smith, D. E., Tyler, G. L., Aharonson, O., Balmino, G., Banerdt, W. B., Head, J. W., Johnson, C. L., Lemoine, F. G., McGovern, P. J., Neumann, G. A., Rowlands, D. D., & Zhong, S. (2000). Internal structure and early thermal evolution of Mars from Mars global surveyor topography and gravity. *Science*, 287(5459), 1788–1793. <https://doi.org/10.1126/science.287.5459.1788>

## CHAPTER 4: Channel head response to anthropogenic landscape modification

Rachel M. Atkins<sup>1</sup>, Karl W. Wegmann<sup>1,2</sup>, and DelWayne R. Bohnenstiehl<sup>1,2</sup>

<sup>1</sup>Department of Marine, Earth and Atmospheric Sciences, North Carolina State University, Raleigh, NC, 27695, USA, <sup>2</sup>Center for Geospatial Analytics, North Carolina State University, Raleigh, NC, 27695, USA

Corresponding author: Rachel Atkins (ratkins@ncsu.edu)

### Key Points:

- Investigations of streams in a previously farmed and reforested Piedmont watershed indicate that 23 of the 40 studied channel heads exist down-valley of their local slope and contributing drainage area predicted locations.
- An average per-channel contribution of 282.6 m<sup>3</sup> [S.D. = 177.6 m<sup>3</sup>] of future erosion is predicted as the channel heads migrate up-valley and an additional 90,419 ± 56,838 m<sup>3</sup> (68% conf.) is expected to erode from the presently unchannelized valley bottom areas within Umstead State Park (23 km<sup>2</sup>), assuming 50% of channel heads migrate.
- Results from soil sampling indicate that erosion of this amount of soil and sediment encompassing the state park will contribute 9.5 x 10<sup>5</sup> ± 2.8 x 10<sup>5</sup> kg (68% conf.) (951 ± 277 t) of carbon, 4.4 x 10<sup>4</sup> ± 1.2 x 10<sup>4</sup> kg (44 ± 12 t) of total nitrogen, and 1.3 x 10<sup>4</sup> ± 3.9 x 10<sup>3</sup> kg (13 ± 4 t) of phosphorus to downstream waterways.

## 1. Abstract

European-American settlement along the southeastern Piedmont of the U.S. introduced agricultural practices and the extensive clearing of previously forested hillslopes to support food and cash-crop agriculture. This land disturbance has long-term effects on stream morphology by displacing channel heads down-valley, impacting downstream sediment and nutrient supply as channel heads migrate up-valley to their pre-disturbance locations. This study investigates 40 stream channels in William B. Umstead State Park in northwest Raleigh, NC using relationships between local slope and contributing drainage area to predict channel head locations and compare with their observed locations. Further, expected erosion volumes and nutrient contributions are quantified using migration distances and sampled soils near channel heads. Of the 40 study channel heads, 23 had observed channel heads down-valley, an average distance of 174.4 m [S.D. = 109.6 m] from predicted locations. Using this distance and measured cross-sectional areas of channel heads ( $1.6 \text{ m}^2$  [S.D. =  $1.4 \text{ m}^2$ ]), the expected erosion volume per channel is  $282.6 \text{ m}^3$  [S.D. =  $177.6 \text{ m}^3$ ]. Drainage density was used to extrapolate these volumes to the  $23 \text{ km}^2$  area encompassing the park, finding that if a conservative estimate that 50% of channel heads will migrate up-valley, an additional  $90,419 \pm 56,838 \text{ m}^3$  (68% conf.) is expected to erode from this area. Finally, applying these volume estimates to sampled soil nutrients indicates that approximately  $9.5 \times 10^5 \pm 2.8 \times 10^5 \text{ kg}$  (68% conf.) ( $951 \pm 277 \text{ t}$ ) of carbon,  $4.4 \times 10^4 \pm 1.2 \times 10^4 \text{ kg}$  ( $44 \pm 12 \text{ t}$ ) of total nitrogen, and  $1.3 \times 10^4 \pm 3.9 \times 10^3 \text{ kg}$  ( $13 \pm 4 \text{ t}$ ) of phosphorus can be expected to enter the fluvial system in response to channel head migration just from within the confines of this relatively small state park. Excess sediment and nutrients can lead to eutrophication of water bodies and have been linked to harmful algal blooms.

## 2. Introduction

### 2.1 Controls on channel head location

Headwater streams comprise over 75% of the cumulative length of global waterways (Downing et al., 2012). These first-order streams play a critical role in mass transport processes as the first sediment removal locations from hillslopes (Milliman & Syvitski, 1992). Drainage network extent is heavily influenced by where a channel begins. Because headwaters play an important role in downstream hydrologic, geomorphic, and biogeochemical processes, channel head locations are an essential factor to consider when delineating drainage networks (Dietrich & Dunne, 1993; Gomi et al., 2002; Wohl, 2018).

Early methods for generating streams from digital elevation models (DEMs) presented challenges when using a constant flow accumulation-area threshold (e.g., Horton, 1945) to define channel initiation, as the method fails to capture the full extent and variability of drainage networks (Tarboton et al., 1991; Montgomery & Foufoula-Georgiou, 1993). It was later discovered that local slope is a significant variable in channel initiation, and the combination of the physical relationship between local slope and contributing drainage area results in the more accurate demarcation of hillslope-to-fluvial geomorphic process zones (Montgomery & Foufoula-Georgiou, 1993; Montgomery, 2001; McNamara et al., 2006; Henkle et al., 2011). Across soil-mantled landscapes, the predicted location of channel heads is determinable by gradient and sign changes in graphs of basin averaged log-slope versus log-area, with diffusive hillslope processes dominating as slope increases and advective fluvial processes dominating when slopes decrease with contributing drainage area (Montgomery & Dietrich, 1988; Tarboton et al., 1991; Willgoose et al., 1991) (Figure 4.1). The hillslope-to-fluvial continuum can be subdivided into process regions with variable degrees of negative relationships between slope and

drainage basin area (Ijjasz-Vasquez & Bras, 1995; Tarolli & Dalla Fontana, 2009). Region I begins at the drainage divide, characterized by positive slope-area relationships, and exhibits unchannelized, convex, diffusion-dominated hillslopes. Conversely, region IV is identified by a strong inverse relationship between slope and area and contains prominent incised valleys with active fluvial activity. Some landscapes also exhibit intermediate regions II and III, representing the transition from diffusive hillslope processes to fluvial incision and sediment transport and are generally where channel heads are found on an undisturbed landscape (Montgomery, 2001; Tarolli & Dalla Fontana, 2009; Wohl, 2018). The region where channel heads are located is a function of climate and dominant hillslope and flow processes.

For soil-mantled hillslopes in humid environments, flow processes at the unchannelized-to-channelized transition are often characterized by shallow subsurface piping or sapping, often with channel heads originating in region II (e.g., Tarolli & Dalla Fontana, 2009). In contrast, for arid-to-semiarid places that exhibit more runoff-generated surface flow, channel heads are most often found in regions III and IV (Henkle et al., 2011). In the densely forested, sub-tropical, low-relief soil-mantled landscapes of the eastern Appalachian Piedmont, ephemeral channel heads initiate where subsurface storm flow intersects the surface.

## 2.2 Anthropogenic impacts on hillslope erosion

Anthropogenic hillslope modification can have long-lasting and often unforeseen effects on landscapes and ecosystems well after the cessation of such activities (e.g., Walter and Merritts, 2008). European-American settlement along the southeastern Piedmont of the U.S. introduced agricultural practices and the extensive clearing of previously forested hillslopes to support food and cash-crop agriculture and supply wood as a fuel source (Auch et al., 2015).

Hillslope farming involves removing vegetation that formerly intercepted rainfall, subjecting the newly exposed and tilled soil to increased effective moisture through decreases in canopy interception and evapotranspiration. In forested landscapes of the Atlantic Piedmont, overland flow is rare because of canopy interception and low bulk-density A horizons, often with an annual leaf litter layer (Figure 4.2a). Following forest clearing and soil disturbance, overland flow conditions develop rapidly during rainfall events, especially where soils are clay-rich (e.g., Jacobson & Coleman, 1986). With less time for infiltration, concentrated surface flow can lead to gully formation and hillslope dissection through soil and sediment transport from hillslope to adjacent valley bottoms (Figure 4.2b). During the interval of intensive land clearing and hillslope agriculture in the southeastern U.S. (c. the late 1700s to 1930s CE), the erosion and subsequent accumulation of hillslope sediments in headwater valley bottoms caused the down-valley displacement of headwater stream initiation locations (Jefferson & McGee, 2013; Avcioglu et al., 2017). The construction and maintenance of low-head milldams on trunk channels and erosion control check dams higher up in the drainage network further contributed to sediment accumulation along low-order Piedmont valley bottoms (Walter & Merritts, 2008; Wegmann et al., 2012). Millponds behind these dams served as accumulation traps for the newly eroded hillslope sediment; the evidence of these reservoirs is observable in streambank sediment records throughout the Piedmont (e.g., Walter & Merritts, 2008; Wegmann et al., 2012; Starek et al., 2013; Lyons et al., 2015). These meters-thick packages are referred to as "legacy sediment" as they record the legacy of anthropogenic disturbances to background sediment erosion, transport, and deposition rates in headwaters and trunk channels across the Atlantic Piedmont of eastern North America (Costa, 1975; Trimble, 1975; Jackson et al., 2005; Walter & Merritts, 2008).

The sedimentation dynamics and morphology of many present-day Piedmont streams are significantly altered from expected fluvial form and behavior, lacking natural floodplains as channels erode through the thick packages of legacy sediment (Jackson et al., 2005; Hupp et al., 2009; Merritts et al., 2013). In addition, near-vertical stream banks are often undercut, leading to pulses of legacy sediment influx to streams when they collapse (Trimble, 1975; Wegmann et al., 2012; Lyons et al., 2015). These legacy sediment influxes alter downstream sediment dynamics and contribute to poor water quality (Voli et al., 2013; Flemming et al., 2019).

Estimates of post-colonial upland erosion rates of  $\sim 950 \text{ m Ma}^{-1}$  during the Anthropocene contrast with much lower background (pre-Anthropocene) erosion rates  $< 10 \text{ m Ma}^{-1}$  from the rivers draining the uplands of the southeastern Piedmont (Trimble, 1975, 1977; Reusser et al., 2015). For example, in North Carolina, Phillips (1992) used variations in mineral composition of Neuse River channel sands collected from Piedmont and Coastal Plain sites to document that despite extensive historic Piedmont upland erosion and soil loss in the basin, the bulk of these legacy sediments have yet to reach the estuary. Similarly, in the upper Piedmont of South Carolina, Jackson et al. (2005) estimate that even though streams there have been in a state of net sediment export since the mid-1950s, under current sediment export rates, it will take six to ten millennia to remove all of the cotton-farming era soil that was eroded from uplands and deposited in headwater basins. The imbalance in sediment erosion and delivery rates between the Piedmont and Coastal Plain suggests that legacy sediments must have accumulated in headwater valley bottoms. Much of it is still awaiting export to receiving streams, estuaries, and ultimately the Atlantic Ocean. Notably, the slow re-erosion and downstream transport of legacy sediments, compared to its emplacement rate, continues to contribute to chronically turbid stream waters that will persist for millennia along the east coast of the United States (Jackson et al., 2005;

Wohl & Merritts, 2007; Voli et al., 2013). While the timespan over which erosion is measured can bias results, with faster rates associated with shorter timespans and vice-versa (e.g., the Sadler effect), a meta-analysis of over 4,000 erosion rate estimates from across North America determined that even when this bias is accounted for, the increase in post-European-settlement erosion is ~10x background (Kemp et al., 2020).

Perturbations of sediment and nutrients to stream networks significantly impact hydrologic, biologic, and chemical functions in downstream aquatic and riparian environments (Walter et al., 2007; Graeber et al., 2012; Inamdar et al., 2012). Thus, quantification of physical and chemical consequences of legacy sediment influx, including volumes of eroded soil/sediment and associated nutrients, will improve our understanding and modeling of nutrient pollution in Piedmont streams and reservoirs (Inamdar et al., 2020; 2021). Moreover, determining this is an essential constraint in ongoing efforts to reduce the contributions of non-point source nutrient loading to the eutrophication of rivers and estuaries along the Atlantic coast (e.g., Paerl, 2009; Lebo et al., 2012; Paerl et al., 2017; Fleming et al., 2019; Bhattacharya & Osburn, 2020).

Channel heads in anthropogenically disturbed landscapes may not be located where their slope-area relationships predict, reflecting a disturbance to the drainage networks. Across the Piedmont of the southeastern U.S., channel heads have been observed downslope of their predicted locations due to aggradation of legacy sediment in zero-to-first order headwater basins (Jackson et al., 2005; Jefferson & McGee, 2013) (Figure 4.2c). Results from Jefferson and McGee's 2013 investigation of reforested watersheds in the North Carolina Piedmont indicated that these landscapes are still recovering from disturbance. Fluvial networks may be capable of

returning to their full extent, i.e., with channel heads located where local slope-contributing area thresholds predict via continued and persistent erosion of previously aggraded legacy sediment.

### 2.3 Study location: William B. Umstead State Park

William B. Umstead State Park (USP) is located in northwest Wake County, North Carolina, in the lower portion of the Appalachian Piedmont physiographic province (Figure 4.3). The park encompasses 22.66 km<sup>2</sup> of reforested rolling hills and bottomlands with maximum relief of 70 m. In CE 1774, the land that is now USP was opened to farming and agricultural practices to encourage local settlement. Sustained poor cultivation and soil preservation practices led to erosion and decreasing crop yields that became untenable during the Great Depression (CE 1929-1939). In 1935, the U.S. Department of Agriculture reported that in the area that would become USP,

*People are obtaining income from stripping the last vestiges of timber from the land...the area is submarginal for agricultural purposes due to the steep and rocky slopes which have been ruined by a continual soil erosion.*

Before 1774, the study area most likely existed as a mature, mixed deciduous-conifer forest (Figure 4.2a). After forest clearing and the subsequent 160 years of agricultural practices, the federal Resettlement Administration and North Carolina state agencies purchased 5,000 acres of private land (~20 km<sup>2</sup>) in 1934 for land restoration and repurposed it as a recreation area. The area was reforested with Loblolly Pines. Natural seedling recruits of oak, beech, and hickory complement the planted pines. Several thousand small rock check dams were built across gullies and the upper reaches of ephemeral channels to slow the once-pervasive hillslope erosion (North Carolina State Parks, 2018). The parklands are now reforested as secondary successional forest with stand ages of c. 80 years.

The soils found across USP are derived from Paleozoic felsic gneiss and schist of the Raleigh Metamorphic belt (North Carolina Geological Survey, 1985). These soils are part of the Pacolet, Wedowee, Nanford, and Cecil sandy loams and the Georgeville silt loam series. In addition, some loamy alluvium (Chewacla and Wehadkee series) exists near the lower reaches of the streams and is flooded frequently (United States Department of Agriculture, 2018).

## 2.4 Research questions

There are several motivations for this study. First, a high-resolution (1 m/pixel) lidar-derived DEM allows for a detailed evaluation of slope-area relationships of first-order channel head locations across anthropogenically disturbed headwater basins in the Piedmont of North Carolina. Second, the lidar permits testing a null hypothesis – that channel heads are positioned across the landscape in concert with their slope-area predicted locations. After testing the null hypothesis, we seek to quantify future erosion potential by modeling the up-valley distance channel heads are likely to travel to reestablish their slope-area predicted equilibrium landscape locations. Finally, we preliminarily estimate the impacts to downstream receiving waters from the addition of sediment and soil-bound nutrients that could be liberated by the cumulative amount of channel-head migration predicted from our model results.

## 3. Methods

### 3.1 Field & Environmental Lab methods

Ephemeral channel heads were located in the field using a 1-meter bare-Earth lidar DEM and hillshade map of Umstead State Park for guidance. Each tributary was traversed from where it entered the trunk channel upslope to its initiation location. Channel heads were identified as

the furthest upslope location of a continuous channel with defined banks (Figure 4.4), a definition commonly used to identify these landscape features in the field (e.g., Montgomery & Dietrich, 1989; Dietrich & Dunne, 1993; Jefferson & McGee, 2013). All channels had visible evidence of recent flow, including sediment or debris transport and lack of tree or vegetation growth in the bottom of the channel downstream from the initiation point. Exposed and suspended tree roots are observed short distances downstream from many channel heads (Figures 4.4c; 4.5), indicating that soil erosion and up-valley channel migration have occurred after the trees' growth. Channel cross-sectional areas (widths and depths) were measured 5 to 10 m downstream of fifteen channel heads.

Channel initiation points were recorded using a Garmin Oregon 4001 handheld GPS during leaf-off conditions (late fall to early spring) during 2018 and 2019 to maximize positional accuracy beneath the forest canopy. Horizontal GPS measurement errors ranged from 4 to 30 meters. Field GPS coordinates were imported into ArcGIS. Often they did not align exactly on top of the GIS-delineated streamlines. Channel heads were repositioned on the 1-meter lidar DEM by creating a circular buffer around each GPS-measured location with a radius equal to the reported GPS uncertainty. Then, using a D8 flow accumulation raster derived from the 1-meter lidar DEM, field-identified points were manually moved to the largest-value flow accumulation pixel found within the uncertainty buffer along the nearest previously delineated trunk channel. DEM-located points were not shifted more than 15 meters.

Soil profiles were compared at four channel head locations 5 to 10 m up-valley from each initiation point. Soil properties, including horizon thickness, grain size, and bulk density, were recorded, and samples for total soil-bound carbon, phosphorous, and nitrogen were collected. Nineteen samples were extracted using a hand auger and trowel to excavate fresh,

uncontaminated surfaces at each soil series transition down to 120 cm depths. The upper reaches of channels are not anticipated to erode below this depth; thus, deeper soils were not sampled. Field samples were stored in a freezer (approx.  $-18^{\circ}\text{C}$ ) before analysis. Quantification of soil layer total carbon (C), nitrogen (N), and phosphorous (P) were conducted at the Environmental and Agricultural Testing Service lab at North Carolina State University. For each sample, a slurry of 10 g of soil and 10 mL of deionized water was stirred with a glass rod and allowed to settle for one hour, with additional stirring at 30 minutes. Soils were then air-dried and sieved to  $<2$  mm. Total C and N concentrations were obtained by thermal combustion and recording with a Perkin Elmer 2400 Organic Elemental Analyzer. Total available P was measured using a Perkin Elmer ICP-Optical Emission Spectrometer and followed EPA Method 3050B strong-acid soluble digestion procedures (U.S. EPA, 1996).

## 3.2 GIS Methods

### 3.2.1 Trunk channel delineation

Topographic and surface hydrologic GIS analyses used the 2015 Phase III QL2 lidar-derived 1-meter bare-earth DEM produced by the state of North Carolina. Stream network delineations were conducted with ChiProfiler (Gallen & Wegmann, 2017), a series of MATLAB functions utilizing TopoToolbox 2 (Schwanghart and Scherler, 2014) to extract and analyze longitudinal river profiles. Trunk channels were defined on a D8 flow accumulation raster by the highest values and extended upslope to a minimum flow accumulation of 10 cells ( $10\text{ m}^2$ ). The use of a D-infinity-derived flow accumulation raster was tested and found to yield the same results as the D8-derived raster. Thus, for computational simplicity, the D8 flow accumulation raster was used for this work. Examples of delineated trunk channels are shown in Figure 4.6.

The lower reaches of these trunk streams are channelized at present, and the largest exhibit perennial flow, while the upper reaches (upslope of the channel head) are currently unchannelized. The local slope (m/m) and flow accumulation values were extracted for each 1-meter pixel along the trunk channels (e.g., Figures 4.6b,d). These values were used to construct slope vs. area plots (e.g., Figures 4.6a,c) for each channel with an identified channel initiation point and to model (predict) future channel head locations (described in section 2.2.2). The future-predicted channel head locations were translated back into locations on the DEM-delineated trunk channels.

### 3.2.2 Predicting channel head locations and migration distances

Slope-area plots in log-log space were used to fit a spline with a smoothing parameter ( $p_{smooth}$ ) of 0.25 to determine the transition from increasing slope (diffusion-dominated) to decreasing slope (fluvial-dominated) in drainage area space along each channel (Figures 4.6a,c). Spline fits were bootstrapped ( $n = 2,000$ ) to determine 95% confidence bounds on the flow accumulation area corresponding to the range of predicted spatial locations (peak of spline curve) for the channel head point along a given trunk channel segment. The range in migration distances was calculated between existing and predicted channel head locations for channels where the present-day flow accumulation areas fell outside (down-valley) of the slope-area predicted spatial position of the contributing areas (Figures 4.6a, c; 4.7a). Drainage areas were translated into locations on the landscape using the contributing area along delineated trunk channels. Horizontal distances along the channel were determined by measuring the stream-line length between the observed channel head position and the 95% confidence interval range of predicted locations from the spline fitting routine. Because contributing drainage areas vary by

catchment, this was done for each channel. Distances were not calculated for channel heads with observed locations within the predicted range of contributing areas (e.g., Figure 4.7).

Additionally, slopes for all channels were binned by 0.25 log area, and a smoothing spline ( $p_{smooth}=0.5$ ) was fit using the same procedure as for individual channels (Figure 4.8a). Finally, channel heads that were predicted to migrate using the individual channel fits (e.g., Figures 4.6a, c; 4.7a) were plotted separately and fit with a smoothing spline ( $p_{smooth}=0.5$ ) to estimate their potential migration distances as a population (Figure 4.8b).

## 4. Results

### 4.1 Predicted vs. observed locations of channel heads

Forty individual trunk channel locations distributed throughout Umstead State Park were used in the analysis (Figure 4.9). Of these, 23 had observed channel heads with contributing flow accumulation areas greater than what would be predicted for the channel head location based on slope-area curve inflections at the 95% confidence level (e.g., Figures 4.6a,c; 4.7a). These 23 channel heads are predicted to migrate upslope to smaller contributing drainage areas. The 17 other observed channel head locations exist within the 95% confidence interval for predicted equilibrium based upon the log-slope versus log-area relationship and therefore are not predicted to migrate further up-valley (e.g., Figure 4.7b). When all channels are combined and binned into 0.25 log area bins, the smoothing spline fit ( $p_{smooth}=0.5$ ) predicts a contributing drainage area range of 1,380 to 8,710 m<sup>2</sup>. The current average contributing area for all observed channel heads is 28,000 m<sup>2</sup> (Figure 4.8a). However, when analyzed individually, only 23 of these channels had observed head locations downslope of their predicted contributing areas; therefore, a spline regression through the aggregate analyses for only those channels with heads predicted to

migrate upslope results in predicted eventual contributing areas of 1,549 to 4,467 m<sup>2</sup> (Figure 4.8b). For these channels, the current average contributing area is 31,743 m<sup>2</sup>.

Horizontal migration distances were calculated by translating contributing basin areas to a physical distance along the delineated trunk channel. These distances were determined for the observed channel head location and the minimum and maximum (upper and lower 95% confidence in predicted) drainage basin areas. For the 23 channels identified above, the resulting up-valley migration distances range from 23.1 to 453.6 m (Table S1 in Chapter 4, Appendix P) with an average (mean) predicted migration distance of 174.4 m [S.D. = 109.6 m] (Figure 4.10). These migration distance ranges are used to estimate potential future sediment/soil loss volumes (section 4.2).

#### 4.2 Sediment/soil volumes

Width and depth measurements immediately downstream from 15 representative channel heads were recorded to estimate future eroded sediment volumes. Central channel depths ranged from 0.30 to 1.68 m, while widths ranged from 0.25 to 2.90 m. As expected, narrower channel widths correlate with shallower channel depths (Figure 4.11). Cross-sectional areas were calculated assuming a rectangular channel geometry. The average cross-sectional area for these measured channels was 1.62 m<sup>2</sup> [S.D. = 1.40 m<sup>2</sup>]. Using the midpoint between the predicted minimum and maximum migration distances from 23 channels (section 4.1) and the average below-head channel cross-sectional area, the future volume of sediment erosion resulting from up-valley channel head migration approximated by using the simple formula  $V = L \times A$ , where  $L$  is the migration distance in meters,  $A$  is the average channel cross-sectional area, and  $V$  is the predicted volume of eroded sediment. Using the predicted migration distances for all 23

channels, an average estimated future per-channel contribution of  $282.6 \text{ m}^3$  [S.D. =  $177.6 \text{ m}^3$ ] of sediment erosion as the channel heads migrate up their valleys.

### 4.3 Soil descriptions

The Piedmont soils sampled for this study were most commonly sandy loam, while some were also characterized by loam, sandy clay loam, and clay loam textures. Percent sand, silt, and clay for all four locations ranged between 36.8-63.9%, 20.0-41.5%, and 10.0-38.6%, respectively. A representative soil profile from all four sample locations indicating weight-percent C and N, the mass of bioavailable P, and grain size values are shown in Figure 4.12. Generally, these soil profiles consisted of modern A, B, and C horizons, followed by a buried A and B horizon, assumed to be the original, pre-legacy surface. Each location also contained a basal layer of quartz gravels, and the fine fraction became progressively more clay-rich and wet at depth. The A horizons were ~10 cm thick, commonly characterized by a dark brown color, and were often dry and friable. These upper-most layers were also very organic-rich, including small root structures. The B horizons were about ~15 and 10 cm thick, respectively. Both  $B_{g1}$  and  $B_{g2}$  were identifiable by their lighter reddish-brown color, friable nature, and few root structures.  $B_{g1}$  was slightly oxidized but became more reduced in the transition to  $B_{g2}$ , where the color changed to a yellowish-brown, sometimes making the boundary between  $B_{g2}$  and  $C_g$  difficult to identify. The  $C_g$  horizon was ~40 cm thick, commonly grey mud mottled with oxidized nodules throughout, with percent sand progressively increasing with depth in the horizon. In addition, a buried ~15 cm thick A horizon ( $A_b$ ) that is medium-to-dark brown loamy sand containing some organic remnants is frequently observed below the C-horizon. The  $A_b$  signifies the land surface before burial by legacy sediments. It is often underlain by ~15 cm of buried b-horizon ( $B_{wgb}$ ),

characterized by a dark brownish-grey mud with mottled oxidized nodules throughout, confined at the bottom by a layer of basal quartz gravels.

## **5. Discussion**

### **5.1 Hillslope-to-valley transition zones in modified landscapes**

Delineating individual trunk channels from high-resolution (1-meter) DEMs to assess slope-area relationships allows for targeted investigations of the expected initiation location of a stream. In contrast, much previous work has used basin-binned-area, which averages slopes across drainage basins, not just along a single stream (e.g., Montgomery and Foufoula-Georgiou, 1993; Tarolli and Dalla Fontana, 2009; Henkle et al., 2011; Vergari et al., 2018). The basin-binned-area method is widely used to reduce uncertainties when using a single channel for associating measured metrics like slope and contributing area by using an average slope over a given drainage area bin across a landscape. This process condenses data across the basin to average slope values across contributing area ranges with a size of 0.25 log area (e.g., all cells with a contributing area between 100 – 325 units<sup>2</sup>, 326 – 550 units<sup>2</sup>, 551 – 775 units<sup>2</sup>, 776 – 1,000 units<sup>2</sup>, etc.). While this basin-averaged binned-area technique may be appropriate for landscapes where anthropogenic modification is not a significant factor, it may fail to appropriately capture the log-slope vs. log-area relationships for hillslope-to-valley transitions in landscapes preserving the topographic signatures of prior human landscape modification, especially when high-resolution topography data is available. For example, in the Umstead State Park study area, relict anthropogenic topographic features are readily observable in the 1-m lidar DEM and hillshade rasters and as localized, short-wavelength deviations in slope and curvature values (Figure 4.13). These features include hillslope gullies caused by forest removal and

decades of poor soil conservation practices, active and abandoned dirt roads and erosion control features like hillside terraces built in the 1930s to reduce soil erosion after federal land purchase and inhabitant relocation. Because these features occur on the upper parts of hillslopes, this leads to higher than normal slopes at low flow accumulation values and hinders the ability to find hillslope-to-channel transitions from the data.

We tested the importance of these anthropogenic topographic features on the binned-area technique at different DEM resolutions (Figure 4.14). We found that their impact on the local slope-contributing area relationship decreases at lower DEM resolutions. The 1-meter DEM (grey line in Figure 4.14) shows that slopes are higher than expected near drainage divides at small contributing areas and are the most prominent at this 1-meter scale. This effect is smaller in a 5-meter DEM downsampled from the original 1-meter DEM (green line in Figure 4.14) and even less at coarser DEM resolutions. Our findings are consistent with previous works finding that the hillslope-to-valley transition is predicted to occur at larger contributing drainage areas when lower resolution DEMs are used (Tarolli & Dalla Fontana, 2009; Tarolli, 2014). The documented differences in DEM resolution and the ability to consistently predict hillslope-to-valley transition locations indicate that more work is needed to understand the role of DEM resolution in this prediction process. However, it likely suggests that combining the binned-area and trunk channel methods yields the most reliable results for high-resolution (lidar) datasets. Therefore, this study employs the binned-area approach for locating channel heads in an effort to mitigate the impacts that anthropogenic landscape artifacts have on these results.

Values of slope and area at channel heads across our study locale are consistent with the few published studies in the same physiographic province (e.g., Julian et al., 2012; Jefferson & McGee, 2013). We compare our results to those presented in Jefferson & McGee (2013) (Figure

4.15) while noting slight differences in DEM resolution (6-meter vs. 1-meter used in this study). For the 40 channel head locations used in this study, we find an inverse relationship between contributing area ( $m^2$ ) and slope ( $m/m$ ). After rearranging the regression, the relationship is given by:  $1163 = AS^{1.05}$ . This relationship is moderate ( $r^2 = 0.41$ ) but is significant ( $p < 0.001$ ). Jefferson & McGee (2013) also identify an inverse relationship given by;  $380 = AS^{1.27}$ , with contributing area and slope also moderately correlated ( $r^2 = 0.65$ ) and significant ( $p < 0.001$ ) for western and central Piedmont channel head locations, also in North Carolina. Drainage networks in undisturbed landscapes typically have slope exponents that range between 1.7 and 2 (e.g., Dalla Fontana & Marchi, 2003; Giannoni et al., 2005; McNamara et al., 2006). Conversely, gullied landscapes often reflect disturbance and have slope exponents closer to 1 (e.g., Istanbuloglu et al., 2002; Bastola et al., 2018). Our finding that the best-fitting slope exponent is close to unity for the channel heads in the eastern Piedmont of North Carolina investigated in this study indicates that these Piedmont landscapes are likely still recovering from anthropogenic disturbance.

## 5.2 Ongoing response to human disturbances

To this point, we have demonstrated that >50% of study area channel heads are located down-valley from their predicted location based upon topographic slope-area relationships. From this, we have estimated the distances they are likely to travel and the volume of sediment they need to erode through to regain topographic equilibrium. Next, we use metrics such as average up-valley channel migration distances, channel cross-sectional areas, and drainage density to explore the extent to which the future migration of channel heads will impact the study area, and by extension, broader expanses of Piedmont similarly impacted by historic upland soil losses and

sediment aggradation in headwater valley bottoms. The findings from the analysis of 40 channel heads are extrapolated to the entirety of Umstead State Park. Ultimately, these results could be scaled further to encompass larger spatial areas (e.g., Hydrologic Unit Codes 12 to 8, or even counties).

Modified Strahler stream orders were calculated for study area channels using the same stream initiation threshold criteria used for the trunk channel delineation; minimum flow accumulation values of 100 m<sup>2</sup> (100 cells). We refer to this as a 'modified' Strahler stream order designation since, traditionally, first-order streams are defined by at least intermittent flow. In contrast, in our case, the ephemeral or intermittent flow may not occur until "channels" reach modified 2<sup>nd</sup> to 5<sup>th</sup> order, 87.5% of which are classified as 4<sup>th</sup> or 5<sup>th</sup> order using the artificially small flow accumulation area threshold. The creation of the modified Strahler ordering aids in highlighting patterns in stream size and their respective density across the study area for extrapolation purposes.

Using the calculated ranges of eroded sediment volumes for the study locations ( $n = 40$ ) and the finding that 23 out of 40 streams in the sample are predicted to migrate, we apply a conservative 50% migration potential to our calculated drainage densities. Application of this threshold means that one out of every two channel heads across the state park is expected to migrate. These volume calculations and 50% migration estimates were applied to the modified Strahler stream order densities to estimate total potential eroded sediment volumes (Table 4.1). Modified Strahler stream orders of 4 or 5 were found at 87.5% of studied channel heads, with over half of the channel heads surveyed residing on 4<sup>th</sup>-order streams. A total of 640 4<sup>th</sup>-order (modified) streams are located within the 23 km<sup>2</sup> area of William B. Umstead State Park. Thus, if we assume that channel heads will continue to migrate up-valley at 50% of the modified 4<sup>th</sup>-

order stream locations ( $n = 320$ ) and the average eroded volume per channel is used ( $282.6 \text{ m}^3$  [S.D. =  $177.6 \text{ m}^3$ ]), the result is an additional  $90,419 \pm 56,838 \text{ m}^3$  (68% conf.) of expected sediment erosion from the presently unchannelized valley bottom areas within the state park. More conservatively, if all channel heads are assumed to reside on modified 5<sup>th</sup>-order streams,  $21,333 \pm 13,410 \text{ m}^3$  (68% conf.) of future erosion should be expected (Table 1).

Although the up-valley channel head migration rate is unquantified at present, anecdotally, we did not observe any appreciable change in the location of nine different channel head sites that were monitored over 12 months. However, large tree roots exposed meters downstream from channel head locations (e.g., Figures 4.4c; 4.5) confirm that some channel heads do sporadically migrate up the valley. Applying a conservative migration rate estimate of  $0.01 \text{ m a}^{-1}$  to the average predicted (modeled) migration distance of 174 m (Figure 4.10) indicates that it might take ~15,000 years for some of the channel heads to reach their predicted equilibrium location set by local slope and upstream contributing area. Most are likely to migrate upstream more quickly, and providing better channel head migration rates is an important next step to understanding erosion persistence. The rate of channel head migration has implications for the persistence and severity of the release of fine-grained hillslope legacy sediment into fluvial networks, receiving reservoirs, and ultimately coastal estuaries.

### 5.3 Implications for downstream ecosystems

Along with introducing large volumes of fine-grained, mostly legacy sediment to fluvial networks that previously existed in unchannelized regions of valley bottoms, eroding channel heads also constitute a potential diffuse, non-point source of nutrient input to headwater streams. Using the average volume of erosion ( $90,419 \pm 56,838 \text{ m}^3$ ; section 5.2) for the  $23 \text{ km}^2$  area that encompasses the state park and an average soil bulk density of  $1.3 \text{ g/cm}^3$  (Bradley, 2020), we

find the mass of soil from future erosion of channel heads to be  $1.06 \times 10^8 \pm 6.68 \times 10^7$  kg (68% conf.) (i.e.,  $106 \pm 67$  t). The proportion of each soil horizon and its respective nutrient content (Figure 4.12) was then determined and totaled to forward-estimate the contributions of nutrients from up-valley migration of channel heads found within the state park (Table 4.2). For this 23 km<sup>2</sup> area, approximately  $9.51 \times 10^5 \pm 2.77 \times 10^5$  kg (68% conf.) ( $951 \pm 277$  t) of carbon,  $4.38 \times 10^4 \pm 1.24 \times 10^4$  kg ( $44 \pm 12$  t) of total nitrogen, and  $1.32 \times 10^4 \pm 3.85 \times 10^3$  kg ( $13 \pm 4$  t) of phosphorus can be expected to enter the fluvial system in response to channel head migration.

In a broader context, the headwaters investigated here impact local reservoirs (Wiltsie et al., 2018) and ultimately empty into the Neuse River estuary (Pamlico Sound). Excess nutrient supply, specifically nitrogen and phosphorus, lead to eutrophication of water bodies and have been linked to harmful algal blooms (e.g., Pearl et al., 2009; Pearl et al., 2016), which can ultimately be ingested by livestock, pets, and humans (Carmichael & Boyer, 2016). While research shows that concentrations of carbon can vary considerably throughout drainage basins (e.g., Inamdar et al., 2012; Bhattacharya & Osburn, 2020), it is known that carbon, particularly in the form of dissolved organic matter (DOM), can influence the rate of photochemical reactions and available light for photosynthesis in the water column (e.g., Tzortziou et al., 2008; Graeber et al., 2012). Thus, changing nutrient and fine-grained sediment inputs to low-energy reservoirs can impact the overall health of the ecosystems that depend on the delicate balance of water quality within them.

Eutrophication is often linked to climate change and present-day land-use changes (e.g., Rabalais et al., 2009; Jokinen et al., 2018); however, our work shows that historical land use may play a larger role than typically appreciated, in part and specifically through the re-establishment of equilibrium channel head locations. The impacts of this geomorphic process is likely to

continue for hundreds to thousands of years to come. More spatially detailed soil investigations are needed to quantify the mass, transport fate, and bio-availability of soil-bound nutrients likely to be liberated from low-relief headwater basin soils as channel heads reestablish their slope-area predicted equilibrium locations via up-valley migration.

## 6. Conclusions

The spatial relationships between predicted hillslope-to-valley transition zones upstream from channel heads in the eastern North Carolina Piedmont was investigated. We found that for ~50% of surveyed streams, 23 of 40 channel heads currently exist at larger drainage areas (average area = 28,000 m<sup>2</sup>,  $n = 40$ ) than their predicted locations in slope-area space (between 1,380 and 8,710 m<sup>2</sup>). For these 23 channel heads, the average difference between the observed and expected locations was 174.4 m [S.D. = 109.6 m]. We interpret this as the result of agricultural practices from the late 1700s to the 1930s that led to increased erosion of upland soils, now preserved in low-order valley bottoms as legacy sediment. Evidence for present-day up-valley migration of channel heads, such as recently exposed tree roots along channels, indicates that this landscape is still recovering from disturbance and that fluvial networks across the region could feel the impacts of European settlement for millennia.

Observed channel heads exhibit a significant inverse relationship between local slope (m/m) and contributing area (m<sup>2</sup>) as described by the equation;  $\text{Area} = 1163 * \text{Slope}^{-1.06}$ . The slope exponent close to unity indicates that this landscape is likely still recovering from anthropogenic disturbance. This finding is consistent with other studies of ephemeral headwater Piedmont stream channels.

Measured channel head widths and depths were used to calculate an average cross-sectional area that, when combined with up-valley migration distances, yielded a per-channel eroded sediment volume of  $282.6 \text{ m}^3$  [S.D. =  $177.6 \text{ m}^3$ ]. This estimated range of future per-channel erosion and the finding that ~50% of channel heads are predicted to migrate was combined with an analysis of the drainage density as a function of stream order to arrive at an average predicted erosion volume of  $90,419 \pm 56,838 \text{ m}^3$  (68% conf.) across the  $23 \text{ km}^2$  state park study area. Finally, results from soil samples were used to quantify the nutrient contributions from the calculated sediment volumes and found that  $9.5 \times 10^5 \pm 2.8 \times 10^5 \text{ kg}$  (68% conf.) ( $951 \pm 277$  metric tons) of carbon,  $4.4 \times 10^4 \pm 1.2 \times 10^4 \text{ kg}$  ( $44 \pm 12$  metric tons) of total nitrogen, and  $1.3 \times 10^4 \pm 3.9 \times 10^3 \text{ kg}$  ( $13 \pm 4$  metric tons) of phosphorus will be released into the drainage network as a result of the upvalley propagation of channel heads. These nutrients and fine-grained sediments have consequences for the quality (light penetration, eutrophication) of downstream receiving waters. In addition, they likely represent a non-point source for fine-grained sediment (TSS) and nutrients previously overlooked in regional water quality modeling efforts. While the daily, monthly, or annual contributions from any single up-valley migrating channel head are small, the cumulative ‘slow bleed’ across anthropogenically modified Piedmont landscape units may be substantial and is likely to persist for hundreds to thousands of years into the future.

## 7. Acknowledgements

The authors would like to thank the Geological Society of America for partially funding the data collection and sample processing through a Graduate Student Research Grant to Atkins. Many thanks to the graduate and undergraduate students who assisted in field data collection, including

Rachael McCaully, Joeseeph Bolla, Justin Bealo, and Daniel Russell. Also to Dr. Matthew Ricker for assisting with Umstead soil characterization. A special thank you goes to Milo and Franklin Wegmann for trekking through Umstead with dad on multiple weekends, looking at channels, and especially Milo for his help with excel calculations!

## Figures

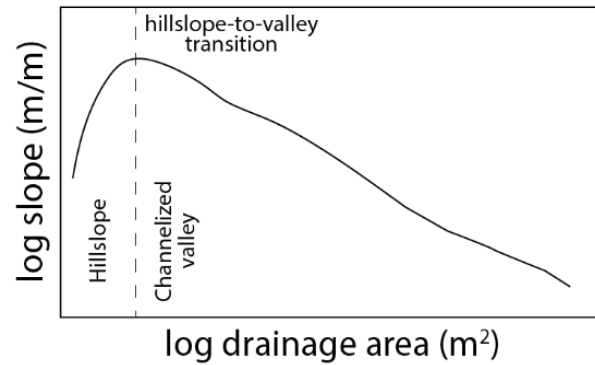


**Figure 4.1** Schematic of the dominant headwater geomorphic process zones for the Piedmont of North Carolina, denoted by a roll-over from a positive-to-negative relationship between the log of the local slope versus the log of contributing drainage area relationship (adapted from Sweeney et al., 2015, Tarolli & Dalla Fontana, 2009; Montgomery & Foufoula-Georgiou, 1993; Willgoose et al., 1991). Note that hillslopes are not steep or long enough to generate debris flows in the Appalachian Piedmont, so that process zone is excluded. Headwater channels commonly exhibit both alluvial and short bedrock-dominated reaches.

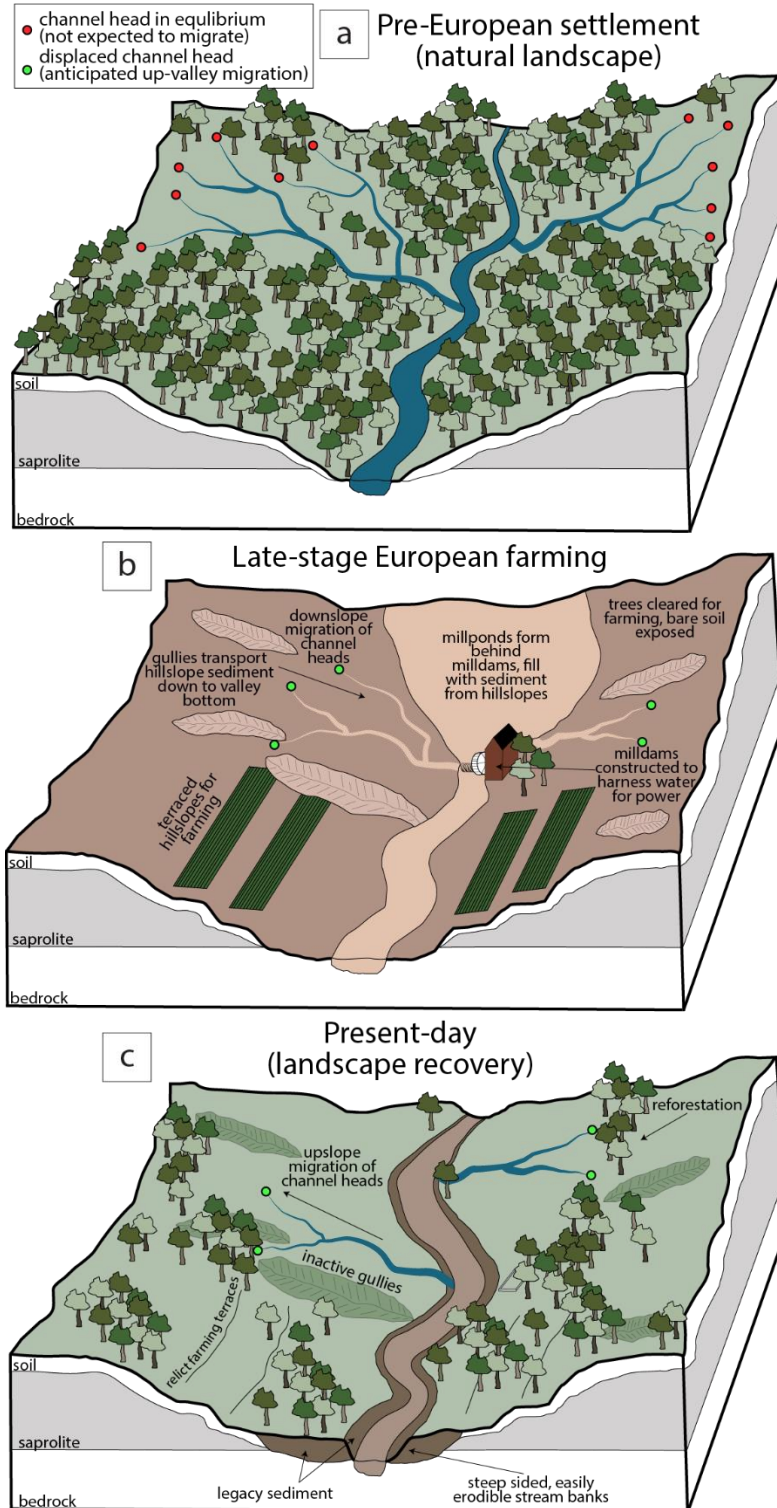


**Figure 4.2** A time-series schematic of (a) an idealized Piedmont landscape before European arrival, (b) immediately after the era of intensive forest clearing and farming, and before the introduction of soil-erosion control measures. (c) Schematic depiction of the landscape recovery (present-day) following disturbance. In the study area, landscape recovery began about 1935 CE.

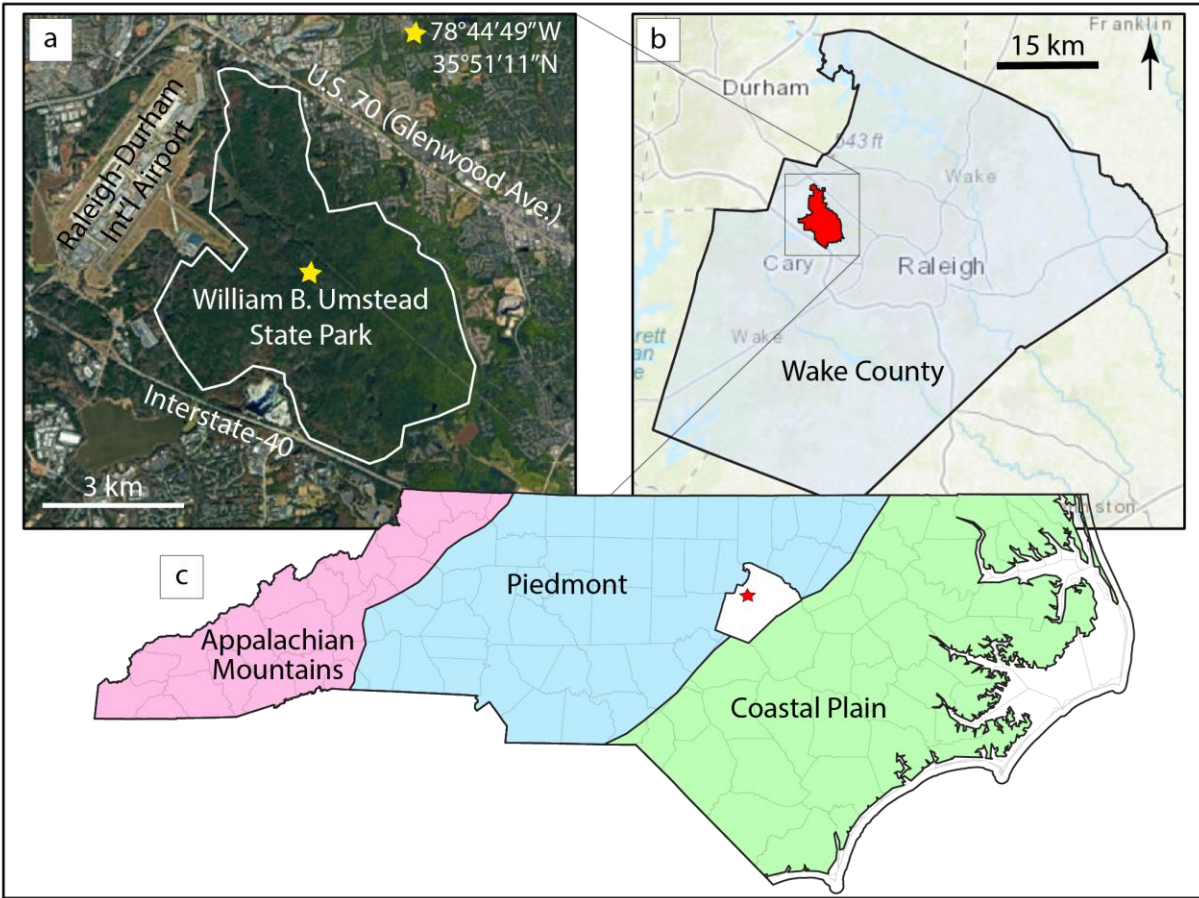


**Figure 4.3** Study area. (a-b) Satellite view and map location of North Carolina’s William B. Umstead State Park (USP) located northwest of Raleigh, in Wake County. (c) Wake County is in the eastern portion of the Piedmont physiographic province of North Carolina. USP location in Wake County is marked by the red star.



**Figure 4.4** Field photos of channel heads located in William B. Umstead State Park showing differing morphologies. Panels (a) and (b) are examples of low-relief channel initiation points, (c) and (d) are examples of channel heads with more significant plunge pools and wider channels. In (c), note the exposed roots of a *Liriodendron tulipifera* tree that attest to recent headward retreat and soil erosion by this channel head. Soil piping may be occurring at this location. The white lines delineate channel margins. The direction of flow is towards the bottom of the photograph in all cases.

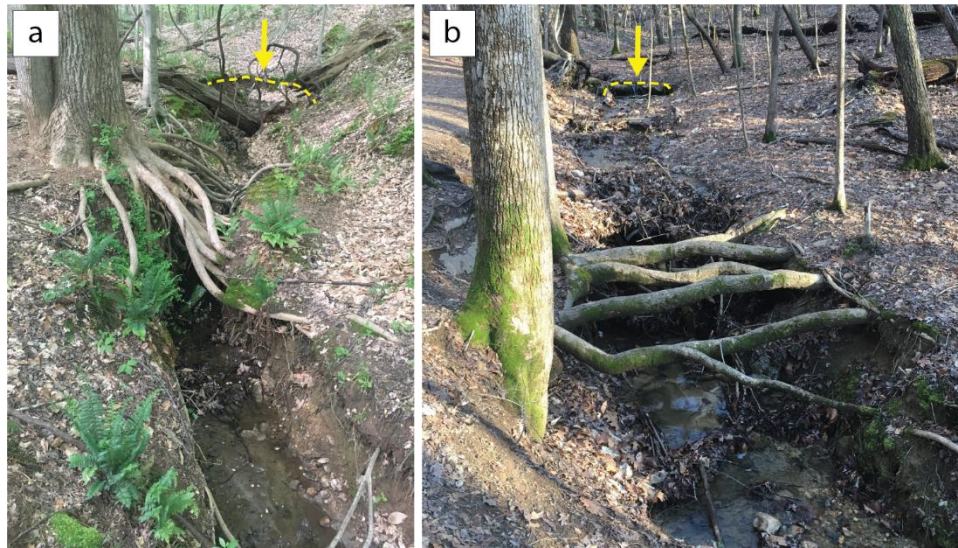


**Figure 4.5** Examples of *Liriodendron tulipifera* roots exposed by recent headward migration of the channel head location along first-order channels of Umstead State Park. The 2018 channel head locations, identified as the upstream most point with clearly defined banks, are marked by the dashed yellow lines and arrows. Flow is toward the bottom of each photograph.

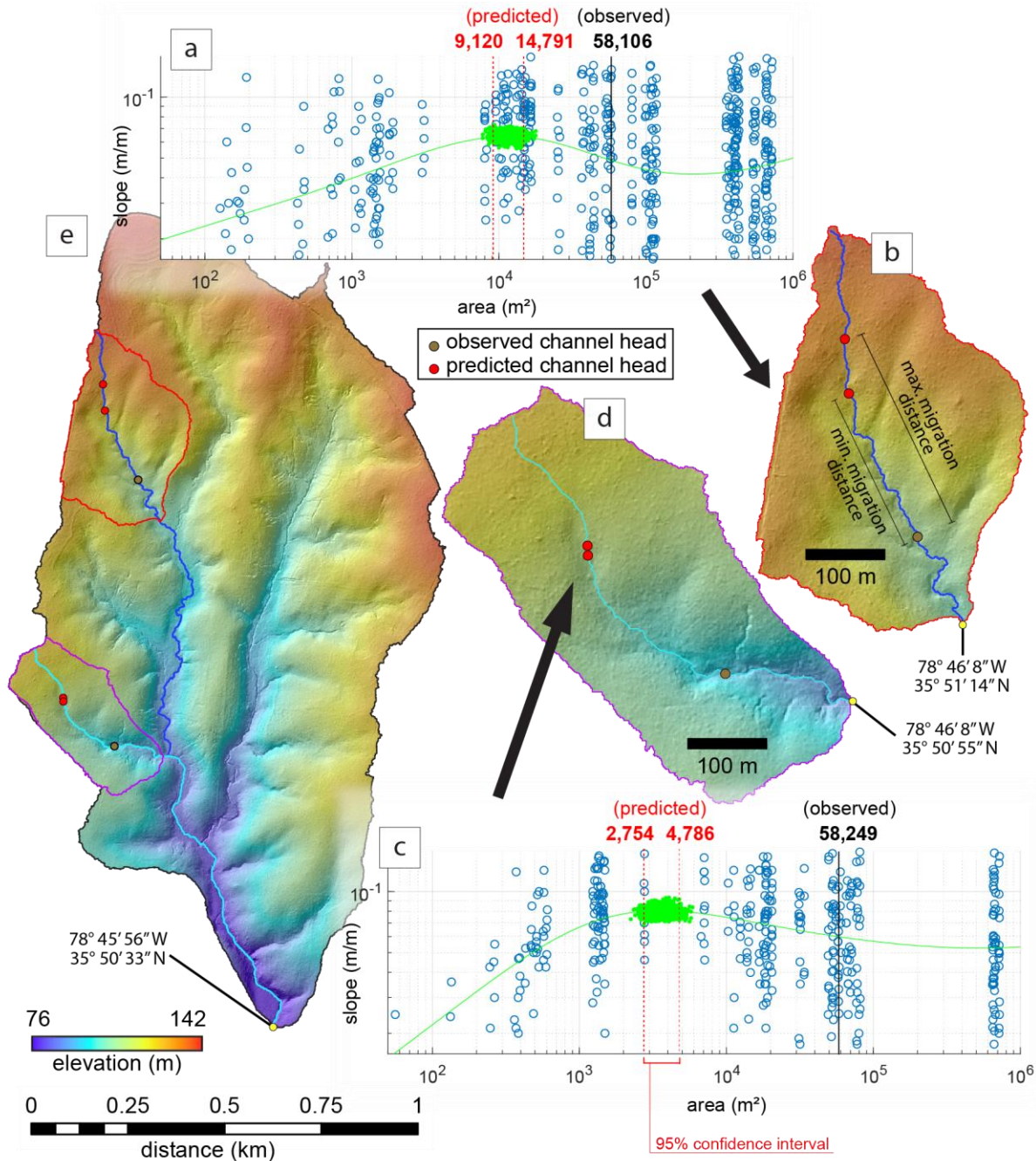


**Figure 4.6** The process for modeling channel head initiation locations in Piedmont basins. (a) Scatter plot of the log of local channel slope vs. the log of contributing area for an individual channel whose length is artificially extended to the drainage divide for the sub-basin shown in (b). The observed channel head position (black line) is located where the contributing area is 58,106 m<sup>2</sup>. A smoothing spline fit (curved green line) was fit to 2,000 predicted spline peaks (green points) using a bootstrap resampling approach to determine the predicted location (maximum along the green line) at 95% confidence (red lines) should lie between 14,791 and 9,120 m<sup>2</sup>. (c) Slope vs. area plot for sub-basin shown in d indicating that the observed channel head at 58,249 m<sup>2</sup> is downslope of the predicted range of contributing areas (4,786 to 1,754 m<sup>2</sup>). These two example sub-basins are both located within the larger basin (e).

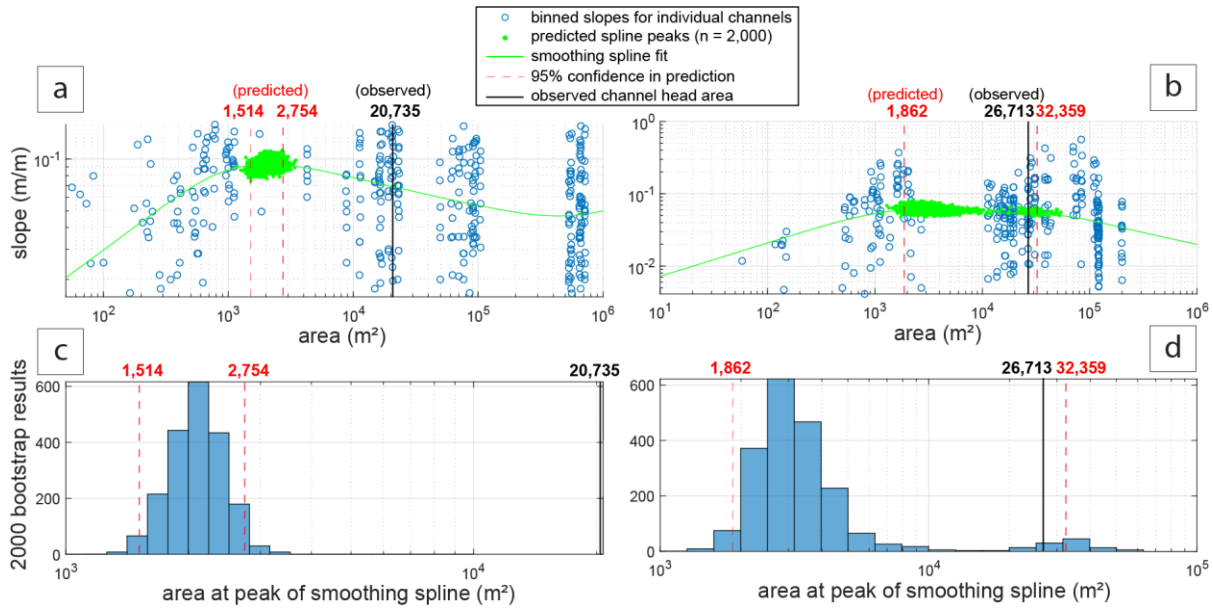


**Figure 4.7** Slope-area plots constructed using 0.25 log bins of area. **(a)** An example where the observed channel head (black line) is positioned down the valley from the predicted location (dashed red lines) as determined by the 2,000 bootstrapped samples (green points) and maximum best fit smoothing spline (curved green line). The channel head in this example is predicted to migrate up the valley until its location falls within the predicted range of contributing area. **(b)** Example basin where the observed channel head location is within the predicted area range and thus not predicted to migrate. **(c & d)** Distribution of contributing areas at the peak of each of 2,000 bootstrapped smoothing splines; dashed red lines are the 95% confidence range.

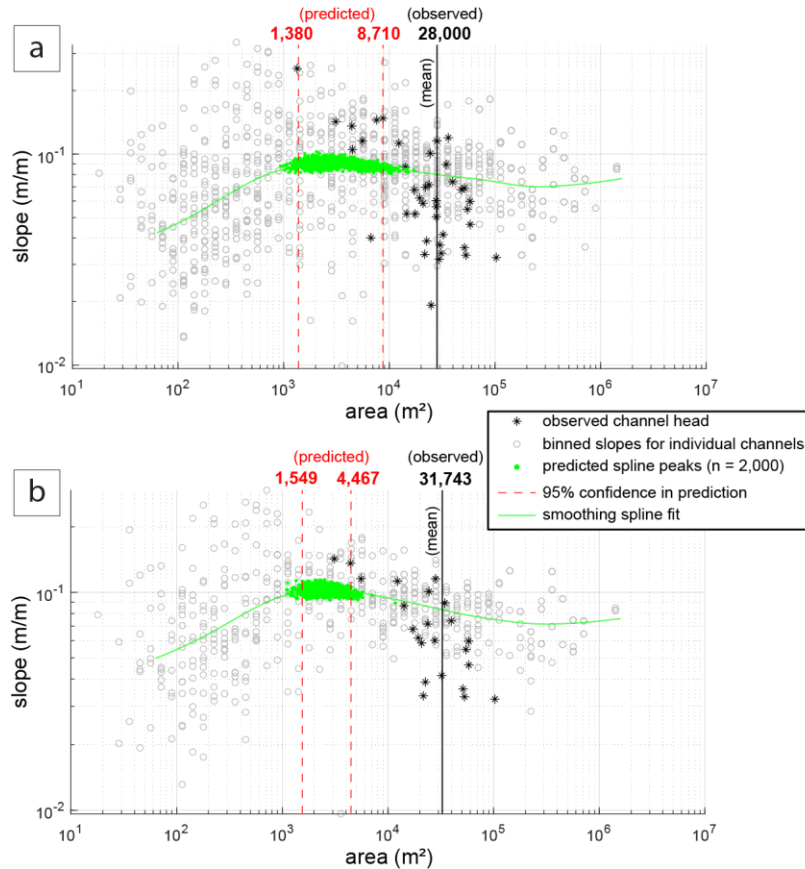


**Figure 4.8** Slope-area plots constructed using 0.25 log bins of area for (a) all study channels ( $n = 40$ ) and (b) the sub-population ( $n = 23$ ) of those predicted to migrate when fit without binning. The average contributing drainage areas of the observed channel heads are displayed as the vertical black lines and the modeled 95% confidence range of predicted locations as vertical dashed red lines for both plots based upon the results of the smoothing spline fit (curved green line) for 2,000 predicted spline peaks (green points) using a bootstrap resampling approach. When predicted migration distances are determined using aggregate data, two of the 23 observed channel head locations predicted to migrate when analyzed individually are no longer predicted to do so (plot-b). A smoothing spline parameter ( $p_{smooth}$ ) = 0.5 is used in both plots.

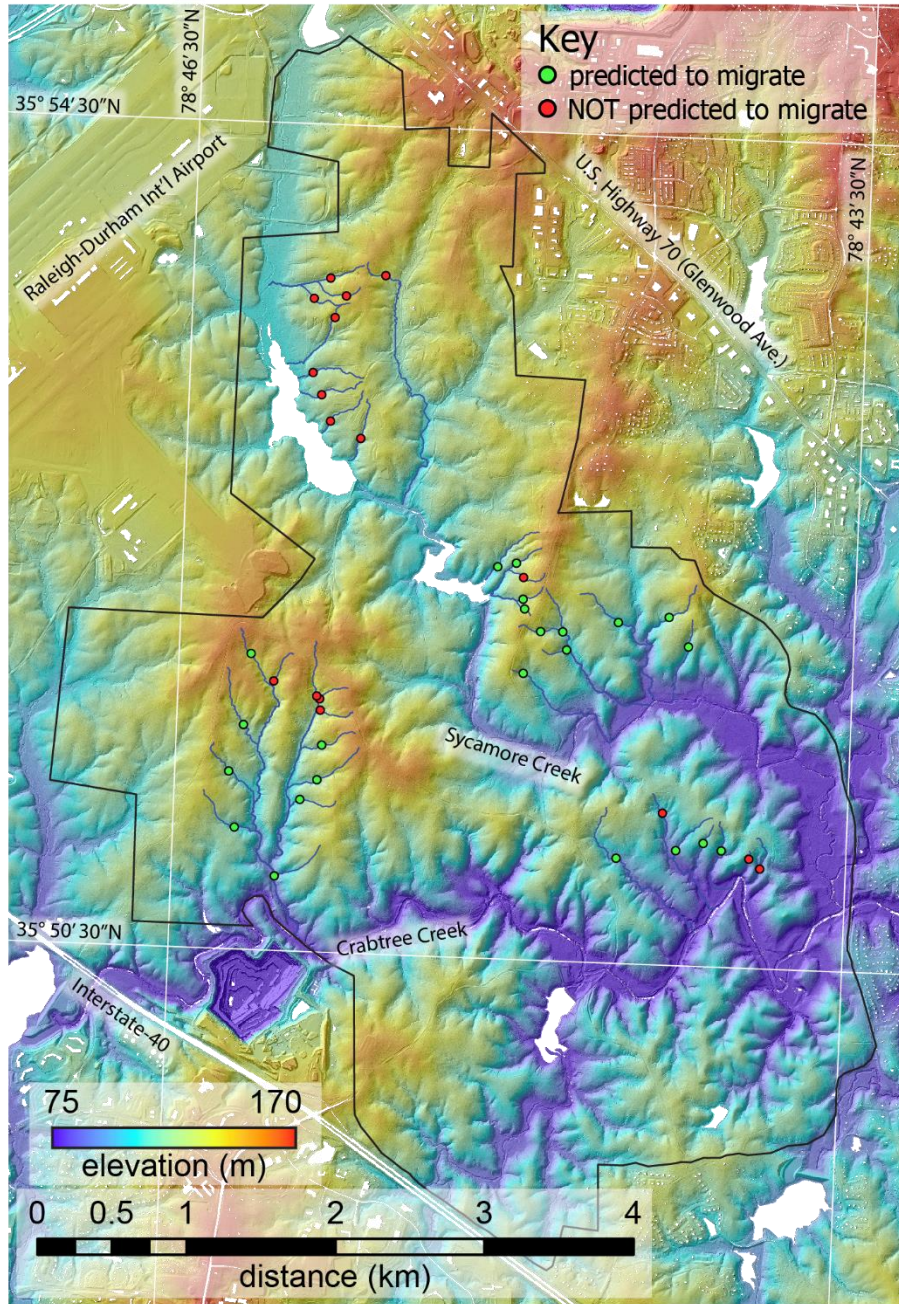


**Figure 4.9** The spatial location of 40 investigated channel heads (green = migration predicted; red = migration not predicted) and their trunk channels (blue lines) in William B. Umstead State Park. The solid black line encloses the park.

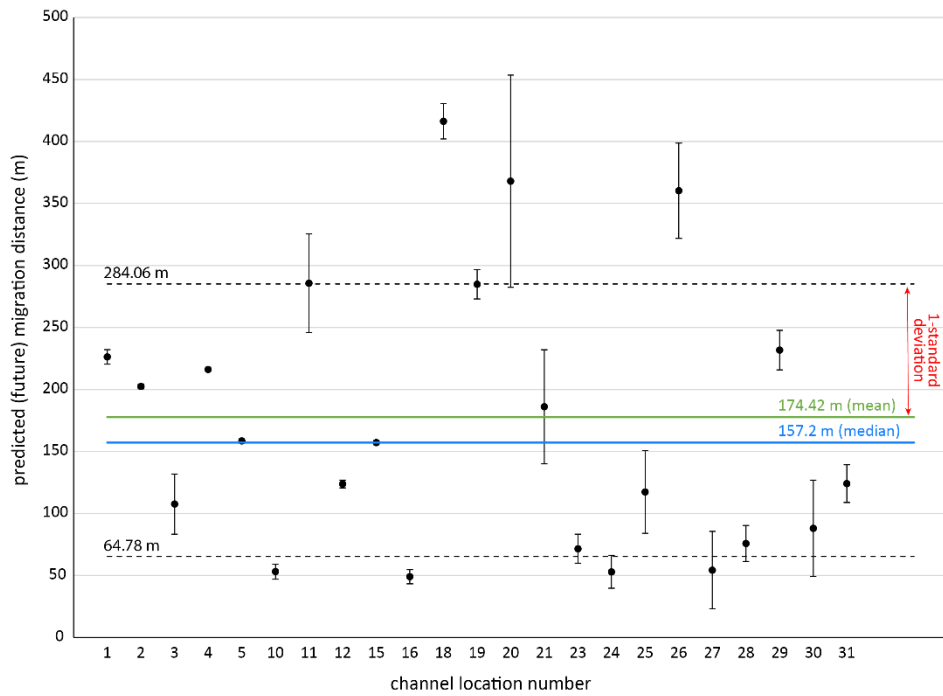


**Figure 4.10** Estimated future up-valley channel head migration distances for the 23 channels that are predicted to migrate. Vertical bars represent the range in distances, with the black dots as the midpoint between the minimum and maximum. Dashed black lines indicate one standard deviation from the median (solid green line) of the population of 23 channels.

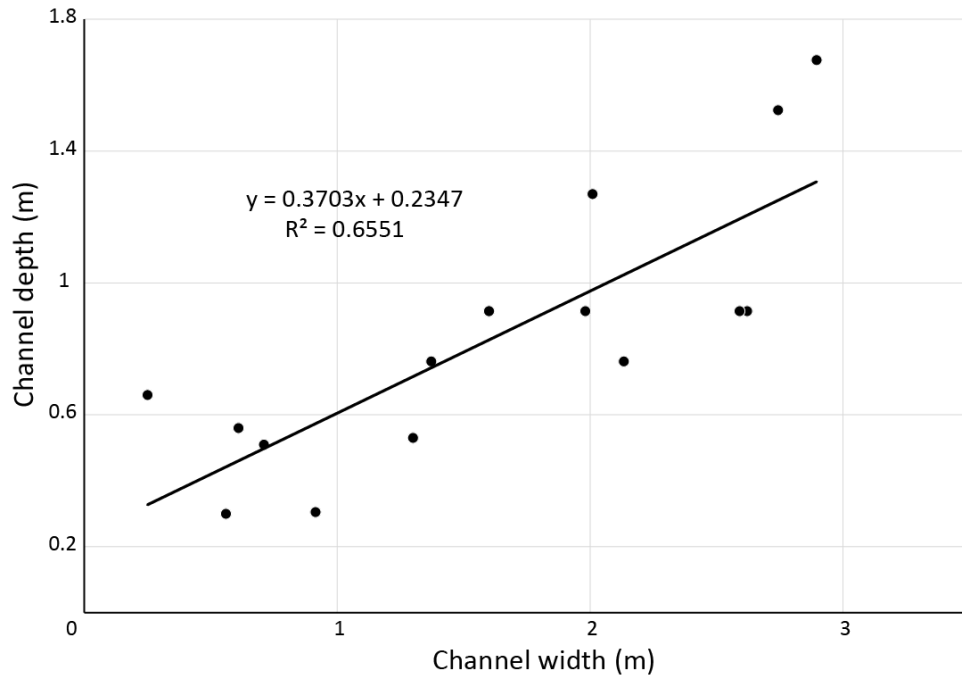


**Figure 4.11** Channel width and depth measurements for 15 channels located 5 to 10 m downstream from current channel heads.

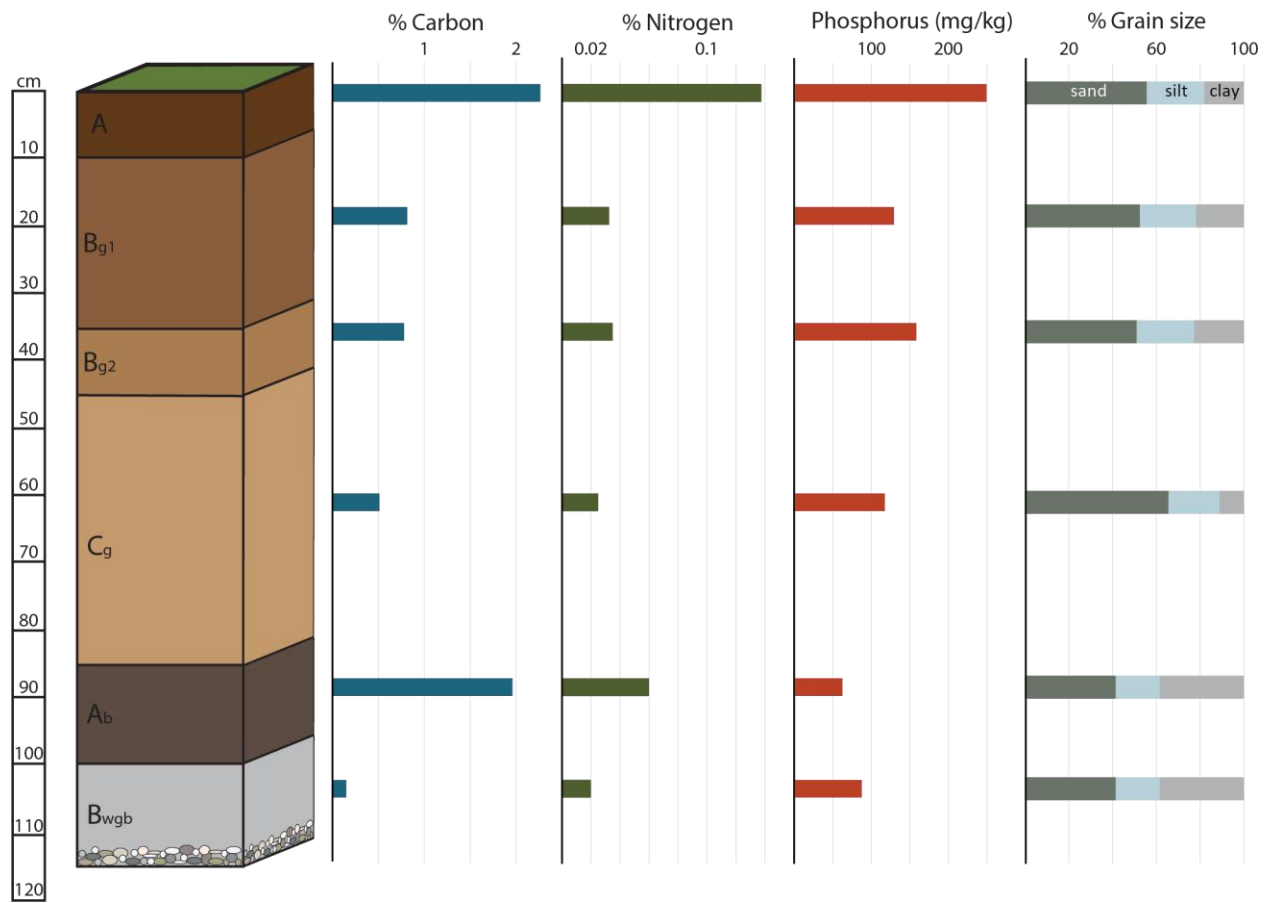


**Figure 4.12** A generalized composite soil profile upslope of sampled channel heads in Umstead State Park with soil horizon thicknesses, nutrient (carbon, nitrogen, and phosphorous) content, and grain sizes. Soil horizon abbreviations follow the suggested nomenclature of the Keys to Soil Taxonomy 12<sup>th</sup> edition (Soil survey Staff, 2014).

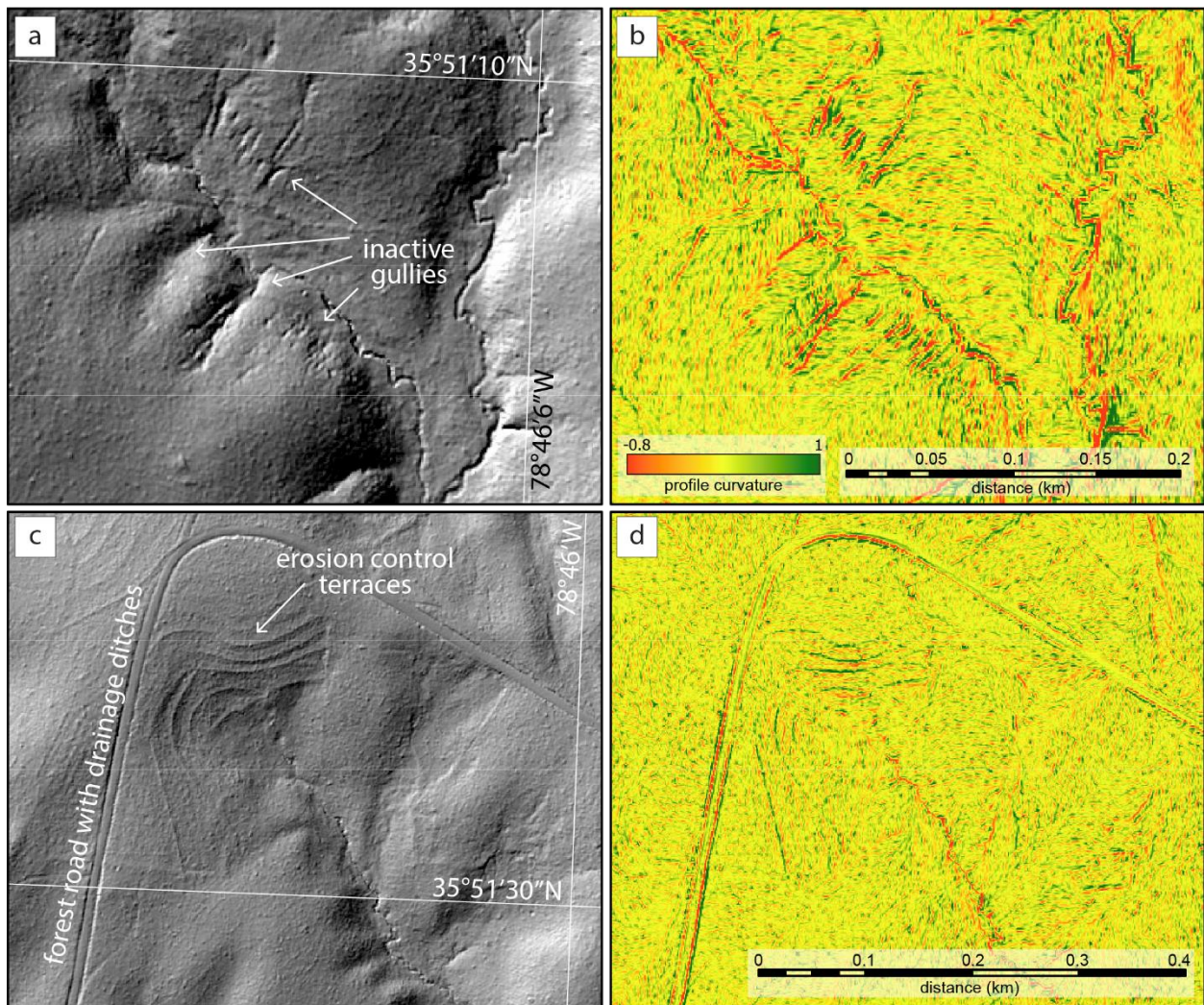


**Figure 4.13** Examples of anthropogenic topographic features visible in 1m lidar topographic data within the study area are present on parts of the landscape with small flow accumulation area values. **(a)** Hillshade and **(b)** profile curvature maps of a sub-basin with several inactive (legacy) gullies. **(c)** Hillshade and **(d)** profile curvature maps identifying erosion control terraces and a forest road. The existence of topographic features such as these in lidar data (here and elsewhere) hinders the identification of hillslope-to-channel transitions when using average slopes from basin-binned areas.

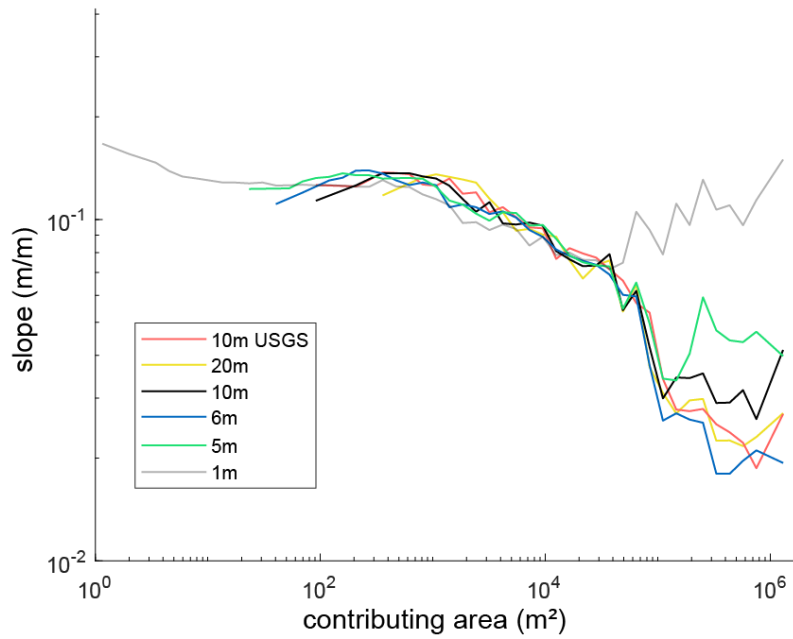


**Figure 4.14** Log-log plot of local slope versus contributing basin area as a function DEM resolution for a single catchment used to explore the impact of DEM resolution on slope-area relationships for predicting channel head locations. Note the steeper slopes at very low contributing drainage areas for the highest resolution topography data. The 1, 5, 10, and 20 m data were downsampled from the 1 m QL2 Lidar, while the 6 m data is the 2002 legacy QL1 Lidar for North Carolina, and the 10 m DEM is from the USGS National Elevation Dataset (Gesch et al., 2002).

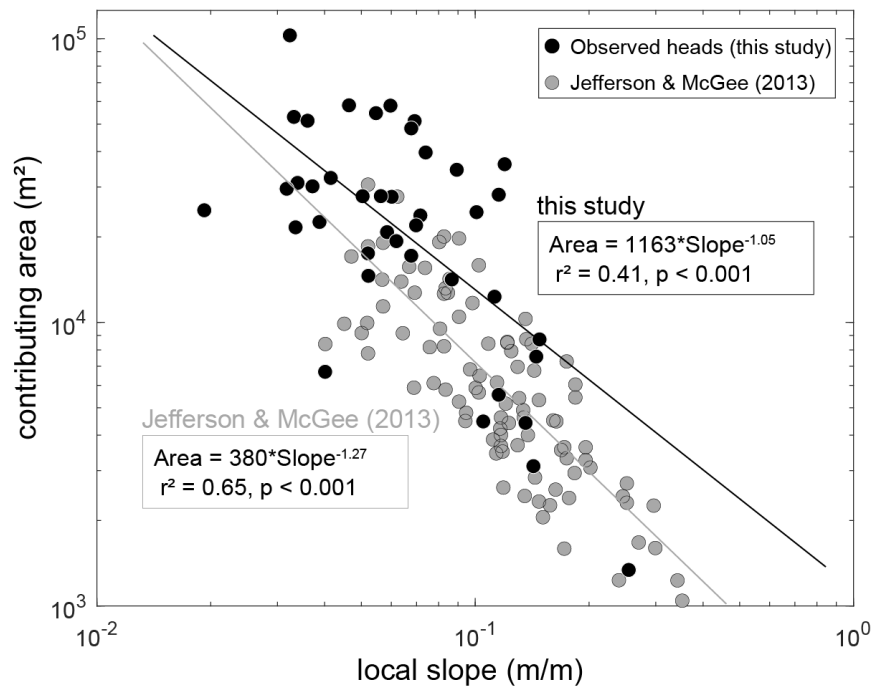


**Figure 4.15** Comparison of local slope and the contributing area at channel head locations between sites in the western and central North Carolina Piedmont (gray points) reported by Jefferson & McGee (2013) and the eastern Piedmont of this study (black points).

**Table 4.1** Future erosion potential for Umstead State Park using average erosion volume per stream ( $282.6 \pm 177.6 \text{ m}^2$ ) and drainage density information from a modified Strahler stream order analysis. These values conservatively assume that 50% of channels of a given stream order will migrate.

<b>Modified Strahler Stream order</b>	<b>4</b>	<b>5</b>
<b>Evaluated Channel Heads (<math>n=40</math>)</b>	21	14
<b>Number of streams in entire USP</b>	640	151
<b>Eroded sediment volume potential (<math>\text{m}^3</math>) if only 50% of streams migrate</b>	$90,419 \pm 56,838$	$21,333 \pm 13,410$
<b>Lower bound of 68% confidence (eroded sediment volume in <math>\text{m}^3</math>)</b>	33,581	7,923
<b>Upper bound of 68% confidence (eroded sediment volume in <math>\text{m}^3</math>)</b>	147,258	34,744

**Table 4.2** Future nutrient contribution potential for Umstead State Park headwater channels resulting from the up-valley expansion of the drainage network. Results, by average soil horizon thickness and in aggregate rely on the average erosion volume, the assumption that 50% of modified 4<sup>th</sup>-order streams will migrate ( $90,419 \pm 56,838 \text{ m}^3$ , calculated in Table 1), a soil bulk density of  $1.3 \text{ g/cm}^3$  (Bradley, 2020), and nutrient values from Fig. 12. Confidence intervals (68%) are listed for each horizon, totals are calculated using appropriate error propagation techniques.

<i>Horizon</i>	<i>% of soil column</i>	<i>Total Carbon (kg)</i>	<i>± (kg)</i>	<i>Total Nitrogen (kg)</i>	<i>± (kg)</i>	<i>Total Phosphorus (kg)</i>	<i>± (kg)</i>
<i>A</i>	8.70	209,356	131,602	12,709	7,989	2,303	1,448
<i>Bg1</i>	21.74	188,241	118,330	7,507	4,719	2,989	1,879
<i>Bg2</i>	8.70	72,096	45,320	3,235	2,034	1,463	920
<i>Cg</i>	34.78	189,066	118,848	9,238	5,807	4,345	2,731
<i>Ab</i>	13.04	271,538	170,691	8,312	5,225	867	545
<i>Bwgb</i>	13.04	20,781	13,063	2,771	1,742	1,216	764
<b>TOTAL</b>	<b>100</b>	<b>951,079</b>	<b>277,139</b>	<b>43,772</b>	<b>12,421</b>	<b>13,183</b>	<b>3,849</b>

## Chapter 4 References

- Auch, R. F., Napton, D. E., Sayler, K. L., Drummond, M. A., & Sorenson, D. G. (2015). The Southern Piedmont's Continued Land-Use Evolution , 1973 – 2011. *Southeastern Geographer*, 55(3), 338–361.
- Avcioglu, B., Anderson, C. J., & Kalin, L. (2017). Evaluating the Slope-Area Method to Accurately Identify Stream Channel Heads in Three Physiographic Regions. *Journal of the American Water Resources Association*, 53(3), 562–575. <https://doi.org/10.1111/1752-1688.12512>
- Bastola, S., Dialynas, Y. G., Bras, R. L., Noto, L. V., & Istanbuluoglu, E. (2018). The role of vegetation on gully erosion stabilization at a severely degraded landscape: A case study from Calhoun Experimental Critical Zone Observatory. *Geomorphology*, 308, 25–39. <https://doi.org/10.1016/j.geomorph.2017.12.032>
- Bhattacharya, R., & Osburn, C. L. (2020). Spatial patterns in dissolved organic matter composition controlled by watershed characteristics in a coastal river network: The Neuse River Basin, USA. *Water Research*, 169. <https://doi.org/10.1016/j.watres.2019.115248>
- Bradley, S. (2020). *Ecosystem Services Provided by Alluvial Soils Across an Urban to Rural Gradient* (Master's thesis, North Carolina State University, Raleigh, NC).
- Carmichael, W. W., & Boyer, G. L. (2016). Health impacts from cyanobacteria harmful algae blooms: Implications for the North American Great Lakes. In *Harmful Algae* (Vol. 54, pp. 194–212). <https://doi.org/10.1016/j.hal.2016.02.002>
- Costa, J. E. (1975). Effects of agriculture on erosion and sedimentation in the Piedmont province, Maryland. *Bulletin of the Geological Society of America*, 86(9), 1281–1286. [https://doi.org/10.1130/0016-7606\(1975\)86<1281:EOAOEA>2.0.CO;2](https://doi.org/10.1130/0016-7606(1975)86<1281:EOAOEA>2.0.CO;2)
- Dalla Fontana, G., & Marchi, L. (2003). Slope-area relationships and sediment dynamics in two alpine streams. *Hydrological Processes*, 17(1), 73–87. <https://doi.org/10.1002/hyp.1115>
- Dietrich, W. E., & Dunne, T. (1993). The Channel Head. In *Channel Network Hydrology* (Issue 7, pp. 175–219). [papers2://publication/uuid/35014F2C-AA83-4D92-AC89-15DA53E9230C](https://doi.org/10.1029/1993JF001993)
- Downing, J. A., Cole, J. J., Duarte, C. M., Middelburg, J. J., Melack, J. M., Prairie, Y. T., Kortelainen, P., Striegl, R. G., Mcdowell, W. H., & Tranvik, L. J. (2012). *Inland Waters Global abundance and size distribution of streams and rivers*. <https://doi.org/10.5268/IW-2.4.502>
- Fleming, P. M., Merritts, D. J. and Walter, R. C.: Legacy sediment erosion hot spots: A cost-effective approach for targeting water quality improvements, *J. Soil Water Conserv.*, 74(4), 67A LP-73A, doi:10.2489/jswc.74.4.67A, 2019.
- Gallen, S. F., & Wegmann, K. W. (2017). River profile response to normal fault growth and linkage: An example from the Hellenic forearc of south-central Crete, Greece. *Earth Surface Dynamics*, 5(1), 161–186. <https://doi.org/10.5194/esurf-5-161-2017>
- Giannoni, F., Roth, G., & Rudari, R. (2005). A procedure for drainage network identification

- from geomorphology and its application to the prediction of the hydrologic response. *Advances in Water Resources*, 28(6), 567–581.  
<https://doi.org/10.1016/j.advwatres.2004.11.013>
- Gomi, T., Sidle, R. C., & Richardson, J. S. (2002). Understanding processes and downstream linkages of headwater systems. *BioScience*, 52(10), 905–916. [https://doi.org/10.1641/0006-3568\(2002\)052\[0905:UPADLO\]2.0.CO;2](https://doi.org/10.1641/0006-3568(2002)052[0905:UPADLO]2.0.CO;2)
- Graeber, D., Gelbrecht, J., Pusch, M. T., Anlanger, C., & von Schiller, D. (2012). Agriculture has changed the amount and composition of dissolved organic matter in Central European headwater streams. *Science of the Total Environment*, 438, 435–446.  
<https://doi.org/10.1016/j.scitotenv.2012.08.087>
- Henkle, J. E., Wohl, E., & Beckman, N. (2011). Locations of channel heads in the semiarid Colorado Front Range, USA. *Geomorphology*, 129(3–4), 309–319.  
<https://doi.org/10.1016/j.geomorph.2011.02.026>
- Horton, R. E. (1945). Erosional development of streams and their drainage basins; Hydrophysical approach to quantitative morphology. *Bulletin of the Geological Society of America*, 56(3), 275–370. [https://doi.org/10.1130/0016-7606\(1945\)56\[275:EDOSAT\]2.0.CO;2](https://doi.org/10.1130/0016-7606(1945)56[275:EDOSAT]2.0.CO;2)
- Hupp, C. R., Pierce, A. R., & Noe, G. B. (2009). Floodplain geomorphic processes and environmental impacts of human alteration along coastal plain rivers, USA. *Wetlands*, 29(2), 413–429. <https://doi.org/10.1672/08-169.1>
- Ijjasz-Vasquez, E. J., & Bras, R. L. (1995). Scaling regimes of local slope versus contributing area in digital elevation models. *Geomorphology*, 12(4), 299–311.  
[https://doi.org/10.1016/0169-555X\(95\)00012-T](https://doi.org/10.1016/0169-555X(95)00012-T)
- Inamdar, S., Finger, N., Singh, S., Mitchell, M., Levia, D., Bais, H., Scott, D., & McHale, P. (2012). Dissolved organic matter (DOM) concentration and quality in a forested mid-Atlantic watershed, USA. *Biogeochemistry*, 108(1–3), 55–76.  
<https://doi.org/10.1007/s10533-011-9572-4>
- Inamdar, S., Peipoch, M., Gold, A. J., Lewis, E., Hripto, J., Sherman, M., Addy, K., Merritts, D., Kan, J. and Groffman, P. M. (2021). Ghosts of landuse past: legacy effects of milldams for riparian nitrogen (N) processing and water quality functions, *Environ. Res. Lett.*, 16(3), 35016.
- Inamdar, S., Sienkiewicz, N., Lutgen, A., Jiang, G. and Kan, J. (2020). Streambank Legacy Sediments in Surface Waters: Phosphorus Sources or Sinks?, *Soil Syst.*, 4(2), 30.
- Istanbulluoglu, E., Tarboton, D. G., Pack, R. T., & Luce, C. (2002). A probabilistic approach for channel initiation. *Water Resources Research*, 38(12), 61-1-61–14.  
<https://doi.org/10.1029/2001WR000782>
- Jackson, C. R., Martin, J. K., Leigh, D. S., & West, L. T. (2005). A southeastern piedmont watershed sediment budget: Evidence for a multi-millennial agricultural legacy. *Journal of Soil and Water Conservation*, 60(6), 298–310.
- Jacobson, R. B., & Coleman, D. J. (1986). Stratigraphy and recent evolution of Maryland

- Piedmont flood plains. *American Journal of Science*, 286(8), 617–637.  
<https://doi.org/10.2475/ajs.286.8.617>
- Jefferson, A. J., & Mcgee, R. W. (2013). Channel network extent in the context of historical land use, flow generation processes, and landscape evolution in the North Carolina Piedmont. *Earth Surface Processes and Landforms*, 38(6), 601–613. <https://doi.org/10.1002/esp.3308>
- Jokinen, S. A., Virtasalo, J. J., Jilbert, T., Kaiser, J., Dellwig, O., Arz, H. W., Hänninen, J., Arppe, L., Collander, M., & Saarinen, T. (2018). A 1500-year multiproxy record of coastal hypoxia from the northern Baltic Sea indicates unprecedented deoxygenation over the 20th century. *Biogeosciences*, 15(13), 3975–4001. <https://doi.org/10.5194/bg-15-3975-2018>
- Julian, J. P., Elmore, A. J., & Guinn, S. M. (2012). Channel head locations in forested watersheds across the mid-Atlantic United States: A physiographic analysis. *Geomorphology*, 177–178, 194–203. <https://doi.org/10.1016/j.geomorph.2012.07.029>
- Kemp, D. B., Sadler, P. M., & Vanacker, V. (2020). The human impact on North American erosion, sediment transfer, and storage in a geologic context. *Nature Communications*, 11(1), 1–9. <https://doi.org/10.1038/s41467-020-19744-3>
- Lebo, M. E., Paerl, H. W., & Peierls, B. L. (2012). Evaluation of progress in achieving TMDL mandated nitrogen reductions in the Neuse river basin, North Carolina. *Environmental Management*, 49(1), 253–266. <https://doi.org/10.1007/s00267-011-9774-5>
- Lyons, N. J., Starek, M. J., Wegmann, K. W., & Mitasova, H. (2015). Bank erosion of legacy sediment at the transition from vertical to lateral stream incision. *Earth Surface Processes and Landforms*, 40(13), 1764–1778. <https://doi.org/10.1002/esp.3753>
- McNamara, J. P., Ziegler, A. D., Wood, S. H., & Vogler, J. B. (2006). Channel head locations with respect to geomorphologic thresholds derived from a digital elevation model: A case study in northern Thailand. *Forest Ecology and Management*, 224(1–2), 147–156. <https://doi.org/10.1016/j.foreco.2005.12.014>
- Merritts, D., Walter, R., Rahnis, M., Cox, S., Hartranft, J., Scheid, C., Potter, N., Jenschke, M., Reed, A., Matuszewski, D., & Kratz, L. (2013). The rise and fall of Mid-Atlantic streams: Millpond sedimentation, milldam breaching, channel incision, and stream bank erosion. In *The challenges of dam removal and river restoration* (21st ed., pp. 183–203). Geological Society of America Reviews in Engineering Geology.
- Milliman, J. D., & Syvitski, J. P. M. (1992). Geomorphic/Tectonic Control of Sediment Discharge to the Ocean: The Importance of Small Mountainous Rivers. *The Journal of Geology*, 100(5), 525–544. <https://doi.org/10.1086/629606>
- Montgomery, D. R. (2001). Slope Distributions, Threshold Hillslopes, and Steady-state Topography. *American Journal of Science*, 301(April/May), 432–454.
- Montgomery, D. R., & Dietrich, W. E. (1988). Where do channels begin? *Nature*, 336(6196), 232–234. <https://doi.org/10.1038/336232a0>
- Montgomery, D. R., & Foufoula-Georgiou, E. (1993). Channel network source representation using digital elevation models. *Water Resources Research*, 29(12), 3925–3934. <https://doi.org/10.1029/93WR02463>

- North Carolina Geological Survey, 1985, Geologic Map of North Carolina: North Carolina Geological Survey, General Geologic Map, scale 1:500,000.
- Paerl, H. W., Gardner, W. S., Havens, K. E., Joyner, A. R., McCarthy, M. J., Newell, S. E., Qin, B., & Scott, J. T. (2016). Mitigating cyanobacterial harmful algal blooms in aquatic ecosystems impacted by climate change and anthropogenic nutrients. In *Harmful Algae* (Vol. 54, pp. 213–222). <https://doi.org/10.1016/j.hal.2015.09.009>
- Paerl, H. W., Rossignol, K. L., Hall, S. N., Peierls, B. L., & Wetz, M. S. (2017). Phytoplankton community indicators of short- and long-term ecological change in the anthropogenically and climatically impacted Neuse river estuary, North Carolina, USA. In *Estuaries and Coasts* (Vol. 12, Issue 10, pp. 2190–2195). <https://doi.org/10.1007/s12237-009-9137-0>
- Paerl W., H. (2009). Controlling Eutrophication along the Freshwater–Marine Continuum: Dual Nutrient (N and P) Reductions are Essential. *Estuaries and Coasts*, 32(4), 593–601. <https://about.jstor.org/terms>
- Phillips, J. D. (1992). The source of alluvium in large rivers of the lower coastal plain of North Carolina. *Catena*, 19(1), 59–75. [https://doi.org/10.1016/0341-8162\(92\)90017-6](https://doi.org/10.1016/0341-8162(92)90017-6)
- Rabalais, N. N., Turner, R. E., Díaz, R. J., & Justić, D. (2009). Global change and eutrophication of coastal waters. *ICES Journal of Marine Science*, 66(7), 1528–1537. <https://doi.org/10.1093/icesjms/fsp047>
- Reusser, L., Bierman, P., & Rood, D. (2015). Quantifying human impacts on rates of erosion and sediment transport at a landscape scale. *Geology*, 43(2), 171–174. <https://doi.org/10.1130/G36272.1>
- Schwanghart, W., & Scherler, D. (2014). Short Communication: TopoToolbox 2 – MATLAB-based software for topographic analysis and modeling in Earth surface sciences. *Earth Surface Dynamics*, 2(1), 1–7. <https://doi.org/10.5194/esurf-2-1-2014>
- Soil Survey Staff. (2014). Keys to Soil Taxonomy, 12th ed. USDA-Natural Resources Conservation Service, Washington, DC.
- Starek, M. J., Mitasova, H., Wegmann, K. W., & Lyons, N. (2013). Space-time cube representation of stream bank evolution mapped by terrestrial laser scanning. *IEEE Geoscience and Remote Sensing Letters*, 10(6), 1369–1373. <https://doi.org/10.1109/LGRS.2013.2241730>
- Tarboton, D. G., Bras, R. L., & Rodriguez-Iturbe, I. (1991). On the extraction of channel networks from digital elevation data. *Hydrological Processes*, 5(1), 81–100. <https://doi.org/10.1002/hyp.3360050107>
- Tarolli, P. (2014). High-resolution topography for understanding Earth surface processes: Opportunities and challenges. *Geomorphology*, 216, 295–312. <https://doi.org/10.1016/j.geomorph.2014.03.008>
- Tarolli, P., & Dalla Fontana, G. (2009). Hillslope-to-valley transition morphology: New opportunities from high resolution DTMs. *Geomorphology*, 113(1–2), 47–56. <https://doi.org/10.1016/j.geomorph.2009.02.006>

- Trimble, S. W. (1975). A volumetric estimate of man-induced soil erosion on the southern Piedmont Plateau. *Present and Prospective Technology for Predicting*, 142–152. <http://scholar.google.com/scholar?hl=en&btnG=Search&q=intitle:A+Volumetric+Estimate+Of+Man-Induced+Soil+Erosion+On+The+Southern+Piedmont+Plateau#0%5Cnhttp://scholar.google.com/scholar?hl=en&btnG=Search&q=intitle:A+volumetric+estimate+of+man-induced+soil+e>
- Trimble, S. W. (1977). The fallacy of stream equilibrium in contemporary denudation studies. *American Journal of Science*, 277(7), 876–887. <https://doi.org/10.2475/ajs.277.7.876>
- Tzortziou, M., Neale, P. J., Osburn, C. L., Megonigal, J. P., Maie, N., & Jaffé, R. (2008). Tidal marshes as a source of optically and chemically distinctive colored dissolved organic matter in the Chesapeake Bay. *Limnology and Oceanography*, 53(1), 148–159. <https://doi.org/10.4319/lo.2008.53.1.0148>
- U.S. Department of Agriculture, 1935, Application for Purchase and Development of Crabtree Creek Industrial Recreational Submarginal Project: Washington, D.C.
- United States Department of Agriculture. (2018). *Web Soil Survey*. <https://websoilsurvey.sc.egov.usda.gov/App/WebSoilSurvey.aspx>
- U.S. EPA. 1996. "Method 3050B: Acid Digestion of Sediments, Sludges, and Soils," Revision 2. Washington, DC.
- Vergari, F., Troiani, F., Faulkner, H., Del Monte, M., Della Seta, M., Ciccacci, S., & Fredi, P. (2018). The use of the Slope-Area function to analyse process domains in complex badland landscapes. *Earth Surface Processes and Landforms*. <https://doi.org/10.1002/esp.4496>
- Voli, M. T., Wegmann, K. W., Bohnenstiehl, D. W. R., Leithold, E., Osburn, C. L., & Polyakov, V. (2013). Fingerprinting the sources of suspended sediment delivery to a large municipal drinking water reservoir: Falls Lake, Neuse River, North Carolina, USA. *Journal of Soils and Sediments*, 13(10), 1692–1707. <https://doi.org/10.1007/s11368-013-0758-3>
- Walter, R. C., & Merritts, D. J. (2008). Natural streams and the legacy of water-powered mills. *Science*, 319(5861), 299–304. <https://doi.org/10.1126/science.1151716>
- Wegmann, K.W., Lewis, R.Q., and Hunt, M.C.2 (2012). Historic mill ponds and piedmont stream water quality: Making the connection near Raleigh, North Carolina, in Eppes, M. C., and Bartholomew, M. J., (eds.), *From the Blue Ridge to the Coastal Plain: Field Excursions in the Southeastern United States: Geological Society of America Field Guide 29: Boulder*, Geological Society of America, p. 93-121, [https://doi.org/10.1130/2012.0029\(03\)](https://doi.org/10.1130/2012.0029(03)).
- Willgoose, G., Bras, R. L., & Rodriguez-Iturbe, I. (1991). A physical explanation of an observed link area-slope relationship. *Water Resources Research*, 27(7), 1697–1702. <https://doi.org/10.1029/91WR00937>
- Wiltsie, D., Schnetzer, A., Green, J., Borgh, M. Vander, & Fensin, E. (2018). Algal blooms and cyanotoxins in Jordan Lake, North Carolina. *Toxins*, 10(2). <https://doi.org/10.3390/toxins10020092>
- Wohl, E. (2018). The challenges of channel heads. In *Earth-Science Reviews* (Vol. 185, pp. 649–

664). Elsevier. <https://doi.org/10.1016/j.earscirev.2018.07.008>

Wohl, E., & Merritts, D. J. (2007). What Is a Natural River? *Geography Compass*, 1(4), 871–900. <https://doi.org/10.1111/j.1749-8198.2007.00049.x>

## CHAPTER 5: Conclusions

This dissertation explores geologic processes that shape the surfaces of both Earth and Mars to improve our understanding of the topographic evolution of planetary surfaces. The work in chapter 2 investigated 49 distributed large thrust fault-related landforms on Mars to explore their growth history and determine if spatial patterns of fault characteristics could be quantified globally. The scarp topography-fault analysis was done using maximum displacement–length scaling ratios and variations in displacement along fault lengths (i.e., displacement profiles). Overall, the surface topographic expression of 96% of the faults was characterized by an asymmetric triangle, with maximum displacement peaks outside the fault's center third. Fault segmentation analyses revealed that the investigated faults contained two to eleven major segments, with 85% characterized by five or fewer. Calculations of  $D_{\max}/L$  ratios using an assumed homoclinal fault dip angle of  $30^\circ$  revealed significant differences between faults in the northern lowlands ( $n = 24$ ;  $D_{\max}/L = 2.9 \times 10^{-3} \pm 0.9 \times 10^{-3}$ ) and southern highlands ( $n = 25$ ;  $D_{\max}/L = 9.2 \times 10^{-3} \pm 1.9 \times 10^{-3}$ ), with faults in the north exhibiting less displacement for a given length than faults in the south.

To first order, the thickness of the brittle layer, along with strain rate, can restrict the amount of displacement that accumulated on a fault (e.g., Ackermann et al., 2001; Schulz and Fossen, 2002). Models of thrust faulting on Mars suggest that underlying faults extend to mid-to-lower crustal depths and are interpreted to be limited by the lithospheric brittle-ductile transition zone (BDT) (e.g., Ruiz et al., 2008; Egea-Gonzalez et al., 2017; Herrero-Gil et al., 2019; 2020a; 2020b). Lower  $D_{\max}-L$  ratios may imply a shallower BDT beneath the northern lowlands, assuming that fault depth is limited by lithospheric strength. However, current interpretations of the crustal dichotomy are such that if the crustal density is assumed to be constant, thinner crust

leads to a deeper BDT depth, with lower crustal rocks and upper mantle remaining strong (Montesi & Zuber, 2003). Thus, while hemispheric differences in the depth of the BDT could be called upon to explain variations in  $D_{\max}/L$ , such an interpretation is not easily reconciled with our current understanding of the Martian crustal dichotomy.

As demonstrated through calculations of differing fault dip angles on calculated  $D_{\max}/L$  scaling, the results may be explained by variations in fault geometry. For example, if fault dip angles in the south were fixed at  $30^\circ$ , statistically significant differences disappear between the northern hemisphere fault population if their assumed dip angles are  $\leq 16^\circ$ . Additionally, contrasting mechanical stratigraphy between successive units can promote fault-bend over homoclinal fault-propagation folding, accommodating horizontal fault displacement without a concomitant vertical surface topographic response. If differences in faulting style are present, surface displacement measurements may under-estimate displacement that has occurred along the fault plane.

Chapter 3 explored the timing of global contraction of Mars using buffered crater counting (BCC) to constrain the age of 28 thrust fault-related landforms, often referred to as lobate scarps, whose timing has been tied to secular cooling of Mars' interior. The purpose of chapter 2 was to investigate topographic variations along the length of faults; thus, candidate scarps were selected based on their lack of impact craters erasing the study scarp. Conversely, because size-frequency distributions of crater populations can be used to provide age constraints on the formation of geomorphic features, and this was the intent for chapter 3, candidate scarps were chosen based on their discernable interaction with craters with a diameter  $\geq 1$  km. Undeformed craters that alter the topography of a fault scarp (i.e., punch through the scarp) are assumed to post-date the most recent movement on that fault and taken as a population, can

provide minimum constraints on the timing of most the recent tectonic activity and thus, an estimate of planetary cooling-induced global contraction.

Successive buffers around the mapped scarps, with buffer sizes based on crater diameters, were used to produce an area to normalize small crater counts. This process yielded individual ages for each scarp and a combined age for the population of scarps in aggregate using the Hartmann (Hartmann, 2005) and Neukum/Ivanov (Ivanov, 2001) chronologies. Absolute model ages for individual scarps ranged from 4.4 to 3.5 Ga using a range of 2-13 craters per scarp, falling within the Early Noachian to Early Hesperian periods of Mars' geologic history. An aggregate of 148 craters was used to provide a model age for the area encompassing all 28 scarps. Ages based on the aggregate counts are  $3.8^{+0.01}_{-0.02}$  Ga (per the Hartmann PF and CF) and  $3.9^{+0.01}_{-0.01}$  Ga (for the Neukum/Ivanov models), respectively. As a whole, then, the most recent activity on these faults appears to terminate at the Noachian-Hesperian boundary.

Thermal evolution models for Mars have used gravity measurements (Zuber et al., 2000), geochemical data (Hauck & Phillips, 2002), as well as radioisotopes from meteorites and their extrapolated concentrations throughout the planets evolution (Schubert & Spohn, 1990; Bhatia et al., 2016). Importantly, providing physical constraints for these models based on observable surface features and timing constraints will provide realistic conditions required to satisfy conditions throughout the planet's evolution. While some have investigated localized structures (e.g., Ruj et al., 2019), this study provides model ages for globally distributed lobate scarps that can be used to constrain the global-scale contraction of Mars to the Noachian-Hesperian boundary.

Finally, chapter 4 investigated landscape responses to European farming on the North Carolina Piedmont. Using local slope and contributing drainage area relationships, the predicted

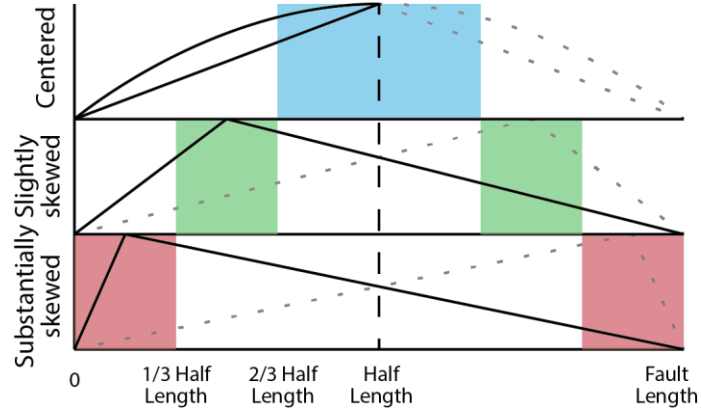
unchannelized-to-channelized transition locations (i.e., channel heads) were determined for a previously farmed and reforested watershed in William B. Umstead State Park, Raleigh, NC. For the 40 channels used for this analysis, slope-area predicted locations were compared to observed channel heads to determine that 23 channel heads were observed downslope of their predicted locations. Taken in aggregate, contributing basin areas were predicted to range between 1,380 and 8,710 m<sup>2</sup>, while the median observed (current) contributing area for all channel heads is 23,719 m<sup>2</sup>. Migration distances were calculated for the channels that were expected to migrate (n = 23) using the range of expected values of each channel's basin area that were translated to physical distances along the trunk channel of each stream. Using this approach, a mean migration distance of 174.4 m [S.D. = 109.6 m] per stream. An average per-channel contribution of 282.6 m<sup>3</sup> [S.D. = 177.6 m<sup>3</sup>] of future erosion is predicted as the channel heads migrate up their valleys from the differences between predicted (future) and observed (current) channel head locations. Drainage densities were used to extrapolate the findings from the 40 channels included in this study to the larger area of Umstead State Park (23 km<sup>2</sup>). These calculations determined that an additional 90,419 ± 56,838 m<sup>3</sup> (68% conf.) is expected to erode from the presently unchannelized valley bottom areas within the state park, assuming conservatively that 50% of channel heads will migrate.

Soil investigations upvalley from four current channel head locations revealed buried A horizons, consistent with legacy accumulations of sediment on top of the former land surface. The weight percent of C and N and the mass of bioavailable P were quantified for each soil horizon from the surface to ~ 1 m depth. Using the estimated average volume of erosion (90,419 ± 56,838 m<sup>3</sup>) for the 23 km<sup>2</sup> area that encompasses the state park and an average bulk soil density of 1.3 g/cm<sup>3</sup> (Bradley, 2020), the mass of soil from future erosion of channel heads was

found to be  $1.1 \times 10^8 \pm 6.7 \times 10^7$  kg (68% conf.) (i.e.,  $106 \pm 67$  t). This amount of soil and sediment contains approximately  $9.5 \times 10^5 \pm 2.8 \times 10^5$  kg (68% conf.) ( $951 \pm 277$  t) of carbon,  $448 \times 10^4 \pm 1.2 \times 10^4$  kg ( $44 \pm 12$  t) of total nitrogen, and  $1.3 \times 10^4 \pm 3.9 \times 10^3$  kg ( $13 \pm 4$  t) of phosphorus. Eutrophication of terrestrial waterways is often linked to present-day human impacts on the landscape (e.g., agriculture, wastewater discharge, lawn fertilization) and the impacts of climate change on hydrologic and biological systems (e.g., Rabalais et al., 2009; Jokinen et al., 2018); however, this work shows that historical land use may play a larger role than typically appreciated, in part and specifically through the re-establishment of equilibrium channel head locations. The impacts of this geomorphic process are likely to continue for hundreds to thousands of years to come.

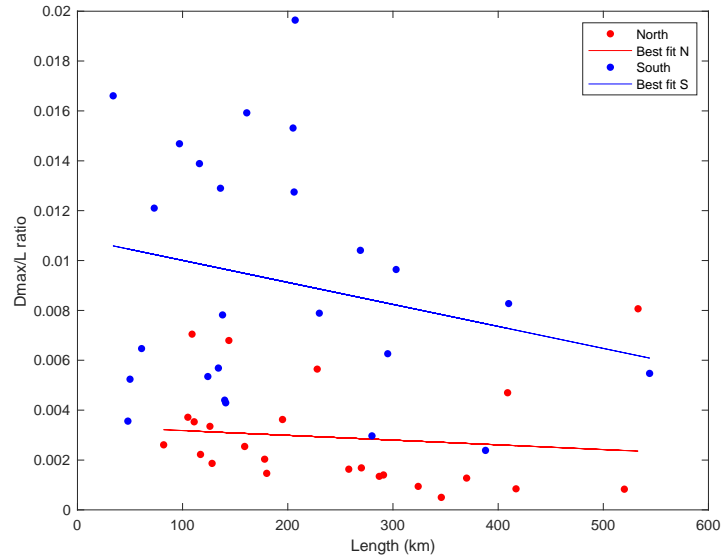
## APPENDICES

## Appendix A: Fault displacement skewness schematic



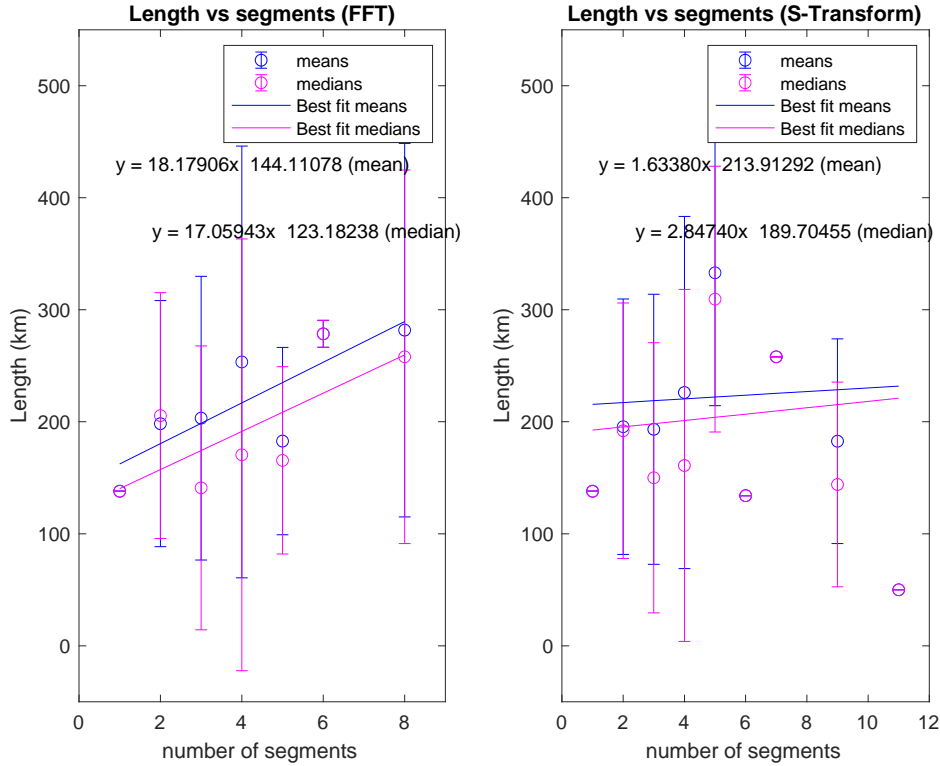
Schematic showing how fault displacement skewness was assessed. Faults were normalized for length, and the peak location of the best-fit shape was categorized as occurring in the middle third of the fault (“central,” blue zone), between one third and two thirds from the fault tips (“slightly skewed,” green zone), or within one third of the fault tips (“substantially skewed,” red zone). (Figure S1 in Chapter 2)

## Appendix B: N vs. S regression plot



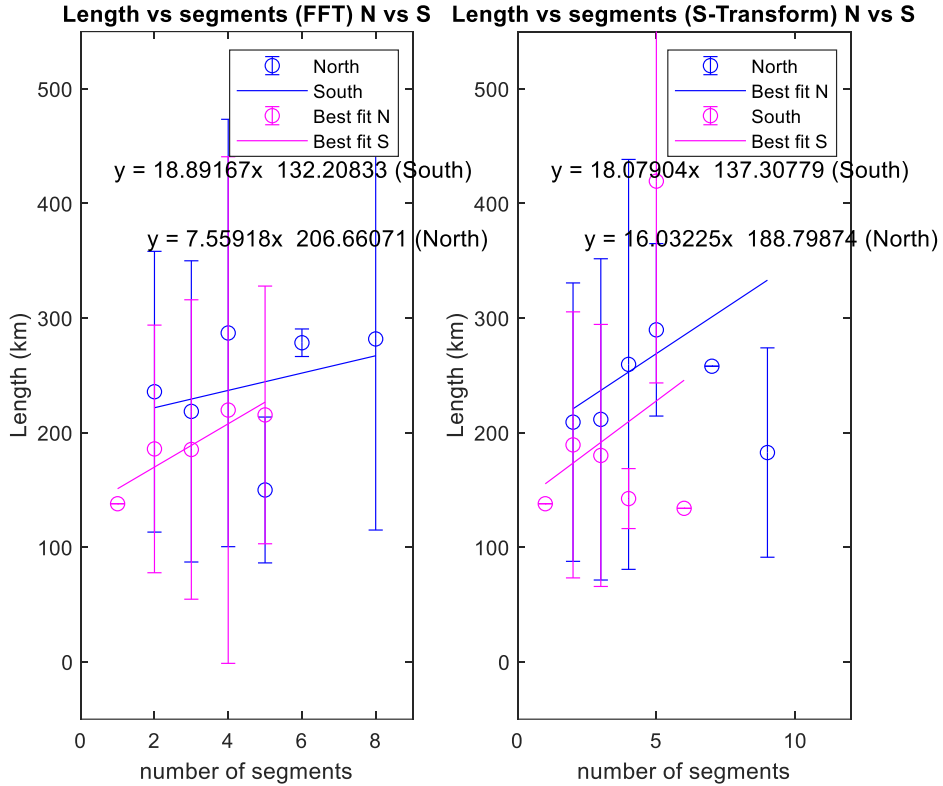
Regression plot for study thrust fault  $D_{\max}/L$  values in the northern lowlands (red:  $y = -1.9 \times 10^{-6} + 0.0037$ ) and southern uplands (blue:  $y = -8.8 \times 10^{-6} + 0.0109$ ). Although the global negative trend of  $D_{\max}/L$  vs. fault length is significant ( $p < 0.05$ ), independently neither population is significantly different from zero ( $p > 0.05$ ). (Figure S2 in Chapter 2, Appendix B)

### Appendix C: Fault length vs. number of segments plots



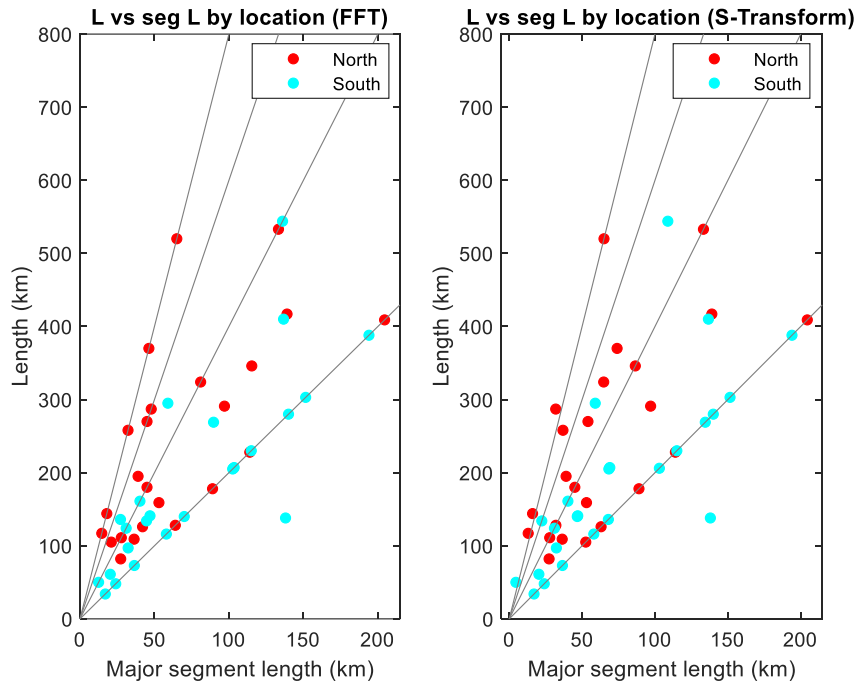
Fault length versus number of segments for our full thrust fault study population ( $n = 49$ ). The positive relationship between length and total segment number for the FFT analysis is significant at  $p > 0.05$ . That relationship for the S-Transform analysis is not statistically significant. (Figure S3 in Chapter 2)

### Appendix D: Fault length vs. number of segments plots (N vs. S)



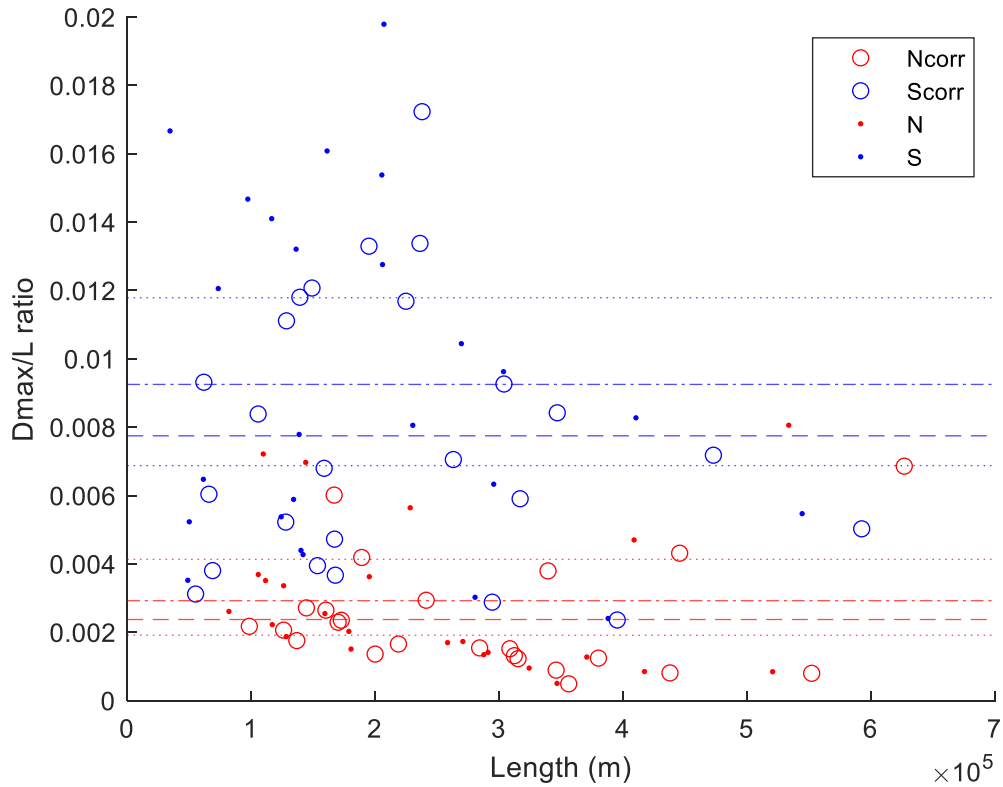
Fault length versus number of segments by northern lowlands and southern highlands. When analyzed as separate populations, the only significant trend is given by the FFT analysis for thrust faults in the southern highlands ( $p > 0.05$ ). The S-Transform analyses do not return significant trends for either population. (Figure S4 in Chapter 2)

## Appendix E: Major segment length vs. total cumulative length plots



Major segment length versus total cumulative length for all study thrust faults, found via FFT (left) and S-Transform (right) analyses. Faults in the northern lowlands are shown in red; those in the southern highlands are cyan. Major fault segment length is obtained by dividing total fault length by number of segments identified by each analysis type. Generally, northern faults exhibit shorter major segments. (Figure S5 in Chapter 2)

## Appendix F: $D_{\max}/L$ vs. Length with missing lengths added



Plot comparing calculated  $D_{\max}/L$  versus fault length used for this study, with faults in the northern lowlands in red and those in the southern highlands in blue; the means of these values are shown with dot–dash lines, and the 99% confidence intervals are shown with dotted lines. Also plotted are ratios modified by including additional fault trace lengths that may not be resolvable with presently available image data; the means for these measurements are shown with dashed lines. A significant difference in  $D_{\max}/L$  ratios can still be observed between N and S (Northern lowlands;  $D_{\max}/L = 2.9 \times 10^{-3}$ ;  $D_{\max}/L_{\text{added}} = 2.5 \times 10^{-3}$ ; Southern highlands;  $D_{\max}/L = 9.1 \times 10^{-3}$ ;  $D_{\max}/L_{\text{added}} = 7.7 \times 10^{-3}$ ). (Figure S6 in Chapter 2)

### Appendix G: Summarized fault metrics

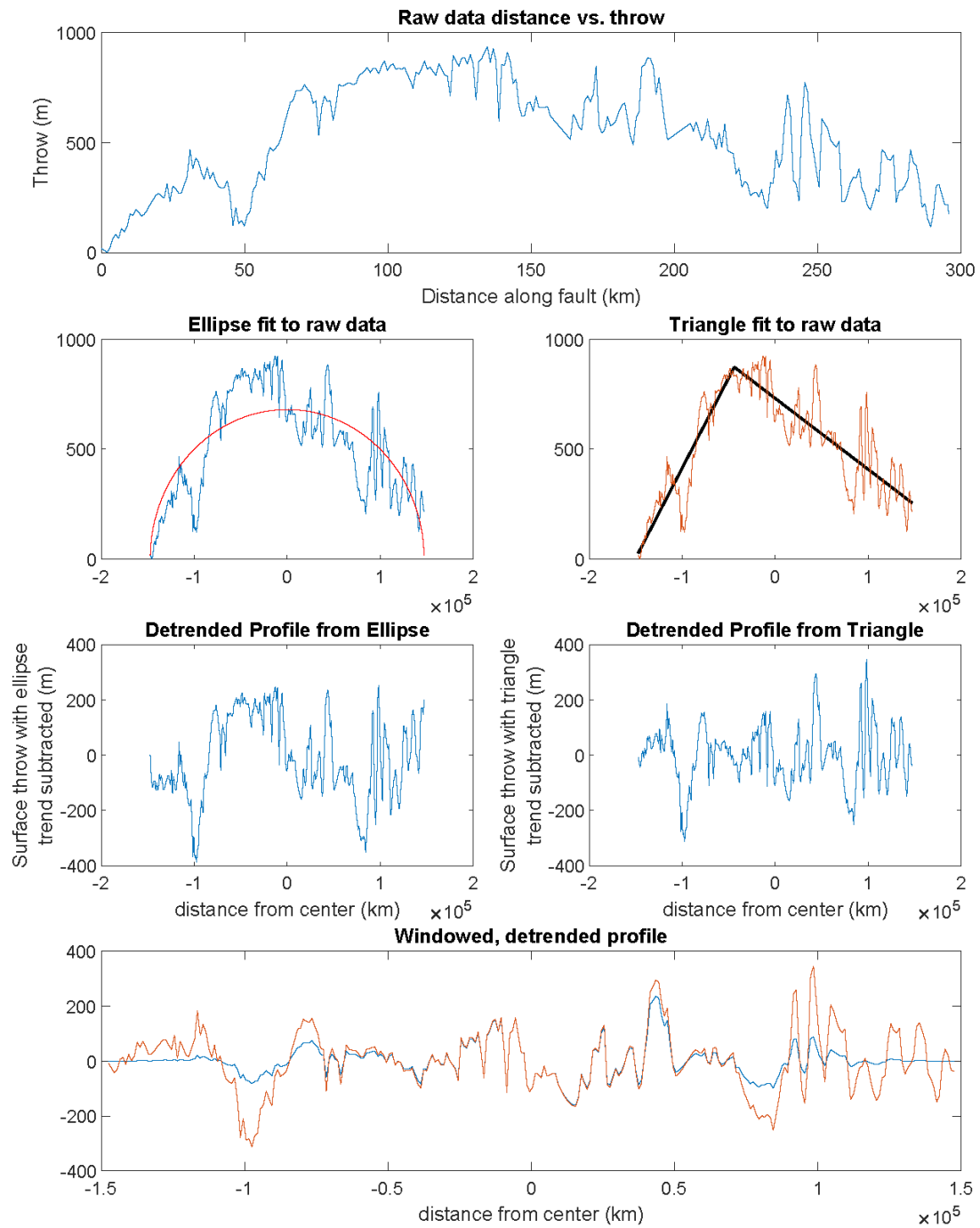
Fault name	Length (km)	$t_{max}$ (m)	$D_{max}$ (m)	$D_{max}/L$ ratio	# of segments (FFT)	# of segments (S-Transform)	Location
1	295	923.8	1847.6	0.00626	5	5	S
2	61	197.3	394.6	0.00647	3	3	S
3	48	85.4	170.9	0.00356	2	2	S
5	141	302.9	605.7	0.00430	3	3	S
6	128	119.4	238.8	0.00187	2	4	N
7	417	176.3	352.6	0.00085	3	3	N
8	109	384.1	768.2	0.00705	3	3	N
9	105	195.0	390.0	0.00371	5	2	N
10	346	87.0	174.0	0.00050	3	4	N
11	126	211.1	422.3	0.00335	3	2	N
12	195	353.3	706.6	0.00362	5	5	N
13	134	381.0	762.0	0.00569	3	6	S
14	34	282.3	564.6	0.01660	2	2	S
15	180	131.8	263.6	0.00146	4	4	N
16	291	203.9	407.8	0.00140	3	3	N
17	117	130.0	260.0	0.00222	8	9	N
18	370	235.9	471.8	0.00128	8	5	N
19	520	215.9	431.8	0.00083	8	8	N
20	82	107.0	213.9	0.00261	3	3	N
21	258	210.5	421.0	0.00163	8	7	N
22	324	152.7	305.4	0.00094	4	5	N
23	73	441.7	883.4	0.01210	2	2	S
24	230	907.2	1814.3	0.00789	2	2	S
25	97	712.2	1424.4	0.01468	3	3	S
26	136	877.1	1754.2	0.01290	5	2	S
Ogygis Rupes	207	2032.8	4065.5	0.01964	2	3	S
28	205	1569.6	3139.2	0.01531	2	3	S
29	116	805.4	1610.7	0.01389	2	2	S
30	140	308.0	616.0	0.00440	2	3	S
31	544	1488.6	2977.1	0.00547	4	5	S
Icaria Rupes	161	1281.8	2563.7	0.01592	4	4	S
Hiddekel Rupes	144	489.1	978.3	0.00679	8	9	N
34	410	1696.2	3392.4	0.00827	3	3	S
Phrxi Rupes	206	1313.0	2626.0	0.01275	2	2	S
37	138	539.4	1078.9	0.00782	1	1	S
38	287	193.0	386.0	0.00134	6	9	N
39	270	227.3	454.6	0.00168	6	5	N
40	178	181.0	362.0	0.00203	2	2	N
41	388	463.0	926.1	0.00239	2	2	S
42	280	415.7	831.4	0.00297	2	2	S
43	533	2149.7	4299.5	0.00807	4	4	N
44	228	643.7	1287.4	0.00565	2	2	N
45	409	961.0	1922.0	0.00470	2	2	N
47	111	196.0	392.0	0.00353	4	4	N
48	50	131.0	262.0	0.00524	4	11	S
49	159	202.1	404.2	0.00254	3	3	N
50	124	331.6	663.2	0.00535	4	4	S

Bosporus Rupes (a)	303	1460.4	2920.8	0.00964	2	2	S
Bosporus Rupes (b)	269	1399.8	2799.6	0.01041	3	2	S

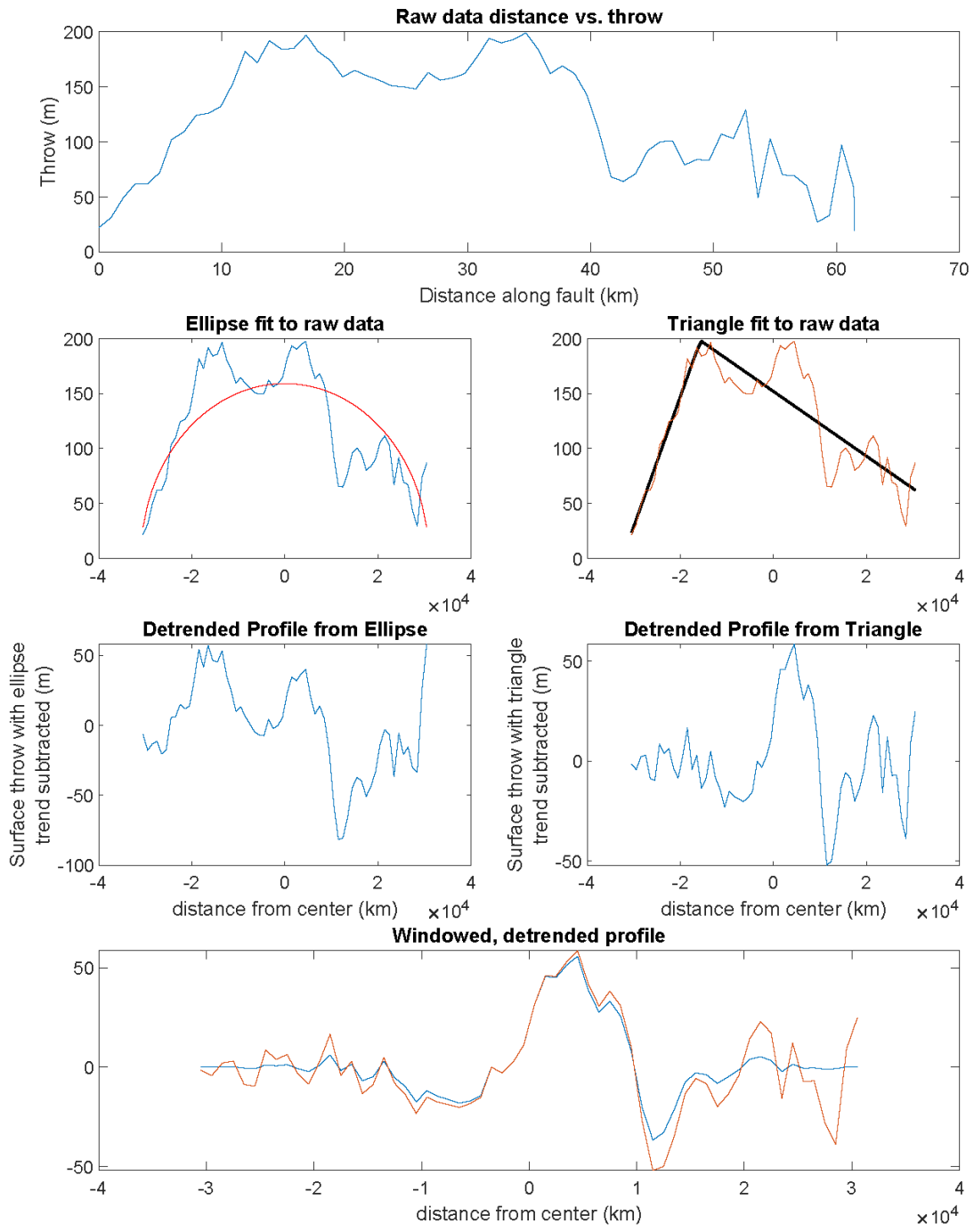
Summarized fault length, throw, displacement, and Dmax/L data for our 49 study faults. The number of segments per our FFT and S-Transform analyses are also given, as are the hemisphere in which each fault is situated. Faults are unnamed unless otherwise specified. (Table S1 in Chapter 2)

## Appendix H: Detrending process for each fault

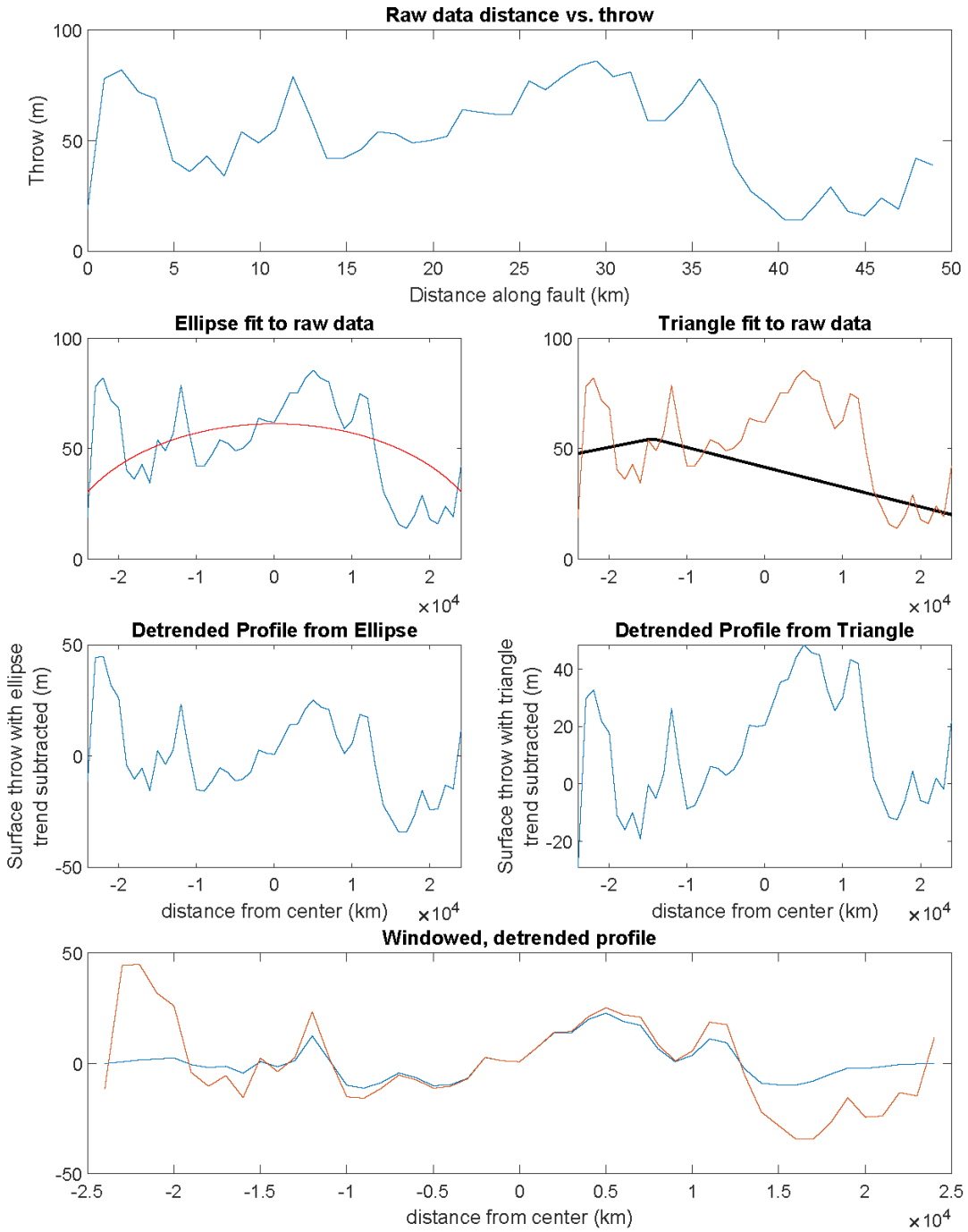
### Fault001



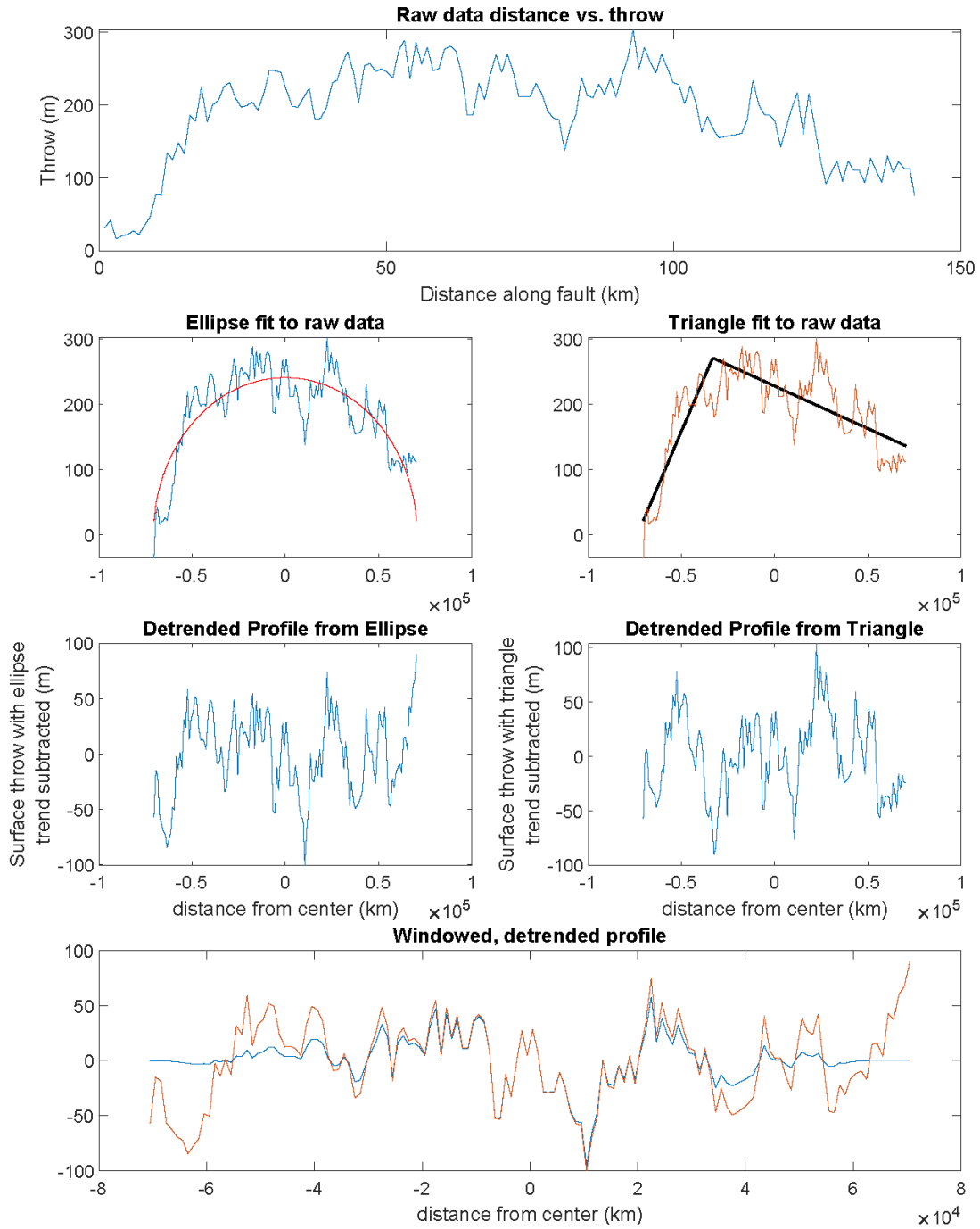
# Fault002



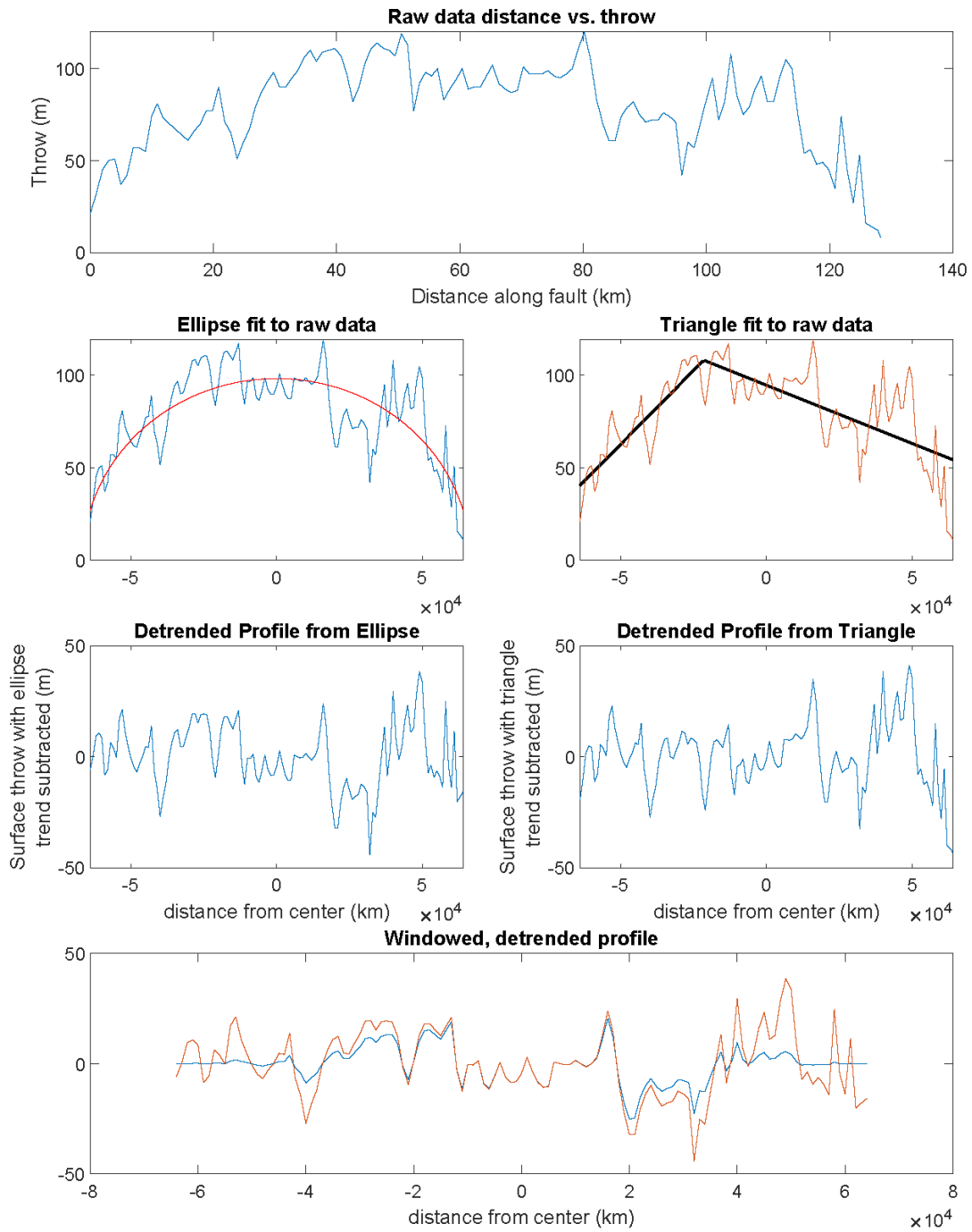
# Fault003



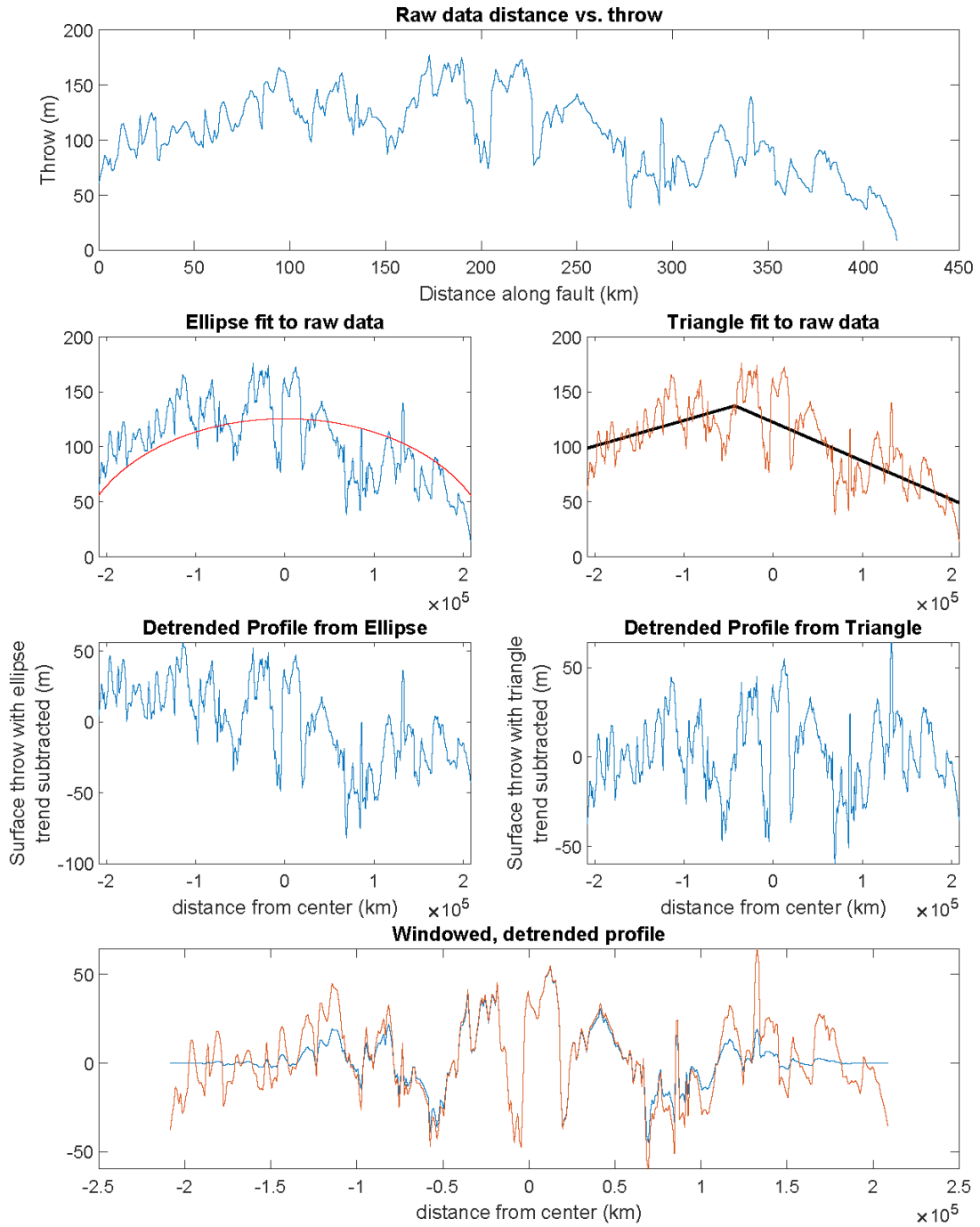
# Fault005



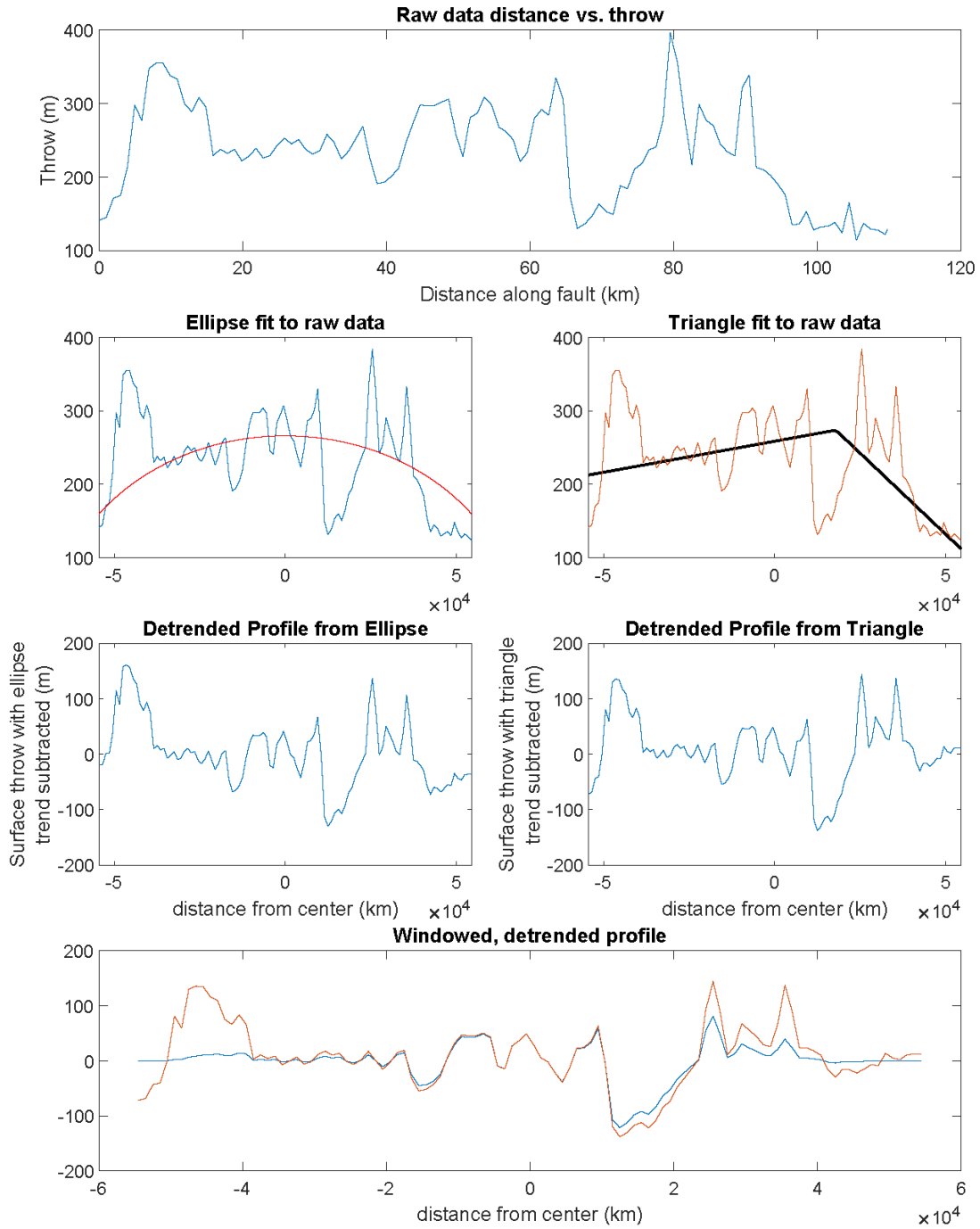
# Fault006



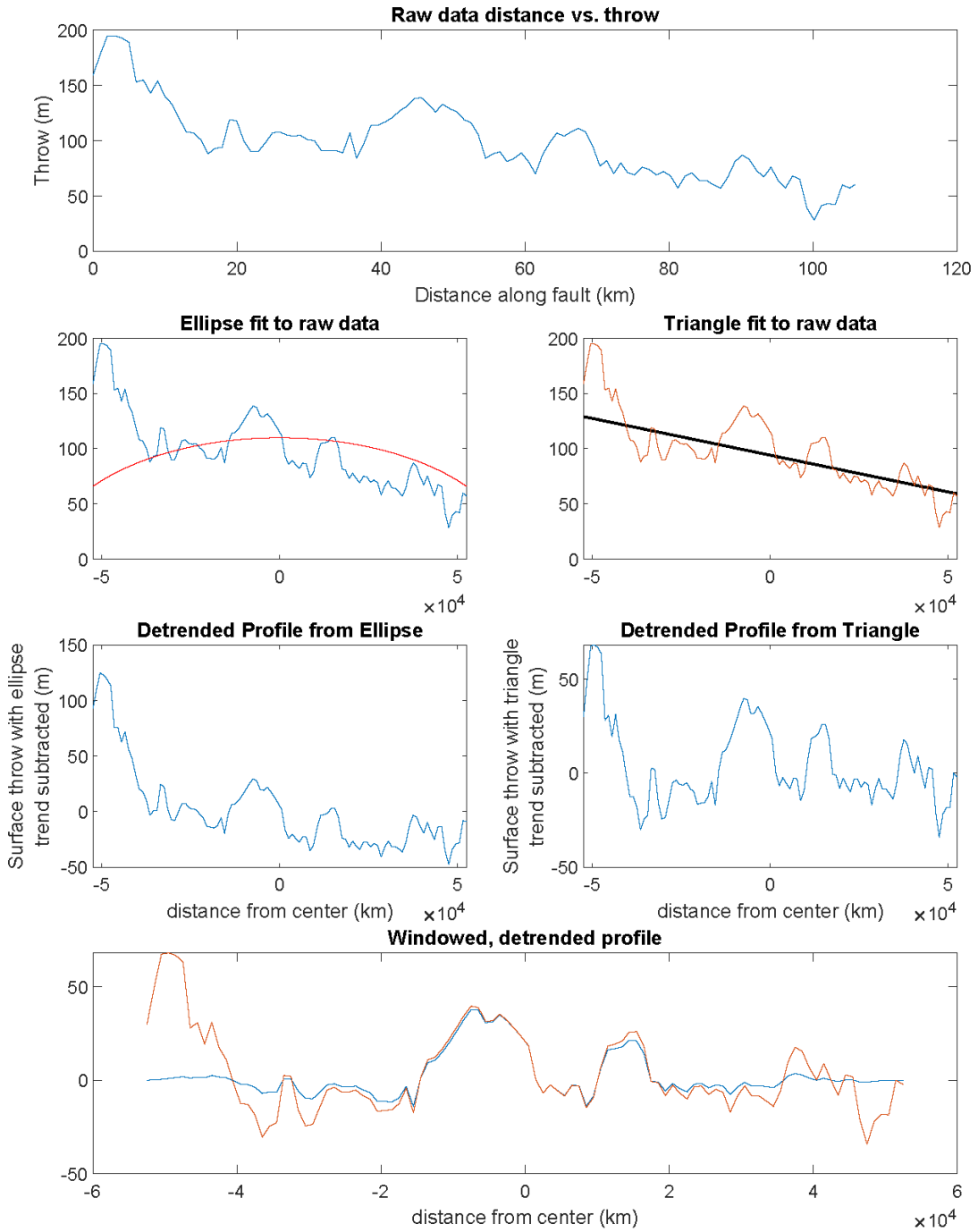
# Fault007



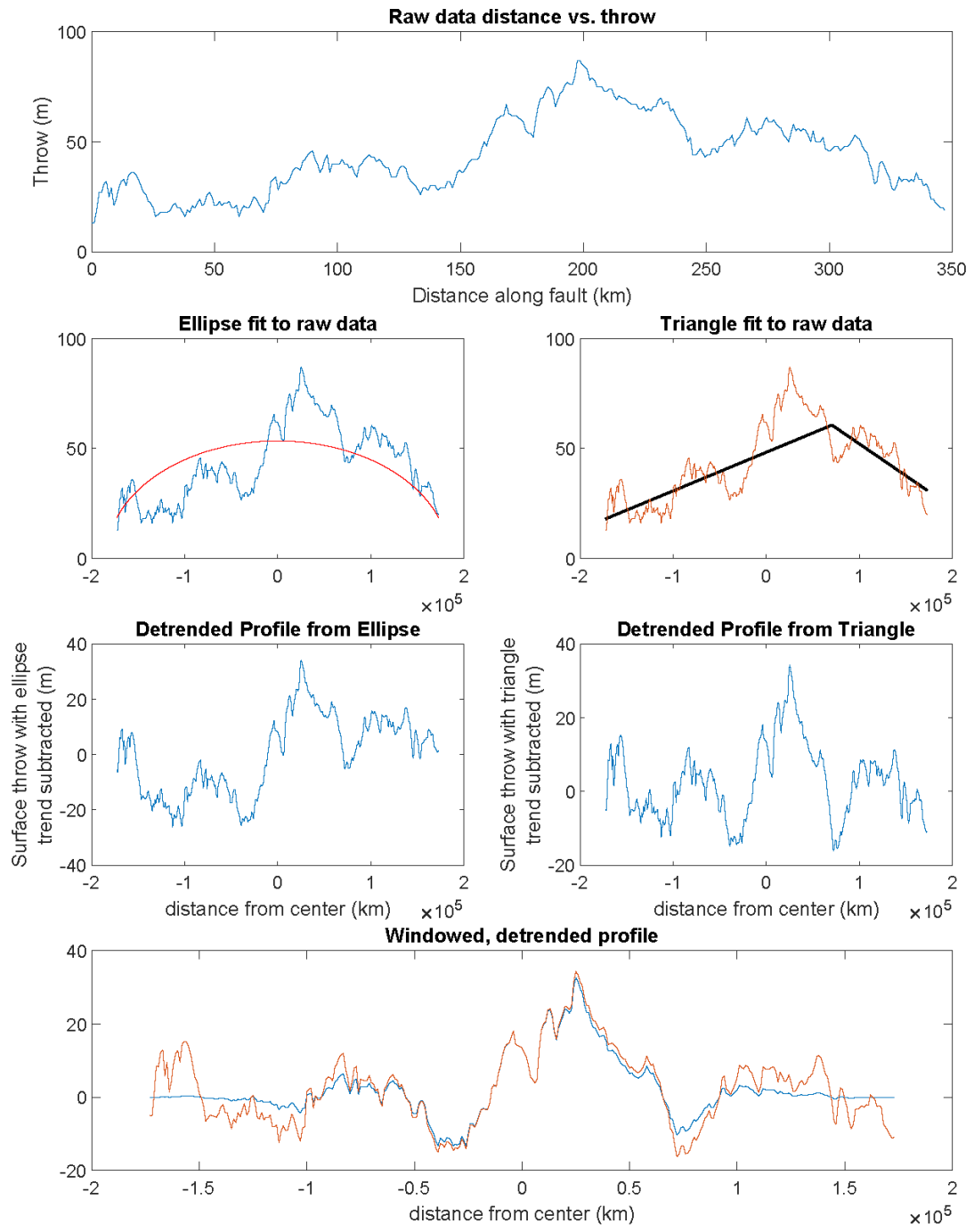
# Fault008



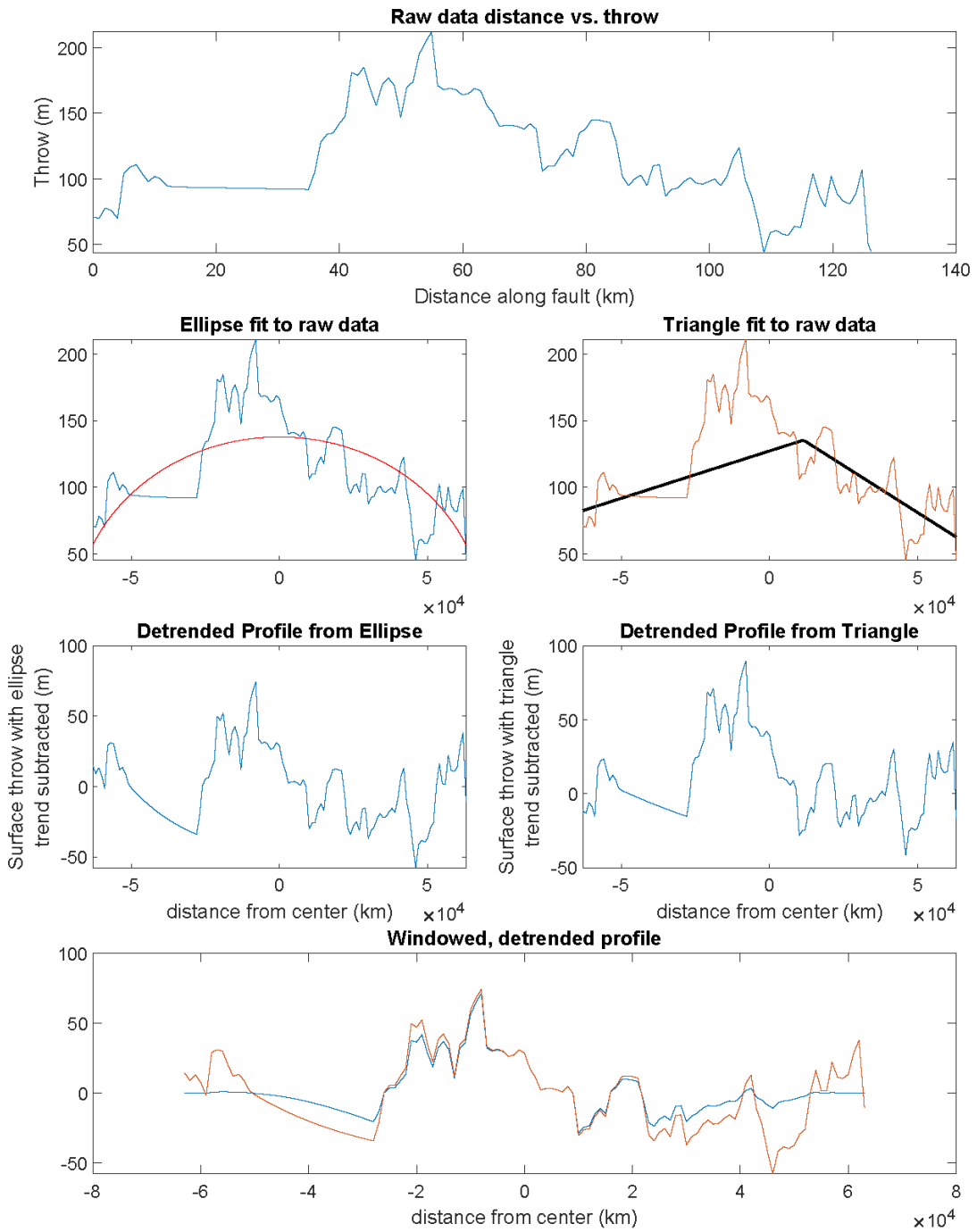
# Fault009



# Fault010

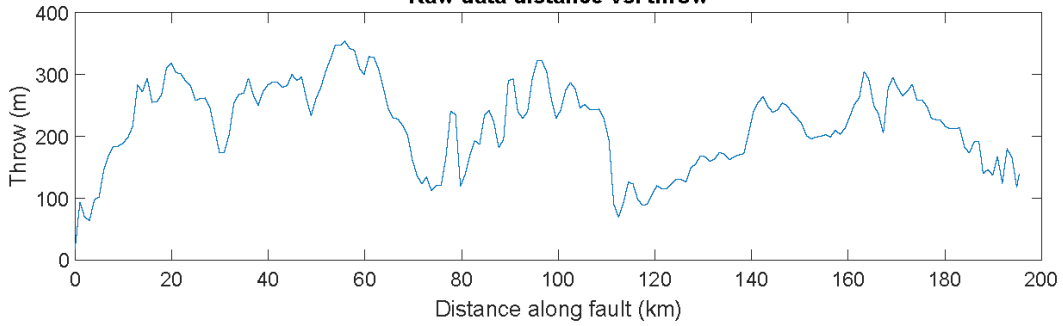


# Fault011

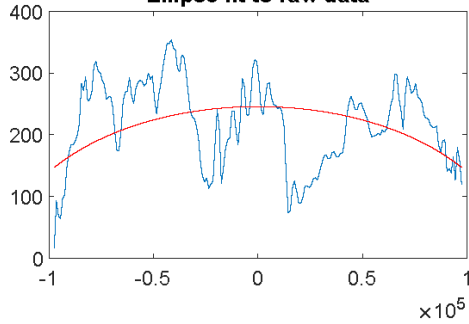


# Fault012

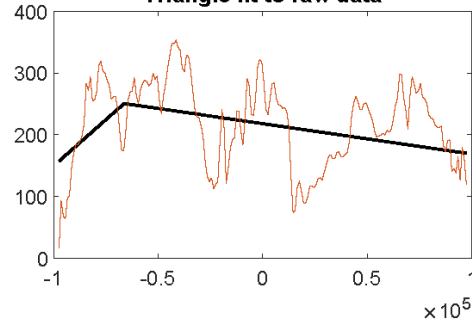
Raw data distance vs. throw



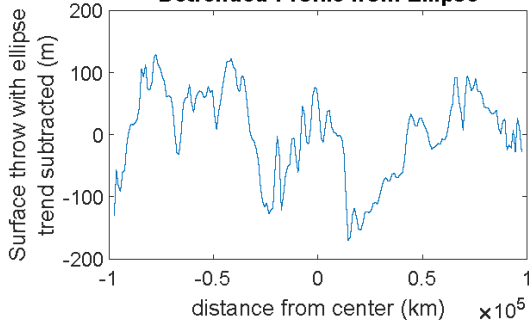
Ellipse fit to raw data



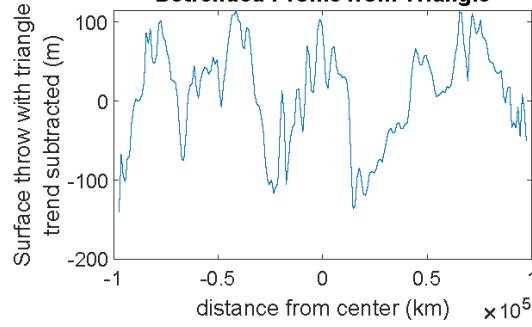
Triangle fit to raw data



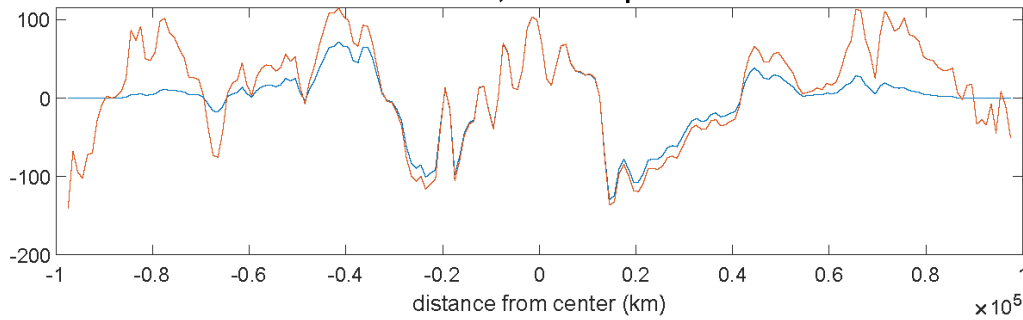
Detrended Profile from Ellipse



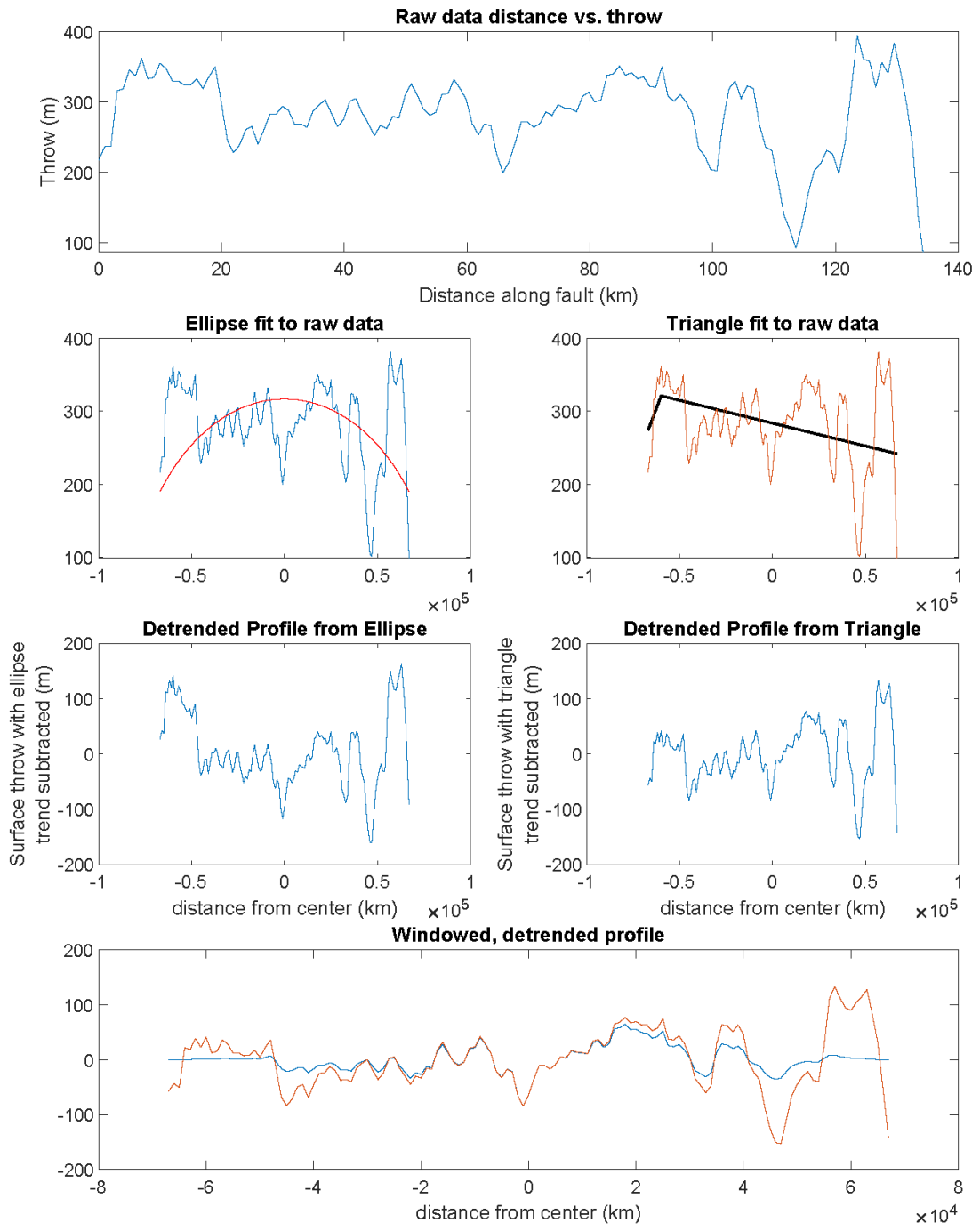
Detrended Profile from Triangle



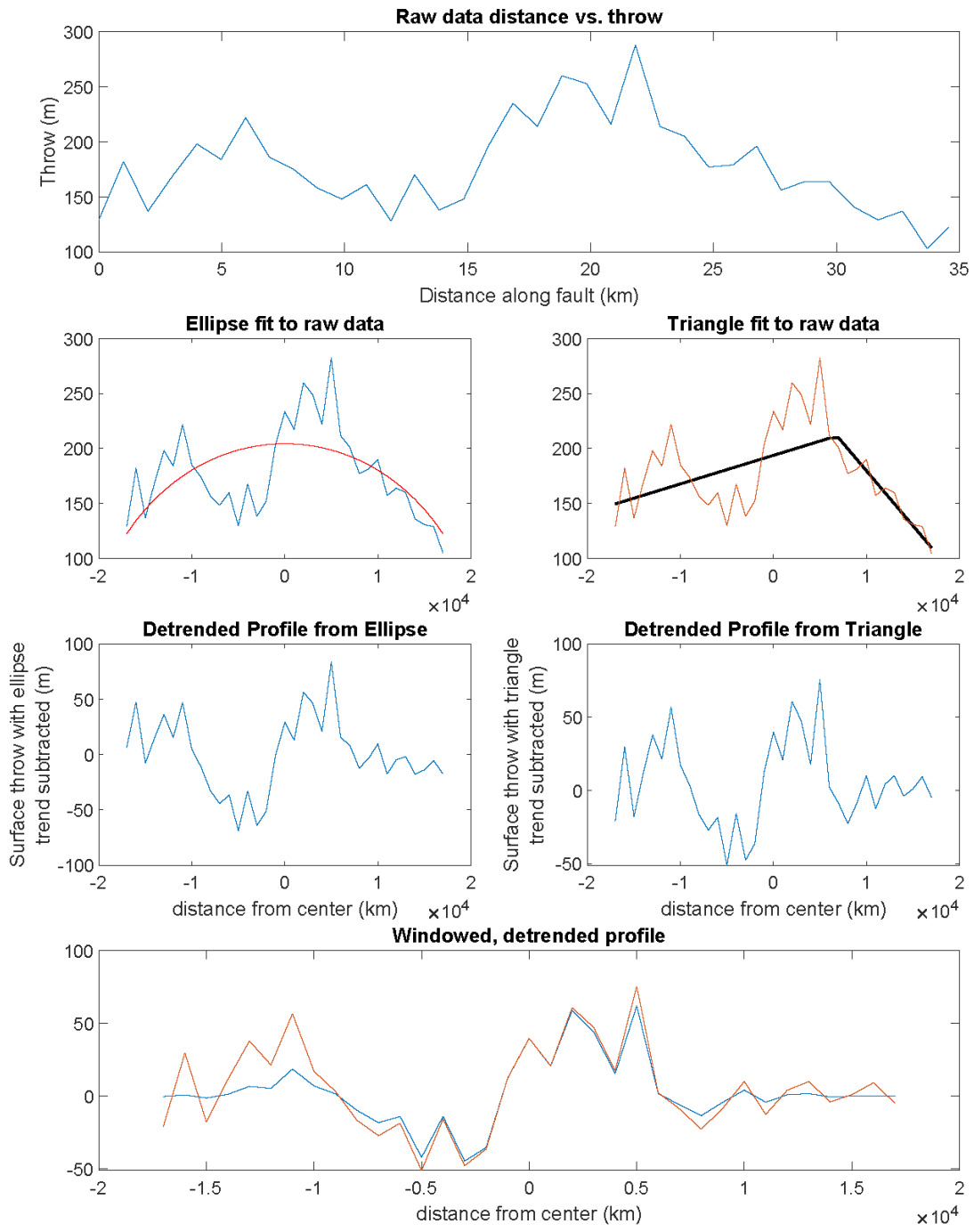
Windowed, detrended profile



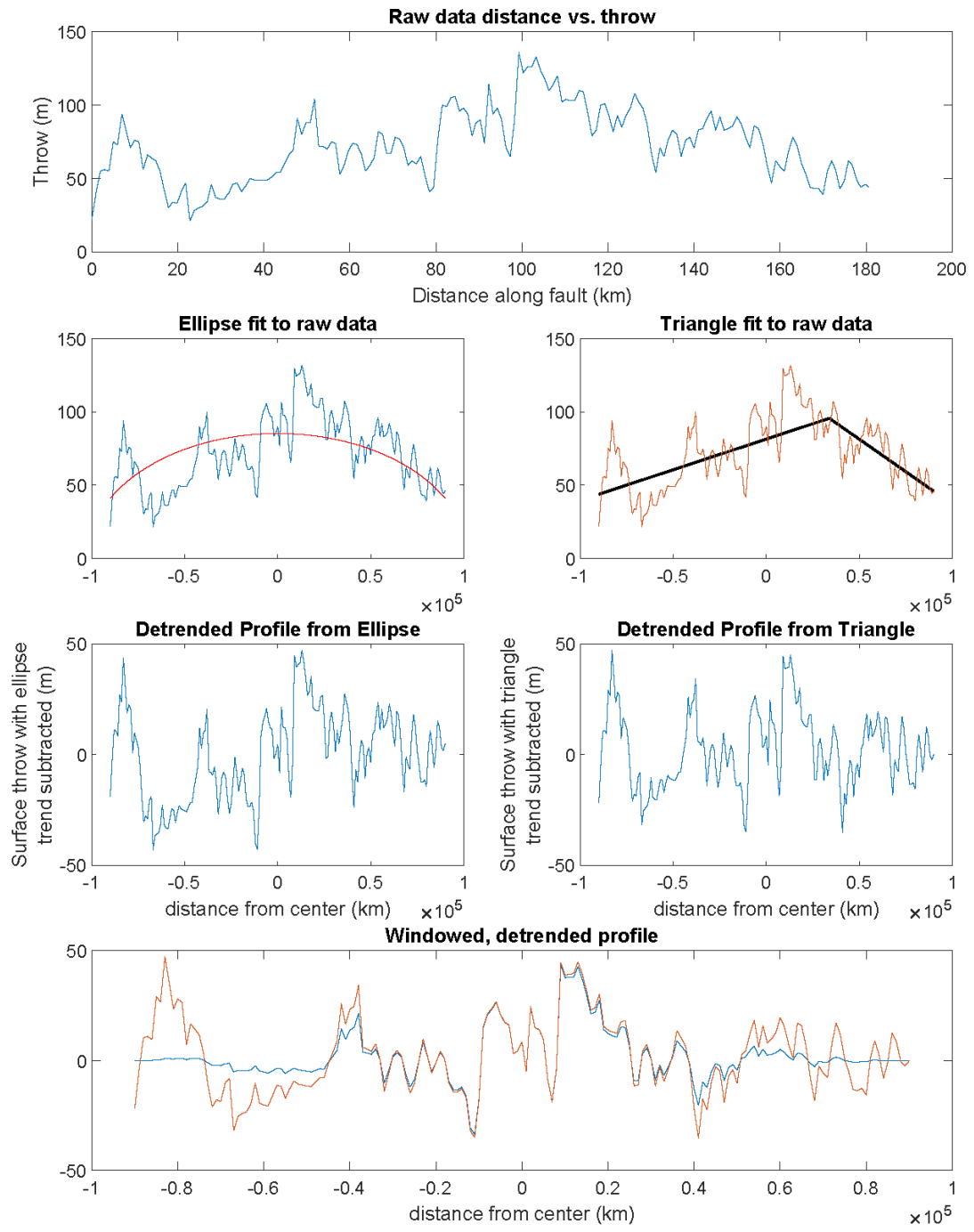
# Fault013



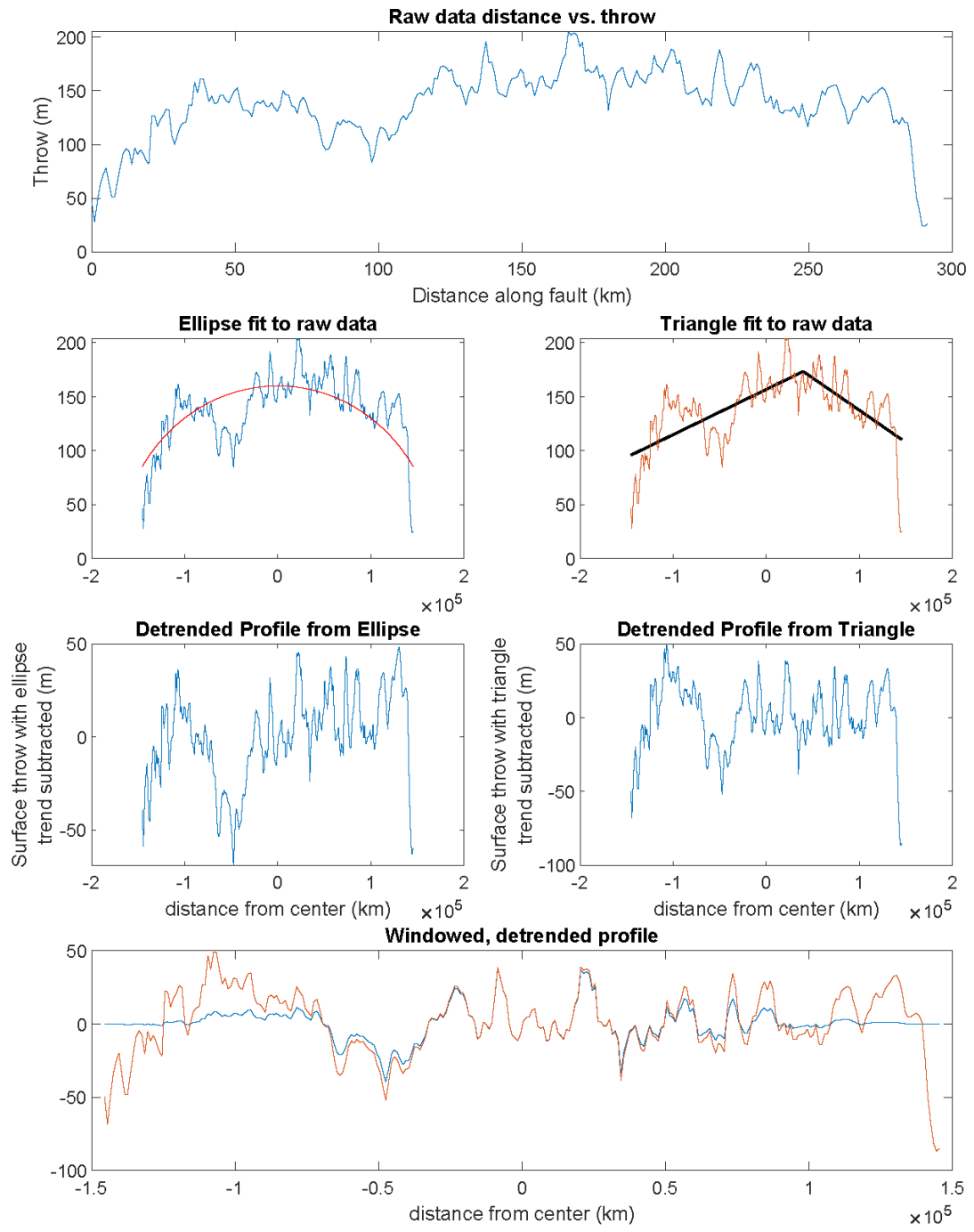
# Fault014



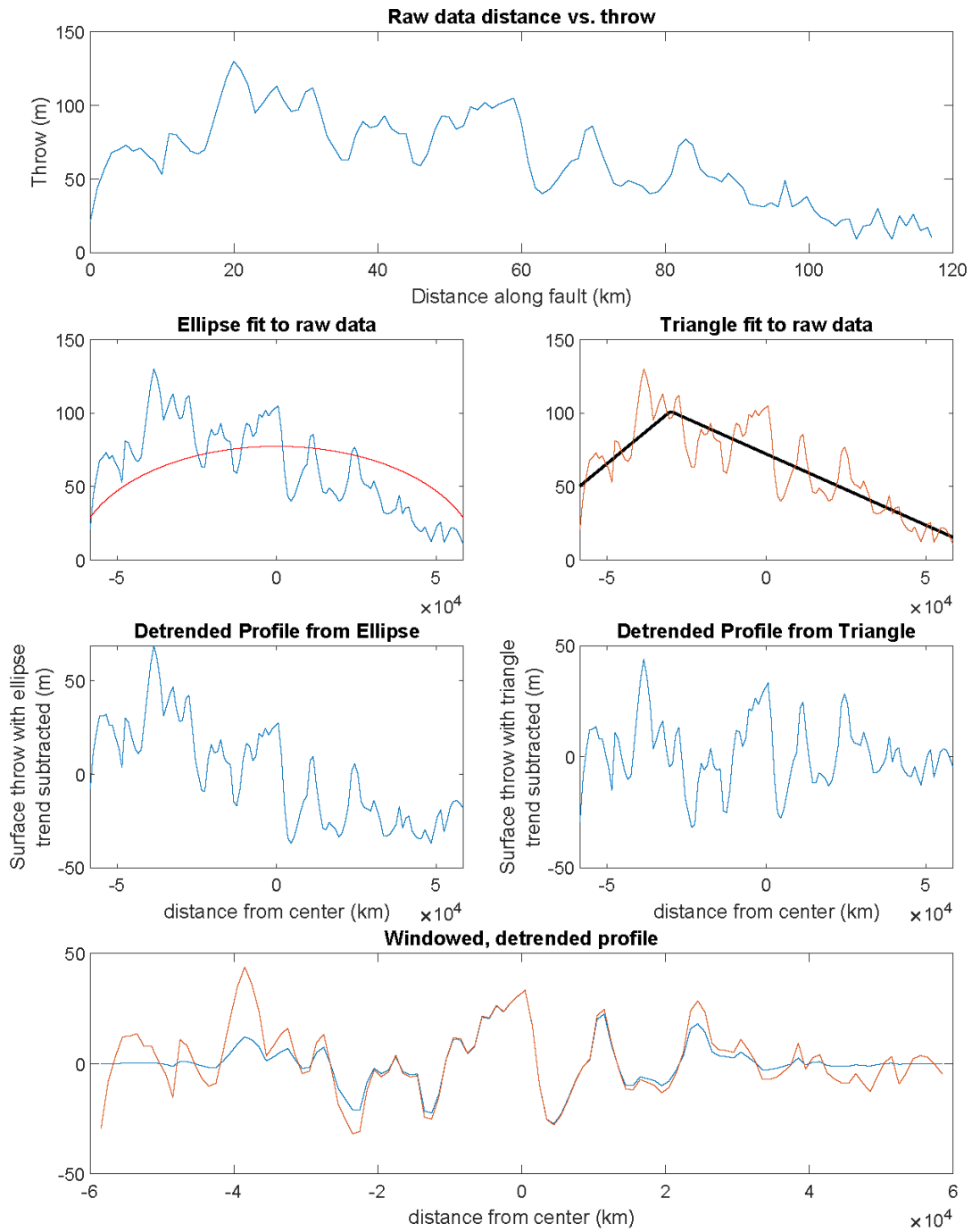
# Fault015



# Fault016

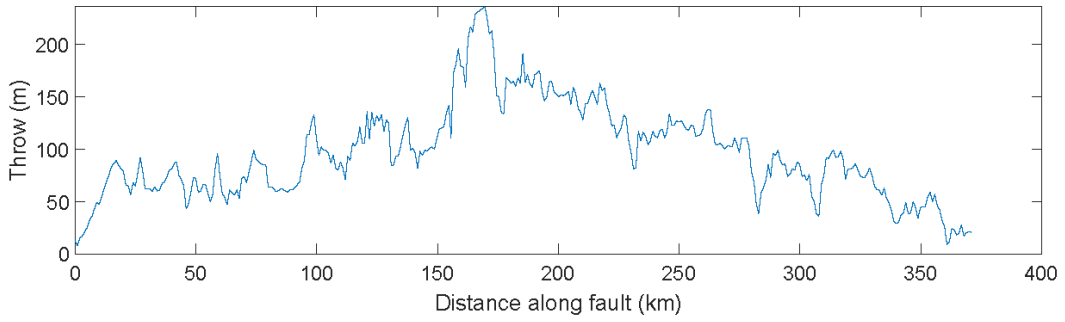


# Fault017

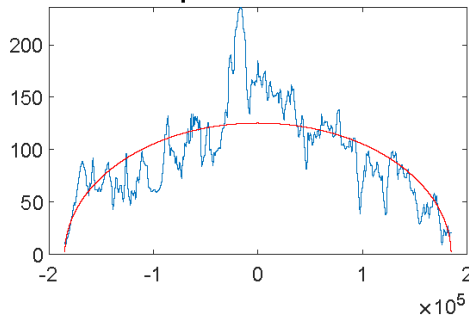


# Fault018

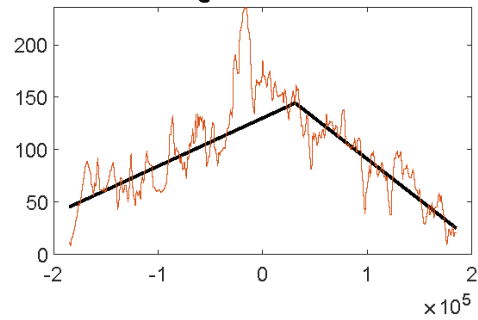
Raw data distance vs. throw



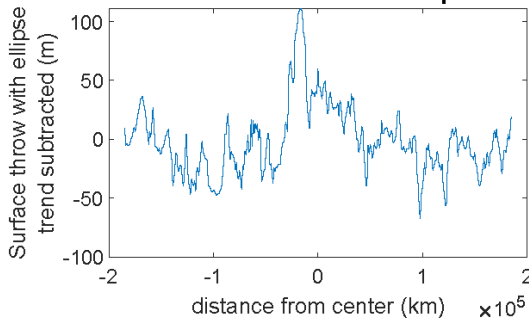
Ellipse fit to raw data



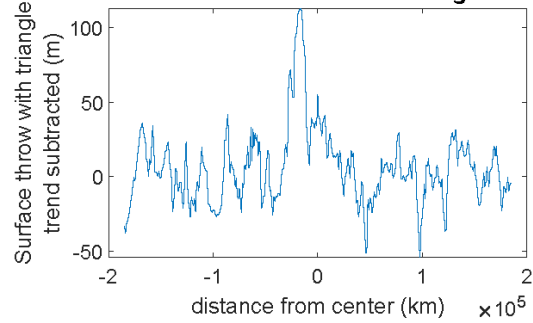
Triangle fit to raw data



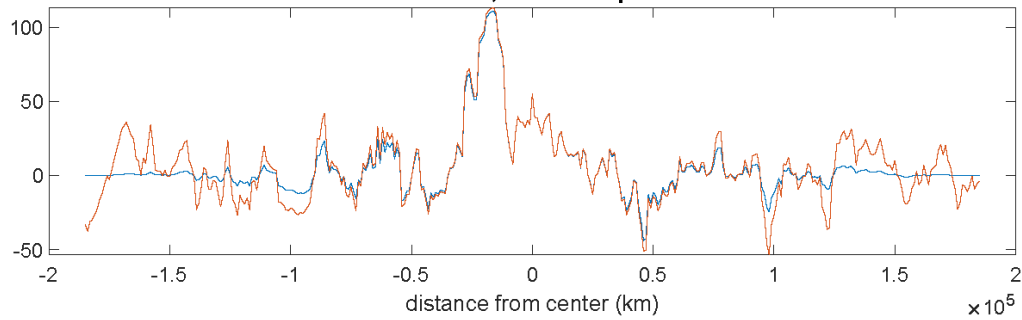
Detrended Profile from Ellipse



Detrended Profile from Triangle

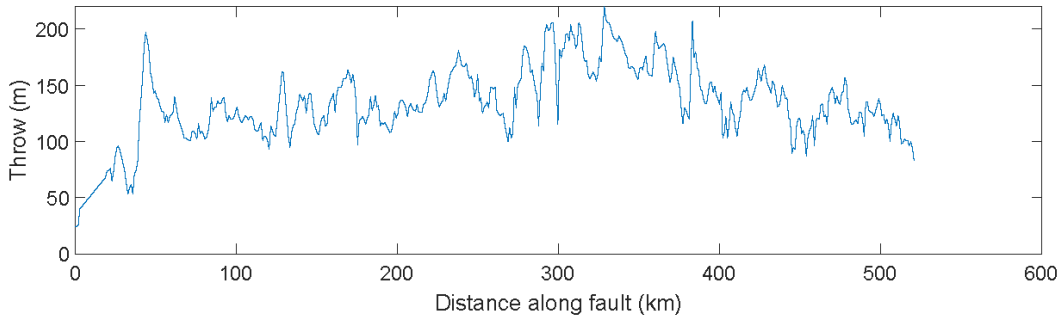


Windowed, detrended profile

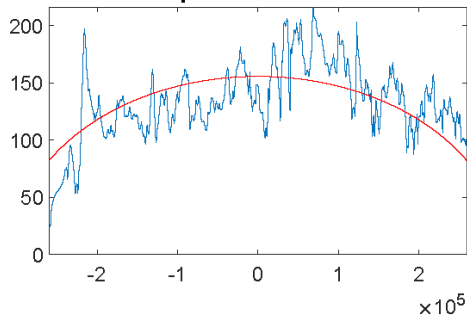


# Fault019

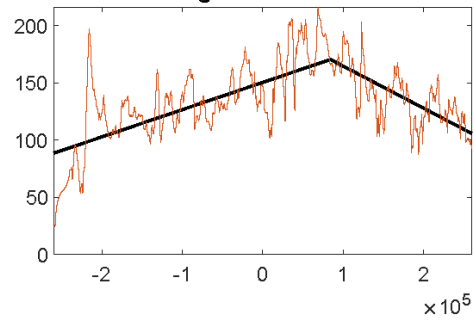
Raw data distance vs. throw



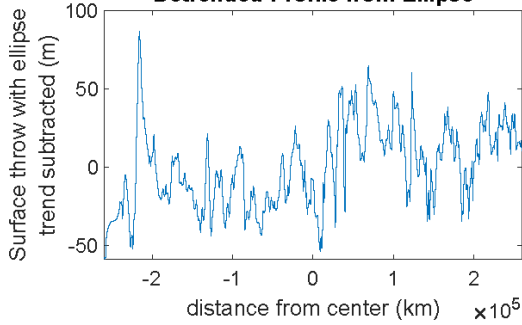
Ellipse fit to raw data



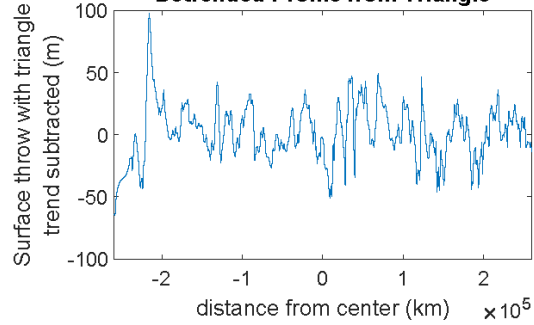
Triangle fit to raw data



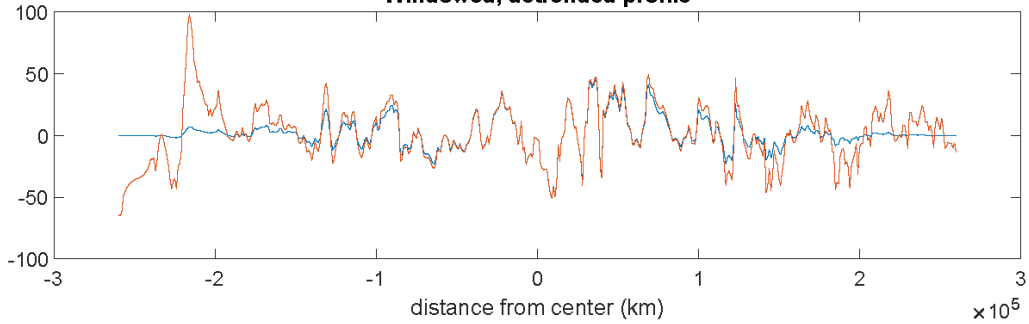
Detrended Profile from Ellipse



Detrended Profile from Triangle

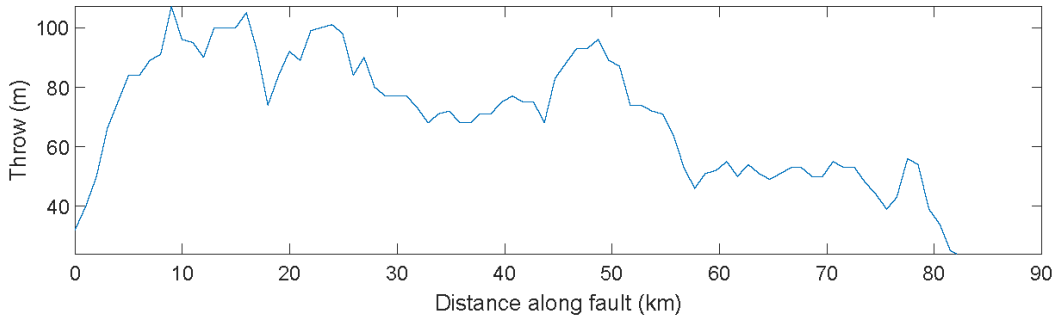


Windowed, detrended profile

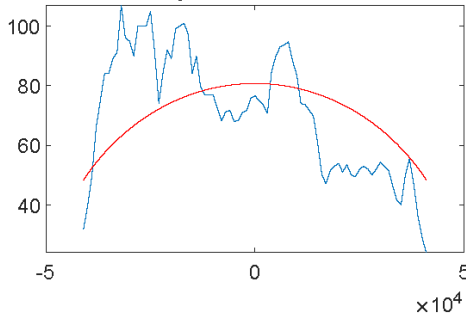


# Fault020

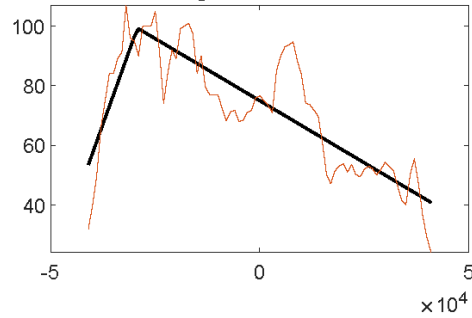
Raw data distance vs. throw



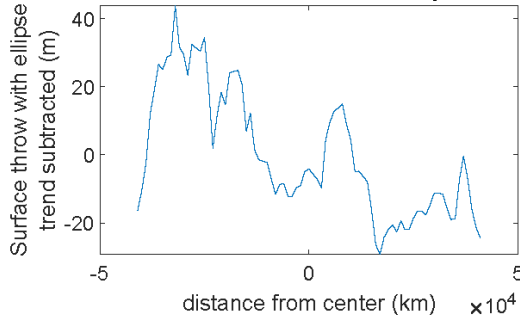
Ellipse fit to raw data



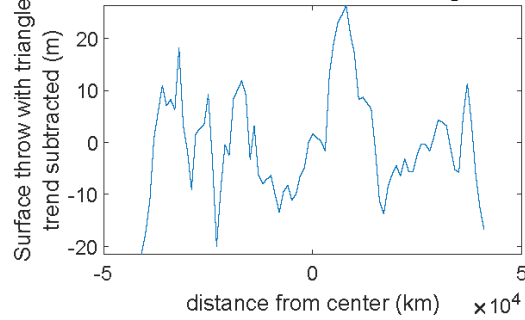
Triangle fit to raw data



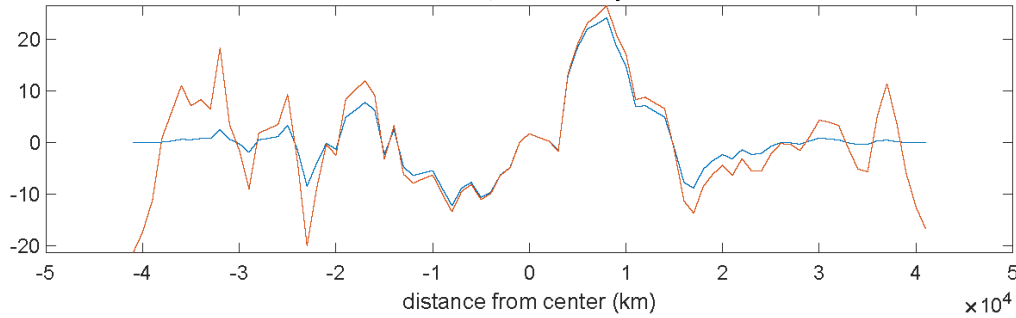
Detrended Profile from Ellipse



Detrended Profile from Triangle

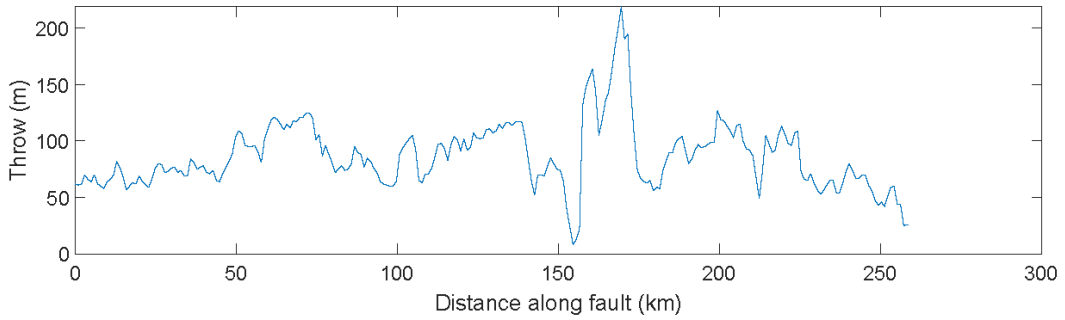


Windowed, detrended profile

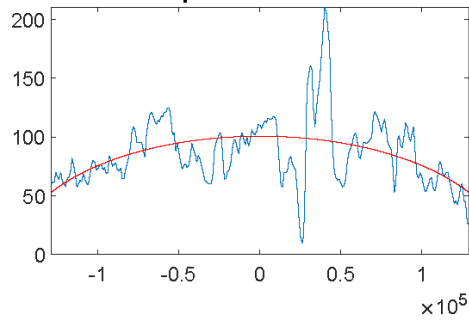


# Fault021

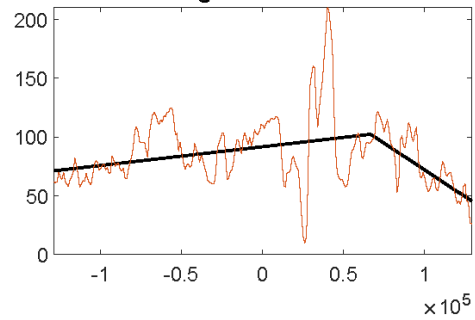
## Raw data distance vs. throw



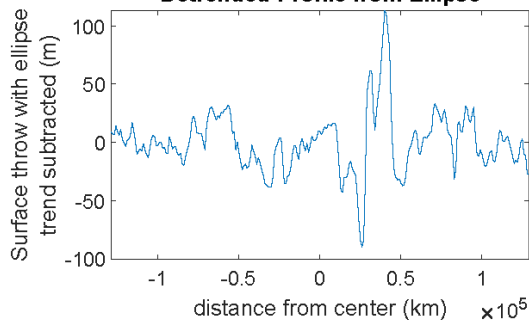
## Ellipse fit to raw data



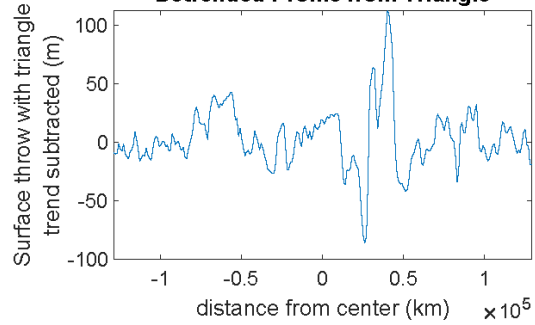
## Triangle fit to raw data



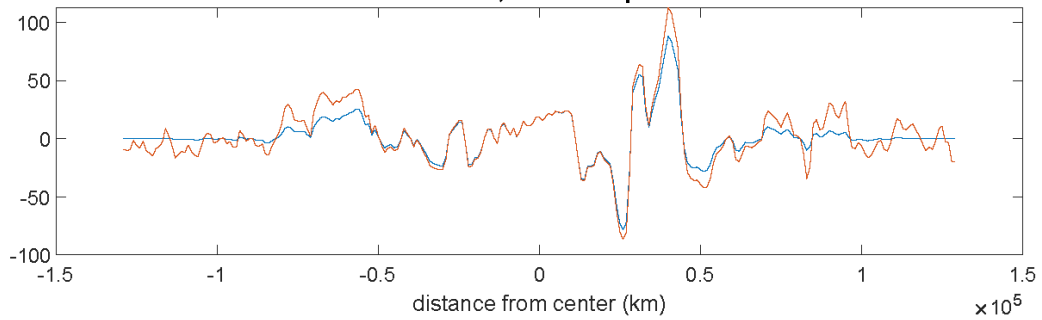
## Detrended Profile from Ellipse



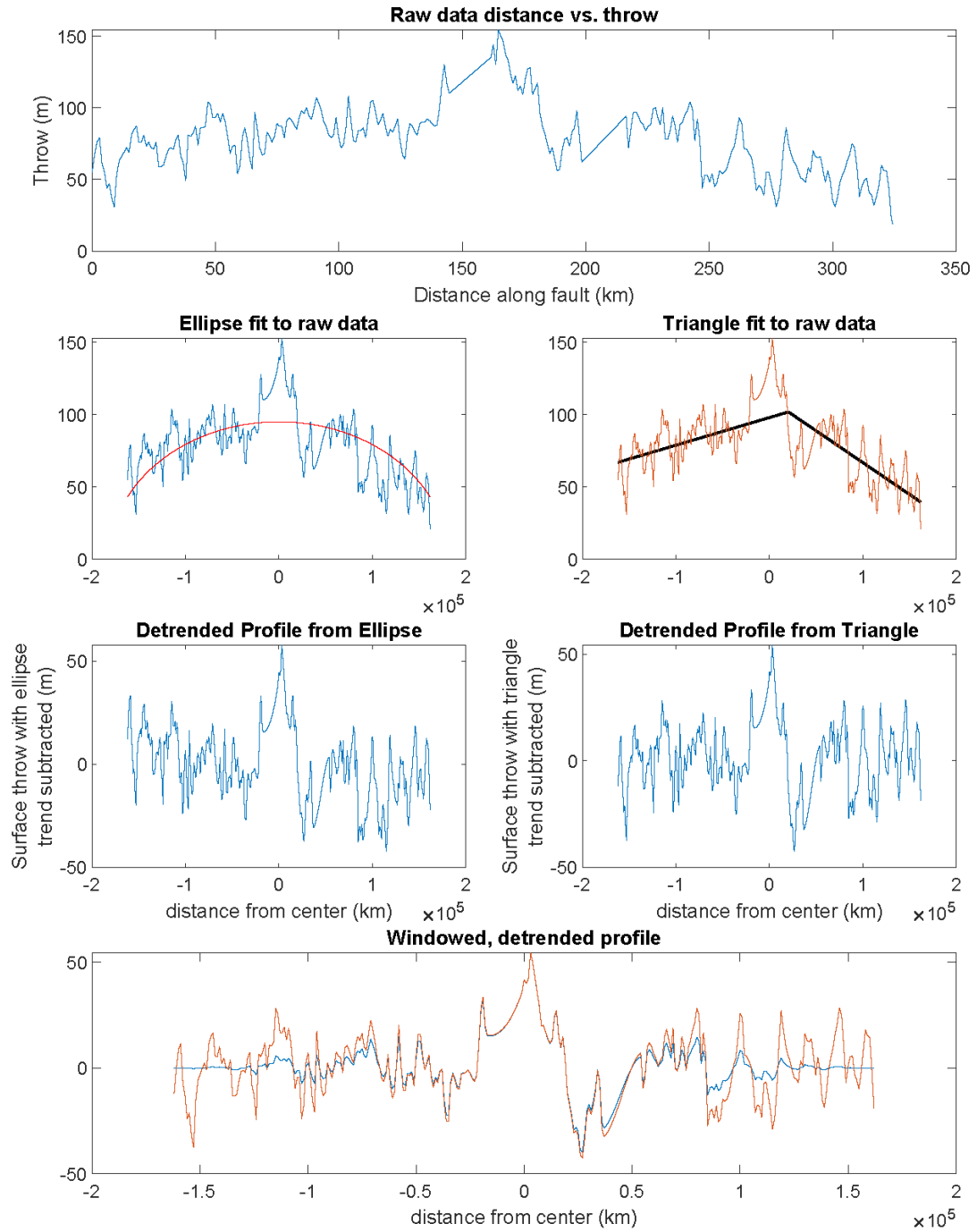
## Detrended Profile from Triangle



## Windowed, detrended profile

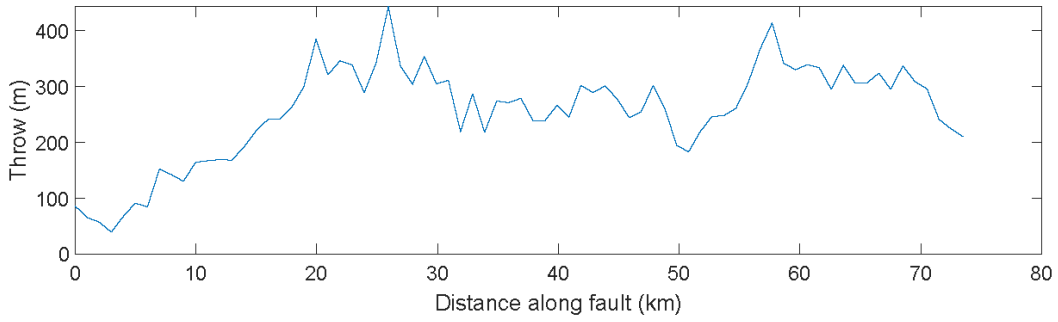


# Fault022

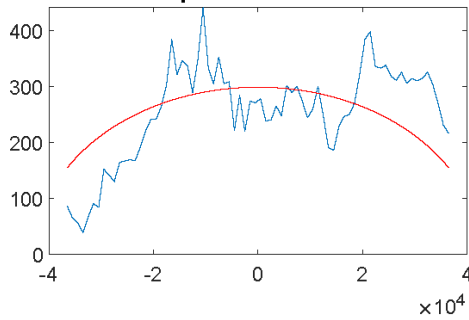


# Fault023

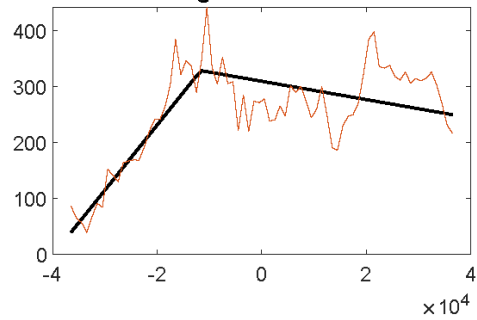
## Raw data distance vs. throw



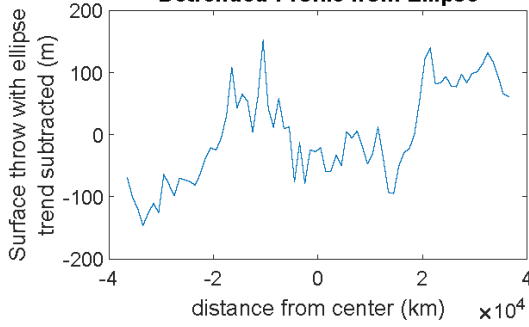
## Ellipse fit to raw data



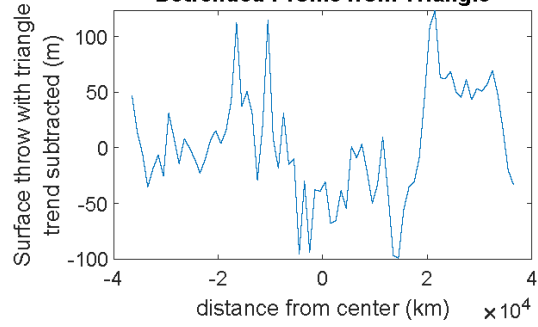
## Triangle fit to raw data



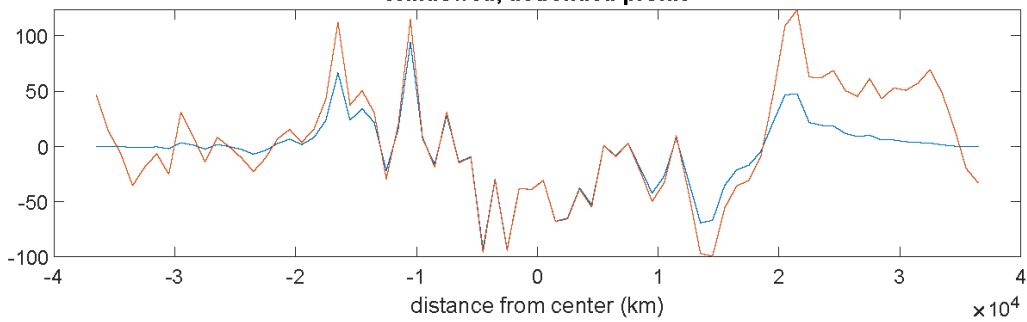
## Detrended Profile from Ellipse



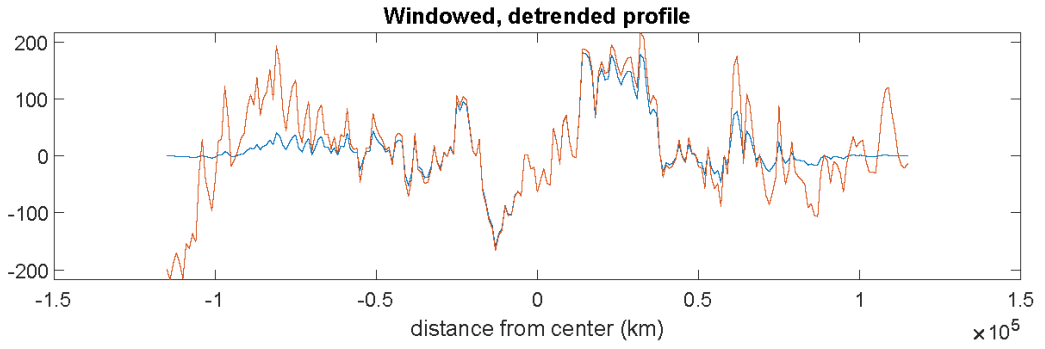
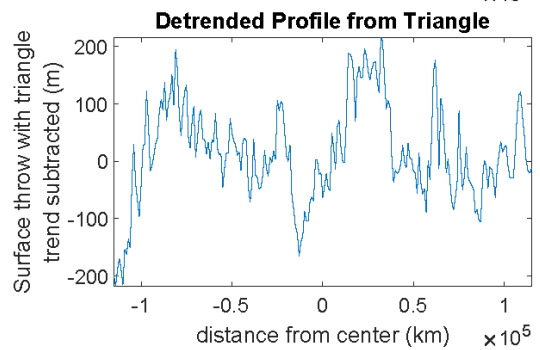
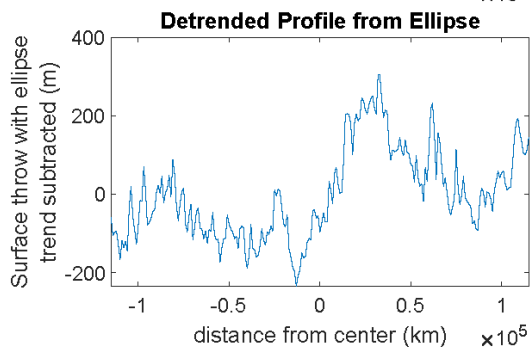
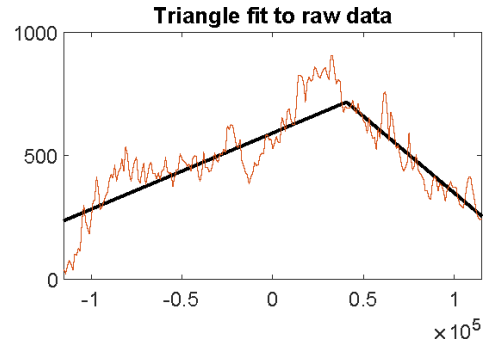
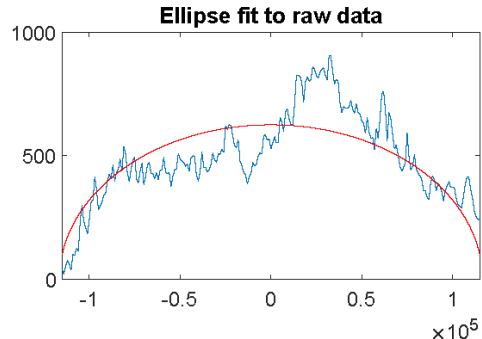
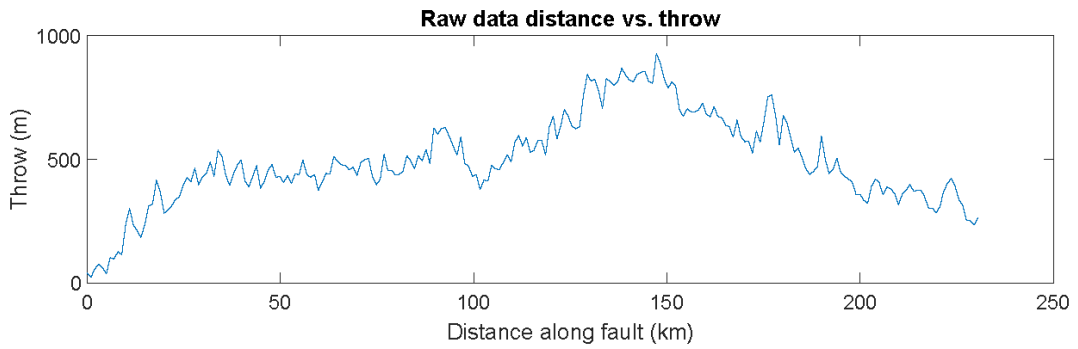
## Detrended Profile from Triangle



## Windowed, detrended profile

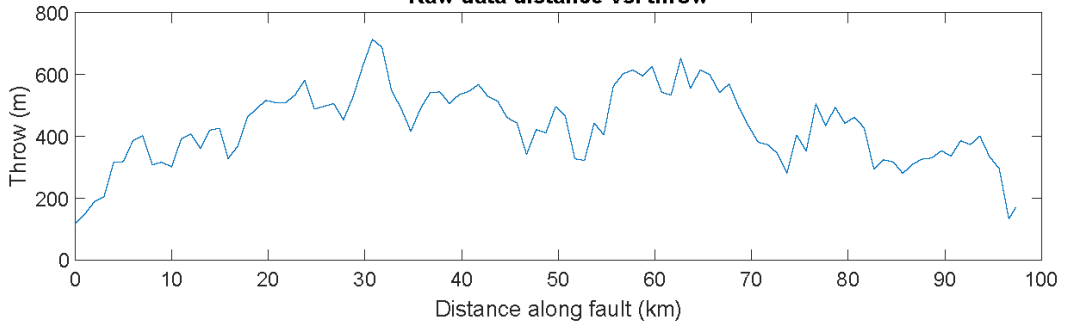


# Fault024

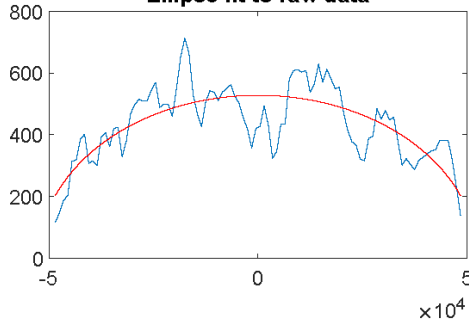


# Fault025

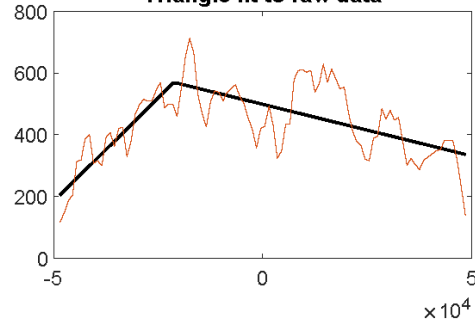
## Raw data distance vs. throw



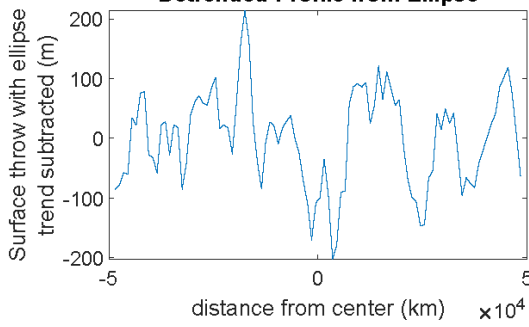
## Ellipse fit to raw data



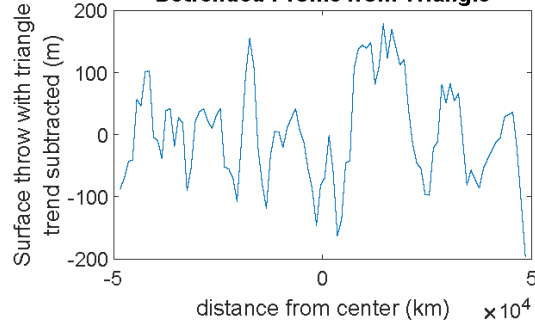
## Triangle fit to raw data



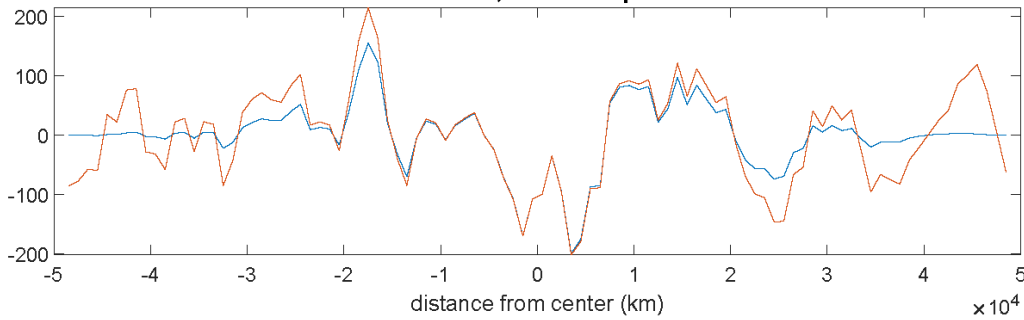
## Detrended Profile from Ellipse



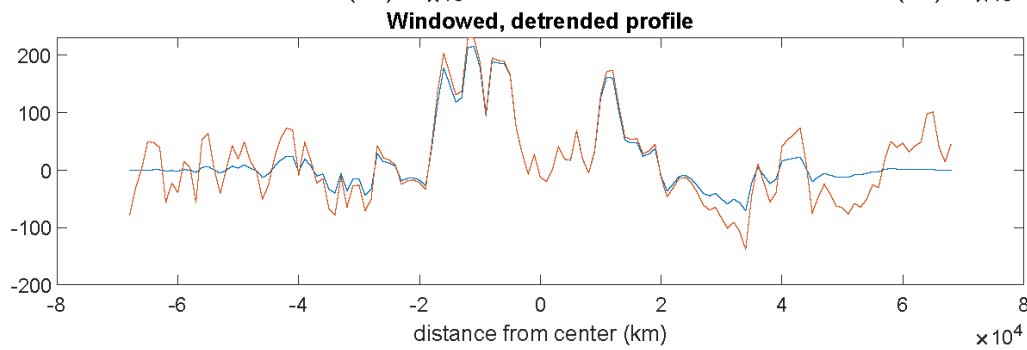
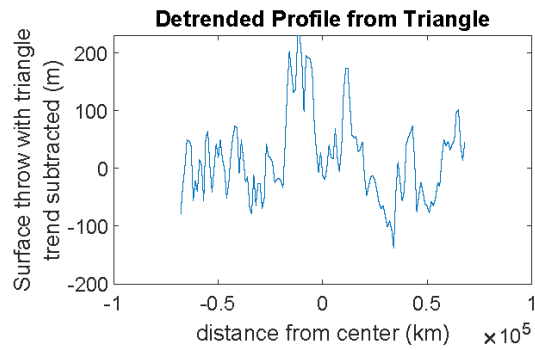
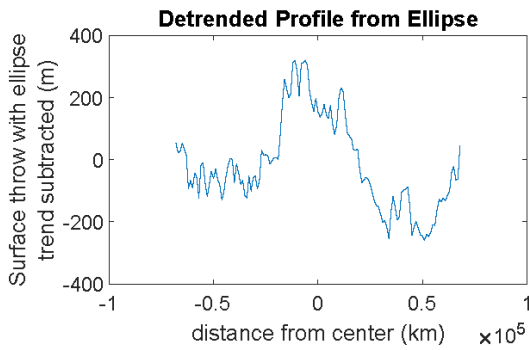
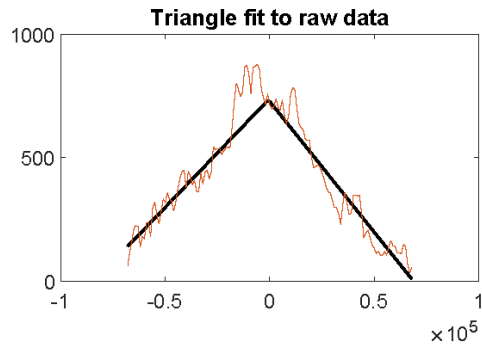
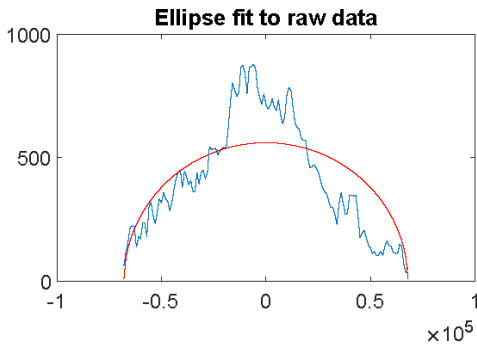
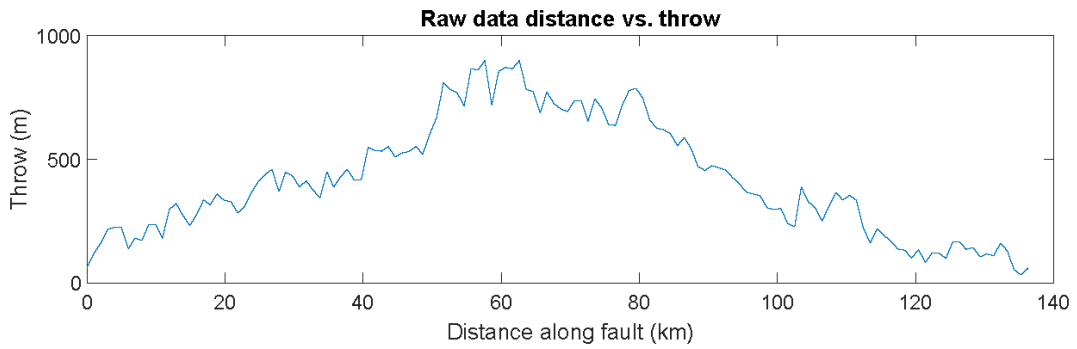
## Detrended Profile from Triangle



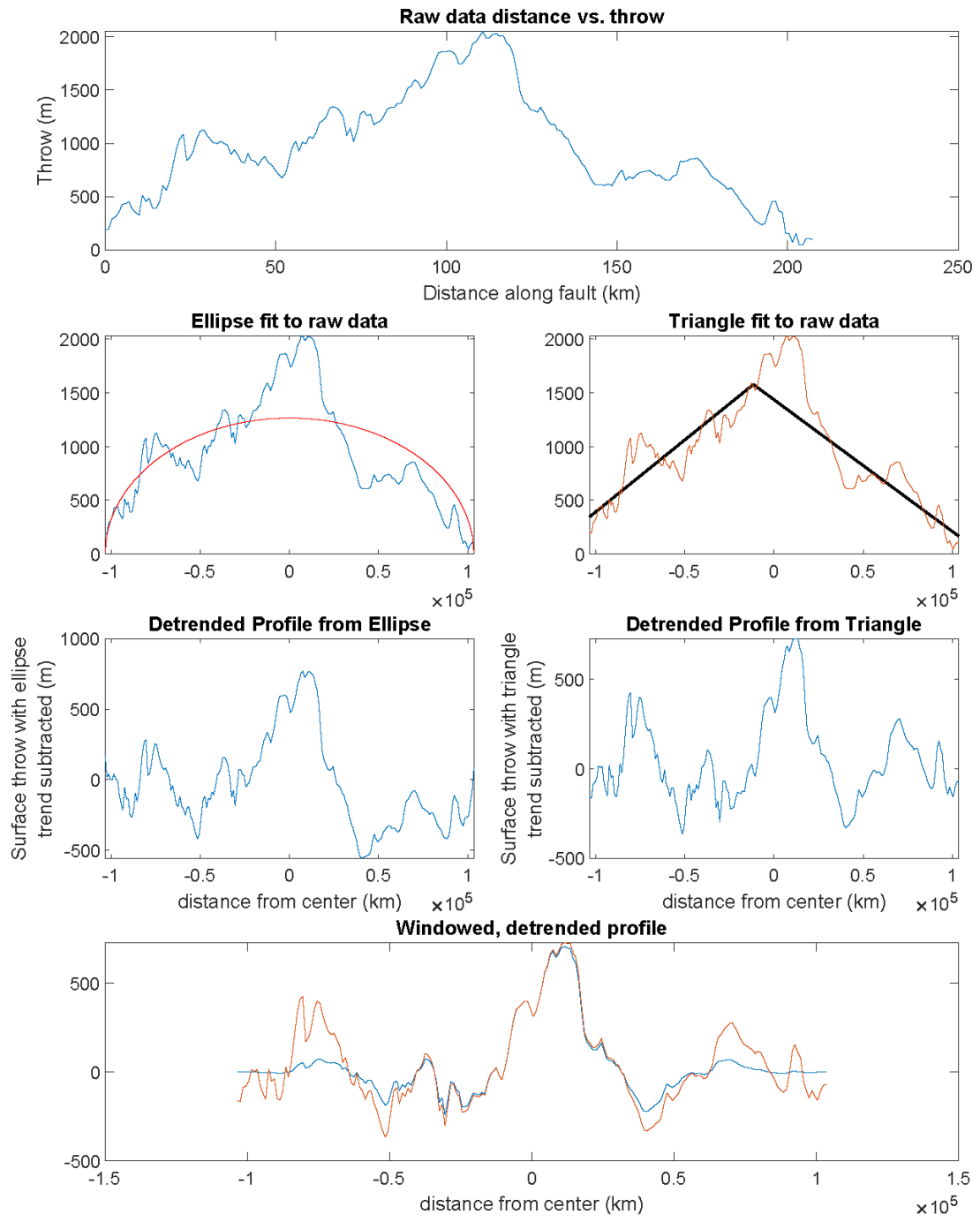
## Windowed, detrended profile



# Fault026

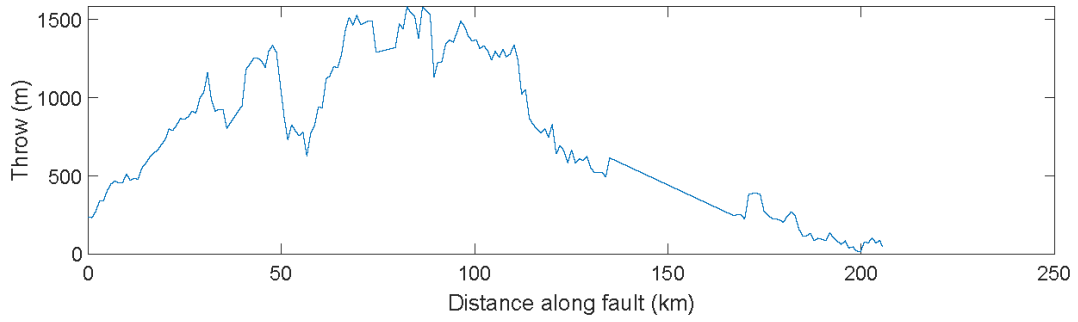


# Fault027

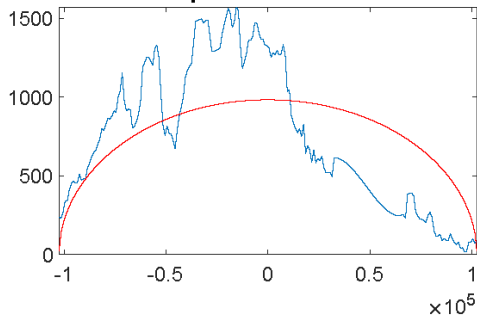


# Fault028

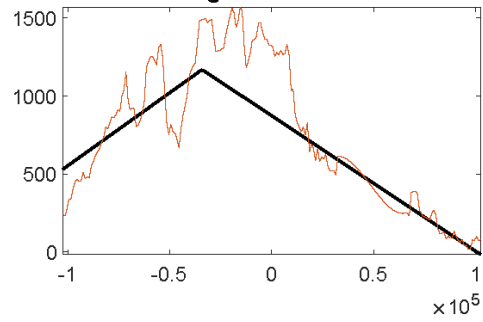
Raw data distance vs. throw



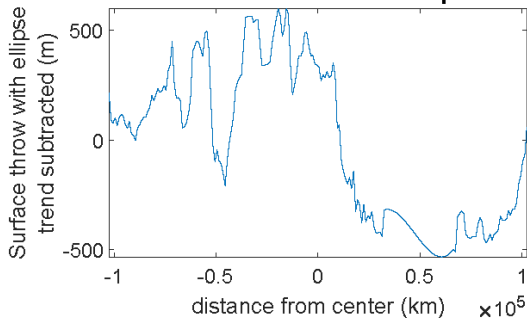
Ellipse fit to raw data



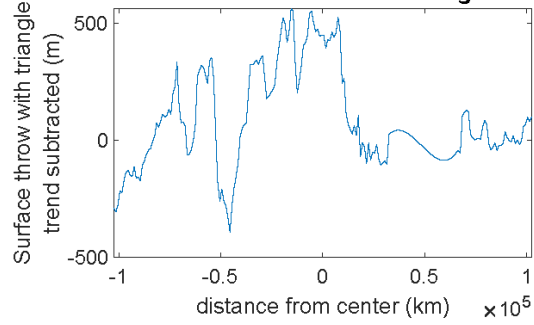
Triangle fit to raw data



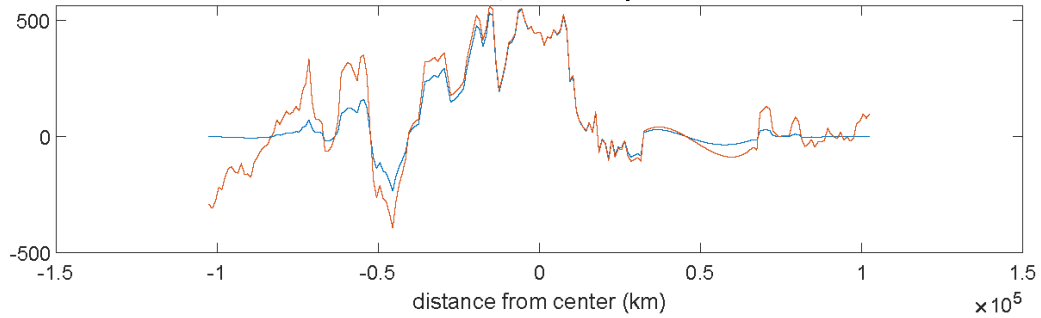
Detrended Profile from Ellipse



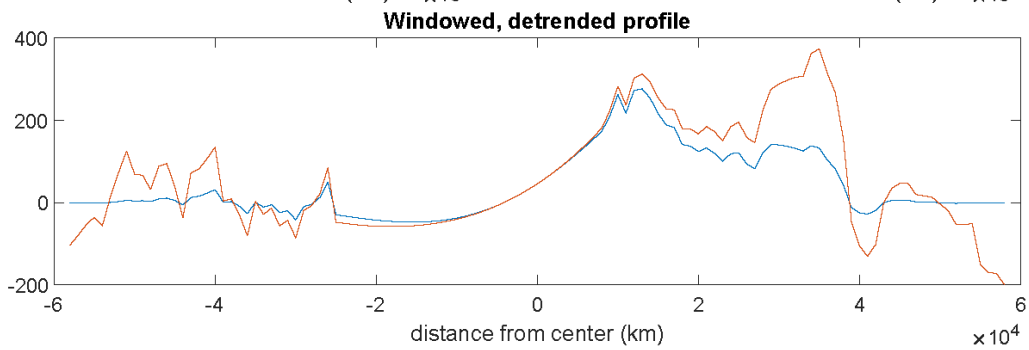
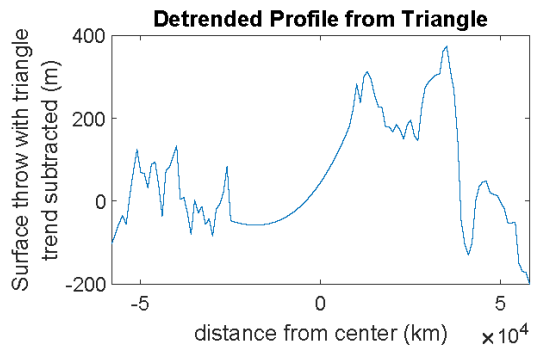
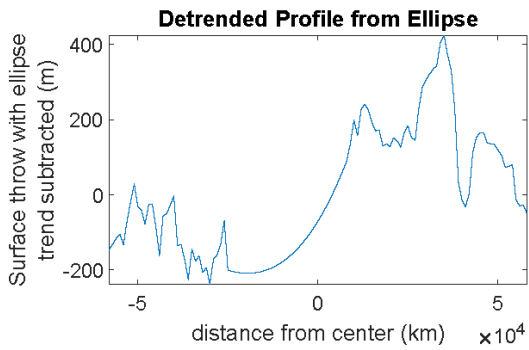
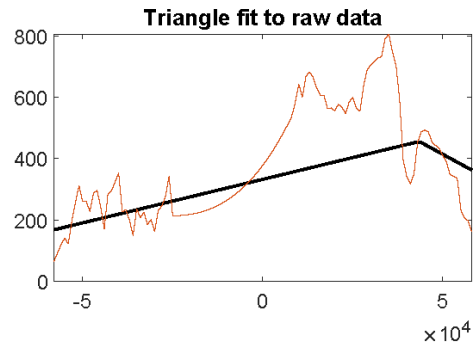
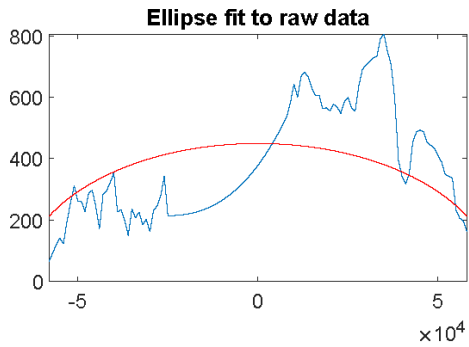
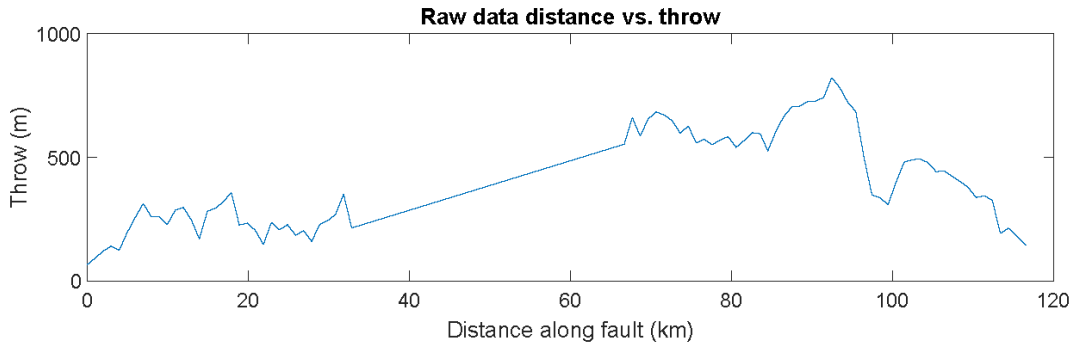
Detrended Profile from Triangle



Windowed, detrended profile

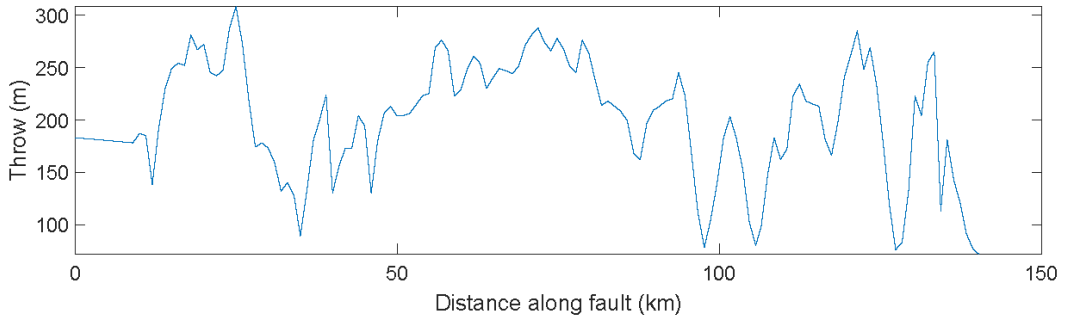


# Fault029

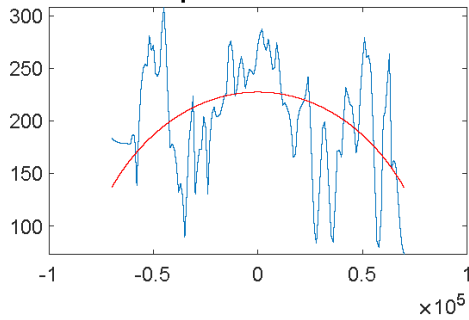


# Fault030

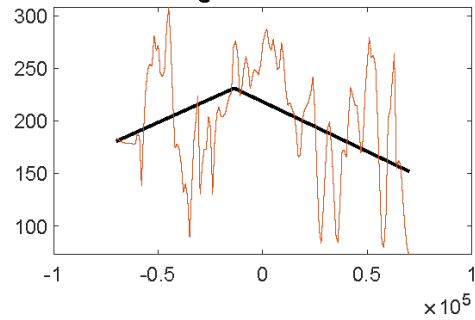
## Raw data distance vs. throw



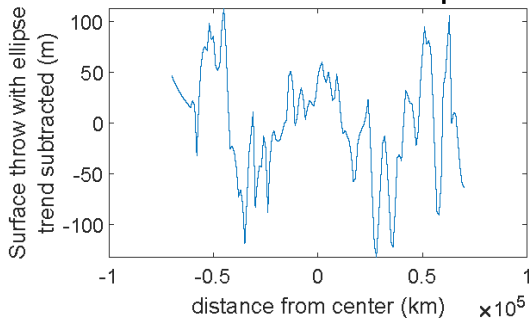
## Ellipse fit to raw data



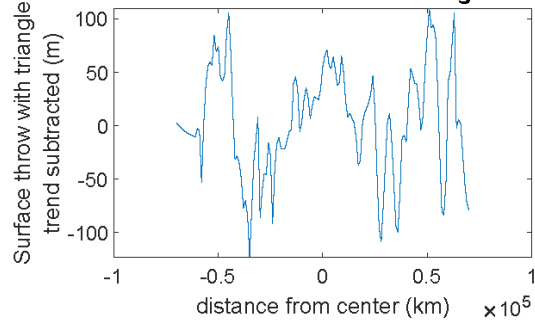
## Triangle fit to raw data



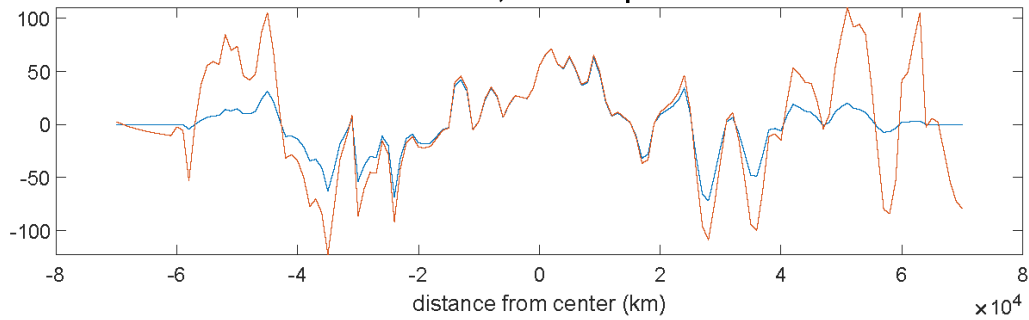
## Detrended Profile from Ellipse



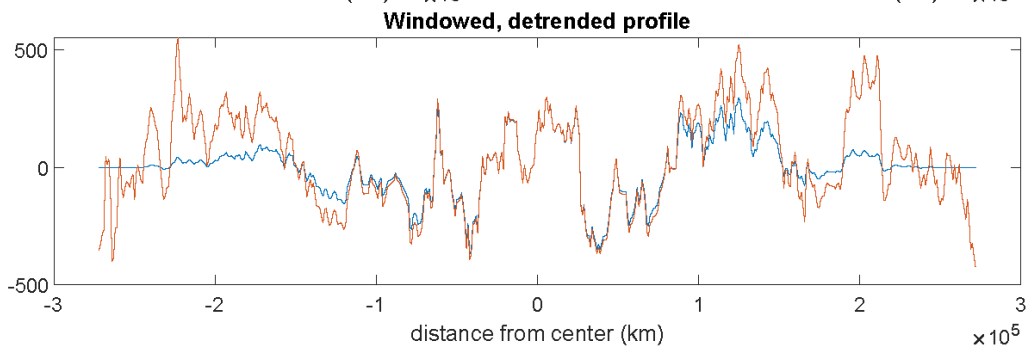
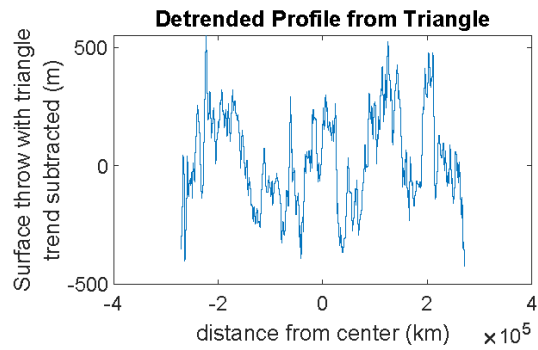
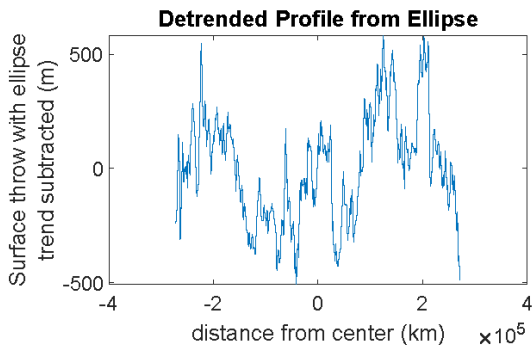
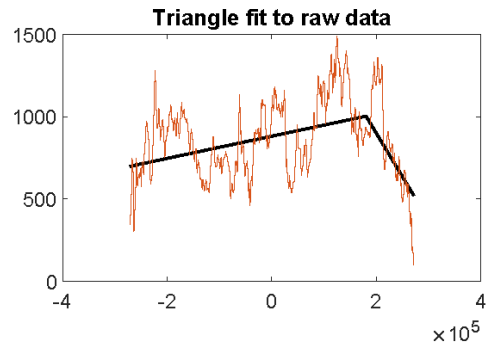
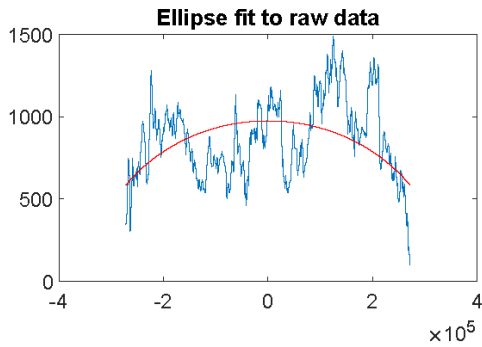
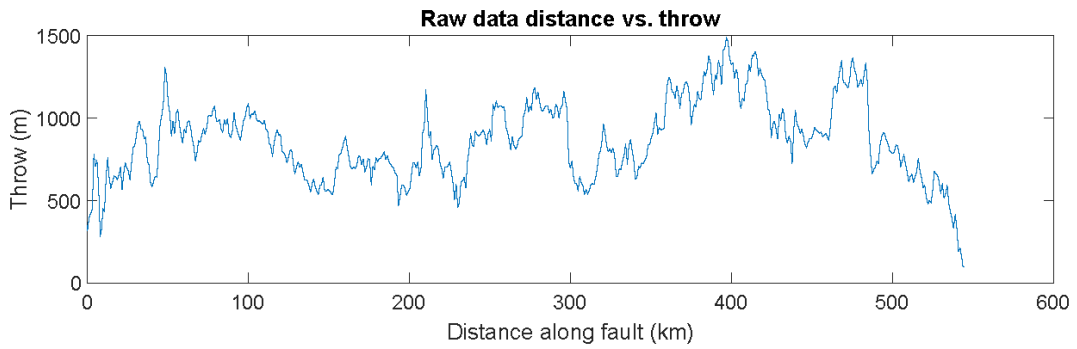
## Detrended Profile from Triangle



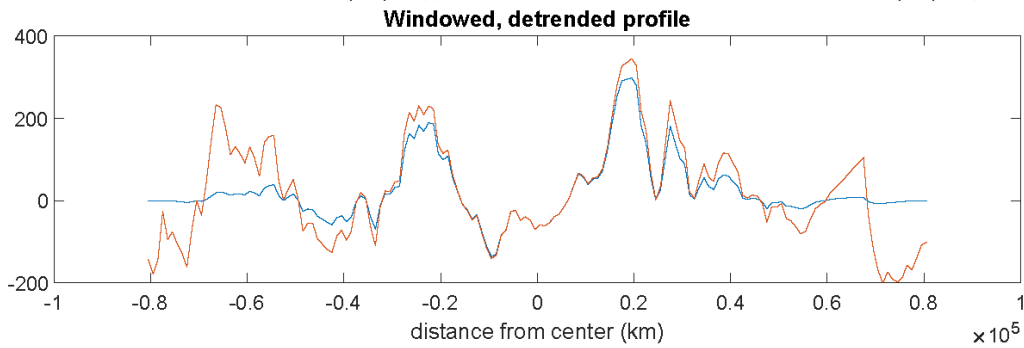
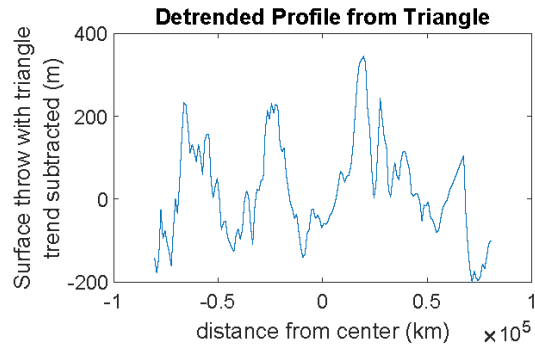
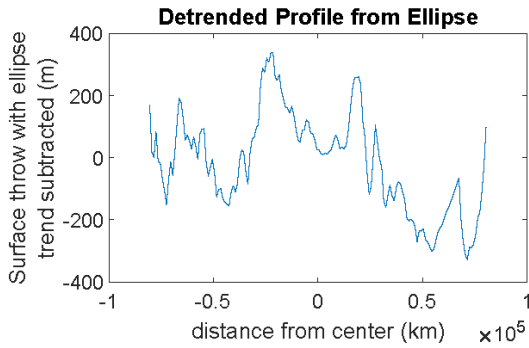
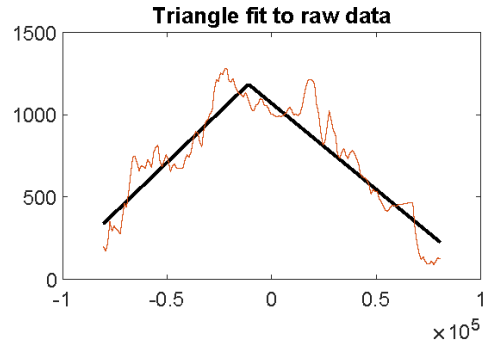
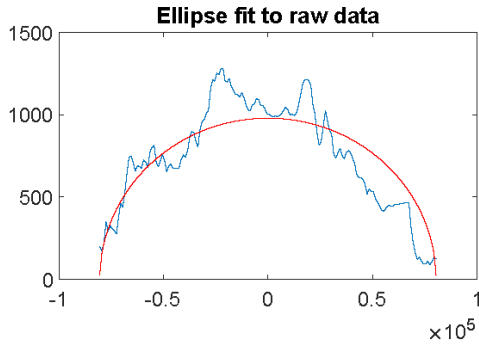
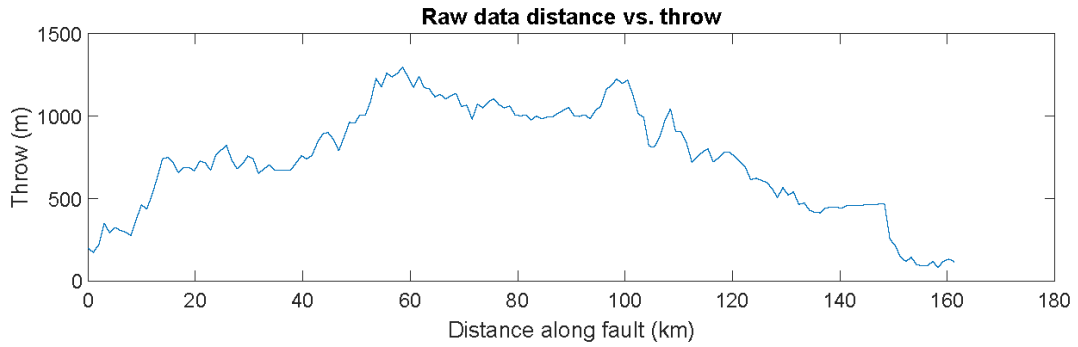
## Windowed, detrended profile



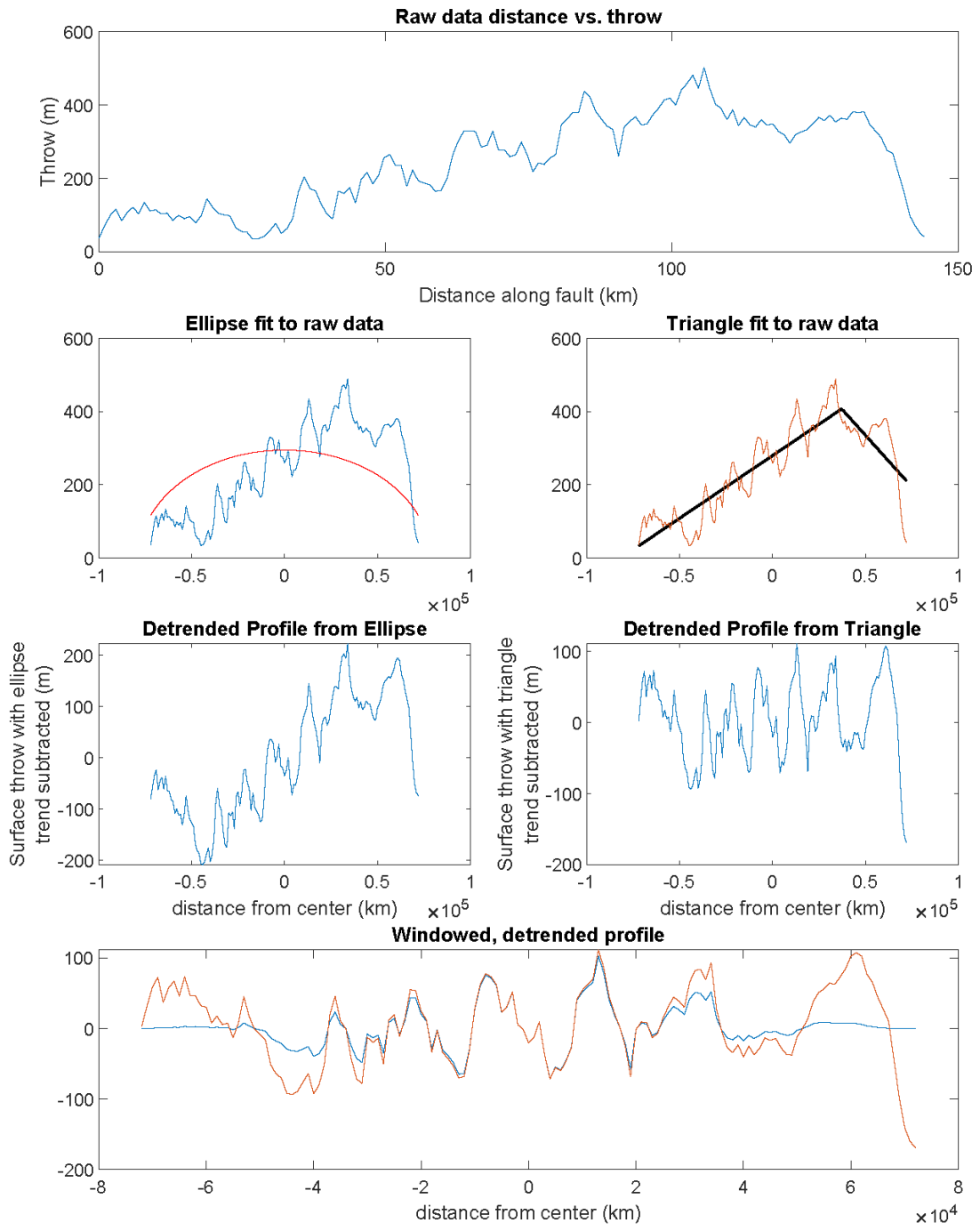
# Fault031



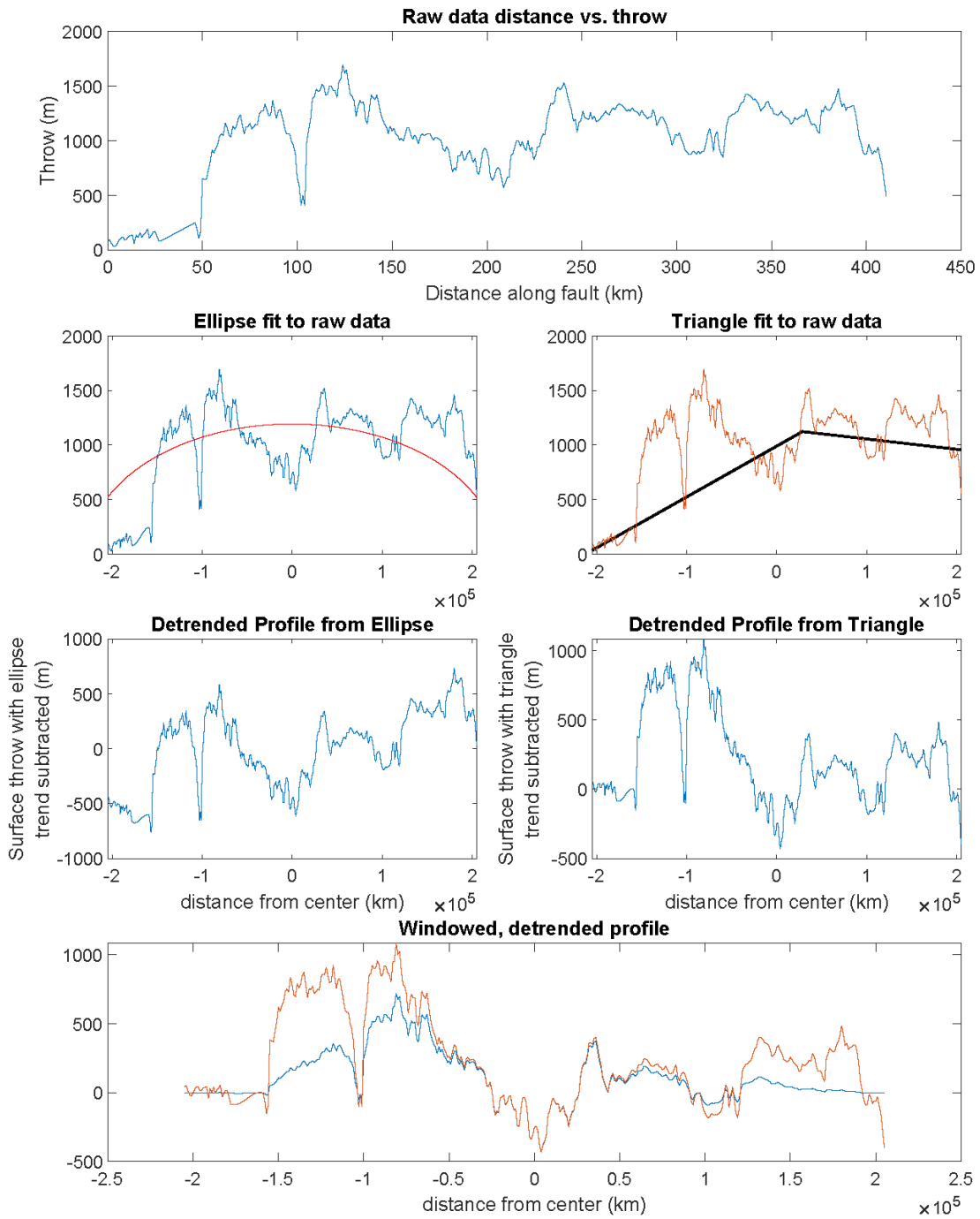
# Fault032



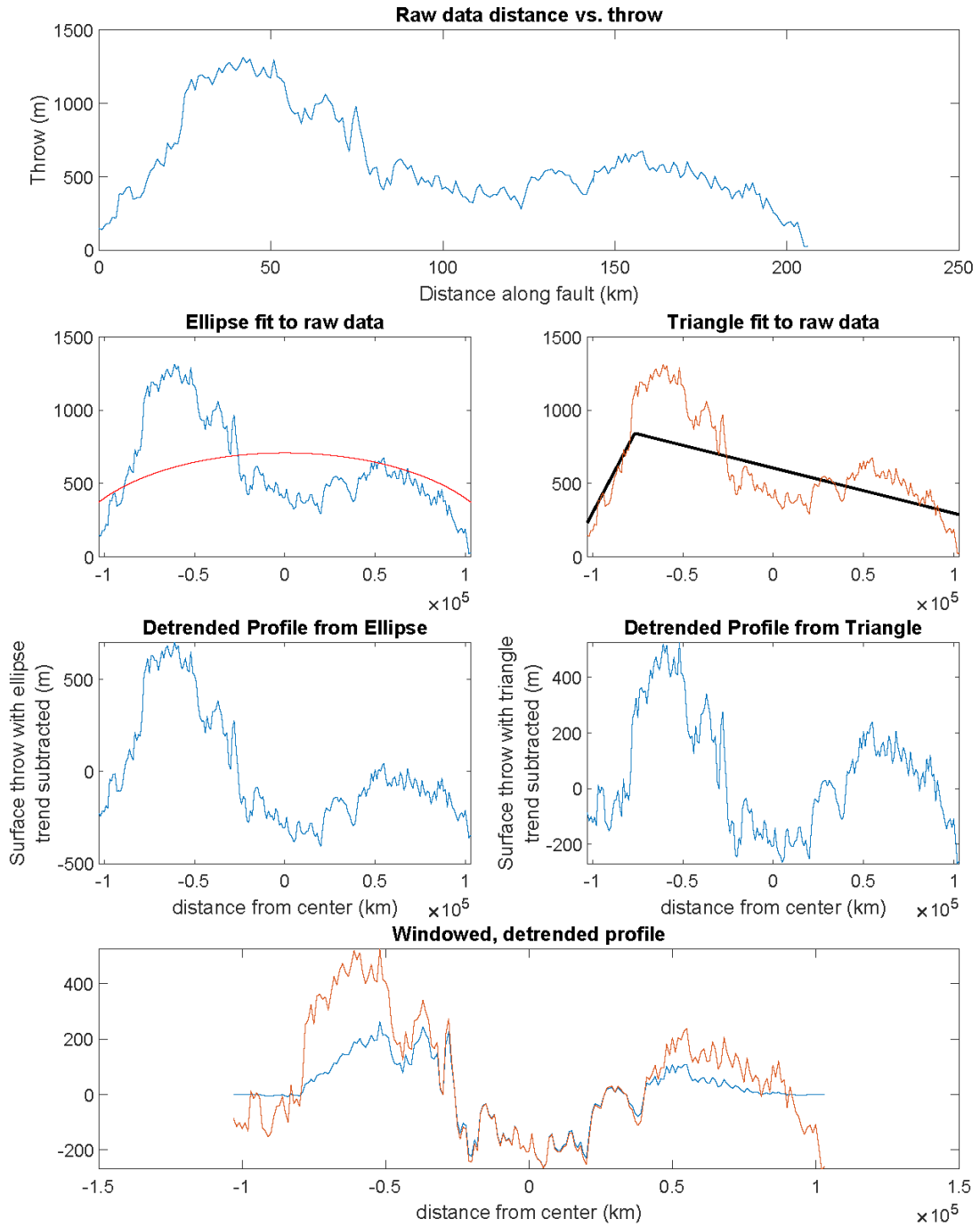
# Fault033



# Fault034

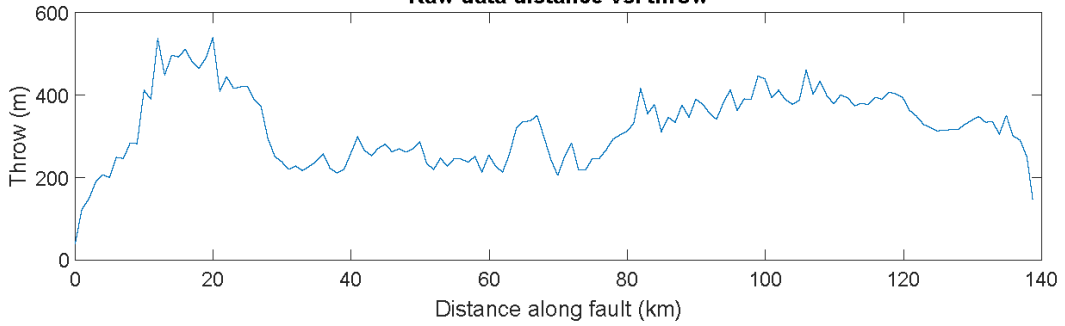


# Fault036

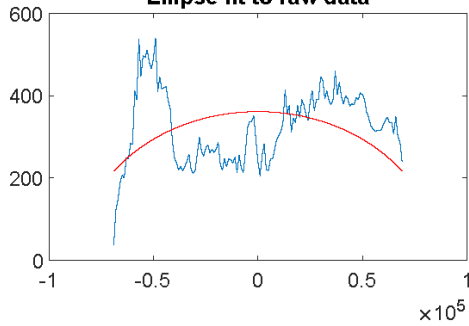


# Fault037

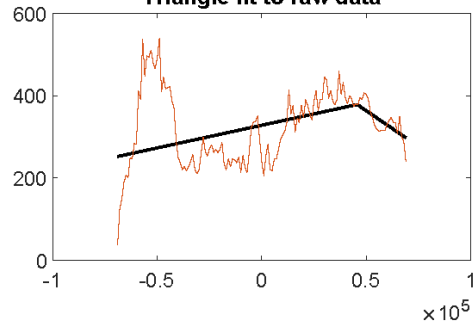
Raw data distance vs. throw



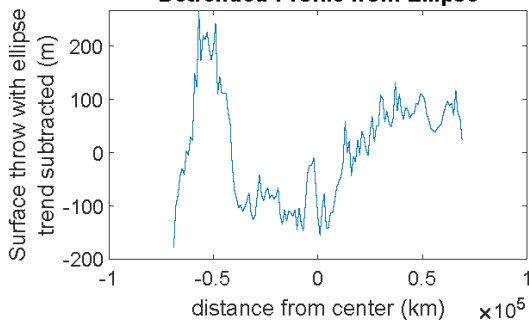
Ellipse fit to raw data



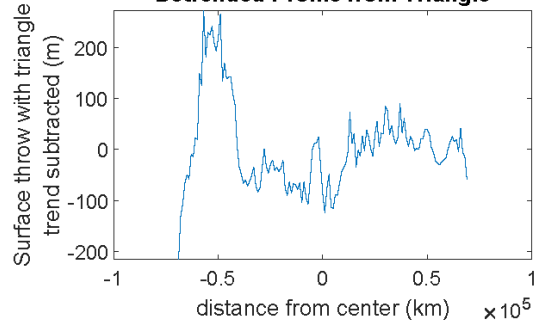
Triangle fit to raw data



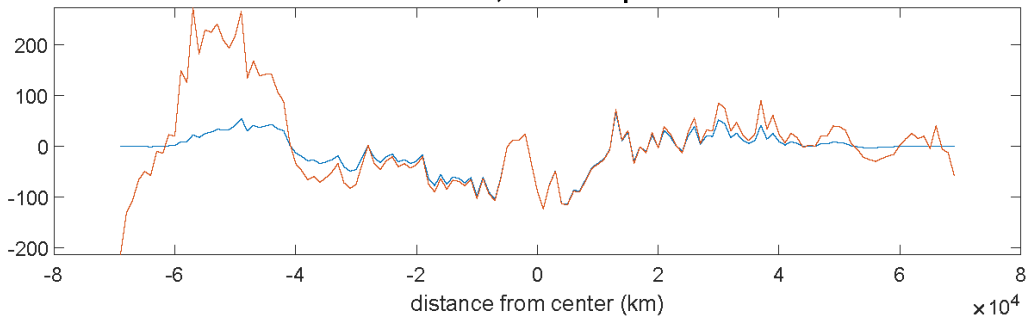
Detrended Profile from Ellipse



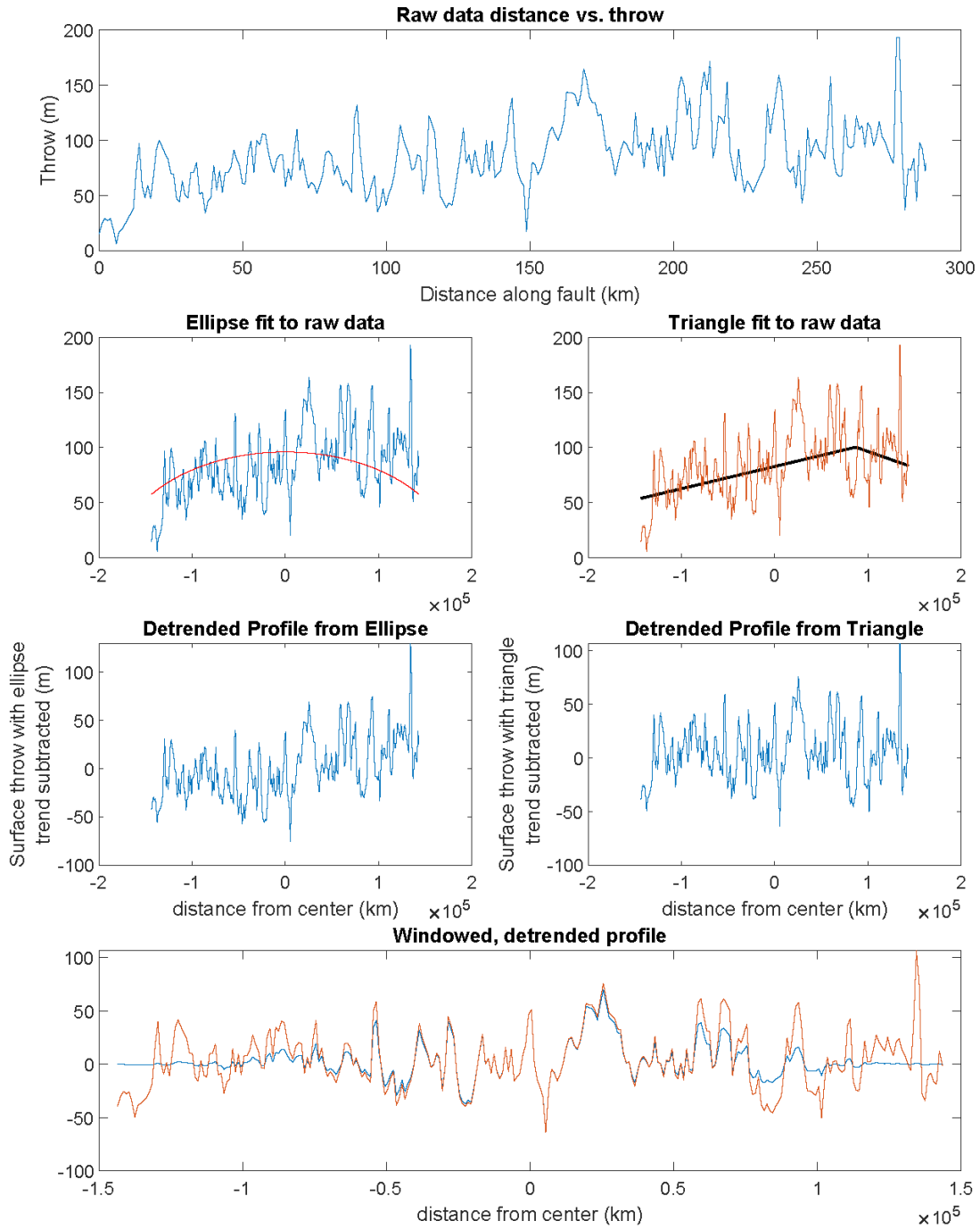
Detrended Profile from Triangle



Windowed, detrended profile

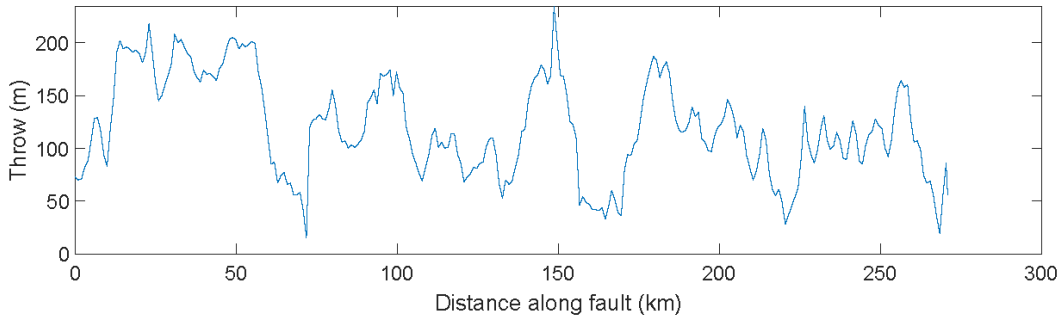


# Fault038

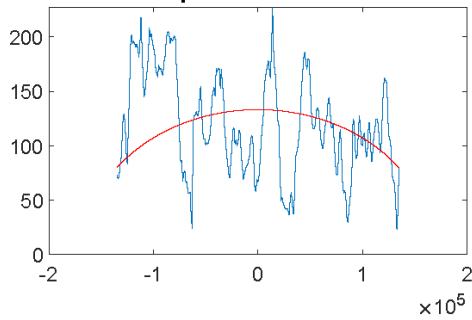


# Fault039

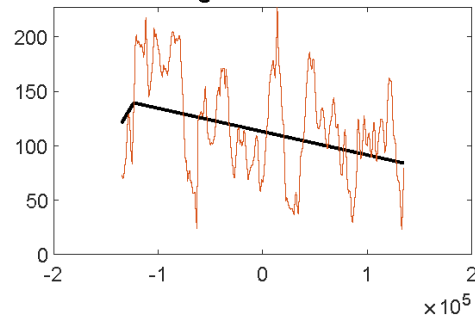
Raw data distance vs. throw



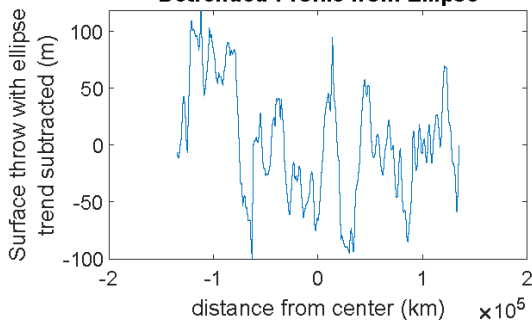
Ellipse fit to raw data



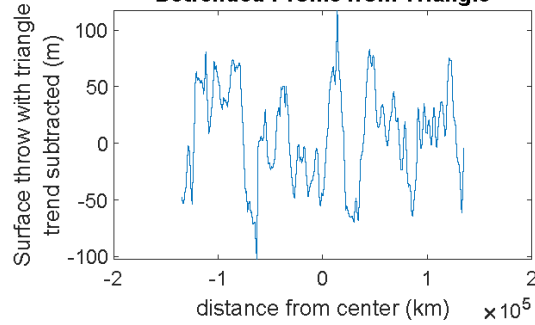
Triangle fit to raw data



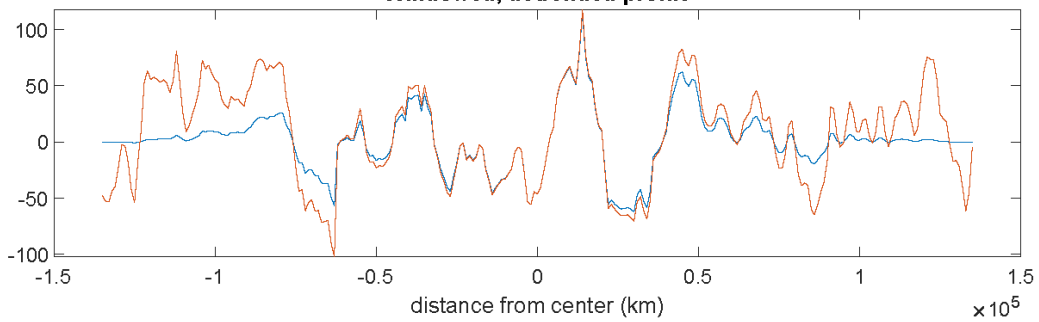
Detrended Profile from Ellipse



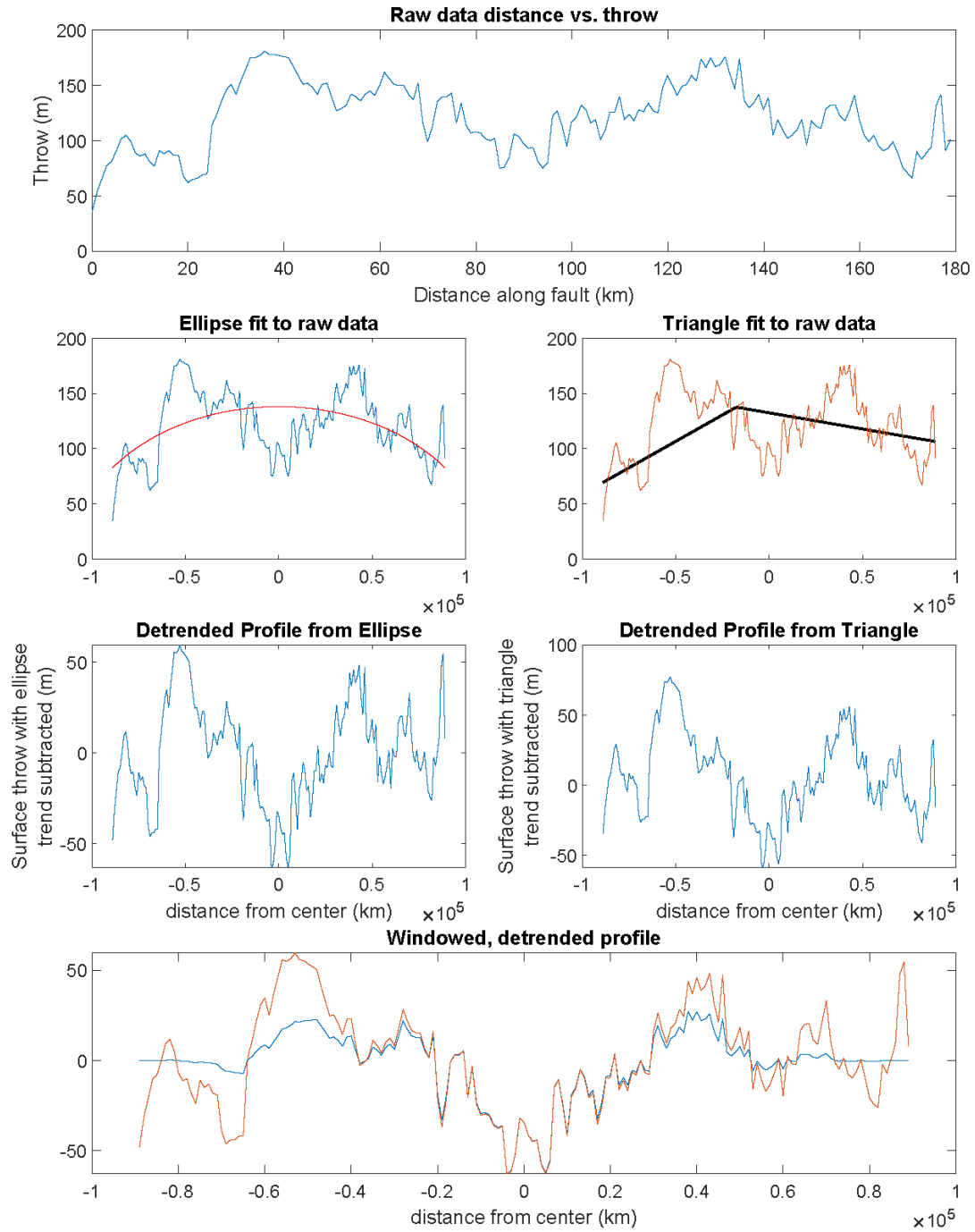
Detrended Profile from Triangle



Windowed, detrended profile

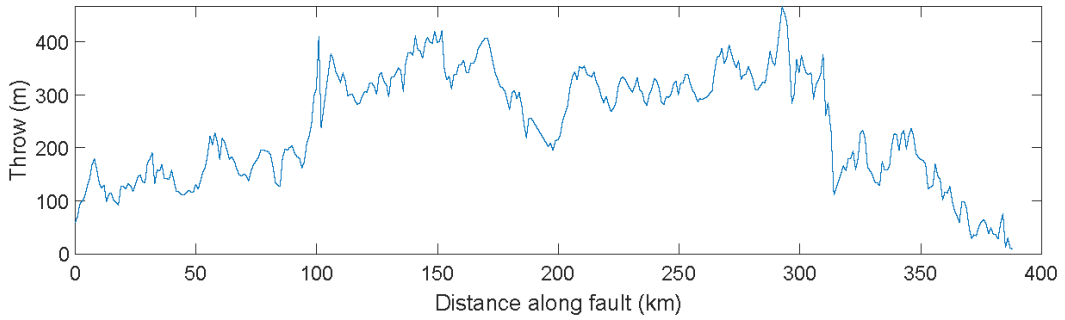


# Fault040

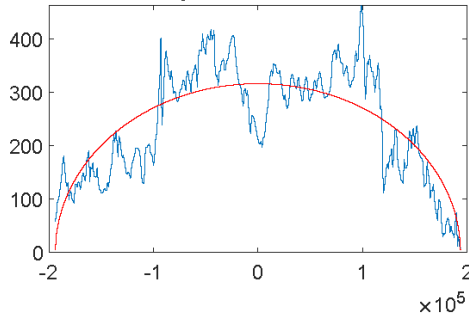


# Fault041

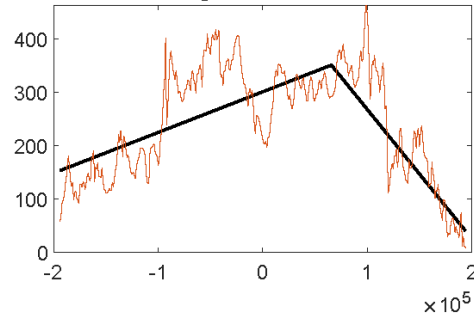
Raw data distance vs. throw



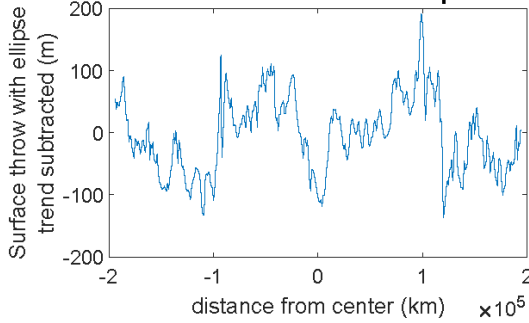
Ellipse fit to raw data



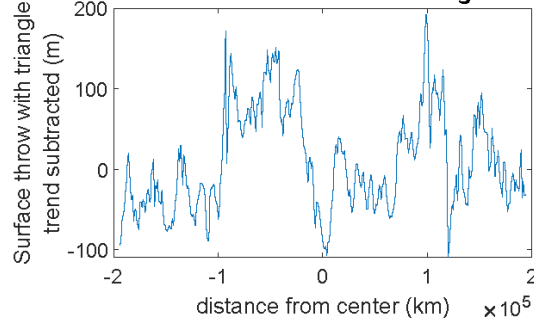
Triangle fit to raw data



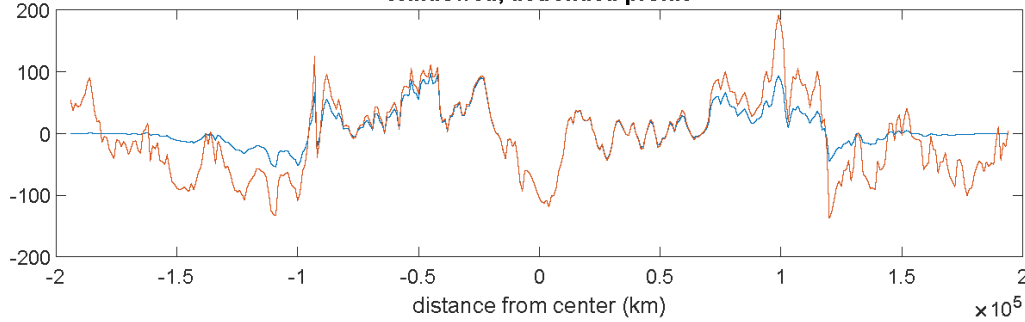
Detrended Profile from Ellipse



Detrended Profile from Triangle

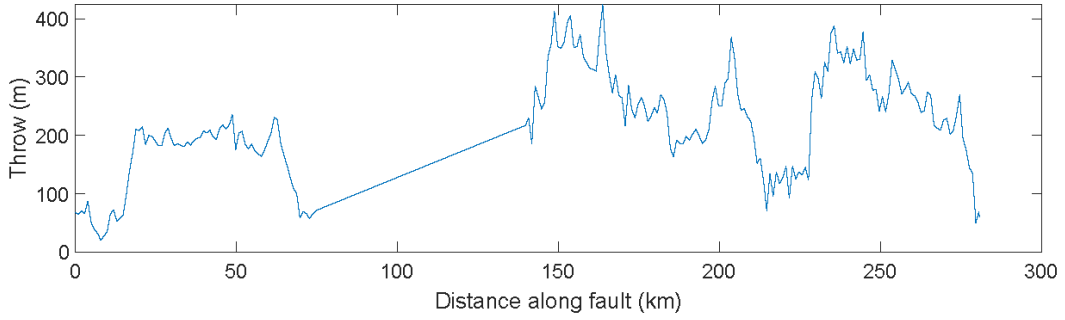


Windowed, detrended profile

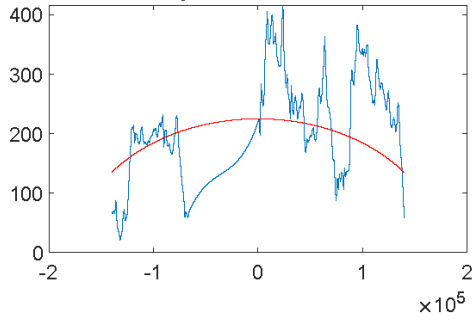


# Fault042

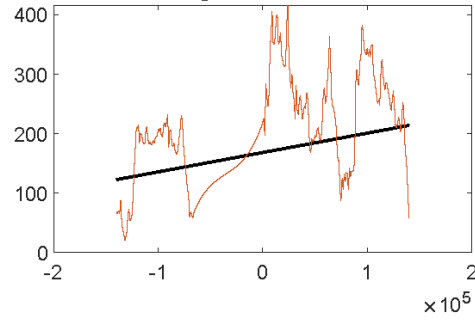
## Raw data distance vs. throw



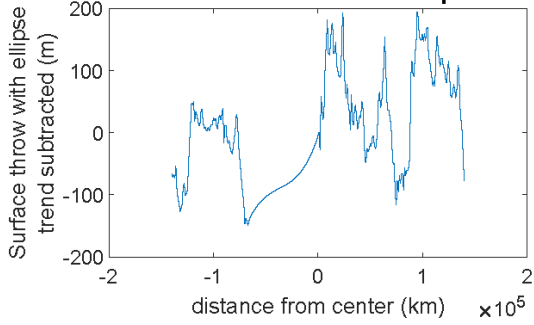
## Ellipse fit to raw data



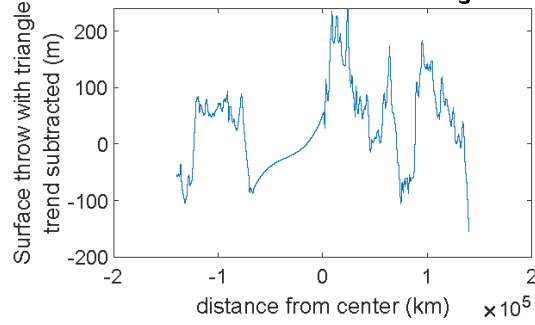
## Triangle fit to raw data



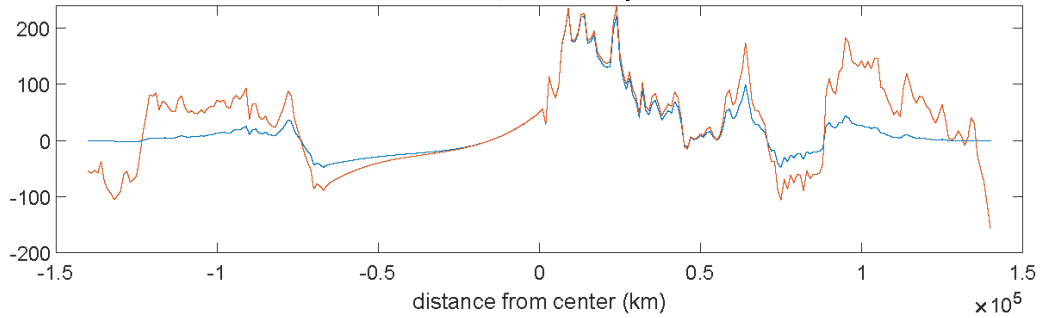
## Detrended Profile from Ellipse



## Detrended Profile from Triangle

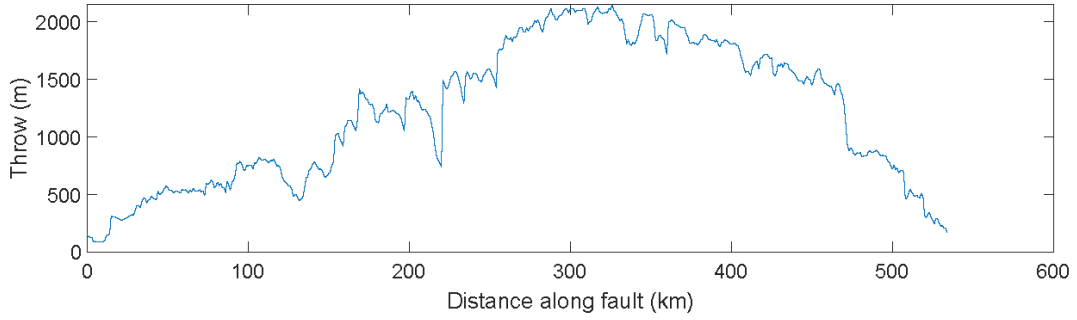


## Windowed, detrended profile

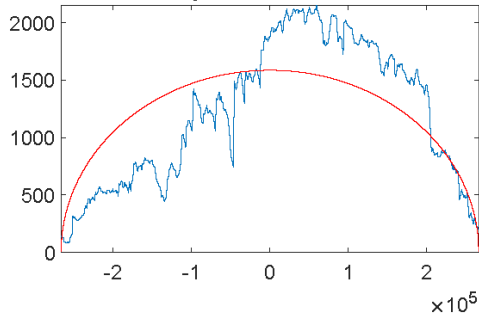


# Fault043

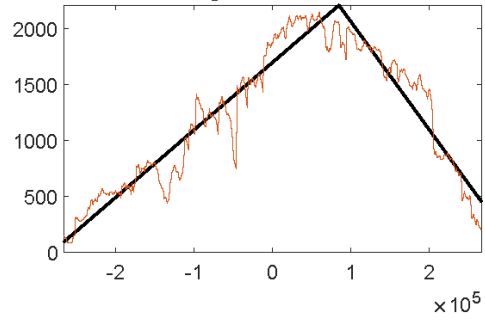
## Raw data distance vs. throw



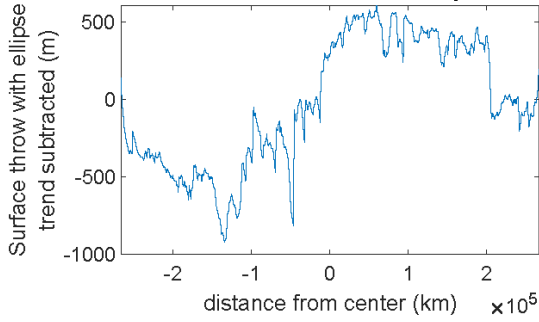
## Ellipse fit to raw data



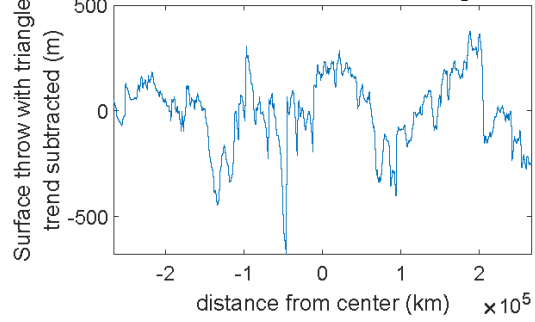
## Triangle fit to raw data



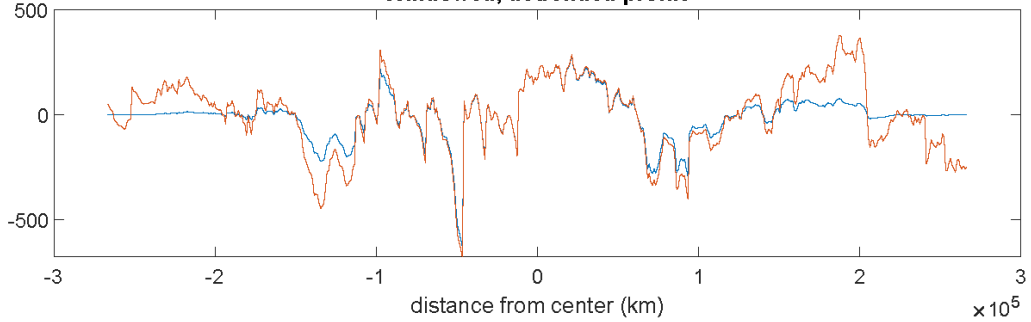
## Detrended Profile from Ellipse



## Detrended Profile from Triangle

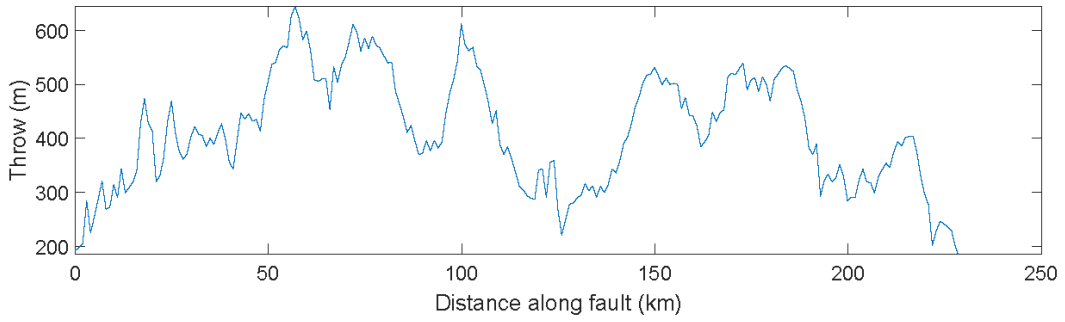


## Windowed, detrended profile

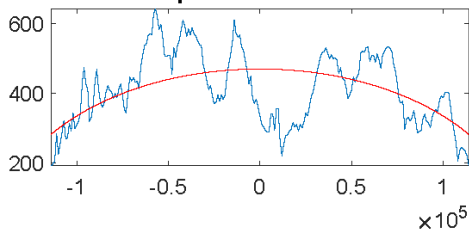


# Fault044

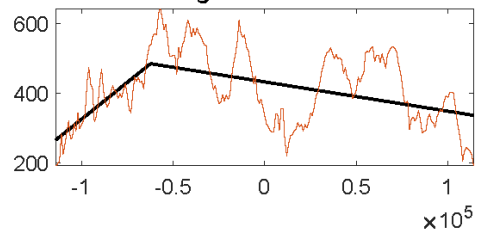
Raw data distance vs. throw



Ellipse fit to raw data

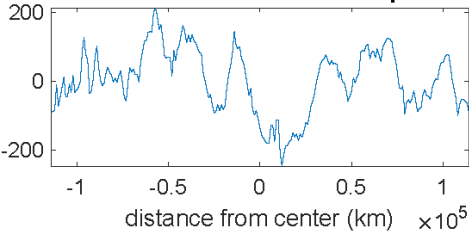


Triangle fit to raw data



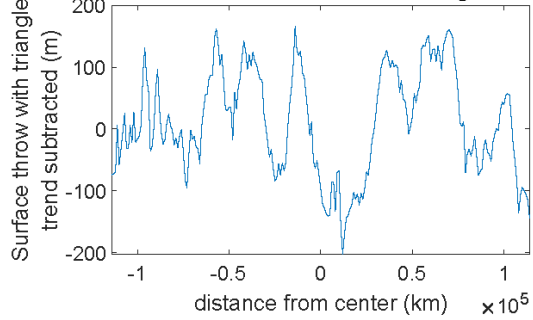
Surface throw with ellipse trend subtracted (m)

Detrended Profile from Ellipse

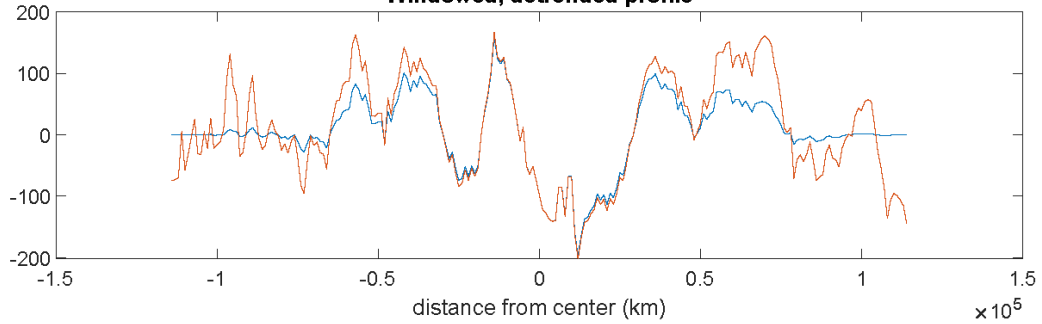


Surface throw with triangle trend subtracted (m)

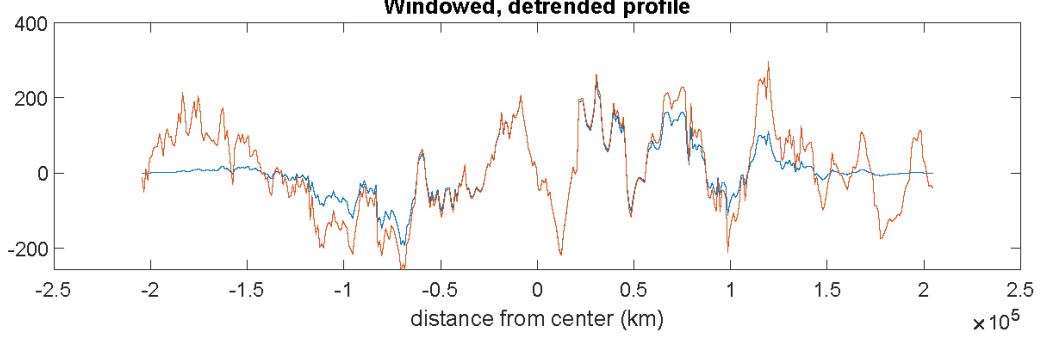
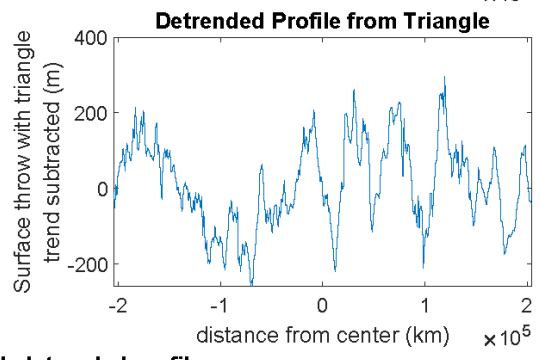
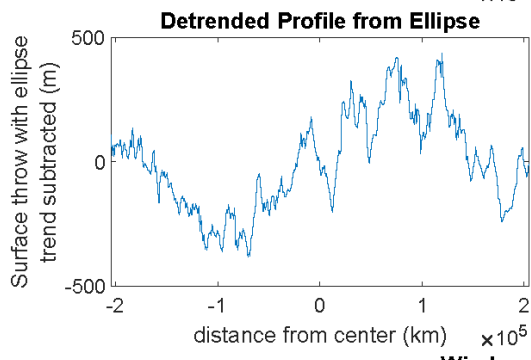
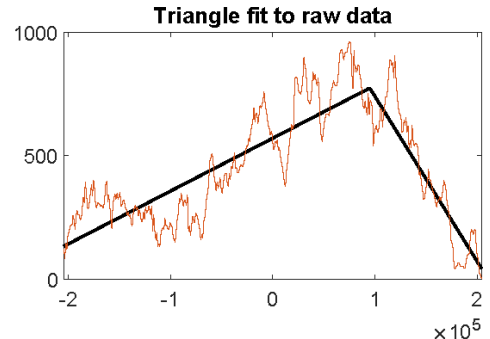
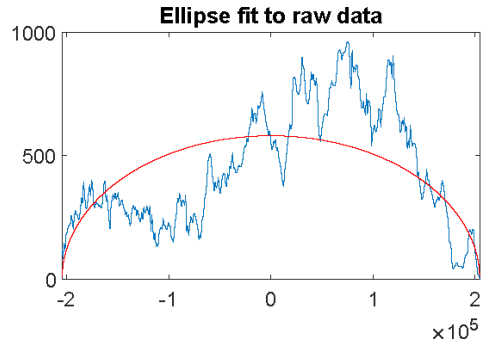
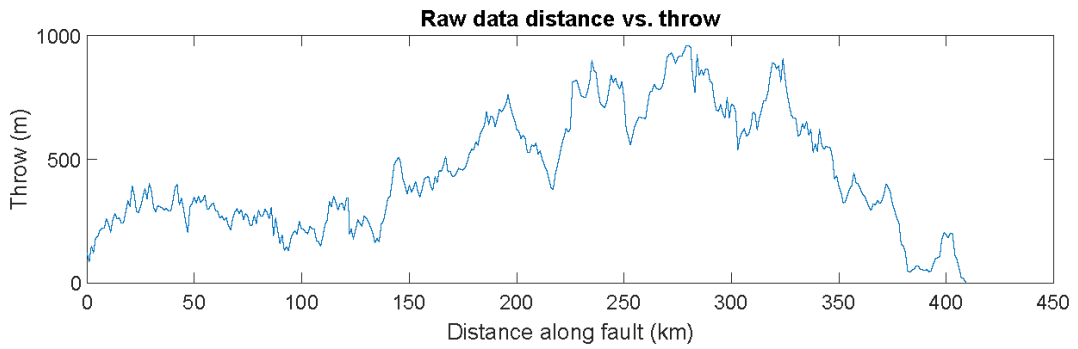
Detrended Profile from Triangle



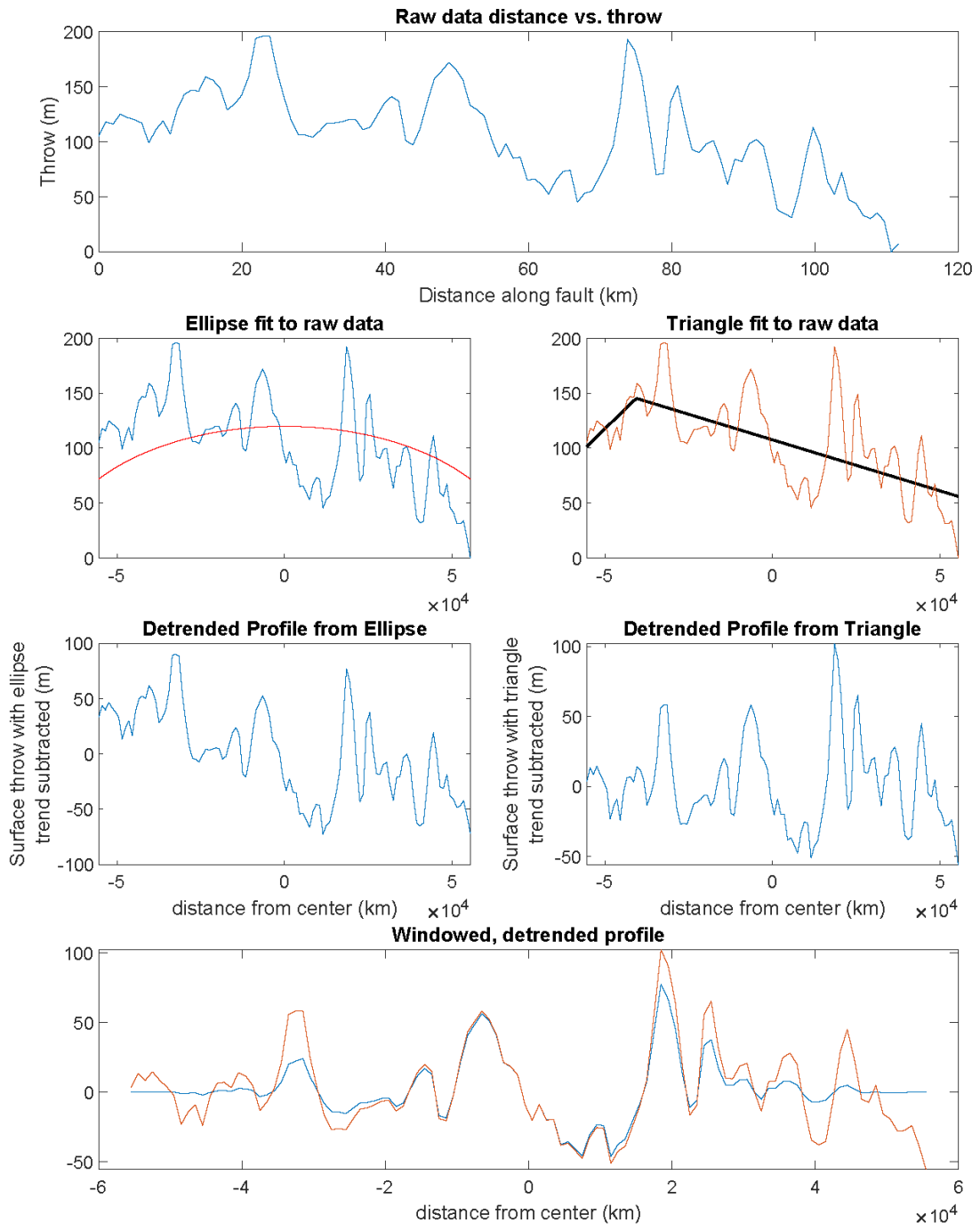
Windowed, detrended profile



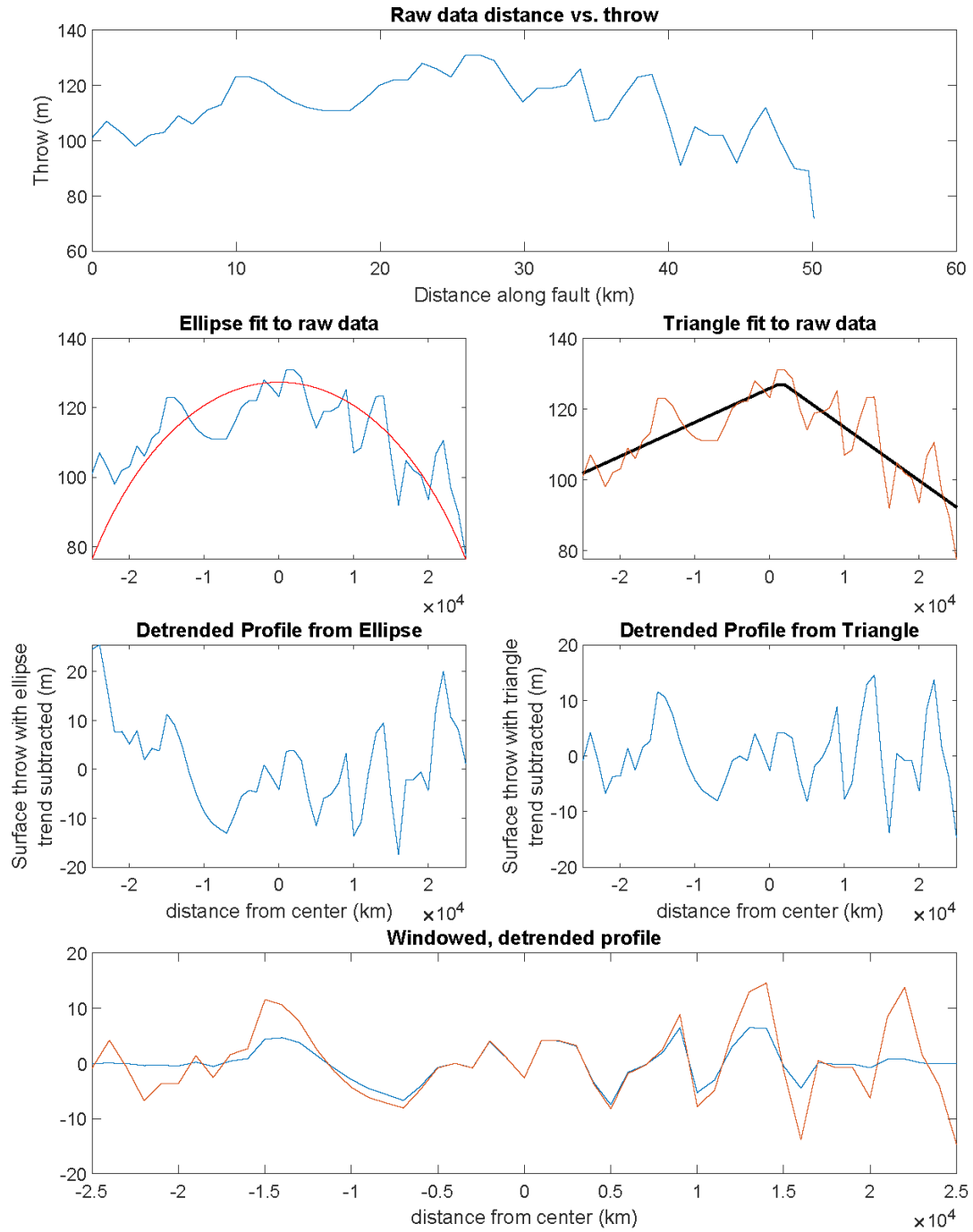
# Fault045



# Fault047

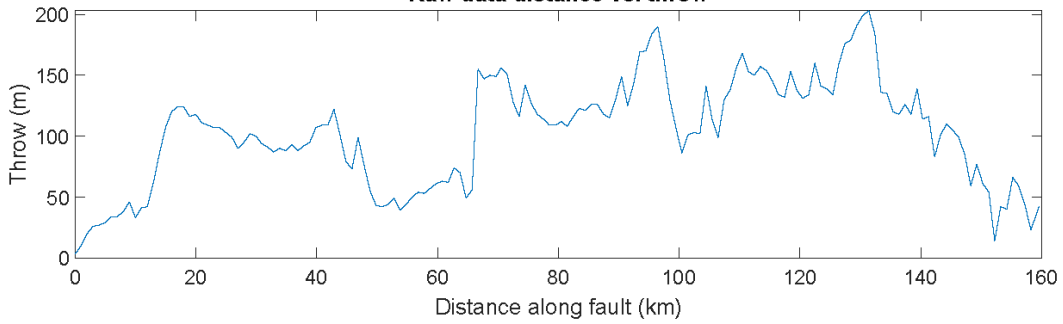


# Fault048

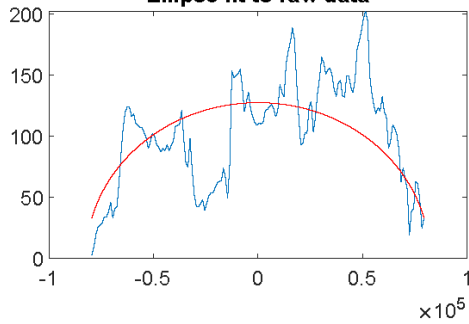


# Fault049

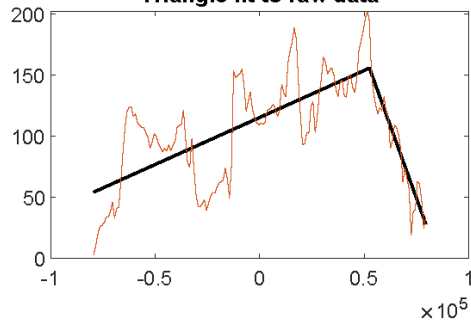
## Raw data distance vs. throw



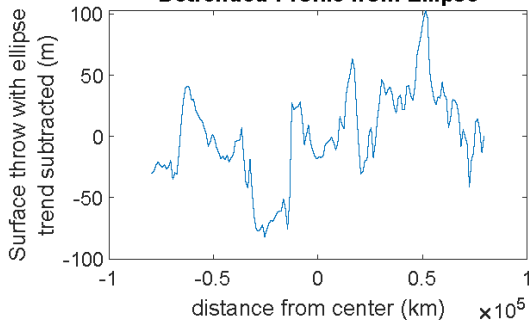
## Ellipse fit to raw data



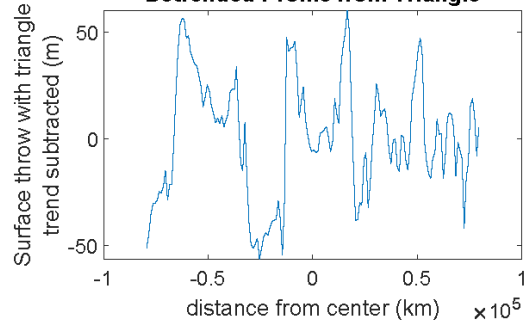
## Triangle fit to raw data



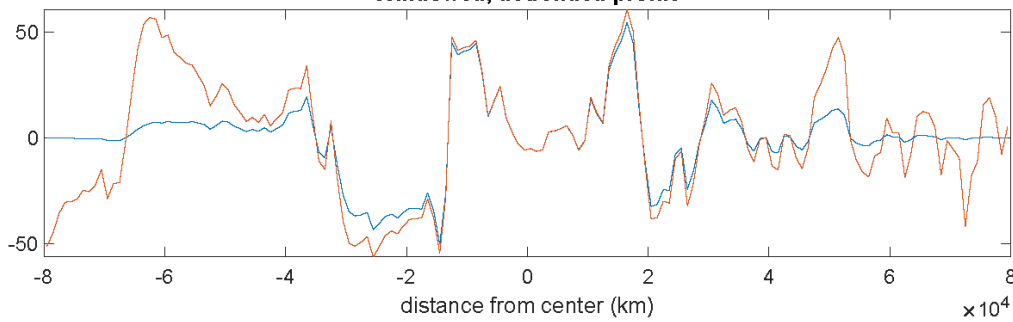
## Detrended Profile from Ellipse



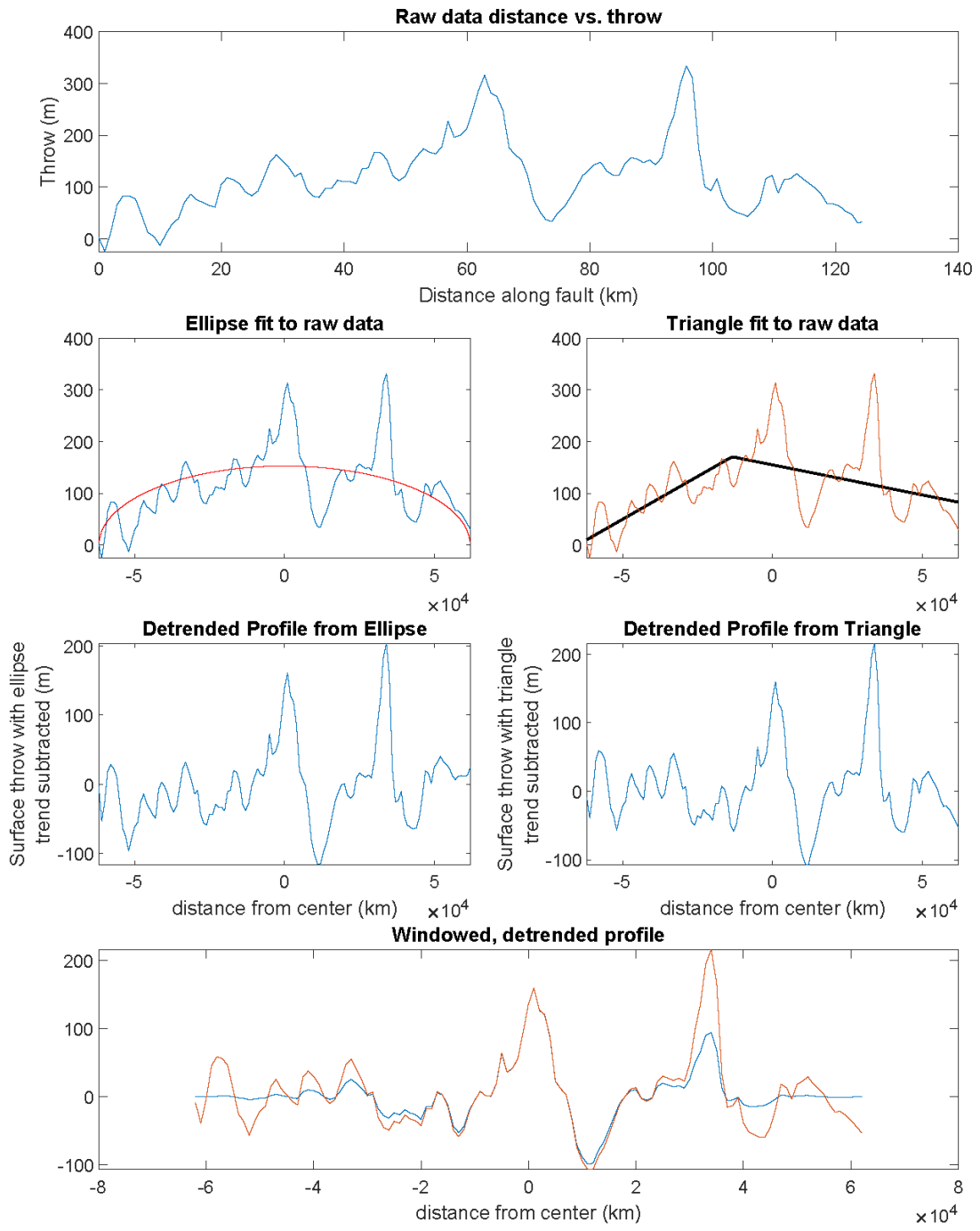
## Detrended Profile from Triangle



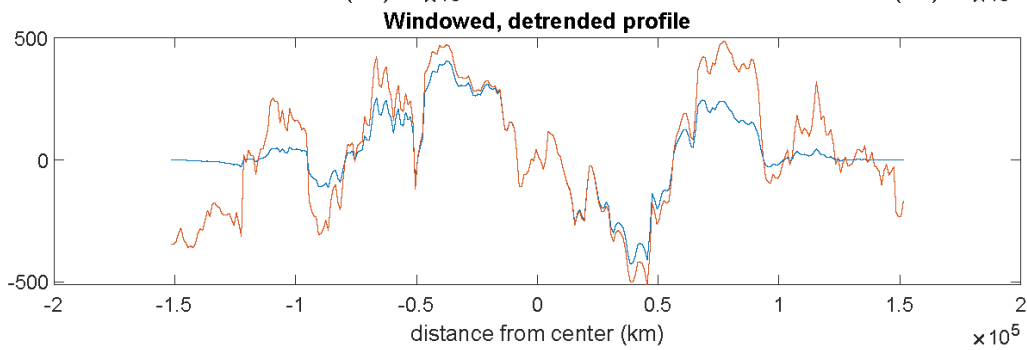
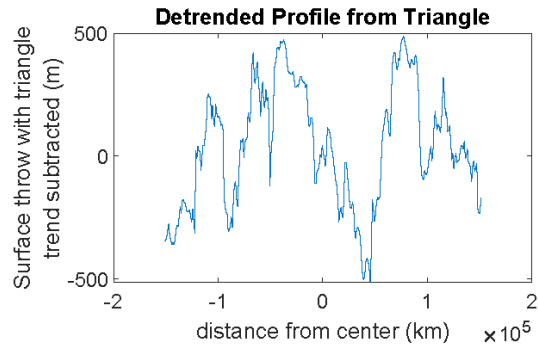
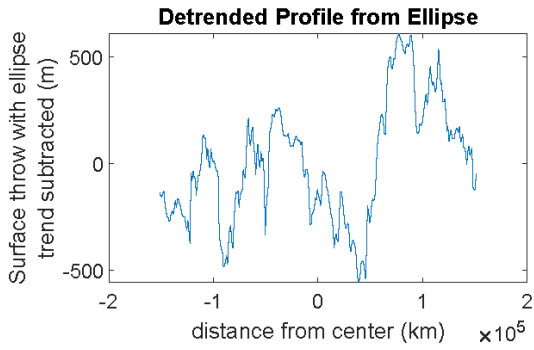
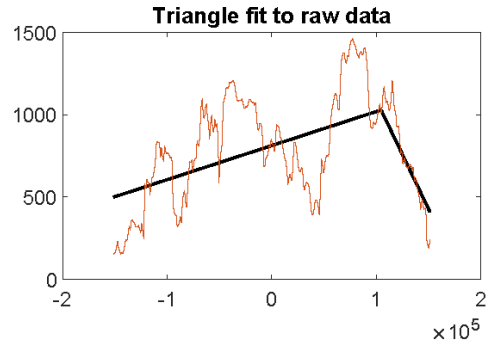
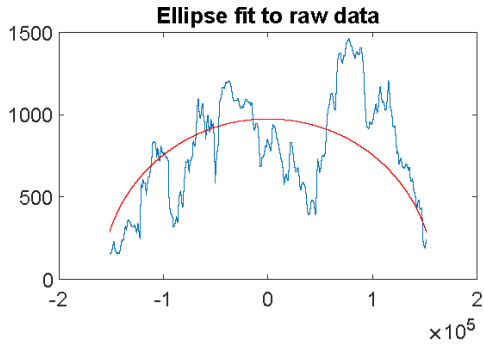
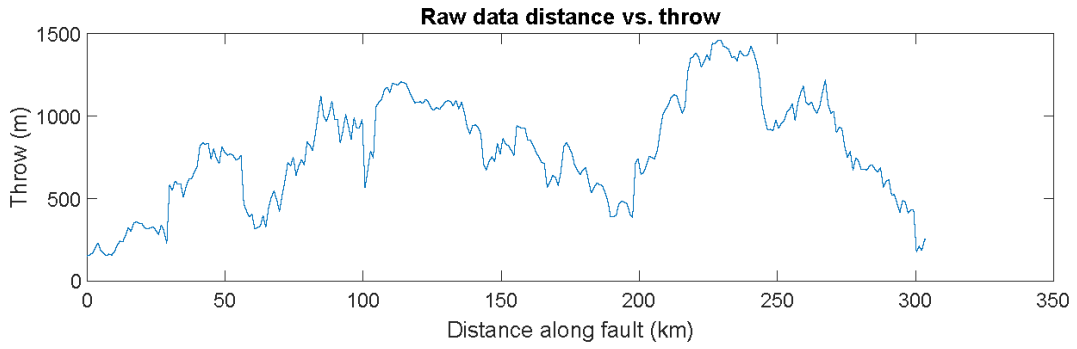
## Windowed, detrended profile



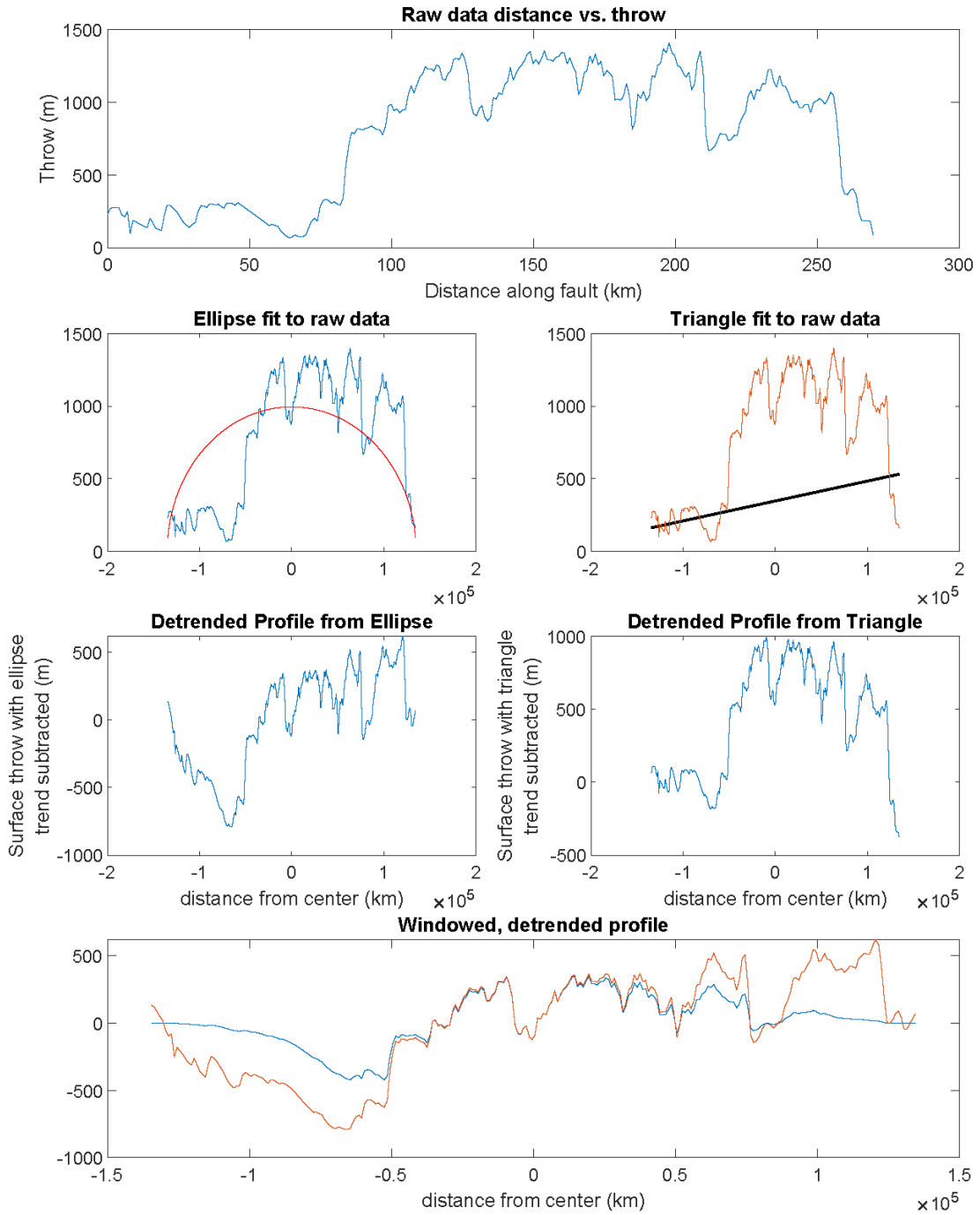
# Fault050



# Fault351

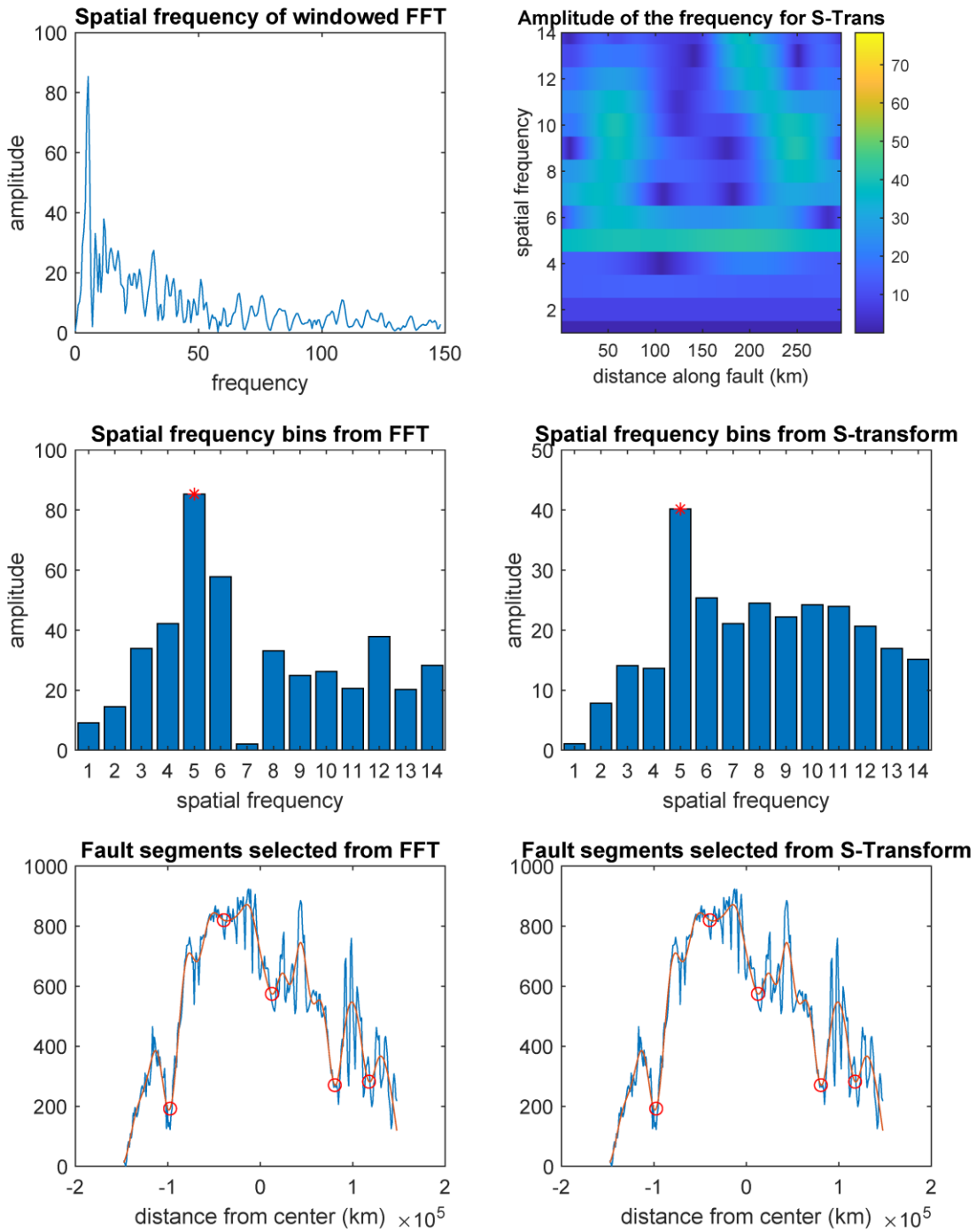


# Fault353

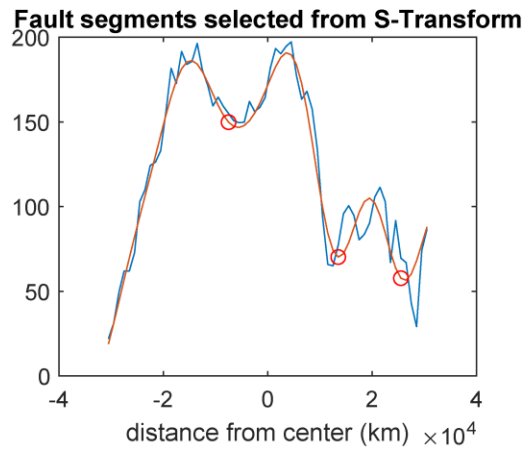
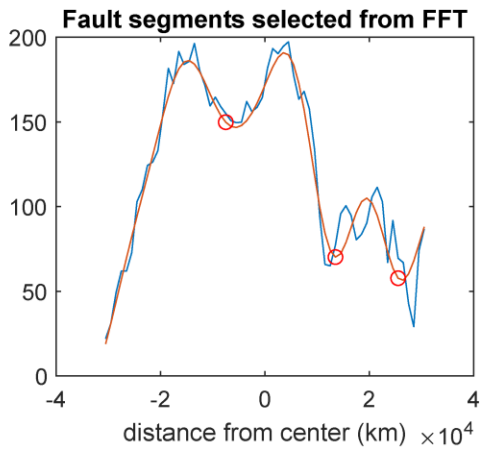
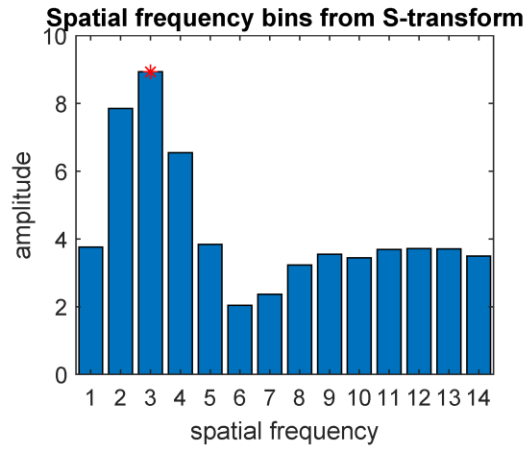
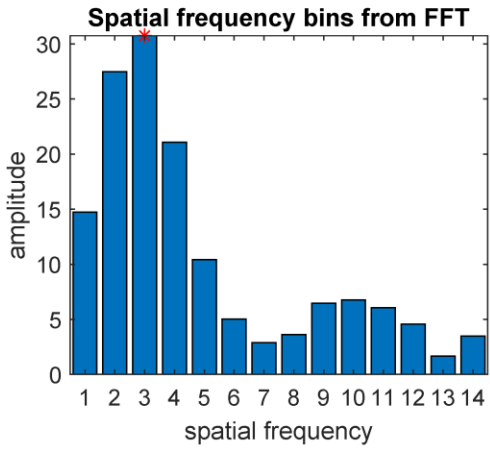
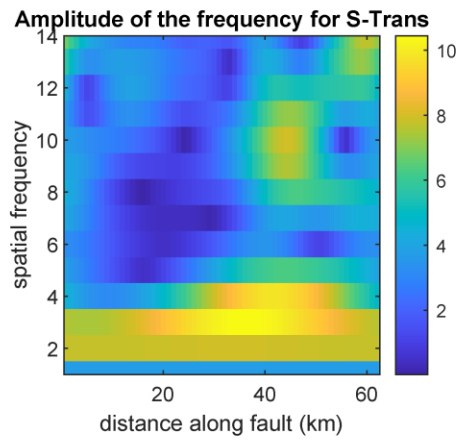
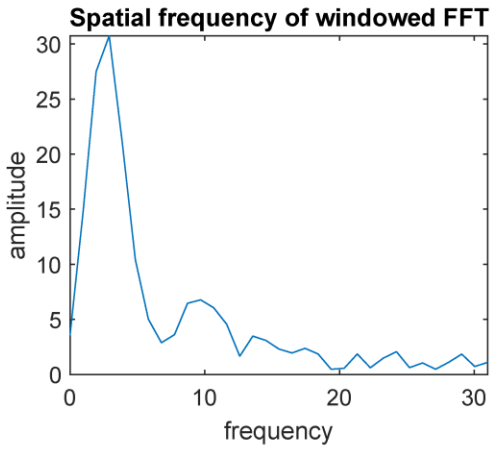


# Appendix I: FFT and S-Transform analysis for each fault

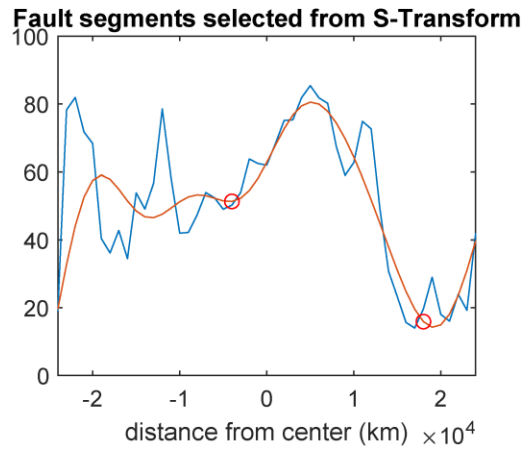
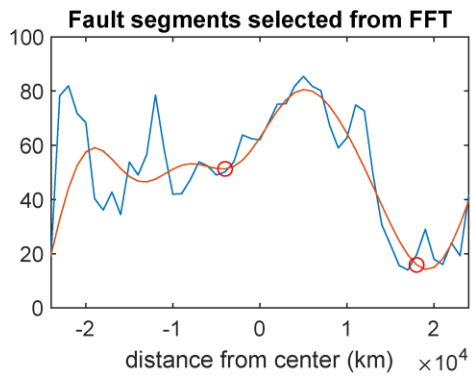
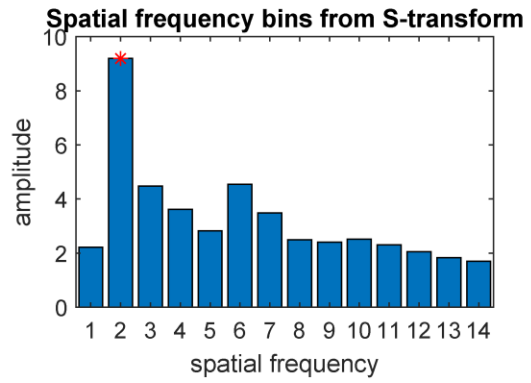
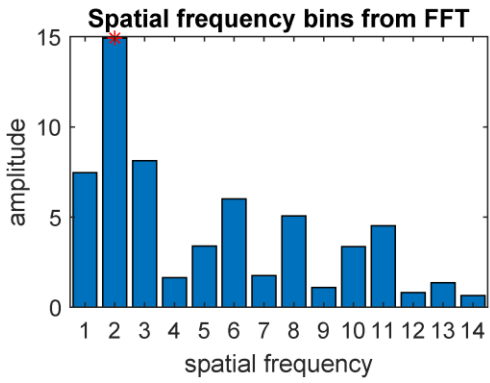
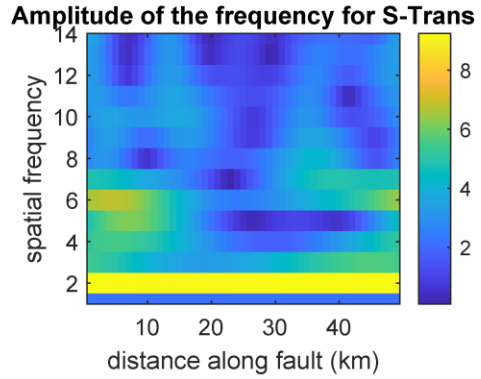
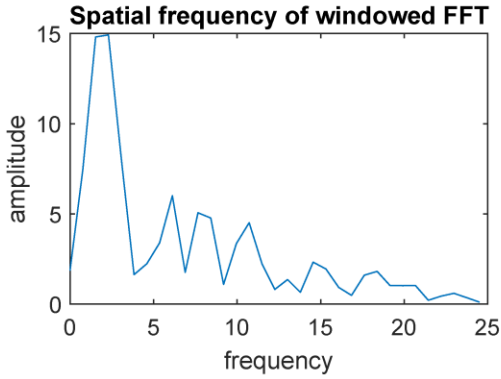
## Fault001



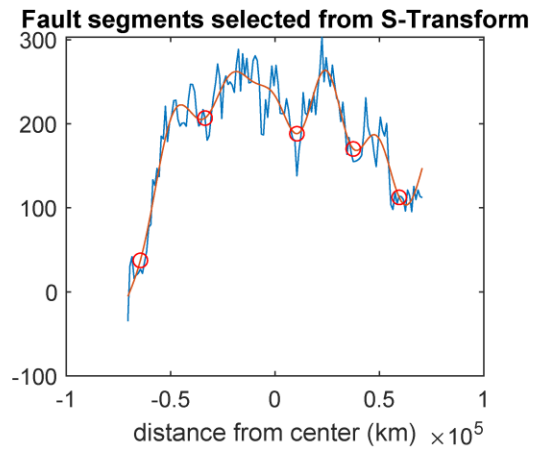
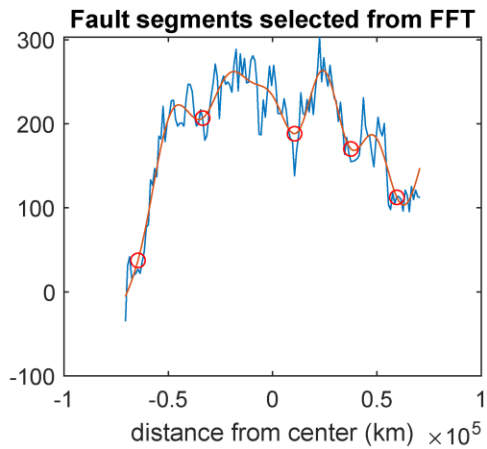
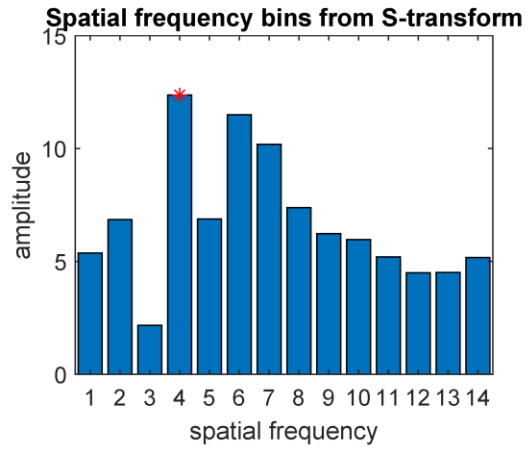
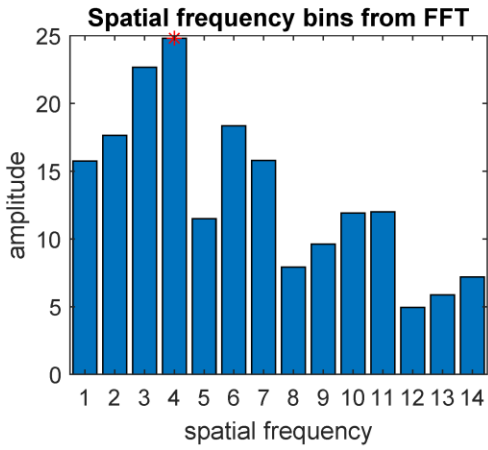
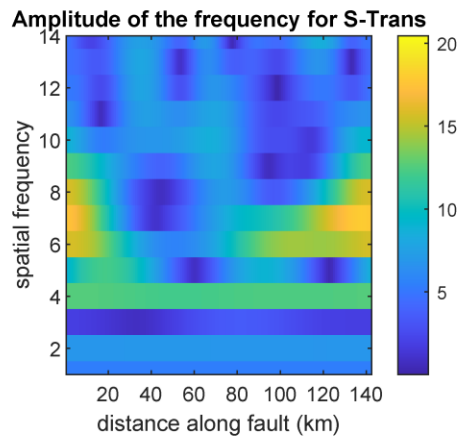
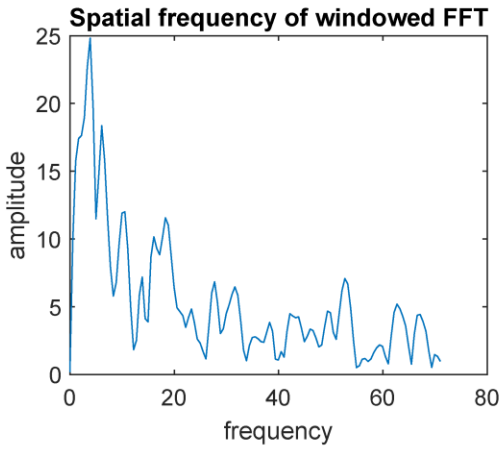
## Fault002



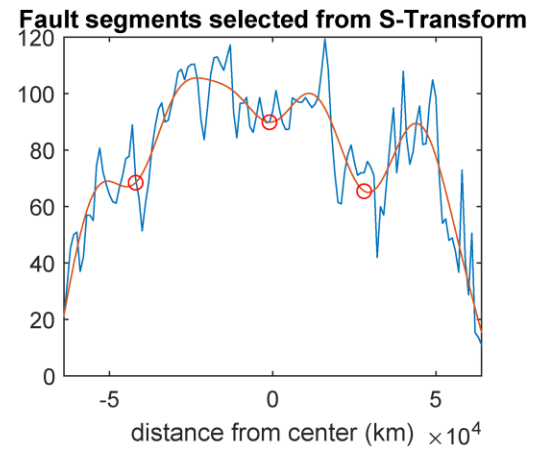
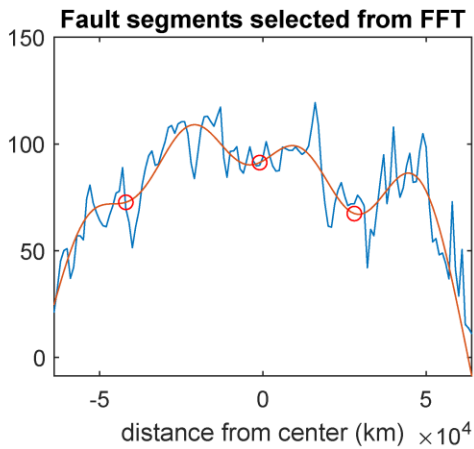
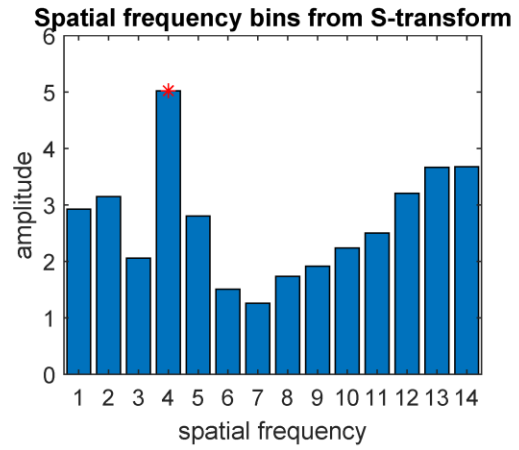
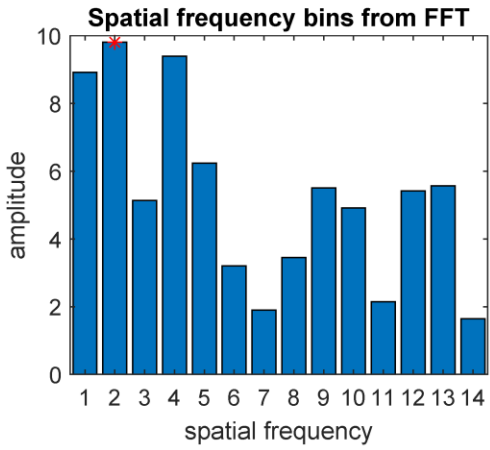
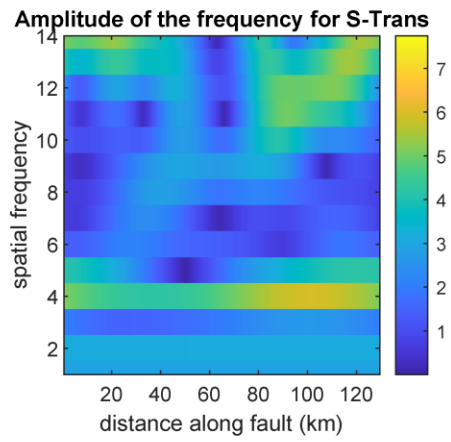
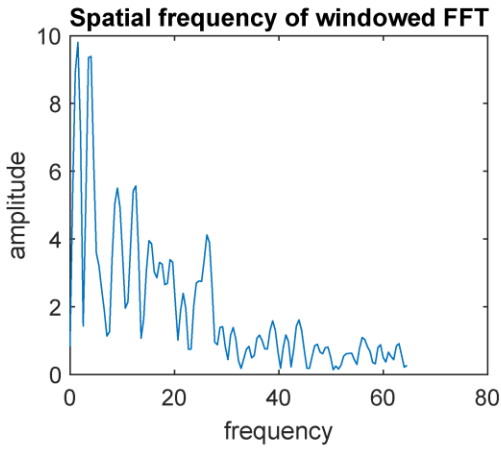
# Fault003



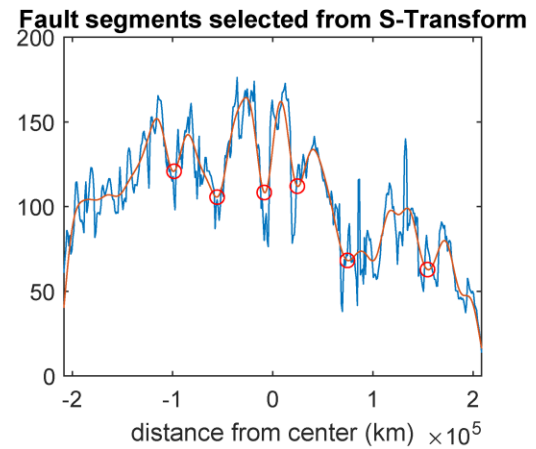
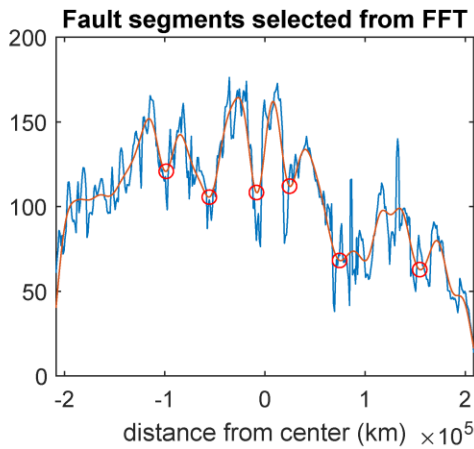
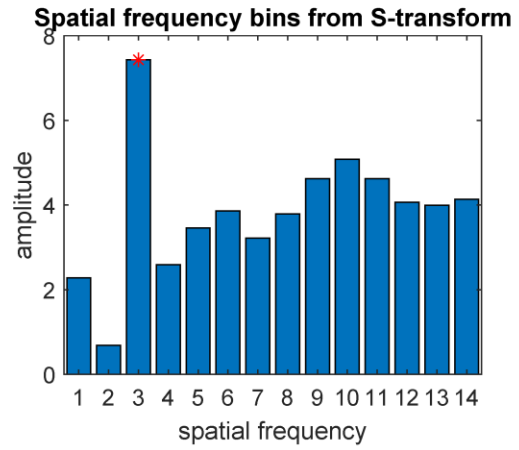
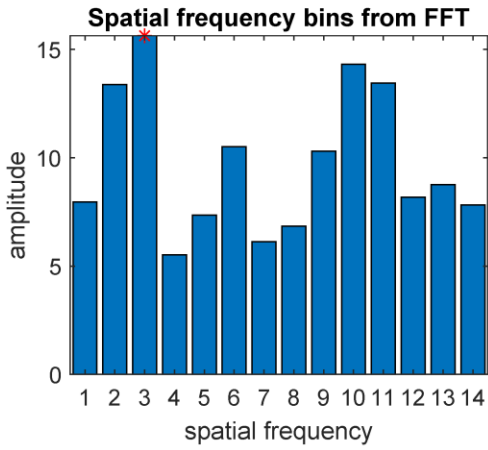
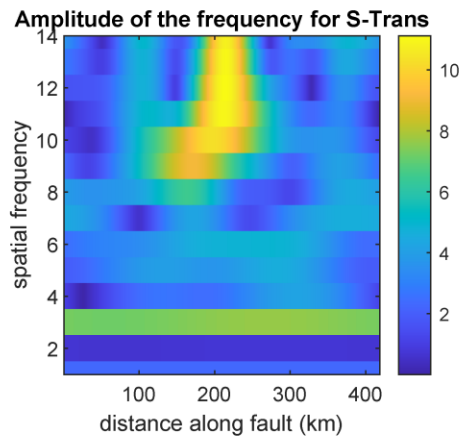
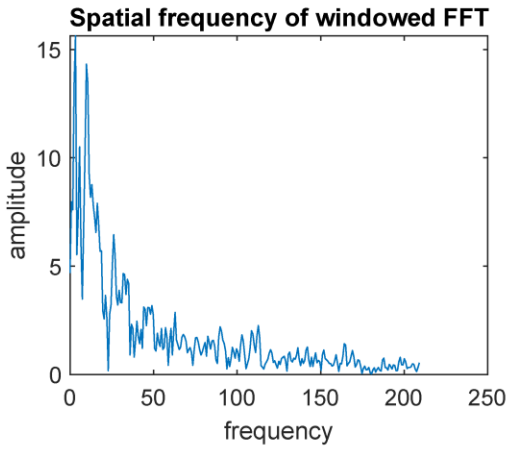
## Fault005



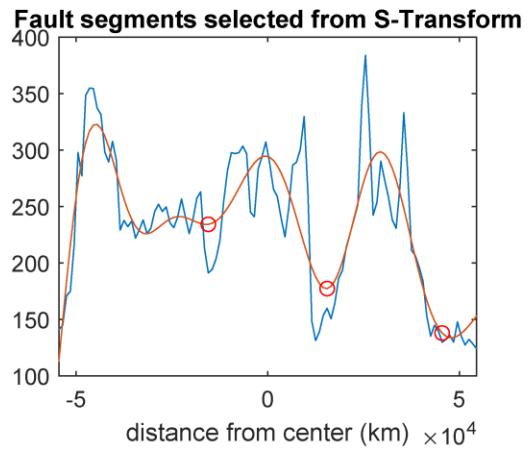
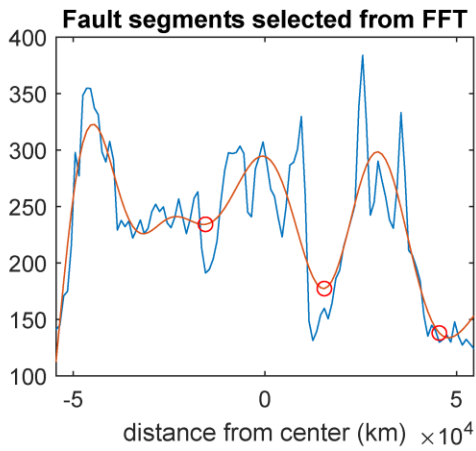
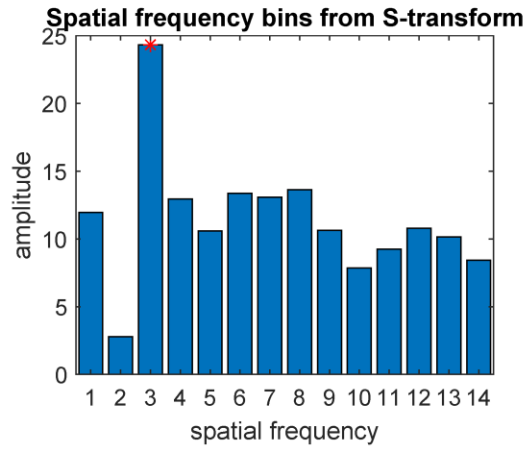
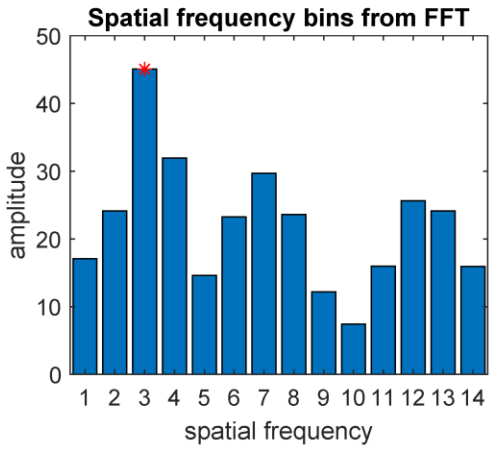
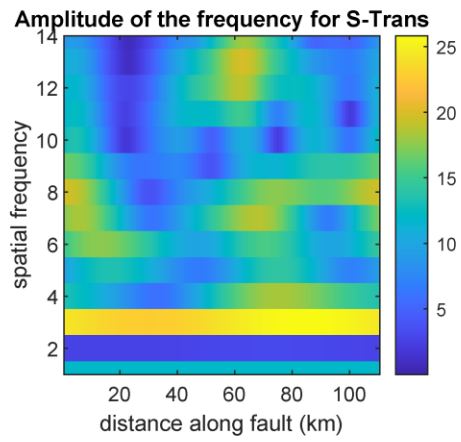
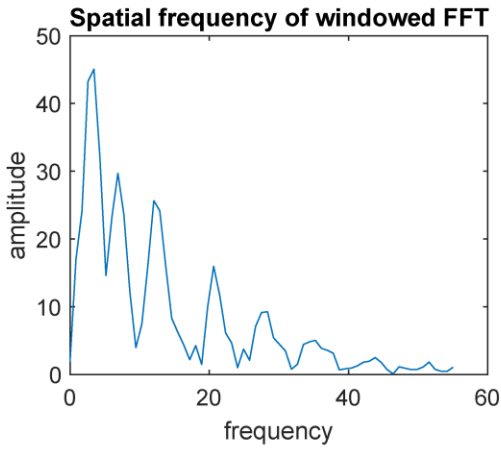
# Fault006



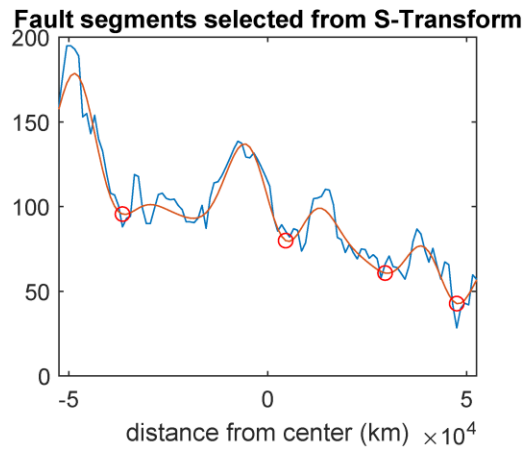
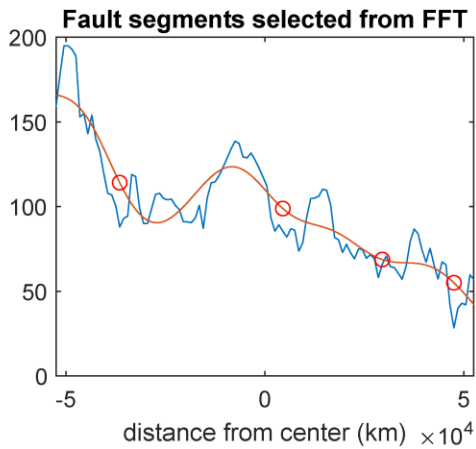
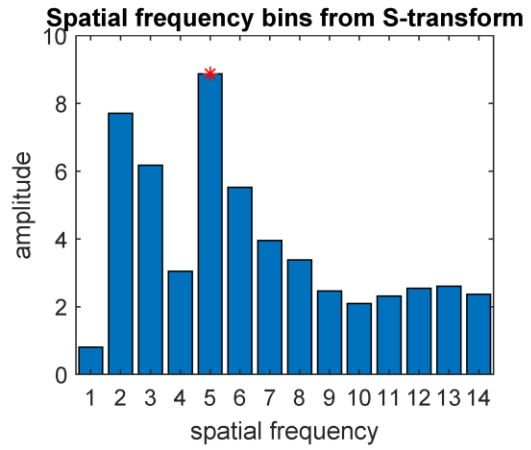
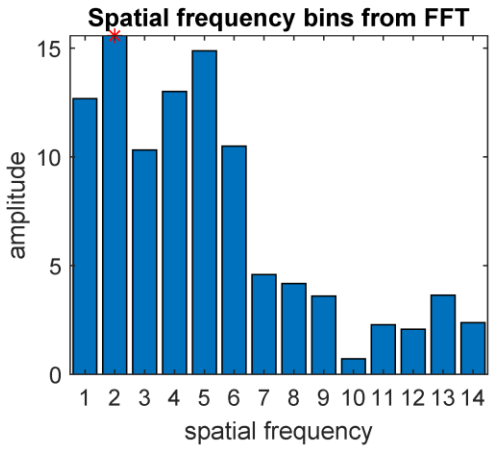
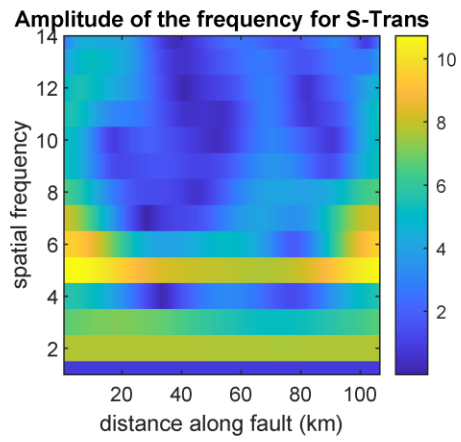
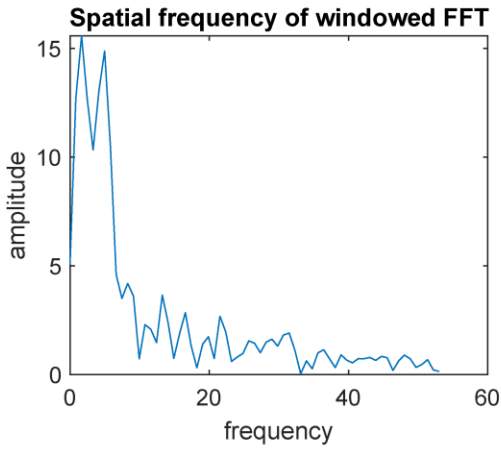
# Fault007



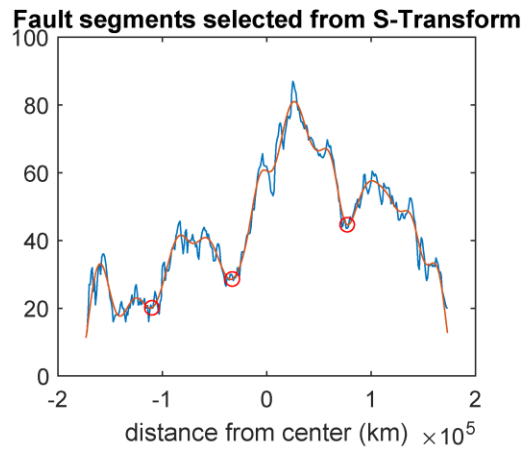
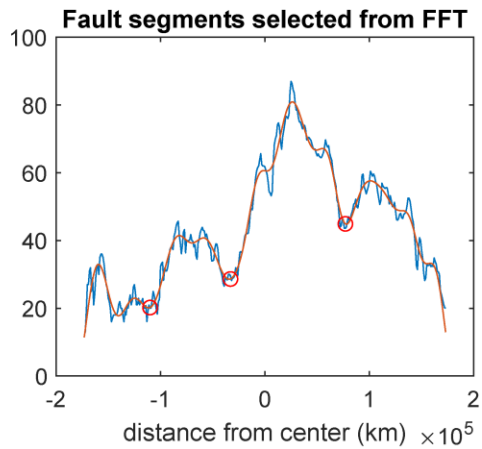
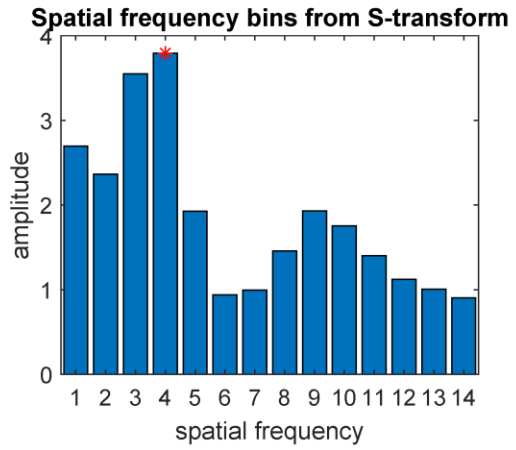
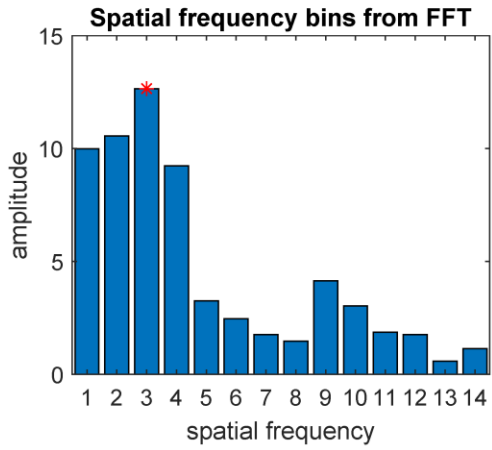
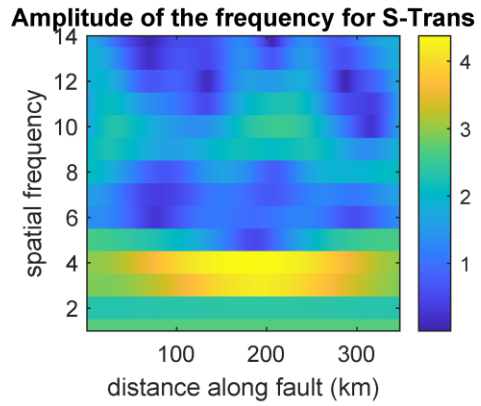
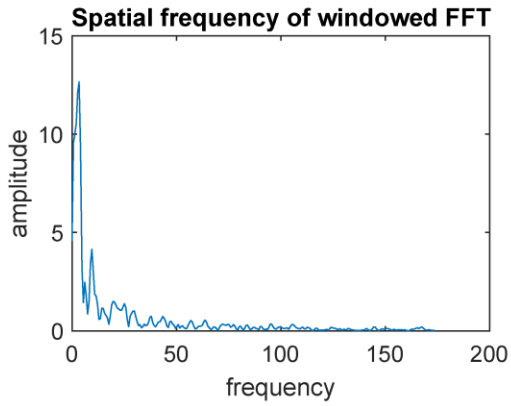
# Fault008



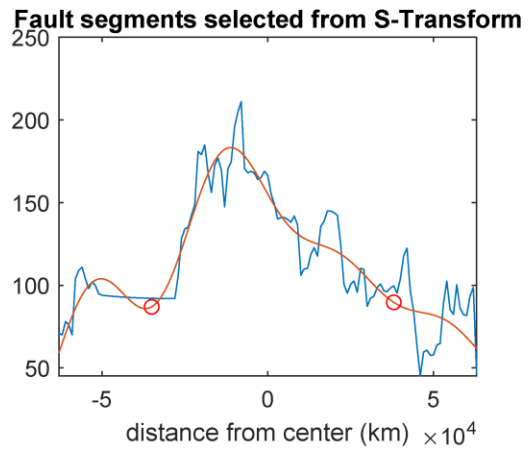
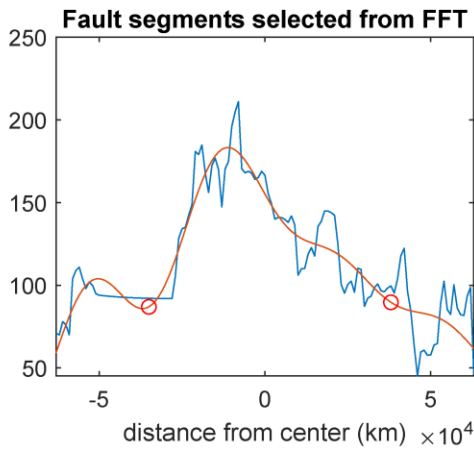
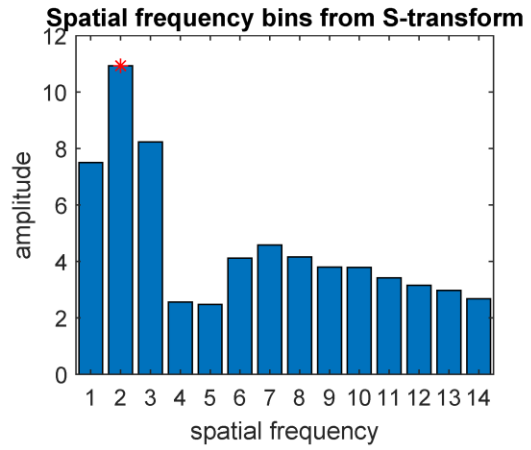
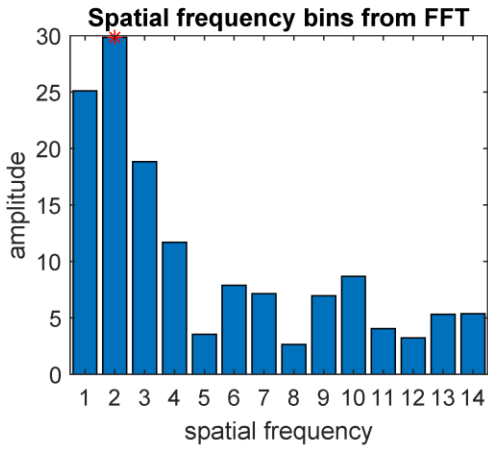
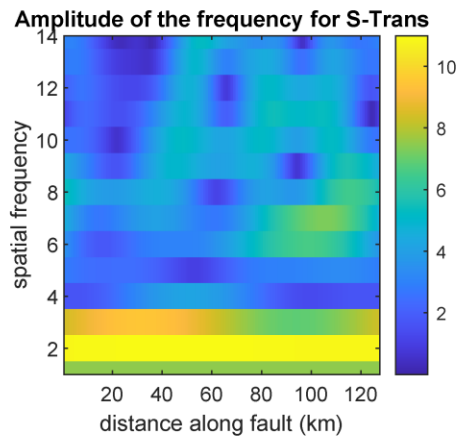
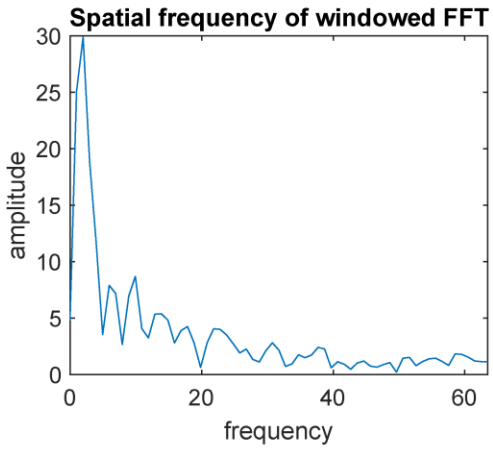
# Fault009



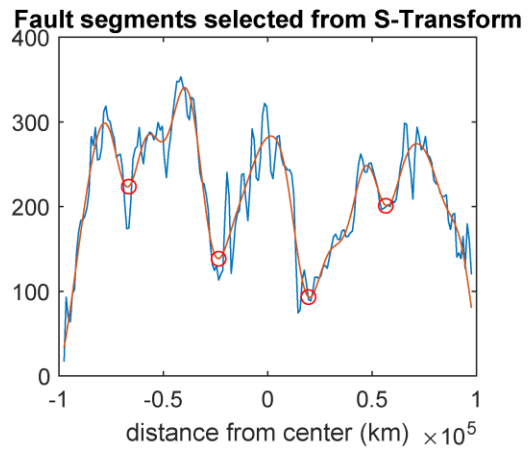
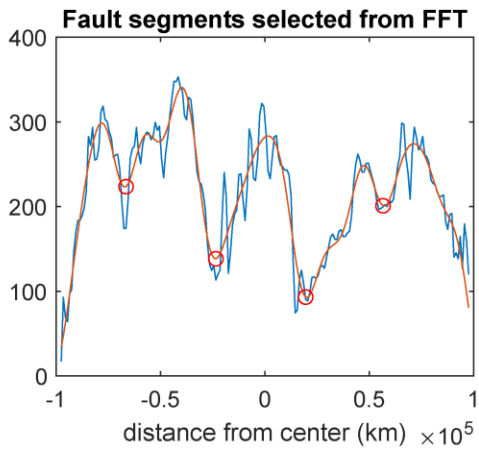
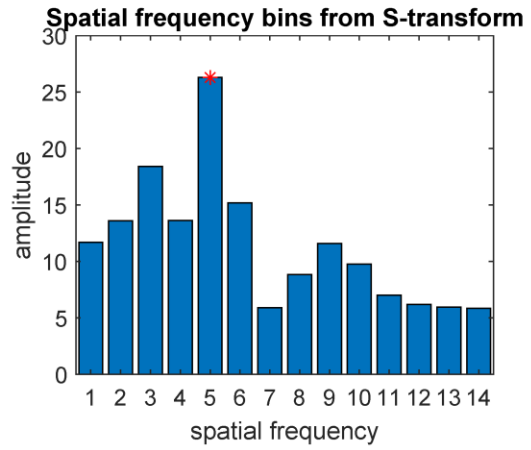
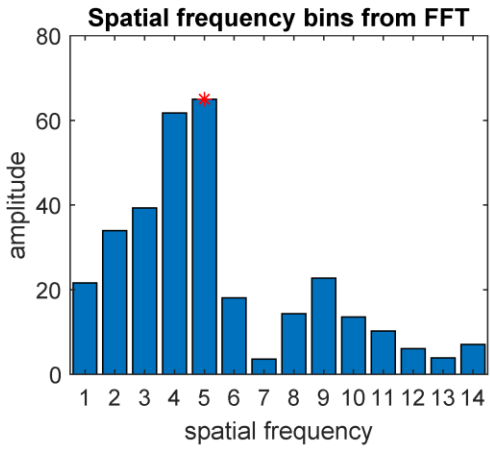
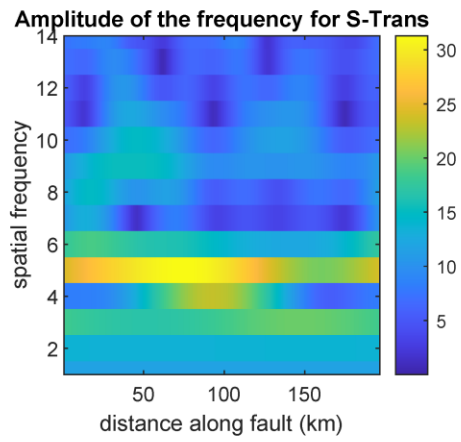
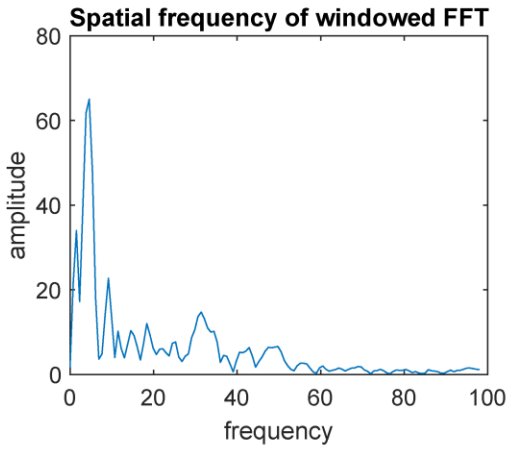
# Fault010



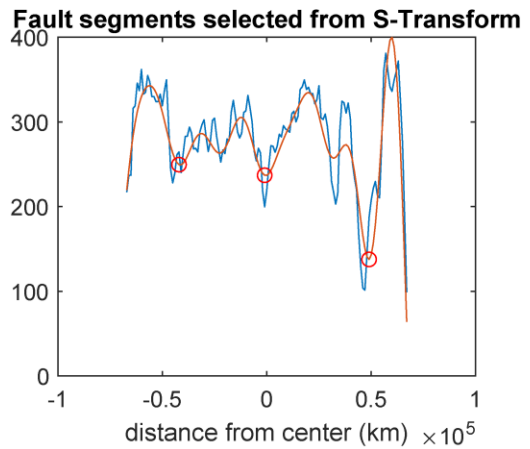
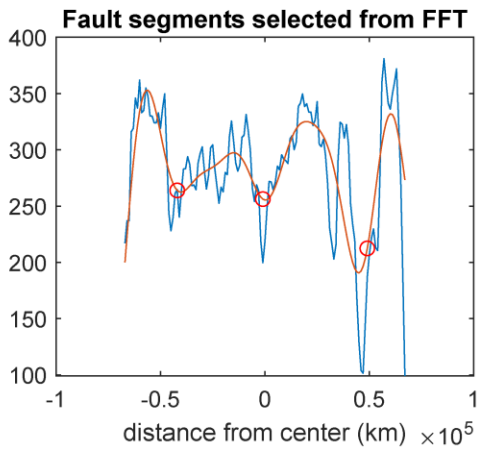
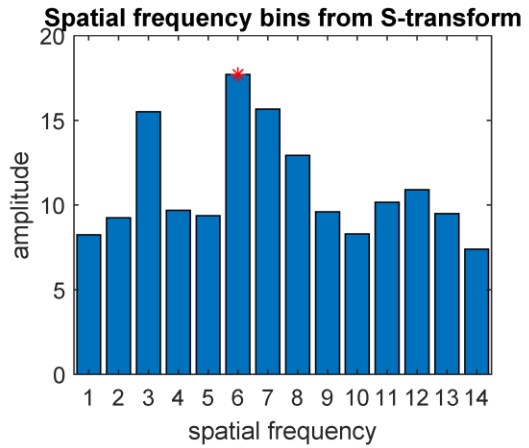
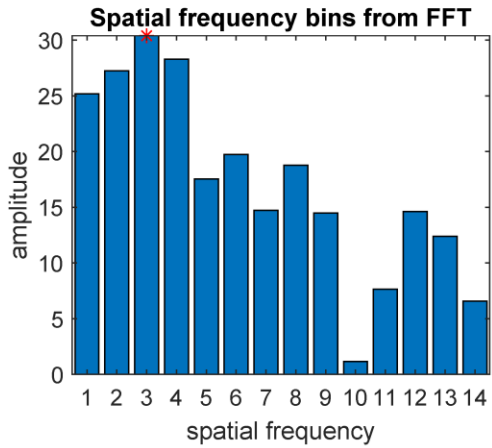
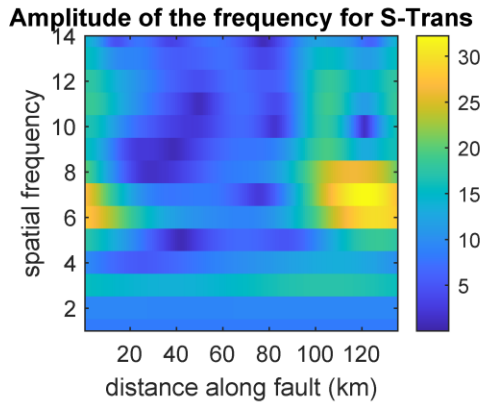
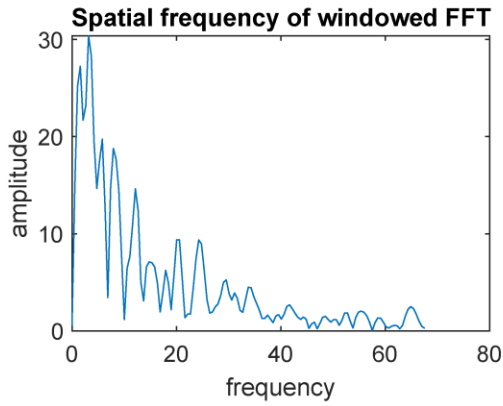
# Fault011



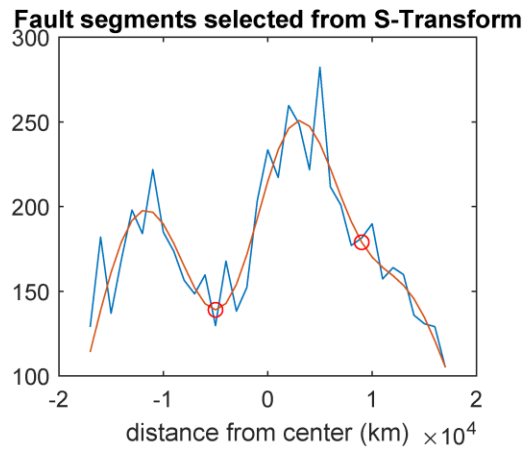
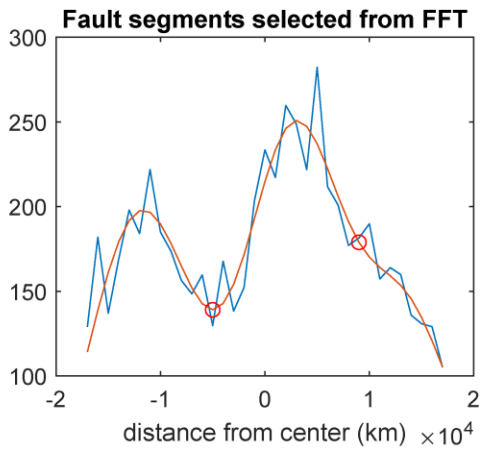
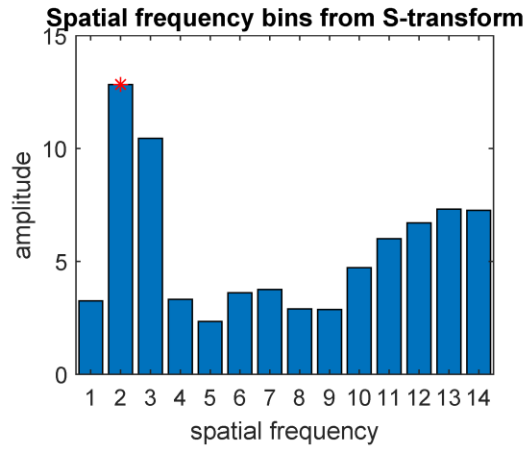
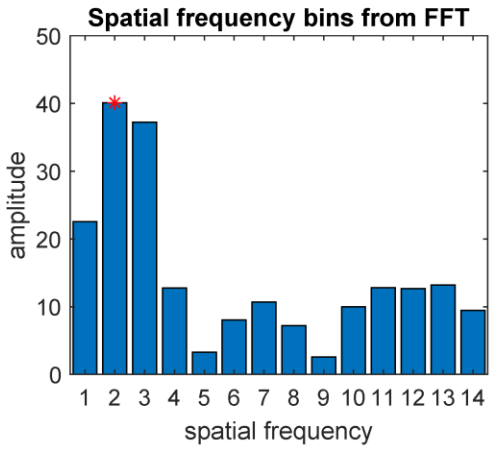
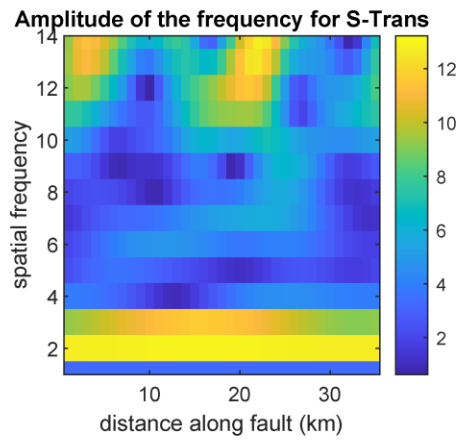
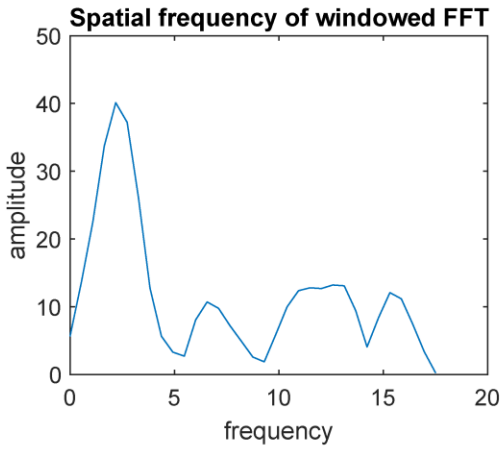
# Fault012



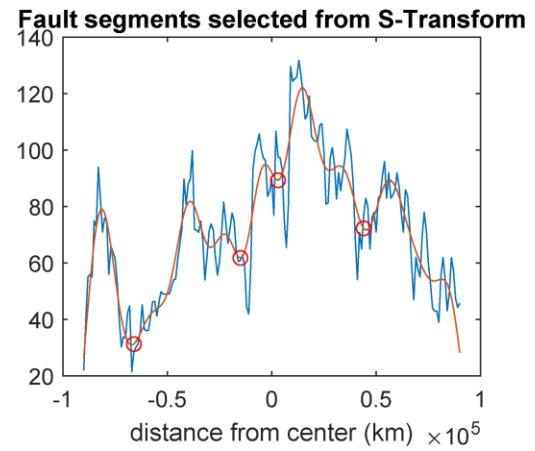
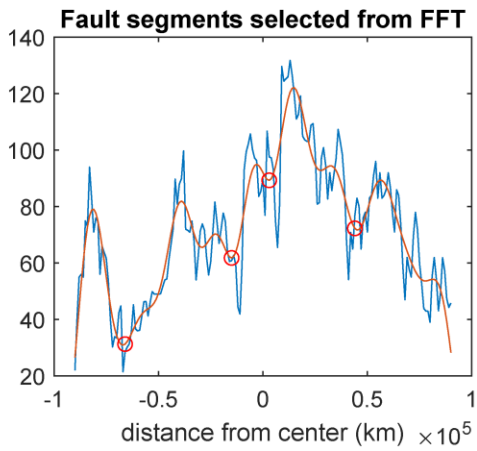
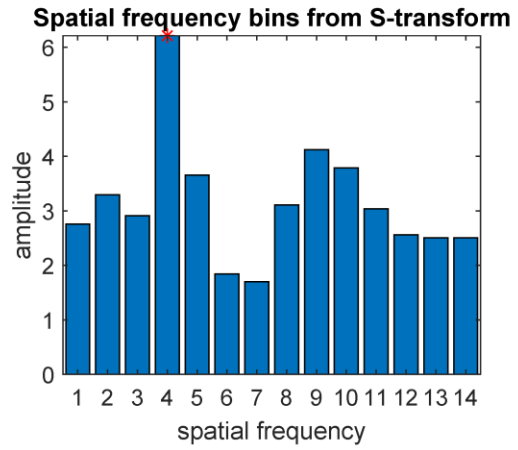
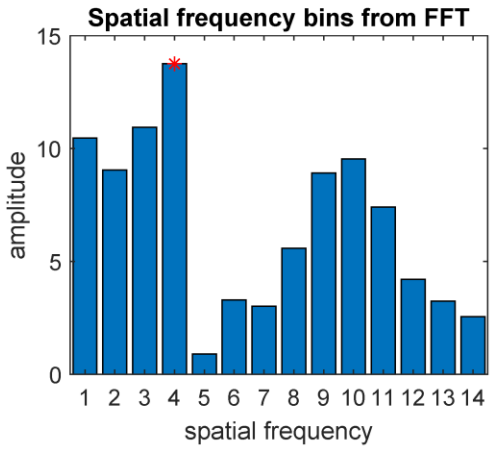
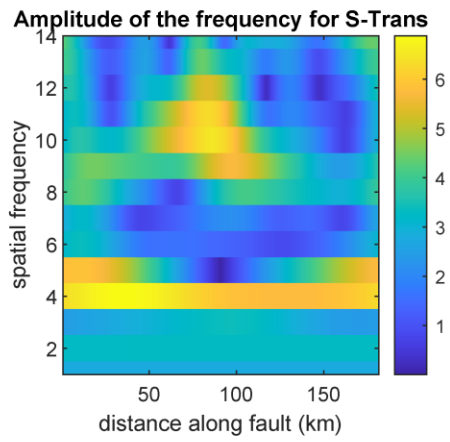
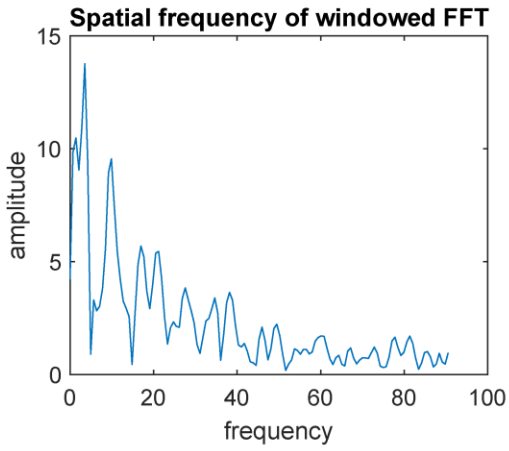
### Fault013



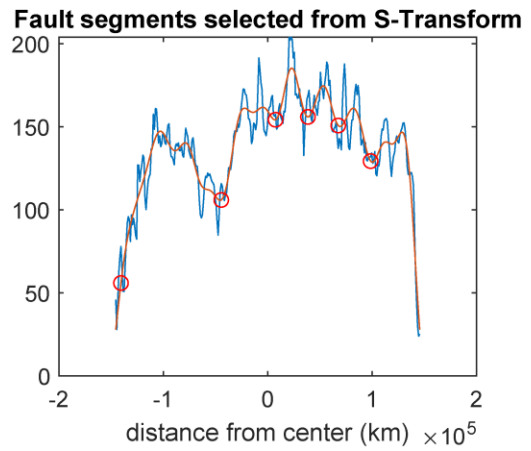
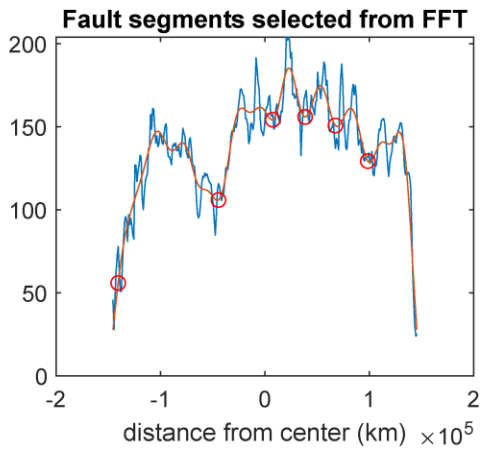
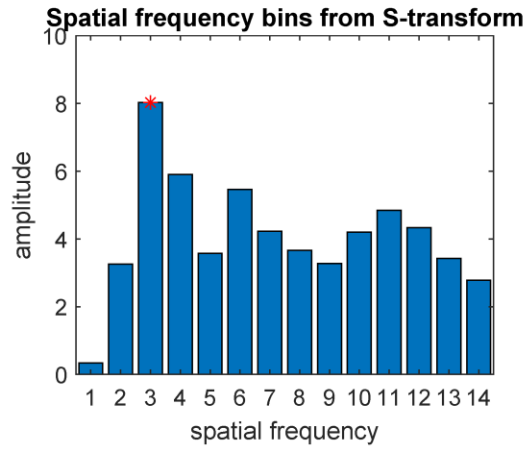
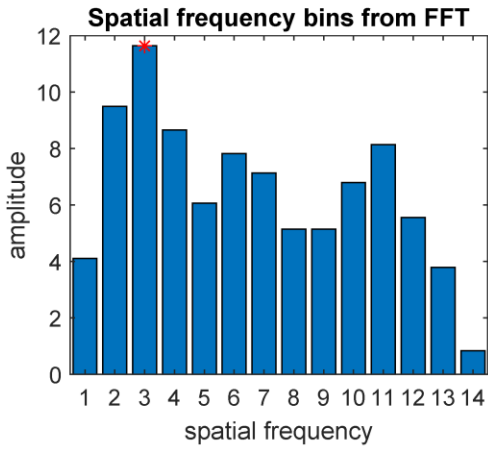
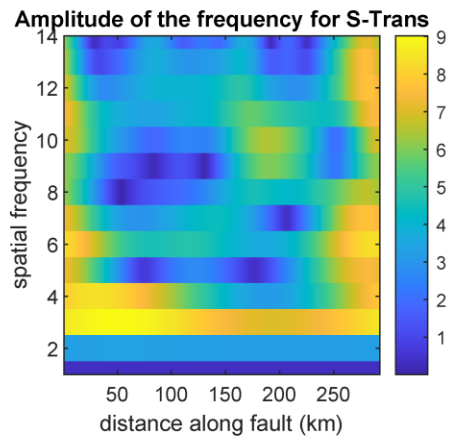
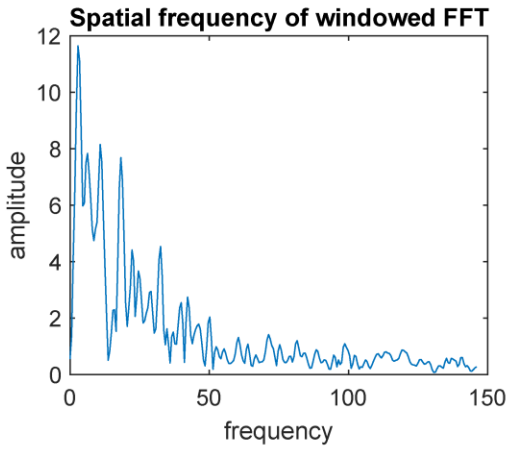
## Fault014



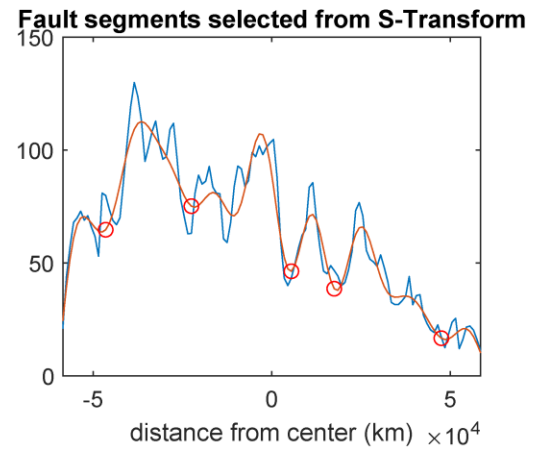
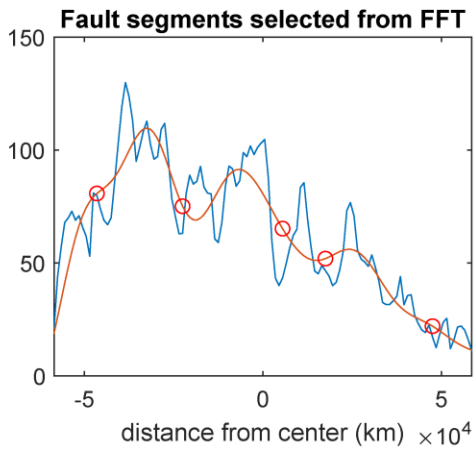
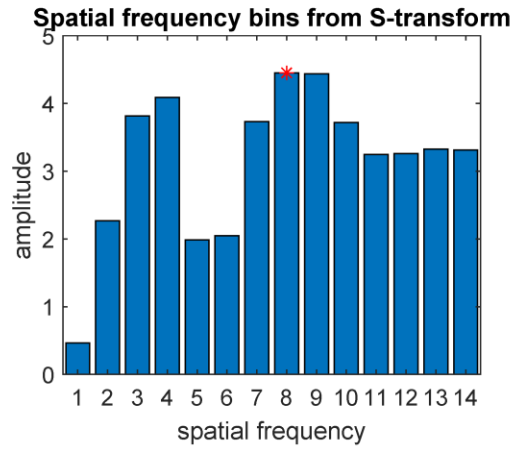
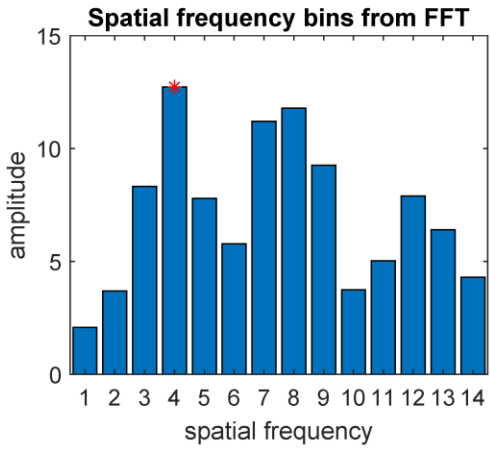
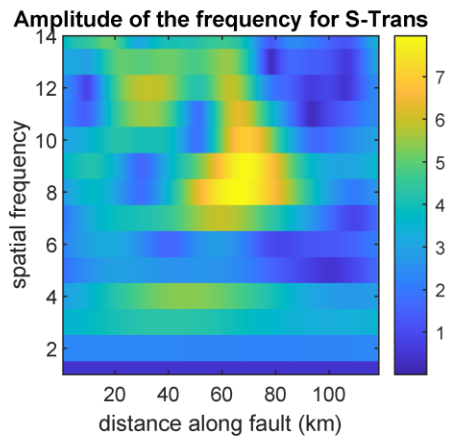
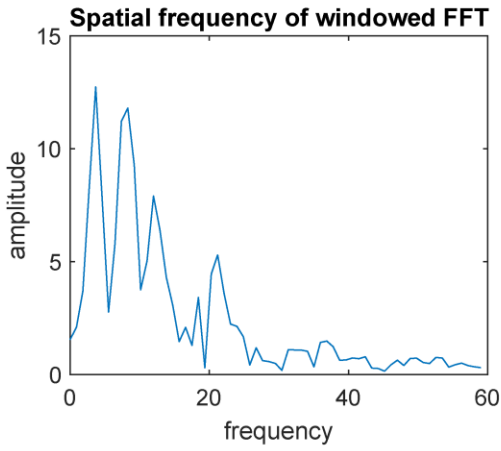
# Fault015



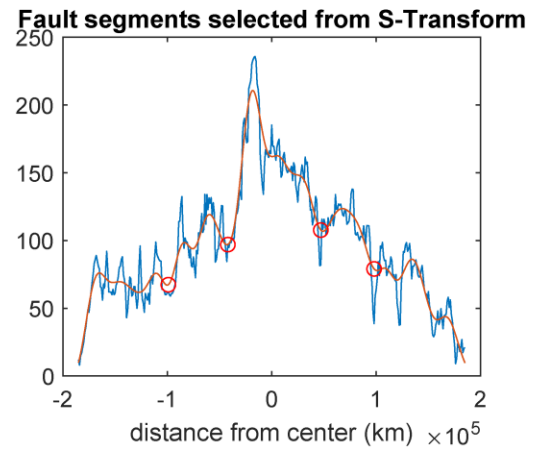
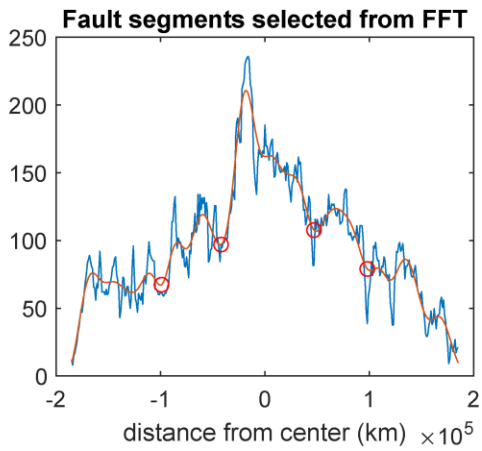
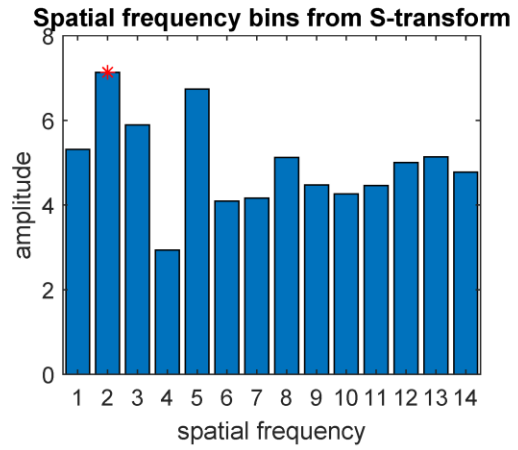
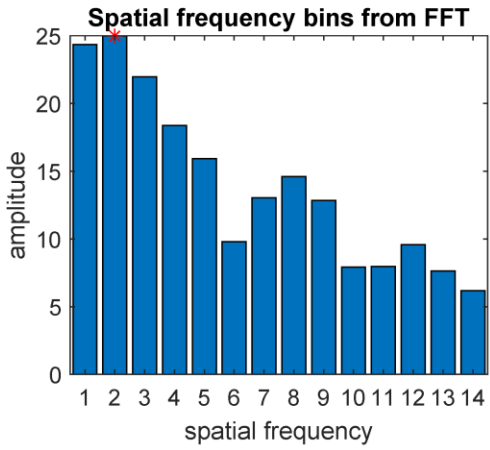
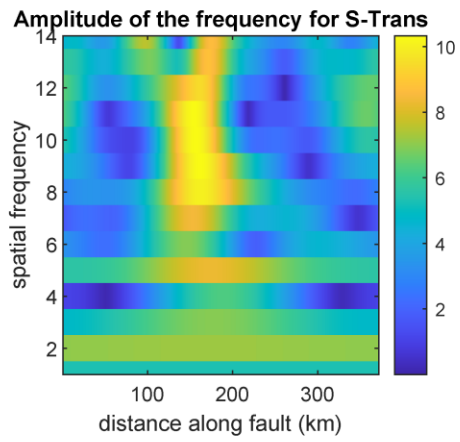
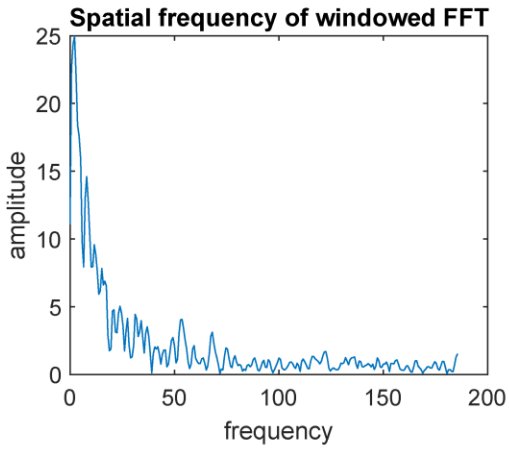
# Fault016



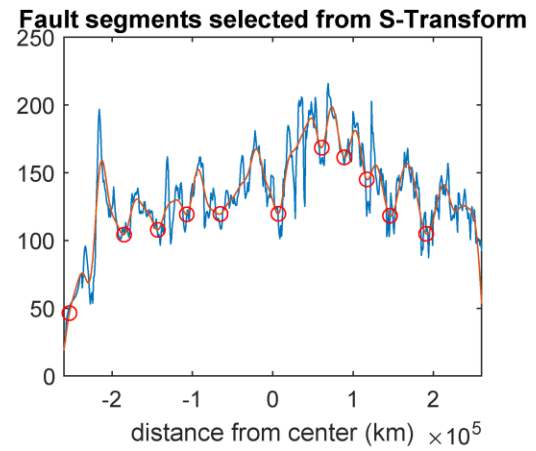
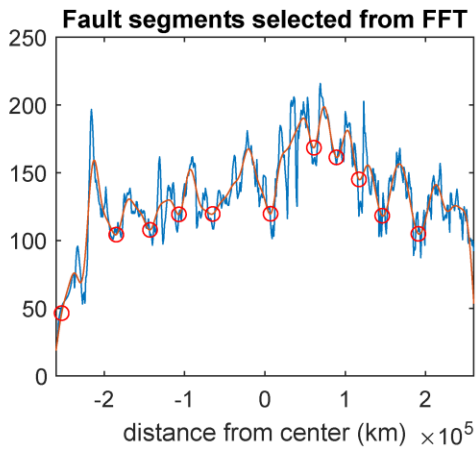
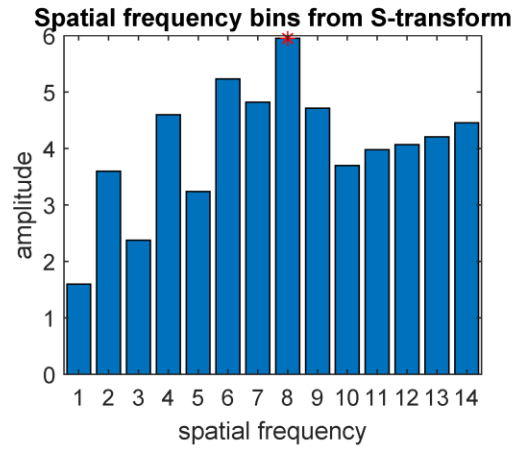
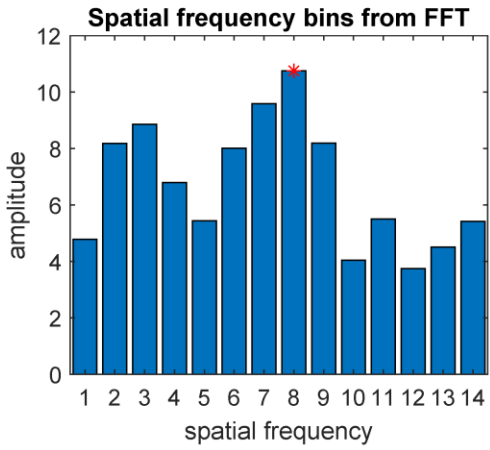
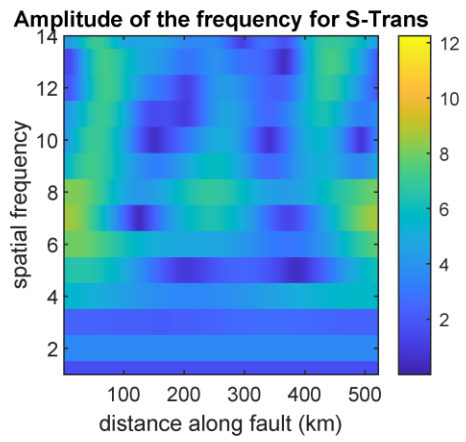
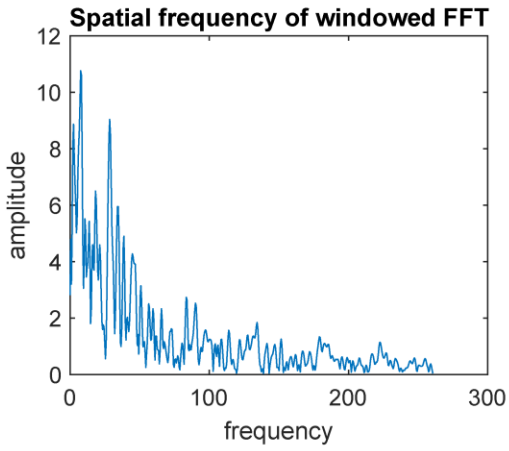
# Fault017



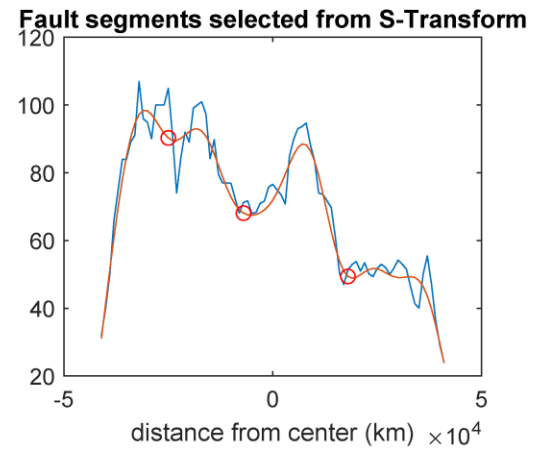
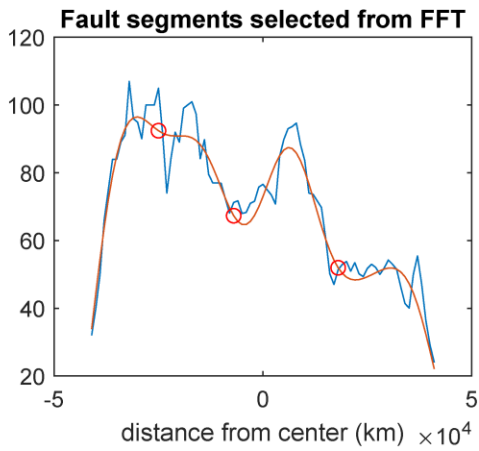
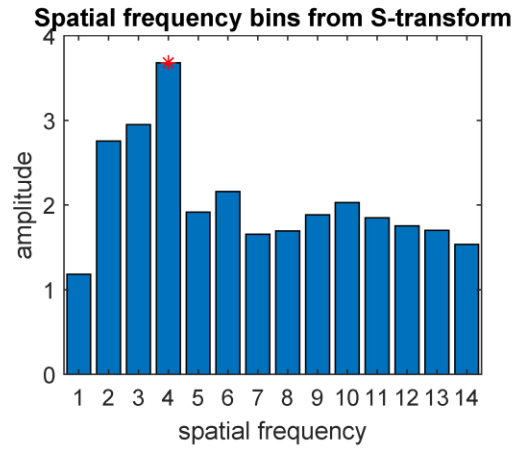
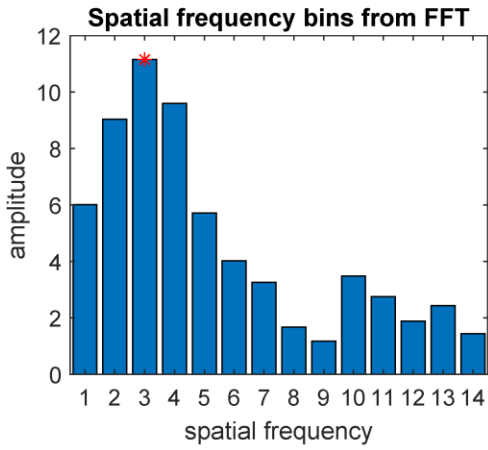
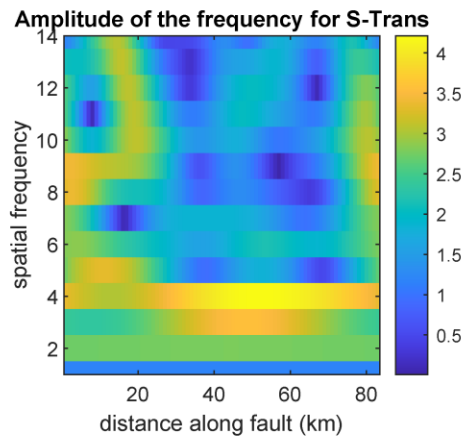
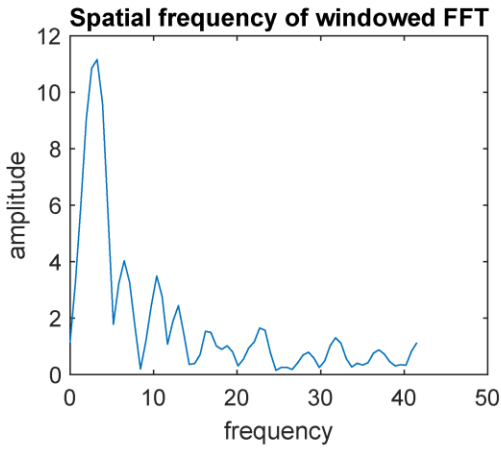
# Fault018



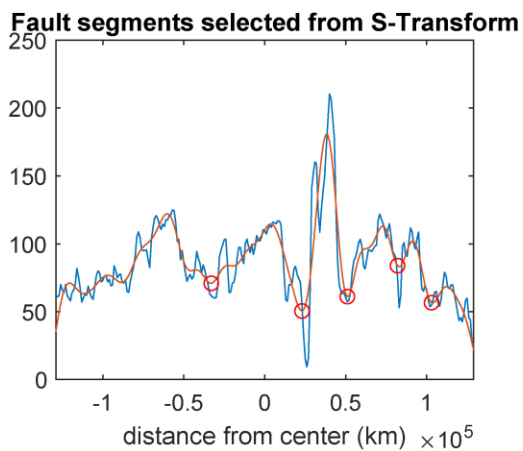
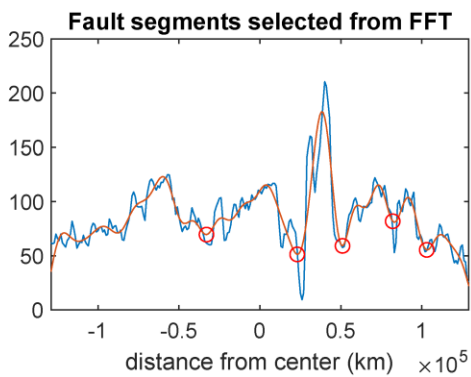
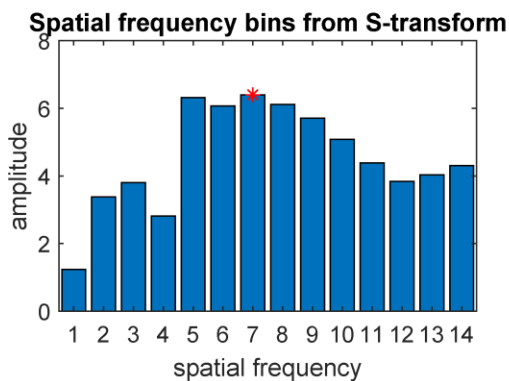
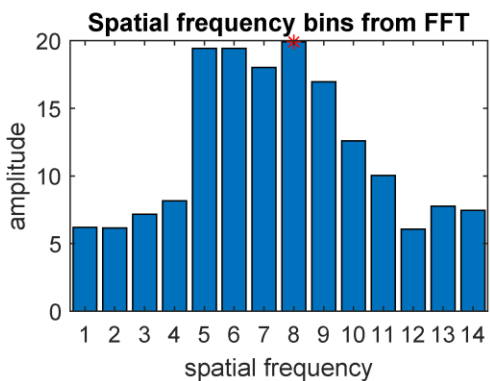
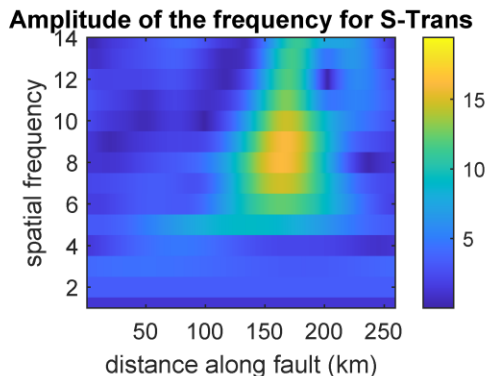
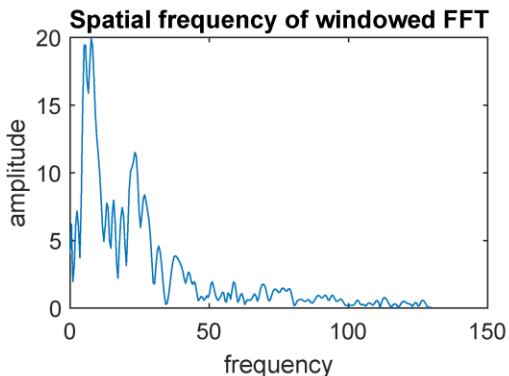
# Fault019



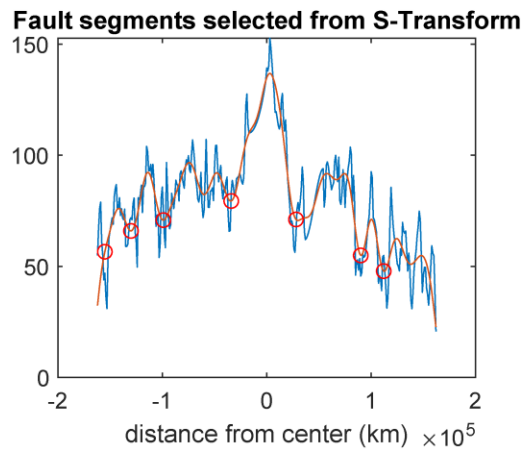
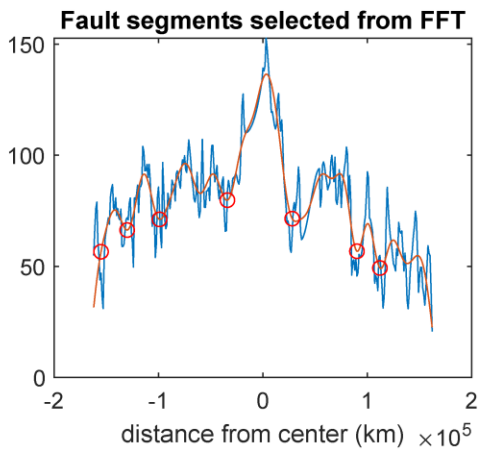
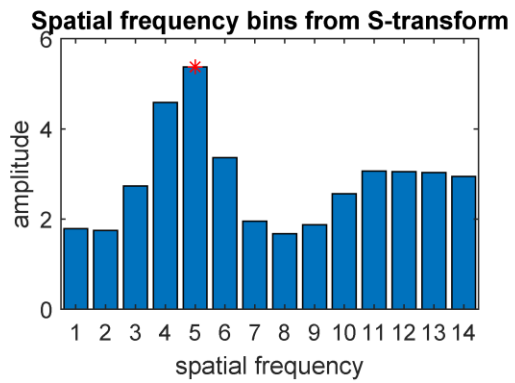
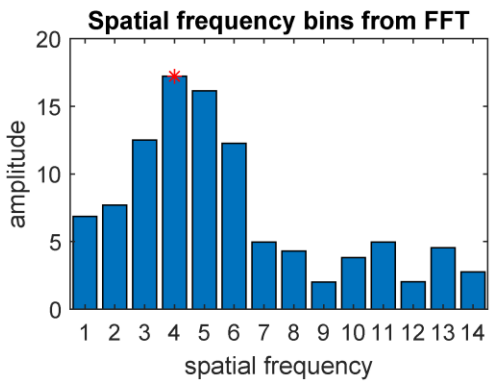
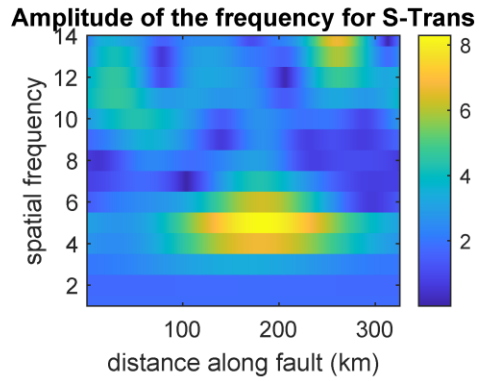
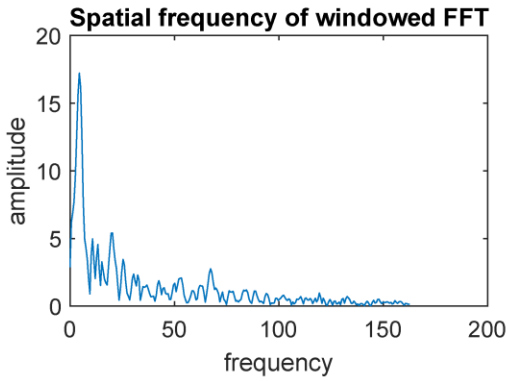
# Fault020



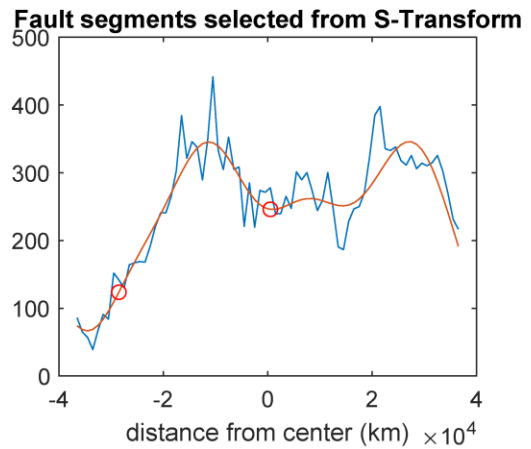
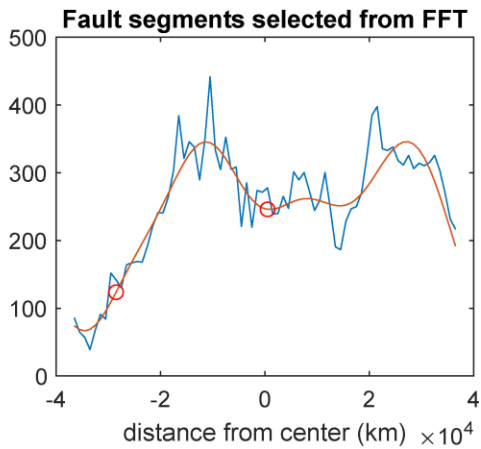
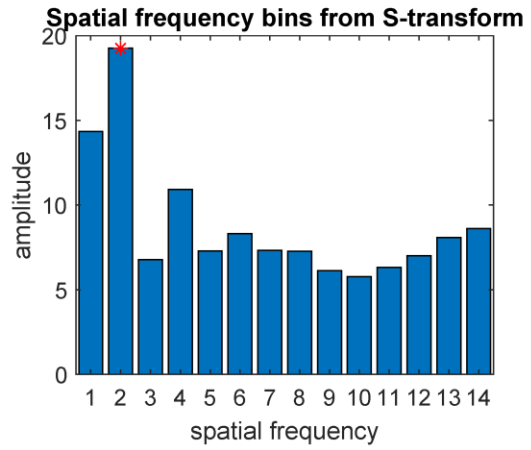
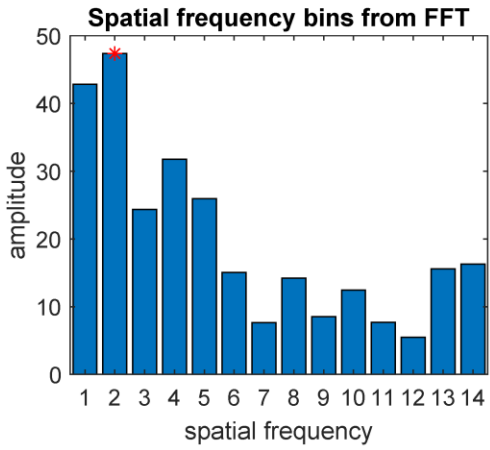
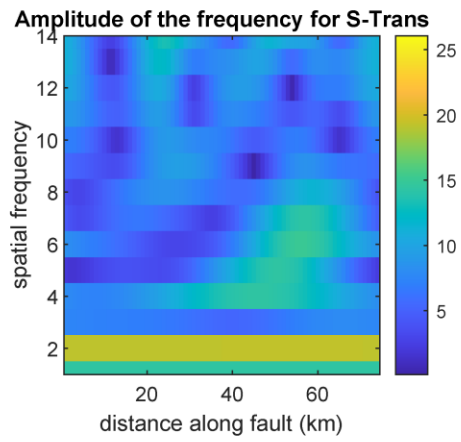
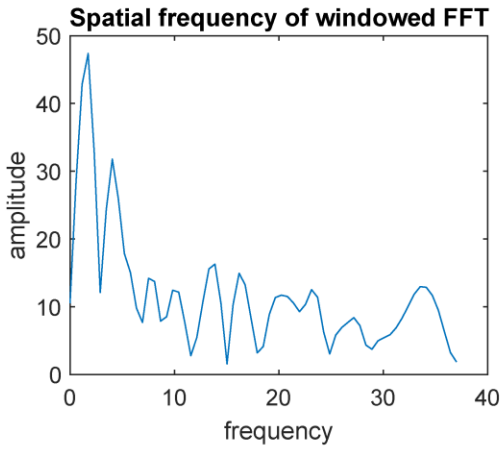
## Fault021



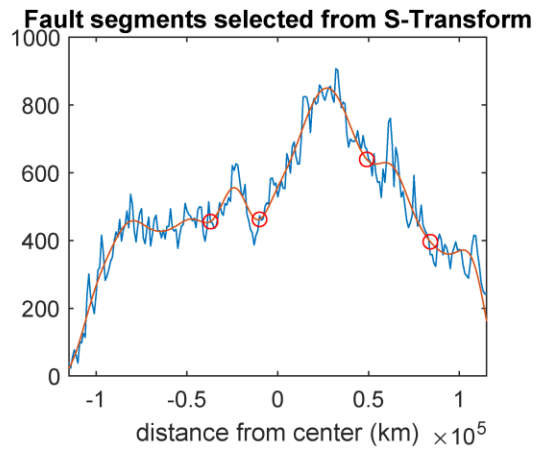
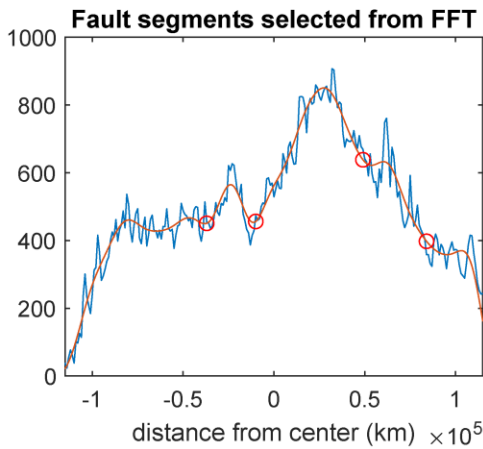
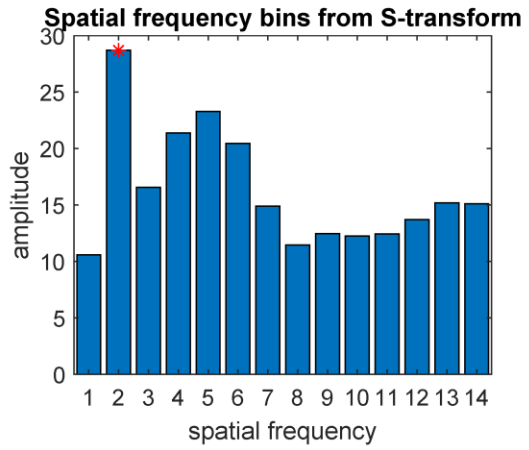
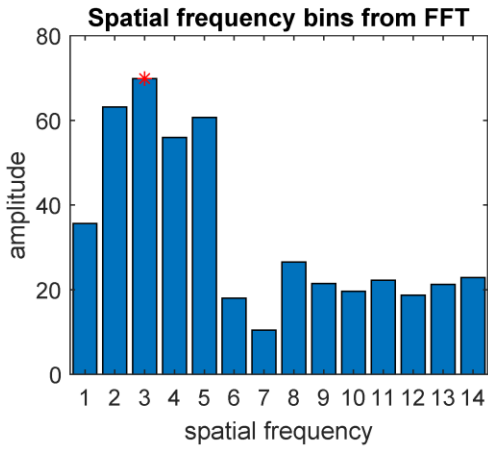
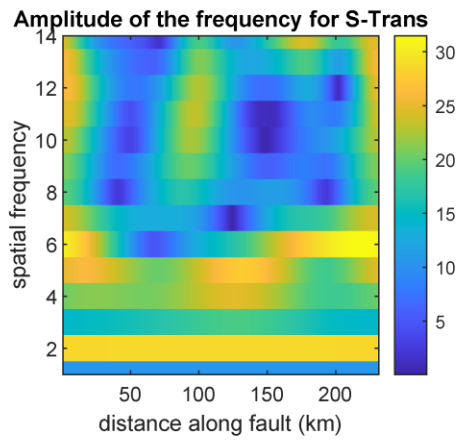
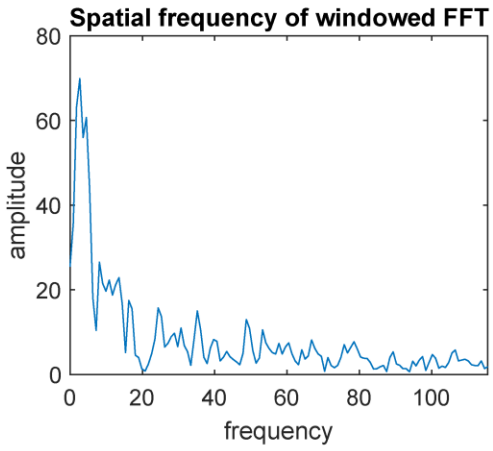
## Fault022



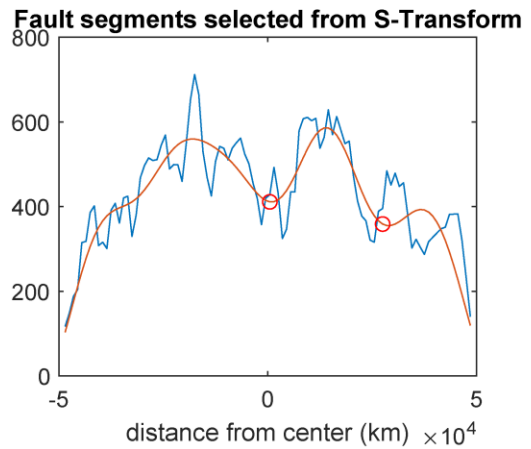
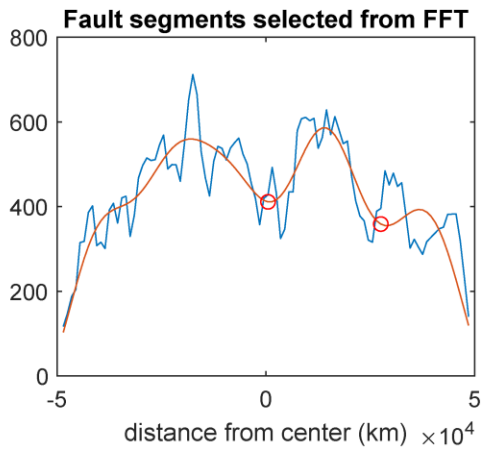
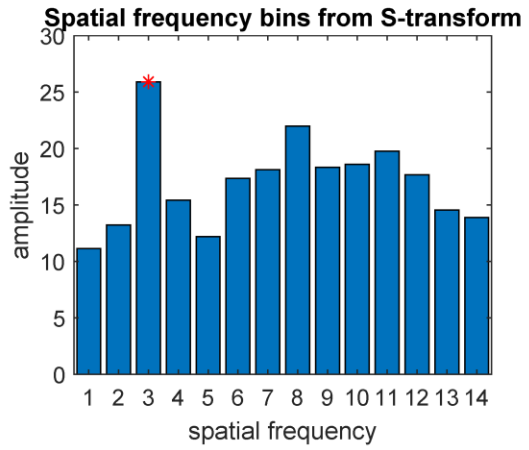
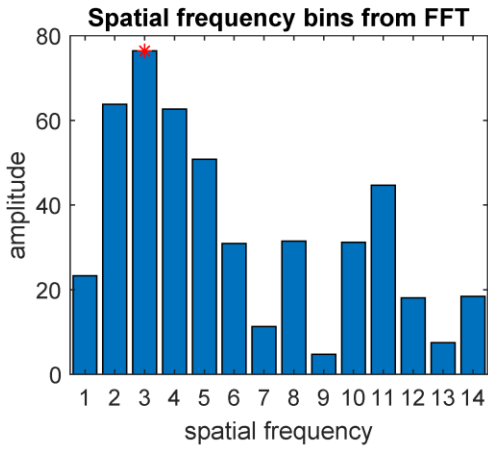
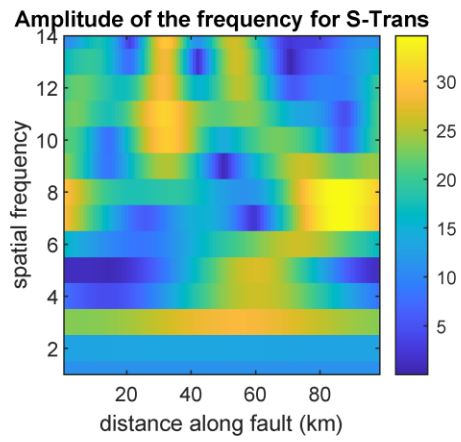
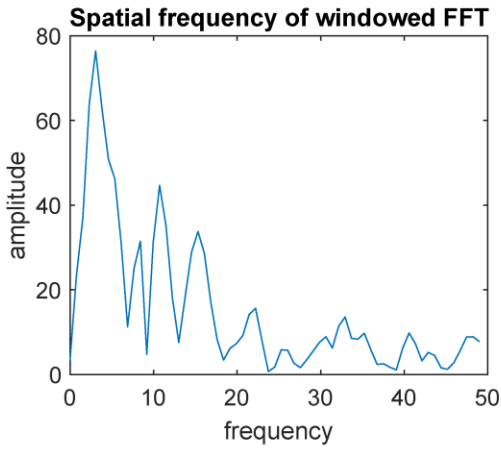
### Fault023



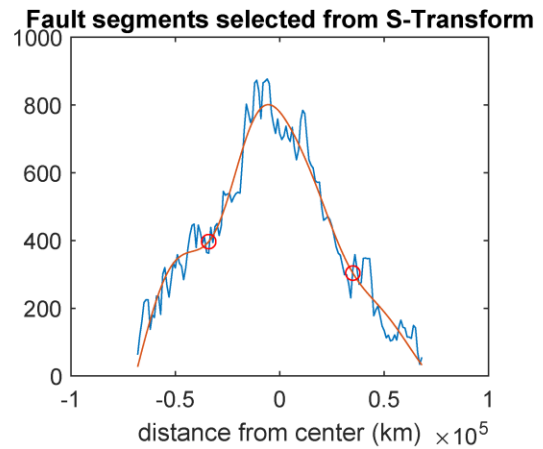
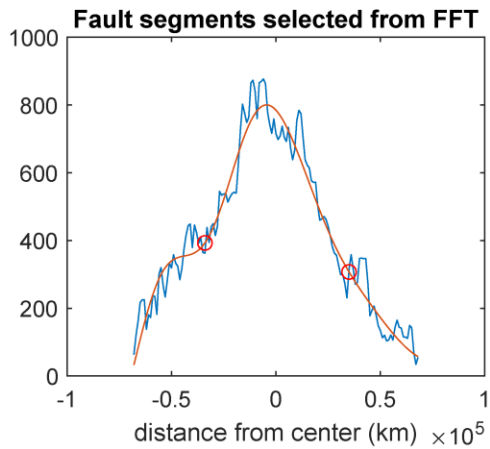
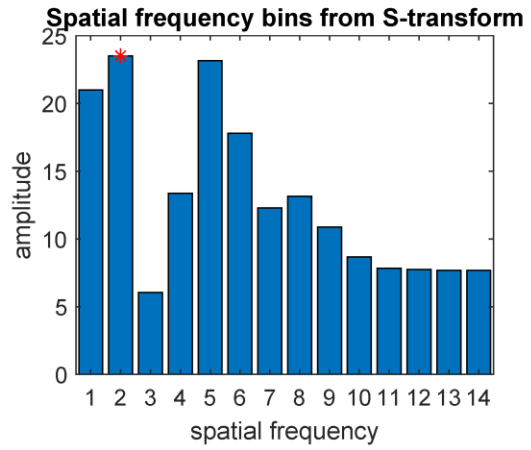
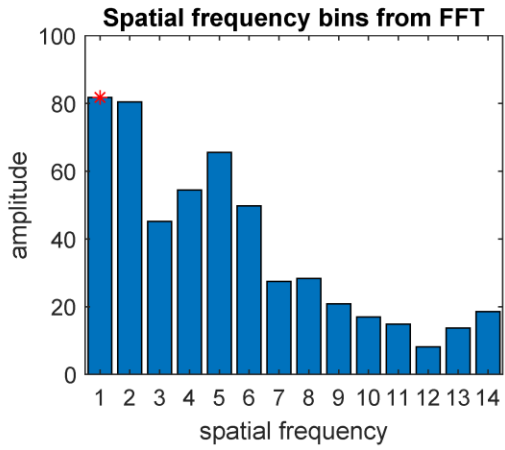
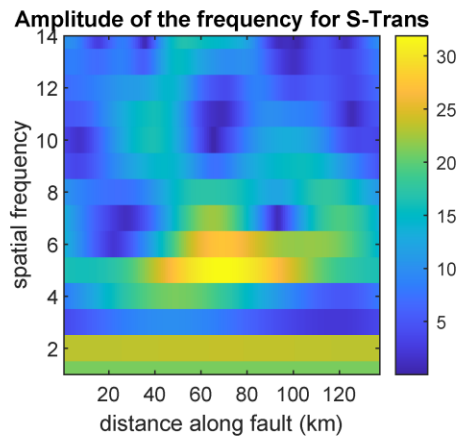
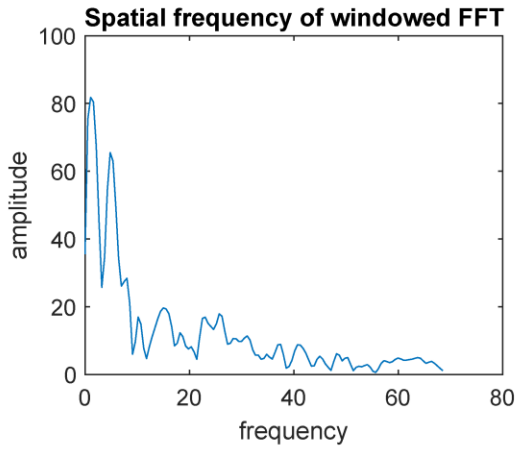
# Fault024



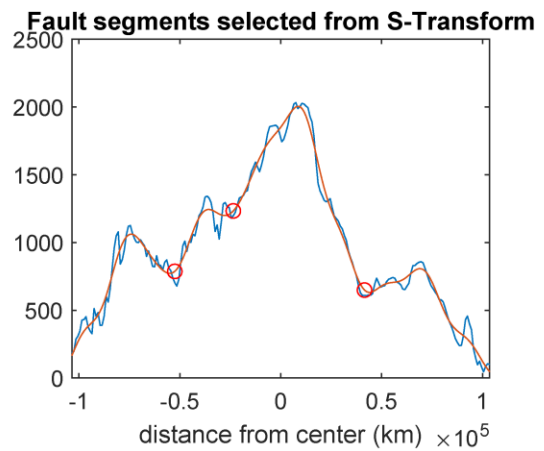
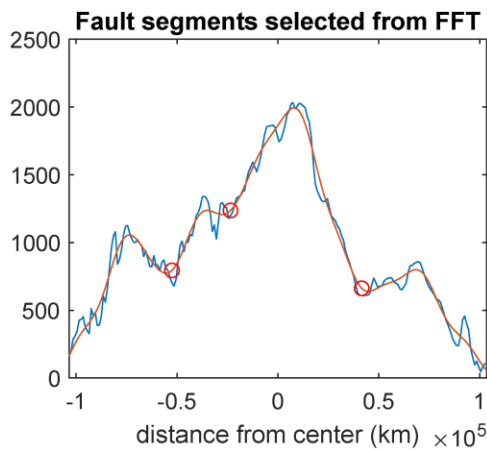
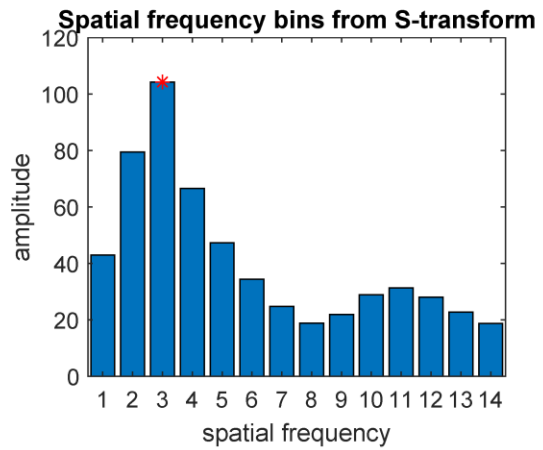
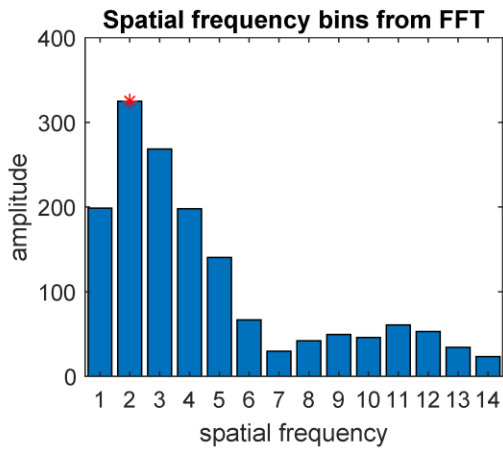
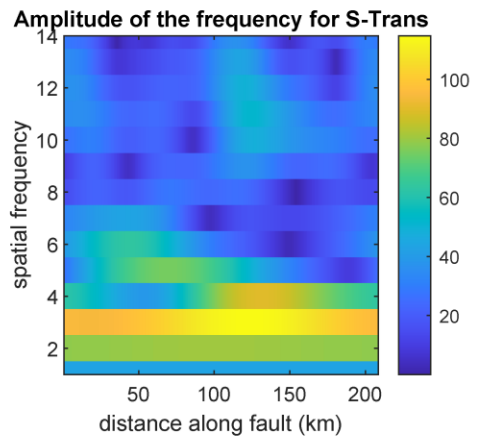
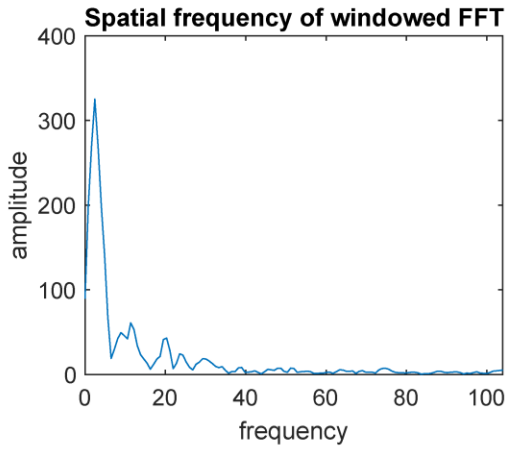
# Fault025



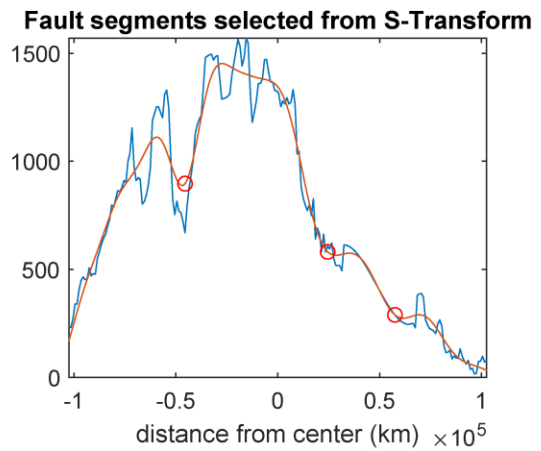
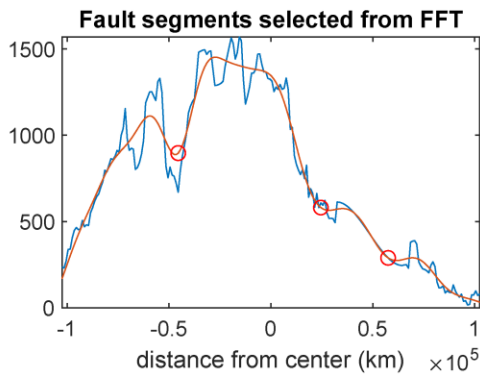
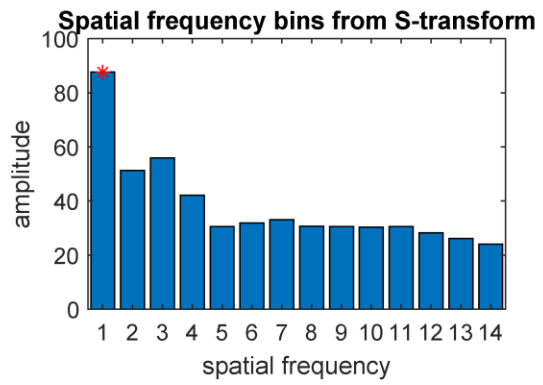
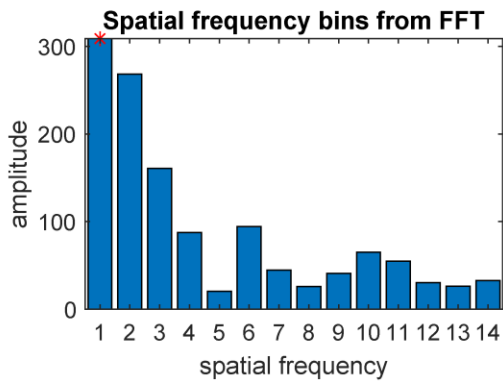
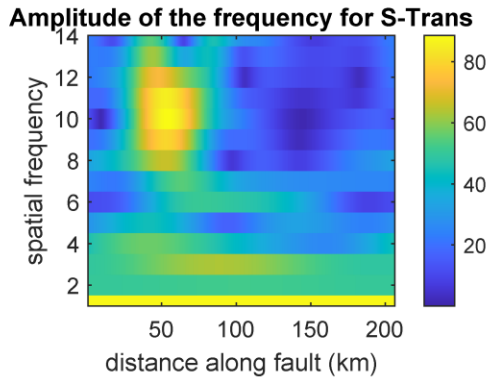
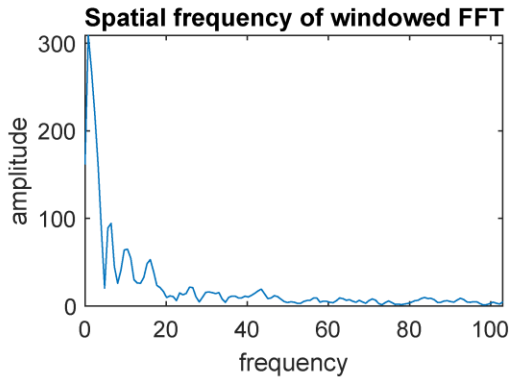
## Fault026



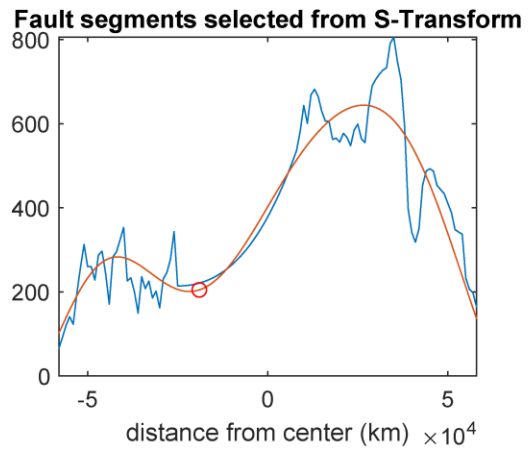
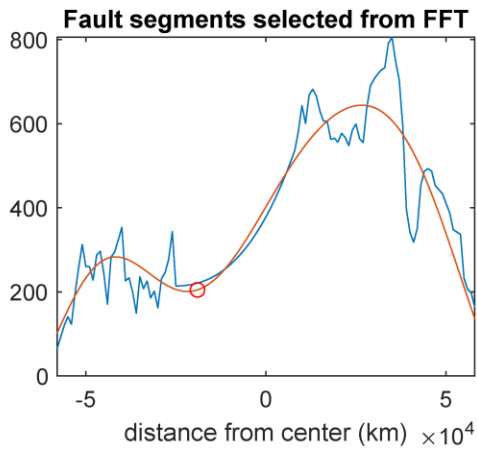
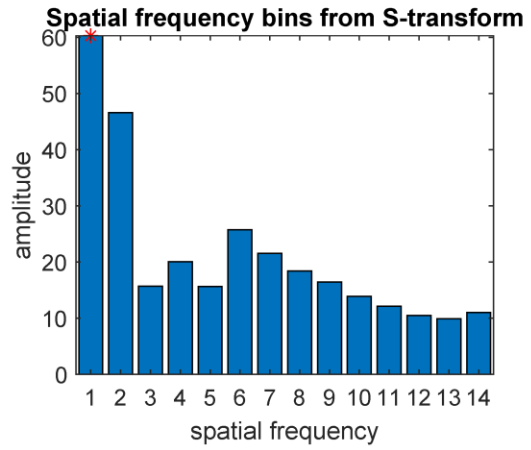
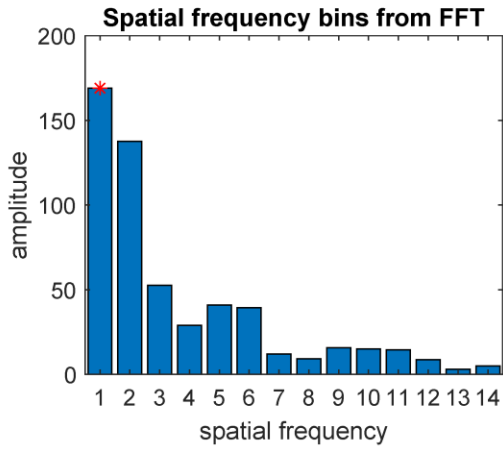
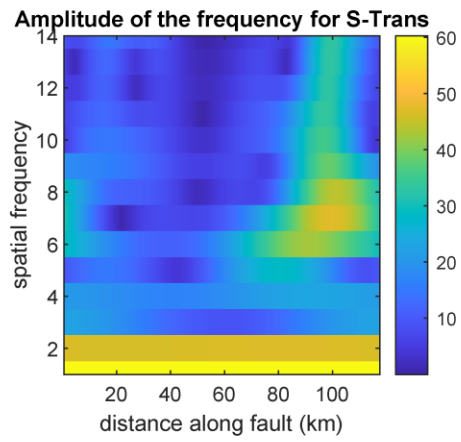
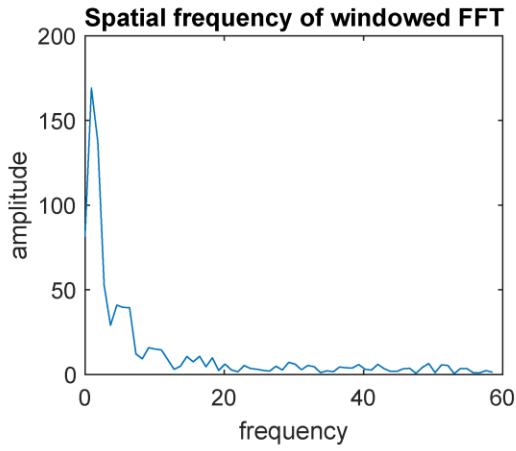
## Fault027



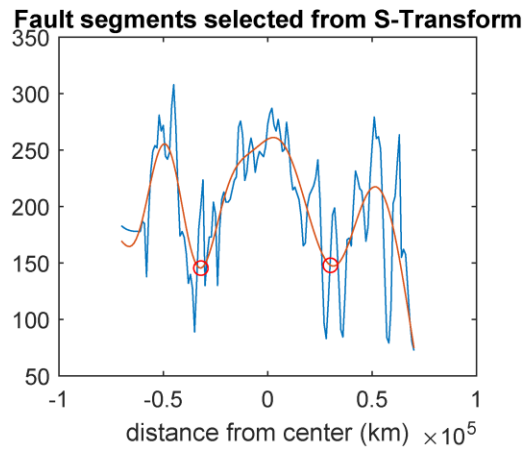
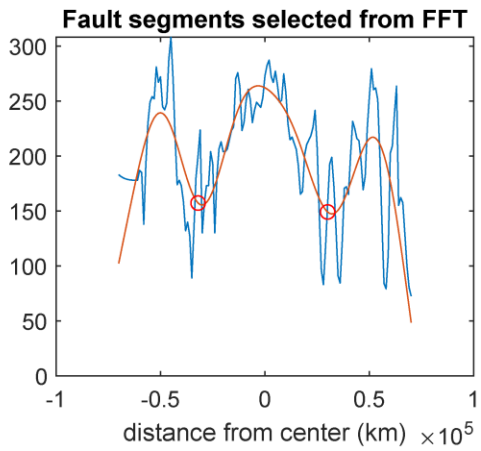
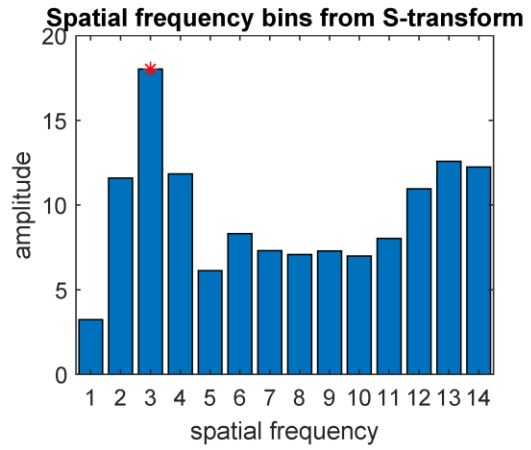
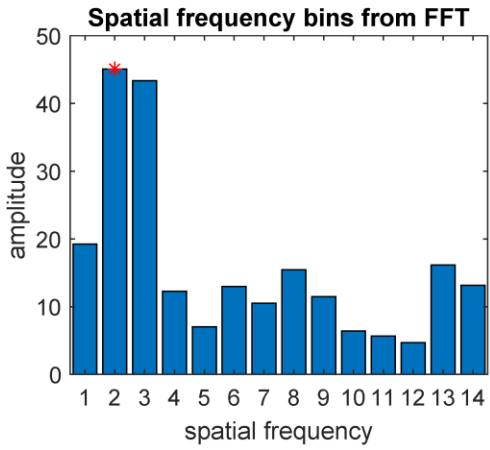
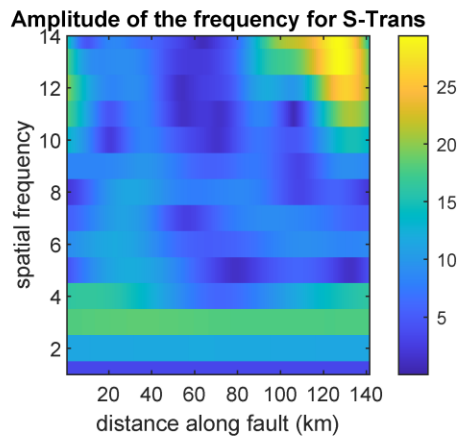
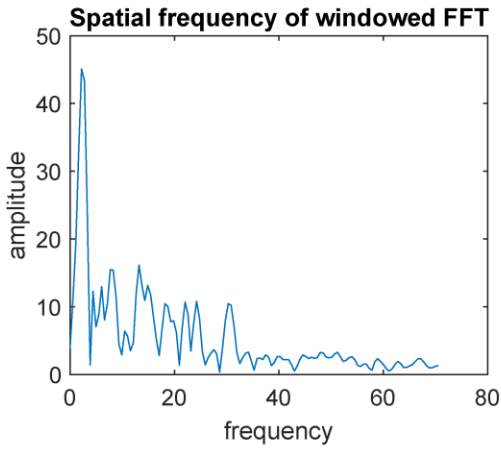
## Fault028



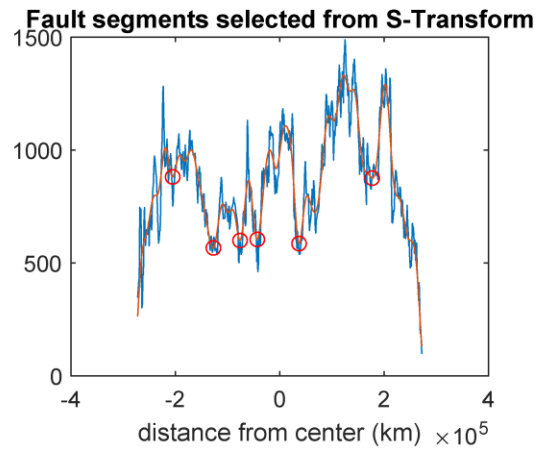
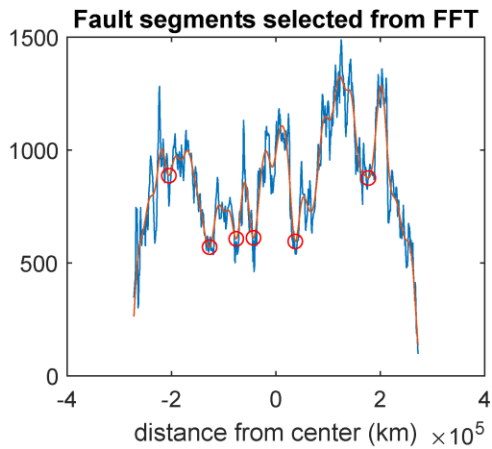
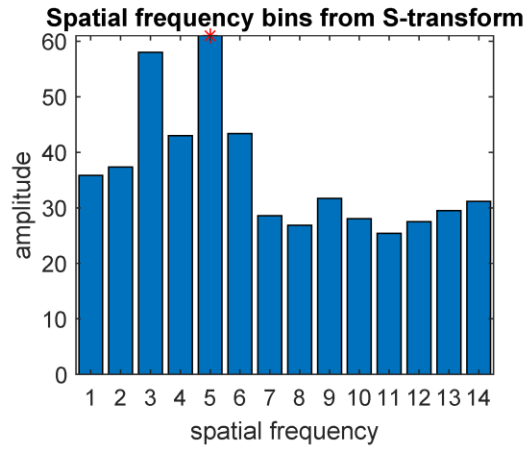
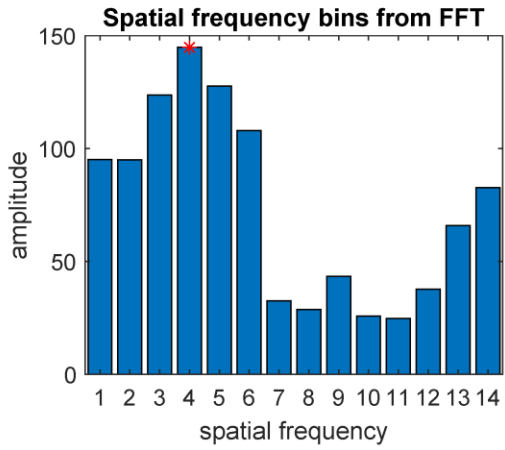
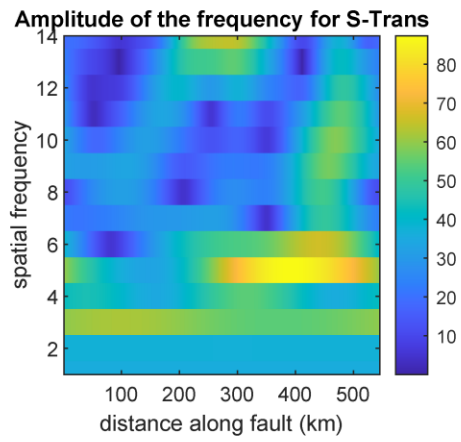
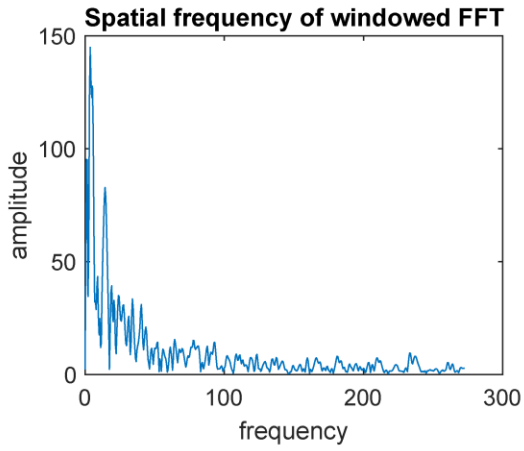
# Fault029



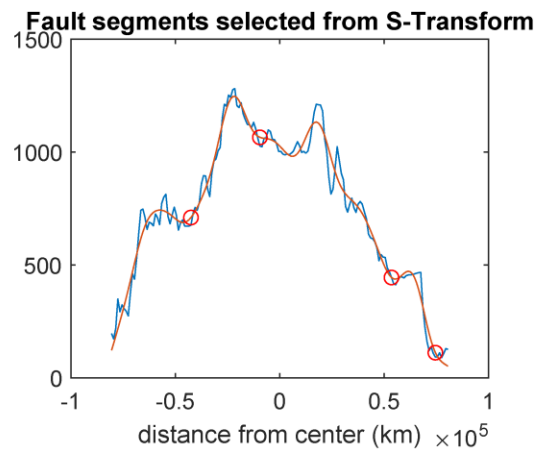
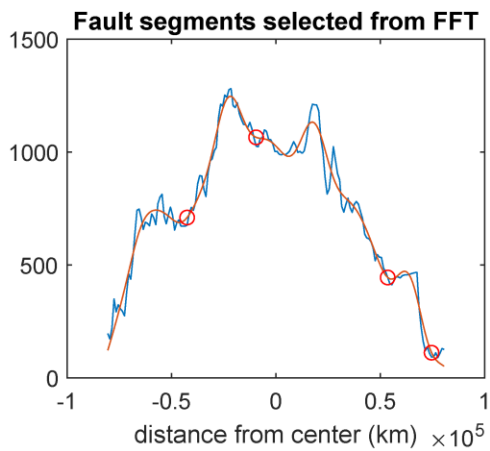
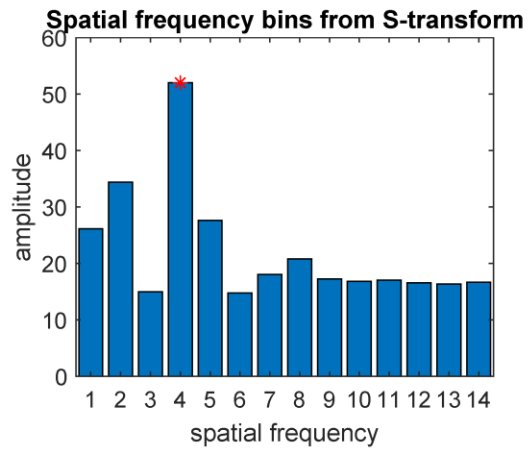
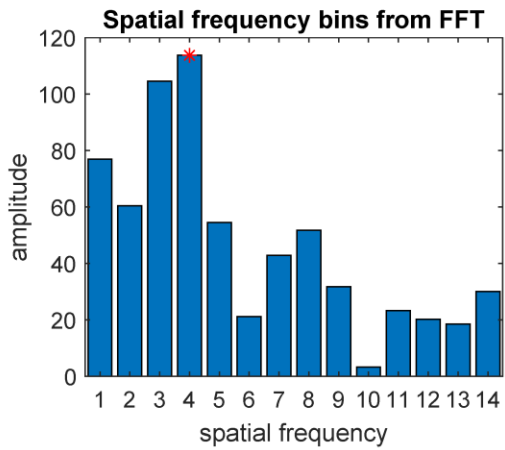
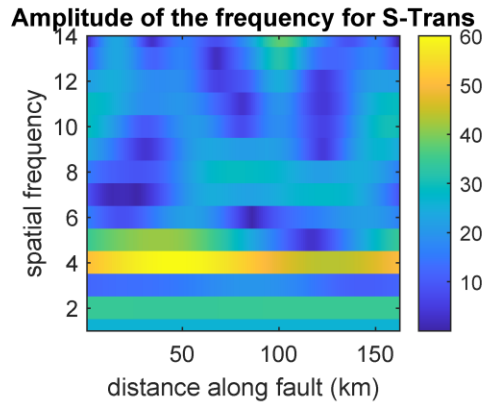
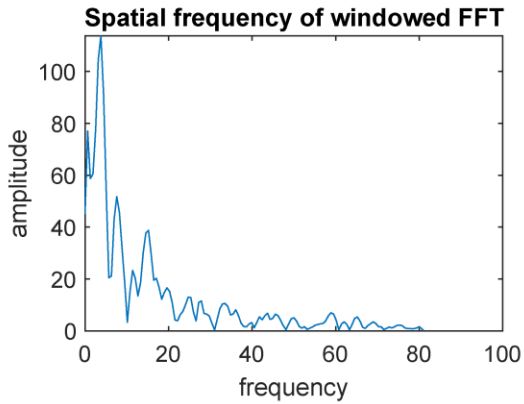
# Fault030



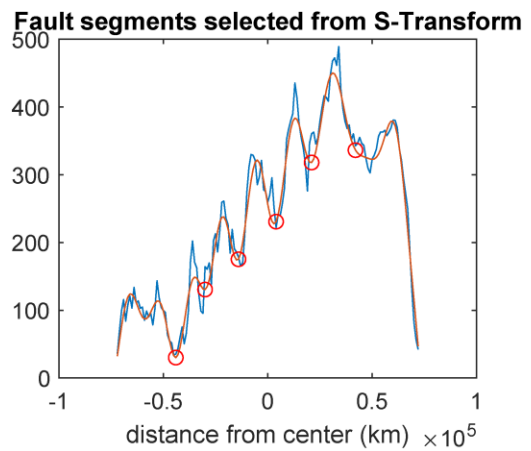
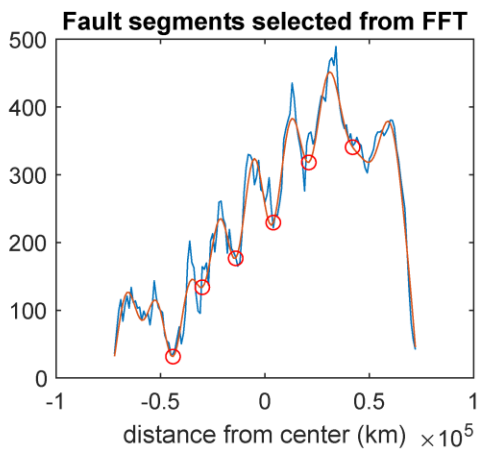
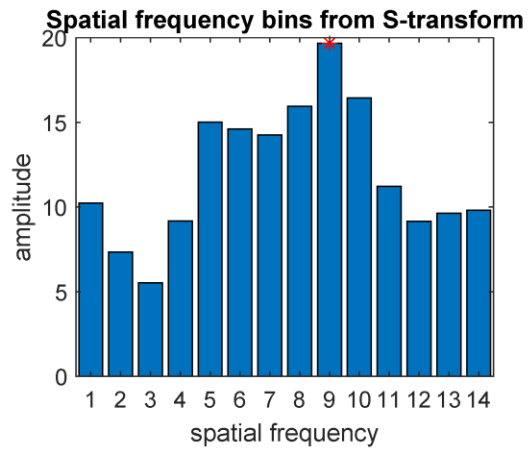
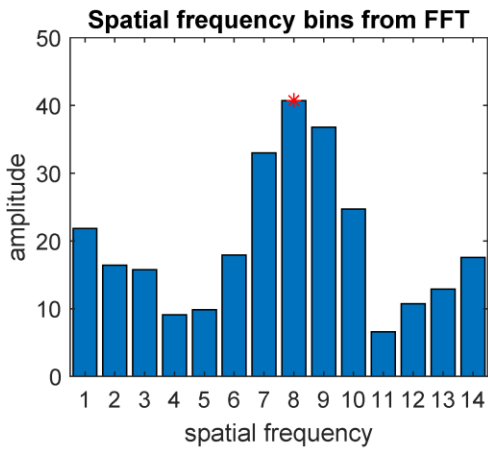
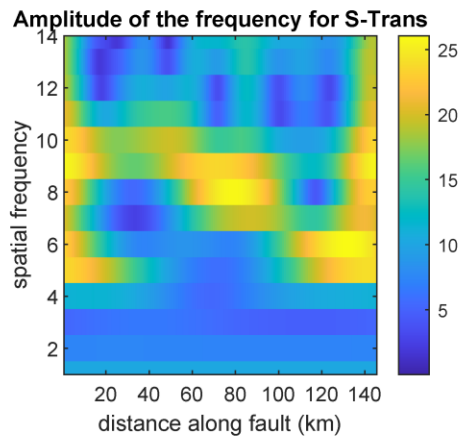
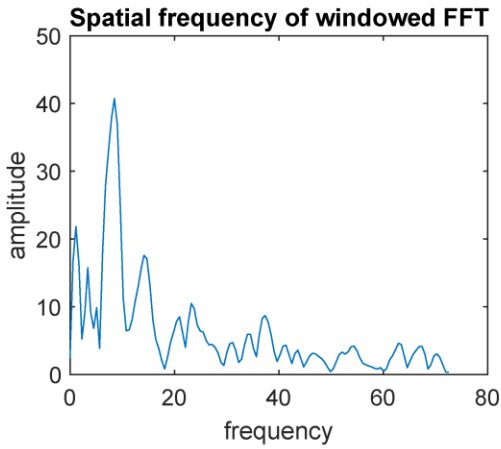
# Fault031



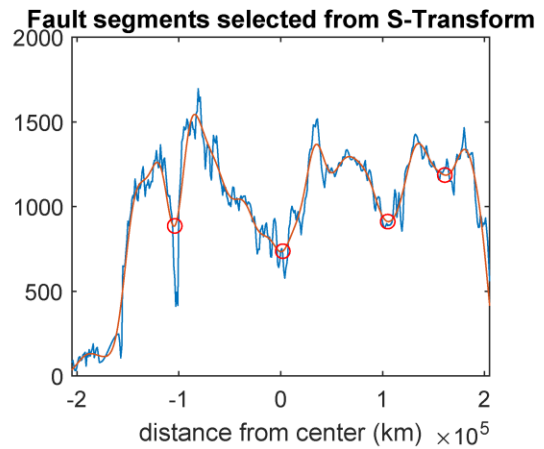
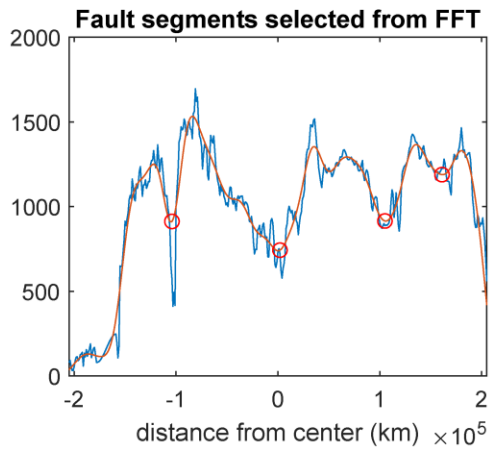
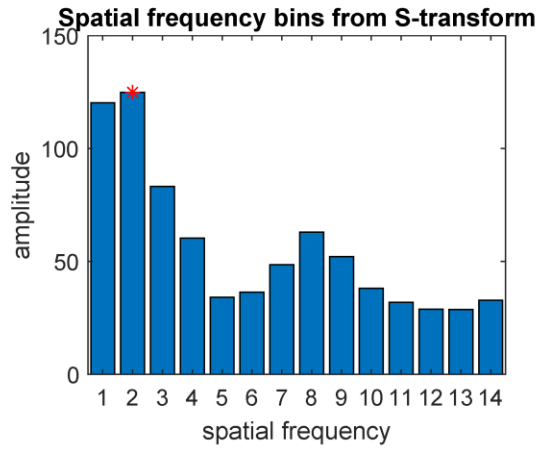
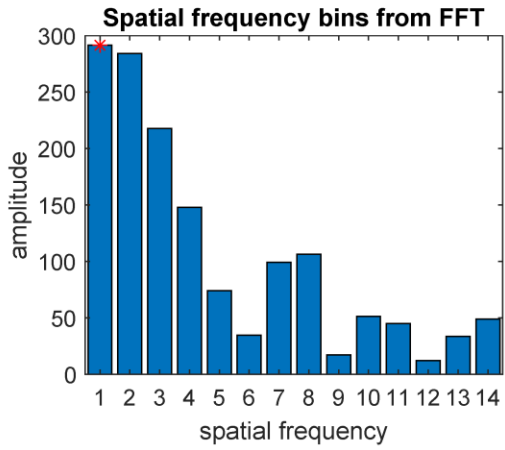
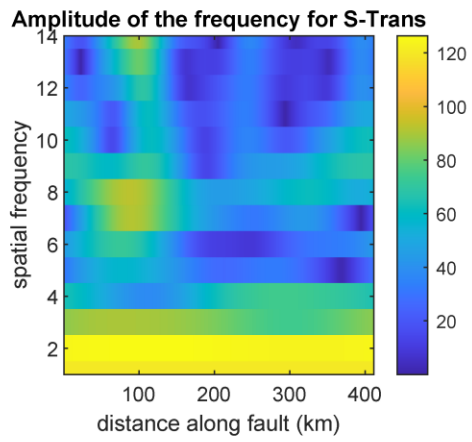
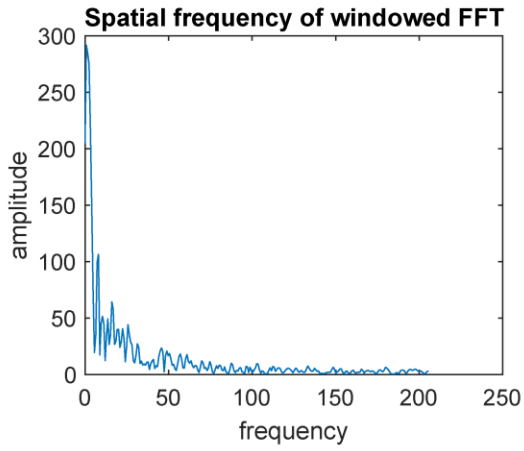
## Fault032



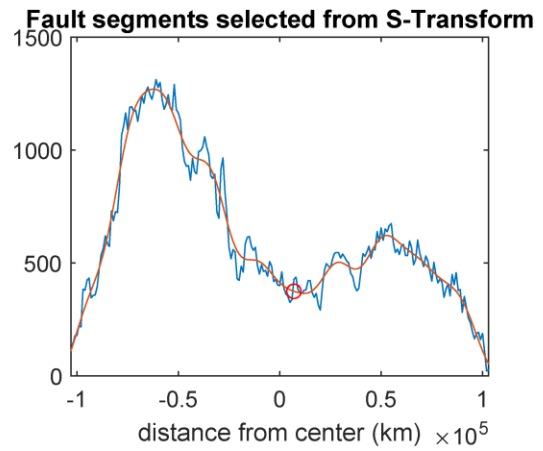
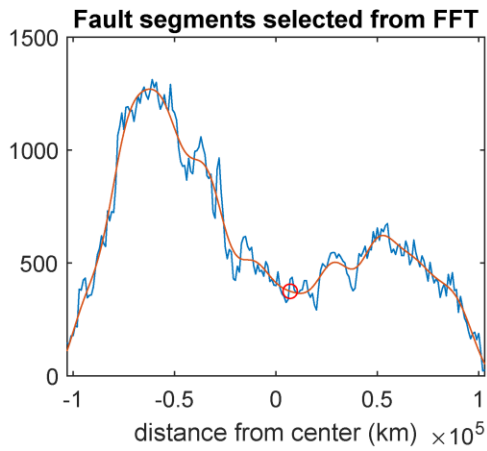
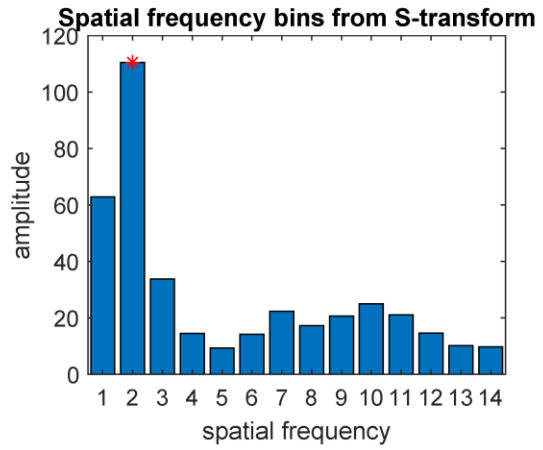
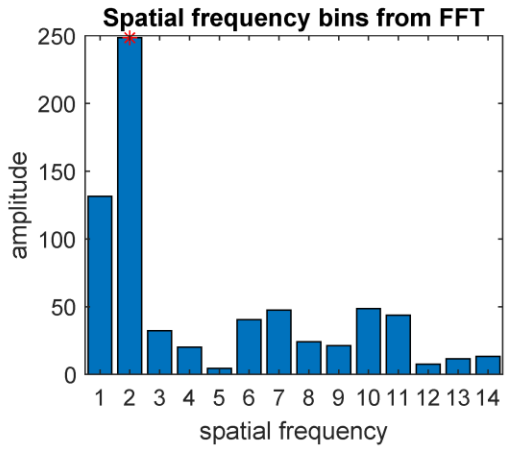
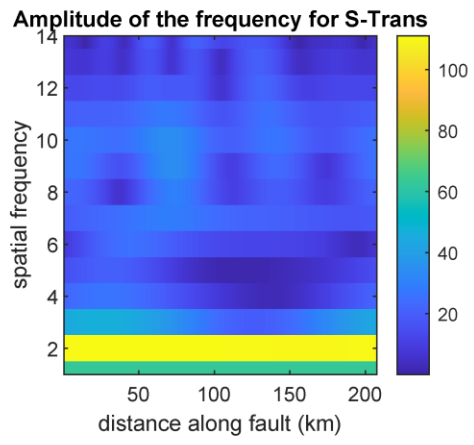
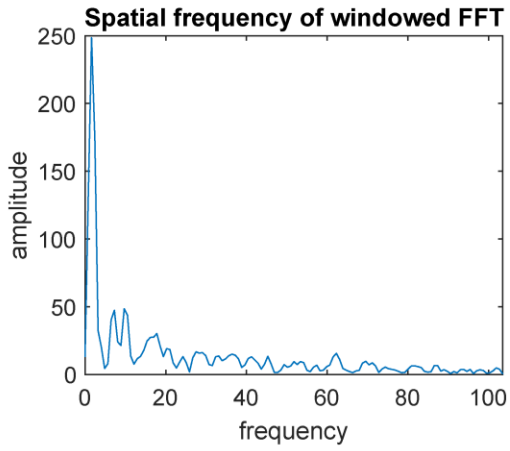
# Fault033



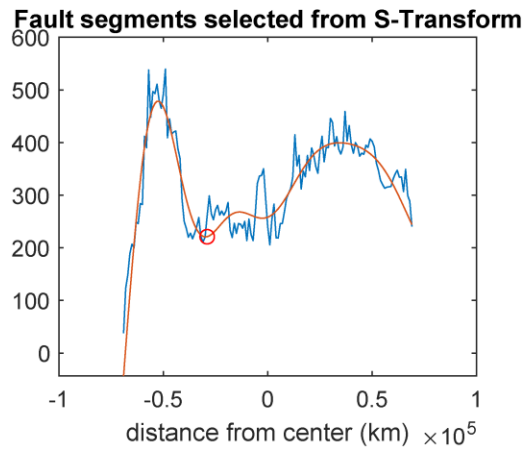
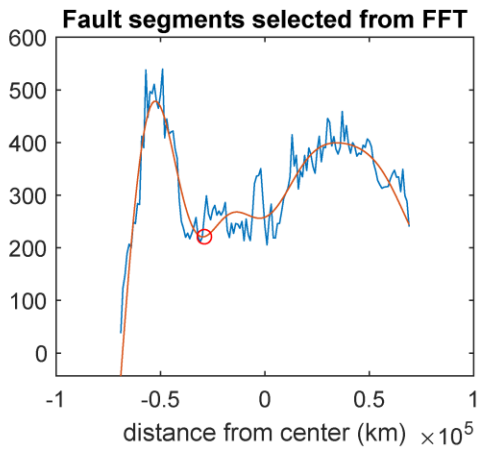
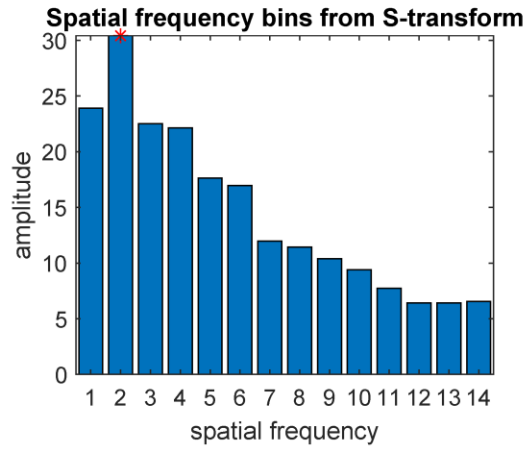
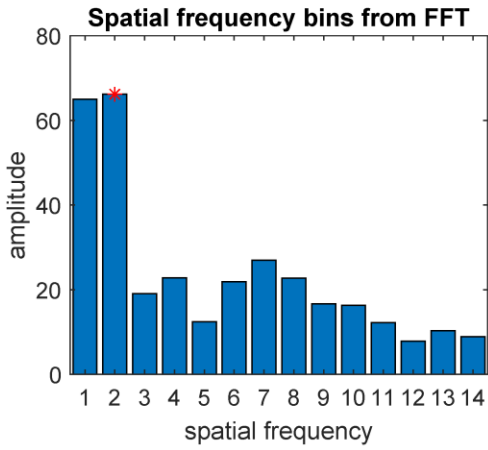
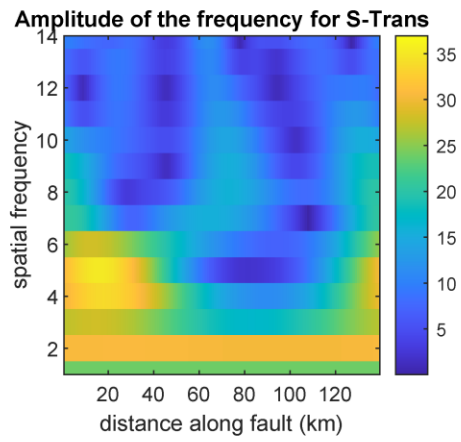
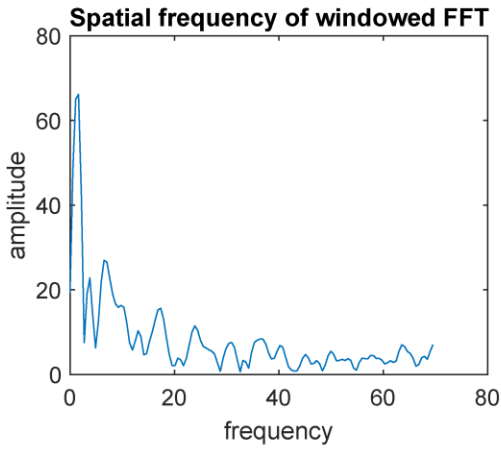
# Fault034



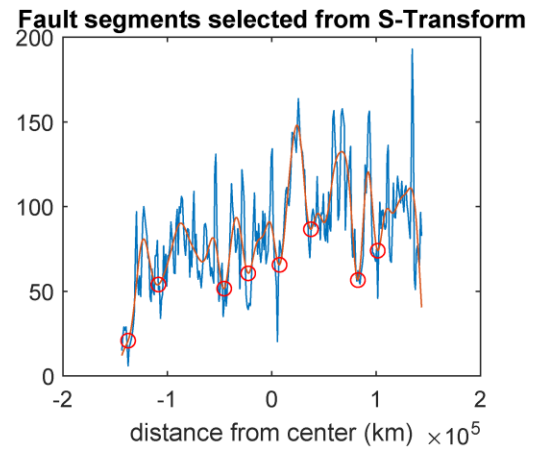
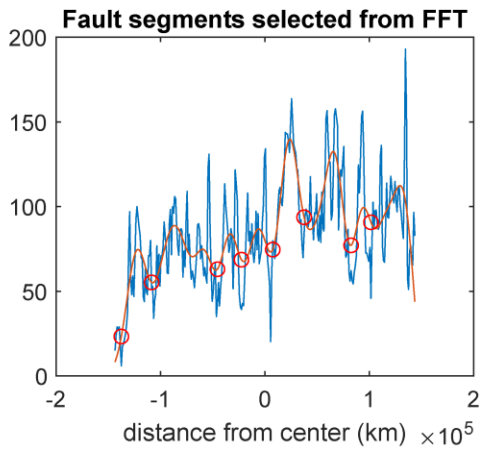
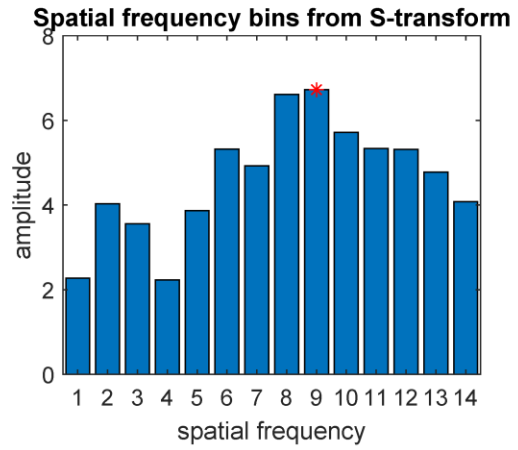
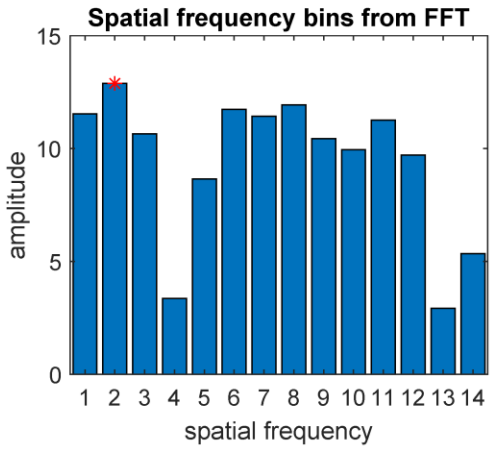
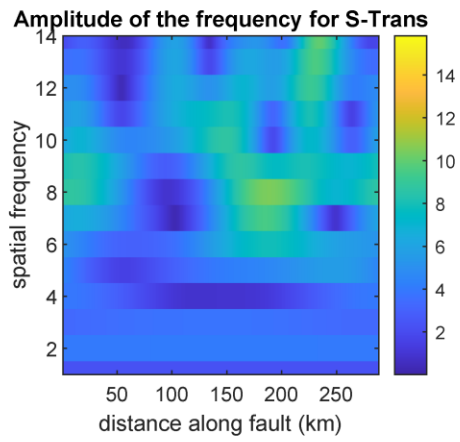
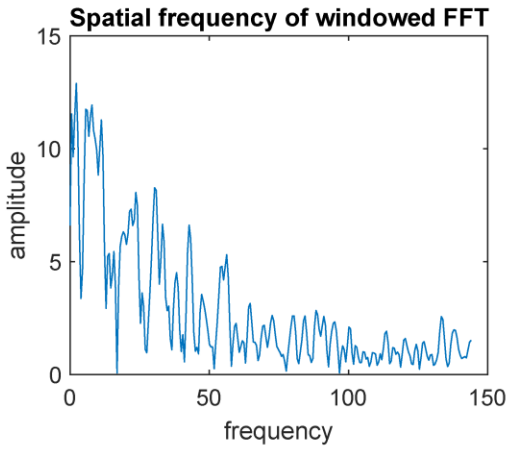
### Fault036



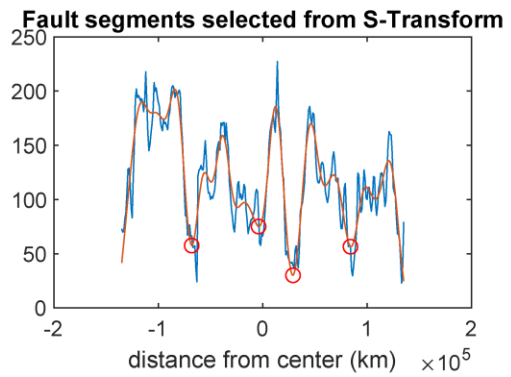
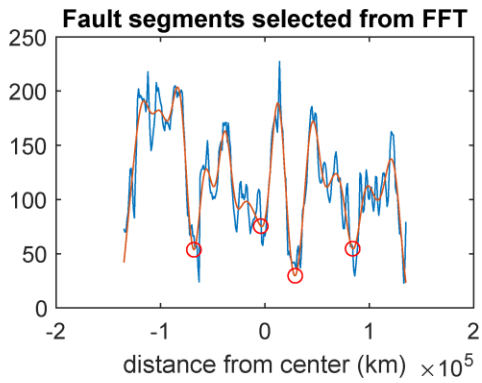
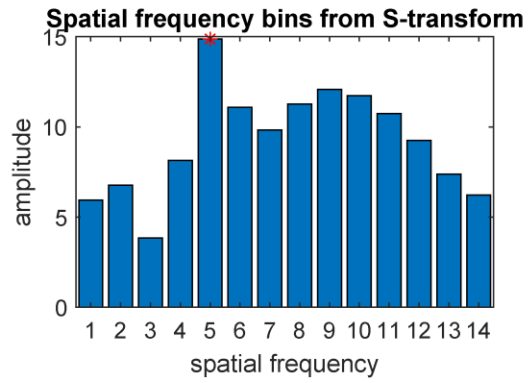
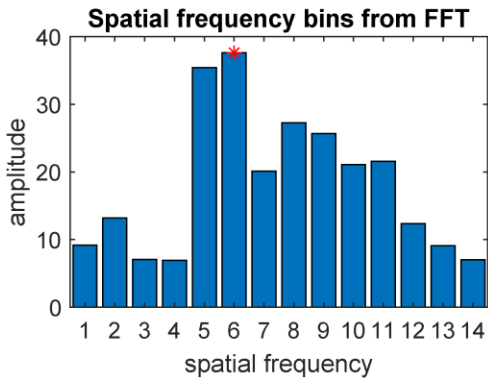
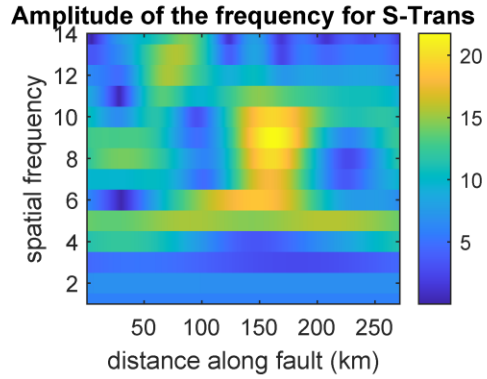
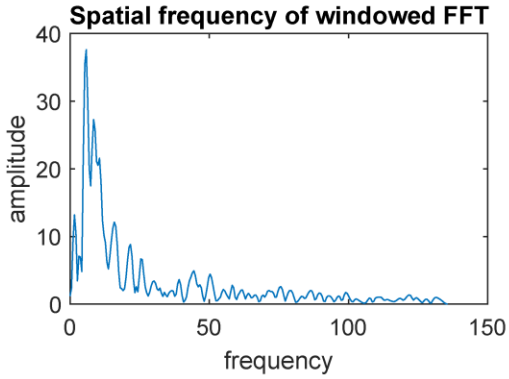
# Fault037



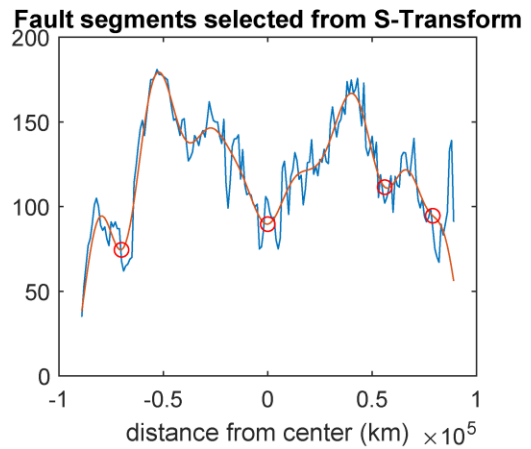
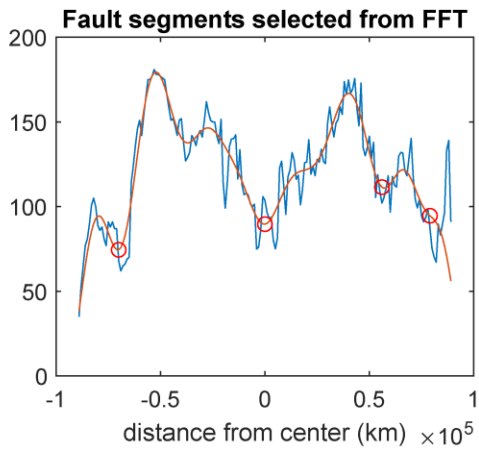
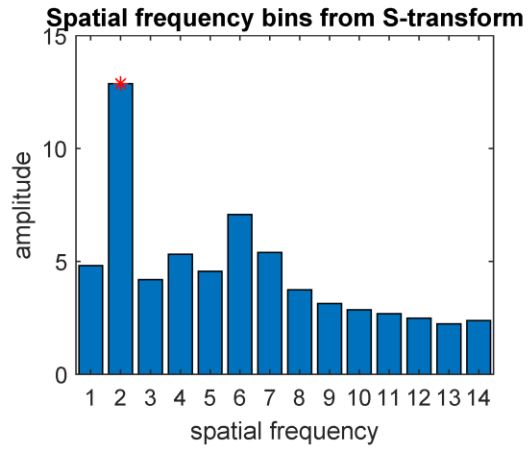
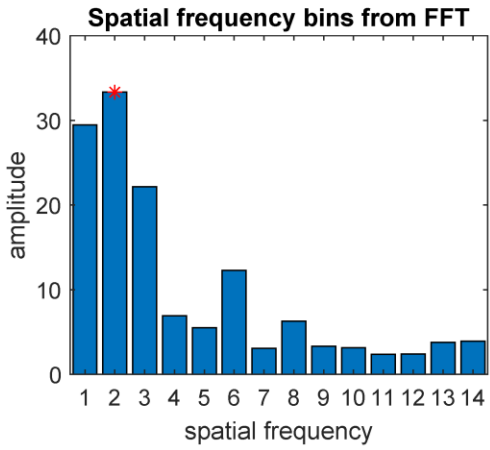
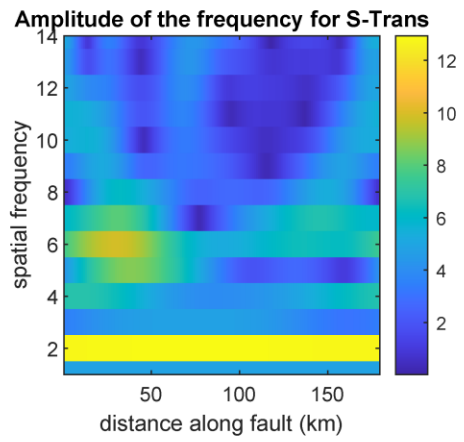
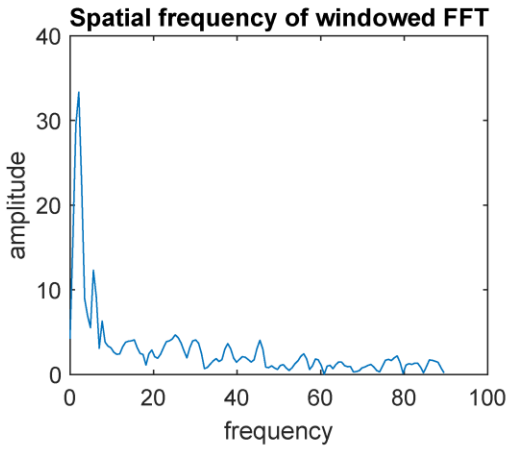
# Fault038



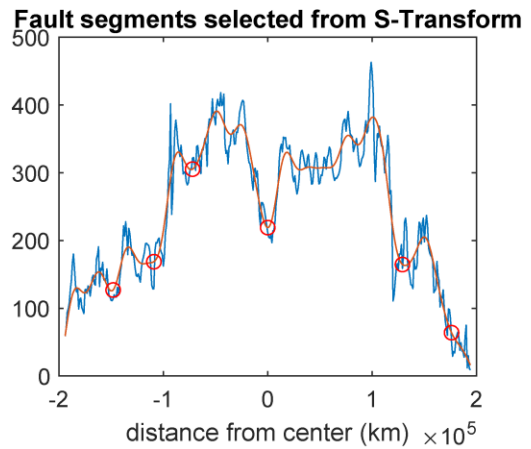
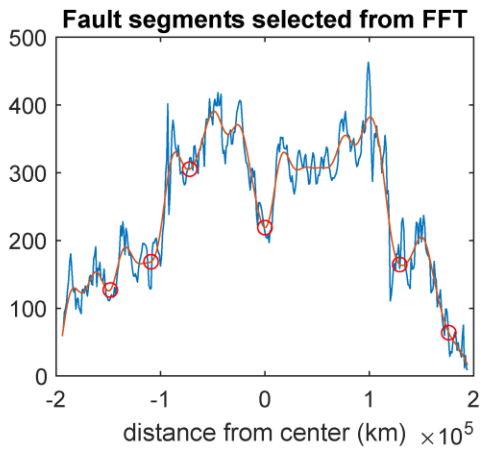
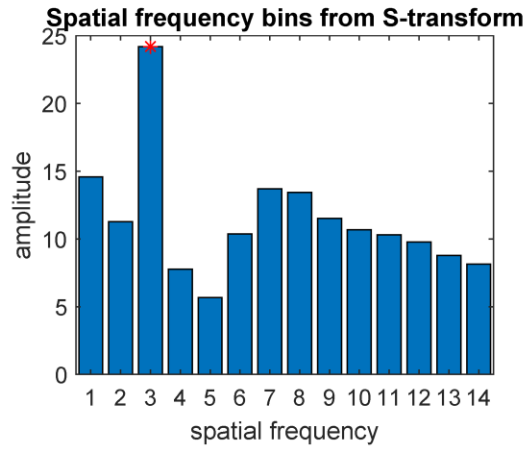
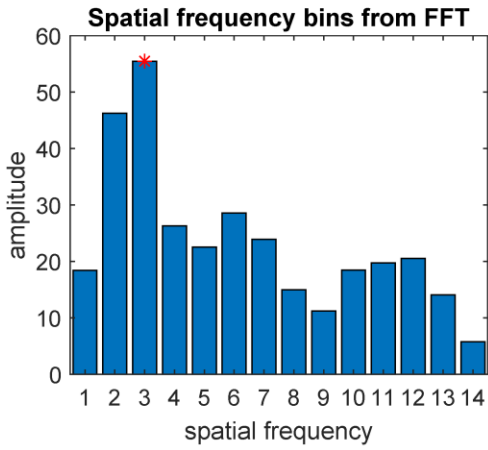
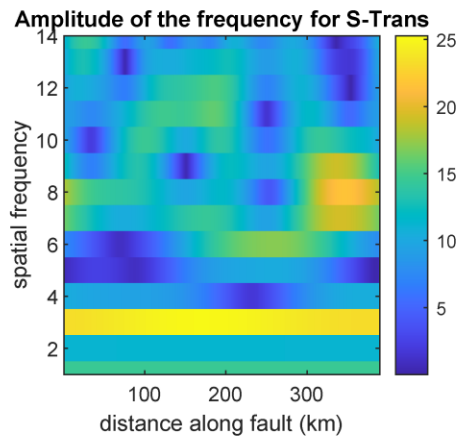
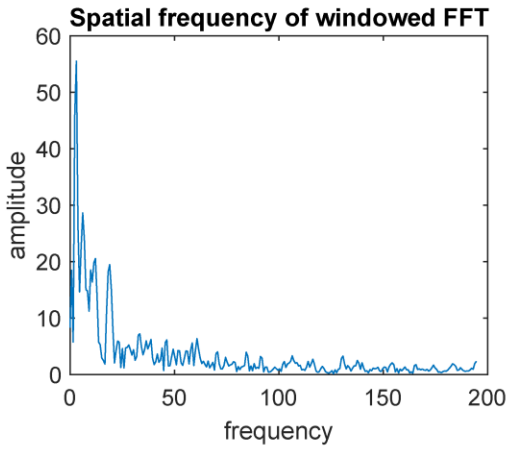
# Fault039



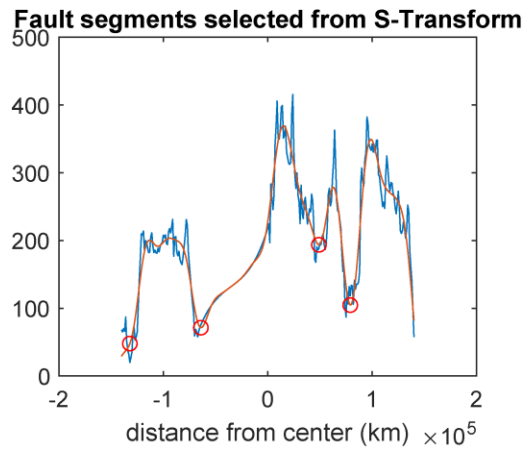
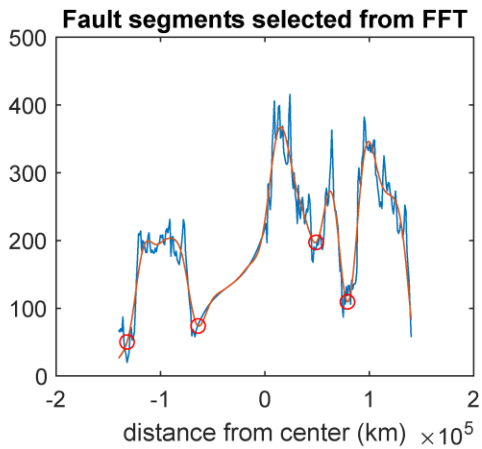
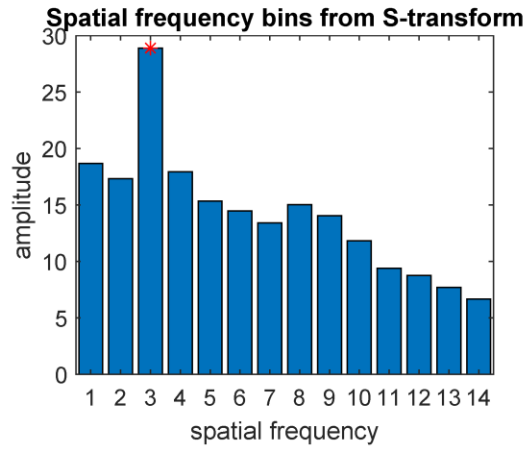
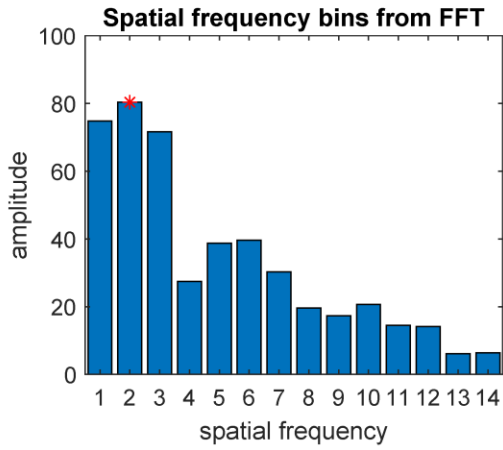
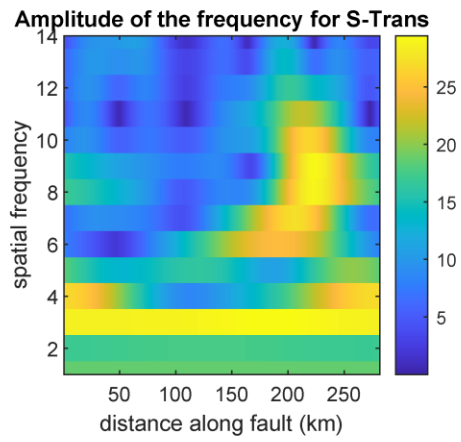
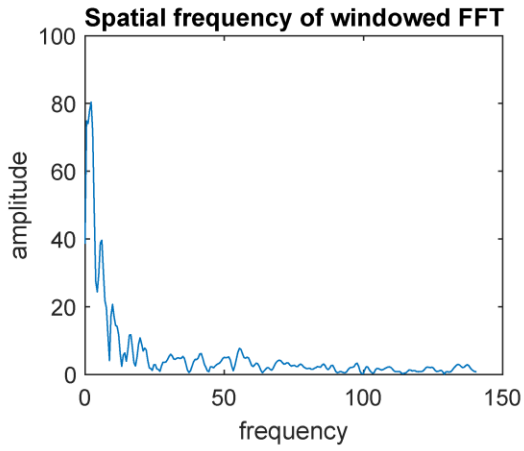
# Fault040



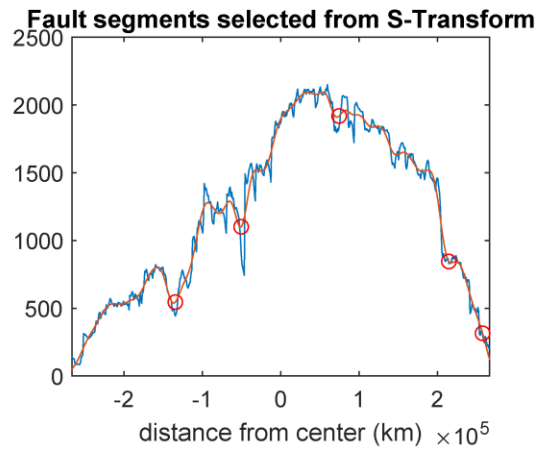
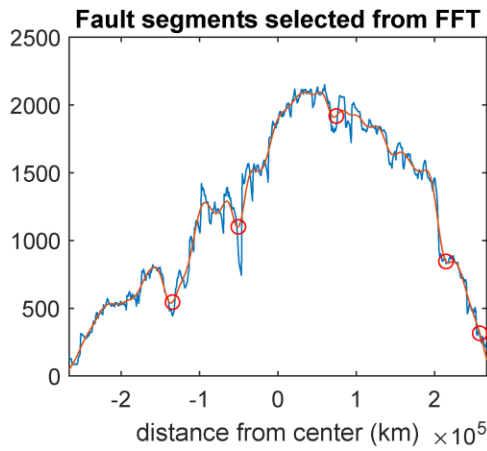
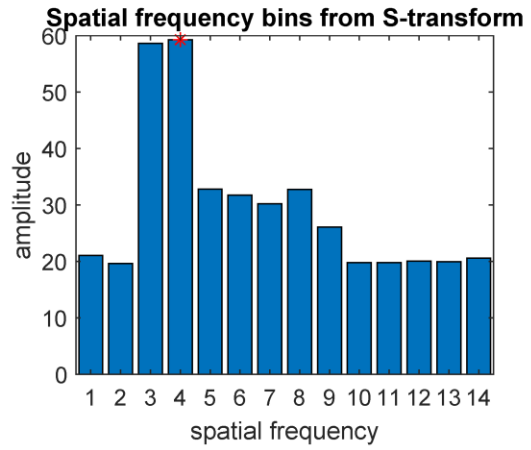
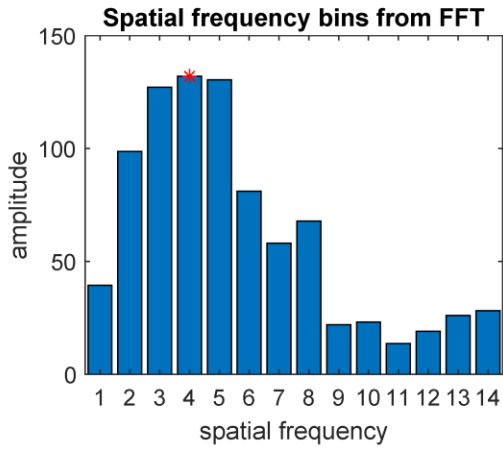
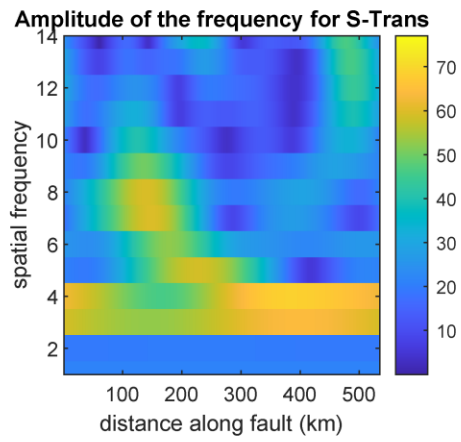
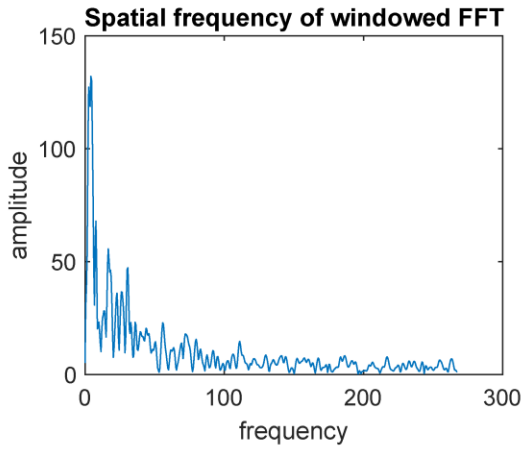
# Fault041



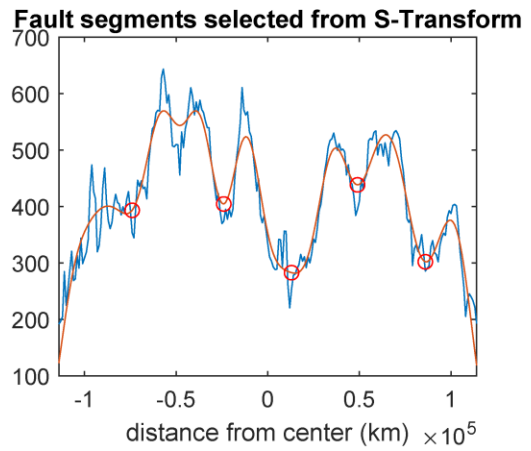
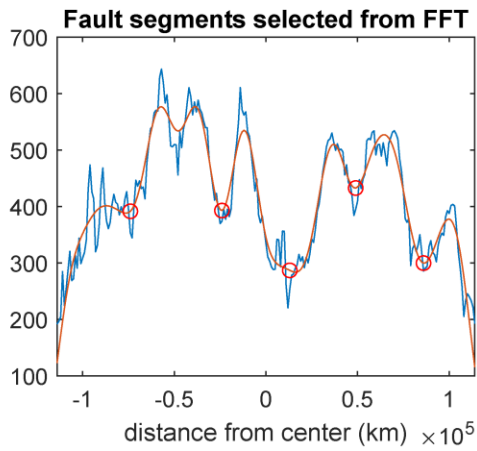
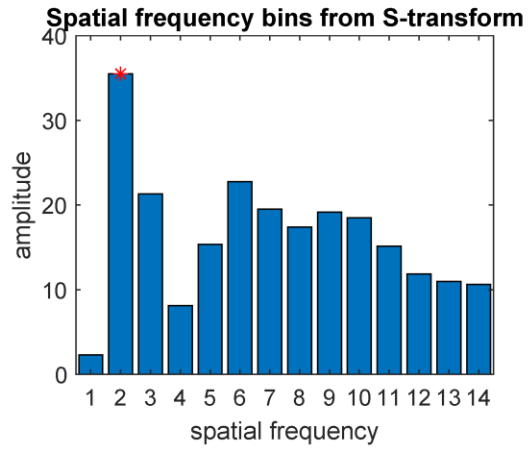
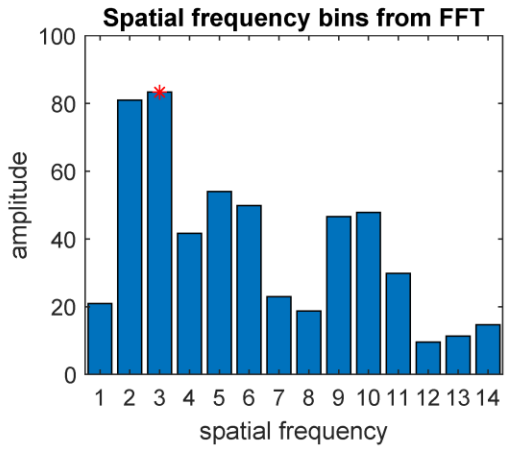
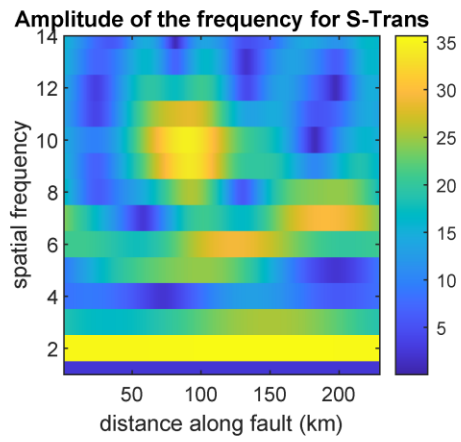
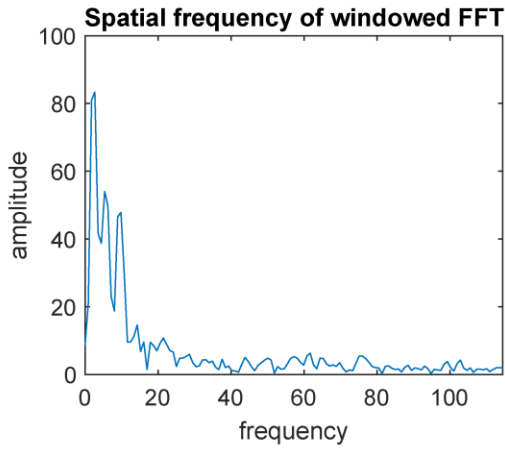
## Fault042



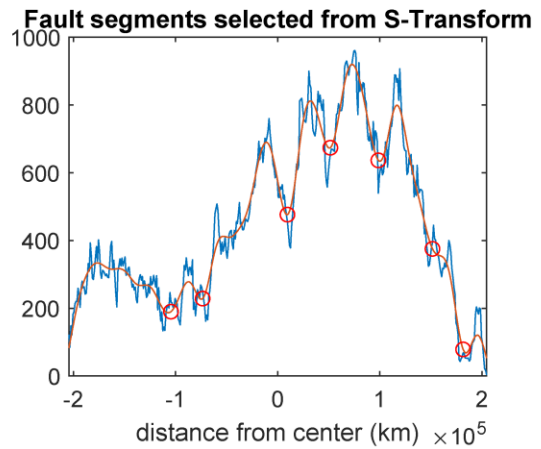
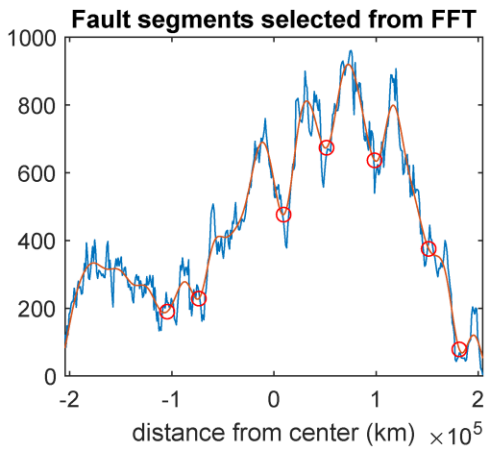
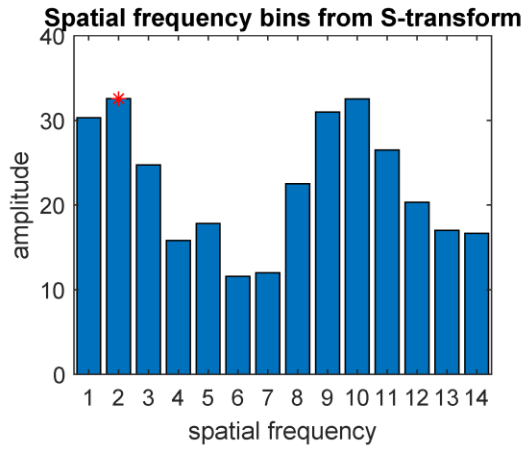
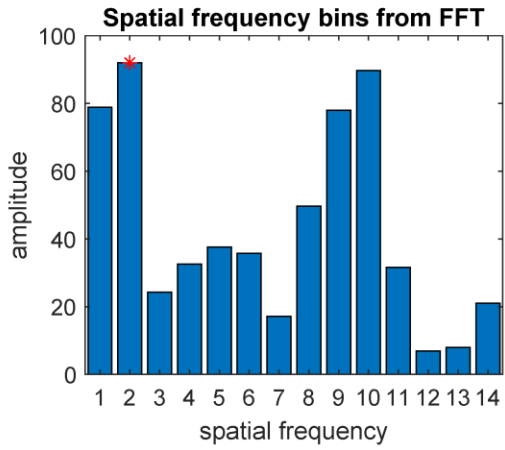
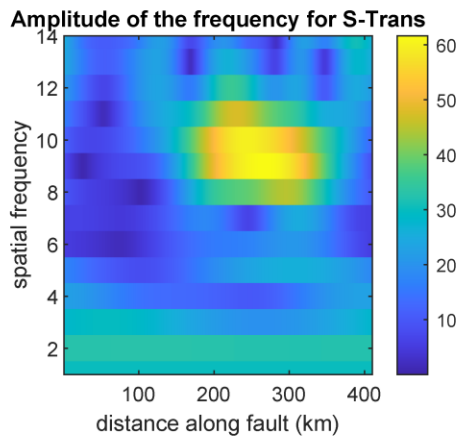
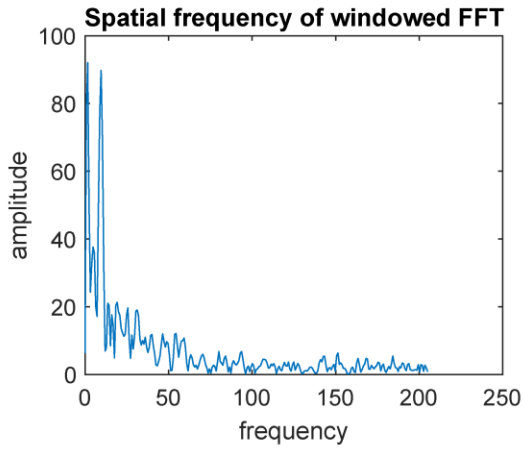
# Fault043



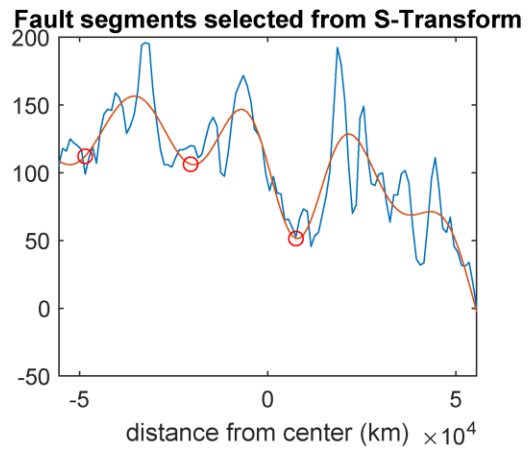
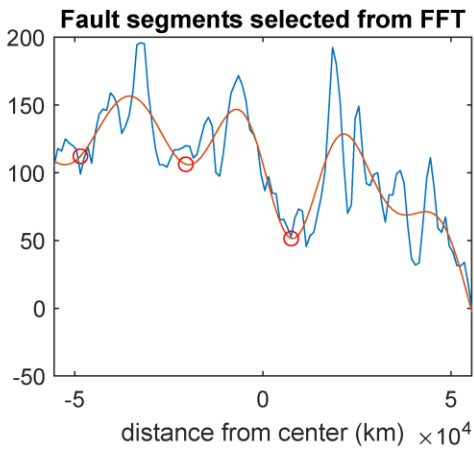
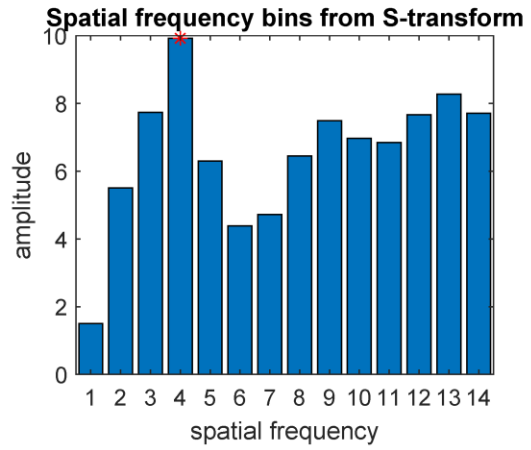
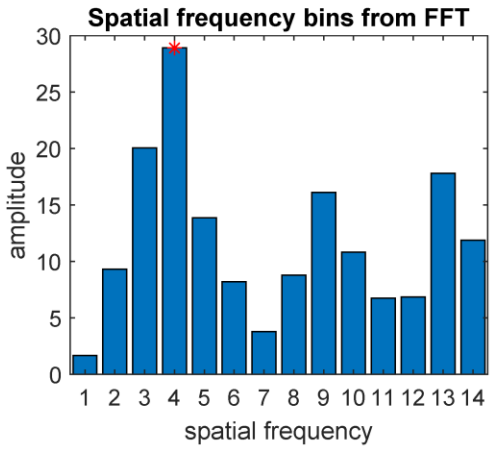
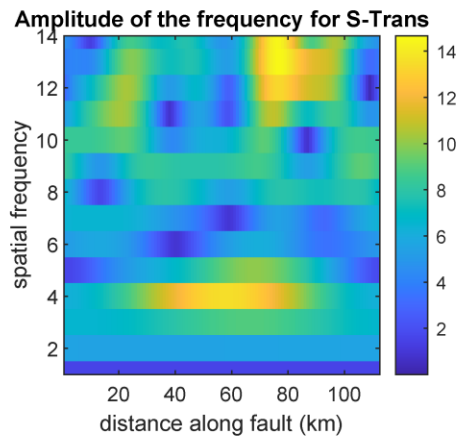
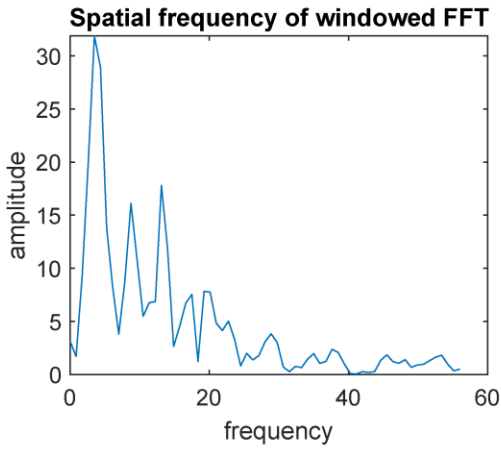
# Fault044



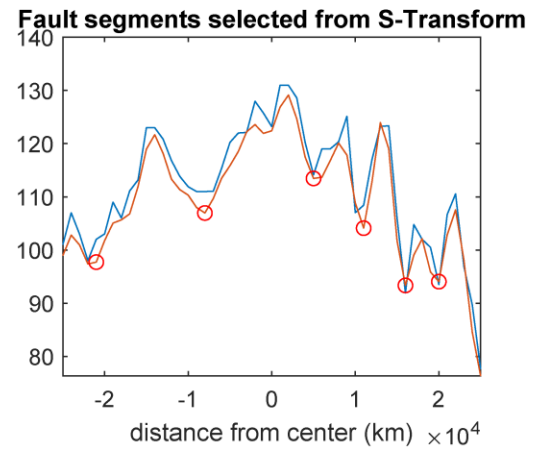
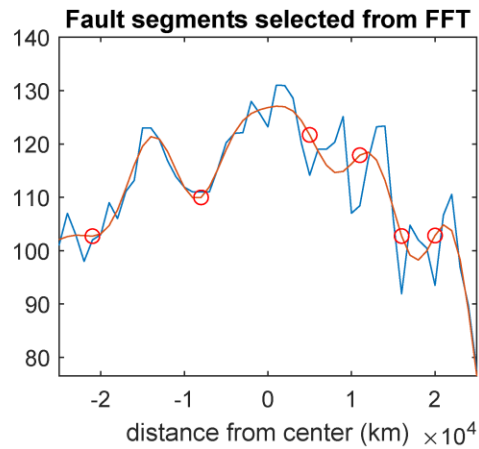
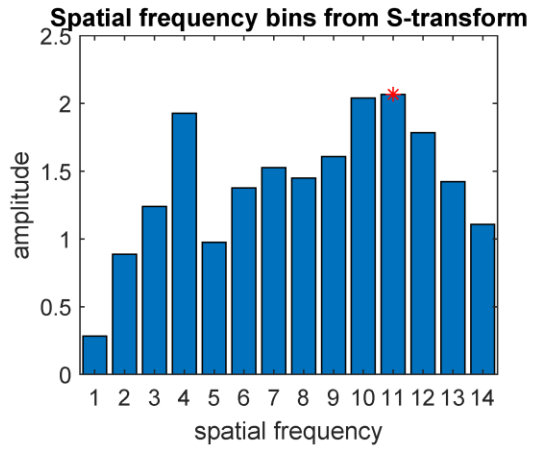
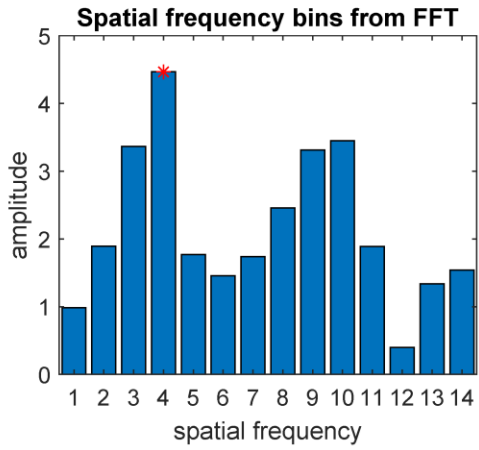
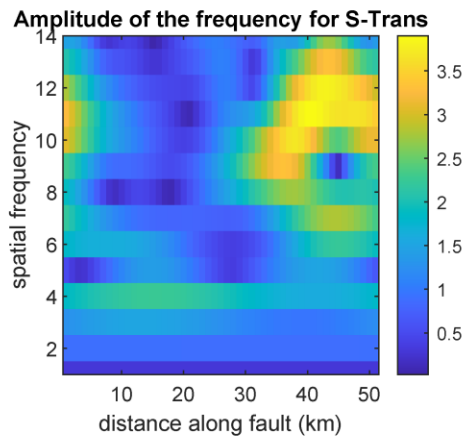
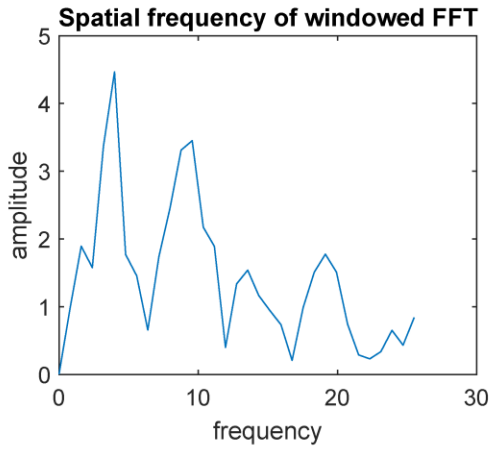
# Fault045



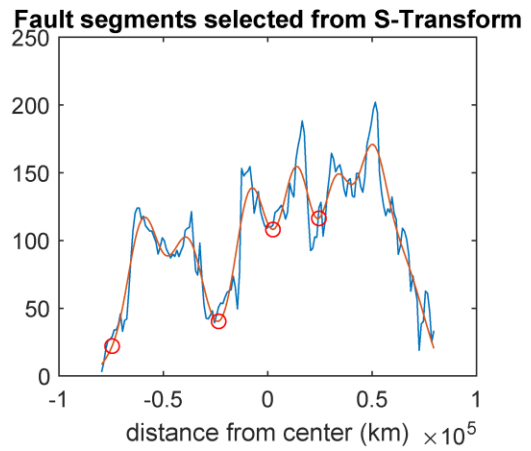
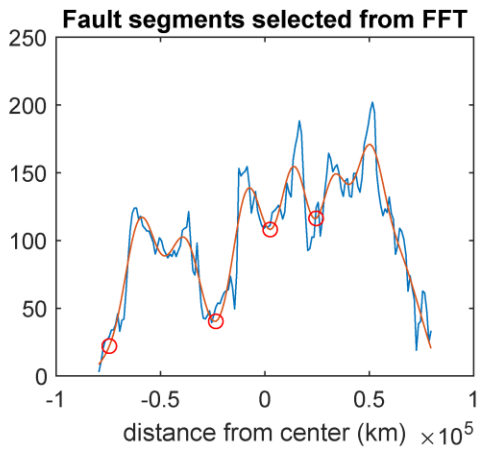
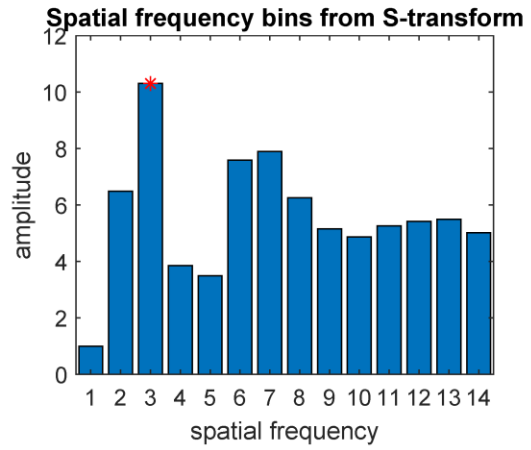
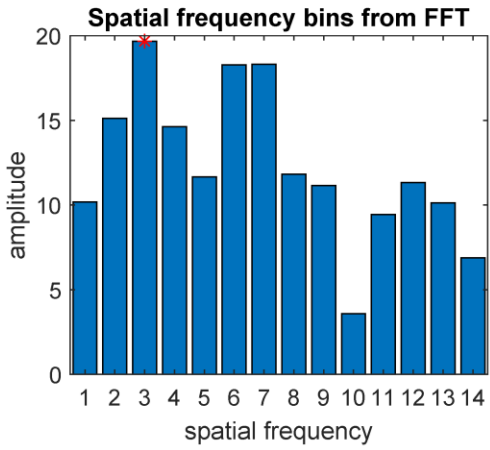
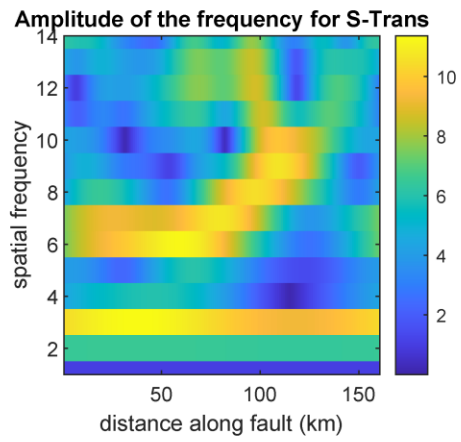
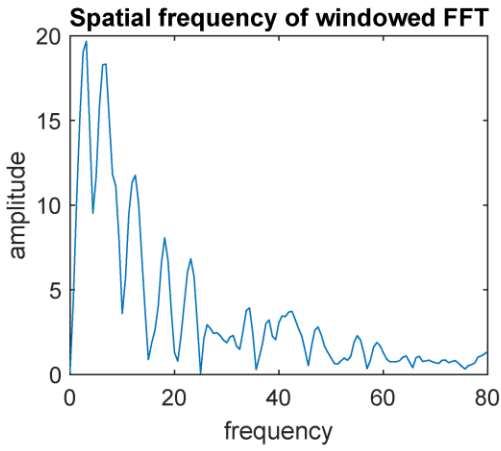
# Fault047



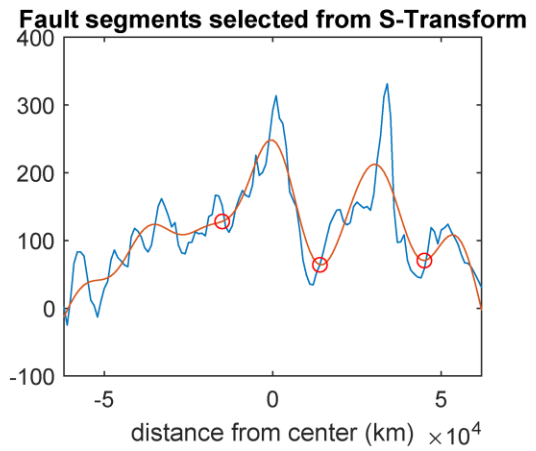
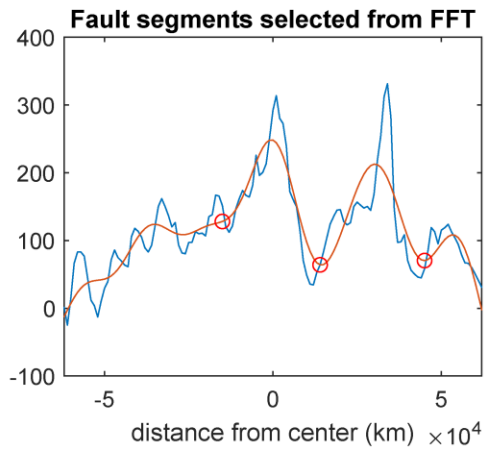
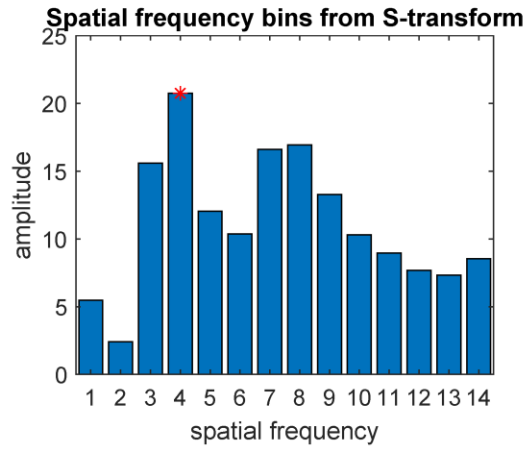
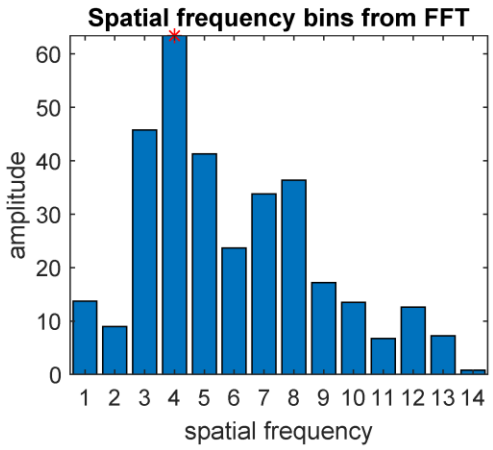
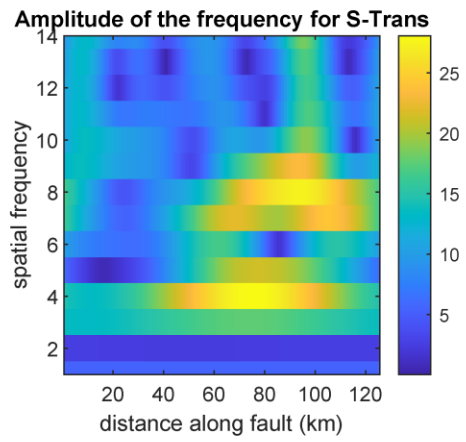
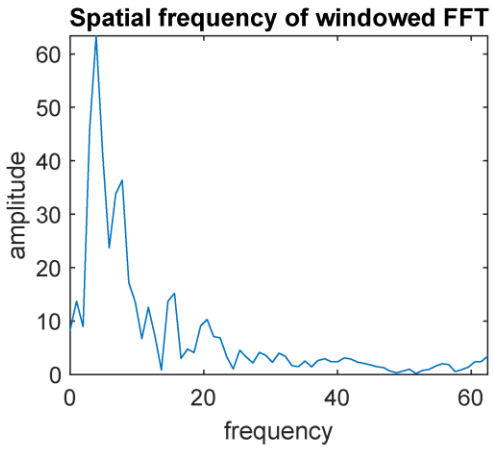
# Fault048



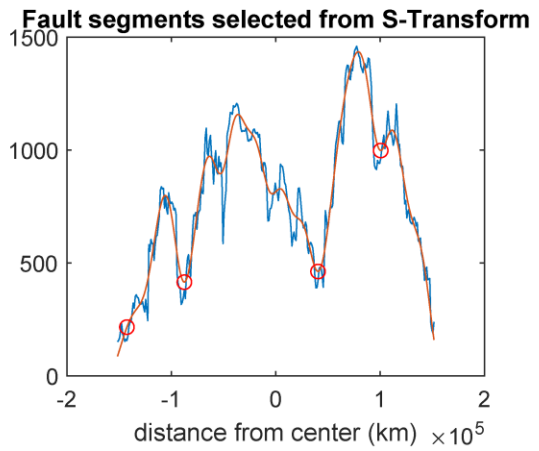
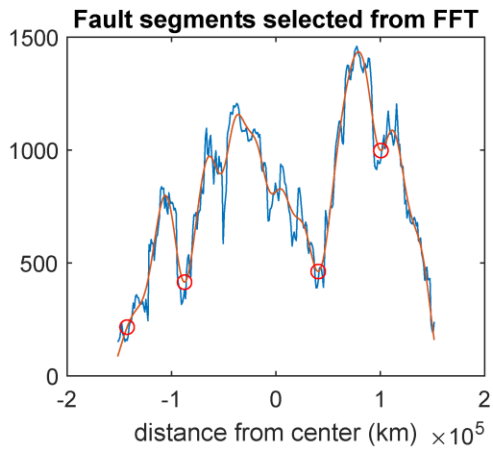
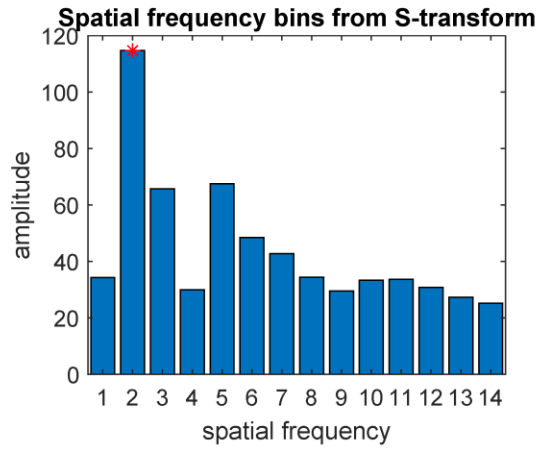
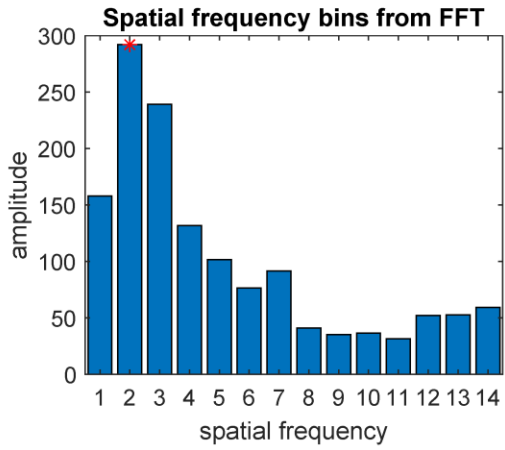
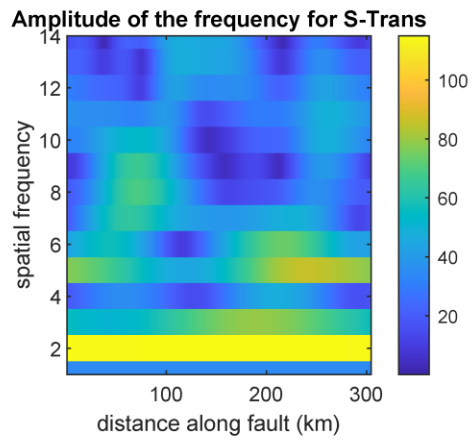
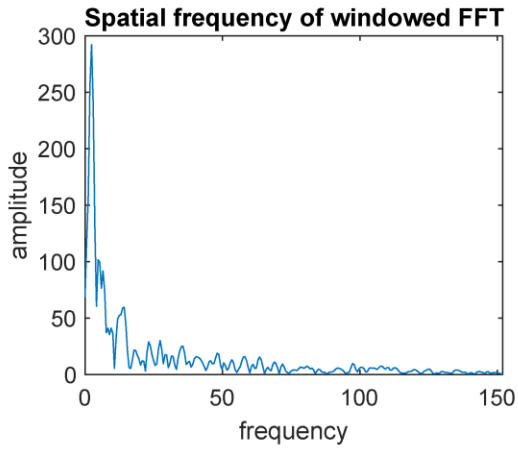
# Fault049



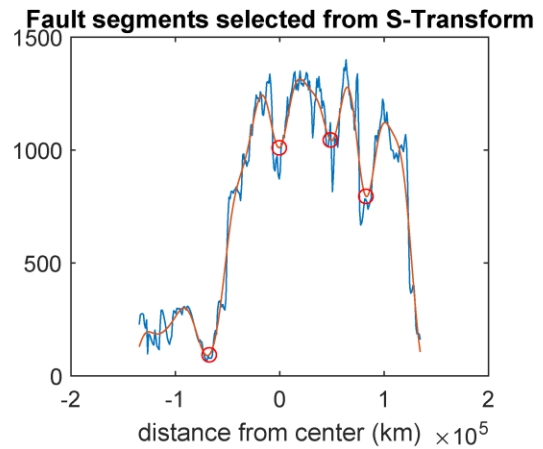
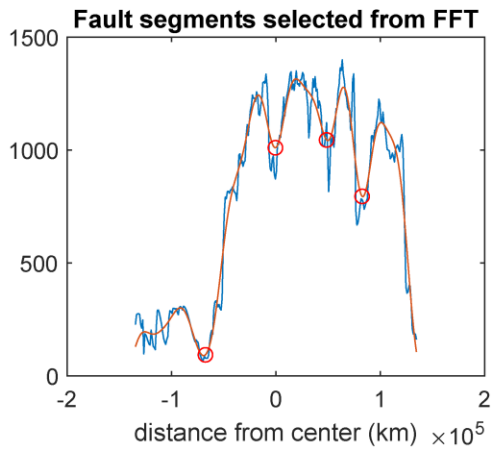
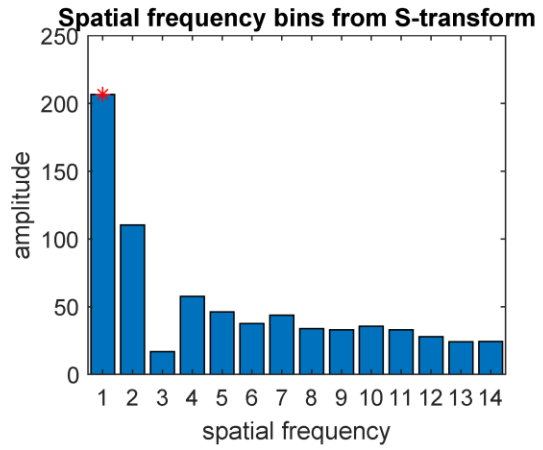
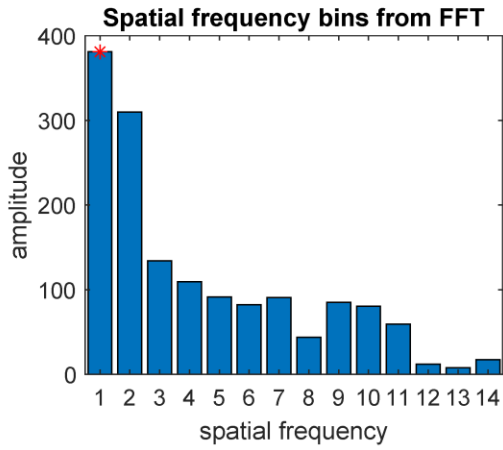
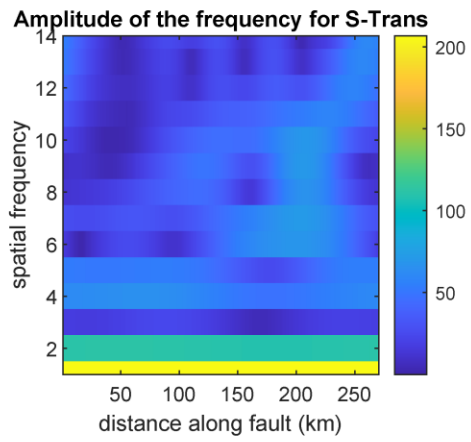
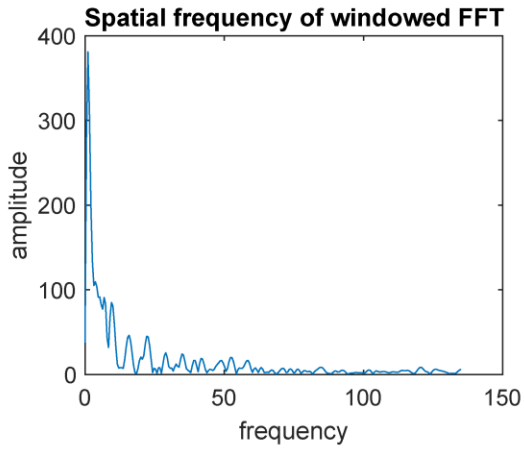
# Fault050



# Fault351



# Fault353



## Appendix J: Mars time period boundaries

Geological time period boundaries as defined by Tanaka (1986) using  $N(D)$  values (i.e., where  $N$  is the cumulative number of craters of diameter  $D$  km or greater in a normalized area, in this case  $10^6$  km<sup>2</sup>). Amazonian boundaries are defined using  $N(2)$ , Hesperian boundaries are defined with  $N(5)$ , and Noachian boundaries are defined using  $N(16)$ . Absolute ages were calculated by Fassett & Head (2008) employing a least-squares approach to fitting the chronology functions from Ivanov (2001) and Hartmann (2005), respectively. This table is modified from Fassett & Head (2008). (Table S1 in Chapter 3)

Boundary	$N(2)$	$N(5)$	$N(16)$	Neukum/Ivanov age (Ga)	Hartmann age (Ga)
Mid–Late Amazonian	40			0.66	0.27
Early–Mid Amazonian	150			2.46	1.02
<b>Hesperian–Amazonian</b>	<b>400</b>			<b>3.54</b>	<b>2.70</b>
Early–Late Hesperian		125		3.65	3.36
<b>Noachian–Hesperian</b>		<b>200</b>		<b>3.74</b>	<b>3.55</b>
Mid–Late Noachian			100	3.86	3.85
Early–Mid Noachian			200	3.97	3.96

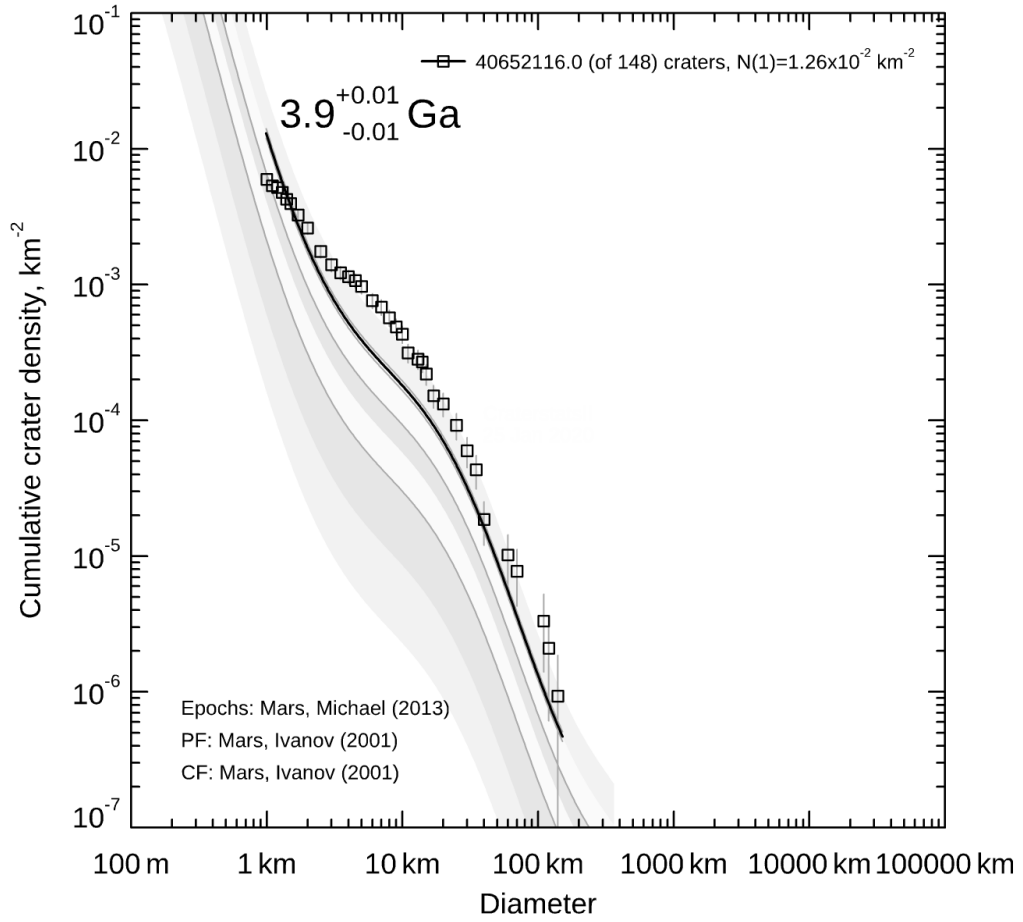
## Appendix K: Crater dating fault metrics summary table

Summarized fault length, measured throw ( $t_{\max}$ ), calculated displacement ( $D_{\max}$ ) for a 30° fault dip angle, calculated  $D_{\max}/L$ , absolute model ages as determined with the Hartmann (2005) and Ivanov (2001) models, coordinates, and the local geological unit (Tanaka et al., 2014) for all 28 faults in this study. (Table S2 in Chapter 3)

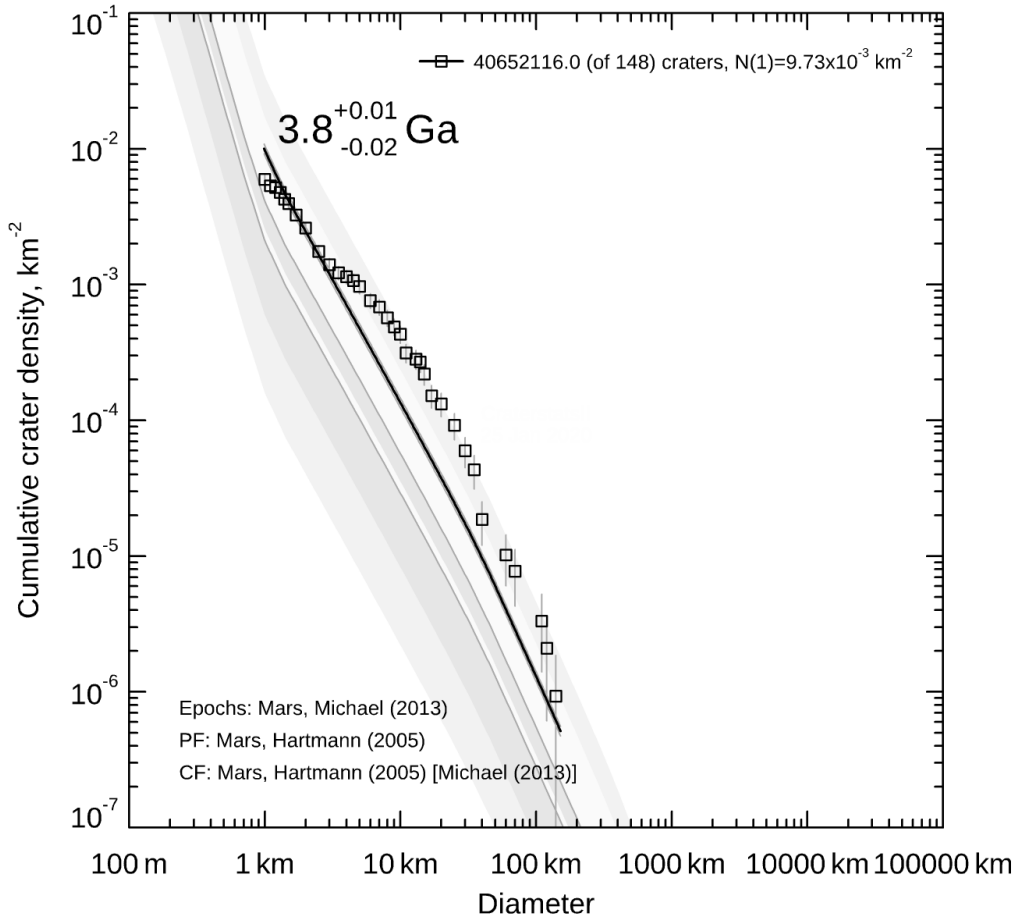
scarp #	L (km)	$t_{\max}$ (m)	$D_{\max}$ (m)	$D_{\max}/L$	Crater count	Hartmann			Neukum/Ivanov			Lat	Long	Geol. Unit*
						Age	+	-	Age	+	-			
1	246	488	976	0.00396	6	3.9	0.05	0.09	4	0.05	0.08	-4.9238	45.4136	mNh/eNh
2	60	182	364	0.00606	2	4.2	0.08	0.2	4.2	0.08	0.2	29.9182	54.6383	mNh
3	79	297	594	0.00749	5	3.9	0.06	0.09	4	0.05	0.09	29.9591	55.282	mNh
4	209	702	1,404	0.00671	3	3.7	0.08	0.2	3.9	0.07	0.1	29.21	44.951	mNh
5	95	397	794	0.00837	4	3.9	0.06	0.1	4	0.06	0.1	28.6386	19.8267	mNh
6	258	520	1,040	0.00403	6	3.8	0.06	0.01	3.9	0.05	0.08	27.4946	39.9203	mNh
7	180	428	856	0.00475	6	3.8	0.06	0.01	3.9	0.05	0.08	-2.6622	122.4348	mNh
8	112	313	626	0.00557	3	3.9	0.07	0.1	4	0.07	0.1	-0.1526	117.1688	mNh/eNh
9	77	391	782	0.01013	4	3.9	0.06	0.1	4	0.06	0.1	-13.3058	115.2849	mNh
10	188	356	712	0.00378	3	3.8	0.08	0.2	3.9	0.07	0.1	-12.3568	95.1244	mNh/eNh
11	82	178	356	0.00435	2	4.1	0.08	0.2	4.2	0.08	0.2	-23.8407	173.2762	mNh
12	260	348	696	0.00268	5	3.9	0.06	0.09	3.8	0.06	0.1	-20.1865	111.236	eHv
13	71	673	1,346	0.01883	3	4.1	0.07	0.1	4.2	0.07	0.1	-6.369	120.7582	mNh
14	610	1,382	2,764	0.00453	12	3.6	0.06	0.01	3.7	0.05	0.07	-6.3171	69.5411	eNh
15	184	502	1,004	0.00546	7	3.8	0.05	0.09	3.9	0.05	0.08	26.2936	14.1014	lNh
16	328	874	1,748	0.00533	13	3.9	0.04	0.05	4	0.04	0.05	-19.3747	-164.5602	mNh
17	241	742	1,484	0.00615	8	3.8	0.05	0.08	3.9	0.05	0.07	-10.0085	-159.7985	mNh
18	341	746	1,492	0.00437	11	3.8	0.04	0.06	3.9	0.04	0.06	-12.5296	-157.4053	mNh
19	138	589	1,178	0.00851	3	3.8	0.08	0.2	3.9	0.07	0.2	-11.754	-164.7447	mNh
20	158	489	978	0.00621	6	3.9	0.05	0.08	4	0.05	0.08	-9.9383	-163.3955	mNh
21	157	162	324	0.00206	4	3.8	0.07	0.1	3.9	0.06	0.1	21.6883	-4.6789	mNh
22	95	319	638	0.00672	2	4.2	0.08	0.2	4.3	0.08	0.2	24.3534	41.2876	mNh
23	109	390	780	0.00716	5	3.9	0.06	0.01	4	0.06	0.09	24.593	43.2004	mNh
24	78	390	780	0.01003	5	3.9	0.06	0.09	4	0.06	0.09	-27.1613	38.2827	eNh
25	110	710	1,420	0.01288	7	3.9	0.05	0.08	4	0.05	0.07	-22.4941	39.4602	eNh
26	95	783	1,566	0.01652	2	3.8	0.09	0.3	3.9	0.08	0.2	-21.3726	34.4336	eNh
27	212	786	1,572	0.00743	7	3.9	0.05	0.08	4	0.05	0.07	-22.7711	20.5826	mNh
28	172	894	1,788	0.01038	5	3.9	0.06	0.01	4	0.06	0.09	-27.2903	18.9537	eNh

\*eNh = early Noachian highland unit, mNh = middle Noachian highland unit, lNh = late Noachian highland unit, eHv = early Hesperian volcanic unit

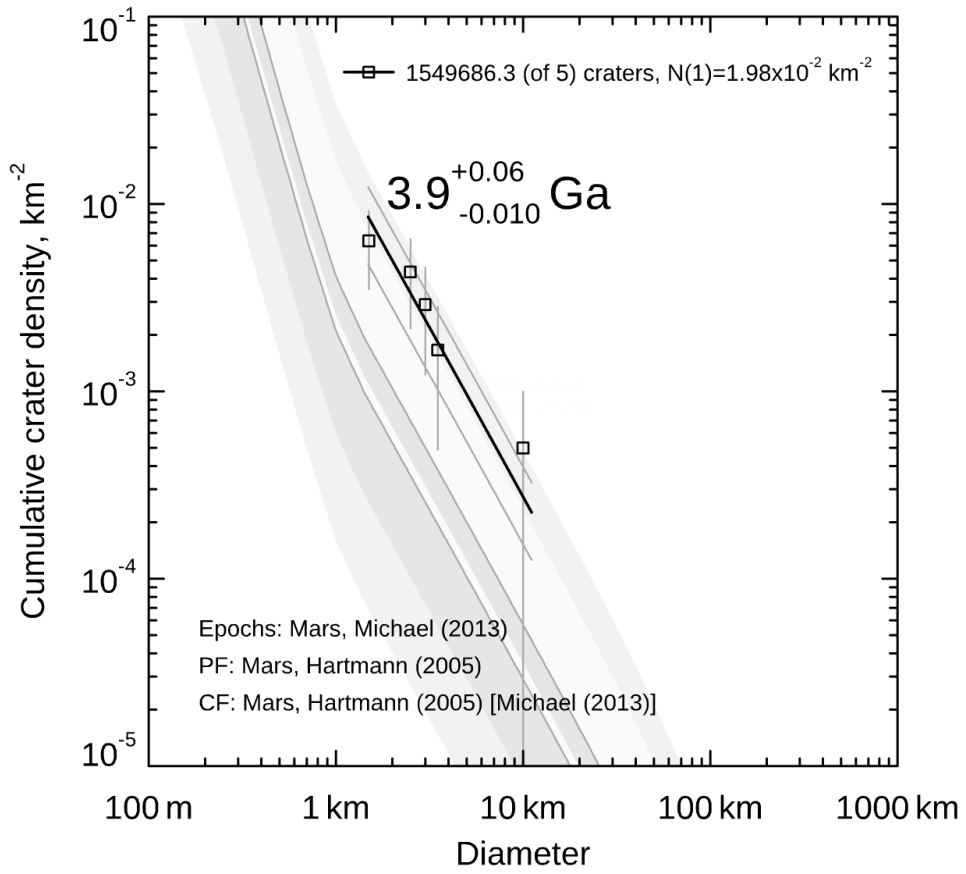
**Appendix L: Aggregate Hartmann Age CraterStats plot ( $n = 28$ )**



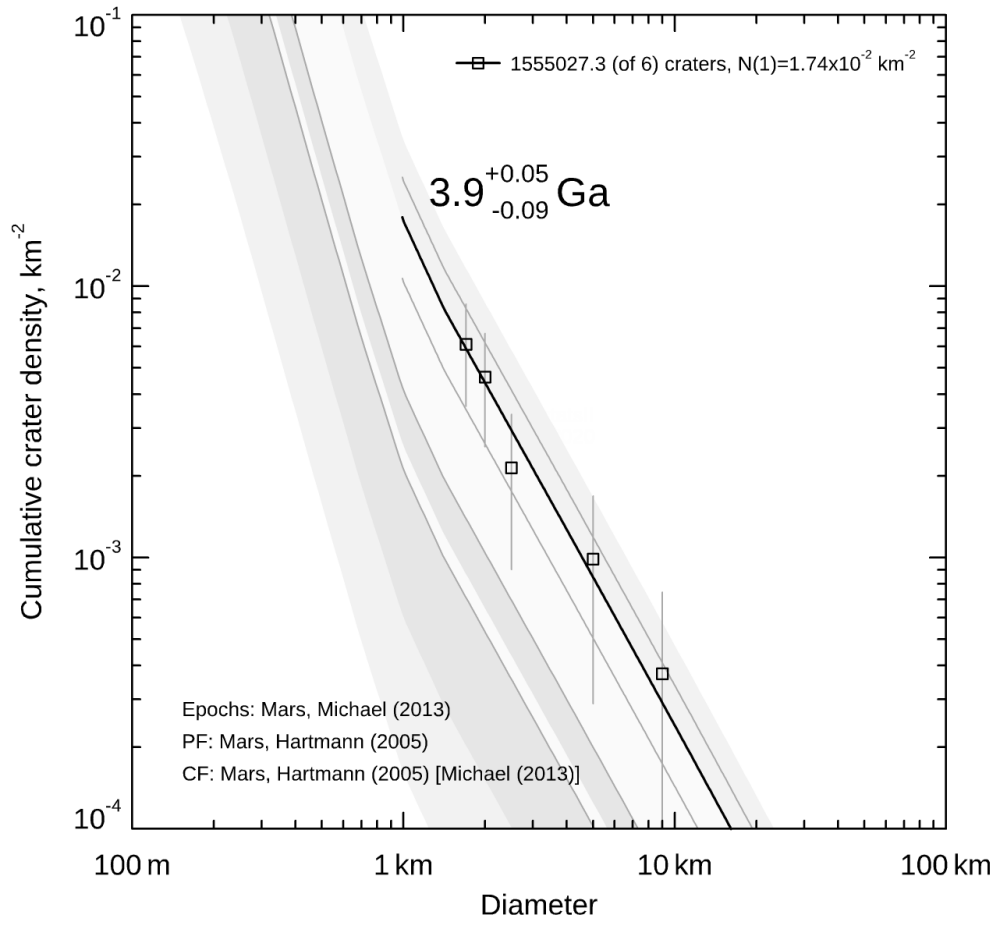
**Appendix M: Aggregate Neukum/Ivanov Age CraterStats plot (n = 28)**



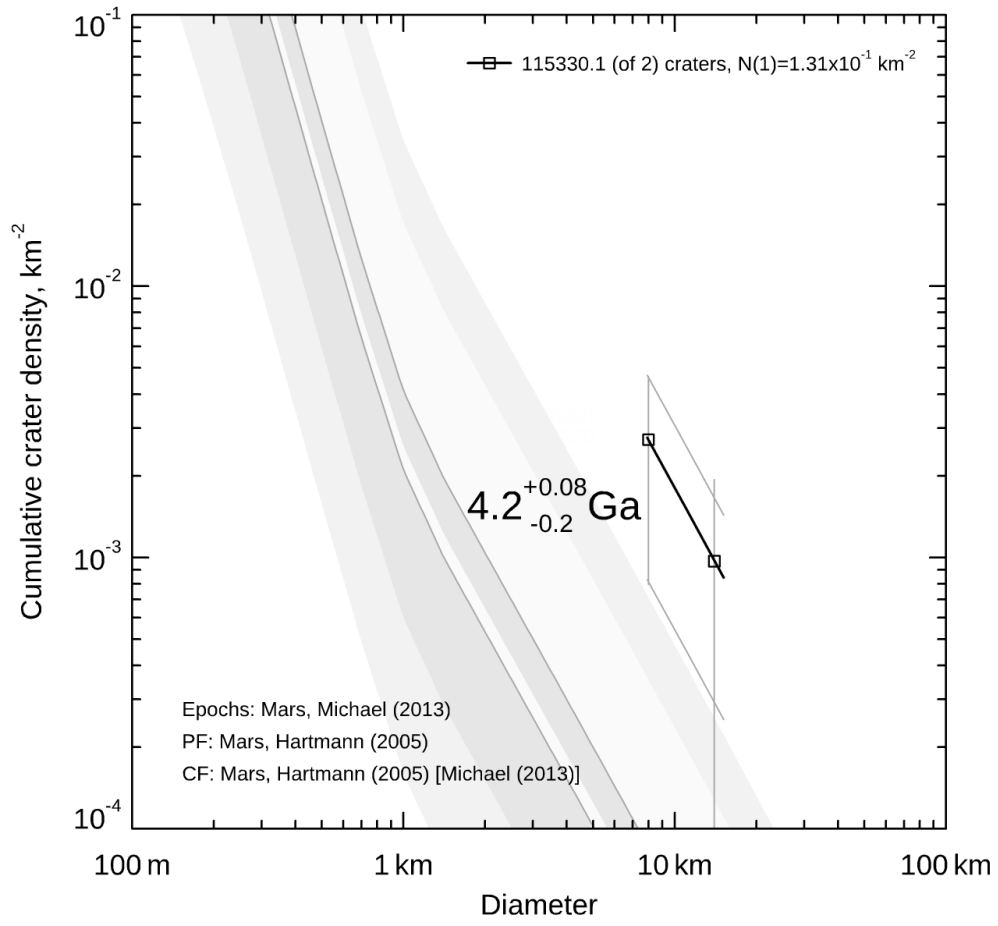
**Appendix N: Hartmann Age for each fault (CraterStats plots)**



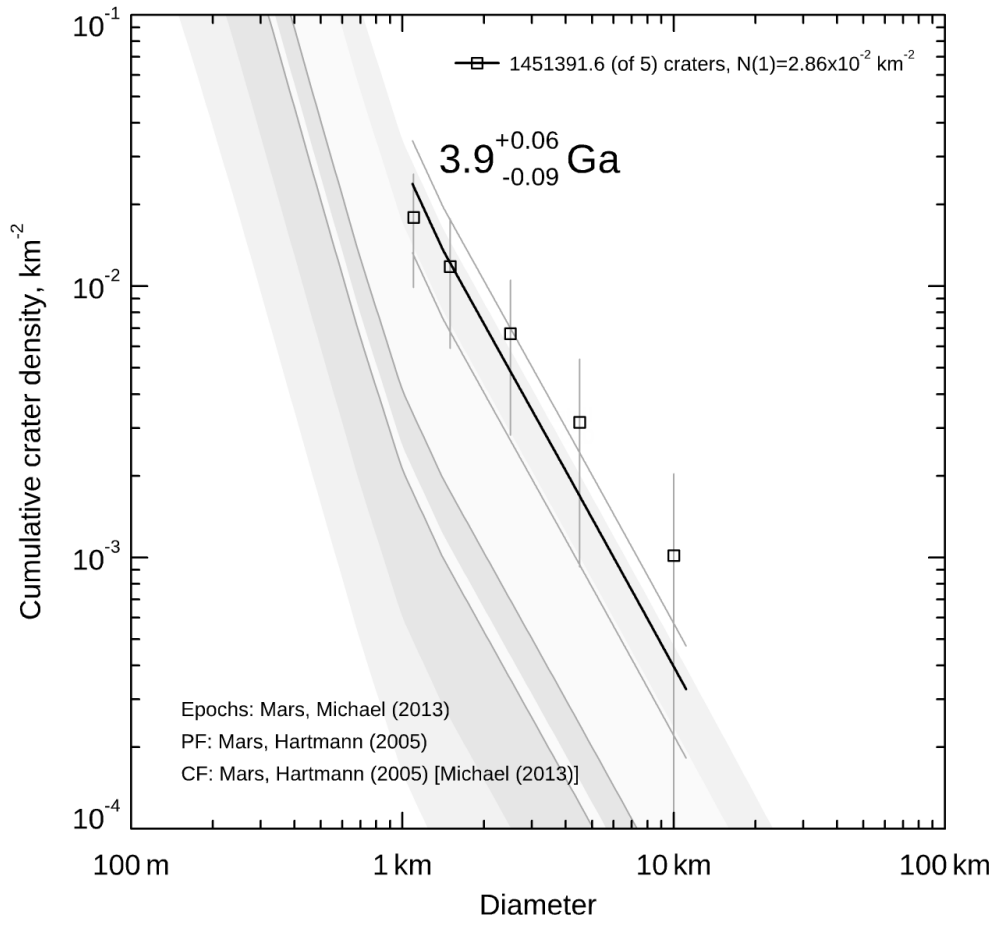
Fault 1 Hartmann age



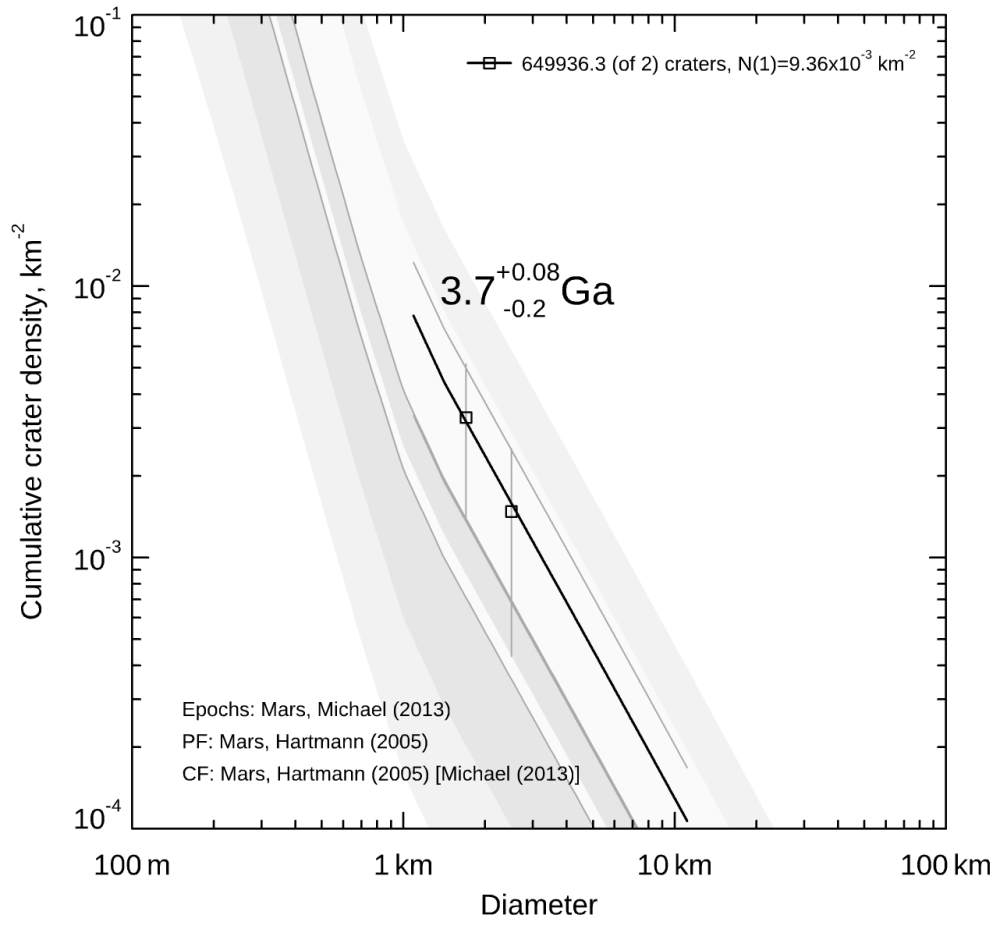
Fault 2 Hartmann age



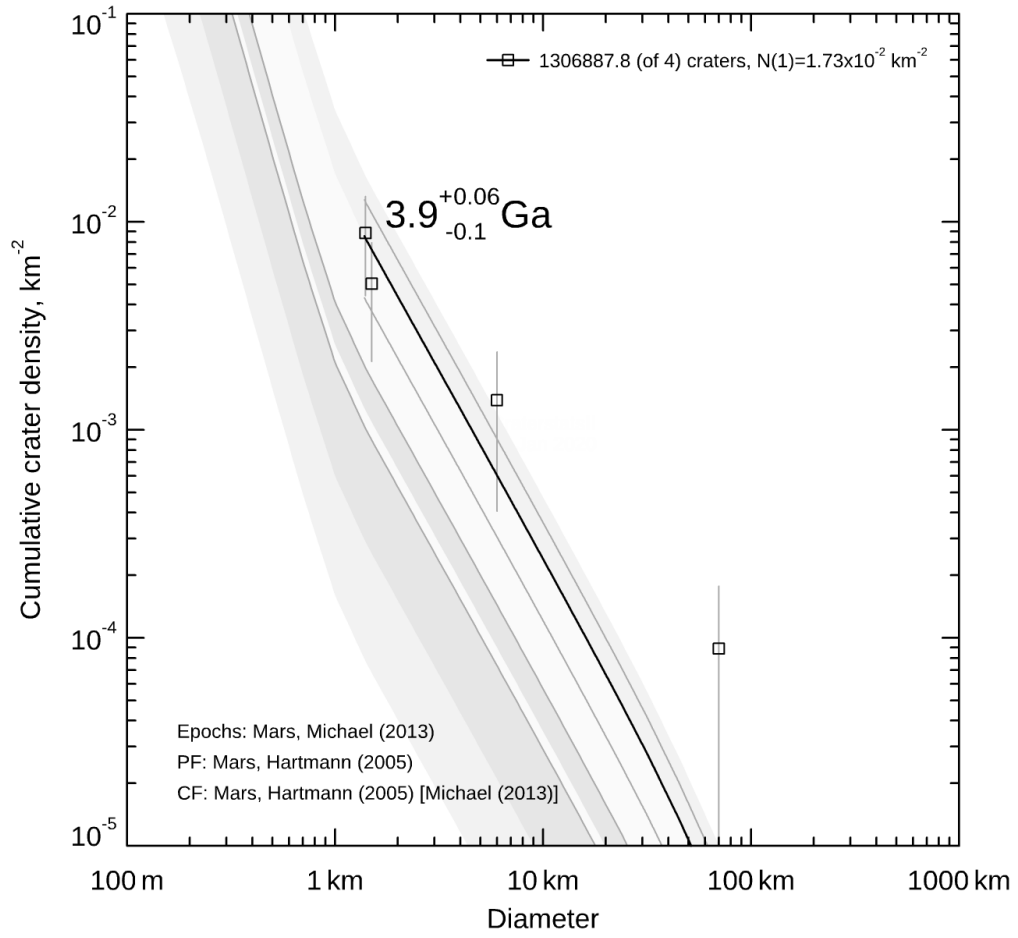
Fault 3 Hartmann age



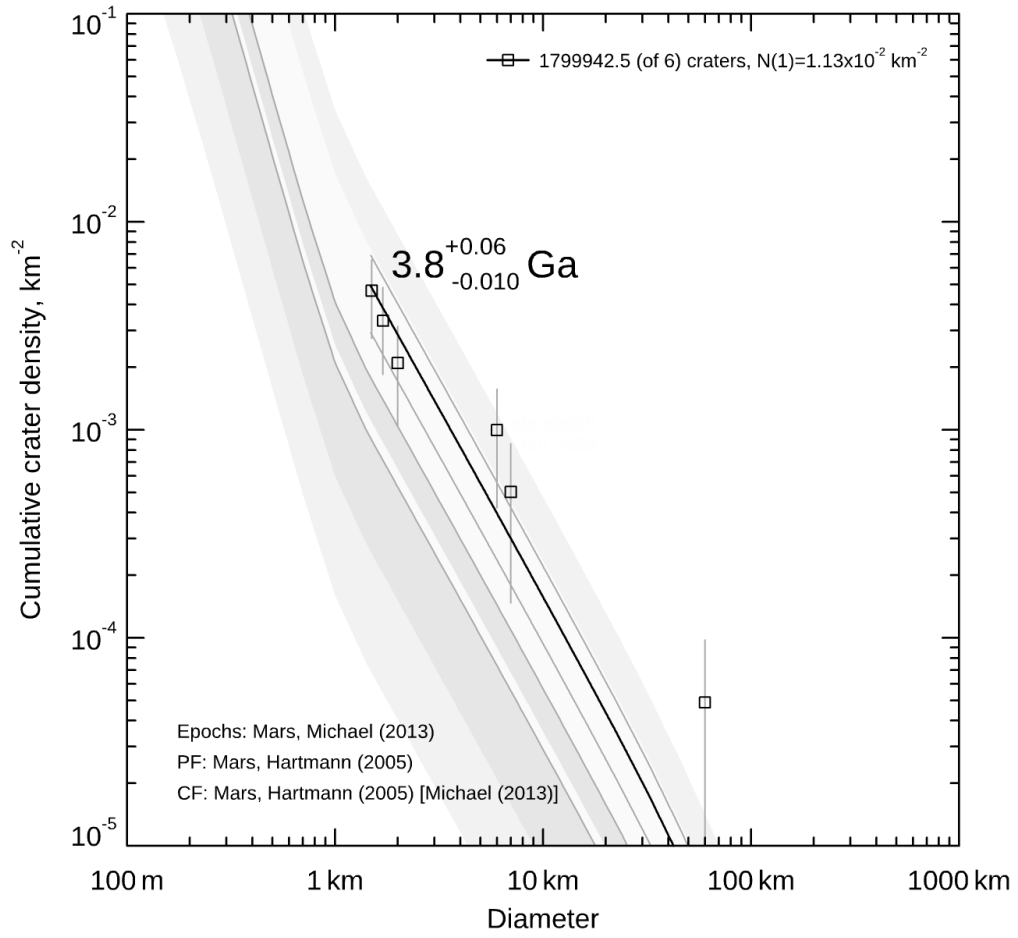
Fault 4 Hartmann age



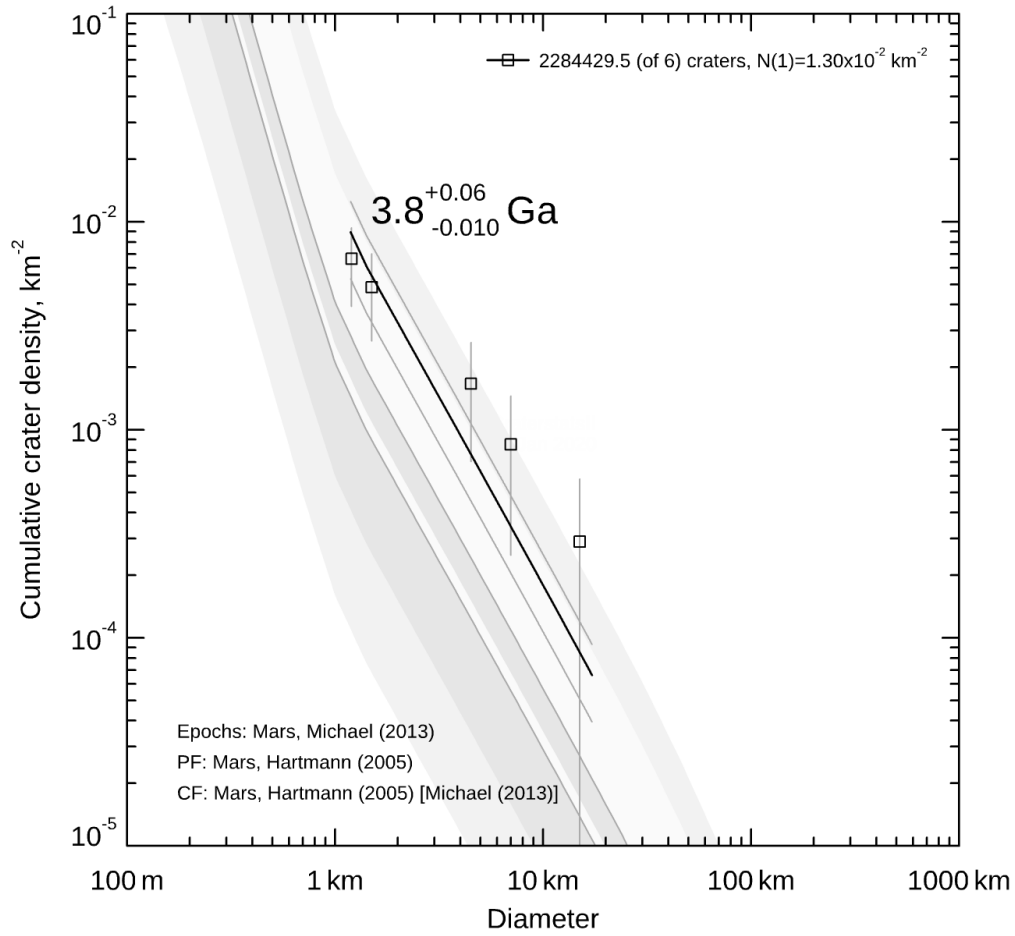
Fault 5 Hartmann age



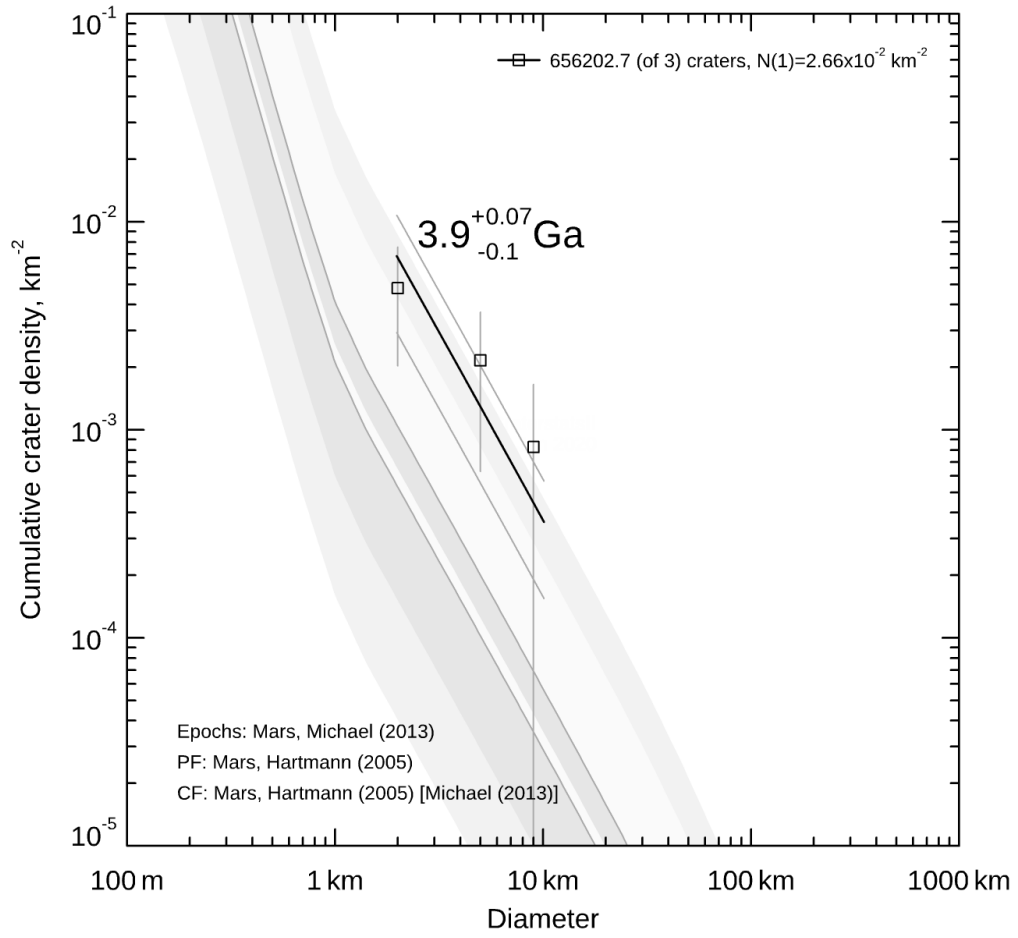
Fault 6 Hartmann age



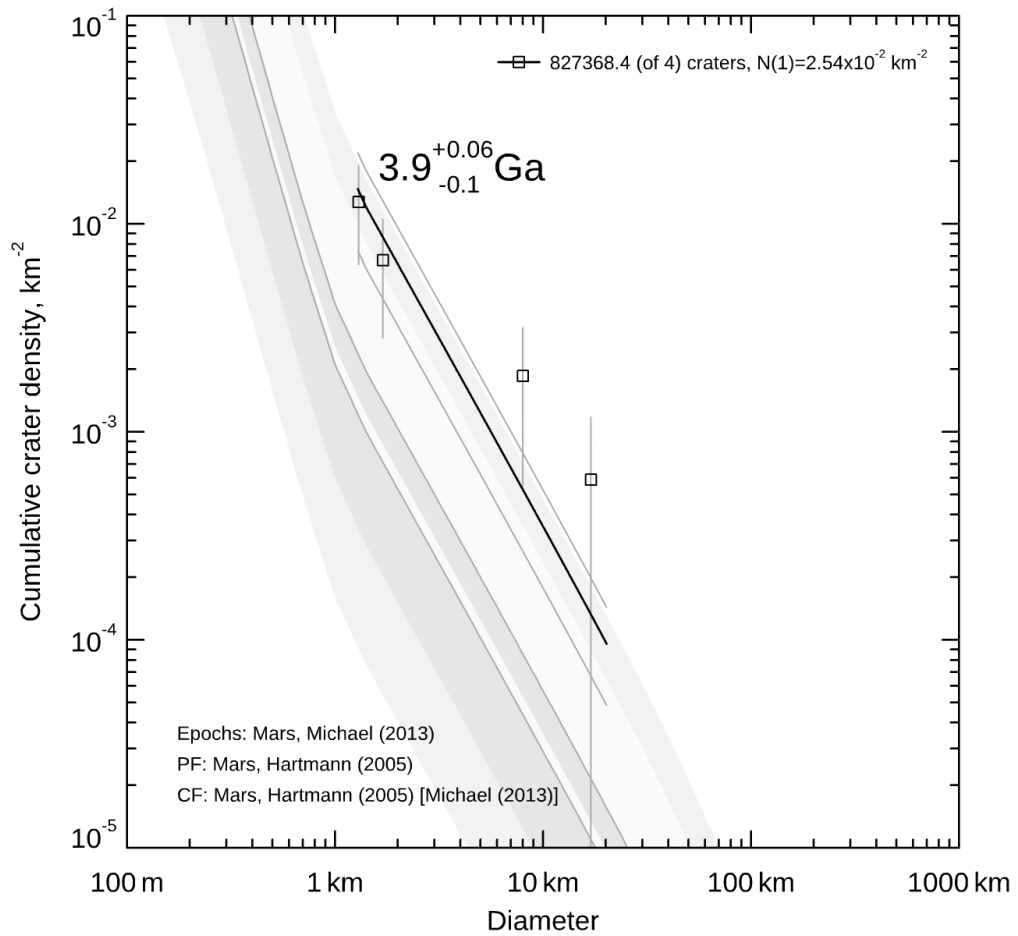
Fault 7 Hartmann age



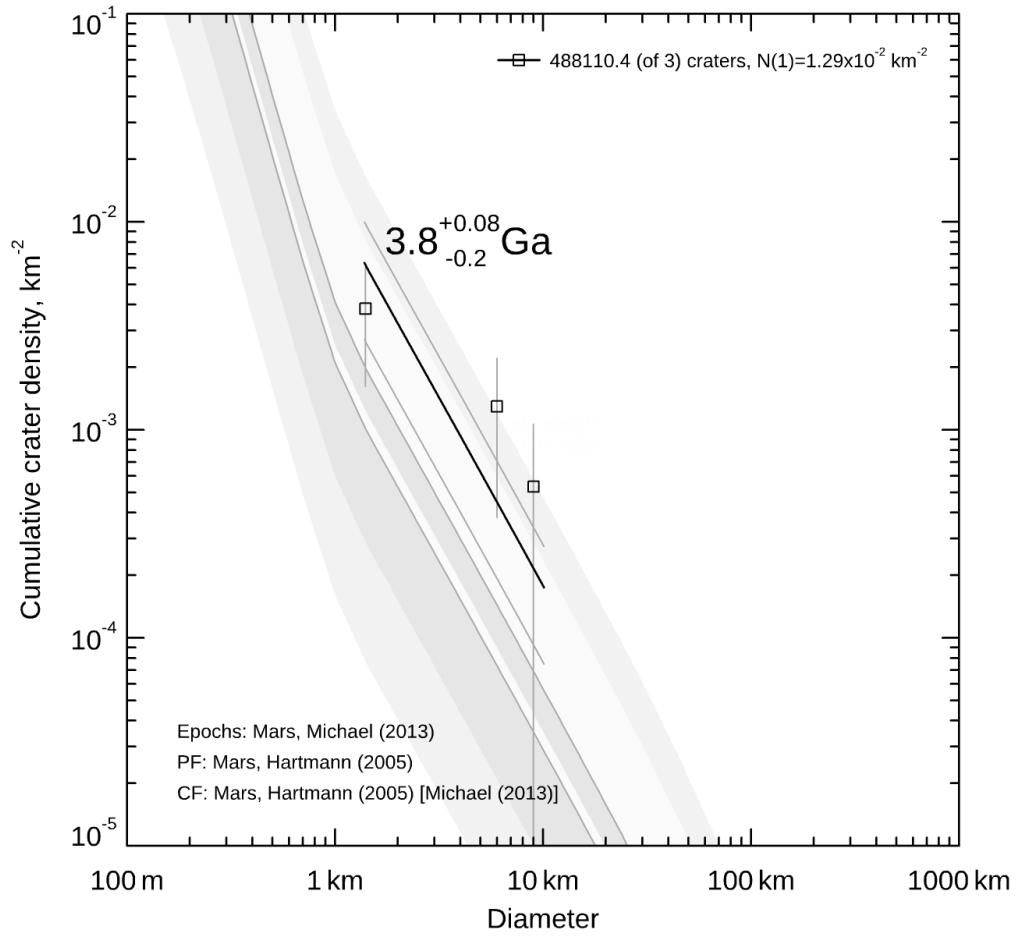
Fault 8 Hartmann age



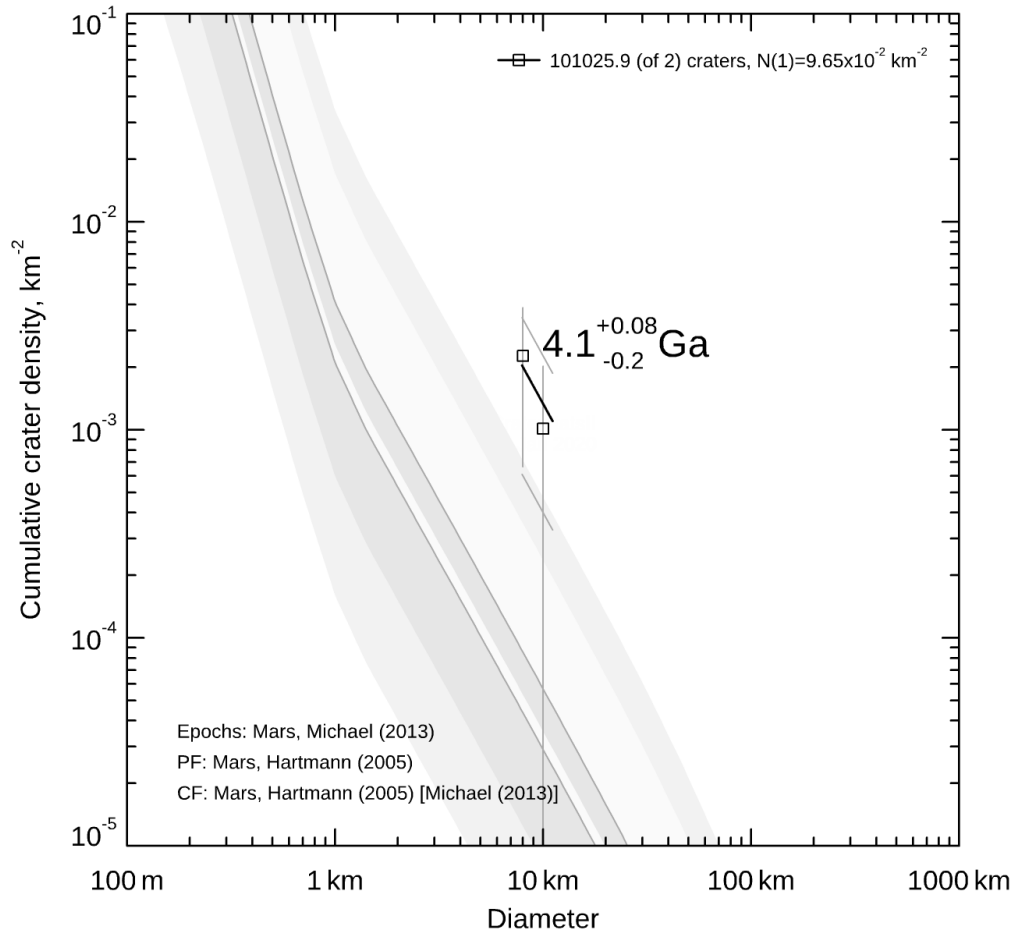
Fault 9 Hartmann age



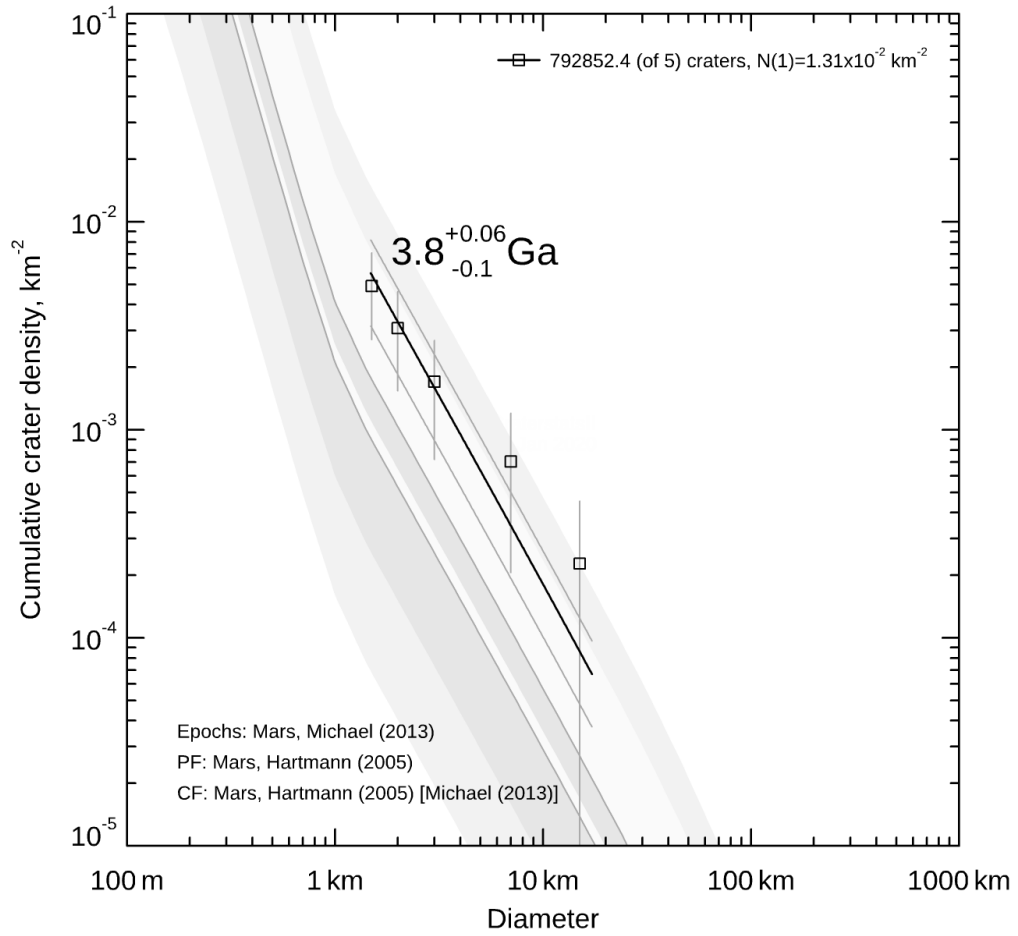
Fault 10 Hartmann age



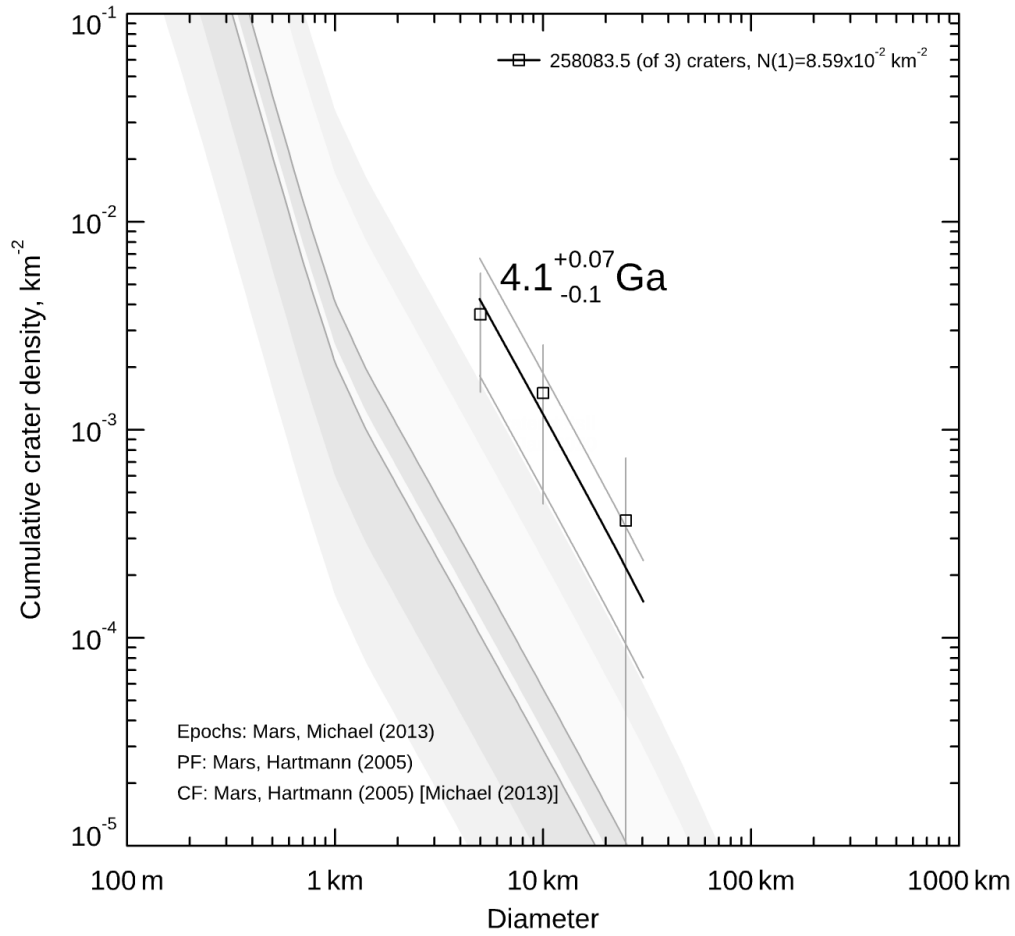
Fault 11 Hartmann age



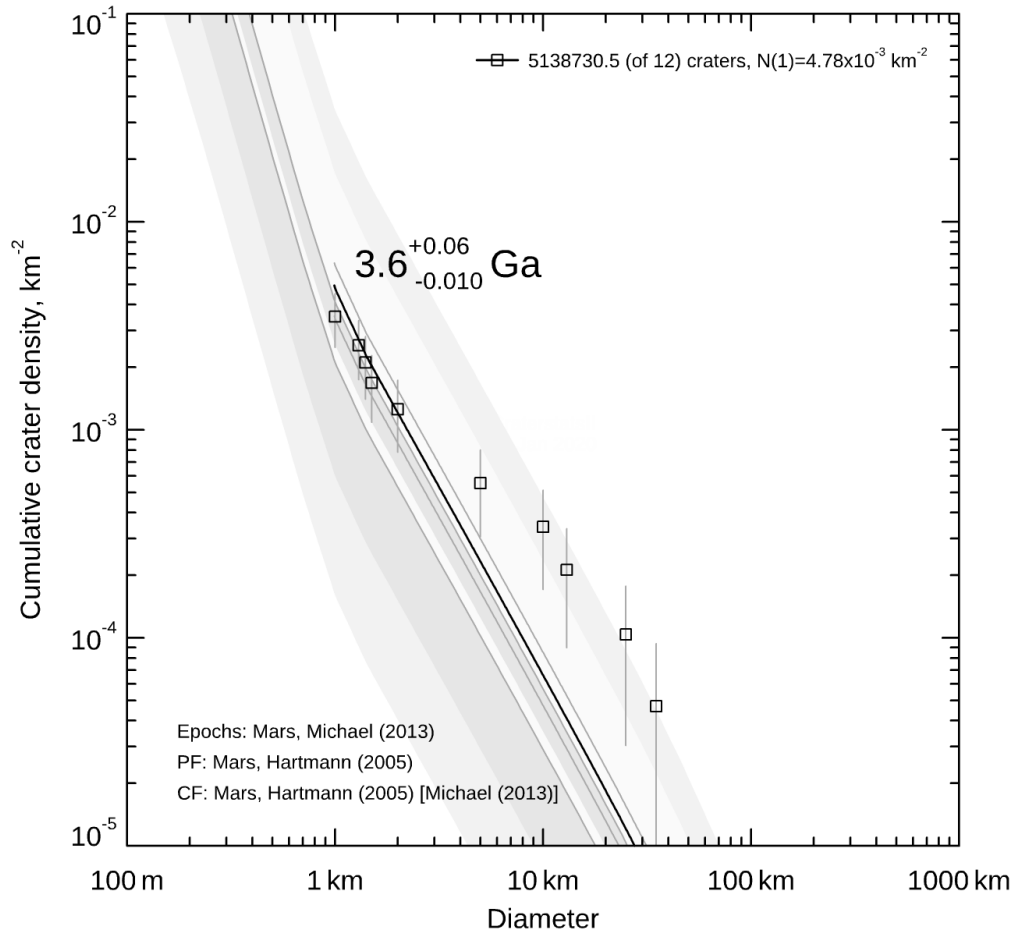
Fault 12 Hartmann age



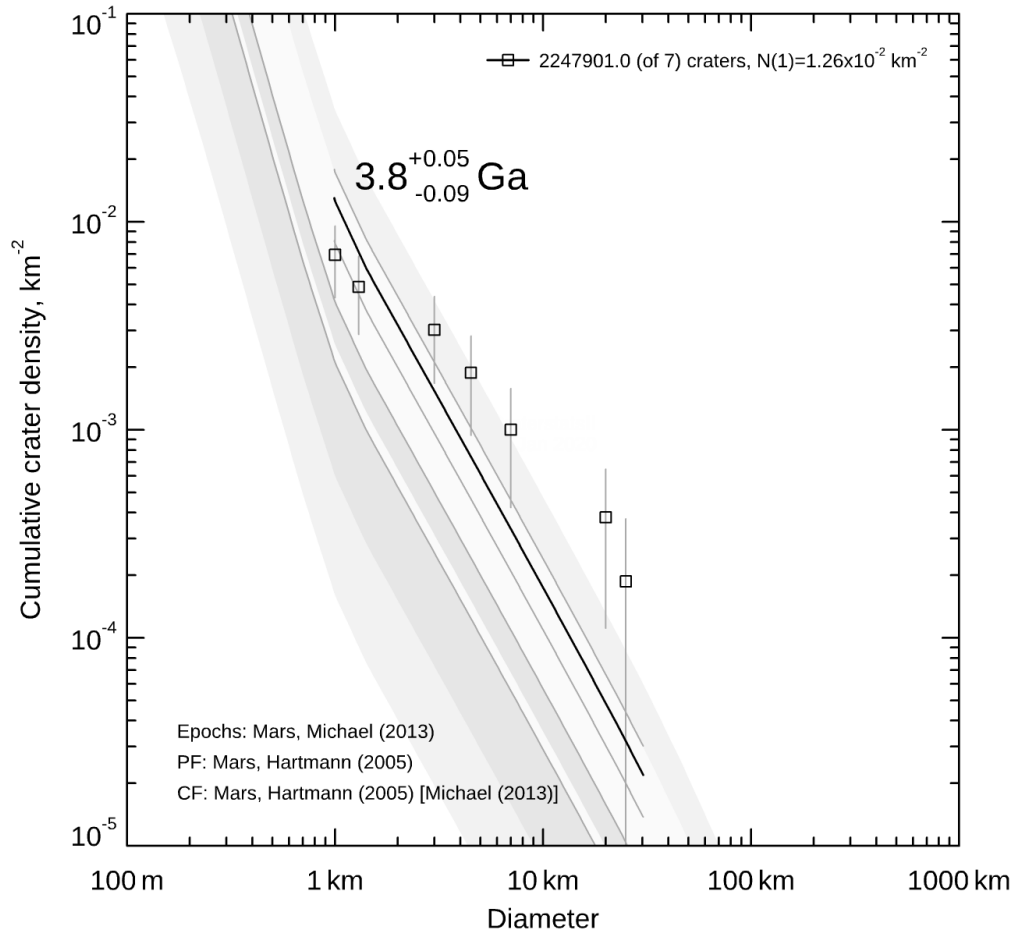
Fault 13 Hartmann age



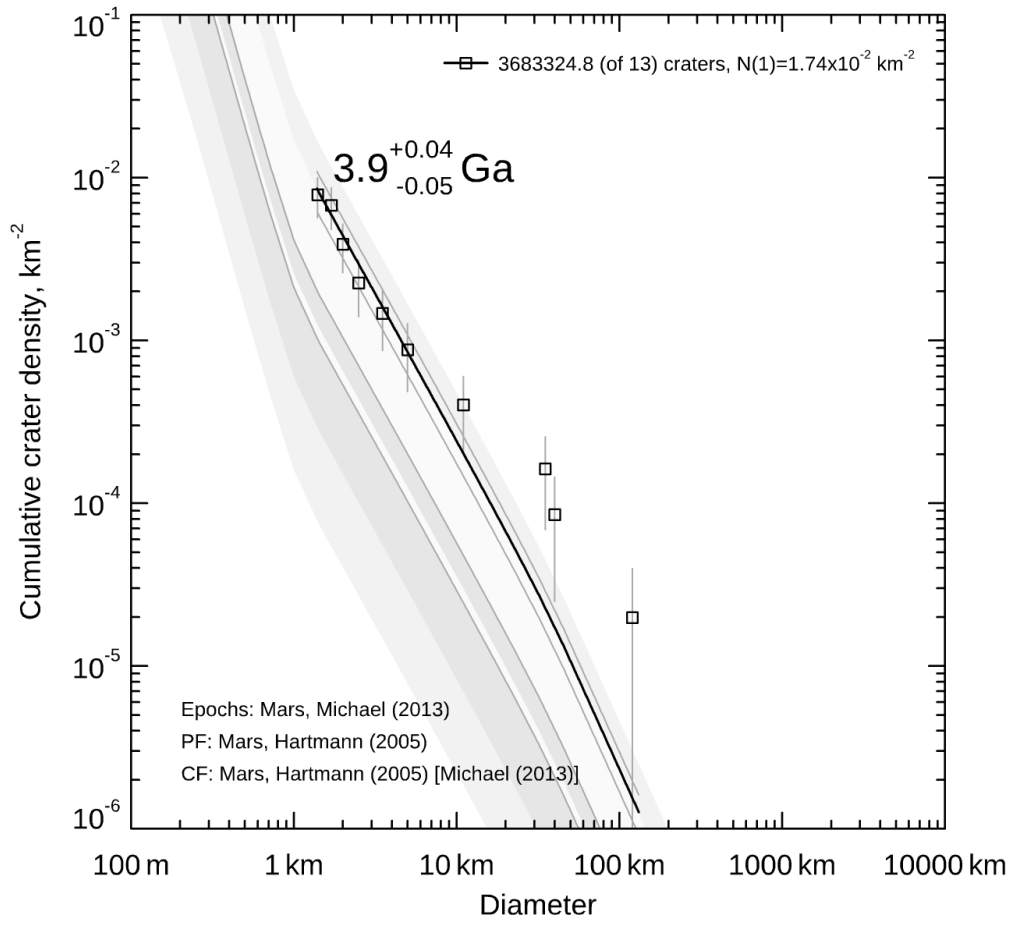
Fault 14 Hartmann age



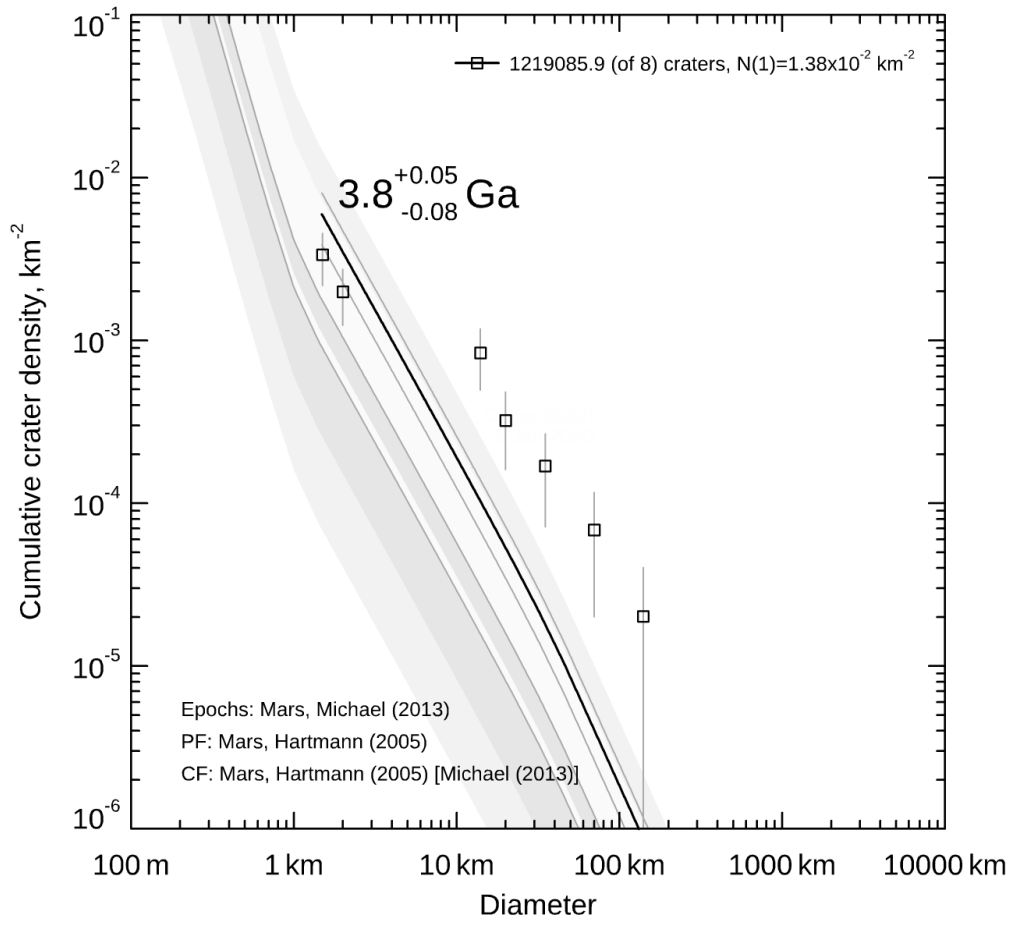
Fault 15 Hartmann age



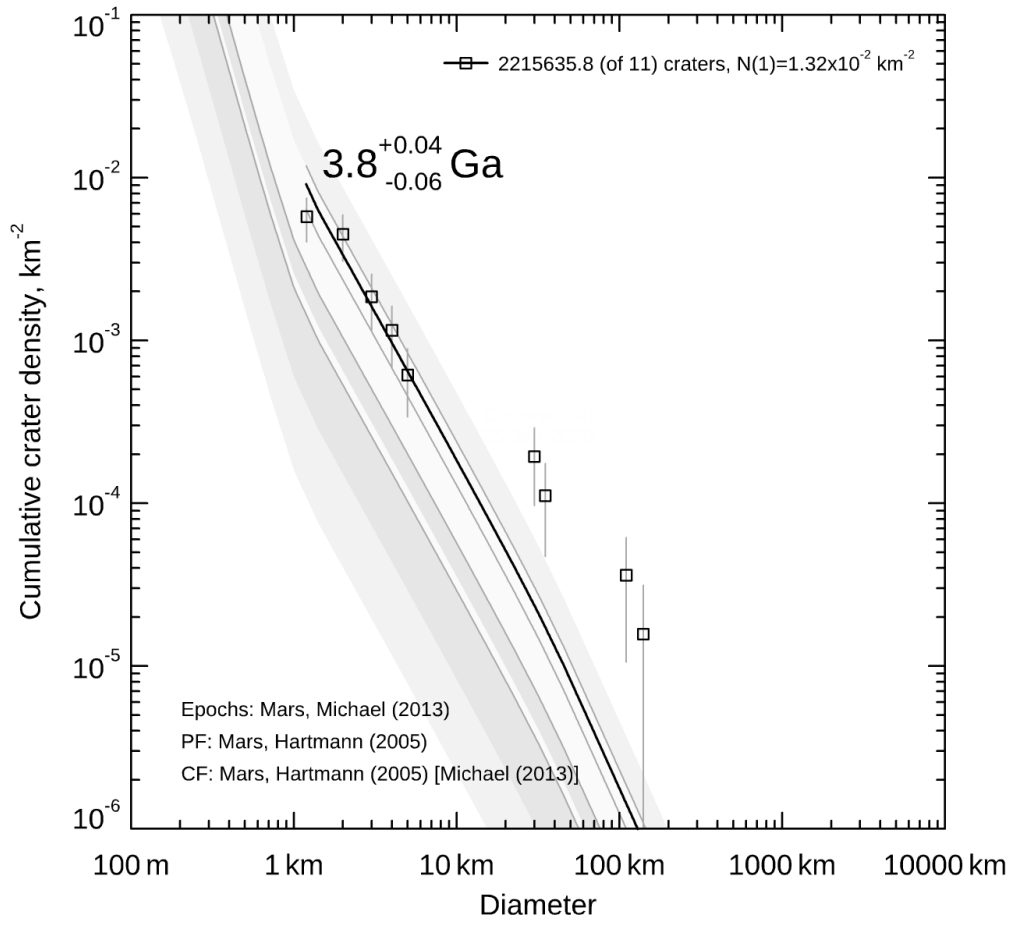
Fault 16 Hartmann age



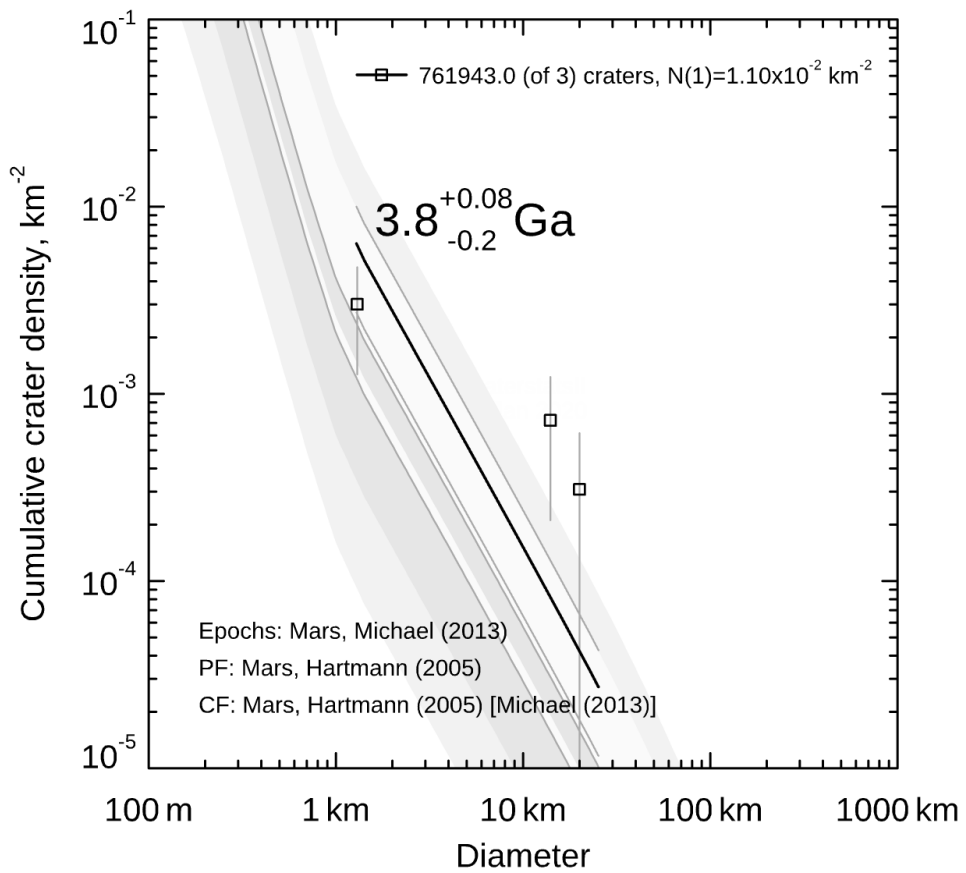
Fault 17 Hartmann age



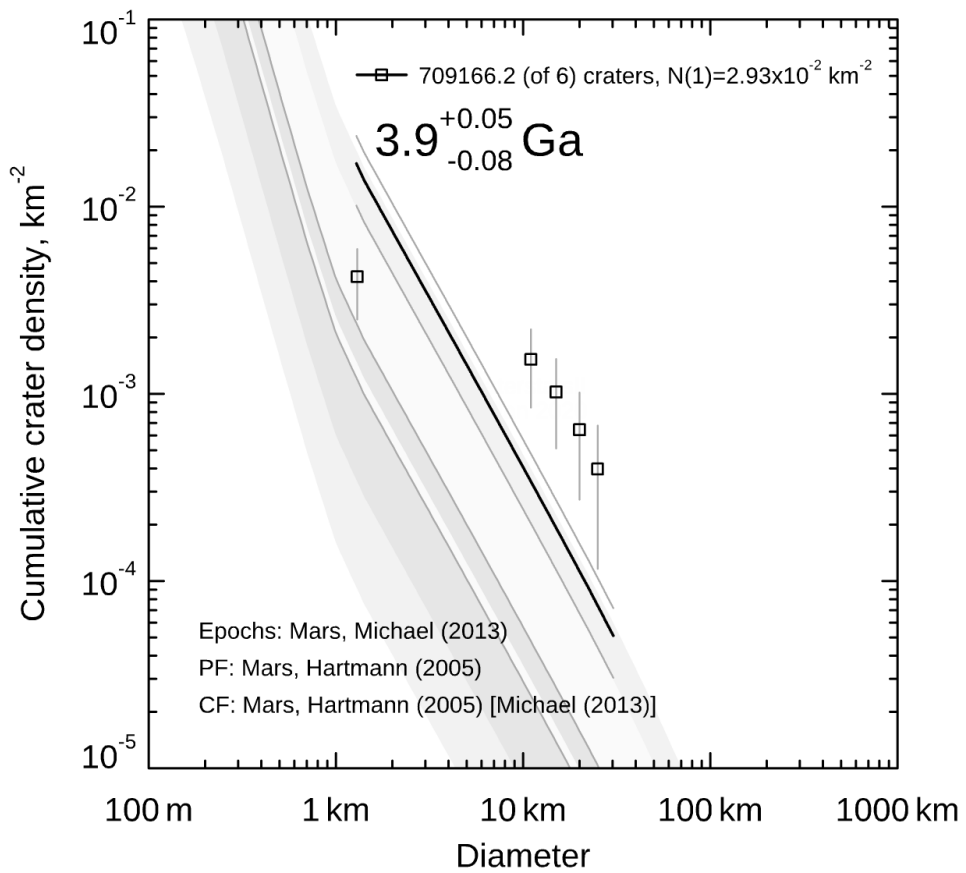
Fault 18 Hartmann age



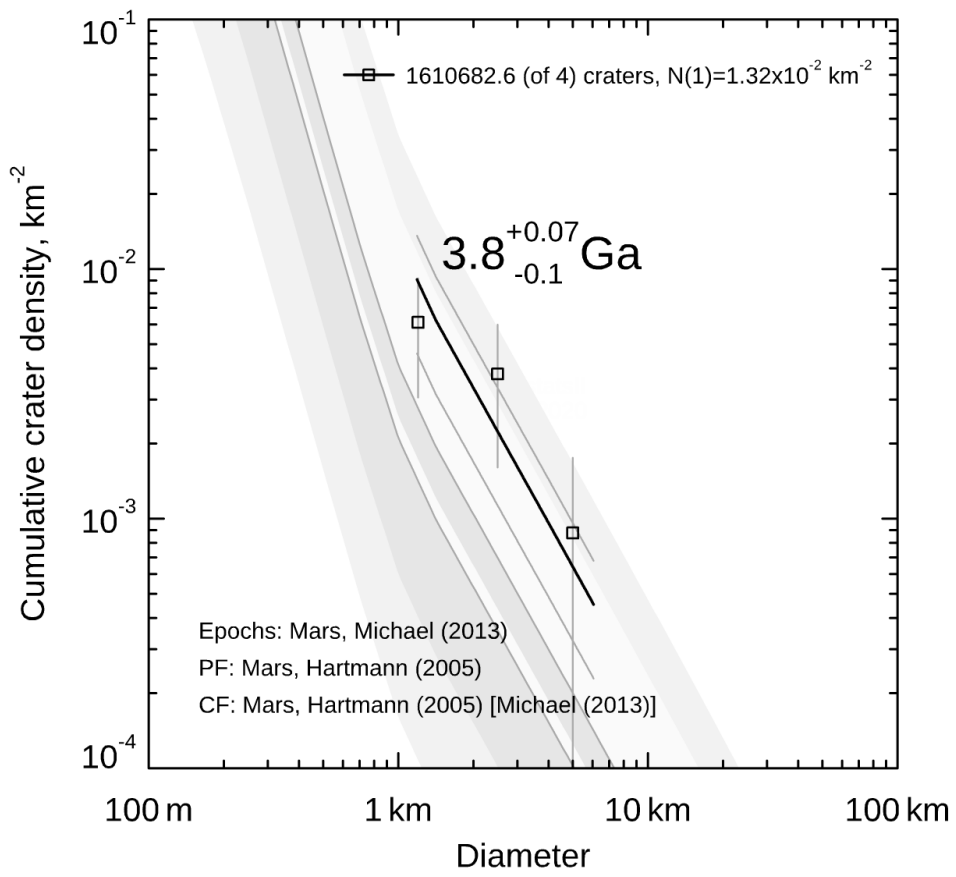
Fault 19 Hartmann age



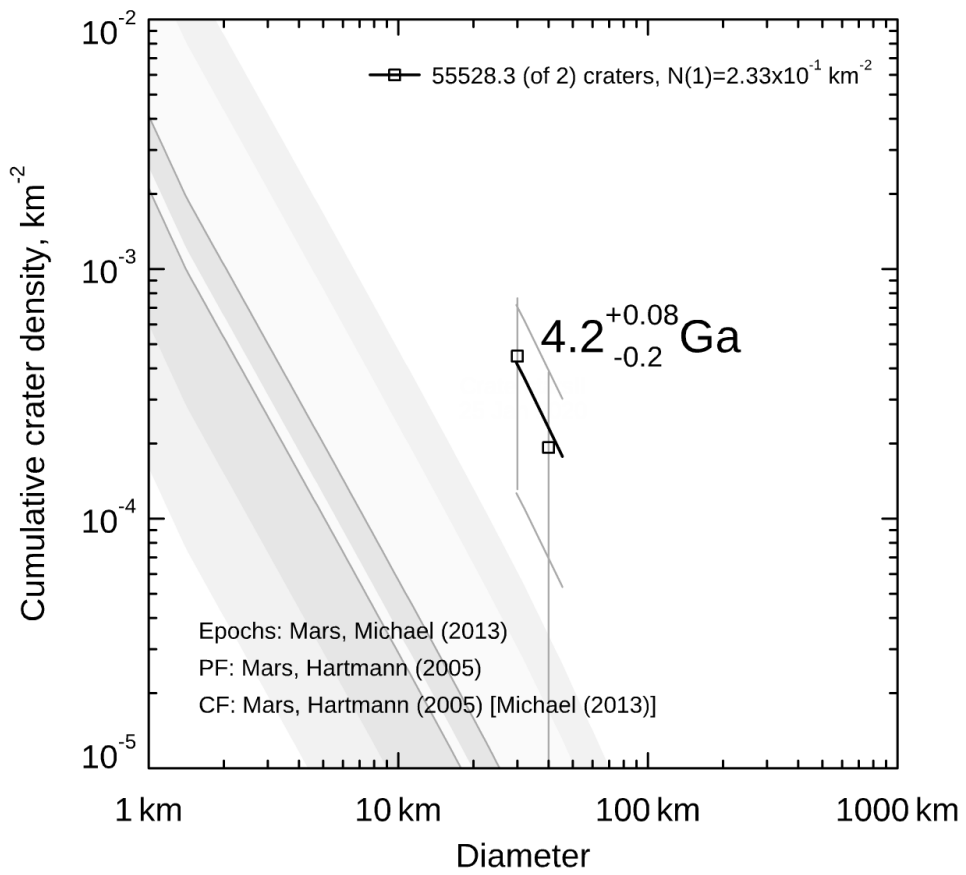
Fault 20 Hartmann age



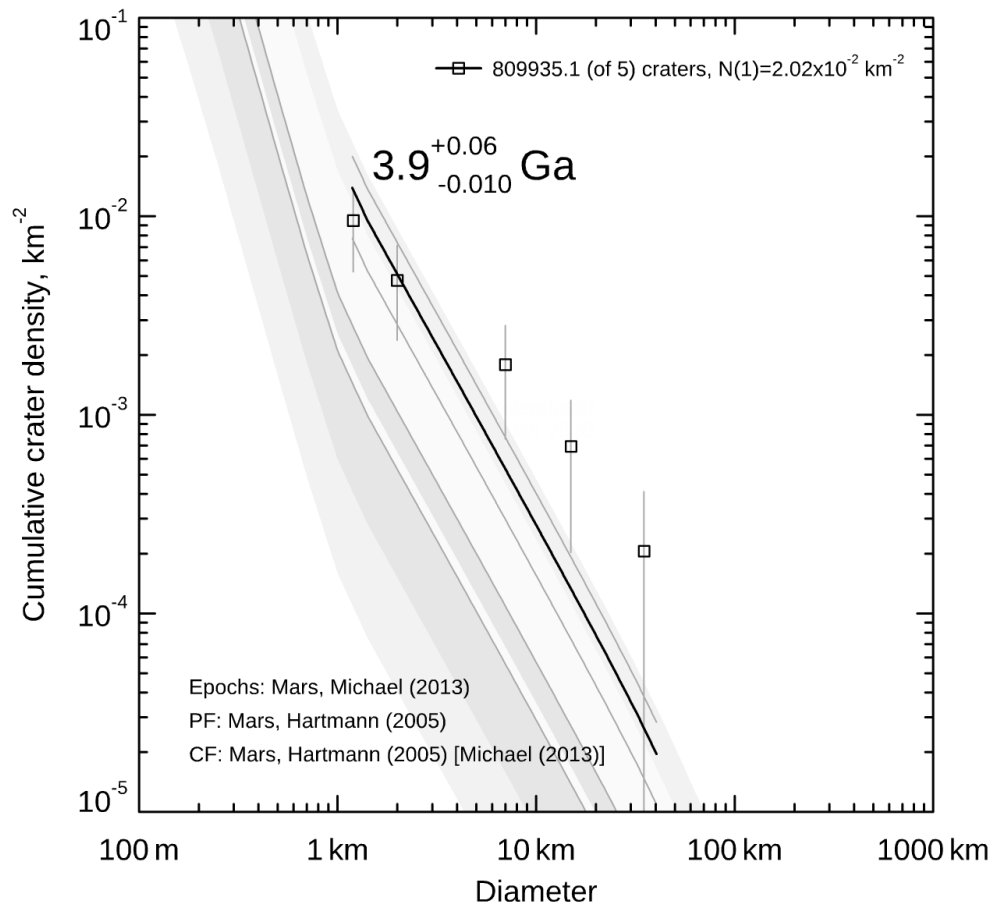
Fault 21 Hartmann age



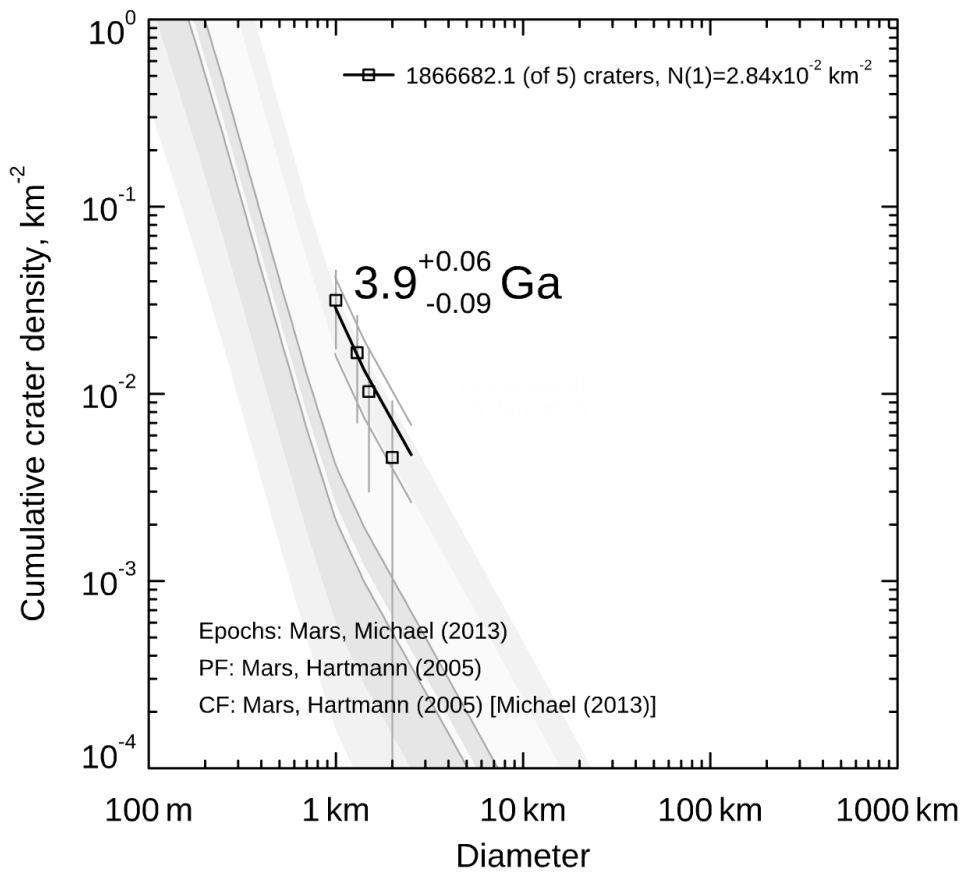
Fault 22 Hartmann age



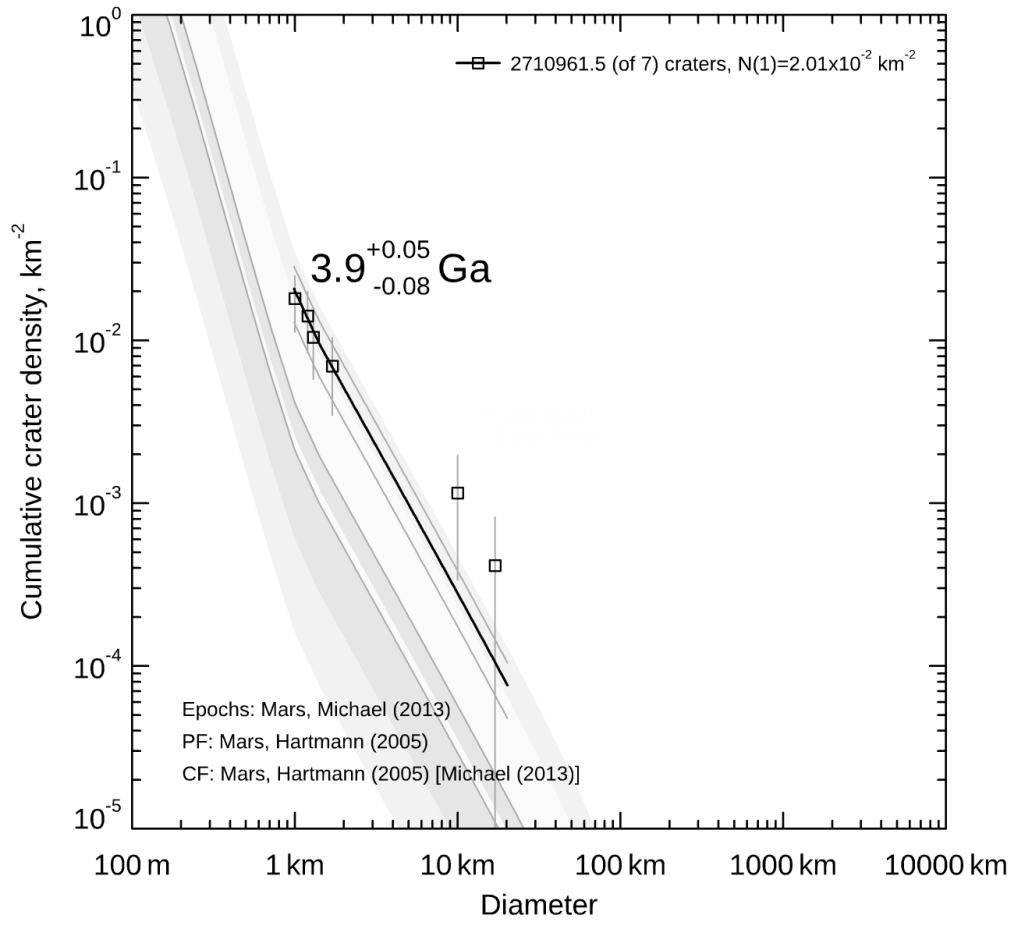
Fault 23 Hartmann age



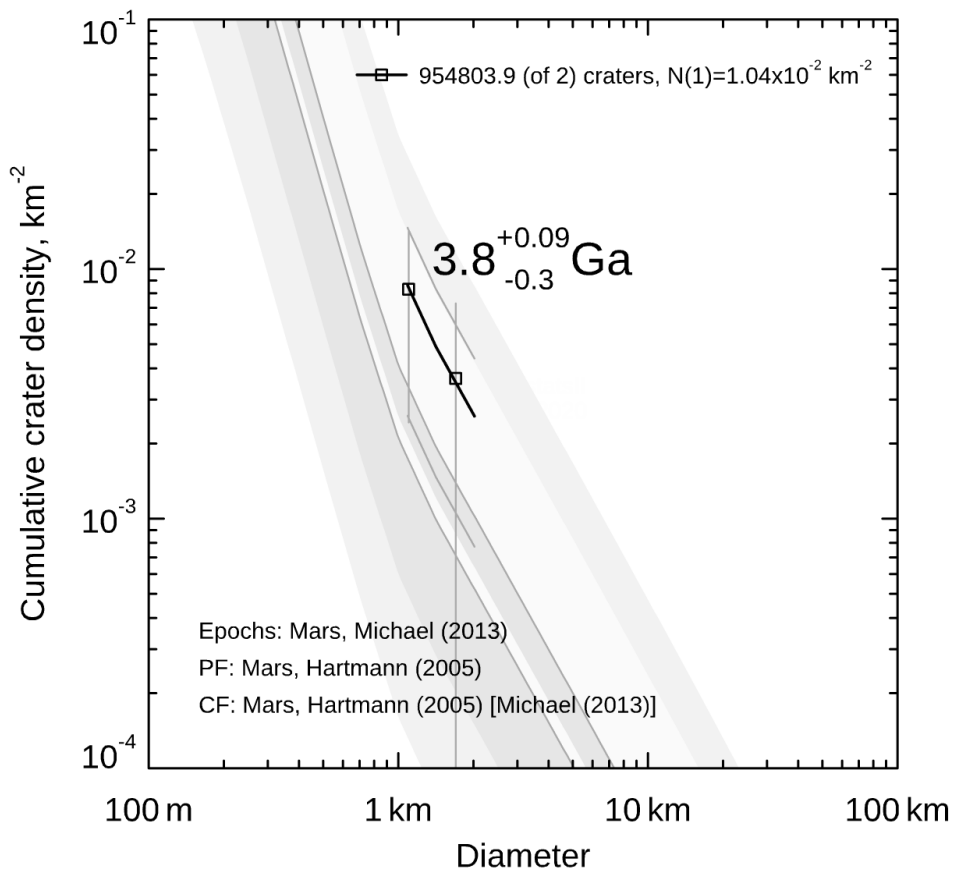
Fault 24 Hartmann age



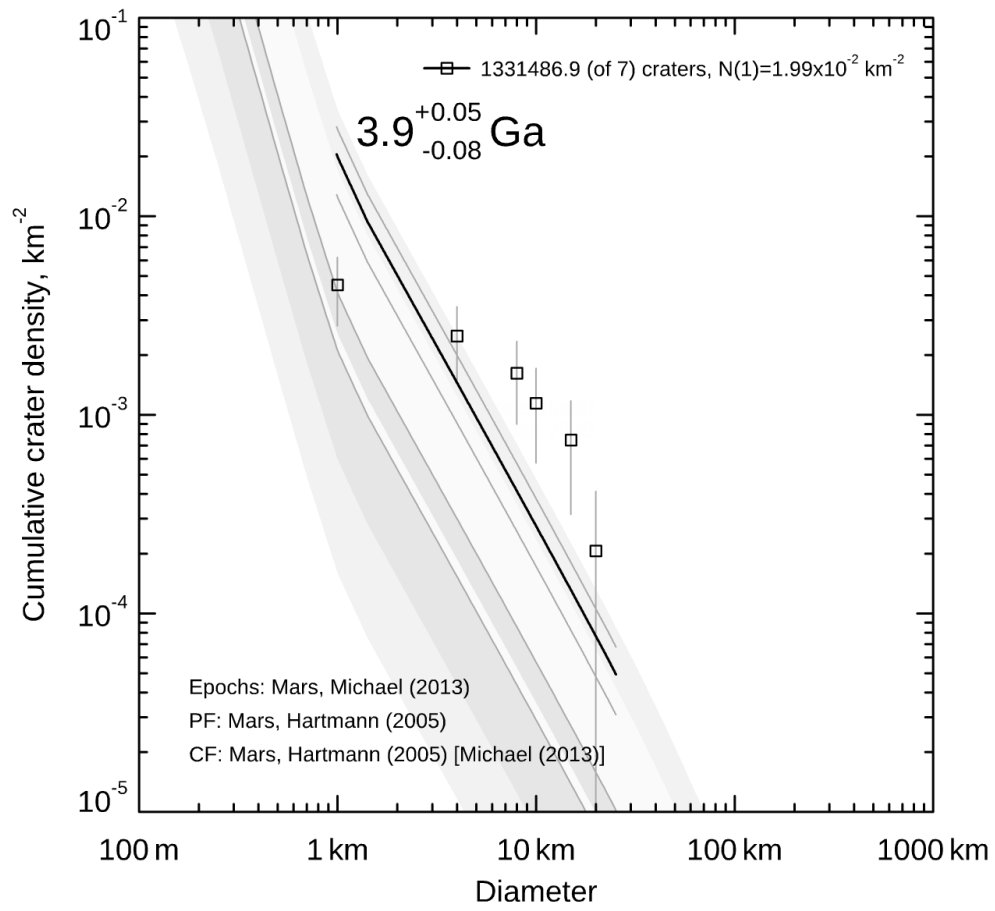
Fault 25 Hartmann age



Fault 26 Hartmann age

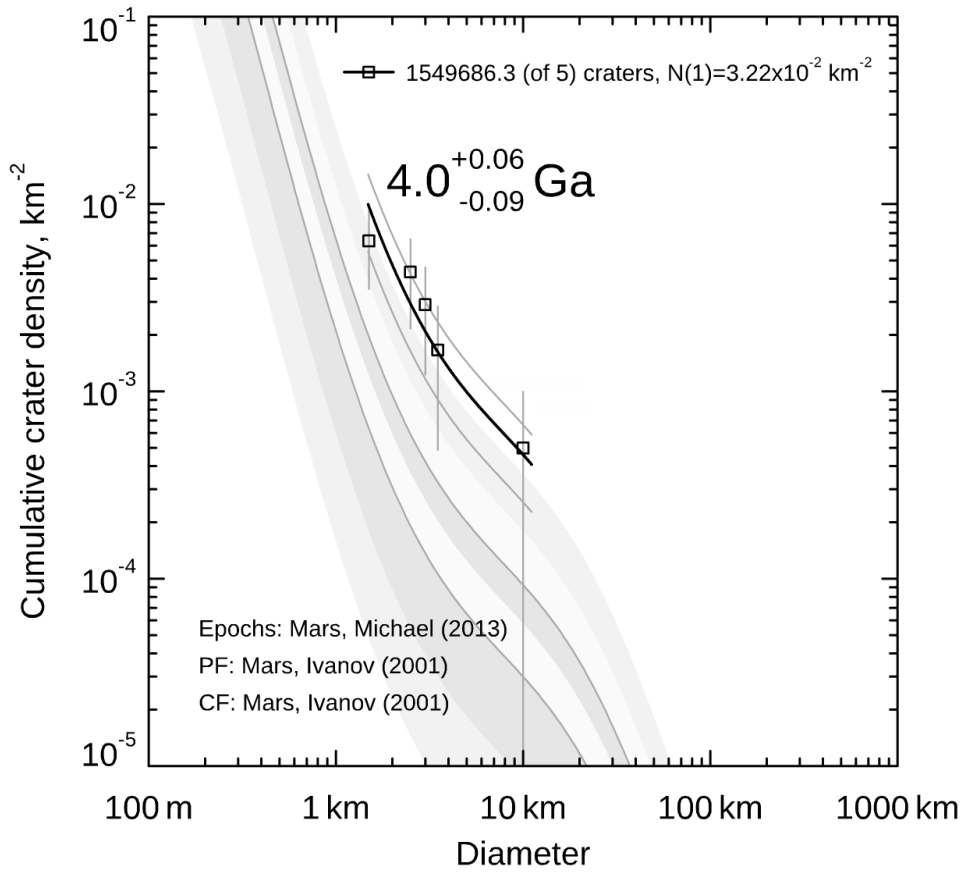


Fault 27 Hartmann age

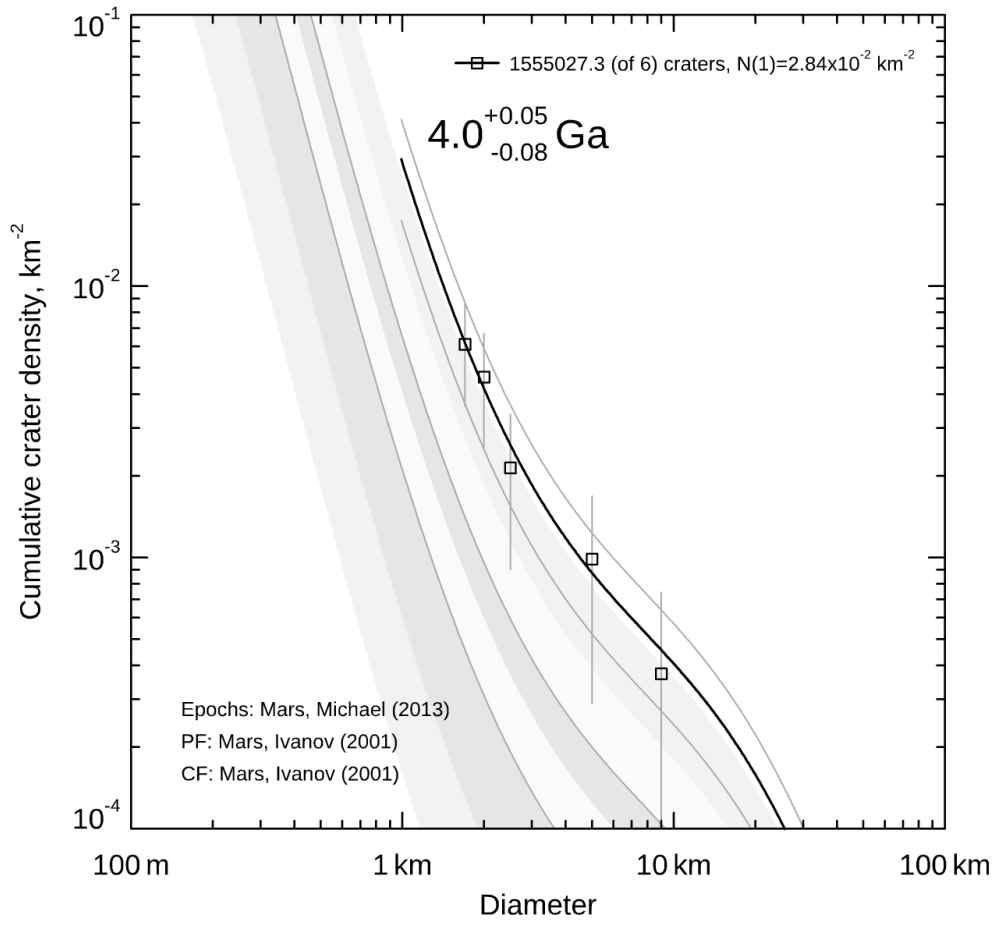


Fault 28 Hartmann age

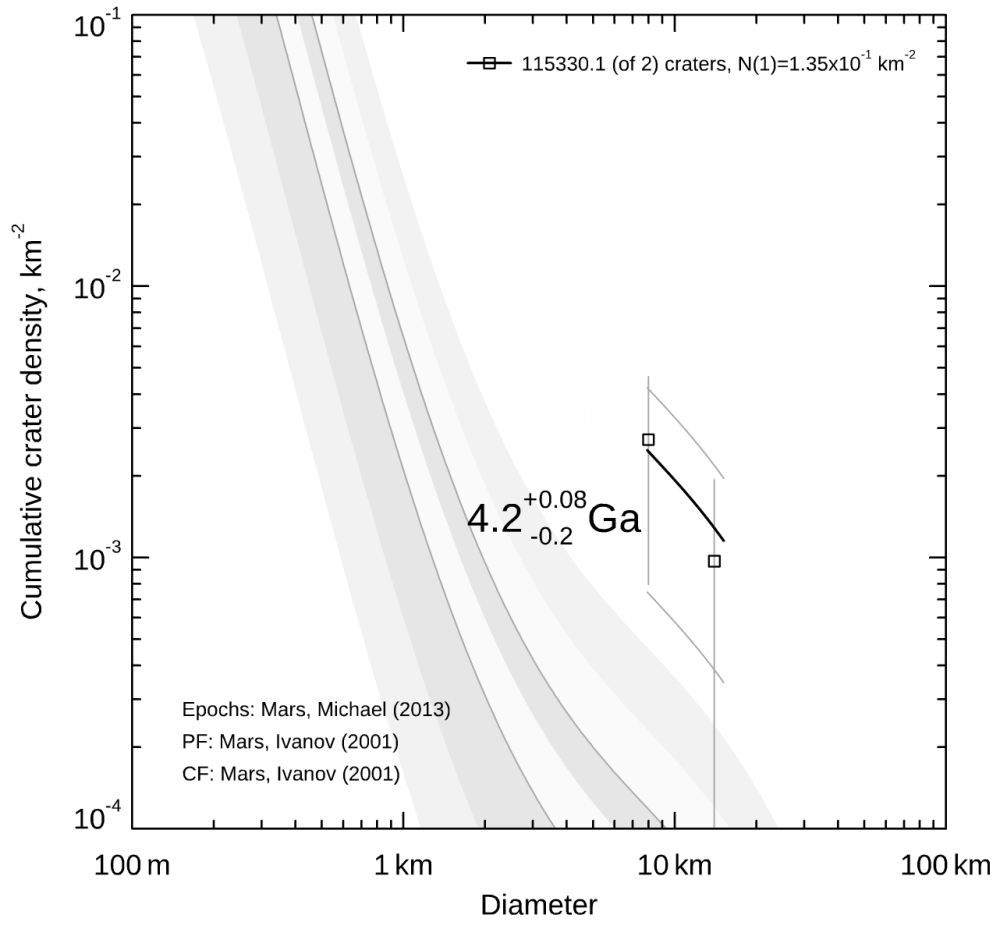
Appendix O: Neukum/Ivanov Age for each fault (CraterStats plots)



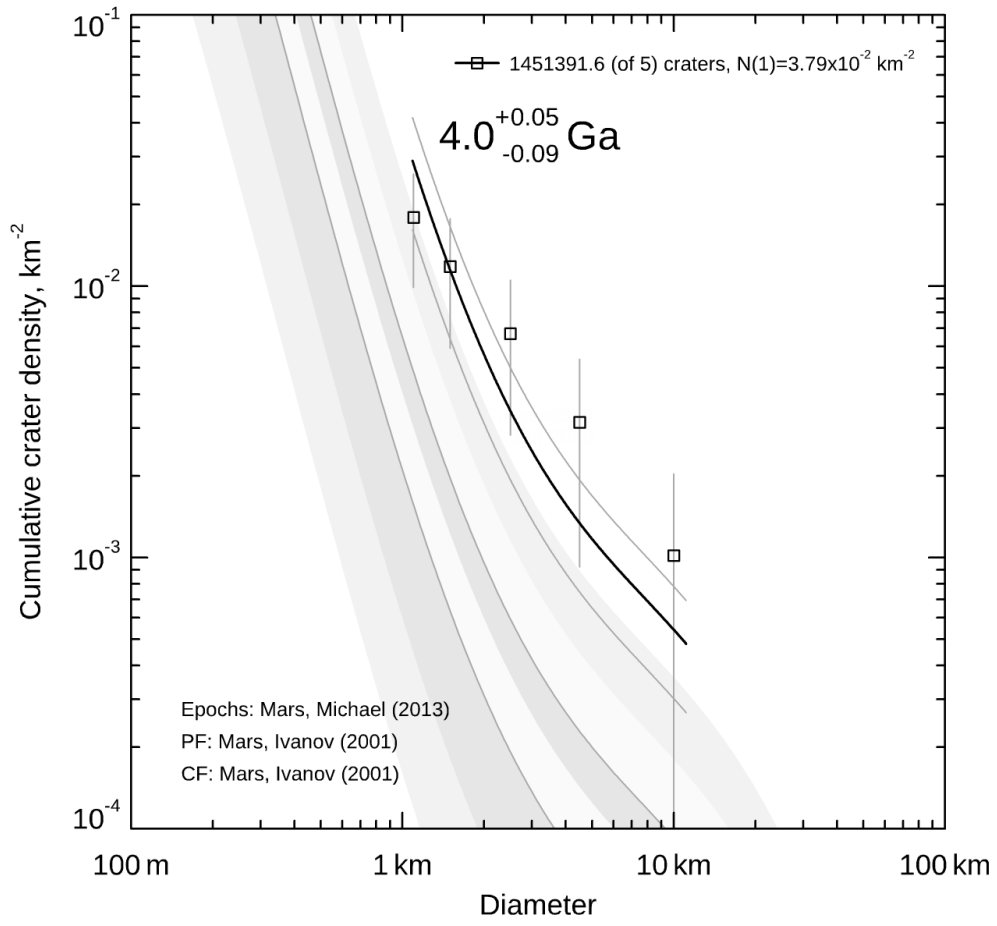
Fault 1 Neukum/Ivanov age



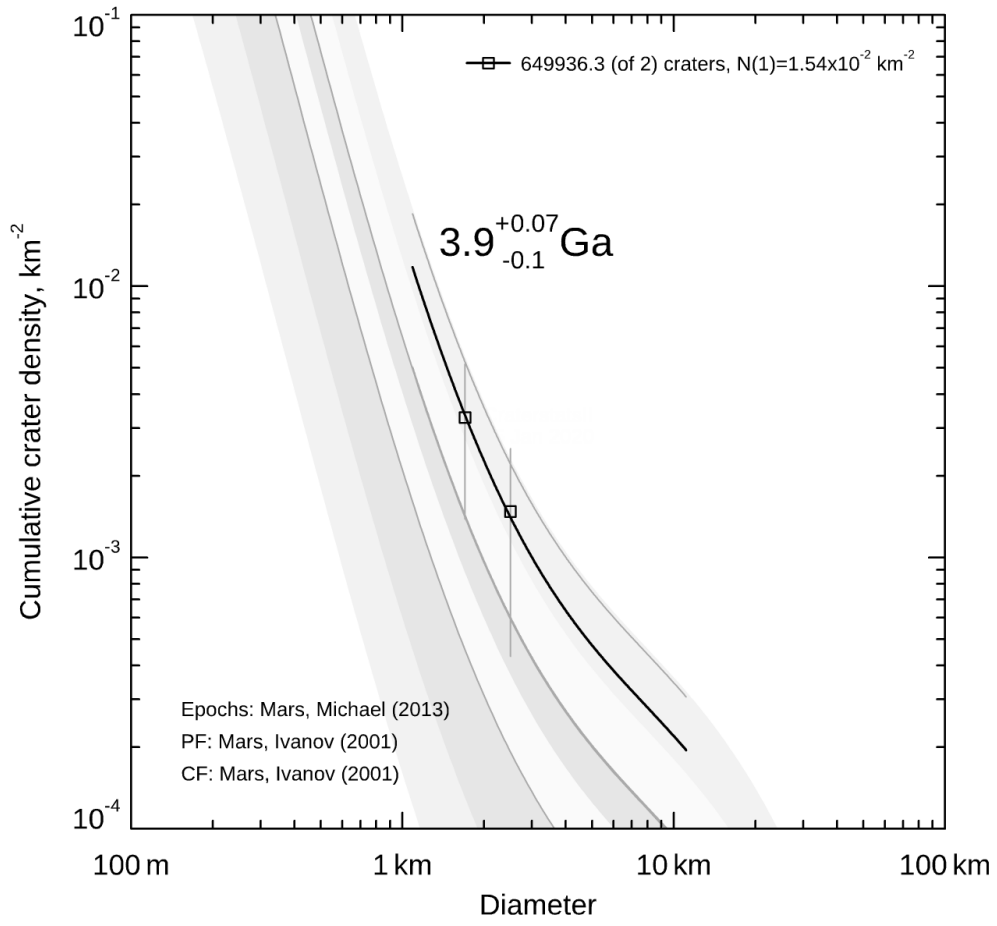
Fault 2 Neukum/Ivanov age



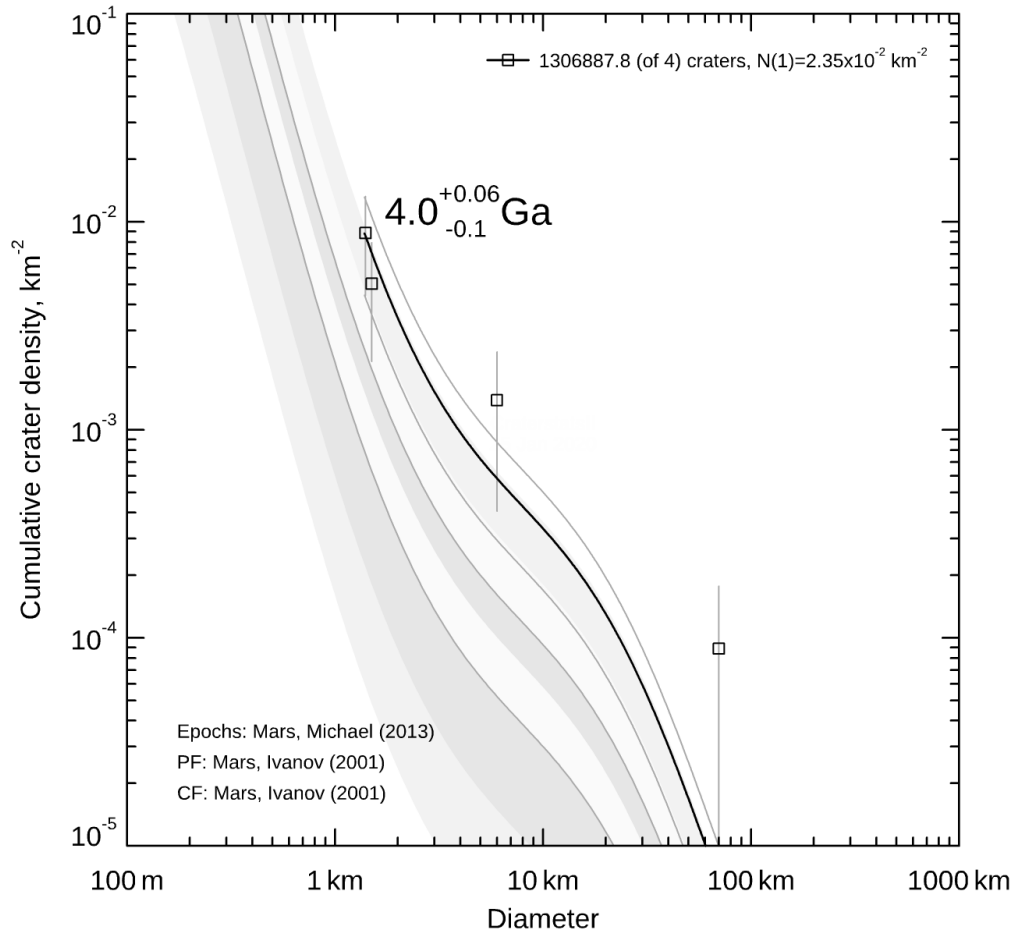
Fault 3 Neukum/Ivanov age



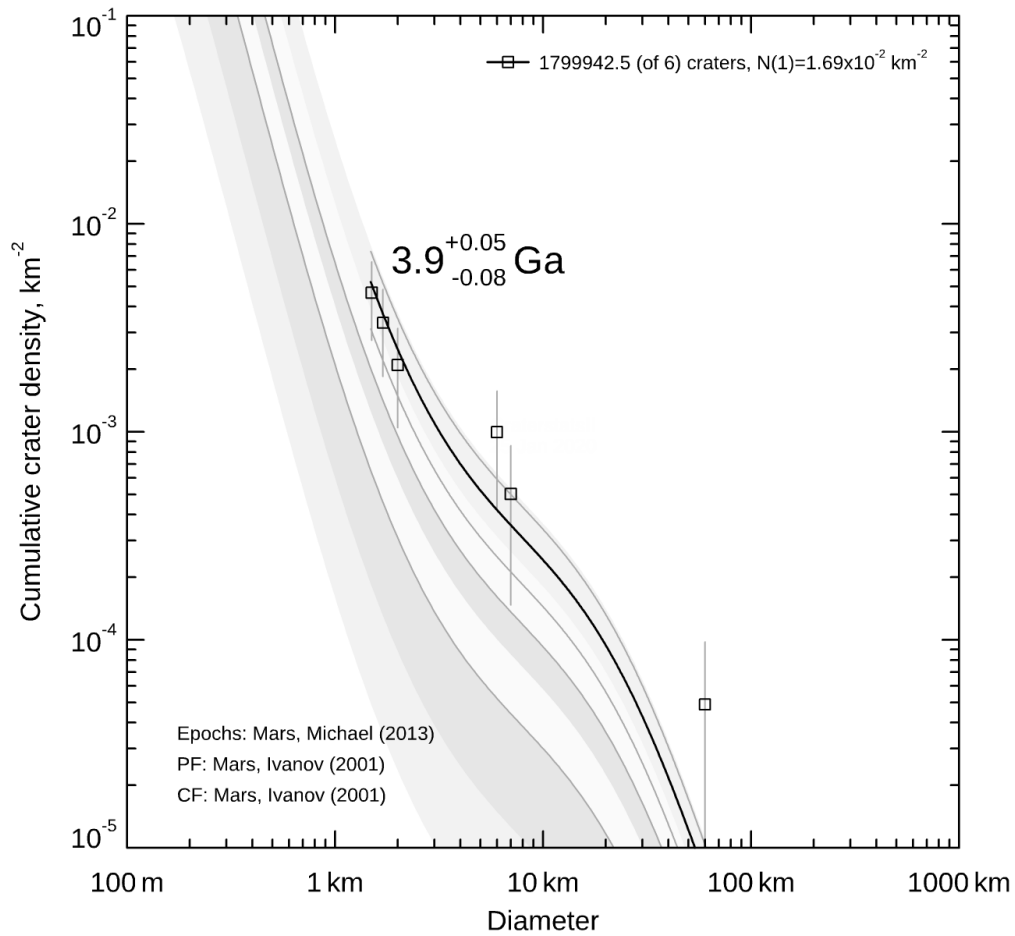
Fault 4 Neukum/Ivanov age



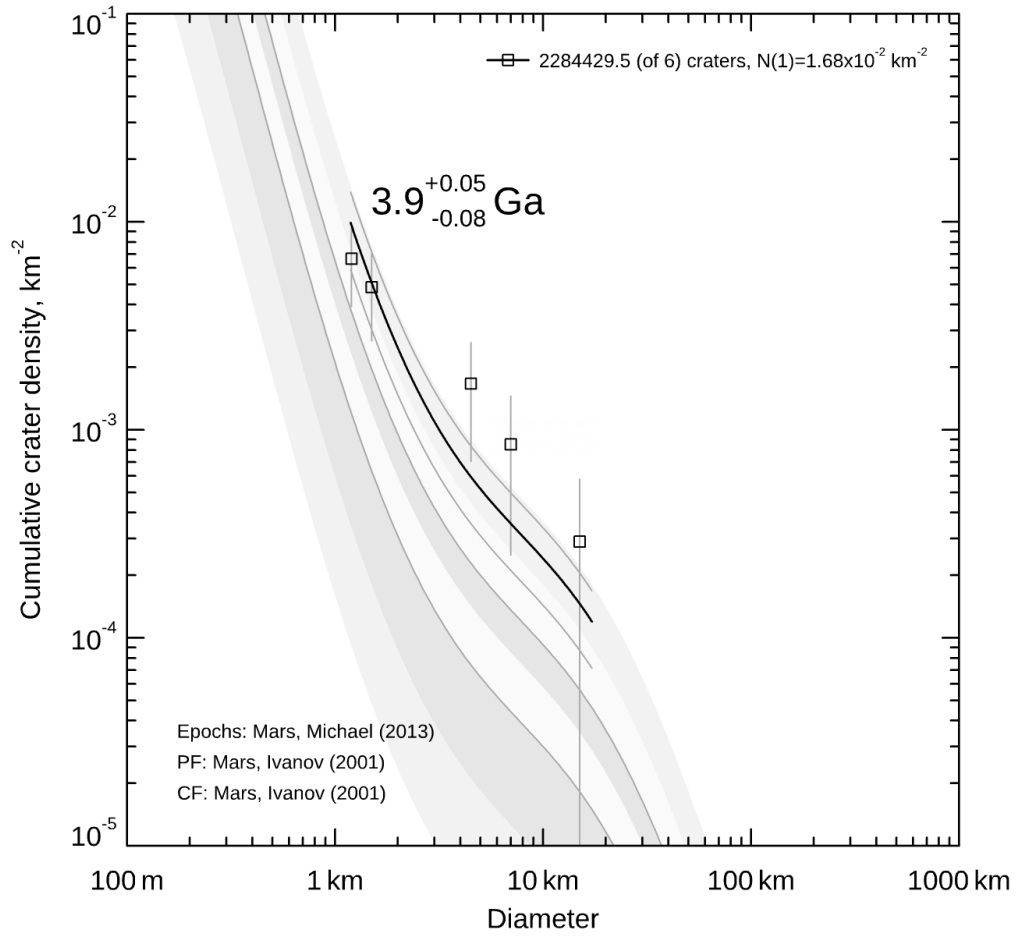
Fault 5 Neukum/Ivanov age



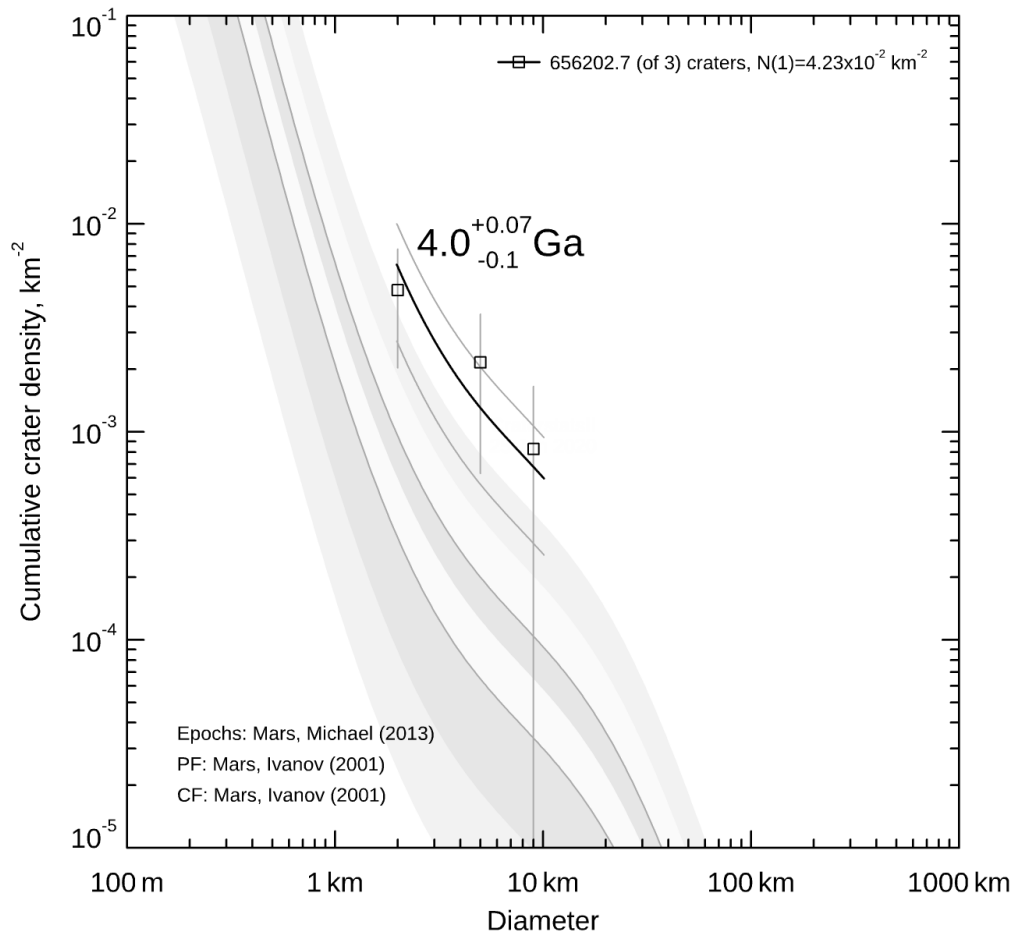
Fault 6 Neukum/Ivanov age



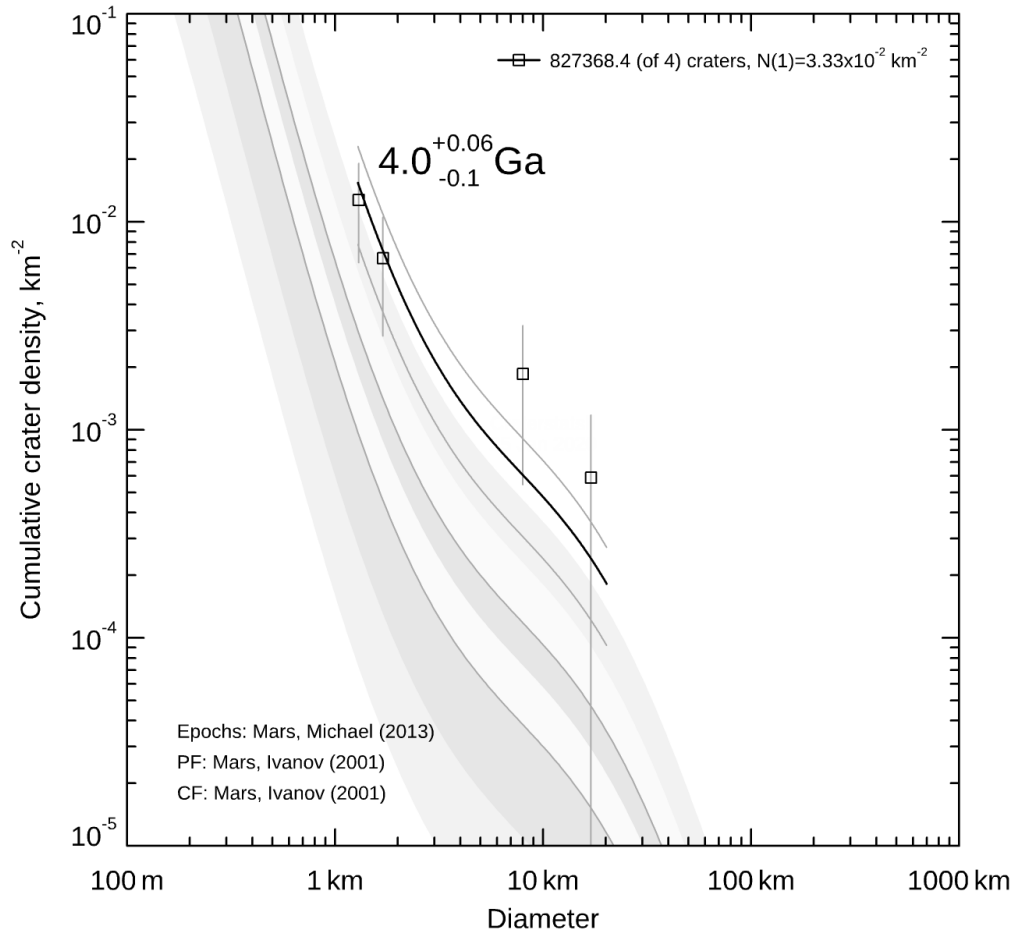
Fault 7 Neukum/Ivanov age



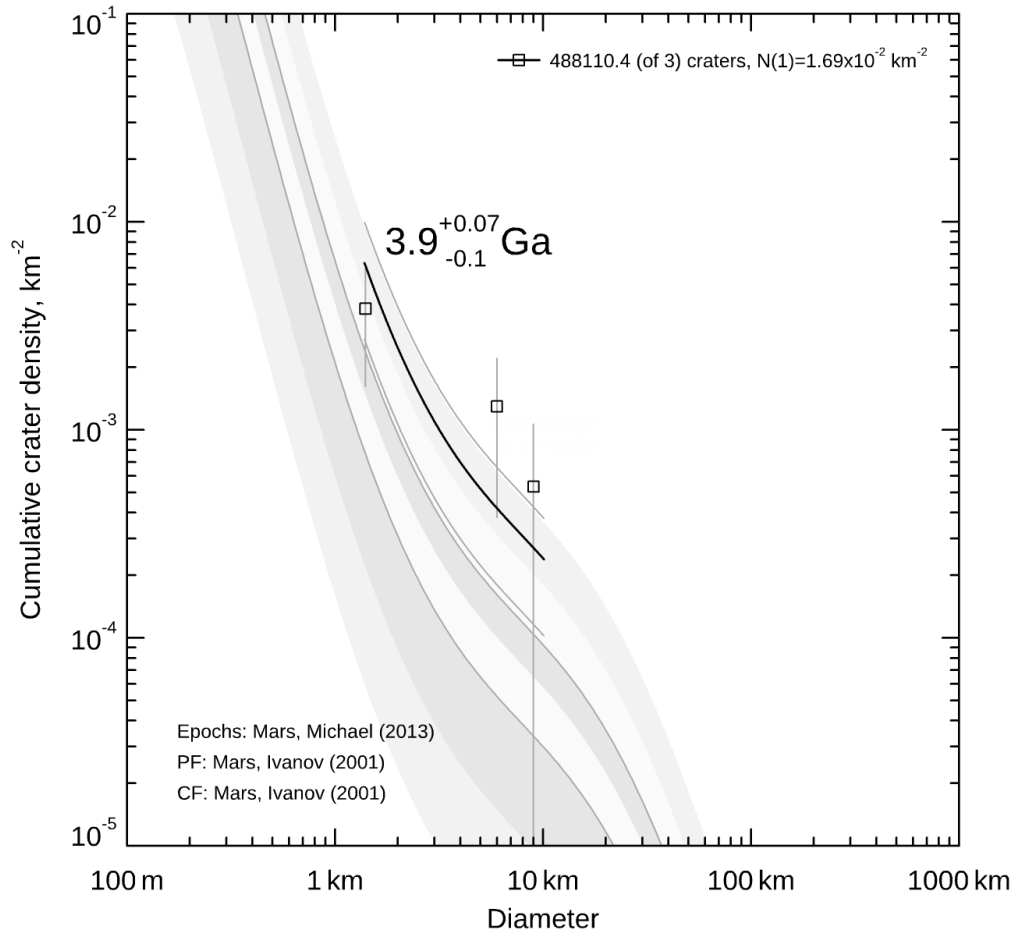
Fault 8 Neukum/Ivanov age



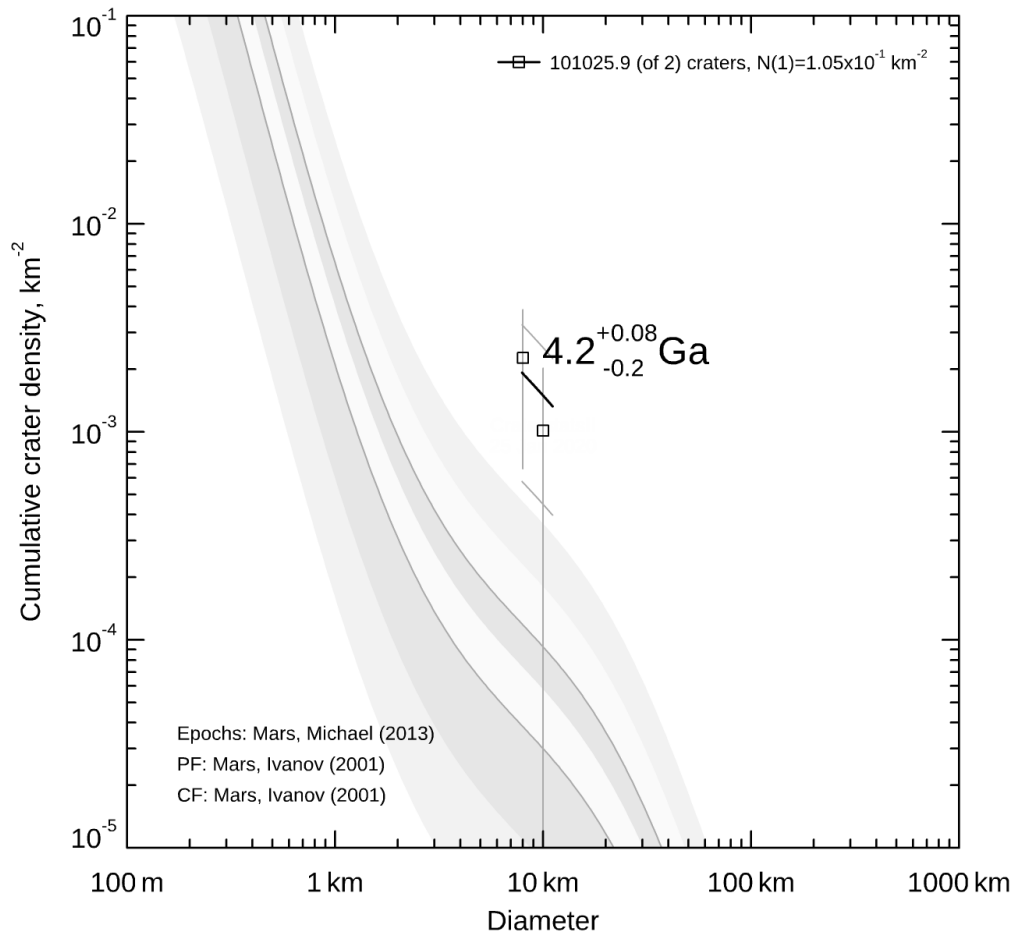
Fault 9 Neukum/Ivanov age



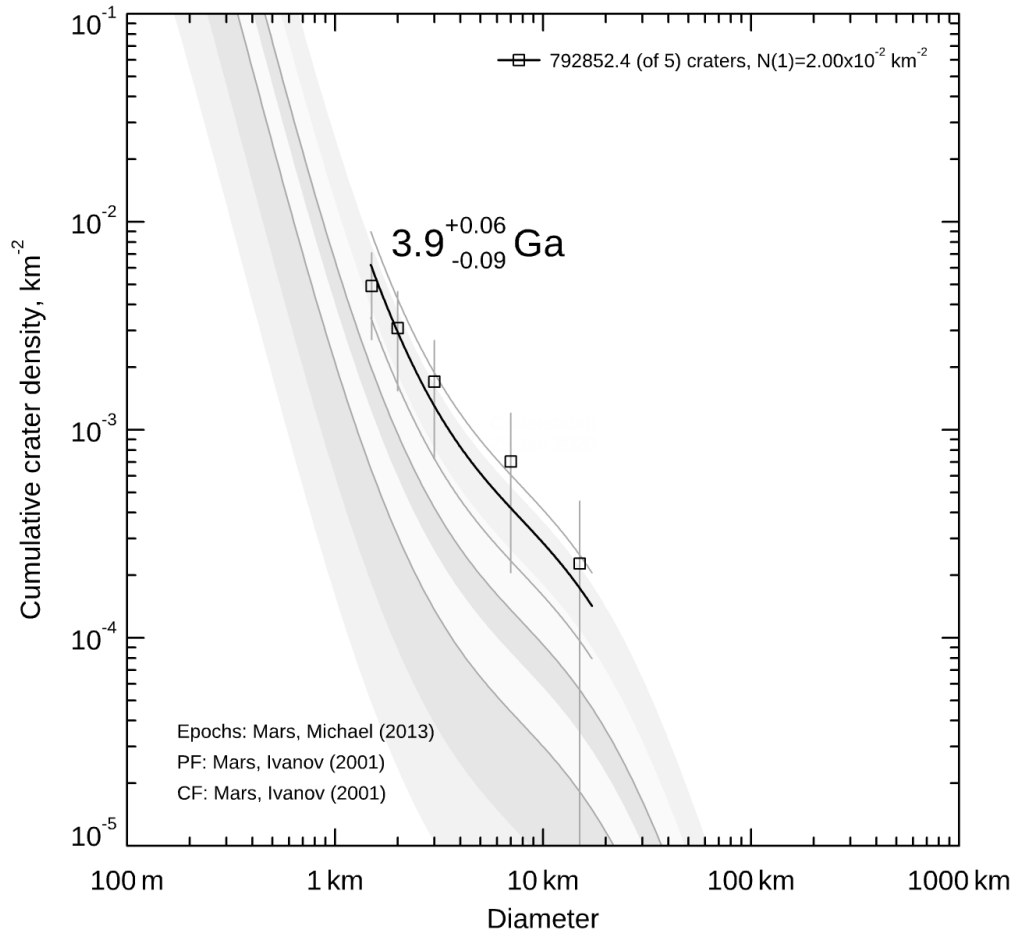
Fault 10 Neukum/Ivanov age



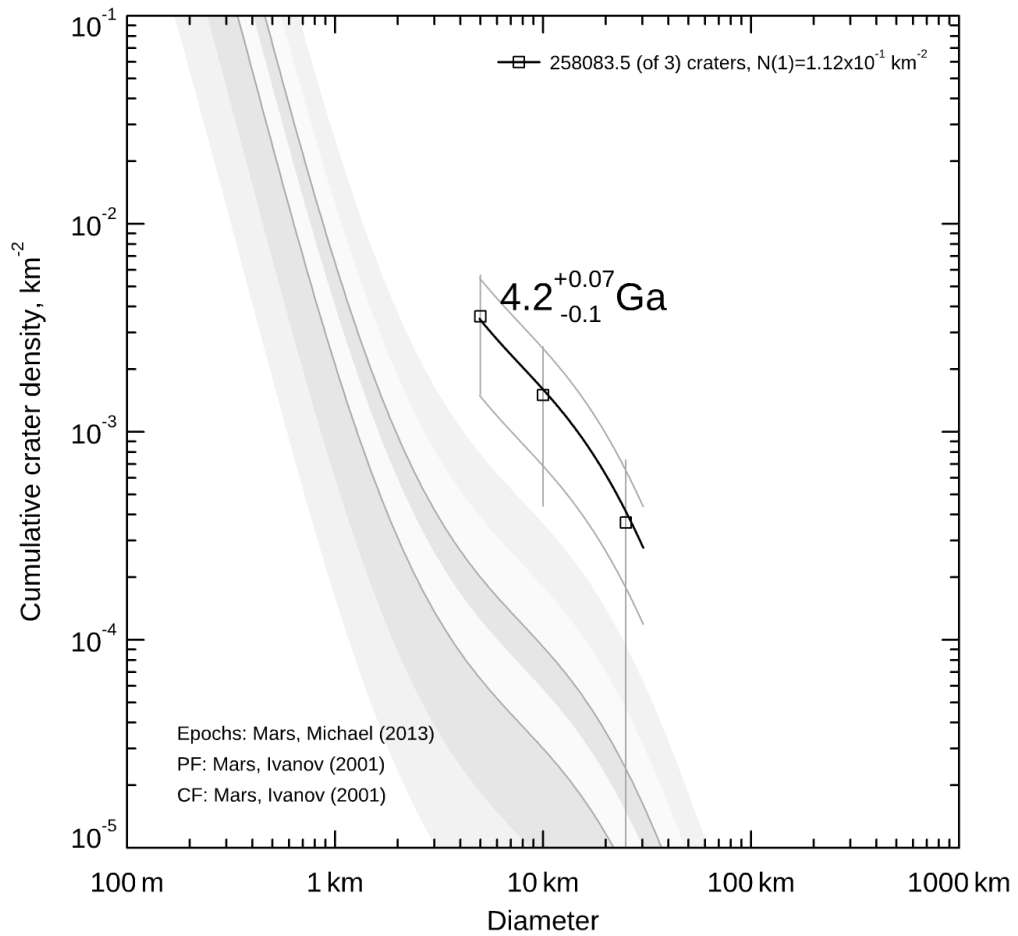
Fault 11 Neukum/Ivanov age



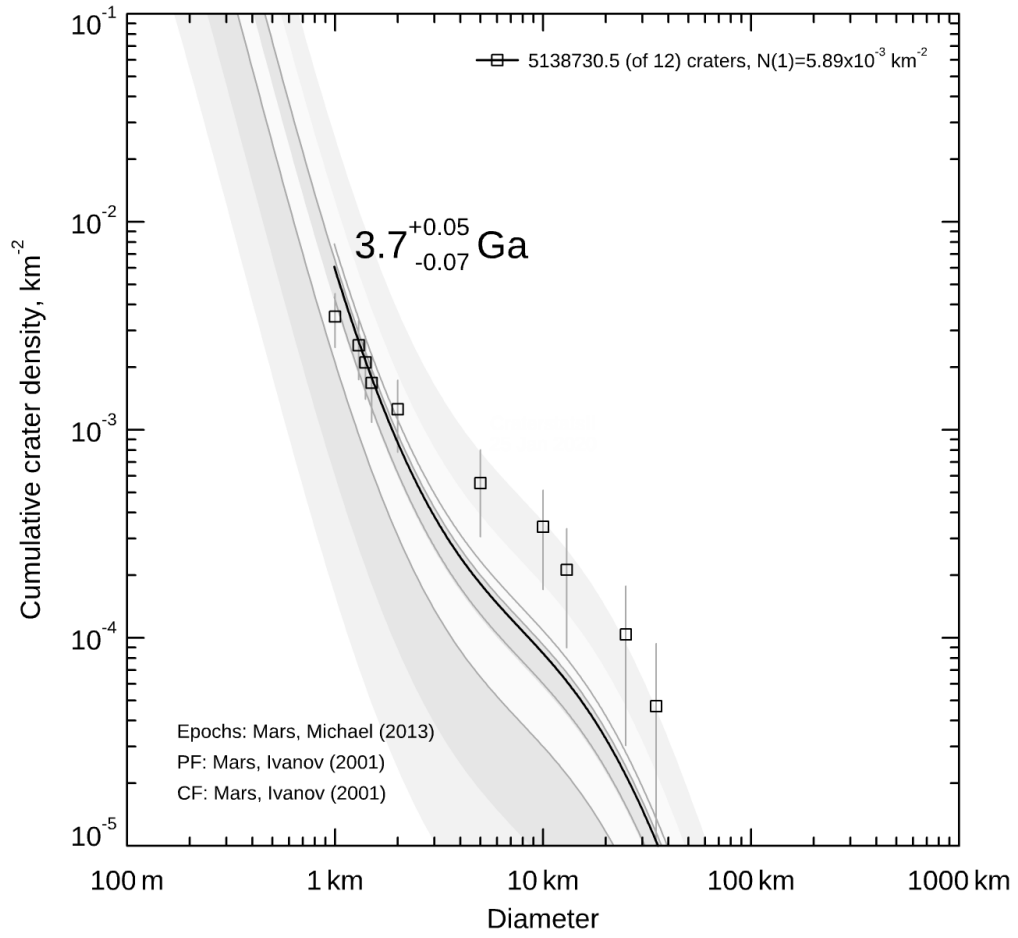
Fault 12 Neukum/Ivanov age



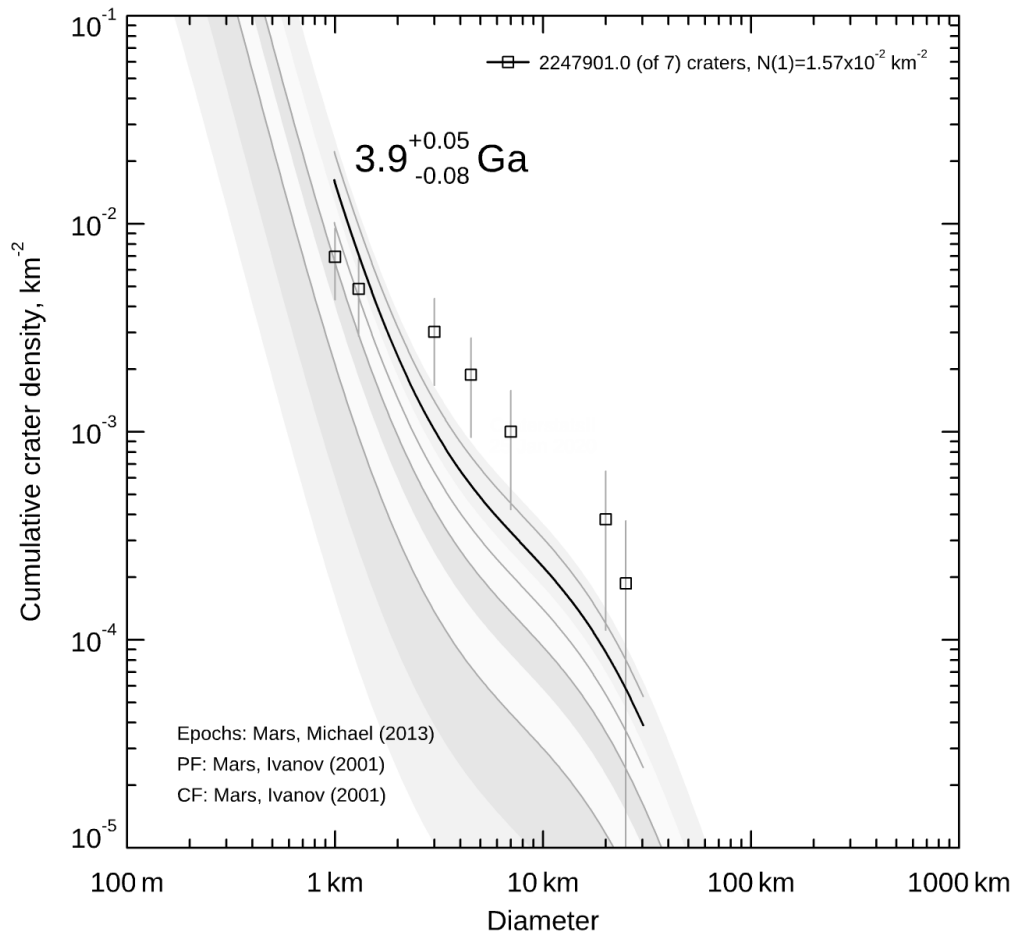
Fault 13 Neukum/Ivanov age



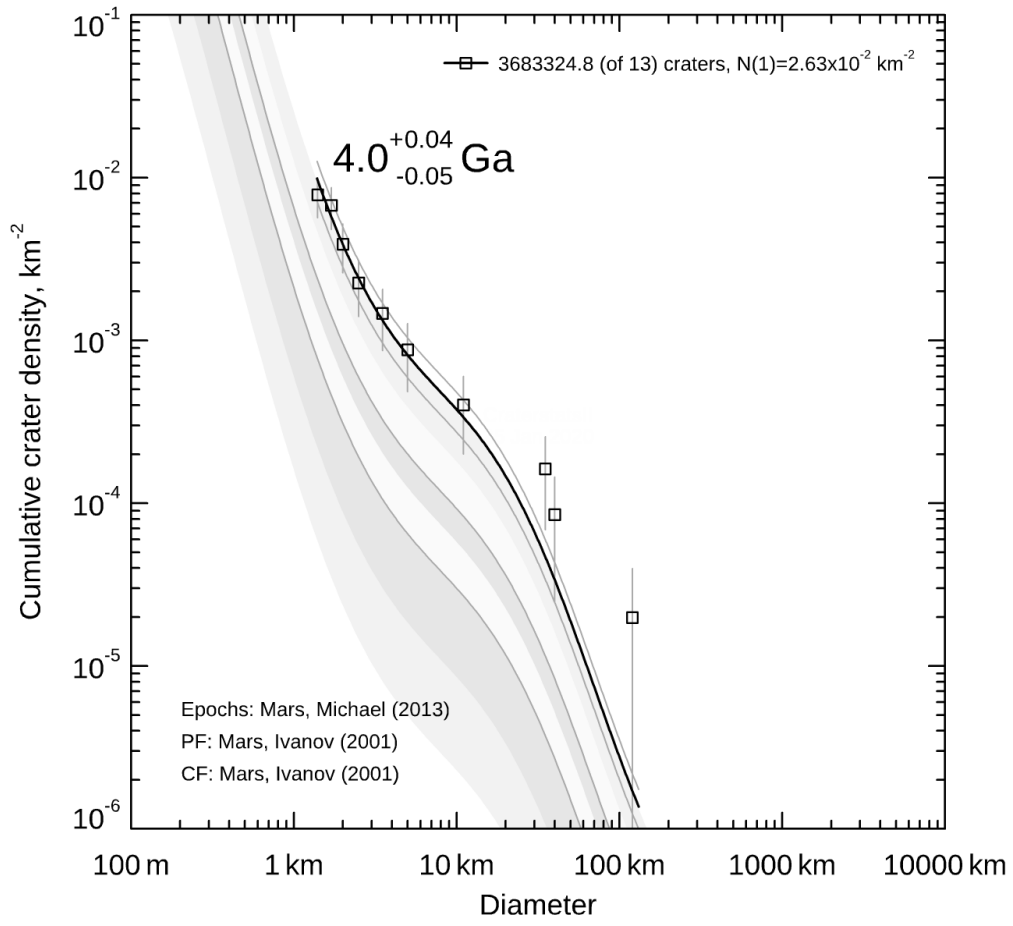
Fault 14 Neukum/Ivanov age



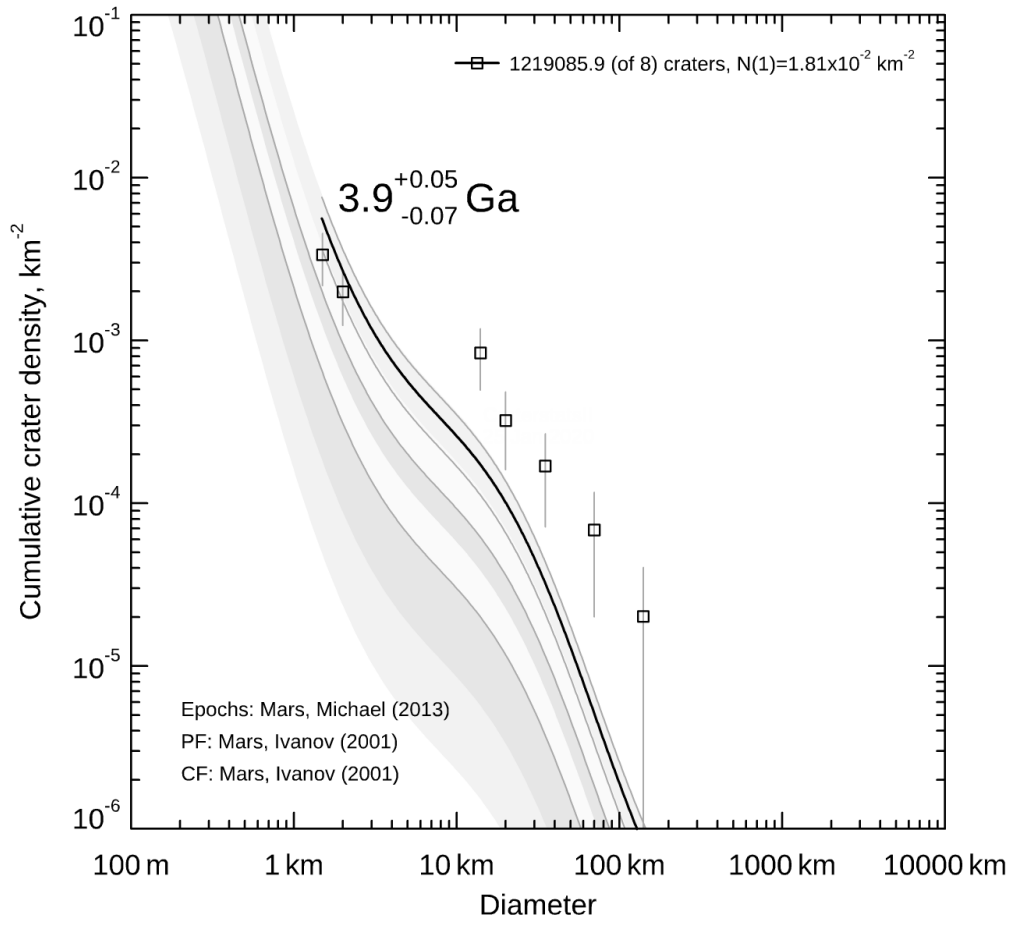
Fault 15 Neukum/Ivanov age



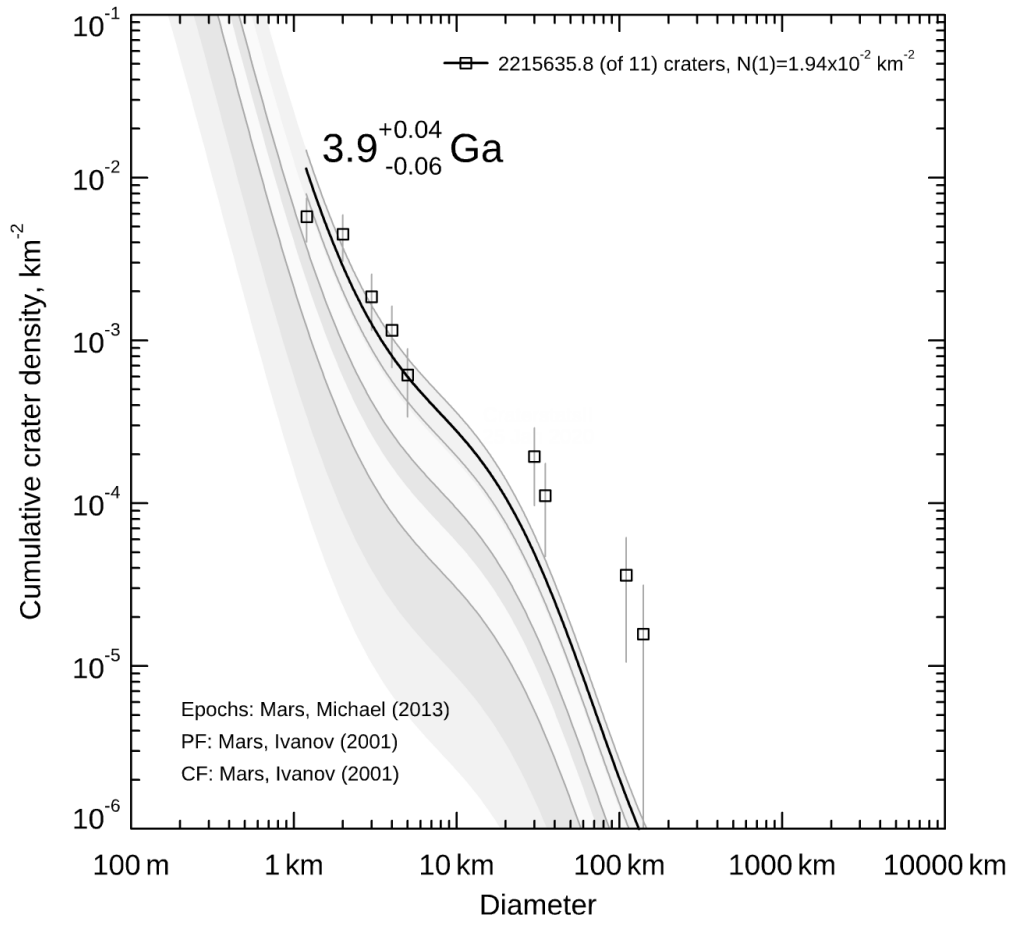
Fault 16 Neukum/Ivanov age



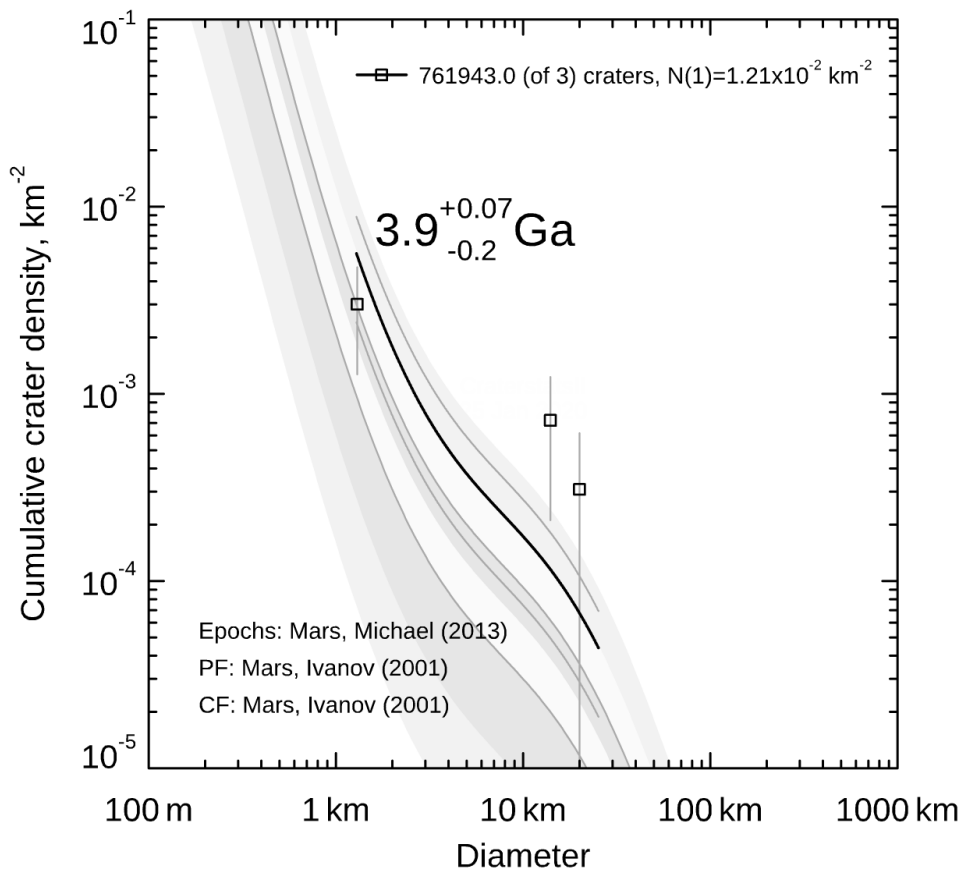
Fault 17 Neukum/Ivanov age



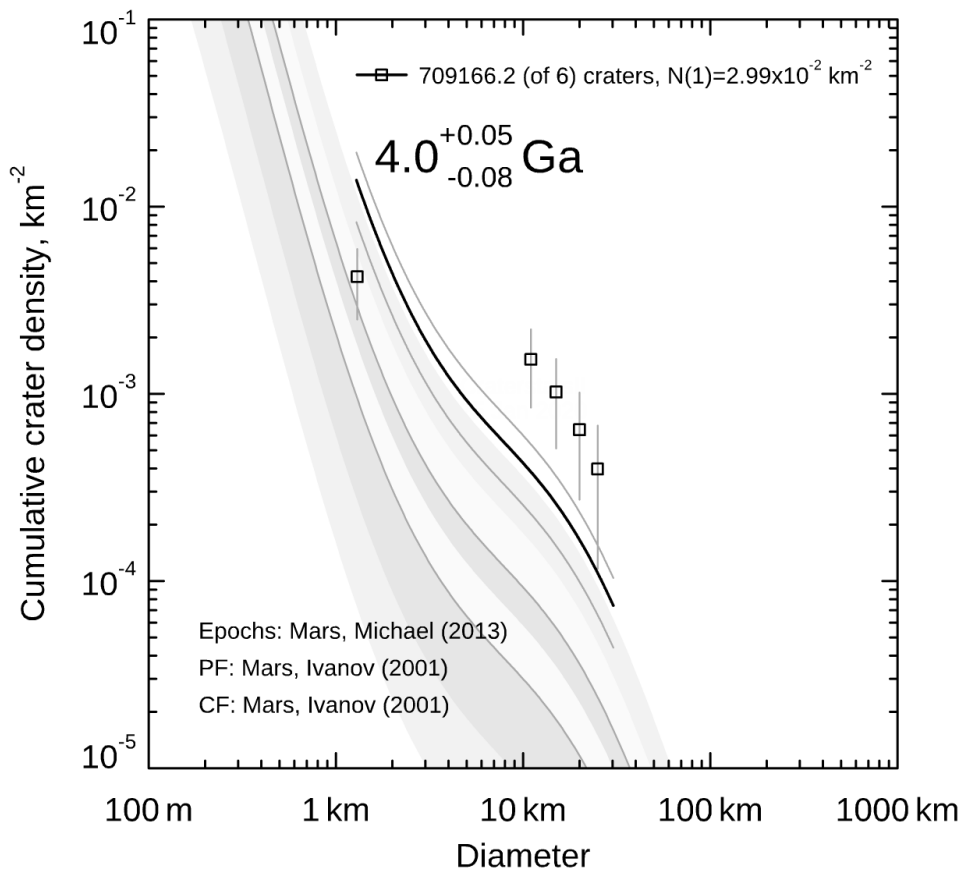
Fault 18 Neukum/Ivanov age



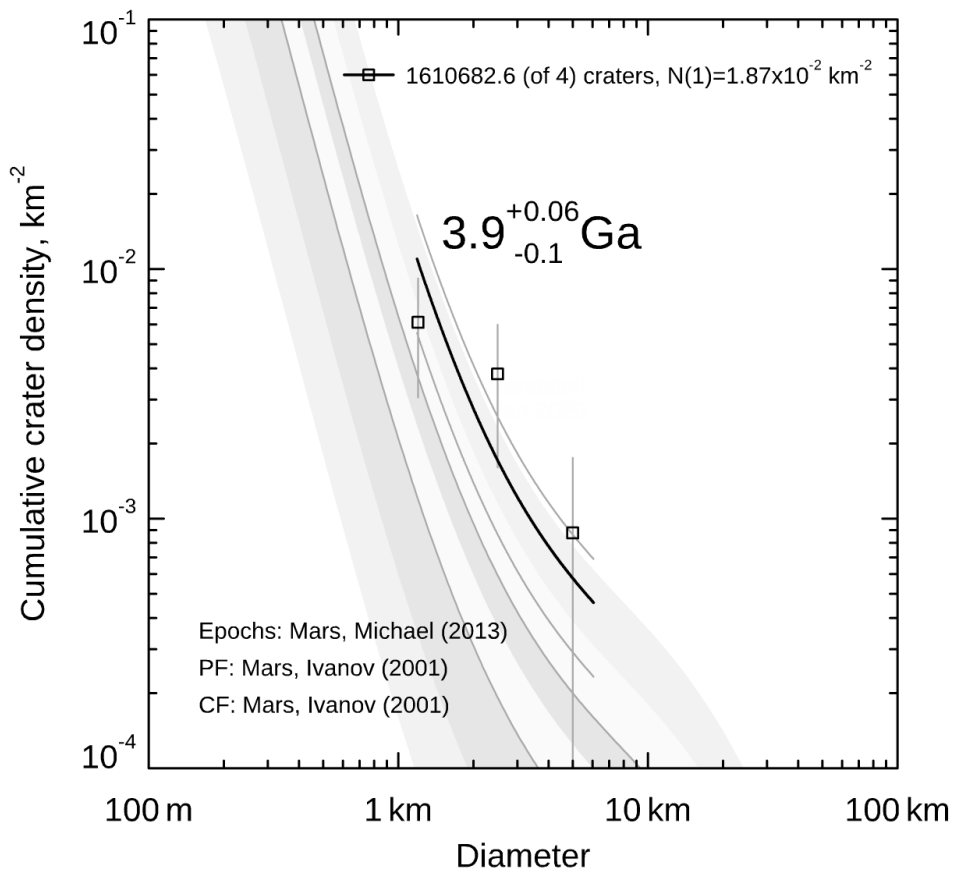
Fault 19 Neukum/Ivanov age



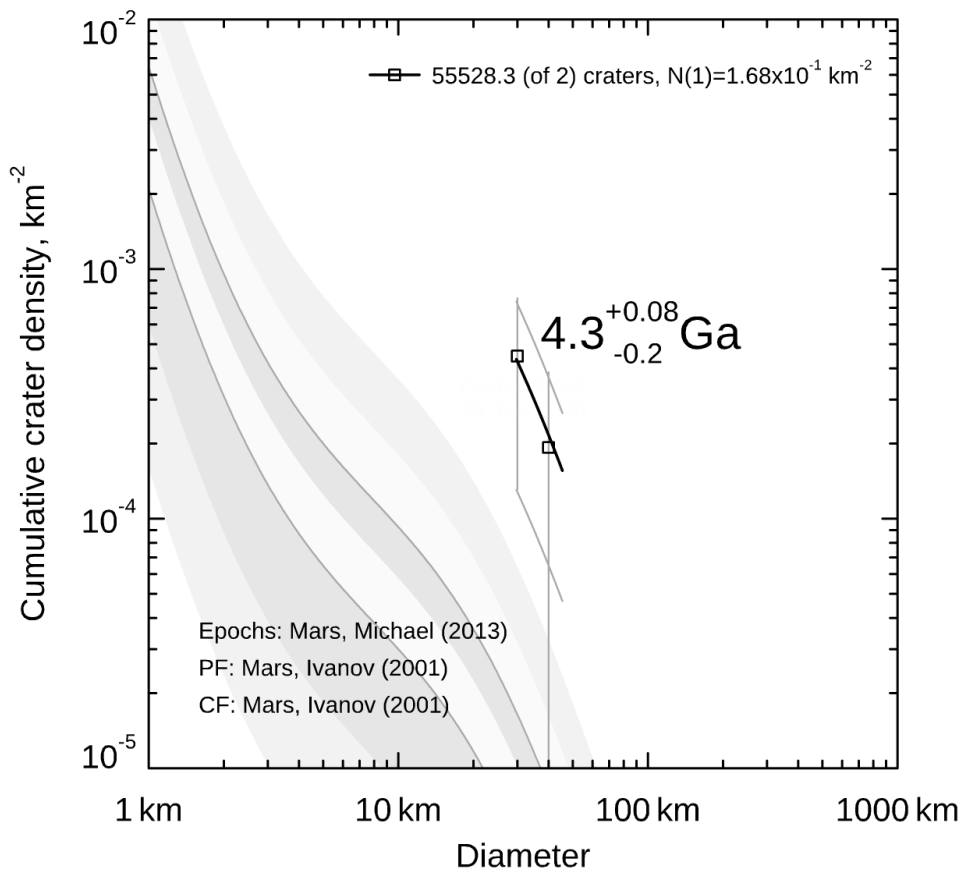
Fault 20 Neukum/Ivanov age



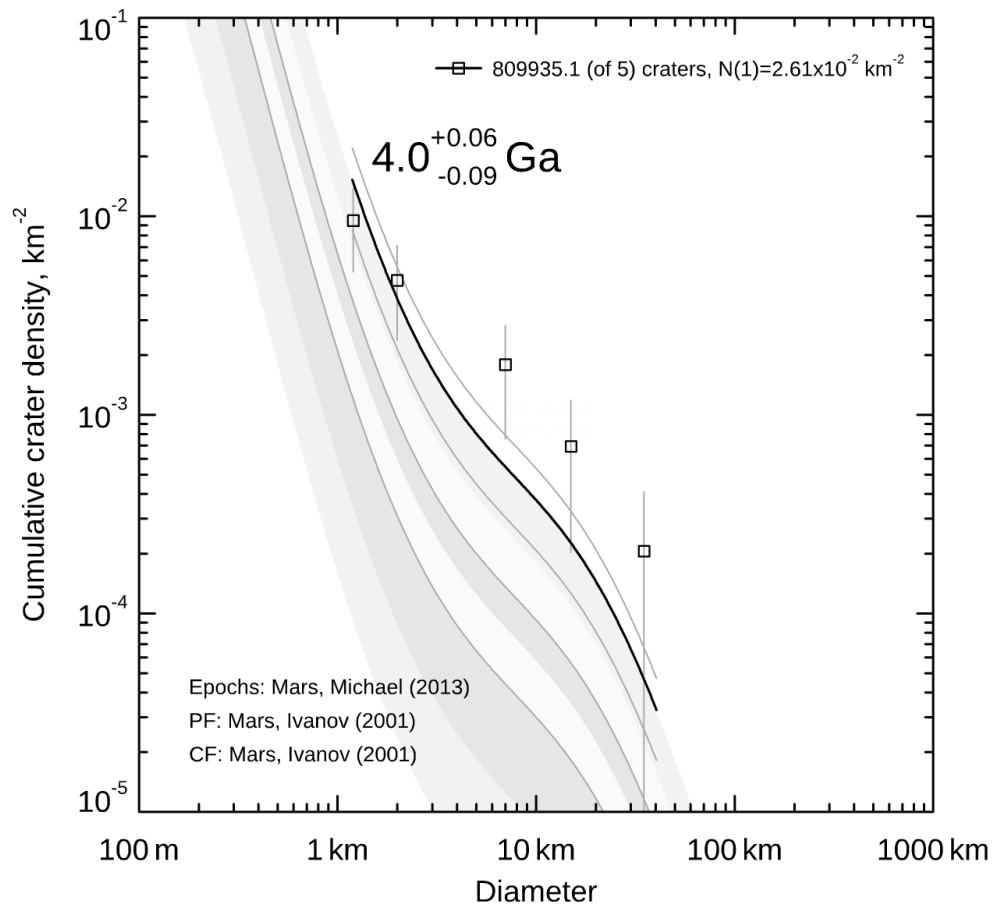
Fault 21 Neukum/Ivanov age



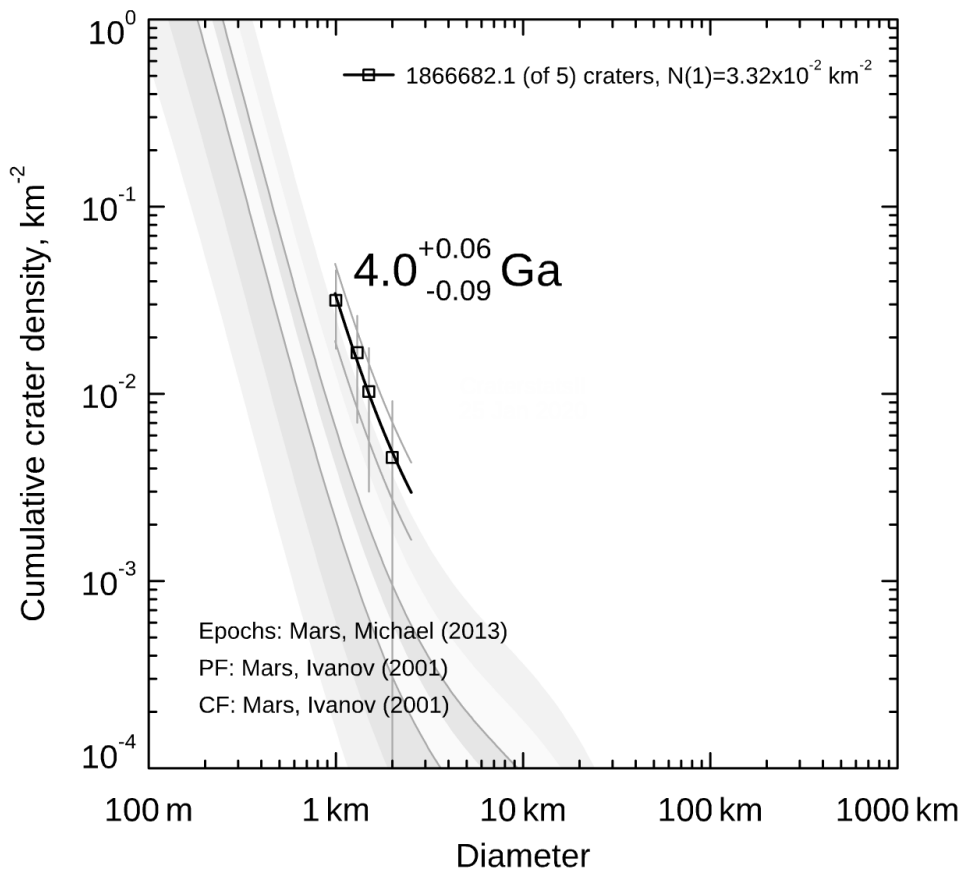
Fault 22 Neukum/Ivanov age



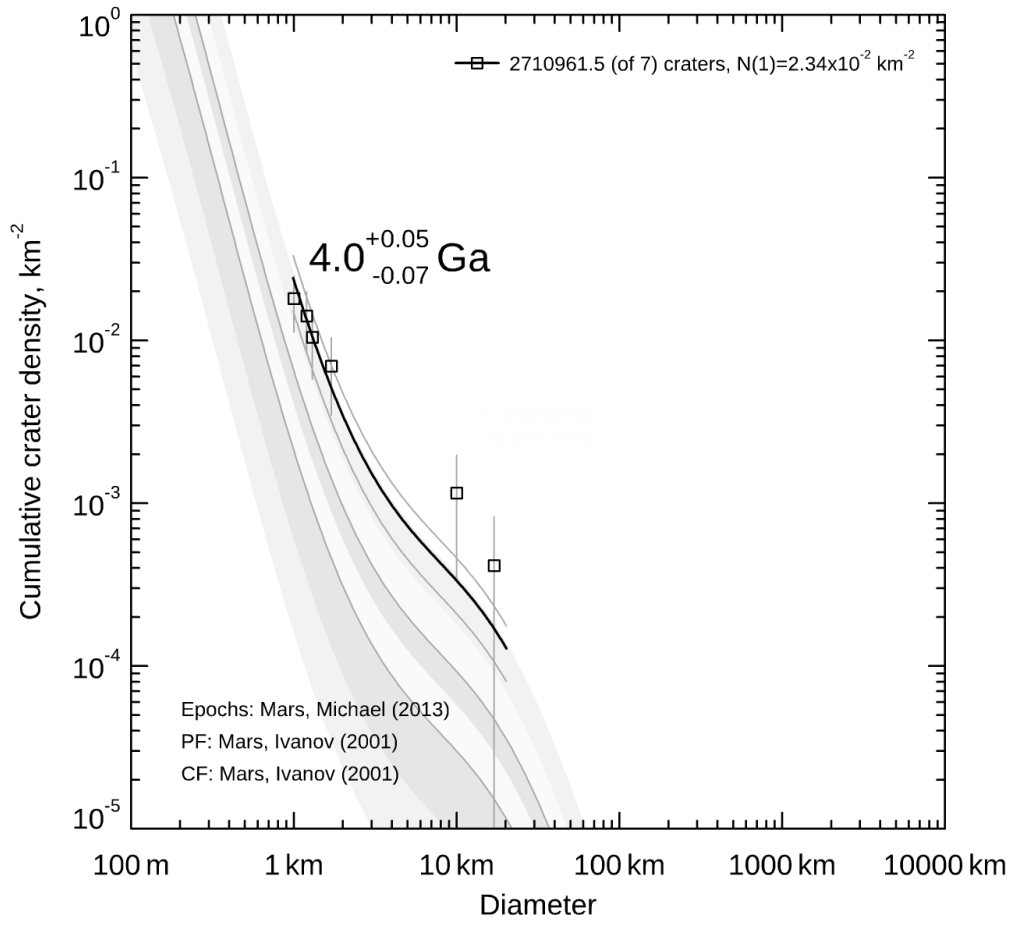
Fault 23 Neukum/Ivanov age



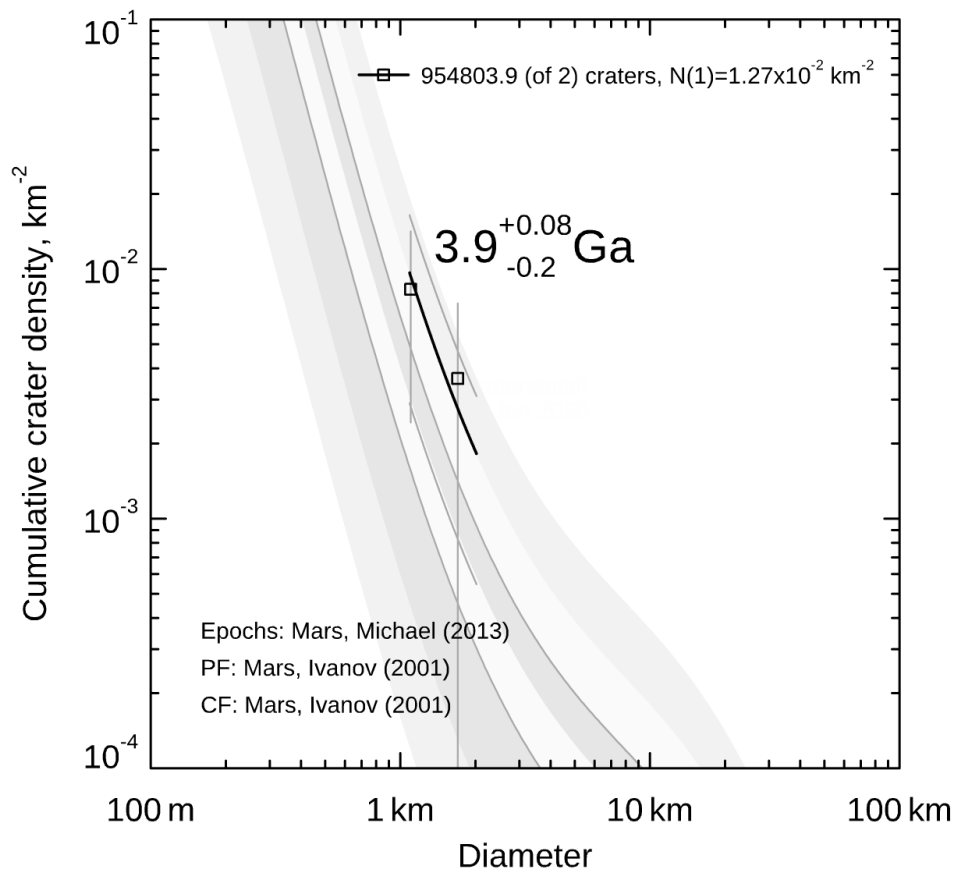
Fault 24 Neukum/Ivanov age



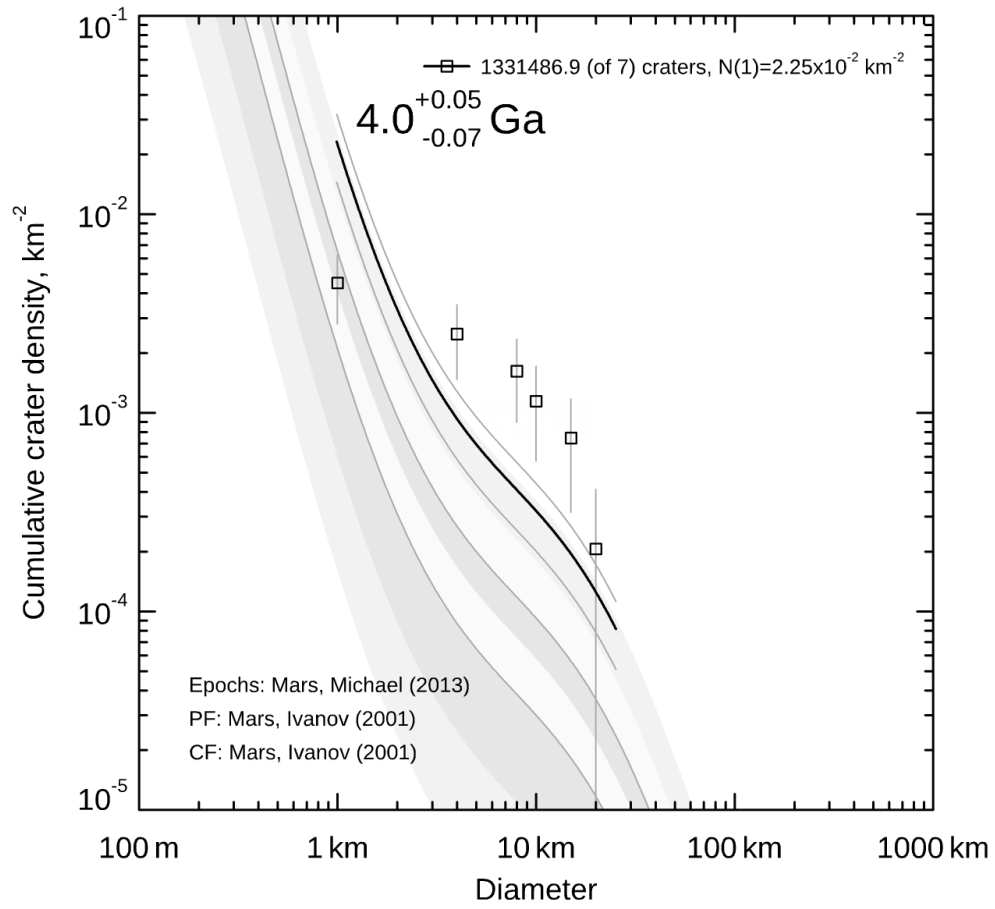
Fault 25 Neukum/Ivanov age



Fault 26 Neukum/Ivanov age



Fault 27 Neukum/Ivanov age



Fault 28 Neukum/Ivanov age

### Appendix P: Channel head summary table

Summary of channel head locations, horizontal accuracy of GPS coordinates, modified Strahler stream orders and predicted horizontal migration distances of channel heads. (Table S1 in Chapter 4)

Loc	Lat	Long	error (m)	Modified Strahler Order	Predicted migration distances (m)	
					Min	Max
1	35.84884	-78.77036	12	5	220.5	232.2
2	35.84621	-78.76726	12	4	200.6	204.4
3	35.85076	-78.76559	12	4	83.4	131.8
4	35.8518	-78.76425	15	5	215.4	216.8
5	35.85404	-78.76411	12	4	156.9	160.3
6	35.85614	-78.76432	9	5	not predicted to migrate	
7	35.85685	-78.76442	10	5	not predicted to migrate	
8	35.85701	-78.76463	10	5	not predicted to migrate	
9	35.85782	-78.76785	7	5	not predicted to migrate	
10	35.85941	-78.7696	9	5	47.1	59.2
11	35.85511	-78.76996	11	5	245.8	325.5
12	35.85231	-78.77088	30	5	120.7	127.0
13	35.84758	-78.73121	5	4	not predicted to migrate	
14	35.84815	-78.73212	7	3	not predicted to migrate	
15	35.8486	-78.73415	5	4	155.5	158.9
16	35.84898	-78.7354	7	3	43.3	54.8
17	35.85073	-78.73866	7	4	not predicted to migrate	
18	35.84779	-78.74199	7	5	402.1	430.6
19	35.84851	-78.73742	11	5	273.0	296.6
20	35.8653	-78.75158	-	4	282.5	453.6
21	35.86542	-78.75017	-	4	140.1	232.1
22	35.86462	-78.74964	6	4	not predicted to migrate	
23	35.86325	-78.74951	12	4	59.9	83.4
24	35.86275	-78.74944	9	2	39.7	66.3
25	35.8614	-78.74821	6	4	84.0	150.9
26	35.86145	-78.74656	10	5	321.8	398.8
27	35.86042	-78.74623	6	4	23.1	85.6
28	35.85881	-78.74937	7	3	61.4	90.3
29	35.86213	-78.74249	11	5	215.9	247.7
30	35.8625	-78.73859	8	4	49.3	126.9
31	35.86082	-78.7372	8	4	108.8	139.3
32	35.87265	-78.76205	7	4	not predicted to migrate	
33	35.87518	-78.76504	5	4	not predicted to migrate	
34	35.87367	-78.76443	4	4	not predicted to migrate	
35	35.87648	-78.76578	5	5	not predicted to migrate	

<b>36</b>	35.87987	-78.76431	6	3	not predicted to migrate
<b>37</b>	35.88101	-78.76585	6	4	not predicted to migrate
<b>38</b>	35.88224	-78.76474	6	4	not predicted to migrate
<b>39</b>	35.88131	-78.76356	4	4	not predicted to migrate
<b>40</b>	35.88255	-78.76069	5	4	not predicted to migrate